A Precision Experiment for the Deformation and Fracture of Blast Loaded Plates

Trevor John Cloete

Department of Mechanical Engineering

University of Cape Town

South Africa

Supervisor:

Prof. G. N. Nurick

February 2022

PhD thesis submitted in fulfillment of the requirements for the degree of Doctor of Philosophy in the Department of Mechanical Engineering at the University of Cape Town

Concise Abstract

A Precision Experiment for the Deformation and Fracture of Blast Loaded Plates

Trevor John Cloete

February 2022

The purpose of this thesis is to present a novel laboratory scale precision test [1] apparatus, developed specifically to study of the deformation and fracture of blast loaded plates.

A review of published laboratory scale blast testing showed that classical ballistic pendulum techniques satisfy several precision testing criteria. However, specific aspects required improvement. Therefore, an instrumented ballistic pendulum has been developed, incorporating a central support, in the form of a Hopkinson bar, for use with a novel peripherally clamped centrally supported (PCCS) plate specimen, which allows the reaction force history at the inner boundary to be captured. Hence, in addition to the traditional impulse vs deflection data, this approach allows details such as the total deformation duration or the exact timing and magnitude of fracture processes to be captured. Furthermore, when used with a peripherally clamped annular (PCA) plate specimen, this approach allows the blast load pressure history to be captured.

A literature review found several classical closed form solutions for the large deflection of impulsively loaded peripherally clamped solid (PCS) circular plates. However, several crucial aspects of the solutions were contradictory and/or incomplete. To address this a generalized energy method for modelling impulsively loaded axisymmetric plates was developed which subsumes previous solutions and facilitated novel analytical solutions that provide a theoretical framework for interpreting the experimental data.

Extensive experimental results reported in this thesis provide a rich set of novel data for code validation. While the PCCS and PCA plate configurations require a refined definition of the observed failure modes, the transitions between the modes and the fracture behaviour are studied in great detail. The data is analysed using dimensionless impulse expressions obtained from the analytical solutions in this thesis. In addition to accurate deflection predictions, these solutions also provide improved deflection duration predictions using a novel two phase solutions that can also accommodate finite load duration.

It is concluded that the instrumented ballistic pendulum, incorporating a central support in the form of a Hopkinson bar, in conjunction with the novel PCCS and PCA plate configurations and analytical solutions, satisfies all the requirement of a precision test.

Declaration

I, Trevor John Cloete, hereby:

1. grant the University of Cape Town free licence to reproduce the above thesis in whole or in part, for the purpose of research;
2. declare that:
   (a) this thesis is my own unaided work, both in concept and execution, and apart from the normal guidance from my supervisor, I have received no assistance except as stated below.
   (b) neither the substance nor any part of the above thesis has been submitted in the past, or is being, or is to be submitted for a degree at this University or at any other university, except as stated below.

Trevor John Cloete

Department of Mechanical Engineering
University of Cape Town

4^{th} February 2022

Acknowledgements

First and foremost, to my long suffering supervisor, Professor Gerald Nurick. Thank you for your wisdom, kindness, patience and faithfulness. Through many days of blast testing and many hours of meetings and proofreading you have remained steadfast. At times calming, at times cajoling, but always positive. I would hope to be even half the mentor to others that you have been to me.

To my current and former colleagues in the Blast Impact and Survivability Research Unit (BISRU): Prof. Genevieve Langdon, Prof. Steeve Chung Kim Yuen, Dr Reuben Govender, Dr Richard Curry and Mr Victor Balden. Thank you for your support, encouragement and constructive criticism.

To my former graduate students who's work contributed in direct and indirect ways to this thesis: Dr Dean Bonorchis, Dr Stephen Marais, Mr Nevile Jacob, Mr Andrew Bowden, Mr Matthew Weyer, Mr Richard Palmer and Ms Rayeesa Ahmed. Thank you for the contribution that you made.

To the current and former members of the Mechanical Engineering workshop: Mr Glen Newins, Mr Dillon Jacobs, Mr Pierre Smith, Mr Jules Mayer, Mr Hubert Tomlinson and Mr Willie Slaverse. Thank you for accommodating my unconventional ideas with grace and producing the equipment and specimens I required with swiftness and professionalism.

To the members of the faculty of Engineering and the Built Environment who assisted me in navigating my course through the university system: There are too many to name, but I would like to mention, Prof. Brandon Collier-Reed, Prof. Harro Von Blottnitz, Ms Marlene Hyland and Ms Denise Botha. Thank you.

To my examiners, the identities of whom I do not know. Thank you for giving of your time and expertise to consider this thesis and uphold the standards of our profession.

To my brothers in Christ, Prof Mark Howells and Mr Wynand Louw. Thank you for your unyielding support and unceasing reminders to never give up.

To my mother, Margaret, and my father, Rodney, who both lived to see the start of this journey, but not the end. Needless to say, I would not even have begun had it not been for you. I wish I could share this with. Thank you.

To my Children, Hannah and Daniel. Thank you for bringing such brightness to my days, especially those where burdens seemed to heavy to bear.

To my wife, Kim. Words fail me to express how grateful I am that you are in my life. Thank you for your faith and strength. The many days and nights you held us together while I worked. The steadfast encouragement. It is done.

Finally, to my Lord and Saviour Jesus Christ. Thank you for your grace and mercy that I have so undeservedly received, and thank you for bringing all the people I have mentioned into my life and many more besides these.

Abstract

The use of numerical simulations has become ubiquitous in engineering practice due to the availability of powerful work stations and the growth in the sophistication of computational mechanics codes. In particular, the resolution to which problems can be analysed has surpassed the level of experimental detail generally available in the literature. Hence, there is a general recognition of the need for novel precision tests that can yield reliable and detailed experimental data for the purpose of code validation. A technical workshop held in Trondheim developed a set of criteria for what constitutes a precision test [1]. The primary purpose of this thesis is to present a novel laboratory scale experimental apparatus developed specifically to satisfy the criteria of a precision experiment for the study of the deformation and fracture of blast loaded plates.

A review of published blast loading studies, with an emphasis on laboratory scale blast testing, found that the majority of the precision testing criteria set out by the Trondheim workshop were satisfied by classical techniques, such as the ballistic pendulum. However, specific aspects were identified for improvement, *i.e.* time resolved response data, load characterization and concurrent analysis. To address this an instrumented ballistic pendulum was developed, incorporating a central support in the form of a Hopkinson bar. When used in association with a peripherally clamped centrally supported (PCCS) plate specimen, the central support allows the entire reaction force history at the inner boundary to be captured. Hence, in addition to the traditional impulse vs deflection data, this approach allows details such as the total deformation duration or the exact timing and magnitude of the fracture process to be captured. Furthermore, when used in association with a peripherally clamped annular (PCA) plate specimen, which does not make contact with the central bar, this approach allows the blast load pressure history to be captured.

The analytical solutions pursued in this thesis were motivated by the precision test requirement that analyses be included in the development of the experimental apparatus to provide a theoretical framework for the presentation of experimental data and lay a foundation for future validation work. A review of published found that the literature contained several classical closed form solutions for the large deflection of impulsively loaded peripherally clamped solid (PCS) circular plates. However, it was also found that several crucial aspects of the published analytical solutions were contradictory and/or incomplete. To address this a generalized energy method for modelling the blast loading of axisymmetric plates was developed which subsumes previous closed form solutions and can extended to include the novel plate configurations, such as those used in this thesis.

An extensive set of experimental results reported in this thesis shows that the instrumented ballistic pendulum succeeds in providing a rich set of novel data for code validation while retaining all the precision features of a classical laboratory scale blast loading apparatus. While the PCCS and PCA plate configurations require a revised definition of the observed failure modes, the transitions between the modes and the fracture behaviour are studied in greater detail. The data is analysed using an expression for the dimensionless impulse obtained from the analytical solutions developed in this thesis. In addition to retaining the accurate deflection predictions previous solutions, these solutions also provide improved deflection duration predictions using a novel two phase solutions that can also accommodate finite load duration. Finally, it will be shown that the instrumented ballistic pendulum, incorporating a central support in the form of a Hopkinson bar, in conjunction with the novel PCCS and PCA plate configurations and analytical solutions, satisfies all the requirement of a precision test.

Glossary

BIRSU	Blast Impact and Survivability Research Unit
CIL	Critical impulsive load
CME	Centre for Materials Engineering
CS	Cowper-Symonds (strain rate equation)
DIC	Digital image correlation
DL	Dynamic load
FFT	Fast Fourier transform
HE	High explosives
HPB	Hopkinson Pressure Bar
IDL	Ideal dynamic load
IIL	Ideal impulsive load
IL	Impulsive load
ISR	Intermediate Strain Rate
JWL	Jones-Wilkins-Lee (equation of state)
PCA	Peripherally clamped annular
PCS	Peripherally clamped solid
PCCS	Peripherally clamped centrally supported
P-I	Pressure-impulse (diagrams)
SSI	Shock-structure interaction
TOA	time of arrival
UCT	University of Cape Town
UNDEX	Underwater explosions

Nomenclature

Latin Alphabet

A	Bessel function constant
a_r	Speed of sound after passage of a reflected shock wave
B	Bessel function constant
D	Strain rate denominator in the Cowper-Symonds equation
E_k	Kinetic energy
$E_{k,0}$	Initial kinetic energy
$\tilde{E}_{k,0}$	Initial kinetic energy according to membrane mode analysis
H	Plate thickness
I	Impulse
$\tilde{I}_0$	Initial impulse according to membrane mode analysis
J_0	Zeroth order Bessel function of the first kind
J_1	First order Bessel function of the first kind
$\tilde{K}$	Plastic Stiffness
$\tilde{M}$	Effective mass
m	Plate mass
n	Strain rate power in the Cowper-Symonds equation
P	Constant or peak pressure
$\tilde{P}$	Effective pressure
P_{abs}	Absolute pressure
P_r	Reflected pressure
$\tilde{R}$	Radial position of maximum sector deflection
R_h	Radial position of a travelling hinge
R_i	Inner boundary radius
R_o	Outer boundary radius
r	Radial position
T	Displacement duration
T_I	Displacement duration of Phase I
T_{II}	Displacement duration of Phase II
T_T	Displacement duration Due to Taylor, *i.e.* 'Taylor duration'
T_L	Load duration
t	Time

u	Radial displacement
v	Uniform velocity of a shock accelerated plate
V	Volume
V_0	Initial uniform plate velocity
W_L	Work done by a pressure load
W_P	Plastic work
w	Transverse deflection
w_h	Transverse deflection at the position of a travelling hinge
w_I	Transverse deflection at the end of Phase I
w_{II}	Transverse deflection at the end of Phase II
$\tilde{w}$	Maximum profile deflection
Y_0	Zeroth order Bessel function of the second kind
Y_1	First order Bessel function of the second kind
z	Through thickness position relative to the midplane

Greek Alphabet

α	Strain rate parameter
α_0	Initial acceleration
β	Effective pressure parameter
γ_c	Ratio of specific heats
γ_S	Stand-off loading parameter
δ	Dimensionless deflection
ϵ_r	Radial strain
ϵ_θ	Circumferential strain
$\dot{\epsilon}$	Strain rate
Λ	Bessel function constant
λ	Plastic dissipation parameter
μ	Effective mass parameter
ρ	Density
σ	Flow or yield stress
σ_d	Dynamic flow stress
$\sigma_d y$	Dynamic yield stress according to the Cowper-Symonds equation
σ_y	Yield stress
σ_r	Radial stress
σ_θ	Circumferential stress
τ	Dimensionless deflection duration
$\tau_I DS$	Dimensionless deflection duration for an ideal dynamic shock
$\tau_{M\&N}$	Deflection duration parameter of Munday & Newitt
ϕ	Dimensionless impulse
$\phi(r)$	Displacement field mode shape

Special Alphabet

$\Re$	Universal gas constant

Contents

List of Figures

List of Tables

Chapter 1

Introduction

> "Theory without practice is empty; practice without theory is blind."
>
> John Dewey (1859-1952)

1.1 Theory and Experimentation

Engineering, as an academic pursuit, exists to develop theoretical models. However, the ultimate aim is not the theory itself, but the application thereof in the engineering profession. Hence, the ultimate validity of a model lies in its ability to systematically describe physical phenomena and predict experimental results.

Engineering has an additional requirement that a theoretical model must be practical and simple enough to be applied routinely. In the past this has placed a limit on the complexity of engineering models. However, with the ever increasing power of modern computers and computational techniques has come the ability to routinely conduct numerical simulations, incorporating theoretical models of increasing sophistication, to design structures in greater detail with smaller tolerances and safety factors. This in turn has increased the demands placed upon experiments that are intended to confirm the validity of the simulations.

In the context of impact engineering, while addressing issues related to the design of hardened shelters, Krauthammer [1] framed the relationship between testing and simulation as follows:

> "...modern fortification technologies are founded upon a combination of precision testing and sophisticated numerical simulations...It is clearly recognized that numerical simulations will play an increasingly more important role in eventually replacing many experimental studies...However, to enable this transition and to insure that it will be effective, it is required to concentrate...on precision testing, as an integral part of development, verification and validation of the eventual numerical capabilities."

The juxtaposition of theory and experiment is at the heart of this thesis, which seeks to investigate the role of precision testing in the context of the shock loading of structures, and present an experimental approach aimed at extending these capabilities.

1.1.1 Verification and Validation

There is general consensus [1, 2] that the process by which the accuracy of a numerical code is evaluated can be separated into two distinct activities, namely verification and validation. Both procedures involve the comparison of simulation results to sets of existing data, but the nature of the data varies.

The objective of code verification is to establish that numerical algorithms are implemented correctly. This is to be accomplished by comparing numerical results with 'known' solutions. Exact analytical solutions are preferable, but if they do not exist then 'benchmark tests' can be used. A benchmark test amounts to a consensus numerical solution obtained by comparing results on code-vs-code basis.

The objective of validation is to establish that a numerical implementation of a given model reproduces 'real world' behaviour. This is accomplished by comparing numerical results with accurate experimental data from precision tests. The term 'validation experiment' is often used to refer to such tests. This latter activity, in the context of blast and shock loading, is the primary motivation for this thesis.

1.1.2 Precision Experiments

While the objective of code validation given in the previous section is widely accepted, what constitutes a precision test is less well articulated. The quote due to Krauthammer, given in the opening section of this chapter, is taken from the proceedings of a technical workshop in which one of the aims was to achieve a consensus definition of a precision test. The title of the workshop was 'Precision testing in support of computer code validation and verification' and took place on 6-8 May 1996 at the Norwegian University of Science and Technology (NTNU), Trondheim, Norway [1][1].

While the report was published over two decades ago, the need for precision tests for code validation appears to be undiminished. In fact, the increasing capabilities of advanced numerical models have only intensified the demand for detailed validation data. Hence, the workshop recommendations have been echoed in similar reports published by other agencies [2]. In other words, the Trondheim proceedings remain an authoritative standard for precision testing and will be used as such in this thesis.

The proceedings cover a wide variety of discussions. For example, the required degree of precision for a validation test was debated, but it was concluded that there is no simple answer to this question. Hence, no quantitative definition was obtained due to the range and variety of possible test configurations and phenomena of interest. However, several essential features of a precision tests were identified. These features were subsequently transposed into a list of requirements that must be fulfilled by laboratory scale experiments to be considered as precise tests for code validation. These requirements were set forth as follows:

[1] The workshop was sponsored by the Norwegian Defense construction service (NDCS), with additional support from the Defense Nuclear Agency (USA), and hence a major focus of the workshop was the impact loading of reinforced concrete structure. Nevertheless, the recommendations of the report are equally valid for other protective structures and for precision testing in general.

1. The structural behaviour must be accurately described and highly repeatable.

   This includes the motion, stress and/or strain at specific points.

2. Failure modes must be individually observable and experimentally decoupled from other effects.

   It was noted that this is more difficult to achieve in dynamics tests due to inertia and strain rate issues.

3. The applied load must be controlled and highly repeatable in terms of magnitude and both spatial and temporal distribution.

   It was emphasized that validation required accurate descriptions of the load in terms of the duration, the rate of application and removal, peak value and area of application. Furthermore, if explosive loading is used, the blast pressure may be influenced by the stand-off distance and the shape and orientation of the charge and detonator. While control was emphasized, it was noted that some control may be relinquished if it is known that a particular parameter will not influence the result. For example, a common approach in short stand-off blast testing is to view the total impulse as being of primary importance, while the blast duration and pressure history are of secondary interest.

4. Boundary conditions must be fully defined, including parameters such as stiffness and friction.

   It was mentioned that support conditions are difficult to define because the support stiffness depends on various other factors.

5. Suitable transducers must be selected.

   The measuring technique should, ideally, be non-invasive and not interfere with the specimen behaviour. Transducer response characteristics must be such that the measurements are accurate and unaffected by mass and stiffness of the transducers or fixtures. The transducer calibration should be dynamic, if possible.

6. The data collected from the experiments must have some redundancy.

   Important experimental parameters should preferably be measured or inferred from more than one sensor or observation.

7. Precision reporting must be provided for all test parameters that could influence the results.

   In other words, the specifications are required for the equipment, sensor, instrumentation, data acquisition, *etc.* Furthermore, analysts require data concerning the initial condition of the structure and its supports, constitutive relations for all materials involved, interface definitions and properties, load characterization, *etc.*

8. The material properties must be well defined, especially with regard to strain rate sensitivity.

   It was emphasized that the material samples must be representative of the material. In other words, the sample must be large enough to contain a representative statistical distribution of defects but small enough to be regarded as a 'mathematical point', *i.e.* a representative unit volume (RUV).

9. Analyses should be included in the development of the experimental apparatus to ensure usable results.

It was noted that there is a need for stronger interaction between testing and analysis. Frequently, the researcher developing the analytical work does not carry out the experimental work and has little experience in high strain rate testing. Though not mentioned explicitly in the report, the converse is equally valid, *i.e.* an experimentalist with little analytical experience may not appreciate the importance of certain subtle parameters.

10. The validation process must involve predictions and not 'postdictions'.

    There must be a clear distinction between tests intended for material and load characterization from those intended as dynamic structural tests. The results from the validation experiments must not be viewed as a guide to 'calibrate' or 'massage' the numerical code or material model until the simulations agree with the validation data. The primary reason for this is that code 'calibration' defeats the purpose of a validation test, which is to assess the ability of a model to predict behaviour outside of its calibrated domain. Nevertheless, a code calibration exercise may lead to a better understanding of the problem by identifying where either the theory or input parameters are lacking.

These requirements were used to guide design decisions throughout this work and will be used in Chapter 9 as a standard against which to evaluate the experiments and analyses presented in this thesis.

1.1.3 Blast and Shock Tube Loading

In addition to the precision test requirements, a topic of great relevance to this thesis was discussed in Session 3 of the Trondheim workshop which was devoted to laboratory scale blast and shock tube experiments. Such experiments have been pursued for their relative economy with respect to large scale blasts, which are expensive and hazardous and for which data is often not readily available or when available consists of few data points.

Several delegates presented work using shock tubes and laboratory scale explosive charges, which they regarded as meeting the requirements of precision tests. Shock tube proponents highlighted the high degree of control that shock tube loading provides, while blast loading proponents emphasized the impulsive nature of explosive tests with high intensity and short duration loading. Both techniques were shown to have good repeatability with respect to the measured parameters.

However, there were a large number of criticisms of the techniques. For example,

> "Shock-tube experiments lack the impulsive loading that is often of interest, and explosive loading is often difficult to define throughout the structure...explosive testing introduces inaccuracies such as unreliable pressure-space-time data." [1]

In addition to the above, the session summary stated that both shock tubes and explosive testing introduce various limitations and difficulties such that they cannot be considered as precision tests. The absolute nature of this statement is surprising given the more measured tone of the rest of the workshop report. Furthermore, it does not anticipate possible improvements in blast and shock loading techniques that could address the stated shortcomings and leaves unanswered the question of how to conduct validation

tests for fluid-structure interaction via shock wave reflections. These and other technical issues relating to laboratory scale blast and shock testing will be discussed in chapter 5.

1.2 Purpose, Scope and Objectives

The central purpose of this thesis is to present a novel experimental apparatus developed specifically to produce data for the validation of simulation codes intended for the study of the deformation and fracture of blast loaded plates.

To this end, the scope of the work encompasses the requirements of a precision test, as presented in Section 1.1, including the development of analytical solutions to provide a theoretical framework for the presentation of experimental data and lay a foundation for future validation work.

Hence, the objectives of this thesis are as follows:

1. Review published blast loading studies, with a particular emphasis on laboratory scale blast testing of structures, and evaluate whether they can be considered as precision tests.
2. Review published theoretical models used to interpret blast loading studies, with particular emphasis on closed form solutions for large displacements, and evaluate whether they are coherent and sufficient to provide basis for the interpretation of precision tests results.
3. Present a novel experimental apparatus for the blast loading of plates, and demonstrate that it meets the requirements of a precision test.
4. Present a unified theory for the blast loading of circular plates which subsumes previous closed form solutions and extends the theory to include the novel specimen configuration presented in this thesis.

1.3 Thesis Outline

The work reported in this thesis is arranged into nine chapters and five appendices, the content and purpose of which are briefly outlined in this section.

1.3.1 Literature Survey

In Chapter 2 the extensive body of literature regarding the experimental and theoretical investigation of impulsively loaded plates is reviewed. For the reasons set forth in the Trondheim workshop, the emphasis is on laboratory scale experiments and associated closed form theoretical models. Various impulsive loading configurations are considered and their relative merits and results discussed. Furthermore, a variety of analytical models are considered, with particular attention given to solutions for plate behaviour that include large deflections, *i.e.* deflections that are greater than the plate thickness, but smaller than the plate radius[2]. In addition to the detailed reviews mention above, brief reviews will be presented for minor

[2] A motivation for this use of the term 'large' is given in Section 2.3.1.

topics that are relevant though peripheral to the central argument of this thesis. These topics include strain rate effects and the interaction of bending and radial displacements with membrane deformation, which is typically assumed to be dominant during large deformations.

1.3.2 Literature Critique

In Chapter 3 a selection of the experimental data and theoretical models reviewed in Chapter 2 are considered in greater detail. Additional analyses and interpretations of the published experimental results are presented, with particular emphasis on the coherence of the data, resulting is new correlations for load intensity, damage and test duration. Furthermore, critical consideration is given to certain theoretical details that do not appear to have been addressed in the literature. For example, novel analyses are presented to show the validity and limitations for several common assumptions used in analytical models, such as membrane dominated deformation and impulsive loading with minimal shock-structure interaction effects. Consequently, the published theoretical models are reinterpreted in terms of a generalized energy approach, which provides a coherent framework for the work reported in subsequent chapters. Finally, the published results are discussed with respect to the precision test requirements set out in Section 1.1.2.

1.3.3 Transient Behaviour of PCS Plates

In Chapter 4 the generalized energy approach, developed in Chapter 3, is extended to include additional effects in the analysis of peripherally clamped solid (PCS) circular plates, such as transient plastic hinges and finite duration loads with various temporal distributions. The intent of this chapter is to address some of the shortcomings of previously published models, such as limitations imposed by the ideal impulse assumption, while maintaining the simplicity and elegance of the solutions. In particular, closed form analytical solutions are presented that incorporate transient deformation profiles and provide more realistic deformation duration estimates. The resulting models provide a basis for comparing and correlating experimental results for circular plates subjected to non-ideal shock loading conditions, and serve as a template for the analytical approach pursued in subsequent chapters.

1.3.4 Experimental Method

In Chapter 5 a novel experimental apparatus, an instrumented ballistic pendulum[3], developed as part of this thesis, is presented. In particular, the apparatus incorporates a novel test plate configuration, a peripherally clamped centrally supported (PCCS) circular plate, that allows boundary reaction forces at a central support to be measured during a blast loading event. In addition, when used with peripherally clamped annular (PCA) plates, the instrumented ballistic pendulum allows the temporal and spatial distribution of a blast load to captured and characterized. The instrumented ballistic pendulum is specifically designed to produce data for the validation of numerical codes intended to study of the deformation and fracture of blast loaded plates. The experimental configuration is described along with the techniques for capturing and processing the experimental data. Specific attention is given to the

[3]The term 'instrumented' is generally taken to imply the use of sensors that provide time resolved measurements in addition to the total impulse measured by a traditional ballistic pendulum.

characterization of the blast loading techniques, where both experimental and numerical results are presented to assess the temporal and spatial distribution of the blast wave.

1.3.5 Experimental Results

In Chapter 6, novel experimental results obtained using the instrumented ballistic pendulum are presented. In keeping with best practice, specific terminology and parameter definitions are introduced to allow for the concise presentation of the experimental results. These definitions represent an extension and generalization of those used in previously published studies to accommodate the novel plate configurations used in this thesis. Particular emphasis is given to the types of data not previously available in the literature and to specific performance parameters, such as repeatability, to assess whether the test results conform to precision test requirements.

1.3.6 Analytical Modelling of PCCS and PCA Plates

In Chapter 7, the analytical models developed in Chapter 4 are extended to incorporate the plate configurations considered in this work. To the author's knowledge, analytical models for PCCS plate configuration have, hitherto, not been reported in the open literature, with the exception of the papers published as part of this work. In keeping with the stipulations of a precision test, the models are intended to aid in the interpretation and presentation of experimental results, in addition to providing a theoretical framework for further numerical studies and model development. In particular, a novel dimensionless damage number, motivated by the analytical solutions, is presented, which allows the experimental results for several distinct plate configurations to be scaled and presented on a single graph.

1.3.7 Discussion of Results

In Chapter 8 the analytical results derived in Chapter 7 are compared to the experimental data reported in Chapter 6 and to previously published results. Particular attention is given to instances where the analytical solutions that capture salient features of the experimental results, thus enhancing the ability of the experimental results to conform to precision test requirements.

1.3.8 Conclusions and Recommendations

In Chapter 9 the conclusions and recommendations arising from this work are discussed with the purpose to consolidate the novel contributions made in this thesis. Firstly, conclusions regarding the novel experimental blast apparatus and associated plate configurations developed and used in this thesis are presented, with a particular focus on the degree to which the experimental results meet the criterion of a precision test. Secondly, conclusions regarding the analytical models developed in this thesis are presented, along with an assessment of the degree to which they provide a unified theory for the blast loading of axisymmetric plates. Thirdly, recommendations for future experimental and analytical work are presented.

1.3.9 Appendices

The Five appendices in this thesis contain theory and/or data that are relevant but not central to the core narrative of this work.

In Appendix B the quasi static and dynamic material properties of the specimen material used in this thesis are reported. This is in keeping with the definition of precision testing, which requires the high strain rate properties of the material used to manufacture the shock/blast test specimens to be obtained using independent material characterization tests. Included is a concise review of the dynamic material testing literature and, in particular, a brief discussion of fundamental elastic stress wave propagation that is relevant to the instrumented ballistic pendulum.

In Appendix C the calculation approach used to determine the total blast impulse from the ballistic pendulum deflection recordings is presented.

In Appendix D the detailed derivations of the Bessel displacement profiles of PCCS plates, as discussed in Section 7.2.1, are presented.

In Appendix E the tabulated impulse and deflection data for blast tests conducted as part of thesis are presented.

Finally, in Appendix F drawings plate specimens used in this thesis are presented.

Chapter 2

Literature Review

> "...engineers have only been well served, *i.e.* educated, if,..., they possess an appreciation of the historical origins of the basic ideas of the disciplines of their profession...."
>
> William Johnson (1922-2010) [3]

2.1 Introduction

The body of literature regarding the impulsive loading of structures is extensive. Several text books and review articles [4–11] on theoretical and experimental impulsive loading of structures have been published, negating the need to repeat the details here. Rather, the focus of this chapter is the subdivision of the field relating to laboratory scale blast and shock loading of thin circular plates in air, so as to establish the context and motivation for the work reported in this thesis.

In the field of general engineering, terms such as 'shock' and 'impact' are often used interchangeably to refer to a load that has a high rate of application. Similar usage also occurs in the titles of specialist fields such as 'impact engineering' or 'impulsive loading', where the terms 'impact' and 'impulsive' are used in a general sense to refer to a range of loading scenarios from high explosive blasts to low speed kinetic collisions. Such generalizations are often unavoidable and specific meaning has to be gained from the context. However, for the sake of clarity in this thesis, certain terms will be reserved to have distinct meaning.

Strictly speaking, the term 'impulsive' refers to a load that has negligible duration, such that the details of load history are irrelevant and only the total impulse is of concern. However, the term 'impulsive loading' has come to be used to describe a range of load cases where the duration is short but not necessarily negligible [6]. This convention will be maintained in this thesis and the term 'ideal impulsive' will be used to imply the stricter definition, as will be given in Section 2.3.3. A load with a duration that is too long to be considered impulsive but still excites an inertial response in a target will be referred to as 'dynamic', and 'ideal dynamic' will imply a dynamic load of constant intensity. The term 'shock' will be used exclusively to refer to a sudden finite discontinuous pressure rise in a fluid due to a pressure wave

propagating through the fluid[1]. Likewise, the term 'blast' will only refer to a load produced using high explosives[2]. Note that a blast wave is a type of a shock wave, *i.e.* it has a discontinuous pressure rise, but a shock wave need not be blast wave, *e.g.* a shock tube type load[3]. A more detailed distinction between impulsive and dynamic loads will be discussed in Section 4.3.

This chapter begins with a brief historical review of impulsive loading research, after which the papers most relevant to this work are considered in detail. The purpose is to provide a context for the papers referred to in this work. These papers are divided into two major sections, namely experimental and analytical results. Literature regarding numerical solutions will only be mentioned in passing, since it is not within the scope of this work. Further analysis, *i.e.* beyond that found in the literature, and discussion is presented in Chapter 3. The literature regarding material characterization and blast modelling is covered in Appendix B and Chapter 5 respectively.

2.1.1 A Brief History of Shock Loaded Structure Research

The experimental study of the effects of blast loads on structures is, in all likelihood, as old as explosive technology itself. However, the analytical treatment of the blast loading of plates is typically traced back to the seminal work of Taylor [15]. Though only openly published in 1950, Taylors original work was carried out in 1942 and was focused on under water explosions (UNDEX). This effort was precipitated by the need to protect Allied ships during the Second World War. Similar work was carried out by Richardson & Kirkwood [16] in 1944 and subsequently published in the same volume as Taylors work. In their paper, Richardson & Kirkwood indicate that they were in private communication with Taylor, indicating the level of collaboration occurring at the time. The well known text on the subject by Cole [17] is based on this and other work during the years 1941-1946.

In these classic papers, Taylor and Richardson & Kirkwood showed great insight into the response of plates to impulsive loading and foreshadowed several of the theoretical approaches that would be pursued by subsequent researchers. Taylor's work, in particular, will be referenced frequently in this thesis. In both papers, the plates were assumed to be perfectly plastic and treated as membranes under constant tension. Taylor primarily employed an energy method with an assumed deformation shape and compared the results to UNDEX tests on relatively large square plates. Richardson & Kirkwood developed an approximate solution of the equations of motion and compared the results to UNDEX tests on small circular plates. Due to the nature of UNDEX threats, the analytical work was focused on finite duration pressure loads with a sudden rise followed by an exponential decay. However, both papers also discuss the effect of a uniform load with a duration significantly shorter than that of the plate motion and describe how a circular plate will initially move at a uniform velocity and be brought to rest by a transverse wave travelling from the boundary to the centre of the plate. These analytical approaches will be discussed in greater detail in Section 2.3.

Following the intense analytical work on the dynamic plastic deformation of membranes in the 1940's, very little work was reported in the 1950's, the only work being extensions of the traveling wave approach

[1] This definition is distinct from that used in the field of structural vibration where the term 'shock' refers to a relatively large transient force with a duration that is short in comparison to the natural period of a structure [12–14].

[2] It is possible, in principle, to reproduce certain characteristics of a blast wave without using high explosives, but this topic will not be considered in this thesis.

[3] The phenomenon of a shock propagating in a solid target is beyond the scope of this thesis.

pursued by Hudson [18] in 1951 and Frederick [19] in 1959. However, during this period there was significant activity on the static and dynamic load carrying capacity of beams and plates where plastic bending was the primary deformation mechanism. Examples of this are the work by Symonds on beams [20] and by Hopkins & Prager [21, 22], Wang & Hopkins [23], Wang [24] and Perzyna [25] on plates. The 1950's also witnessed important work regarding plastic flow rules. In particular, the work of Prager [26], Onat & Prager [27], Onat & Haythornthwaite [28] and Hodge [29] will be discussed in Sections 2.3.8 and 3.3.6, along with the work by Weil & Newmark [30] on the large static deflections of membranes. Hitherto, work on the bending response regime has remained active and has resulted in a large body of literature [4]. However, the structural response considered in this thesis involves large displacements and hence the bending regime will not be considered in detail, although an estimate for the error incurred by ignoring bending will be presented in Section 3.3.7.

Up to the end of the 1950's the experimental focus appears to have been on UNDEX events. The exception being Hoffman [31], in 1955, and Gerard [32], in 1956, who appear, respectively, to be the first to conduct systematic blast loading experiments in air [6] and shock loading experiments on plates using a shock tube. The work of Gerard is noteworthy as the first investigation of the response of a structure to a fluid shock that was not generated by explosives. These two papers mark the start of laboratory scale shock loading experiments in air[4]. The results of Hoffman were only published by Witmer *et al.* [33] in 1963, which is the same year Munday & Newitt [34] described the response of thin circular copper plates to loading via a shock tube. This paper is significant in that it contains the first high speed photographic evidence of the transverse wave deformation mechanism, as shown in Figure 2.1, and employed a non-contact technique to capture the first continuous recording of the central deflection of a plate.

During the mid 1960's, researchers started using sheet explosives at very small stand-off distances to obtain experimental loadings as close as practically possible to an ideal impulsive loading, *i.e.* a load with a duration that is insignificant in comparison to the deformation duration of the structure. Furthermore, in order to characterize the load, the emphasis shifted from obtaining pressure history curves to measuring the total impulse imparted by the blast load. Humphreys [35], in 1965, appears to be the first to use a ballistic pendulum[5] to measure the total impulse imparted to beam specimens. The following year Florence [36], and later Wierzbicki & Florence [37], obtained the total impulse transferred by a given charge configuration by applying the blast load to an unconstrained plate specimen and measuring the resulting velocity using flash x-ray photography. During the same period Duffey & Key [38, 39] pursued a similar approach but used contact pins. Jones *et al.* [40], in 1970, appear to be the first to use sheet explosive in combination with a ballistic pendulum to investigate the behaviour of rectangular plates. Several other structural configurations were tested in a similar manner from 1965 to 1972 [6], marking this as a relatively intense period in the history of laboratory scale blast testing.

The experimental work on the blast loading of plates in the mid to late 1960's coincided with a renewed theoretical interest in the finite deflection of blast loaded structures. The first papers on the numerical modelling of blast loaded structures appeared at this time [33, 41]. Work on closed form analytical solutions included the development of the mode approximation technique by Martin & Symonds [42], while Duffey [38] and Jones [43, 44] considered the finite deflections of circular and annular plates. This

[4] While UNDEX work has continued, it is beyond the scope of this thesis and will not be considered any further.

[5] The ballistic pendulum appears to be the oldest of the impulse measurement techniques, developed independently by J Cassini (1707) and B Robins (1742) for projectile velocity diagnostics. A fascinating discussion of this topic is given by Johnson [3].

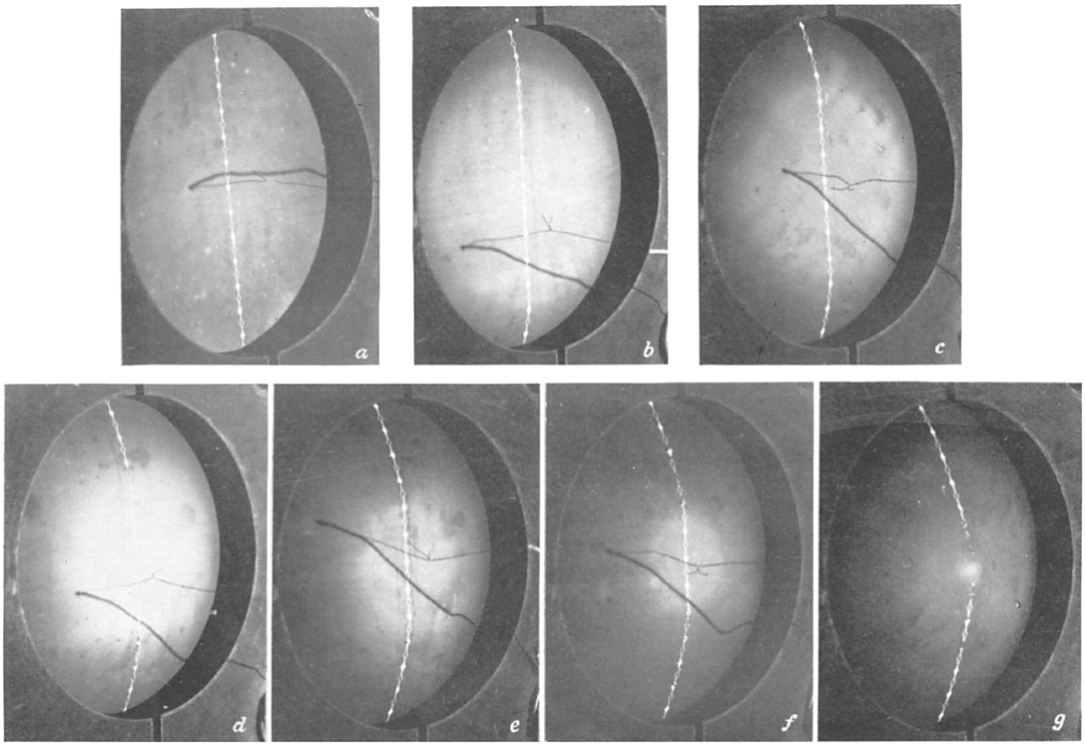

Figure 2.1: Transient plate shapes captured by Munday & Newitt [34]

was followed by the analytical models of Wierzbicki & Florence [37] and Lippmann [45] in the early 1970's. The early 1970's also marked the start of the work of Youngdahl [46] who sought to eliminate the effect of a pressure pulse shape on the response predictions for various structures. He developed an expression for an effective pressure load that reduced an arbitrarily shaped pulse into an equivalent load of equal impulse but rectangular shape, *i.e.* a pressure pulse of finite duration and constant intensity. Since the work of Youngdahl, this approach has developed into the distinct field of pressure-impulse isodamage diagrams [8, 47] for which a brief synopsis is given in Section 2.5.2.

For most of the 1970's there appears to have been little experimental work on the blast loading of plates, though work continued on other structures. Of particular significance is the paper concerning the blast loading of beams by Menkes & Opat [48], who were the first to draw attention to distinct failure modes for impulsively loaded structures. This topic forms an important part of this work and will be discussed further in Section 2.1.4. Another interesting study was that due to Ghosh *et al.* [49, 50] who investigated the inertia forming of plates. They developed an apparatus to accelerate a clamped plate up to 55 m/s and then arrest the clamp motion via impact, while the plate would then deform under its own inertia. In addition to clamped solid plates, Ghosh *et al.* also tested peripherally clamped annular plates and peripherally clamped plates with additional central supports. Apart from this work and that published as part of this thesis [51–53], there does not appear to be any other published experimental results for these two impulsively loaded plate configurations. Unfortunately, Ghosh *et al.* restricted their work to lead plates.

The early 1970's marked the initial work of Johnson [54] who proposed a dimensionless number with which to identify various impact regions in metals. This approach has made a significant contribution to experimental blast loading work on plates, where it has allowed the work of various researchers, over varying scales and material types, to be compiled and interrelated as a coherent set of data. It is interesting to note that Johnson's work coincided with that of Youngdahl which had a similar aim, *i.e.* to develop a unified approach to the study of impulsively loaded structures. Several reviews of this field exist [6, 7, 11, 55] and only the work related to circular plates will be considered in Section 2.2.1.

An important paper appeared in 1979 by Bodner & Symonds [56] concerning the blast loading of circular plates using a ballistic pendulum. It is significant not only for the quality of the resulting data, which is still often cited, but also for the motivation provided for the work. The first sentence of the paper states that the experiments are primarily intended for comparison with the predictions of the mode approximation method. In other words, this may be viewed as the first instance of a validation experiment. This intention is reflected in the design of the experiments, which included a capacitive sensor to obtain the deflection history. Furthermore, the capacitive deflection sensor was isolate from the plate fixture by mounting it on a separate long cantilever arm, the other end of which was secured to the ballistic pendulum. In essence, any structural disturbance caused by a blast load on the plate specimen had to travel down the plate fixture supports and then back up the sensor arm before it could affect the sensor, by which time the complete plate response had been captured. This approach will be discussed further detail in Section 5.2.4.

At this point it is enlightening to consider the contribution to the field of impulsively loaded structures made by researchers associated with Brown University. As previously mentioned, Cole [17] was involved in the UNDEX work during the Second World War. After the war Prager assembled a group that included Symonds, Drucker, Onat and Kolsky [57], the last mentioned being the inventor of the split Hopkinson bar [58]. At various times in subsequent decades the group included, amongst others, Martin, Bodner, Jones and Wierzbicki. These four researchers are mentioned, in particular, because they went on to lead, or strongly influence, impact research groups at the University of Cape Town (UCT), the Israel Institute of Technology (Technion), the University of Liverpool (UL) and the Massachusetts Institute of Technology (MIT) respectively. The UCT group has since diversified with the blast focused research falling under the Blast Impact and Survivability Research Unit (BISRU) under the auspices of which the present work was conducted.

The 1980's were a relatively quiet period with respect to blast testing, though some work continued at UCT on beams by Wegener & Martin [59] and plates by Nurick & Martin [60]. Of particular interest for this work is the data on the blast loading of mild steel circular plates. The experiments were very similar to those of Bodner & Symonds [56] in that a pendulum was used to measure the total impulse and the deflection history was recorded [61]. The two sets of data show excellent correlation and will be discussed in detail in Section 2.2.1.

Nurick & Martin [5] indicate that by the 1980's the analytical treatment of the impulsively loaded plates had begun to give way to numerical solutions. The reason for this was the need to include non-linear effects such as strain rate sensitivity and radial displacements [62] into the formulations. This trend has continued through the 1990's and well into the 2000's, during which time only a small number of closed form solutions for the large displacement of blast loaded circular plates appear to have been

published [52, 63–66]. Furthermore, since the work of Nurick & Martin [5], no comprehensive reviews focusing on the analytical and/or numerical investigation of blast loaded plates appear to have been presented.

In contrast to the 1980's, the 1990's saw a marked increase in blast loading work. In particular, the UCT group conducted numerous blast experiments on various beam, plate and stiffened plate configurations with varying boundary conditions. Of interest to this work are the test results for uniformly loaded circular plates [67–70], which will be discussed in Section 2.2.1. This trend has continued through the 2000's, during which laboratory scale blast work has continued at UCT and has begun in other centres [71–79]. Some of the techniques developed in the laboratory have been carried over to outdoor use with Hanssen *et al.* [80] and Enstock & Smith [81] reporting on blast work carried out on a large outdoor pendulum, on which initial work began in 1997. In this same period, similar techniques have been developed for measuring the vertical impulse delivered by buried charges [77, 82–85]. Finally, the new millenium has witnessed the application of new diagnostic techniques to laboratory scale blast loading, such as digital image correlation (DIC) [72,77,79,86–88] to capture plate motion and high speed pressure sensors, such as piezoelectric pressure transducers [79, 87, 89] or Hopkinson pressure bars [51–53, 90–93], for blast pressure characterization[6].

2.1.2 Alternative Impulsive Loading Techniques

In addition to blast testing using explosives, the 1990's witnessed a renewed interest in alternative experimental techniques to replicate air blast loading effects. This trend continued into the present century and it is noteworthy that this coincided with the realization that precision experiments are required to validate the increasingly powerful numerical codes [1]. The alternative techniques fall into three groups, namely impact arresting, pulsed pressure and shock tubes.

Impact arresting is the least used of the three techniques, with only Nemat-Nasser *et al.* [94] reporting on work in 2007. The technique used is similar in concept to that of Ghosh *et al.* [49, 50], except that the plate assembly is launched from a gas gun and allowed to impact against a Hopkinson tube to arrest the motion of the clamp. This technique is promising in that it closely approximates the short duration impulsive loading assumption. However, the range of impact velocities is limited by the yield strength of the arresting device. For example, Nemat-Nasser *et al.* limited their impact speeds to $60\,ms^{-1}$. By contrast, the velocities induced by impulsive blasts can be significantly higher [67].

A novel pulse pressure loading rig was developed at the University of Liverpool from 1994-1996 [95]. The technique can create a well controlled spatially uniform pressure pulse by the timed blow-down of two pressure chambers on either side of a test specimen. The pulse is typically triangular in time and the specimens are relatively large ($0.5\,m \times 0.5\,m$ to $1\,m \times 1\,m$). However, the pressures are in the order of a few bar and lasts several milliseconds, *i.e.* the loads are more dynamic than impulsive.

The renewed interest in shock tube work began with Toutelmonde *et al.* [96] in 1995, who reported on a large shock tube developed in the early part of that decade for the testing of concrete. This appears to be the first instance of the use of a shock tube for structural loading since the work of Munday & Newitt [34].

[6]Some of the aforementioned studies have been published as part of the work of this thesis [51–53, 90] and are discussed in detail in Chapter 5.

The interest in shock tube work has continued into the 2000's [97, 98] including the development of some large facilities [99, 100]. A common criticism of the shock tube technique is that it cannot reproduce the intensity of an explosive blast [1]. The highest shock pressure reported is that due to LeBlanc & co-workers [101, 102] who achieved reflected pressure intensities of up to 12.5 MPa. This compares well to pressures achieved in the chemical shock tube field, where reflected pressures of 5 MPa are considered high pressures [103], but is still at the lower end of blast loading pressure range, which, depending on the stand-off, can vary from near atmospheric to several tens of GPa. Furthermore, at a laboratory scale, the reported duration of 1.2 ms is too long to be considered an impulsive load.

An alternative approach to the classical shock tube technique, which typically incorporates a bursting diaphragm, is a blast driven shock tube [104–107]. Ågårdh [1, 105] showed that an explosively driven shock tube can produce a fairly plane pressure front while maintaining the intensity of a blast event. The blast tube technique has also been used at UCT by Jacob *et al.* [107] to investigate the effect of stand-off. This approach is of particular relevance to this work and will be discussed in greater detail in Section 2.2.4 and Chapter 5. In this thesis, a blast driven shock tube will simply be referred to as a 'blast tube' to draw a distinction with a conventional shock tube.

2.1.3 Shock Loading Diagnostic Techniques

A variety of diagnostic techniques have been used to investigate the shock loading of structures. The origins of some diagnostic techniques have been reviewed in Section 2.1.1. What follows here is an attempt to categorize impulsive diagnostic techniques to provide a context for the techniques presented in Chapter 5.

Shock loading diagnostic techniques can broadly be grouped as either load or response measurements, with load diagnostics being either pressure history or total impulse measurements and response diagnostics being primarily displacement measurements.

Pressure history diagnostics are typically used for pressure loads that are of a relatively low intensity and long duration, such as occur in shock tubes or open air large stand-off blast tests. Under these conditions, the target response time tends to be in the order of the pulse duration or shorter, *i.e.* the loads would be classified as dynamic, and piezoelectric sensors are the preferred sensing device [72, 101, 108, 109], although various other types of sensors have been used [108]. Recently, Piezoelectric sensors have been used at relatively short stand-off distances for laboratory scale blast tests [79, 87, 89]. An alternative approach is to use a Hopkinson pressure bar (HPB) as a high speed pressure sensor for short stand-off blast characterization. This is, of course, the original purpose of the HPB [110], and although it has seldom been used for this purpose [111–113], the new millennium has seen an increased interest in the technique [52, 90–92, 114, 115] This technique is of particular interest for this thesis and is discussed in greater detail in Chapter 5.

Total impulse measurements tend to be used for small stand-off blast tests where the structural response duration is significantly longer than the load duration, *i.e.* impulsive loads [6]. Under these circumstances the precise load history is generally considered to be of secondary importance and the initial plate velocity, obtained from the total impulse, is assumed to be valid [5], *i.e.* it is considered to be an ideal impulsive load. The effect of finite duration impulsive loads will be considered in Sections 4.3

and 7.5. At a laboratory scale, the total impulse is either measured using a ballistic pendulum [5] or implied from explosive calibration experiments [36,37]. For large scale short stand-off blast tests ballistic pendulums [80] or alternative ballistic methods [83,84] are used, but no explosive calibration experiments appear to be used. The ballistic pendulum has the advantage of directly measuring the impulse for every test but there can be some uncertainty regarding possible impulse transfer through specimen mountings. By contrast, the explosive calibration method has the advantage of definitively measuring only the impulse that has been transferred through the target structure but, per definition, does not provide a unique measurement for every test. Fortunately, both these techniques are well established and give essentially identical results, as will be shown in Section 3.2.2.

From the literature it is apparent that certain diagnostic techniques have traditionally been associated with particular loading techniques and, with the exception of papers published in connection with this work [51–53], the pressure history and total impulse do not appear to have been measured simultaneously. The usefulness of such an approach to increase the redundancy of the data, as required by validation tests, will be discussed in Section 9.2.

The response of a structure to an impulsive load has traditionally been described in terms of the amount of damage incurred. The use of the term 'damage' can lead to confusion. In the blast testing literature both plastic deformation and fracture are referred to as 'damage', while in the field of damage mechanics the terms is used exclusively to refer to discontinuous displacement mechanisms, *i.e.* fracture through crack propagation, coalescent void growth and shear banding. A similarly confusing term, 'failure mode', will be discussed in Section 2.1.4.

In many of the early experimental blast studies fracture was of secondary interest and only the large inelastic structural response was reported. For simple beams and plates structures this is succinctly captured by measuring the final central (*i.e.* maximum) deflection as the primary response diagnostic. In many studies, the final deflection is reported for every specimen, along with a characteristic parameter of the imposed loading [6]. However, few studies provide information regarding the deflection profiles, the radial displacements or the strain distributions [6].

While the final maximum deflection is the dominant displacement diagnostic in blast tests, several studies have also reported deflection histories, which can be continuous or discrete [6]. Continuous deflection histories have been measured using light occlusion techniques [61] or capacitive sensors [56,116] Continuous techniques have traditionally captured the motion of a single point on the structure, such as the central deflection. By contrast discrete methods, such as high speed analog cameras, have been used to capture deflection distributions at specific instances of deformation. More recently, full field data has been captured via discrete high speed digital photography and DIC [72,77,86,88]. In the near future, the increasing capacity of modern photonic technology may well render the distinction between continuous and discrete measurements superfluous.

Various alternative approaches have been used, but to a lesser degree than the above mentioned techniques. Dynamic strain measurements have typically involved the use of strain gauges [38]. However, under impulsive blast loads, gauge spalling appears to limit the usefulness of this approach [56]. Trip wires have been used by Teeling-Smith & Nurick [67] to measure the velocity of blast fragments. Though used for impulse calibration, flash x-rays and contact pins do not appear to have been used for deflection diagnostics, nor streak photography or laser Doppler systems. The precise reasons for this are unknown,

Table 2.1: Modes of Failure according to Menkes & Opat [48]

Mode	Description
I	Large inelastic deformation
II	Tearing (tensile failure) in outer fibers, at or over the support
III	Transverse shear failure at the support

though it is likely that flash x-ray images will be obscured by the plate clamps, while the number of contact pins required to capture non-uniform displacement is prohibitive. Furthermore, the setting up of sensitive equipment close to a hazardous environment, like a blast test, probably accounts for the lack of streak camera and laser Doppler work. However, new digital image processing [72, 86, 88] and laser fibre optic techniques [117] may alleviate these restrictions in the near future.

To the author's knowledge, other experimental parameters such as temperature, crack growth or boundary reaction forces have rarely been measured, if at all, though these parameters are all important in the study of dynamic fracture under blast loading conditions. A central theme of this work is the development of a technique to facilitate the measurement of boundary reaction forces.

2.1.4 Modes of Failure

Precision blast testing requires not only accurate diagnostics, but also precision reporting [1], which implies accurate documentation of all measurements along with a comprehensive and unambiguous description of the observed behaviour. This is not a trivial exercise since displacements and strains can be large or small, elastic or plastic and fracture can manifest as necking, tearing, shearing and petalling. Furthermore, a single structure may exhibit all of these responses simultaneously, depending on its configuration. Hence, a nuanced system of classification is required to characterize the structural response of the target specimens. Hitherto, no single system of description has been developed that comprehensively describes the responses of all possible structural configurations.

Menkes & Opat [48] appear to have been the first to delineate distinct modes of failure, based on their study of the response of clamped beams to impulsive loads. From their experimental results, as shown in Figure 2.2, they defined the three modes of failure given in Table 2.1.

At first glance, the succinct descriptions given in Table 2.1 may appear to be merely a renaming of types of failure. However, the stated intent of Menkes & Opat was not only to identify damage mechanisms, but also to order them in the sequence in which they occur with respect to an increasing load and distinguish the controlling variables. Furthermore, Menkes & Opat qualified Mode III by emphasizing that, "...shear failure is characterized by *no significant deformation* in the severed central section..." (emphasis in original).

Teeling-Smith & Nurick [67] showed that the classification system worked equally well for circular plates and included a sub-category, Mode II*, to indicate partial rupture along the boundary by tensile necking and tearing. Nurick *et al.* [70] further subdivided the classification system to that shown in Table 2.2.

The failure mode definition of Menkes & Opat are relatively easy to apply to simple structures, such as simply connected unstiffened beams and plates, but require slight modifications for more complex

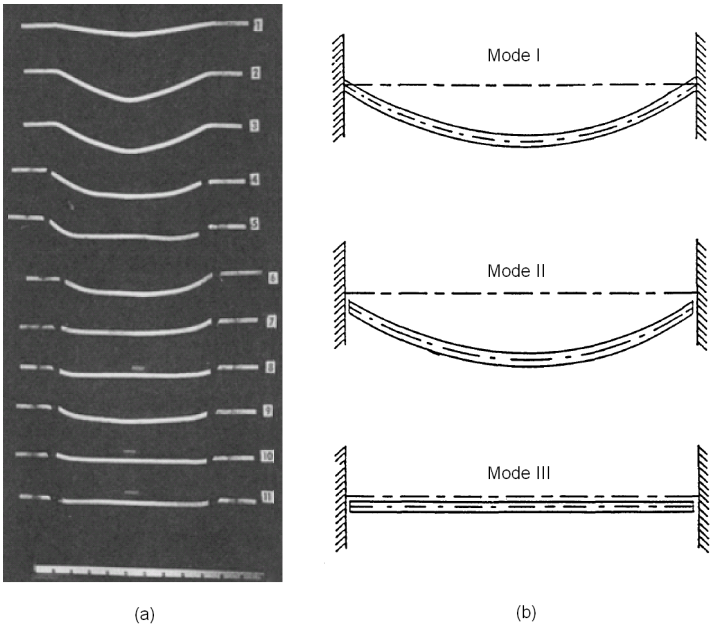

Figure 2.2: Failure modes as defined by Menkes & Opat [48]

Table 2.2: Modes of Failure according to Nurick & Co-workers [67, 70]

Mode	Description
I	Large inelastic deformation
Ia	Large inelastic deformation with necking around part of the boundary
Ib	Large inelastic deformation with necking around the entire boundary
II*	Large inelastic deformation with partial tearing around part of the boundary
II	Tensile tearing at the boundary
IIa	Tearing with increasing midpoint deflection with increasing impulse
IIb	Tearing with decreasing midpoint deflection with increasing impulse
III	Transverse shear failure at the boundary

Note: Modes IIa and IIb are only applicable to quadrangular plates.

structures. Note that in both Tables 2.1 and 2.2 the definition of Mode III does not include a reference to the plastic deformation, or lack thereof. In fact, some authors have focused on the nature of the rupture, *i.e.* necking or shear, regardless of the global plastic deformation [4, 66]. This approach has certain drawbacks. A rupture focused definition reduces the notion of failure modes to become merely another term for tensile necking or shear. It does not allow for the possibility that Mode I behaviour could transition directly into shear rupture, or that localized Mode III failure could be accompanied by large plastic deformation, as could occur in structures that have a more complex form than simple beams or plates. Furthermore, Langdon & Schleyer [118] conducted microstructural investigations of the fracture zone and observed dimples elongated in the direction of plate motion indicating mixed mode failure.

It will be argued in Section 6.1.1 that the distinction should focus on whether global plastic deformation occurs prior to rupture or not, regardless of the type of rupture. Furthermore, it will be shown that this approach retains the original distinctions with respect to the work of Menkes & Opat [48] and

Nurick *et al.* [67, 70], while also allowing for the logical extension of the classification system to more complicated structural elements.

2.2 Uniform Shock Loading of Circular Plates in Air

Shock loading research has produced an extensive literature, as shown in Section 2.1.1, and yet suitable code validation data is surprisingly sparse. Three decades ago Nurick & Martin [6] remarked that there are far more theoretical studies published on the blast loading of plates than there are papers with experimental data. The present situation is much the same despite a significant increase in published data. The reason for this is that many of the reported experimental investigations do not involve a sufficient number of specimens and the reported data is often incomplete or not presented in a convenient form. In other words, there are a limited number of systematic experimental studies that are sufficiently documented for numerical model validation as defined in Chapter 1. In this work, the term 'systematic' implies a series of tests that is large enough for statistically significant trends to the discerned. Furthermore, the implications are that the loading increments are small enough to facilitate the identification of various modes of failure and the load intensities where transition from one mode to another occur.

This section contains a detailed review of experimental data for the uniform shock loading[7] of circular plates in air, with particular attention given to the results for mild steel plates. While the studies considered in this section do not conform to the strict definition of precision experiments as defined in Chapter 1, they represent the best data available in the open literature, as can be seen by the fact that they are still extensively referenced [7, 9–11]. Results from both explosive and shock tube loading techniques will be considered, including results from explosive driven shock tubes, *i.e.* 'blast tubes'.

2.2.1 Blast Loaded Plate Deflection Data

The experimental studies outlined in Section 2.1.1 cover a range of target shapes, sizes, material and loading conditions. Even within the subfield of circular plates there is considerable variation. Hence, to facilitate meaningful comparative and theoretical studies, the data from diverse tests need to normalized in some way. In their 1989 review of experimental work, Nurick & Martin [6] presented a dimensionless damage number ϕ, refered to as the dimensionless impulse, for circular plates subjected to a uniform impulsive load, which has the form,

$$\phi = \frac{I}{\pi R_o H^2 \sqrt{\rho \sigma_y}} \tag{2.1}$$

where I is the total impulse while R_o, H, ρ and σ_y are the radius, thickness, density and quasi-static yield stress of the plate, respectively. Equation (2.1) is an extension of the Johnson damage number [5] and was formulated using dimensionless analysis. Furthermore, Cloete *et al.* [52] defined the dimensionless

[7] In this thesis, the term 'blast loading' will be used exclusively to imply explosive loading, while 'shock loading' can include shock tube data. Pressure pulse loads with significant rise times will not be considered.

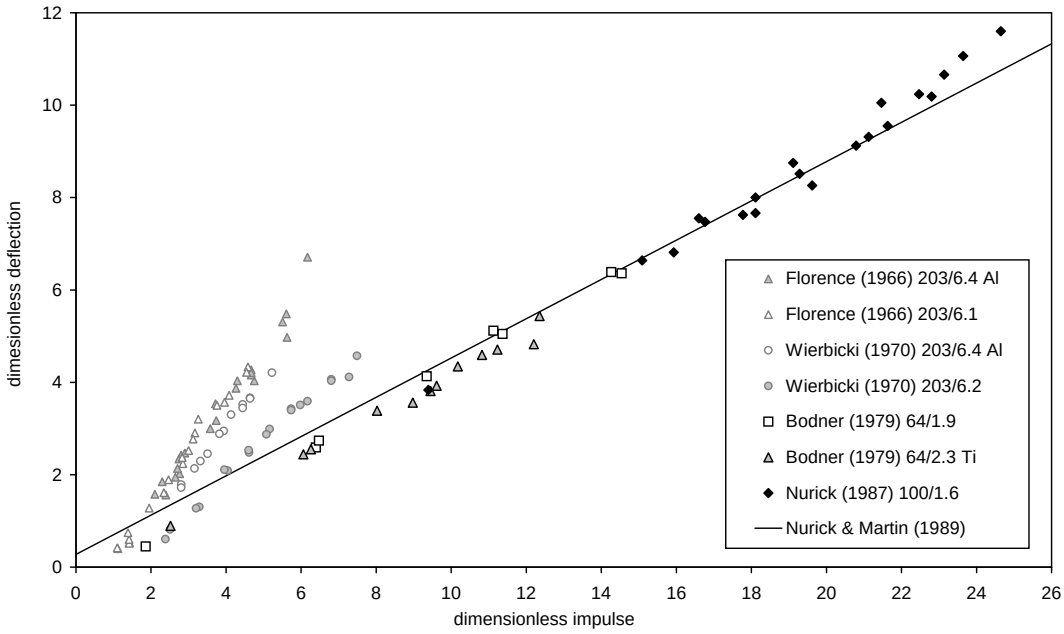

Figure 2.3: Experimental data for impulsively loaded circular plates due to Florence [36], Wierzbicki & Florence [37], Bodner & Symonds [56] and Nurick *et al.* [60] superimposed on the regression fit due to Nurick & Martin [5] given in Equation (2.3). The numbers after the dates in the legend indicate the diameter and thickness of the plate in mm, while materials other than steel are indicated by Al (aluminium) and Ti (titanium).

deflection δ as,

$$\delta = \frac{\tilde{w}}{H} \tag{2.2}$$

where $\tilde{w}$ is the maximum deflection. Figure 2.3 shows the result of applying equations (2.1) and (2.2) to the data of Florence [36], Wierzbicki & Florence [37], Bodner & Symonds [56] and Nurick *et al.* [60]. In addition, Figure 2.3 shows the regression fit derived by Nurick & Martin [5] which has the form,

$$\delta = 0.425\phi + 0.277 \tag{2.3}$$

with a correlation coefficient of 0.974.

Figure 2.3 represents all the data for uniformly loaded plates available to Nurick & Martin at that time. Figure 2.4 shows the data from further work by Nurick & co-workers [60, 68–70] along with the data for mild steel due to Bodner & Symonds [56]. To the author's knowledge, Figure 2.4 constitutes all the data available in the open literature for the large deflection of circular mild steel plates subjected to uniform impulsive loads due to short stand-off explosive charges.

While the regression derived by Nurick & Martin is correct for the data they considered, it nevertheless possesses the curious feature of a positive y-intercept. The physical implication is that a plate would have a non-zero positive deflection before any load is applied, which cannot be correct. This data will be revisited in Section 3.2.1, where reasons for the positive y-intercept of the regression derived by Nurick & Martin will be considered and a new correlation will be presented.

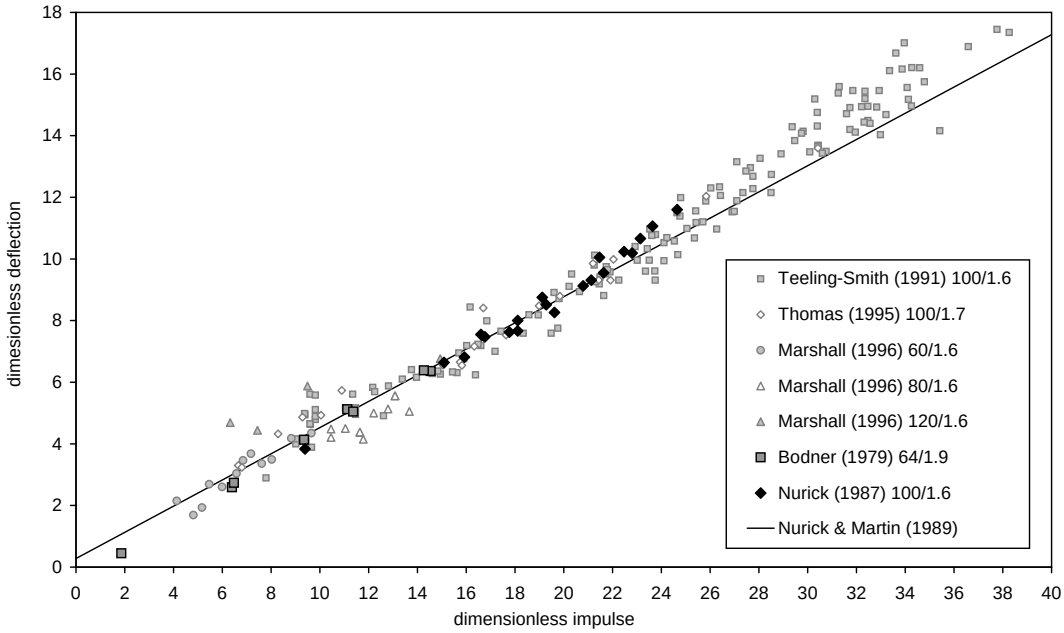

Figure 2.4: Experimental data for impulsively loaded circular steel plates due to Bodner & Symonds [56] and Nurick & co-workers [60, 68–70] superimposed on the regression fit due to Nurick & Martin [5] given in Equation (2.3). The numbers after the dates in the legend indicate the diameter and thickness of the plate in mm.

2.2.2 Blast Loaded Plate Response Duration

As mentioned in Section 2.1.3, the final maximum deflection is the dominant displacement diagnostic in blast tests and, by comparison, relatively few studies have reported deflection histories. Furthermore, among this smaller set of results, only Bodner & Symonds [56] and Nurick *et al.* [60] used short stand-off non-localized charge configurations, *i.e.* an experimental loading as close as practically possible to a uniform ideal impulsive loading. This data, though over twenty years old, still constitutes the best available in the literature[8]. Continuous central plate deflection histories where reported by Nurick [61], who used a light occlusion technique, and by Bodner & Symonds [56], who used a capacitive sensor. The time to peak deflection as a function of blast impulse is shown in Figure 2.5.

Two features of the duration data show trends that contrast with those of the deflection data, namely: the duration does not appear to increase with impulse and the data shows more scatter. The former trend was anticipated by Taylor [15], who was the first to analytically consider the impulsive deformation of plastic plates. He argued that the response would be analogous to that of a linear vibrating membrane, which is well understood and known to have a constant period regardless of the displacement. The implication is that the response time is independent of the magnitude of the deflection, and consequently, independent of the magnitude of the impulse. This observation suggests that it is possible to define a dimensionless time parameter that is consistent with the displacement and impulse parameter. A definition of a dimensionless time parameter will be proposed in Section 3.2.3 since there does not appear to be such a definition in the literature for the large deflection of plastic plates.

[8]This situation is expected to change in the near future as digital image correlation techniques become more widespread and are applied to short stand-off blast testing.

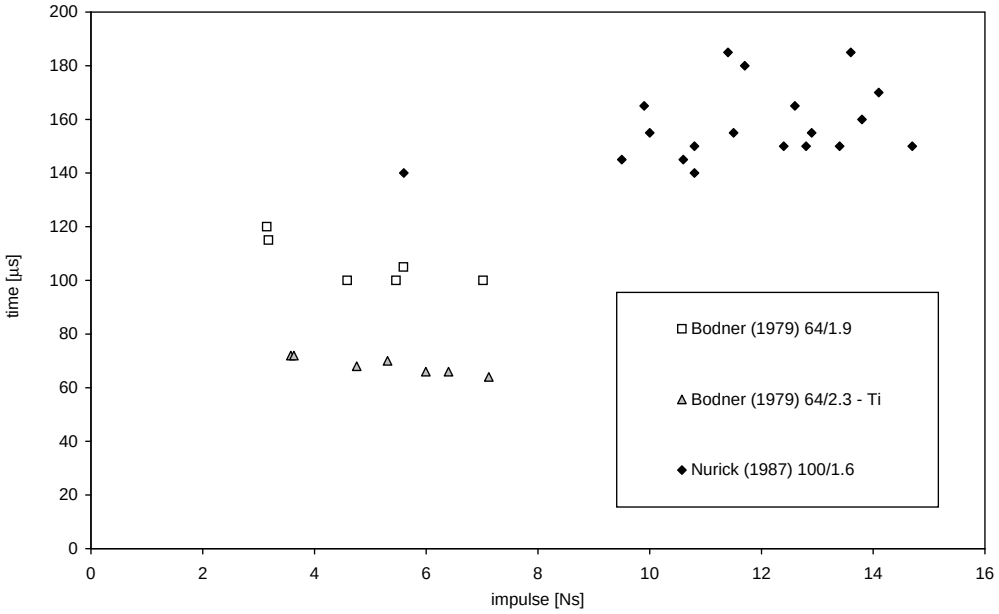

Figure 2.5: Deflection duration, *i.e.* time to maximum deflection, data for impulsively loaded circular plates due to Bodner & Symonds [56] and Nurick *et al.* [60]. The numbers after the dates in the legend indicate the diameter and thickness of the plates in mm, while materials other than steel are indicated by Ti (titanium).

Since the work of Taylor, the membrane analogy has been used extensively and is reviewed in detail in Section 2.3.5. It will be shown that the membrane approach leads to great insight, but contains a problematic feature in that it implies a sinusoidal deformation history for any point on the plate. This is not supported by experimental results, such as those shown in Figure 2.1. A shock loaded plate does not immediately assume the shape of a vibrating membrane. In fact, under impulsive loading the plate centre has a constant velocity, and hence linear displacement curve, for the majority of the response duration, as shown in Figure 2.6, which is due to Nurick [61]. A closed form model that captures both the membrane like behaviour and the initial constant velocity of the plate centre will be presented in Section 4.2.

The second feature mentioned above, *i.e.* the relatively large scatter in the response time, does not appear to have been addressed in the literature. This feature is of particular interest because the very same data

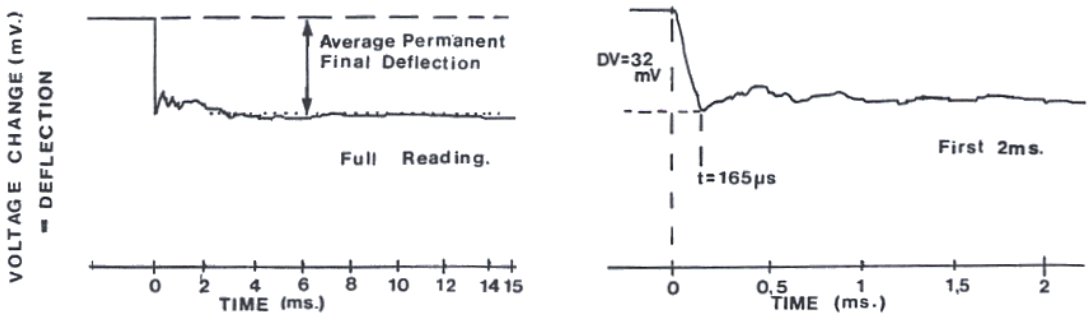

Figure 2.6: Measured deformation history for a blast loaded circular plates due to Nurick [61] using a light occlusion technique where an increasing deflection produced a decreasing signal.

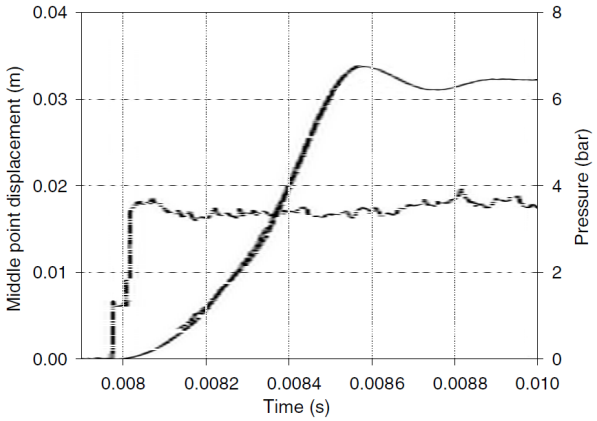

Figure 2.7: Measured pressure and deformation history for a shock loaded circular plates due to Stoffel [98].

shows little scatter when plotted in terms of deflection, as shown in Figure 2.3. Furthermore, the data due to Nurick *et al.*, which shows greater spread, appears to have a distinct lower limit. This behaviour will be discussed further in Section 3.3.4.2.

2.2.3 Shock Tube Loaded Plate Deflection Histories

The data considered in Section 2.2.1 all result from systematic short stand-off blast testing, *i.e.* impulsive shock loading. There do not appear to be any systematic laboratory scale tests on circular plates subjected to uniform dynamic shock loads. A number of studies involving the shock loading of plates or panels in air using a shock tube have been reported [34, 96, 98, 99, 101, 102]. However, the published results for metal plates are insufficient for statistically significant dimensionless regression analysis, similar to that conducted for impulsively loaded plates. Nevertheless, the available data from the experiments of Munday & Newitt [34] and Stoffel [98] are reviewed here for the sake of comparison with results reported in Sections 3.2.4, 3.2.5 and 4.3.8.

An example of the shock tube data due to Stoffel is shown in Figure 2.7. The pressure history approximates that of an ideal dynamic shock load, *i.e.* a pressure load that is applied instantaneously and held at a constant intensity until the plate motion is arrested. The resulting plate motion shows a gradually increasing plate velocity, which is distinct from the linear response curve for an impulsive load, as shown in Figure 2.6.

Munday & Newitt produced the first detailed deflection history recordings, which are reproduced in Figure 2.8. The tests were conducted on thin copper plates[9] that were between 0.033 mm and 0.081 mm thick with radii of 50.8 mm or 76.2 mm. Hence, rapid plate response was obtained despite the modest shock pressures of between 0.39 bar and 1.6 bar. Munday & Newitt employed a novel light occlusion technique to measure the deformation history of the centre of the plate. However, the specimen clamping fixture obscured the initial plate response, leading to the incomplete curves in Figure 2.8 and uncertainty regarding the point where the plate began to move. Furthermore, while viewing ports were installed in the

[9]In this thesis, for consistency, the test specimens of Munday & Newitt will be referred to as 'plates', since the term 'diaphragms', which may be more descriptive, will be used exclusively to imply the initiation mechanism of a shock tube.

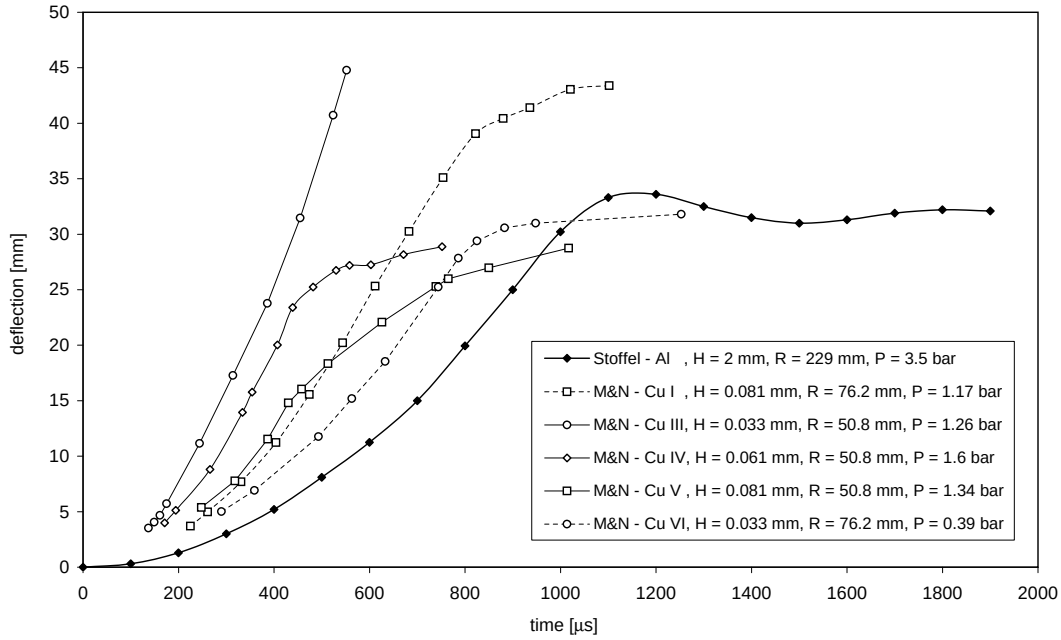

Figure 2.8: Deflection history data for dynamically loaded circular plates due to Munday & Newitt [34] and Stoffel [98]. The values in the legend represent the thickness and radius of the plate and the peak gauge pressure of the shock load. The initial portions of the curves due to Munday & Newitt were obscured by the clamping fixture.

test section of the shock tube to measure the shock velocity and trigger the recording equipment, neither the shock velocity nor the trigger delay is reported and hence the arrival time of the shock cannot be accurately determined. In lieu of a measured value, the temporal offsets of the curves in Figure 2.8 were estimated using shock wave theory, the details of which are discussed in Section 3.2.4. In addition to the deflection history, Munday & Newitt reported the permanent residual shape of the plates. However, this may not represent the deflection distribution of the plates after the initial shock loading since subsequent pressure pulse reverberation in the shock tube may have caused reloading[10]. Hence, the final plate shapes will not be considered for comparison with theory.

Following the work of Munday & Newitt there does not appear to have been any studies of shock loading of metal plates using a shock tube until the work of Stoffel [98], almost fifty years later[11]. Stoffel reports that the primary motivation for the shock tube work was for code validation with a focus on long term behaviour. A test is reported on a 2 mm thick aluminium plate with a clamped radius of 229 mm. The displacement of the centre of the plate specimen was measured using a capacitive sensor, giving a complete displacement history, and the pressure history was measured a short distance before the clamped boundary of the plate, using a piezoelectric sensor. The plate response is shown in Figures 2.7 and 2.8. The construction of the shock tube and the measured pressure history indicate that subsequent loading due to pressure pulse reverberations in the shock tube are small, which implies that the recovered plate

[10] Modern shock wave analysis packages are capable of resolving this issue, but it was not pursued during this work.

[11] Stoffel does not appear to be aware of the work of Munday & Newitt, but does refer to the work of Gerard [32] in 1956, who recorded strain but not deflection histories.

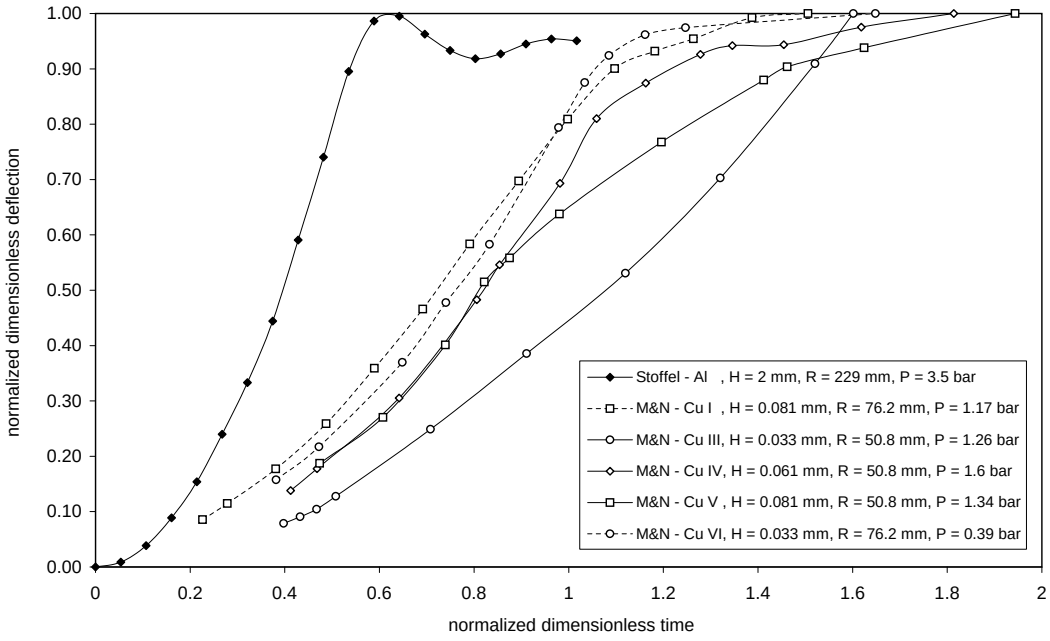

Figure 2.9: Deflection history data due to Munday & Newitt [34] and Stoffel [98] for shock tube loaded circular plates, normalized according to Equation (2.4).

shape should correspond to the plate shape after the initial shock. Unfortunately, only plate shapes obtained from numerical simulations appear to be reported.

While the data reported in Figure 2.8 is too limited to support general conclusions, certain trends are evident. The most evident trend is that increasing the pressure or decreasing the plate thickness leads to greater acceleration and final displacement, *e.g.* Munday & Newitt plates III, IV and V. However, the pressure and plate thickness do not appear to influence the time to reach the inflection point on the curves, *i.e.* the point on the curve where the gradient, and hence velocity, begins to decrease[12]. In other words, for a given diameter and nominal pressure, thicker plates deflect less, but take a similar time to reach their maximum deflection. By contrast, a comparison of curves I and V shows that, for the same plate thickness and nominal shock pressure, an increase the plate radius increases both the final deflection and deflection duration, but not the initial acceleration.

Munday & Newitt expressed their data in nondimensional form by normalizing the deflection with respect to the maximum deflection and using a dimensionless time parameter defined as,

$$\tau_{M\&N} = t\sqrt{\frac{a_0}{R_o}} \tag{2.4}$$

where a_0 is the measured initial acceleration. Munday & Newitt report that Equation (2.4) provided for a good correlation for all the plates, but this result could not be confirmed from the data provided in their paper. The data of Stoffel and Munday & Newitt expressed in terms of Equation (2.4) are shown in Figure 2.9. While the alignment is reasonable for most of the Munday & Newitt data, especially for a given plate radius, the data for plate III, which burst, does not correlate. The data for plate III

[12]Plate III of Munday & Newitt burst during testing.

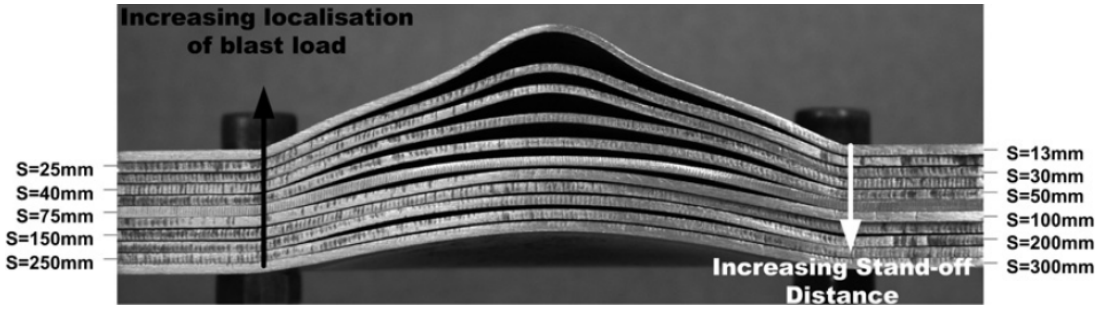

Figure 2.10: Effect of explosive stand-off distance 'S' for the blast tube loading of mild steel plates with a 5 g charge according to Jacob *et al.* [107].

are problematic because Munday & Newitt do not explain how the displacement of a burst plate is to be normalized, *i.e.* a definition for maximum displacement, analogous to that of the other plates, is not given. Furthermore, Equation (2.4) does not provide a good correlation when the data of Stoffel is added. An alternative to Equation (2.4) will be proposed in Section 3.2.4.

2.2.4 Blast Tube Data and Stand-off Effects

An alternative to the conventional diaphragm type shock tube is a blast tube, *i.e.* an explosively driven shock tube. As mentioned in Section 2.1.2, blast tubes can produce uniform shock loads of greater intensity than conventional shock tubes. Blast tubes have been used extensively [104, 106], but their application to laboratory scale blast loading of structures has been limited [105, 107].

Of particular interest is the work of Jacob *et al.* [107]. Jacob *et al.* conducted a series of blast tests on circular plates placed at the end of thick walled tubes of various lengths and loaded with an explosive charge at the other end, which was open. The plates were 1.9 mm thick and 106 mm in diameter, while tubes varied in length from 13 mm to 300 mm. The explosive charges were disk shaped with a constant diameter of 34 mm but with masses varying from 4 g to 15 g. The total impulse was measured by mounting the specimen fixture and loading system on a ballistic pendulum. The experimental configuration is very similar to that used in this work, which will be discussed in greater detail in Section 5.2.

The primary focus of the work of Jacob *et al.* was to investigate the effect of explosive charge stand-off distance on the deformation of mild steel plates. An example of the specimen response is shown in Figure 2.10, where the cross-sections of plates loaded with a 5 g charge are compared. Jacob *et al.* note that at short stand-off distances there is pronounced localized deformation in the form of a central bulge superimposed upon the global plate deformation. However, as the stand-off increases, the localized deformation reduces until it is no longer discernible.

Jacob *et al.* argued that a lack of localized deformation indicates that from a stand-off of 75 mm the blast load can be considered to be essentially uniformly distributed across the plate specimen. Furthermore, it was noted that for a given charge mass, the final central deflection is essentially constant for all the blast tube lengths from 75 mm to 300 mm, as is shown in Figure 2.11. The nature of a blast tube pressure distribution is discussed further in Section 5.3.2.3.

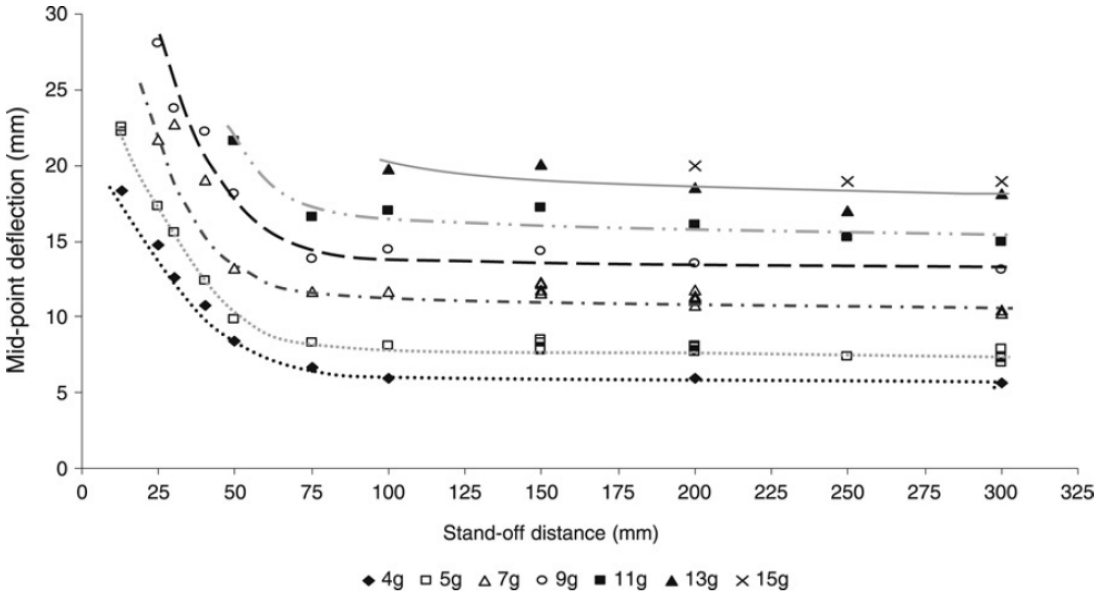

Figure 2.11: Effect of charge stand-off distance on central deflection for blast tube loaded of mild steel plates according to Jacob *et al.* [107].

Jacob *et al.* extended the dimensionless damage number proposed by Nurick & Martin [6], which accounts for differences in charge and plate diameters, to have the form,

$$\phi_S = \frac{I\gamma_S}{\pi R_o H^2 \sqrt{\rho\sigma_y}} \tag{2.5}$$

where the γ_S is a loading parameter with the form,

$$\gamma_S = \frac{1 + ln\frac{R}{R_c}}{1 + ln\frac{S}{R_c}} \quad \text{for} \quad (S \geq R_c) \tag{2.6}$$

where S is the stand-off distance and R_c is the charge radius. For instances where the stand-off distance is less than the charge radius, *i.e.* a localized load, the denominator is reduced to unity and the damage number of Nurick & Martin is recovered. The numerator of Equation (2.6) was introduced by Nurick & Martin to account for the fact that a localized load produces a greater central displacement than a uniform load of equivalent impulse. The denominator, added by Jacob *et al.*, has the effect of cancelling out the numerator when the stand-off distance is equal to the plate radius. In other words, Equation (2.6) states that, with respect to Mode I response, a localized load at a stand-off distance of one plate radius will produce that same effect as a uniform impulsive load of the same total impulse. The results reported by Jacob *et al.* show that Equation (2.5) produces an excellent correlation between the blast tube data and uniform short stand-off blast data considered in Section 2.2.1. Further analysis of the data of Jacob *et al.* is presented in Section 3.2.6.

2.2.5 Shock Loaded plate shapes

Many of the solution strategies pursued in the analytical investigations mentioned in Section 2.1.1 were inspired by the plate shapes produced during blast loading events. Hence, before presenting a more detailed review of some of the analytical methods, it is instructive to consider the shapes of recovered plate specimens.

Figure 2.12 shows typical final shapes of plate specimens recovered after blast testing. The shapes have been normalized with respect to the maximum deflection to aid comparison. The three experimental data sets represent a reasonably broad range of loading durations. The data due to Bodner & Symonds [56] was obtained using thin sheets of rolled sheet explosive mounted on 6.35 mm polystyrene disks. In other words, the blast load was evenly spread with a short stand-off distance and thus represents the experimental charge configuration that most closely approximates an ideal short duration impulsive load. Teeling-Smith & Nurick [67] used a similar configuration where concentric rings of plastic explosive mounted on 12 mm polystyrene disks. It will be shown in Section 5.3.1.3 that this configuration also gives a reasonably uniform impulse distribution, but does not have a negligible blast duration, *i.e.* it is not an ideal short duration impulsive load. Finally, the data due to Jacob *et al* [107] was obtained using a blast tube which, as shown previously, attenuates the blast load, causing it to be less ideally impulsive and more dynamic in character. It is interesting to note that despite the differences in the load configurations, Figure 2.12 shows that the final plate shapes are reasonably similar. Unfortunately, for reasons mentioned previously, experimental plate shapes from dynamic shock tests such as the work of Munday & Newitt [34] and Stoffel [98] are not available.

Also shown in Figure 2.12 are four curves used in theoretical models. As will be discussed in Section 2.3, the parabola and Bessel function represent the displacement profile of a circular membrane under static pressure and vibrating conditions. The cosine and conical functions are included since they are used by some authors. It is evident that the Bessel function most closely approximates the experimental data. This is in keeping with the view of Taylor [15], as discussed in Section 2.2.2, who argued that the response would be analogous to that of a linear vibrating membrane. Furthermore, it is also clear that the parabolic and cosine curves are reasonable approximations which should be considered if the use of a Bessel function ever proves to be mathematically intractable. By contrast, the data indicates that the conical shape prediction purely on the basis of moving plastic hinges is not a good approximation. However, the aforementioned does not imply that moving plastic hinges should not be considered. In fact, Figure 2.1 would indicate that travelling hinges are an intrinsic part of dynamic plate behaviour, but that they should not be considered in isolation. The relationship and interaction between travelling hinges and other deformation mechanisms is considered in Chapter 4.

2.3 Analytical modelling of Circular Plates

The theoretical analysis of the behaviour of impulsively loaded structures is a complicated problem. The experiments reviewed in Section 2.2 show that plate deformations are typically large and take place over short time intervals, inducing both geometric and material non-linearities through large strains and high strain rates. Additional complications arise from boundary conditions, which vary from rounded to sharp

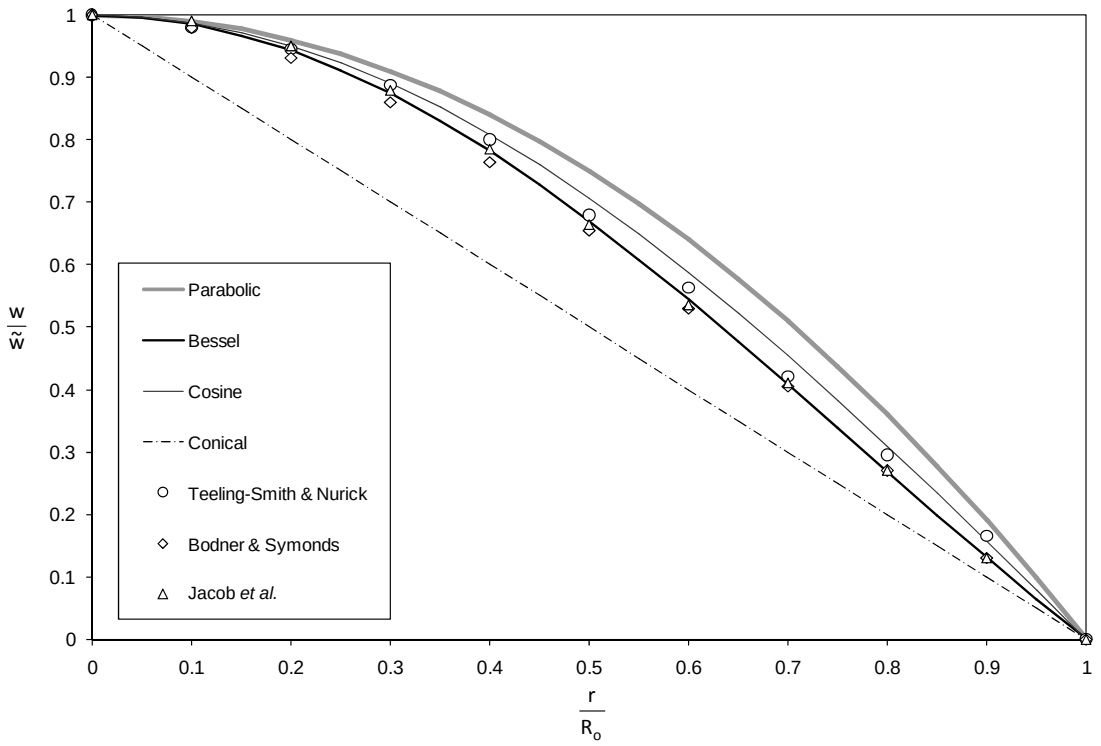

Figure 2.12: Various assumed plate shapes compared with normalized experimental data due to Bodner & Symonds [56], Teeling-Smith & Nurick [67] and Jacob *et al.* [107].

and clamped to built-in, and loading conditions, which vary from near ideal short duration impulsive or constant pressure shock loading to pressure pulses of variable profiles and durations, such as exponentially decaying blast waves. Furthermore, the structural response can affect the nature of the load, such as shock-structure interactions discussed in Section 2.2.3.

The challenging nature of the aforementioned impulsive loading and response phenomena renders the problem intractable for exact theoretical analysis. There appear to be no published closed form analytical solutions for the general problem and a detailed treatment thereof invariably requires the use of numerical techniques. Nevertheless, experimental investigations have inspired the large variety of analytical approaches, some of which are reviewed in Section 2.1.1. Consequently, despite their inherent difficulties and limitations, several approximate analytical solutions have been developed for specific cases where simplifying assumptions can be made.

Approximate analytical solutions are useful for a variety of reasons. For the early studies, there was simply no other option since computers, and associated techniques, were in their infancy. However, even when numerical techniques became widely available, there was a sustained effort in developing analytical solutions. This is partly due to their form, which is typically compact and hence useful for preliminary design work or as starting points for numerical studies, but the primary motivation is the physical insight that analytical solutions provide. The simplifying assumptions required to obtain a solution for a given response regime reveal the dominant mechanisms of deformation that characterize the response regime and govern the behaviour. Furthermore, closed form solutions allow for the extraction of dimensionless

parameters which are useful for the interpretation and reporting of experimental and numerical results. In essence, while numerical techniques are required for detailed analysis, it is the analytical solutions that provide the 'big picture' theoretical framework within which numerical results can be interpreted.

Analytical impulsive loading studies are typically focused on relatively simple structures, such as beams and plates of various cross-sections and configurations (circular, quadrangular, built in, *etc.*) [5]. A complete and unambiguous categorization of these solutions is beyond the scope of this work. Instead, the area of relevance is the subsection of the literature devoted to impulsively loaded circular plates. The majority of these studies have focused on peripherally clamped solid (PCS) plates with the remainder focused on peripherally clamped annular (PCA) plates. There do not appear to be any analytical studies of peripherally clamped centrally supported (PCCS) circular plates other than that those published as part of this work [51–53], which will be discussed in Chapter 7. The area of interest is further curtailed by the observation that the experimental results reviewed in Section 2.2 all exhibit large deflection behaviour. The majority of the theoretical studies on PCS and PCA plates are concerned with small deflections, where bending effects are considered to be dominant [4]. By contrast, a relatively small number of studies consider PCS and PCA plates with large deflections, where membrane effects are regarded as dominant.

In light of the preceding considerations, the primary focus of this section is to provide a detailed review of closed form solutions for shock loaded circular plates in the large deflection regime, although some small displacement and static solutions will be discussed as required. Firstly, the governing differential equation of motion and typical deformation profiles will be discussed. Thereafter, published solutions for both PCS and PCA configuration will be considered. Particular emphasis will be placed on models that result in simple closed form solutions, as opposed to series solutions[13]. This will include a detailed review of three most common analytical models for the large deflection of impulsively loaded circular plates. These will be referred to as the energy method, the membrane mode method and the travelling hinge method. The relative merits of these models will be discussed in Chapter 3. All three models approximate the load as an ideal short duration impulsive load and hence this will be considered beforehand. The purpose throughout is to provide a basis for comparing and correlating the published experimental results and provide a starting point for the analyses in Chapter 7.

2.3.1 Displacement Profiles

The primary distinction between the various published analytical solutions for blast and shock loaded plates depends, in essence, on the way in which the deflection profile is obtained. The most rigorous method of determining the plate profile is through solving the relevant differential equations of motion. In other words, the deformed shape is not assumed *a priori*, but is a result of the analysis. Reissner [119] presented the full non-linear differential equilibrium equations for a statically loaded elastic plate undergoing large deflections, which Jones [43] extended to included inertia terms. These equations represent an extremely difficult mathematical problem and, to the author's knowledge, no exact solution for the full non-linear dynamic problem has been published.

Published analytical solutions typically reduce a plate deformation problem to a tractable form by using various approximations and assumptions to simplify the equations of motion. A significant assumption

[13] Bessel functions, which are in themselves series solutions, will be used, but their evaluations lead to constants that are invariant for a given plate configuration and therefore the final expressions are not regarded to be series solutions.

relates to the relative magnitude of the maximum deflection expected to occur. This approach has met with great success for circular plates undergoing small deflections, *i.e.* a maximum deflection of less that a plate thickness, where bending effects tend to dominate and membrane effect can be ignored [4], rendering the equations of motion tractable. Conversely, for large deflections, *i.e.* a maximum deflection of more than a plate thickness and less that a plate radius, membrane effects dominate and bending effects are not typically considered, making the equation of motion more amenable to analytical treatment, but not to the degree that the small deflection assumption achieves. The definitions of the terms 'small' and 'large', given above, are representative of terminology used in the field of impact mechanics [4], and will be used in this context throughout this thesis.

Greater mathematical obstacles are encountered in problems involving moderate deflections, *i.e.* a maximum deflection of greater than half a plate thickness but a small fraction of a plate radius, where both bending and membrane effects, and their interactions, are present. Strictly speaking, neither the small nor large deflection approaches are applicable to moderate displacement problems and plate profile have to be assumed rather than derived. A few approximate solutions of this kind are discussed in Section 2.3.8, with a more detailed model presented in Section 3.3.7.

This work is primarily concerned with large deflections and hence, considering only the membrane terms in the equations of Reissner [119] and Jones [43], the equation of motion for a dynamically loaded axisymmetric membrane is,

$$\frac{d^2w}{dt^2} = \frac{\sigma_d}{\rho}\left[\frac{d^2w}{dr^2} + \frac{1}{r}\frac{dw}{dr}\right] + \frac{P}{\rho H} \tag{2.7}$$

where w is the out of plane displacement, t is the temporal variable, r is the radial position, σ_d is the dynamic flow stress, ρ is the density, P is the load pressure and H is the plate thickness.

Unfortunately, even when ignoring bending effects, Equation (2.7) still does not lend itself to analytical treatment, and only a few authors appear to have attempted such an approach. Richardson & Kirkwood [16] developed several approximate solutions for finite duration UNDEX loading of circular membranes, including a truncated series solution. For the case of an ideal impulsive load, Jones [43] developed a two phase solution where the first phase is assumed to be bending dominated, while the second phase is viewed as being membrane dominated with the solution of the first phase serving as initial conditions for the second phase. Both these aforementioned papers report solutions in the form of infinite series of Bessel functions, which are, in themselves, infinite series. In other words these solutions are not convenient or compact and have not been used extensively[14]. As mentioned previously, this work is primarily concerned with closed form solutions and hence the aforementioned analyses will not be considered in detail.

An alternative approach to seeking to derive the plate profile directly from Equation (2.7), is to assume *a priori* a deformed plate shape to be used in the analysis. Several authors have used variations of this approach and their efforts can be grouped into three distinct subsets, which, in this work, will be referred to as the membrane mode method, the energy method and travelling hinge method[15]. These three methods will be discussed in the Section 2.3.

[14] Wierzbicki & Nurick [63] and Wierzbicki & Florence [37] used infinite Bessel series, but, when applied to large deflections, the series were truncated to form single term descriptions.

[15] It is remarkable to note that all three these methods were introduced in the seminal work of Taylor [15].

In lieu of an exact treatment, Equation (2.7) can still be used to suggest which plate profiles would be useful for use in an approximate method. Ignoring the inertia term in Equation (2.7) gives,

$$\frac{d^2w}{dr^2} + \frac{1}{r}\frac{dw}{dr} + \frac{P}{\sigma_d H} = 0 \tag{2.8}$$

which is the differential equation for a circular membrane under a quasi-static pressure load. The solution for this case is well known [120],

$$w(r) = \bar{w}\left[1 - \left(\frac{r}{R_o}\right)^2\right] \quad \text{where} \quad \bar{w} = \frac{R_0 P}{4H\sigma_d} \tag{2.9}$$

where w is the deflection of the plate at radius r, $\bar{w}$ is the maximum quasi-static displacement and R_o is the outer radius of the plate.

As shown in Figure 2.12, the simple parabolic plate shape of Equation (2.9) provides a reasonable first order approximation to experimental data. Furthermore, it is convenient for analytical work and has been used extensively to study the dynamic behaviour of circular plates, even though it is not strictly applicable [15, 38, 66]. In this work, the parabolic shape will be used repeatedly in Section 3.3.7 and Chapter 7 to estimate the effects of membrane strain, radial displacement, bending strain and moving plastic hinges.

An alternative assumption for Equation (2.7) is to ignore the load term, which gives,

$$\frac{\partial^2 w}{\partial t^2} = c^2\left(\frac{\partial^2 w}{\partial r^2} + \frac{1}{r}\frac{\partial w}{\partial r}\right) \quad \text{where} \quad c^2 = \frac{\sigma_d}{\rho} \tag{2.10}$$

Equation(2.10) describes the free vibration of an axisymmetric membrane for which the solution is also well known [121],

$$w(r,t) = F(r)G(t) \tag{2.11}$$

The form of Equation (2.11) is based on the intrinsic assumption that the deformation profile of the plate is constant and that only the amplitude of the deformation changes. Figure 2.1 clearly shows that this is not true under impulsive loading conditions. Nevertheless, the technique has been pursued by several authors and will be discussed further in Section 2.3.5.

Differentiating and substituting Equation (2.11) into Equation (2.10) gives,

$$\frac{\rho}{\sigma_d} F\ddot{G} = G\left[F'' + \frac{1}{r}F'\right] \tag{2.12}$$

where the dot and prime superscripts represent temporal and spatial derivatives respectively. Equation (2.12) can be separated into two ordinary differential equations,

$$\frac{d^2F}{dr^2} + \frac{1}{r}\frac{dF}{dr} + k^2\frac{\rho}{\sigma_d}F = 0 \tag{2.13}$$

and,

$$\frac{d^2G}{dt^2} + k^2G = 0 \tag{2.14}$$

Equation (2.14) deals with the temporal response which will be considered in Section 2.3.5, whereas Equation (2.13) describes the shape of the plate for which the general solution is,

$$w(r) = \tilde{w}A\left[J_0\left(\Lambda\frac{r}{R_o}\right) + BY_0\left(\Lambda\frac{r}{R_o}\right)\right] \quad \text{where} \quad k = \frac{\Lambda}{R_0}\sqrt{\frac{\sigma_d}{\rho}} \tag{2.15}$$

The coefficients A and B are constants while the functions J_0 and Y_0 represent zeroth order Bessel functions of the first and second kind. The form of the argument of the Bessel functions has been chosen such that a root of Equation (2.15) will coincide with the outer edge of the circular plate where the displacement vanishes. In the case of a solid circular plate the second Bessel term must fall away since it is unbounded at the centre of the plate. This implies that the value of Λ corresponds to the first root of J_0 [16]. Hence,

$$w(r) = \tilde{w}J_0\left(\Lambda\frac{r}{R_o}\right) \quad \text{where} \quad \Lambda = 2.4048 \tag{2.16}$$

Despite the simple form of Equation (2.16) it provides an accurate fit to the experimental data, as shown in Figure 2.12. This observation suggests that it may be appropriate to view other plate shapes in terms of vibrating membranes.

The parabolic and Bessel shapes, given in equations (2.9) and (2.16) respectively, represent the extreme plate profiles of a dynamically deformed plastic membrane. In other words, a complete solution of Equation (2.7) will, in all likelihood, be a combination of these two solutions and must lie between the two extreme cases. Hence, many analytical approaches to the present problem have been based in these two profiles as will be discussed in Section 2.3. This reasoning also explains why the sinusoidal profile was used by Duffey [38].

The data in Figure 2.12 and the preceeding analyses do not support the assumption of a conical plate profile. However, the conical profile has been used extensively in small displacement studies where it represents the static collapse profile of circular and annular plates undergoing bending deformation [4]. A conical profile also results from using a travelling hinge analysis approach, as will be discussed in Section 2.3.6. In this thesis the conical profile will be used to analyse annular plate motion in Section 7.2.2.

2.3.2 The Perfectly Plastic Membrane Assumption

Several published analytical models for impulsively loaded circular plates use the perfectly plastic membrane assumption [37, 38, 43, 45, 63, 122, 123]. In this approach, the stress in the plate is assumed to be constant and homogeneous, while all strains are assumed to arise from membrane type deformations. This implies that the effects such as elastic deformation, radial displacements, bending strains, strain hardening and strain rate effects are ignored.

[16] Note that the interpretation of Λ used here differs from that used by Symonds & Wierzbicki [122].

Taylor [15] appears to be the first to have considered a blast loaded plate to behave as a perfectly plastic diaphragm and argued that its response would be analogous to a soap film or stretched elastic membrane. He noted that the stress in a soap film or stretched membrane is uniform regardless of the amount of deformation and that this would also be the case for a perfectly plastic diaphragm. An analogous membrane would have the same dimensions and mass as the plate, with the tension equal to the product of the yield stress and thickness of the plate. As shown in the previous section, the shape of a vibrating or hydrostatically loaded membrane corresponds closely to the measured shapes of recovered blast loaded thin plates. This alone would vindicate Taylor insight and justify several subsequent studies that were based on similar assumptions.

The majority of the models reviewed in this chapter and those developed as part of this thesis, which will be presented in Chapters 4 and 7, have been based on Taylor's membrane assumption. However, the models will be used to interpret experimental data obtained using metal plate specimens for which the strains and strain rates are neither constant nor homogeneous. Consequently, the flow stress distribution does not strictly conform to the membrane analogy. To address this, published models that account for strain and strain rate effects will be reviewed in Section 2.3.7, while bending strains and radial displacements will be considered in Sections 2.3.8, 3.3.6 and 3.3.7. It will be shown that these refined models establish the domain within which the membrane assumption is valid and provide simple correction factors that allow various effects, such as strain and strain rate sensitivity, to be accounted for in an averaged sense.

2.3.3 Ideal Impulsive Loading

As mentioned in Section 2.1.1, researchers have used sheet explosives at very small stand-off distances to obtain experimental loadings that approach the ideal limit of an impulsive loading, *i.e.* a load with a duration that is negligible compared to the duration of the structural response. From the seminal work of Taylor [15] and Richardson & Kirkwood [16], it was realized that under these instances the precise pressure history is irrelevant and only the total impulse needs to be considered. The implication is that the acceleration phase of the plate can be ignored and that the total impulse is transferred instantaneously to the plate, giving it an initial velocity distribution. Implicit in this approximation is the assumption that plastic dissipation in the region of the boundary during load application may be neglected. In this thesis, this type of load will be referred to as an ideal impulsive load (IIL), so as to distinguish it from loads of a small but finite duration, which are generally also referred to as impulsive loads. The validity of the ideal impulsive assumption will be considered in Section 4.3.

Ideal impulsive loads with a variety of initial velocity distribution are found in the literature. Some velocity distributions are chosen to represent a particular blast load distribution [63] while others are chosen to suite a particular form of analytical solution [122] or to avoid certain phenomena like plastic hinges [44]. However, the typical assumption is that of a simple uniform velocity distribution [38, 45, 66].

For an instantaneous uniform initial velocity field, Duffey [38] gives the initial momentum and kinetic energy in the following form,

$$I = mV_0 \quad \text{and} \quad E_{k,0} = \frac{1}{2}mV_0^2 \tag{2.17}$$

where I is the impulse transmitted by the load, m is the mass of the plate, V_0 is the initial uniform plate velocity and $E_{k,0}$ is the initial kinetic energy. The mass of a solid circular plate is,

$$m = \rho \pi R_o^2 H \tag{2.18}$$

Eliminating the initial velocity gives the initial kinetic energy for a given impulse,

$$E_{k,0} = \frac{I^2}{2m} \tag{2.19}$$

The effect of a non-uniform initial velocity will be considered in Section 2.3.5.

2.3.4 Energy Methods

One of the simplest, and most widely used, methods for analyzing the large deflections of impulsively loaded plates is the energy method [15, 38, 45, 66]. Taylor [15] appears to be the first to use the energy method to analyse blast loaded plates and assumed the deformed plate shape to be identical to a hydrostatically loaded membrane, *i.e.* a parabola. The essential principle of this approach can be traced back to Lord Rayleigh's energy method for estimating the natural frequencies of continuous structures using their quasi-static shape as a starting assumption [124]. Other researchers who used this method are Duffey [38], who used various sinusoidal and power law profiles to match experimental profiles, Lippmann [45], who used a Bessel profile based on a derivation similar to that in Section 2.3.1, and Wen [66], who used a parabolic profile and included bending and strain rate effects which will be discussed in Sections 2.3.8 and 2.3.7. In this thesis the notation of Duffey [38] will be used (with some modification and extension) and the work of other authors will be translated for the sake of comparison.

2.3.4.1 Parabolic Displacement Profile

Duffey [38] considered a uniform ideal impulsive load exerted on solid circular perfectly plastic plate. The initial kinetic energy of the plate is given by Equation (2.19). This energy is dissipated through plastic work as the plate deforms and by equating the total initial kinetic energy to the total plastic work, the final deflection can be calculated. To calculate strain energy the displacement profile of the plate must be assumed *a priori*. Duffey investigated various transverse displacement profiles, including a parabolic profile with the form,

$$w(r) = \tilde{w}\left[1 - \left(\frac{r}{R_o}\right)^2\right] \tag{2.20}$$

where $\tilde{w}$ is the central deflection. Duffey considered only transverse displacements, which is a common assumption that has been used by many researchers when addressing the topic of impulsively loaded plates [37, 43, 45, 63, 66, 122, 123]. Duffey justified this approach by presenting arguments to show that the effect of bending and radial displacements on the total strain energy are negligible. These arguments will be considered in greater detail in Section 2.3.8. Given this assumption, the radial strain can be obtained

from the displacement distribution using,

$$\epsilon_r \approx \frac{1}{2}\left(\frac{dw}{dr}\right)^2 \tag{2.21}$$

The expression for the radial strain is written as an approximation to emphasize that terms related to bending, radial displacements and higher order effects have been omitted [38, 43, 119]. Hence, accurate predictions can only be expected for large deflections, as defined in Section 2.3.1. The effect of radial displacements and bending are considered in Sections 3.3.6 and 3.3.7 respectively. Equation (2.21) begins to become inaccurate toward the upper end of the large displacement regime and additional non-linear terms are required beyond this point. However, in practice, failure mechanism, such as boundary shear, tend to manifest before displacement magnitudes approach a plate radius, and, therefore, additional non-linear terms will not be considered.

In the case of a parabolic distribution, the radial strain can be expressed as,

$$\epsilon_r = 2\tilde{w}^2\frac{r^2}{R_o^4} \tag{2.22}$$

Consequently, the expression for plastic work has the form,

$$W_P = \int_V \sigma_d \epsilon_r \, dV \quad \text{where} \quad dV = 2\pi r H \, dr \tag{2.23}$$

The integral subscript V implies integration over the volume of the plate, while σ_d is the dynamic flow stress. Duffey assumed that the dynamic flow stress is equal to the quasi-static yield stress. However, in this thesis, to facilitate the comparison of various models, the mean flow stress will be expressed as,

$$\sigma_d = \alpha\sigma_y \tag{2.24}$$

where α is a constant intended to account for strain hardening and strain rate sensitivity and σ_y is the quasi-static yield stress. A simple iterative procedure to estimate α as a function of the average strain and strain rate will be reviewed in Section 2.3.7. Substituting equations (2.22) and (2.24) into Equation (2.23), the plastic work done during the deformation of the plate is thus,

$$W_P = \int_0^{R_o} \alpha\sigma_y \left(2\tilde{w}^2\frac{r^2}{R_o^4}\right) 2\pi r H \, dr = \pi H \alpha\sigma_y \tilde{w}^2 \int_0^{R_o} 4\frac{r^3}{R_o^4} \, dr = \pi H \alpha\sigma_y \tilde{w}^2 \tag{2.25}$$

Finally, equating the plastic work to the initial kinetic energy using equations (2.19) and (2.25) results in an expression for the final central deflection in terms of the total impulse[17]

$$\tilde{w} = \frac{I}{\pi R_o H\sqrt{2\rho\alpha\sigma_y}} \tag{2.26}$$

[17] In this thesis, unless otherwise stated, $\tilde{w}$ will refer to the final maximum deflection of a plate and δ will refer to the final maximum dimensionless deflection. However, for a solution that includes time $\tilde{w}$ and δ will refer to the maximum deflection at a given time, while the subscript 'max' will be added to indicate the final state. For multi-phase models the subscript 'I' and 'II' will indicate the state at the end of Phases I and II.

2.3.4.2 Bessel Displacement Profile

There do not appear to be any published solutions for impulsively loaded circular plates using the energy method in conjunction with an assumed displacement profile in the form of a Bessel function, as given in Equation (2.16). The Bessel function is typically used when treating the plate as a vibrating membrane [15, 45, 122]. However, Lippmann [45], in addition to reporting a membrane solution, also provides an expression for the energy dissipated by the plastic membrane as a function of the central displacement. When expressed in the notation used in this thesis, the plastic work for Bessel function displacement profile has the form,

$$W_P = \frac{1}{2}\lambda\pi H\alpha\sigma_y\tilde{w}^2 \quad \text{where} \quad \lambda = \Lambda^2 J_1^2(\Lambda) = 1.5589 \tag{2.27}$$

Note that the result has the same form as the solution based on the parabolic distribution, but has a different constant. In Section 3.3.1, it will be shown that Equation (2.27) can be derived using Duffey's energy approach and the results will be compared to those obtained using the parabolic displacement distribution.

2.3.5 Membrane Mode Methods

A well known solution[18] for the ideal impulsive loading of a circular plate is that due to Symonds & Wierzbicki [122], who made use of the "mode approximation" technique developed by Martin & Symonds [42]. They argued that qualitatively meaningful results could be obtained by considering only the equations of the final phase of motion, *i.e.* the solution would not account for transient plate profiles such as those shown in Figure 2.1. The result of this simplification was that the plate could be treated as a perfectly plastic membrane, although some corrections for strain and strain rate effects were included, which will be discussed in Section 2.3.7.

While, a detailed review of the membrane mode method is beyond the scope of this work, the salient features will be discussed. In accordance with the technique, Symonds & Wierzbicki assumed that the plate deformation profile can be approximated as[19],

$$w(r,t) = \tilde{w}(t)\phi(r) \tag{2.28}$$

where $\tilde{w}(t)$ is a scalar function of time and $\phi(r)$ defines the mode shape of the displacement field. Equation (2.28) is essentially identical to Equation (2.11) and consequently led to a set of differential equations identical to Equations (2.13) and (2.14) for which the solution is given by Equation (2.16), *i.e.* the mode shape is a Bessel function.

The Bessel function form of the solution obtained by Symonds & Wierzbicki, originally suggested by Taylor [15], had been reported previously by Lippmann [45]. However, neither Taylor nor Lippmann provided a means of accommodating the starting condition of the plate. Taylor sought only to obtain an expression for the deflection duration and, therefore, did not consider the initial velocity for reasons that will be discussed later in this section. Similarly, Lippmann presented the expression given in

[18] Jones [4] refers to Symonds & Wierzbicki's work as a 'more exact' solution.
[19] The notation of Symonds & Wierzbicki has been modified to conform to that used in this thesis.

Equation (2.27) for the energy dissipated during plate deformation and implied that this should be equated to the initial kinetic energy of the plate, but did not report a means of calculating the initial kinetic energy for a given impulsive load. An energy solution using Lippmann's plastic work expression in conjunction with Duffey's initial kinetic energy expression will be discussed in Section 3.3.2.2.

Symonds & Wierzbicki assumed that an impulsive load imparts an initial uniform velocity V_0 to the plate and obtained the magnitude of V_0 using a similar approach to that of Duffey given in Equation (2.17) and (2.18). However, unlike energy methods, where V_0 is used to determine the initial kinetic energy, the mode approximation technique seeks to replace the initial uniform velocity distribution with a "best" approximation based on the assumed mode shape [42]. Obtaining the "best" approximation involves finding the initial maximum velocity of the mode shape by minimizing a functional as defined by Martin & Symonds [42], the details of which are beyond the scope of this thesis. For the problem considered by Symonds & Wierzbicki the minimization procedure resulted in the criterion,

$$\frac{\dot{\tilde{w}}_0}{V_0} = \frac{\int_0^{R_o} \phi r \, dr}{\int_0^{R_o} \phi^2 r \, dr} = \frac{\int_0^{R_o} r J_0\left(\frac{\Lambda}{R_0} r\right) \, dr}{\int_0^{R_o} r J_0^2\left(\frac{\Lambda}{R_0} r\right) \, dr} = \frac{\Lambda J_1(\Lambda)}{\frac{1}{2}\Lambda^2 J_1^2(\Lambda)} = \frac{2}{\Lambda J_1(\Lambda)} = 1.602 \tag{2.29}$$

where $\dot{\tilde{w}}_0$ is the initial velocity at the point of maximum velocity of the mode shape, *i.e.* the initial velocity of the centre of the plate. The value of 1.602 implies that an equivalent Bessel velocity distribution must have a maximum, *i.e.* central, velocity that is 60 % greater than that of the uniform velocity. A physical interpretation of the criterion will be discussed in Section 3.3.3.1.

Using the initial velocity condition given in Equation (2.29), Symonds & Wierzbicki found that solution to Equation (2.13) to be that given in Equation (2.16), while Equation (2.14) has the solution,

$$\tilde{w} = \tilde{w}_{max} \, sin\left(\frac{\pi}{2}\frac{t}{T}\right) \tag{2.30}$$

where $\tilde{w}_{max}$ is the final plate deflection and T is the deformation duration. The expression for final plate deflection reported by Symonds & Wierzbicki has the form,

$$\tilde{w}_{max} = \left(\frac{2}{\Lambda^2 J_1(\Lambda)}\right) \frac{I}{\pi R_o H \sqrt{\rho \alpha \sigma_y}} \tag{2.31}$$

Note the inclusion of the parameter α which is intended to account for the effect of strain and strain rate sensitivity. Symonds & Wierzbicki proposed a means of estimating α which will be discussed in Section 2.3.7. The expression for the response duration is,

$$T = \frac{\pi}{2\Lambda} R_o \sqrt{\frac{\rho}{\alpha \sigma_y}} = 0.6532 \, R_o \sqrt{\frac{\rho}{\alpha \sigma_y}} \tag{2.32}$$

An interesting feature of Equation (2.32) is that it does not depend on the magnitude of the initial impulse, but does depend on the dynamic flow stress. The impulse independent nature of the displacement duration has also been highlighted by Lippmann and Taylor and agrees with the experimental observations discussed in Section 2.2.2. Based on these results, a definition of dimensionless time will be proposed in Section 3.2.3, and more detailed comparisons and discussions will be given in Section 3.3.4.2.

2.3.6 Travelling Hinge Methods

Experimental observations, such as those shown in Figure 2.1, show that when a circular plate experiences a uniform shock load, giving the plate an initially uniform acceleration, a flexural wave initiates at the plate boundary and propagates toward the centre. This is the mechanism by which the effect of the boundary is communicated across the plate such that the initial uniform motion is converted to a non-uniform deformation profile.

The travelling wave mechanism has been extensively studied in the context of small displacement problems [4], where bending effects dominate and the mechanism is typically treated as a travelling plastic hinge. However, when membrane effects dominate, the travelling wave will be caused by in-plane tractions and should therefore not, strictly speaking, be referred to as a 'plastic hinge'. The essential difference is that a travelling plastic hinge is typically treated as a curvature discontinuity, while a travelling membrane wave need not be. Nevertheless, the term 'hinge' has become entrenched in the literature and hence a travelling membrane wave will be referred to as such in this thesis.

Taylor [15] was the first to outline an analytical approach that explicitly accounts for a travelling hinge. Taylor argued that, in accordance with the membrane analogy, the wave speed for radially travelling disturbances in an axisymmetric plate is given by the constant which appears in the governing differential equation, *i.e.* the constant c in Equation (2.10)[20],

$$c = \sqrt{\frac{\alpha\sigma_y}{\rho}} \tag{2.33}$$

Furthermore, Taylor reasoned that any given particle of the plate will come to rest as the hinge passes over it. Therefore, the duration of deformation is simply the time taken for the hinge to reach the centre of the plate. If the dynamic flow stress is assumed to be constant, Equation (2.33) implies that the hinge speed is constant and hence the deformation duration is simply,

$$T_{_T} = R_0\sqrt{\frac{\rho}{\alpha\sigma_y}} \tag{2.34}$$

In this thesis, Equation (2.34) will be referred to as the 'Taylor duration', hence the subscript T. Note that the form of the Taylor duration is similar to that of Equation (2.32), except that the coefficient is unity. In other words, under identical conditions, the Taylor duration is 53 % greater than the deformation duration predicted using the membrane mode method. The aforementioned predictions will be compared to experimental results in Section 3.3.4.2.

Taylor assumed that the load is uniform and ideally impulsive, giving the plate a uniform initial velocity. Furthermore, he noted that under these assumptions a given plate radius would continue displacing at the initial velocity until arrested by the arrival of the hinge. In other words, the final shape of the plate would be conical and the maximum displacement would be the product of the initial velocity and the deformation duration,

$$\tilde{w} = \frac{I}{m}R_0\sqrt{\frac{\rho}{\alpha\sigma_y}} = \frac{I}{\pi R_o H\sqrt{\rho\alpha}\sigma_y} \tag{2.35}$$

[20] In this thesis, the symbol, c, will also be used for the acoustic wave speed in a Hopkinson bar and the relevant definition must be gained from the context.

From the literature it would appear that relatively few researchers have consider models similar to Taylor's travelling hinge approach for the large plastic deformation of thin plates. Hudson [18] and Frederick [19], who worked in the same era as Taylor, developed more detailed travelling hinge models, but their work does not appear to have continued. A half century later Wierzbicki & Nurick [63] and Lee & Wierzbicki [125] developed a two phase model for the localized impulsive loading of thin plates where the first phase used the concept of membrane type travelling hinges. This approach is similar in concept to the two phase model of Jones [43] who restricted the first phase to small displacements so as to include a bending type travelling hinge. A brief critique of the above mentioned models will be given in Section 3.3.3.2.

2.3.7 Strain Hardening and Strain Rate Sensitivity

In this thesis, the hardening parameter α is used to denote the ratio of the dynamic flow stress σ_d, of a given plate material, to the quasi-static yield stress σ_y, as given in Equation (2.24). An extensive body of literature is devoted to the microscopic physical mechanisms that cause hardening in metals and the material models that are based on them. Aside from physically based models, there is also a large body of literature dedicated to phenomenological models that seek to describe hardening in terms of macroscopic engineering variables, such as strain, strain rate and temperature. A detailed discussion of these topics is beyond the scope of this thesis, although a limited review will be given in Appendix B. In this section, only the hardening models that have found widespread use in analytical models will be considered.

In this thesis the term 'hardening' will be used to denote an increase in the stress required to cause plastic flow due to an alteration of the microstructure of a material, while 'sensitivity' implies an increase in the flow stress without an alteration of the microstructure. While these effects are coupled they are often treated separately. One of the most widely used strain rate sensitivity models is that due to Cowper & Symonds [126] and has the form,

$$\frac{\sigma_{dy}}{\sigma_0} = 1 + \left(\frac{\dot{\epsilon}}{D}\right)^{\frac{1}{n}} \tag{2.36}$$

where σ_{dy} is the dynamic yield stress, with $\dot{\epsilon}$ being the associated strain rate. Using the annealed mild steel data of Manjoine [127], Cowper & Symonds found the coefficients D and n to be $40.4\,\mathrm{s}^{-1}$ and 5 respectively. The resulting curve fit is shown in Figure 2.13, along with subsequent data by Campbell & Cooper [128] and Zhao [129]. Some authors interpret σ_0 as the quasi-static yield stress, although, strictly speaking, it is the hypothetical static yield stress, that must be obtained from the experimental data using Equation (2.36). Consequently, the value of D represents the strain rate at which the yield stress is double that of the σ_0 value. The n parameter defines the shape of the curve, with a larger value leading to a flatter curve when plotted on a log axis, which is the customary format to report strain rate sensitivity data.

The constants for the Cowper-Symonds (CS) equation as reported by Bodner & Symonds [56] and Nurick *et al.* [60] are summarised in Table 2.3. The titanium parameter are reported for completeness, but will not be considered in detail. However, the mild steel parameter will be considered further in Appendix B since it is the material for which experimental data will be reported in Chapter 6.

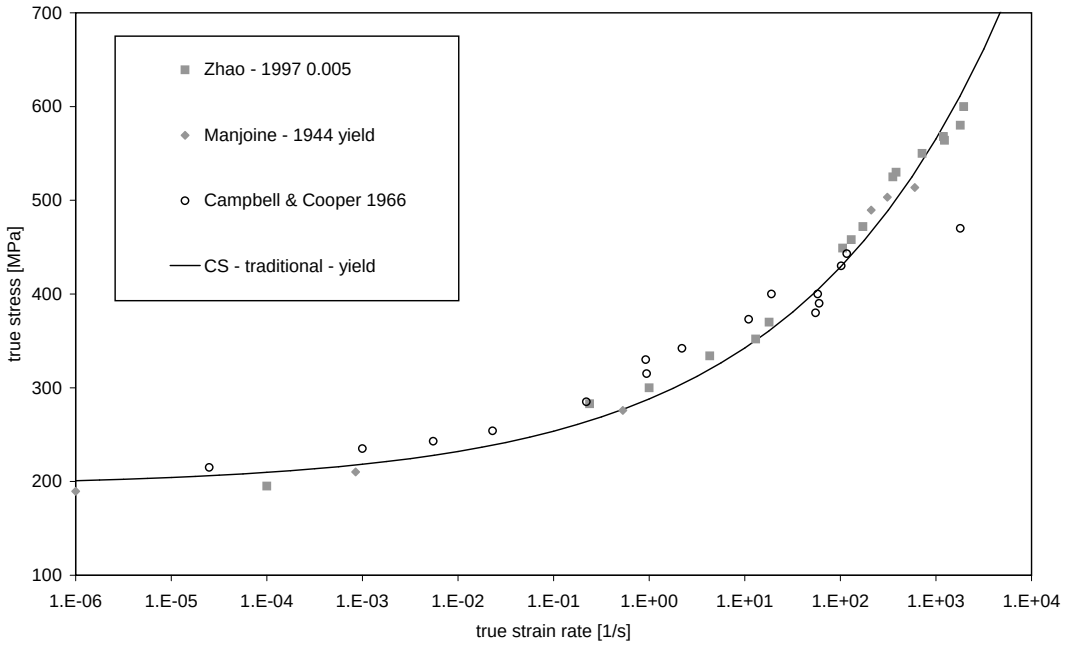

Figure 2.13: The traditional Cowper-Symonds strain rate sensitivity curve compared to published experimental yield strength data for annealed mild steel as a function of strain rate.

Table 2.3: Material data for the plates tested by Bodner & Symonds [56] and Nurick *et al.* [60].

Source	Material	R_o mm	ρ kg/m^3	σ_0 MPa	D s^{-1}	n
Nurick *et al.*	steel	50	7800	282	40	5
Bodner & Symonds	steel	31.8	7800	223	40	5
	titanium	31.8	4500	250	120	9

Note that the static yield stress for the Bodner & Symonds data is 223 MPa while Nurick *et al.* is 282 MPa, and that these were the values used to non-dimensionalise the deflection data in Figure 2.3. Both Bodner & Symonds and Nurick *et al.* tested their plates in the as received condition, *i.e.* the plates were not annealed before testing. However, the yield stress of the material used by Bodner & Symonds is essentially the same as that of the quasi-static regime for annealed mild steel, as shown in Figure 2.13, suggesting that the plates were received in an annealed state [21]. By contrast, the material used by Nurick *et al.* appears to have undergone a certain amount of work hardening prior to delivery. Nevertheless, Nurick *et al.* calculated their value of σ_0 using the rate sensitivity coefficients derived by Cowper & Symonds for annealed mild steel. The validity of this approach will be discussed further in Appendix B.

The non-linearities introduced by strain hardening and strain rate sensitivity effects tend to render impulsively loaded plate problems analytically intractable. Nevertheless, a few analytical models have been published that incorporate these effects. Jones [44] presented an annular plate model that included

[21] A possible scenario is that, after being hot rolled, the plates were not finished with a cold roll to induce significant work hardening.

included both strain hardening and strain rate sensitivity, while Wen [66] used an energy method that included strain hardening effects to model a circular plate with a parabolic displacement profile. Of particular relevance to this thesis is the model by Symonds & Wierzbicki [122], who used the traditional Cowper-Symonds rate sensitivity coefficients to introduce rate sensitivity into their circular plate model in an averaged sense, as will be discussed below[22].

Applying Equation (2.21) to a Bessel function plate shape, as given in Equations (2.16) and (2.30), gives an expression for the radial strain as,

$$\epsilon_r = \frac{1}{2}\,\tilde{w}_{max}^2 \left(\frac{\Lambda}{R_o}\right)^2 J_1^2\left(\frac{\Lambda}{R_o}r\right) sin^2\left(\frac{\pi}{2}\frac{t}{T}\right) \quad \text{where} \quad T = \frac{\pi}{2\Lambda}\,R_o\sqrt{\frac{\rho}{\alpha\sigma_y}} \tag{2.37}$$

The maximum value of ϵ_r will occur at time $t = T$, *i.e.* at the end of the deformation, and at position $r = r_m = 0.7659R_o$, *i.e.* the radius at which $J_1(r)$ is a maximum, resulting in,

$$\epsilon_{r,max} = \frac{1}{2}\left(\frac{\tilde{w}_{max}}{R_o}\right)^2 \Lambda^2 J_1^2\left(\frac{\Lambda}{R_o}r_m\right) \quad \text{where} \quad \Lambda^2 J_1^2\left(\frac{\Lambda}{R_o}r_m\right) = 1.9580 \tag{2.38}$$

The radial strain rate distribution is obtained by taking the temporal derivative of Equation (2.37), giving,

$$\dot{\epsilon}_r = \frac{1}{2}\tilde{w}_{max}^2 \left(\frac{\Lambda}{R_o}\right)^2 J_1^2\left(\frac{\Lambda}{R_o}r\right)\left(\frac{\pi}{2T}\right) sin\left(\pi\frac{t}{T}\right) \tag{2.39}$$

The maximum value of $\dot{\epsilon}_r$ will also occur at radial position r_m, but, unlike the maximum strain, it will occur at time $t = \frac{1}{2}T$, *i.e.* half way through the deformation duration, resulting in,

$$\dot{\epsilon}_{r,max} = \frac{1}{2}\left(\frac{\tilde{w}_{max}}{R_o}\right)^2 \left(\frac{\pi}{2T}\right) \Lambda^2 J_1^2\left(\frac{\Lambda}{R_o}r_m\right) = \frac{\pi}{2}\left(\frac{\epsilon_{r,max}}{T}\right) = 1.5708\frac{\epsilon_{r,max}}{T} \tag{2.40}$$

In other words, the maximum strain rate at any time during the deformation is 57 % higher than the simple average estimate obtained from the quotient of the maximum strain and deformation duration.

The average radial strain over the entire duration of motion is given by the double integral,

$$\epsilon_{r,ave} = \frac{1}{\pi R_o^2\, T}\int_0^T \int_0^{R_o} \epsilon_r\, 2\pi r\, dr dt \tag{2.41}$$

Due to the multiplicative form of Equation (2.37), the double integral can be written as the product of a spatial and temporal integral. The spatial integral represents the average radial strain in the plate at time T, and has the form,

$$\begin{aligned}\epsilon_{r,T\text{-}ave} &= \frac{1}{R_o^2}\int_0^{R_o} \frac{1}{2}\,\tilde{w}_{max}^2 \left(\frac{\Lambda}{R_o}\right)^2 J_1^2\left(\frac{\Lambda}{R_o}r\right) 2rdr \\ &= \frac{1}{2}\left(\frac{\tilde{w}_{max}}{R_o}\right)^2 \Lambda^2 J_1^2\left(\Lambda\right) \quad \text{where} \quad \Lambda^2 J_1^2\left(\Lambda\right) = 1.5586\end{aligned} \tag{2.42}$$

[22] Symonds & Wierzbicki [122] used a different notation and presented and abbreviated derivation. The derivation presented here is a reconstruction of their results.

while the temporal integral is,

$$\frac{1}{T}\int_0^T sin^2\left(\frac{\pi}{2}\frac{t}{T}\right)\,dt = \frac{1}{2} \tag{2.43}$$

In other words, the average radial strain over the entire duration of motion is equal to half the average radial strain at the end of the motion, or when expressed symbolically,

$$\epsilon_{r,ave} = \frac{1}{2}\epsilon_{r,T\text{-}ave} \tag{2.44}$$

Furthermore, a comparison Equations (2.38) and (2.42) gives the ratio of the maximum and average radial strain at the end of the motion as,

$$\frac{\epsilon_{r,max}}{\epsilon_{r,T\text{-}ave}} = \frac{J_1^2\left(\frac{\Lambda}{R_o}r_m\right)}{J_1^2\left(\Lambda\right)} = 1.2562 \tag{2.45}$$

In other words, the maximum radial strain is a quarter larger than the average radial strain at the end of the motion.

As with the average radial strain, the average radial strain rate over the entire duration of motion is given by the double integral in Equation (2.41), with $\dot{\epsilon}_r$ replacing ϵ_r in the integrand. Furthermore, Equation (2.39) also has a multiplicative form that allows for seperate spatial and temporal integral, where the spatial integral is identical to Equation (2.42), while the temporal integral is,

$$\frac{1}{T}\int_0^T \left(\frac{\pi}{2T}\right) sin\left(\pi\frac{t}{T}\right)\,dt = \frac{1}{T} \tag{2.46}$$

Therefore, since spatial integral is identical to Equation (2.42), *i.e.* it represents the average radial strain in the plate at time T, the average strain rate can be written as,

$$\dot{\epsilon}_{r,ave} = \frac{\epsilon_{r,T\text{-}ave}}{T} \tag{2.47}$$

In other words, the average radial strain rate over the entire duration is simply the quotient of the average radial strain at the end of the motion and the duration of the motion.

Finally, the ratio between the maximum and average radial strain rates can be obtained by combining Equations (2.40), (2.45) and (2.47) to give,

$$\frac{\dot{\epsilon}_{r,max}}{\dot{\epsilon}_{r,ave}} = \frac{\pi}{2}\,\frac{J_1^2\left(\frac{\Lambda}{R_o}r_m\right)}{J_1^2\left(\Lambda\right)} = 1.9733 \tag{2.48}$$

In other words the maximum and average radial strain rates differ by just under a factor of 2. Symonds & Wierzbicki [122] noted that since strain rate sensitivity is best expressed on a log scale, a difference factor of two would not have a great effect on the estimated strain rate. Consequently, either the maximum or average radial strain rate could be used to estimate strain rate effects.

Symonds & Wierzbicki observed that their approach could not lead to a closed form solution and proposed an iterative approach. As a first guess, the flow stress was assumed to be equal to the quasi-static yield

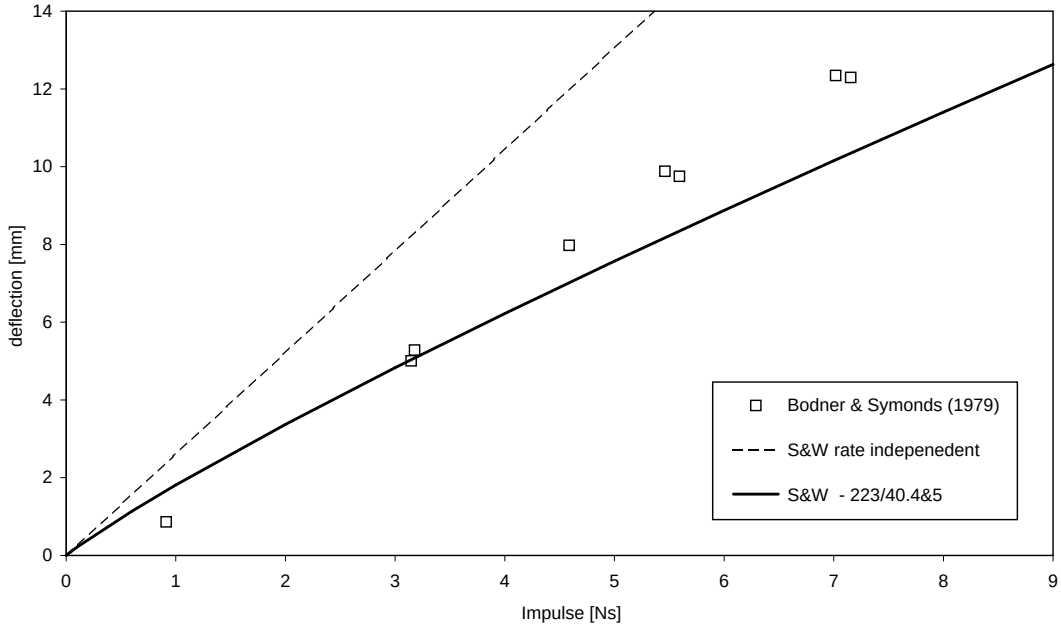

Figure 2.14: Comparison of experimental data due to Bodner & Symonds (B&S) [56] for a circular mild steel plate subjected to a uniform impulsive load with predictions of Symonds & Wierzbicki (S&W) [122], which incorporate averaged strain rate effects. The numbers in the legend indicate the yield stress and Cowper-Symonds hardening coefficients.

stress and used in Equations (2.31) and (2.32), respectively, to obtain first estimates for the maximum final deflection and deformation duration. These values were then used in Equations (2.38) and (2.40) to obtain the maximum strain rate during deformation. The calculated value for the strain rate was then used to obtain an updated estimate of the flow stress using Equation (2.36). The cycle was repeated until the problem parameters converged.

Symonds & Wierzbicki [122] compared the results of their iterative approach to the experimental data due to Bodner & Symonds [56] for impulsively loaded circular plates. The result for mild steel plates subjected to a uniform impulsive load is shown in Figure 2.14. In general, the results showed that solutions incorporating strain rate effects provide improved predictions compared to the rate independent solutions based on the yield stress. The analysis also predicted that the displacement duration would decrease with increasing impulse, with a steep initial gradient at small impulses that rapidly levels off and appears to approach an asymptote at large impulses. Consequently, this effect was expected to be very slight in the range of practical blast loading experiments, though some experimental support was found in the data of Bodner & Symonds [56], as shown in Figure 2.5, where both the duration data for titanium and mild steel show a gradual decrease.

Despite the improved correlation, Figure 2.5 shows certain features of the experimental data that are not captured by the analytical solution of Symonds & Wierzbicki. It will be shown in Section 3.2.1 that the experimental data conforms closely to a linear regression that does not intersect with the origin. By contrast, the predicted response is non-linear and passes through the origin. These features will be discussed further in Section 3.3.5.

2.3.8 Bending and Radial Displacement

A common feature of the models considered in Sections 2.3.1 to 2.3.6 is the assumption that the effects of bending strains and radial displacements are negligible when considering the large deflection behaviour of impulsively loaded circular plates. This assumption is required to justify the description of strain as depending only on the transverse deflection, as given in Equation (2.21), and has been used by several researchers [15,37,38,45,63,122,123]. This approach would appear to be validated by the good agreement between the theoretical and experimental displacement profiles shown in Figure 2.12. Furthermore, it will be shown in Sections 3.3.2.4 and 3.3.4.2 that the predicted maximum displacements and durations show reasonable agreement with experimental data. Nevertheless, some authors have developed analytical impulsively loaded plate models that incorporate bending and/or radial displacement effects [43, 44, 66], which will be reviewed in this section.

2.3.8.1 Bending Effects

Jones [43] appears to be the first to incorporate both bending moments and membrane forces in a large deflection solution for impulsively loaded plates. Jones presented a brief survey of the field up until 1968, and stated that all previous studies had considered either bending or membrane behaviour, but never both. He argued that these approaches were appropriate since the previous studies had considered only small or large deflections, where bending or membrane effects dominate, respectively. By contrast, Jones considered an ideal impulsively loaded rigid plastic circular plate, where the impulse intensity was of such a nature as to cause intermediate displacements, *i.e.* deformations where both bending and membrane strains must be considered. The plate response was divided into two phases. In phase I a radially inward travelling plastic hinge is considered, with the phase terminating as the hinge arrives at the plate centre. Thereafter, phase II involves further plate deformation until the plate comes to rest. Jones reasoned that, for intermediate displacement problems, phase I would be bending dominated and obtained a solution for the plate shape at the end of phase I that is identical to the solution of Wang [24] except that kinetic energy had not been completely dissipated. Furthermore, Jones assumed that phase II would be membrane dominated and used the final phase I displacement and velocity distributions as initial conditions for a membrane solution.

The analysis of Jones [43] has three limitations. Firstly, it is not applicable to problems where the travelling hinge persists into the large deflection regime, such as is the case with a significant portion of the data considered in Section 2.2. Secondly, while the analysis was the first to incorporate both membrane and bending actions in a single solution, it did not consider their combined action and interaction, *i.e.* the bending and membrane effect were uncoupled. Thirdly, radial displacements were not considered, the merits of which are discussed in Section 2.3.8.2.

Jones [4,44], in subsequent work, and Wen [66] considered impulsively loaded plate problems incorporating combined, but uncoupled, bending and membrane effects. These analyses are based on a yield condition originally proposed by Hodge [29], which is a simplification of that presented by Onat & Prager [27]. Onat & Prager derived their yield condition for shells of revolution based on Tresca's yield theory with an associated flow rule, while assuming rigid perfectly plastic material behaviour. The yield condition is expressed in terms of two bending moment and two membrane force components, leading to a closed

convex hypersurface in four-dimensional stress space, where moment and force components display non-linear interactions [27, 29]. These relations have proved to be mathematically intractable for all but the simplest problems [43] and will, therefore, not be discussed in detail. Hodge [29] proposed a simplified yield surface that maintains force-force and moment-moment interactions, but neglects interactions between forces and moments. In other words, bending and membrane effects are combined, *i.e.* they are treated as occurring simultaneously, but independent, *i.e.* the work done by bending moments and membrane forces are evaluated separately as if the other is not present and then summed. This uncoupled approach renders the problem mathematically tractable, as shown by Jones, who developed solutions for the equations of motion.

The analyses of Jones [4, 44], who applied the equations of the motion to a conical displacement profile, and will not be considered in detail since the focus of this thesis is on energy methods and a conical profile provides a poor approximation to the deformed plate shapes considered in this thesis, as shown in Figure 2.12. Instead, the work of Wen [66], who used an energy method and assumed a parabolic plate profile, will be reviewed.

Wen considered a circular plate subjected to an ideal impulsive load and deforming with a parabolic profile. In other words, the plate shape is identical to that used by Duffey [38] as stated in Equation (2.20). Furthermore, like Duffey, Wen assumed that all radial displacements are negligible. However, unlike Duffey, Wen argued that flexural strains are important in addition to membrane strains. In this case the expression for the radial and circumferential strains are,

$$\epsilon_r = \frac{1}{2}\left(\frac{dw}{dr}\right)^2 - z\frac{d^2w}{dr^2} \quad \text{and} \quad \epsilon_\theta = -\frac{z}{r}\frac{dw}{dr} \tag{2.49}$$

where z is the height above the midplane of the plate. The first term in the expression for the radial strain is identical to Equation (2.21) and is thus identified as the membrane contribution $\epsilon_{r,m}$ and, consequently, the second term is the bending contribution $\epsilon_{r,b}$. The circumferential strain is due entirely to bending, *i.e.* $\epsilon_{\theta,b}$. Substituting Equation (2.20) into Equation (2.49) gives,

$$\epsilon_r = \frac{2\tilde{w}^2}{R_o^4}r^2 + \frac{2\tilde{w}}{R_o^2}z \quad \text{and} \quad \epsilon_\theta = \frac{2\tilde{w}}{R_o^2}z \tag{2.50}$$

Equation (2.50) indicates that the membrane strain is always positive, *i.e.* tensile, but that the bending strains are tensile above and compressive below the midplane of the plate due to the sense of z. The implication is that above that mid plane the radial membrane and bending strains will always sum and the flow stress will, consequently, always be tensile. However, below the mid-plane the radial membrane and bending strains are opposed and the sense of the flow stress will depend on which deformation mechanism dominates. This is an example of the coupling between membrane and bending deformations that is ignored when using the simplified yield criterion of Hodge, resulting in an overestimate of the plastic dissipation.

Wen assumed an uncoupled yield criterion similar to that of Hodge and, from the expression for plastic work given Equation (2.23), obtained an expression for the membrane strain energy, which for the case

of perfect plasticity has the form,

$$W_{P,m} = \int_0^{R_o} \sigma_d \frac{2\tilde{w}^2}{R_o^4} r^2 \, 2\pi r H \, dr = \pi H \sigma_d \tilde{w}^2 \tag{2.51}$$

which is identical to Equation (2.25). The corresponding expression for the radial bending strain energy is,

$$W_{P,b} = \int_0^{R_o} 2 \int_0^{\frac{H}{2}} \sigma_d \frac{2\tilde{w}}{R_o^2} z \, 2\pi r \, dz \, dr = \frac{1}{2} \pi H^2 \sigma_d \tilde{w} \tag{2.52}$$

Note that in Equation (2.52) the change in sense of the flow stress is accounted for by integrating over half the plate thickness and then doubling the result. The strain energy due to circumferential bending, when similarly considered in isolation, has the same form as Equation (2.52).

Wen considered the ideal impulsive loading case, which, using Equation (2.26), gives,

$$E_{k,0} = \frac{I^2}{2\pi R_o^2 H \rho} = W_P = W_{P,m} + 2W_{P,b} = \pi H \sigma_d \tilde{w}^2 + \pi H^2 \sigma_d \tilde{w} \tag{2.53}$$

which results in a quadratic equation,

$$\left(\frac{\tilde{w}}{H}\right)^2 + \frac{\tilde{w}}{H} = \frac{\phi^2}{2\alpha} \quad \text{where} \quad \phi = \frac{I}{\pi R_o H^2 \sqrt{\rho \alpha \sigma_y}} \tag{2.54}$$

Considering only the positive root, the final solution is,

$$\frac{\tilde{w}}{H} = \sqrt{\frac{1}{4} + \frac{\phi^2}{2\alpha}} - \frac{1}{2} \tag{2.55}$$

This solution represents an 'upper' bound to the exact plastic dissipation for the parabolic plate shape and, therefore, will tend to underpredict the displacement response. The implications of this analysis will be discussed in Section 3.3.7.

Equation (2.55), which applies to a perfectly plastic material, is a special case of the solution reported by Wen, whose analysis included strain hardening and shear sliding effects. The inclusion of these effects appears to have necessitated the use of an uncoupled yield model, similar to that of Hodge, in conjunction with an energy method. However, the simplification proposed by Hodge [29] was specifically intended for problems in which the equations of motion were to be integrated directly, and in an energy method, where the equations of motion are not solved directly, restrictions to the yield surface can be avoided. In the context of circular plates subjected to a static central load, Onat & Haythornthwaite [28] argued that if a function can be chosen *a priori* that accurately describes the plate shape, then the plastic dissipation can be calculated and the magnitude of the loading obtained using virtual work. Furthermore, they showed that the coupled expression for plastic strain, given in Equations (2.49), can be integrated directly without requiring a limited interaction approximation. This approach does not appear to have been applied to dynamic plate deformation problems and will be considered in Section 3.3.7.

2.3.8.2 Radial Displacement Effects

There do not appear to be any published analytical models for impulsively loaded circular plate that incorporate radial displacements. Some authors have indirectly taken radial displacements into account by assuming that radial strains vanish, as is approximately the case for annular plates [44] and unclamped simply supported circular plates that are free to draw-in [28]. However, this approach is not applicable to clamped solid circular plates.

The original reason for neglecting radial displacements is unclear but may be inferred from the literature. The most likely explanation lies in the pioneering work of Taylor [15] where both the travelling hinge and membrane approaches were limited to transverse displacements. In the case of the membrane approach, the model is based on an analogy with a vibrating membrane, the analysis of which implicitly assumes small transverse displacements. In the case of the travelling hinge approach, the central portion of the plate is assumed to move as a rigid body until the arrival of the plastic hinge, *i.e.* the transverse motion assumption is implicit. In other words, no explicit reasons for neglecting radial displacements were given by Taylor and it merely appears to have been a default assumption that has been adopted by subsequent researchers.

A number of authors have attempted to provided some justification for neglecting radial displacements. For example, Jones [43] justified the assumption on the basis of experimental data presented by Griffith & Vanzant [130], who reported that radial displacements during the impact loading of plates are significantly less than during static loading. However, Griffith & Vanazant investigated plates subjected to projectile impact, which produces a displacement profile that is distinctly different from that produced by impulsive loading. In addition, Griffith & Vanzant were careful to point out that the circumferential strains were non-zero, *i.e.* radial displacements did occur. Furthermore, Munday & Newitt [34], who are cited by Jones, provide experimental results suggesting that any given point on a plate with initially displace transversely until the arrival of the travelling hinge and subsequently experience both transverse and radial displacements. By contrast, Duffey [38] used the results of numerical simulations where radial displacements were a small fraction of the transverse displacements to argue that strains due to radial displacements are negligible. However, as will be shown, radial displacements have a large effect on the strain distribution, even though they are small. These two examples are typical of the justifications given in the literature, if any are given at all.

A consequence of neglecting radial displacements is that the maximum radial strains are predicted to occur at the outer periphery for a parabolic plate shape, as shown in Equation (2.22), while for a Bessel displacement profile, as given in Equation (2.37), the maximum strain occurs at a dimensionless radius of 0.7659. Furthermore, both Equations (2.22) and (2.37) predict zero radial strain at the centre of the plate, which implies that the centre plate thickness should be constant. However, this prediction does not agree with experimental observations. Karunes & Onat [131] point out that experiments show marked thinning in the central portion of plates. Similar results were obtained by Nurick & co-workers [62, 70], who measured plate thickness and grain elongation to assess the final strain distributions and found that the greatest strain occurs in the plate centre. This type of behaviour is also seen in UNDEX work, such as that by Kosing & Skews [132] who reported strain results from a grid painted onto circular copper plates that were loaded using a liquid shock tube.

The aforementioned experimental evidence implies that the strain distribution obtained when assuming a pure transverse displacement is incorrect. Nurick *et al.* [62] conducted an experimental and numerical investigation of the radial displacement profile of blast loaded plates and found a significant error in the theoretical strain distribution obtained when radial displacements are neglected. This result is significant since ignoring radial displacements will affect failure predictions based on a critical strain approach and may alter the assessment of strain hardening and strain rate effects. Nevertheless, the deflections predicted when using this erroneous strain distribution in the energy method are reasonably accurate, as will be shown in Section 3.3.2.4. To the author's knowledge, there appears to be no discussions in the literature regarding this apparent contradiction, *i.e.* the notion of how an energy method based on an incorrect strain distribution can produce accurate displacement results is not raised, nor the effect that radial displacements would have on the energy dissipated through plastic work. Furthermore, a fundamental theoretical justification for neglecting radial displacements, other than for mathematical convenience, does not appear in the literature prior to the work published as part of this thesis [133]. These issues will be considered further in Sections 3.3.6 and 3.3.7.

While absent in dynamic models, deformation theories that include radial deflections have been including in the analysis of quasi-statically loaded membranes. Taylor [15] presented an approximate radial deflection solution that will form the basis of an analysis presented in Section 3.3.7 and will, therefore, be reviewed in detail[23].

Taylor considered the radial equilibrium of a static membrane undergoing small deflection. The angle between the membrane and the horizontal plane was assumed to be small and, hence, the cosine of the angle was treated as unity, leading to a radial equilibrium equation of the form,

$$r\frac{d\sigma_r}{dr} + \sigma_r - \sigma_\theta = 0 \tag{2.56}$$

where σ_θ is the membrane stress is the circumferential direction. Assuming that the membrane thickness does not change appreciably, the constant flow stress assumption satisfies Equation (2.56), since the variation of stress in the radial direction vanishes and the radial and circumferential stresses are equal at every point. Consequently, the Mises yield criterion and associated flow rule states that the radial and circumferential strain will also be equal [15].

According to Taylor, the expressions for the radial and circumferential membrane strain, including both transverse and radial displacements, are,

$$\epsilon_r = \frac{1}{2}\left(\frac{dw}{dr}\right)^2 + \frac{du}{dr} \quad \text{and} \quad \epsilon_\theta = \frac{u}{r} \tag{2.57}$$

where u is the radial displacement. Taylor ignored higher order terms that appear in more complete derivations, such as that due to Reissner [119]. Substituting the expression for the transverse strain given in Equation (2.9) and equating the radial and circumferential membrane strains, gives,

$$\frac{du}{dr} - \frac{u}{r} = -\frac{1}{2}\left(\frac{dw}{dr}\right)^2 = -\frac{2\bar{w}^2}{R_o^4}r^2 \tag{2.58}$$

[23]It is curious to note that that the seminal paper of Taylor [15] which provided the initial impetus for neglecting radial displacements also contains an analysis that implies the opposite.

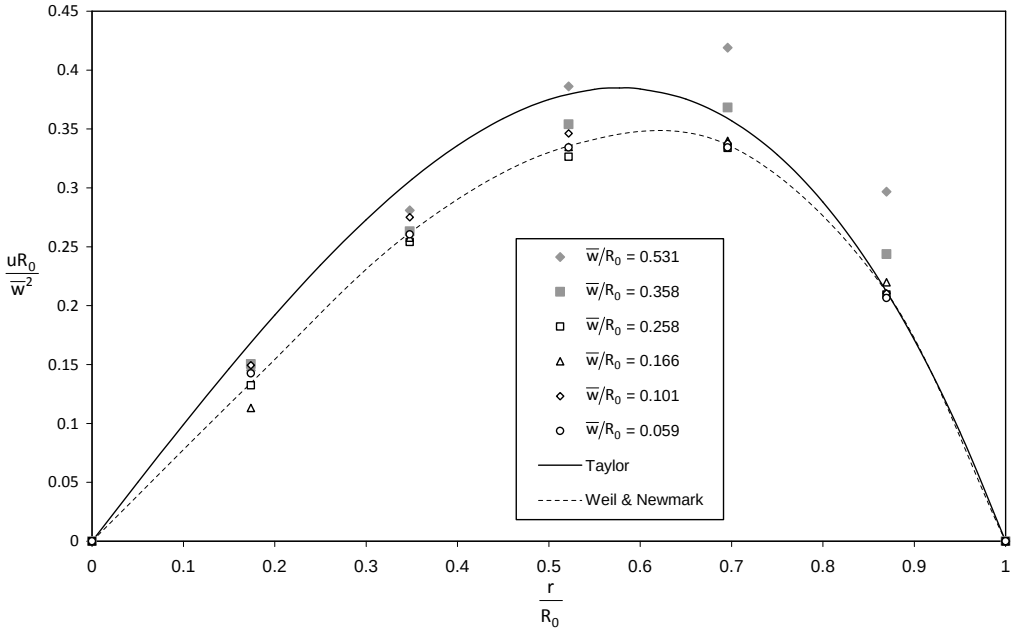

Figure 2.15: Comparison of the published radial displacement results by Weil & Newmark [30] with the prediction of Taylor [15] using a parabolic transverse displacement profile. The dashed curve represent a smoothed interpolation of the experimental results $\bar{w}$ values of less than $0.3R_o$.

Solving Equation (2.58) and noting that the radial displacement is zero at the plate centre and periphery, Taylor found that the radial displacement distribution is,

$$u = \frac{\bar{w}^2}{R_o}\left[\frac{r}{R_o} - \left(\frac{r}{R_o}\right)^3\right] \tag{2.59}$$

This result indicates that if the transverse deflection is small, then the radial displacement is negligible. Rearranging Equation (2.59) provides a dimensionless expression of radial displacement, in the form,

$$\frac{uR_o}{\bar{w}^2} = \frac{r}{R_o} - \left(\frac{r}{R_o}\right)^3 \tag{2.60}$$

A comparison between Equation (2.60) and the quasi-static experimental data of Weil & Newmark [30][24] is shown in Figure 2.15. The analysis of Taylor is considered to provide an acceptable prediction for the radial displacement distribution. Furthermore, Figure 2.15 shows that the expression for the dimensionless radial deflection obtained from Equation (2.60) causes the data for central deflections of less than $0.3R_o$ to collapse onto a single curve. This result supports the validity of Taylor's approach, but indicates that higher order terms should be included in Equation (2.57) for central deflections greater than $0.3R_o$.

From Equations (2.57) and (2.59) the strain distribution is,

$$\epsilon_r = \epsilon_\theta = \left(\frac{\bar{w}}{R_o}\right)^2\left[1 - \left(\frac{r}{R_o}\right)^2\right] \tag{2.61}$$

[24] Weil & Newmark presented an accurate numerical solution, which is beyond the scope of this thesis.

Note that Equation (2.61) predicts that the maximum strain occurs at the plate centre while the strain at the outer periphery vanishes, which agrees with experimental results mentioned previously. In Section 3.3.7 it will be argued that Taylors approach is also applicable to impulsive loading problems and the effect of radial displacement on dynamic plate behaviour will be considered. In particular, the effect of radial displacements on energy dissipation and failure prediction will be considered.

2.4 Analytical modelling of Annular Plates

As discussed in the preamble of Section 2.3, the majority of analytical studies have focused on impulsively loaded PCS plates. By contrast, relatively few analytical models for impulsively loaded peripherally clamped annular (PCA) plates have been published [4, 44, 134, 135], a short review of which is provided by Lellep & Torn [135].

The majority of the PCA plate models appear to focus on small displacement behaviour where bending strains are dominant and membrane effects can be ignored [4]. For example, Aggarwal & Ablow [134] considered an annular plate subjected to a uniform impulse. The plate was assumed to be rigid-perfectly plastic with a Tresca yield condition and associated flow rule. Both peripherally clamped and simply supported boundary conditions were considered. Lellep & Torn [135] considered a similar model but retained the shear forces in the yield surface.

In contrast to the preceding models, Jones [44] considered an annular plate model that included both bending and membrane strains along with finite deflections, radial displacements, strain hardening and strain rate sensitivity. Jones states that to enable the study of these interacting phenomena, a conscious attempt was made to simplify the problem. To this end, only the simply supported case was considered and both the initial velocity and displacement profiles were assumed to have a linear distribution of the form,

$$\dot{w} = \dot{\tilde{w}}\frac{R_o - r}{R_o - R_i} \quad \text{and} \quad w = \tilde{w}\frac{R_o - r}{R_o - R_i} \tag{2.62}$$

If the inner radius vanishes, Equation (2.62) is identical to the conical profile obtained using the travelling hinge method discussed in Section 2.3.6. The linear displacement profile as applied to the PCS and PCA configurations will be considered further in Sections 3.3.2.3 and 7.2.2 respectively.

In addition to the above mentioned simplifications, Jones also assumed that the radial strains vanish. This has the implication that, unlike the PCS models reviewed in Sections 2.3.4, 2.3.5 and 2.3.6, the radial displacement cannot be assumed to be negligible. Jones gave the resulting radial displacement as,

$$u = \frac{\tilde{w}^2(R_o - r)}{2(R_o - R_i)^2} \tag{2.63}$$

This expression can be confirmed by substituting it and Equation (2.62) into Equation (2.57) and noting that the radial strain reduce to zero for all r values. The effect of including radial displacements will be considered further in Section 7.3.2.2.

The radial strain assumption used by Jones is justified, in part, by the inertia forming experiments of Ghosh *et al.* [49, 50], which included the deformation of PCA plates and showed that the inner radius increased with increasing deflection. These experimental results are in agreement with those published as part of this work [52, 53], which will be presented in Chapter 6. Furthermore, a theoretical justification for the inclusion of radial displacements in PCA models will be given in Section 3.3.6.

Jones reported that although his analysis included finite displacements, it was only valid for maximum displacements in the order of two plate thicknesses. Despite this, he was able to conclude that membrane effects tend to become dominant at displacements greater than a plate thickness. Furthermore, Jones suggested that at greater displacements it is only necessary to consider membrane effects. The validity of this suggestion for PCS plates will be considered in Section 3.3.7.

There do not appear to be any published large deflection models for impulsively loaded PCA plates, other than those published as part of this work [52]. These models will be considered and extended to include radial displacements in Section 7.3.2.

2.5 Miscellaneous Topics

This section contains brief synopses for topics that are either central to this thesis but for which an extensive literature does not exist, or for topics that are only tangentially relevant to this thesis and for which a detailed survey is outside the scope of this thesis.

2.5.1 Finite Duration Loading

Hitherto, only literature dealing with ideal impulsive loading cases have been discussed. The reason for this is because the open literature contains few closed form analytical solutions for the finite plastic deflection of a circular plate subjected to a finite duration load. This stands in contrast to the large number of solutions that exist for finite duration loading in the small deflection regime where bending strains are predominant [4].

To the authors knowledge, only Jones [4] has reported a solution for the finite plastic deflection of a circular plate subjected to a 'rectangular' load, *i.e.* a load of constant intensity and finite duration. In the solution, a conical plate shape was chosen *a priori* and both bending and membrane strains were included in an uncoupled manner, *i.e.* similar to the yield condition proposed by Hodge [29] as discussed in Section 2.3.8.1. However, it will be shown in Section 3.3.7 that membrane strain dominate at large deflections and overwhelm the influence of bending strain such that the yield condition of Hodge is not applicable. Consequently, the literature does not appear to contain a solution for the large plastic deflection of a circular plate subjected to a finite duration load. This topic will be addressed in detail in Chapter 4 for PCS plates and in Chapter 7 for PCCS plates.

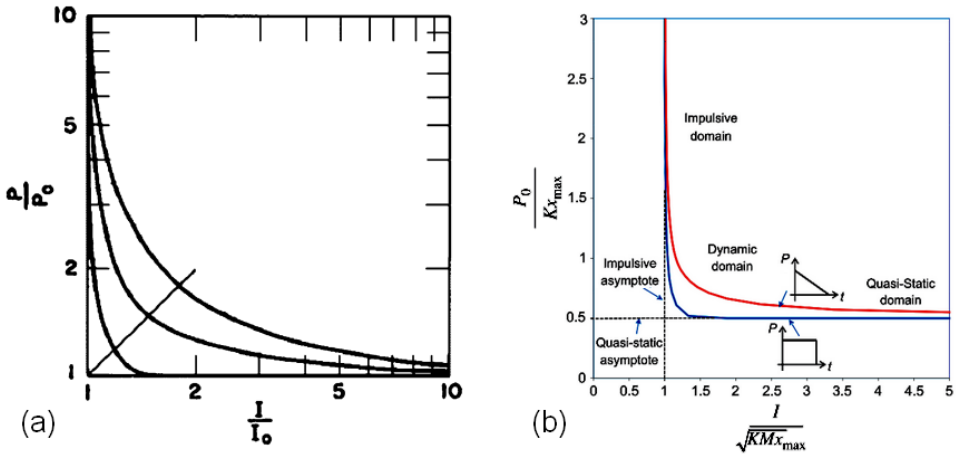

Figure 2.16: Examples of pressure-impulse diagrams for linear spring-mass systems as reported by (a) Abrahamson & Lindberg [138] and (b) Krauthammer *et al.* [47]. In both diagrams I is the total impulse. For diagram (a) P is the peak pressure while P_0 is the magnitude of the step load and I_0 the ideal impulse that individually produce a critical displacement. For diagram (b) x_{max} is the maximum dynamic displacement, K is the spring stiffness, P_0 is the peak force, M is the lumped mass, t is the load pulse duration. In both diagrams the first two response curves represent rectangular and triangular loads while the third curve in (a) is for an exponential load.

2.5.2 Pressure-Impulse Isodamage Diagrams

It is well known that the temporal shape, *i.e.* pressure history, of a fluid pulse has a significant influence on the dynamic plastic response of a structure [8,46,47,136–141]. Early examples of analytical studies is that due to Hodge [136] who studied circular cylindrical shells and Biggs [137] who considered single degree of freedom (SDOF) mass-damper-spring systems. However, as mentioned in Section 2.1.1, Youngdahl [46] was the first to develop an expression for an effective pressure load that reduced an arbitrarily shaped pulse into an equivalent rectangular pulse of equal impulse. Youngdahl found that pressure pulses with the same total impulse and maximum load but with different shapes produced different final deflection results. However, the differences are virtually eliminated if the pulses have the same total impulse and 'effective load'. The 'effective load' was defined as the total impulse divided by twice the mean time, *i.e.* the interval between the onset of plastic deformation and the centroid of the pulse. Youngdahl showed that the effective load approach is valid for four classical problems in dynamic plasticity, one of which is a circular plate under uniform pressure.

Shortly after the work of Youngdahl, Abrahamson & Lindberg [138] considered analytical solutions for critical displacements due to rectangular, triangular and exponentially decaying loads acting on a variety of structures. While Youngdahl aimed to collapse the data onto a single dimensionless deflection vs pressure curve, Abrahamson & Lindberg expressed their results using the concept of a pressure-impulse (P-I) diagram, *i.e.* several curves denoting different pulse profiles on a single dimensionless pressure vs impulse diagram, as shown in Figure 2.16(a). As noted by Abrahamson & Lindberg, pressure-impulse characterization schemes have been in use since the second world war. However, the work of Youngdahl and Abrahamson & Lindberg appears to have been the catalyst for this approach to develop into the distinct field of pressure-impulse isodamage diagrams.

A thorough review of the pressure-impulse diagram approach is beyond the scope of this thesis since it includes a wide variety of structures and analysis techniques that are not immediately relevant. However, certain trends and definition in the P-I diagram literature should be noted for context and contrast. For example, it appears that the analytical solutions used to construct P-I diagrams are restricted to small deflections [46, 138], while numerical schemes are used for elaborate problems [47, 141]. Furthermore, certain aspects of the loading regime classification system used in P-I diagrams are relevant to provide a context for the work presented in Chapters 4 and 7.

The development of pressure-impulse isodamage diagrams has resulted in the recognition of distinct response domains. A typical example is shown in Figure 2.16(b) where Krauthammer *et al.* [47] identify three domains representing three loading regimes, namely impulsive, dynamic and quasi-static. The impulsive domain is associated with the vertical asymptotes in Figure 2.16 where the level of 'damage', *i.e.* deflection in this case, depends only on the total impulse, *i.e.* it is independent of the peak load and load history. By contrast, the quasi-static domain is associated with the horizontal asymptotes in Figure 2.16 where the level of 'damage' depends only on the peak load, *i.e.* it is independent of the total impulse and load history. Finally, the dynamic domain is not associated with either of the asymptotes in Figure 2.16 and the level of 'damage' is dependent on the peak load, load history and total impulse. These definitions are similar to those used in this thesis, as given in Sections 2.1, 2.3.3, 4.2 and 4.3. However, there are some subtle, but important, distinctions which are highlighted in the remainder of this section.

Krauthammer *et al.* [47] discuss an 'energy balance method' that is 'widely used'[25] to obtain analytical solutions for the impulsive and quasi-static asymptotes. For the impulsive asymptote, Krauthammer *et al.* argue that, due to inertia effects, the initial total energy imparted to a system can be assumed to be in the form of kinetic energy only and equating this to the total strain energy stored in the system in its final state provides the maximum response. This is, essentially, identical to the definition of an 'ideal impulsive' load given in Section 2.3.3 and implies a load with a duration that is significantly shorter than that of the structural response.

For the quasi-static asymptote, Krauthammer *et al.* argue that the load can be assumed to be constant before the maximum deformation is achieved and equating the work done by load to the total strain energy gained by the system provides the maximum response. While this is a valid analytical approach, the use of the term 'quasi-static' is a misnomer. According to Young & Budynas [142], the term 'quasi-static' describes a response where accelerations are negligible due to the gradual application of a monotonically increasing load, *i.e.* the inertia of the structure does not play a significant role in the deformation. By contrast, the 'quasi-static' regime of Krauthammer *et al.* involves a rectangular load profile with a sudden pressure increase. It will be shown in Section 4.3.7 that this loading profile produces significant plate accelerations and inertia effects. Therefore, in this thesis, a rectangular load with a duration equal to that of the plate deformation will be referred to as an ideal dynamic load (IDL)[26].

For the dynamic domain, where the load is viewed as having a duration similar to that of the structural response, Krauthammer *et al.* argue that the energy balance method is not applicable and suggest that P-I curves must be obtained using numerical solutions. It will be shown in Section 4.3 that this

[25] Krauthammer *et al.* [47] make this claim but, unfortunately, do not provide a specific list of references.

[26] Zhao *et al.* [143] and Zhu & Yu [144] use the term 'saturation impulse' for this type of load since any further increase is pulse duration does not lead to further deformation.

view is incorrect by presenting analytical solutions for finite duration loads based on energy methods. Furthermore, in Section 4.3.2 of this thesis, the 'dynamic' domain of Krauthammer *et al.* is subdivided into an impulsive domain, where load duration that does not exceed the plastic hinge phase of plate motion[27], and a dynamic domain, where load duration is similar to that of the complete plate motion. In summary, in this thesis the term 'ideal impulsive' is corresponds to the term 'impulsive' as used by Krauthammer *et al.*, while the term 'impulsive' and 'dynamic' correspond to two subdivisions the 'dynamic' domain defined by Krauthammer *et al.*, *i.e.* the meaning of the term 'impulsive' is closer to the general meaning as discussed in Section 2.1.

Finally, while the energy based definitions of Krauthammer *et al.* are well motivated with regard to the asymptotes evident in Figure 2.16, they do not provide clear boundaries for each domain. To address this, Li & Meng [140] suggest threshold values for peak pressure and total impulse corresponding to a 5% error in the damage estimate. In this thesis, more specific criterion to distinguish between impulsive and dynamic loads is presented in Section 4.3. Furthermore, the regime limits and transitions will be treated as special cases as defined in Sections 2.3.3, 4.3.4 and 4.3.7.

2.5.3 Shock-Structure Interaction

In addition to pressure history effects, the impulse delivered by a finite duration load can be affected by the response of a structure. In particular, if a structure responds rapidly and attains a significant velocity, the motion of the structure can relieve the pressure acting on it, thus reducing the transmitted impulse. This shock-structure interaction (SSI) effect was first discussed by Taylor [145] who considered the interaction between a plane blast wave and a plate[28]. Taylor showed that in the case of negligible compressibility effects the interaction is governed by a single nondimensional parameter representing the relative time scales of the duration of the blast load and of the shock-structure interaction. At the upper limit, where the plate has a large mass leading to a small acceleration, the pressure history corresponds to the values produced by a wave reflection on a fixed boundary. In this case, the maximum impulse is transferred to the plate. At the opposite limit, *i.e.* a plate of negligible mass, the plate is rapidly accelerated, which reduces the reflected pressure and limits the momentum transferred to the plate. By assuming the acoustic limit, Taylor found a closed form solution to the problem, including an expression for the relative transmitted impulse in terms of a SSI parameter that is independent of the blast intensity.

Taylor's analysis was reconsidered and extended by Kambouchev *et al.* [146, 147] and Peng *et al.* [148] who included nonlinear compressibility effects, which are significant in the case for explosions in air. Kambouchev *et al.* found analytical solutions for the limit cases, *i.e.* plates with large or small masses, with arbitrary blast load intensities and presented a modified nondimensional SSI parameter representing the mass of compressed fluid relative to the mass of the plate. The intermediate SSI regime was studied using a numerical method based on a Lagrangian formulation of the Euler equations of compressible flow and conventional shock-capturing techniques. Peng *et al.* extended the work of Kambouchev *et al.* by including the effect of shock waves formed on the distal face of the plate. The main conclusion of

[27] This definition is analogous to the that of a 'shock' load in the field of structural vibration, *i.e.* a relatively large transient force with a duration that is finite but short in comparison to the natural period of a structure [12–14]. However, the distinction is that a structural 'shock' load analysis applies to small stain elastic vibrations whereas, in this thesis, an impulsive analysis applies to large plastic strains.

[28] The generic term for this effect is fluid-structure interaction (FSI).

these studies was that nonlinear fluid compressibility enhances the effects of SSI in reducing the impulse transmitted to a free plate.

A means to assess the potential influence of SSI effects is relevant to this thesis for two reasons. Firstly, the analytical models reviewed in Section 2.3 do not take SSI effects into account. This is also the case for the models developed as part of this thesis and presented in Chapters 4 and 7. To the author's knowledge, there are no analytical models for deformable plates that include SSI effects. Secondly, an instrumented ballistic pendulum designed to measure the reflected blast pressure exerted on a plate will be presented in Section 5.2. However, the instrument measures the stagnation pressure adjacent to a plate, *i.e.* the local effect of the plate motion on the reflected pressure is not measured directly. For these two reasons, a simple means of estimating potential SSI effects is required, ideally in the form of a dimensionless number. The analysis of Kambouchev *et al.* and Peng *et al.*, while insightful, does not result in a single dimensionless number. Furthermore, Kambouchev *et al.* and Peng *et al.* do not compare their results to experimental data, *i.e.* no validation has been provided. To address this, an alternative analysis resulting in a compact dimensionless number is presented in Sections 3.2.4 and 3.2.5, with validation data sourced from the work of Stoffel [98] and Munday & Newitt [34], as reviewed in Section 2.2.3.

Chapter 3

Literature Critique

> "The more extensive a man's knowledge of what has been done, the greater will be his power of knowing what to do."
>
> Benjamin Disraeli (1804-1881)

3.1 Introduction

The extensive body of literature regarding the impulsive loading of structures was reviewed in Chapter 2, with particular emphasis placed on the subfield of laboratory scale blast and shock loading of thin circular plates in air. It was shown that the literature is rich in both variety and detail. However, for the purposes of this thesis, additional analysis and interpretation of the literature data is required, along with critical consideration of certain theoretical details that do not appear to have been addressed in the literature. Hence, the purpose of this chapter is to reconsider the data, theories and conclusions reviewed in Chapter 2 and, where necessary, to provide further analysis and discussion. The intent is to provide a coherent framework that will serve as the basis and motivation for work reported it this thesis.

3.2 Uniform Shock Loading of Circular Plates in Air

This section contains further analysis of the published experimental data reviewed in Section 2.2. In particular, certain data regressions will be revised, in addition to the proposal of new dimensionless numbers. The purpose is not to imply that the published regressions are incorrect, but merely include data sets that do not correspond to the analyses discussed in Sections 2.3 and 3.3 and Chapter 4.

3.2.1 Blast Loaded Plate Deflection Data

In Section 2.2.1, published data [36, 37, 56, 60, 68–70] for circular plates subjected to uniform impulsive loads is presented using the dimensionless number of Nurick & Martin [5] given in Equations (2.1)

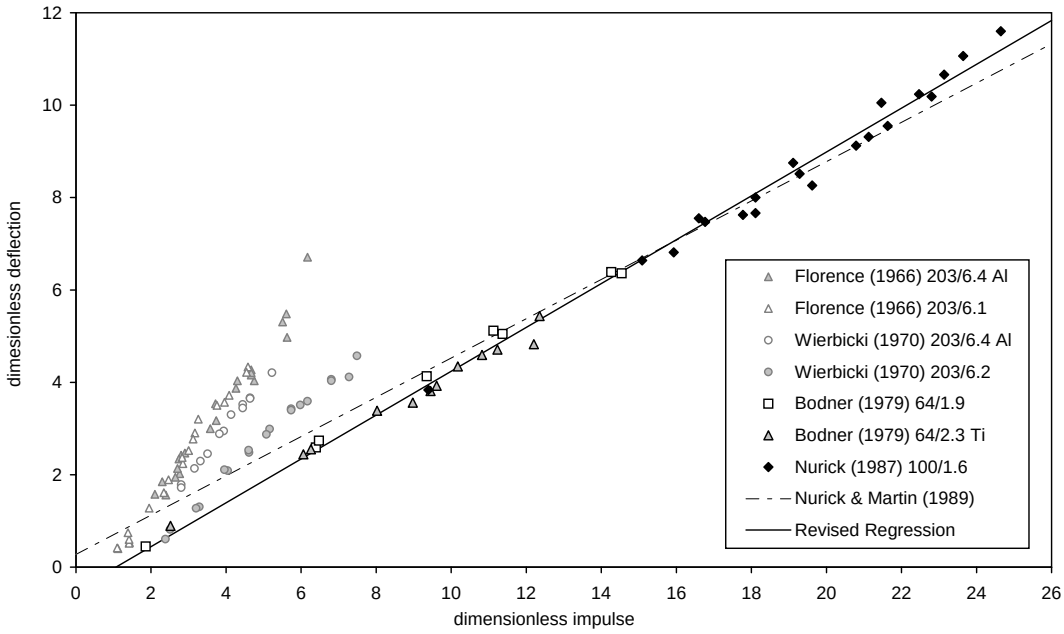

Figure 3.1: Experimental data for impulsively loaded circular plates due to Florence [36], Wierzbicki & Florence [37], Bodner & Symonds [56] and Nurick *et al.* [60] superimposed on the regression fits given in Equations (2.3) and (3.1). The numbers after the dates in the legend indicate the diameter and thickness of the plate in mm, while materials other than steel are indicated by Al (aluminium) and Ti (titanium).

and (2.2). Figures 2.3 and 2.4 show the data superimposed upon the regression fit due to Nurick & Martin [5], given in Equation (2.3), which has a correlation coefficient of 0.974. It was noted that the regression has a positive y-intercept, which is physically impossible in that it implies a non-zero positive deflection as the load impulse tends to vanish. In fact, the opposite would be expected, *i.e.* the impulse of the load would have to be above a certain threshold before any permanent deformation occurs. In this respect it is interesting to note that the individual test series in Figure 2.3 all appear to project to a positive x-intercept in the region of unity.

Sections 2.2.1 and 2.3 show that laboratory blast test data have excellent reproducibility and that several theoretical studies support a linear regression, eliminating these as reasons for the positive y-intercept. Alternatively, the regression may be skewed by an inappropriate combination of data sets. Considering only the data due to Bodner & Symonds [56] and Nurick *et al.* [60] results in a revised regression with the form,

$$\delta = 0.475\phi - 0.507 \tag{3.1}$$

with a correlation coefficient of 0.994, which is an improvement upon the Nurick & Martin result. The new regression is shown in Figure 3.1. The new x-intercept of 1.068 has the physical interpretation that a finite load is required to cause permanent deformation, which is reasonable.

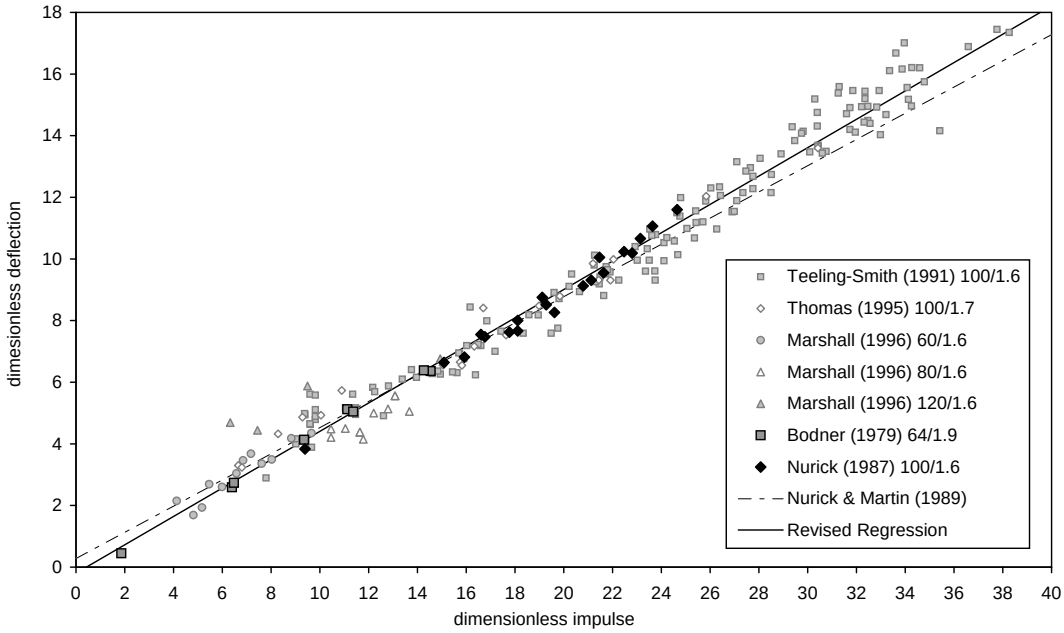

Figure 3.2: Experimental data for impulsively loaded circular steel plates due to Bodner & Symonds [56] and Nurick & co-workers [60, 68–70] superimposed on the regression fit given in Equations (2.3) and (3.2). The numbers after the dates in the legend indicate the diameter and thickness of the plate in mm.

Figure 3.2 shows the data from further work by Nurick & co-workers [60, 68–70] along with the data for mild steel due to Bodner & Symonds [56]. The regression fit for this data is,

$$\delta = 0.46\phi - 0.197 \tag{3.2}$$

with a correlation coefficient of 0.98.

A valid reason for removing the Wierzbicki & Florence data is mentioned by Jones [44], who was at Brown University at the time and remarked that the blast experiments performed by Florence [36] showed a significant amount of 'pull-in' at the clamped edge. From the literature, it appears that Wierzbicki & Florence used the same blast rig. By contrast both Bodner & Symonds and Nurick & Martin used a large clamping area to prevent pull-in. Pull-in leads to additional deflection for a given impulse, as will be discussed in Section 3.3.6. Hence, it can be argued that the data due to Wierzbicki & Florence should be separated from that due to Bodner & Symonds and Nurick & Martin, on the basis that the boundary conditions are distinct.

The data in Figure 3.2 represents two decades of work by six different researchers and at least three different explosive technicians. Hence, the high degree of correlation engenders much confidence in the results, which will be referred to frequently in this work. In particular, the former correlation of Equation (3.1), which is based on data with slightly less scatter, will be used for comparison with theoretical predictions. A further reason is that only Bodner & Symonds and Nurick & Martin recorded the deflection history, which will be discussed in Section 3.2.3

3.2.2 Correlation of Blast Loading Techniques

In the preceding section the lack of correlation between the data of Florence & Wierzbicki on the one hand, and Bodner & Symonds and Nurick & Martin on the other, was attributed to pull-in at the boundaries. However, as mentioned previously, both Bodner & Symonds and Nurick & Martin used a ballistic pendulum while Florence & Wierzbicki used a charge calibration approach. Hence, it must be shown that there is no systematic error due to the load characterizing technique.

All three groups used explosive charges at short stand-off distances, with the charges mounted on neoprene or polystyrene (*i.e.* Styrofoam) attenuators to reduce the peak pressure applied to the plate so as to avoid spalling. Florence & Wierzbicki [36, 37] used Detasheet D (EL-506D) sheet explosive, manufactured by DuPont, while Bodner & Symonds [56] used Detasheet C (EL-506C). Data for Detasheet C is readily available [149] but DuPont no longer produce Detasheet D [150]. Florence & Wierzbicki calibrated their charges in terms of impulse transferred per mass of explosive and reported that the relationship was linear over the range of calibration with a gradient of 2.7×10^3 dyn-s/cm^3 for the 1018 steel tests. Assuming that Detasheet D had a density similar to Detasheet C of 1480 kg/m^3, the gradient can be expressed as 1.824 Ns/g. The charge mass and impulse data reported by Bodner & Symonds is shown in Figure 3.3. Also plotted is a correlation based on all the data except the two points below 2 Ns, which are regarded as representing deflagration. It is noticeable that the intercept crosses essentially at the origin and the regression gradient of 1.821 Ns/g is virtually identical to the result of Florence & Wierzbicki. This excellent agreement supports two important conclusions. Firstly, for small stand-off explosions a ballistic pendulum can be used for precision measurement of the impulse applied to a target structure, *i.e.* there is no impulse transfer through the clamping fixtures. Secondly, the discrepancy between the deflection data of Florence & Wierzbicki and Bodner & Symonds is not due to differences in the charge arrangement.

Also shown in Figure 3.3 are the charge mass and impulse data due to Nurick *et al.* [60], who used Metabel sheet explosive. Metabel is reported as having a density of 1470 kg/m^3 [151] and the data regression shown in Figure 3.3 has a gradient of 1.921 Ns/g, both of which are very similar to the Detasheet explosives. However, the Metabel regression has a positive x-intercept. A possible reasons for this may lie in the difference in the charge configuration. Metabel would not detonate when rolled below a certain thickness and hence, for small charge masses, concentric rings of explosive were employed [151]. The detonation of the explosive rings occurred via a thin strip of explosive, referred to as a 'cross-leader', that was placed across the centre of the polystyrene disk. The entire charge was initiated via a detonator placed in the centre of the polystyrene disk. The mass of the cross-leader was kept as small as possible, which may have reduced the detonation pressure or even lead to deflagration. In this scenario the rings of explosive would still detonate successfully, but the cross-leaders may not have contributed significantly to the total impulse while their mass would still be tallied with the total charge mass. Nurick [151] does not report the mass of the cross-leader, nor its contribution to the total impulse. However, other results [52] indicate that cross-leaders may contribute less impulse per unit mass than the ring charges and hence, since the cross-leader were the same for every charge, could explain the positive x-intercept. The issue of charge configuration will be discussed further in Section 5.2.5.

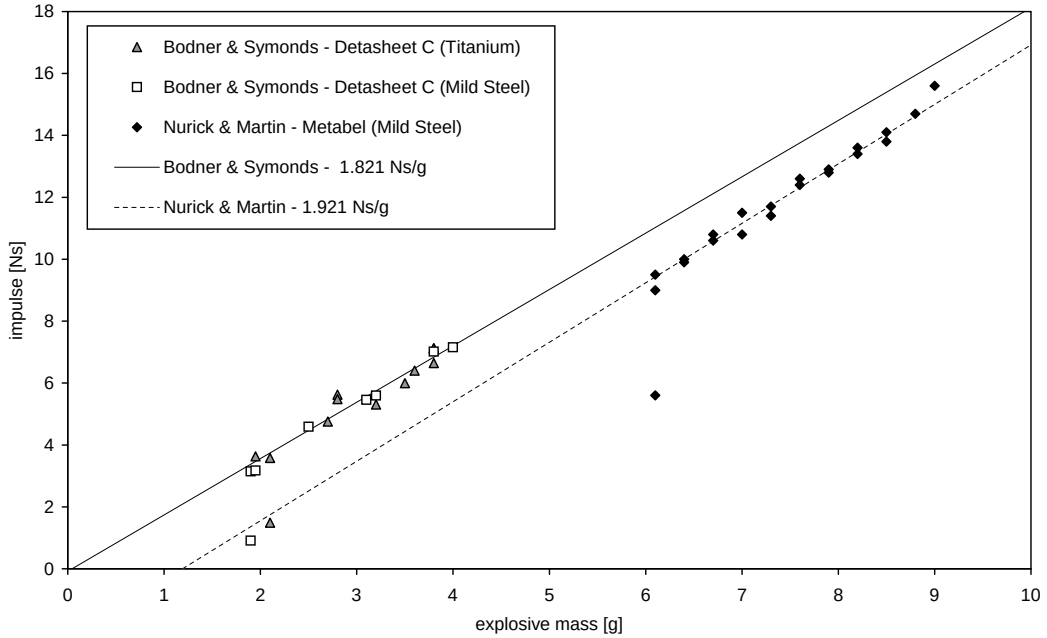

Figure 3.3: Experimental data for charge mass vs impulse for circular plates due to Bodner & Symonds [56] and Nurick *et al.* [60].

3.2.3 Blast Loaded Plate Response Duration

As mentioned in Sections 2.2.2 & 2.3.2, Taylor [15] argued that the response of an impulsively loaded plastic plate would be analogous to that of a linear vibrating membrane. Consequently, the response duration is equal to the first quarter of the period of a vibrating membrane of the same dimensions and mass as the plate, with the tension equal to the product of the yield stress and thickness of the plate. Since the membrane analogy is applicable to an arbitrary plate shape, it provides a convenient basis for non-dimensionalizing the response duration of impulsively loaded plates. For circular plates, the final expression for the response duration is identical to Equation (2.32) reported by Symonds & Wierzbicki [122]. Hence, the proposed form for the non-dimensional deformation duration of an impulsively loaded circular plastic plate is[1],

$$\tau = \frac{T}{0.6532 R_o \sqrt{\frac{\rho}{\sigma_y}}} \tag{3.3}$$

where τ and T are the dimensionless and actual response times and the expression in the denominator is Equation (2.32) with α set to unity.

An alternative definition of a non-dimensional time parameter can be obtained using the travelling hinge approach, which was also proposed by Taylor, as discussed in Section 2.3.6. This implies the use of Equation (2.34) and would result in an identical expression for the dimensionless duration, except for the magnitude of the coefficient in the denominator, which would be unity. While this alternative represents the form that would be obtained using strict dimensional analysis, it is not easily extended to non-circular

[1]This is not to be confused with the definition of an impulsive load as being of negligible duration with respect to the elastic vibration period of the plate.

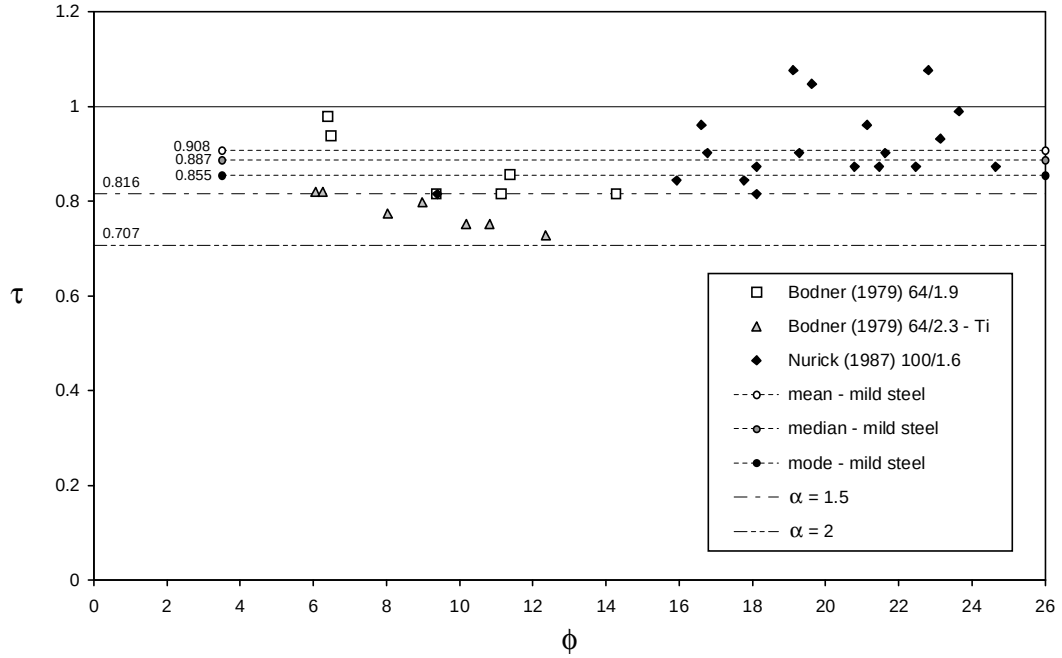

Figure 3.4: Dimensionless deflection duration data for impulsively loaded circular plates due to Bodner & Symonds [56] and Nurick *et al.* [60].

plate shapes. This is due to ambiguity arising from the need to choose an appropriate length parameter. For a circular plate the choice of R_o is axiomatic, but for shapes with more than one characteristic length the choice is not clear. By contrast, the membrane analogy can be applied to any plate shape for which a unique membrane solution exists[2].

Figure 3.4 shows the result of applying Equations (3.3) and (2.1) to the data of Bodner & Symonds [56] and Nurick *et al.* [60], as given in Figure 2.5. Equation (3.3) causes the data to collapse into a band that is relatively narrow, considering that the absolute response durations vary from $65\,\mu$s, for the titanium plates, to $187\,\mu$s, measured by Nurick *et al.* for mild steel plates, *i.e.* a factor of 2.88. This result, along with the convenience of general applicability of the membrane analogy, is regarded as sufficient justification for the use of Equations (3.3). However, this result does not necessarily imply that the vibrating membrane analogy provides an accurate solution. It will be shown, in Sections 3.3.4.2 and 4.2.2, that the membrane analogy provides a lower bound to the actual plate response.

The data in Figure 3.4 preserves the trends noted in Section 2.2.2, *i.e.* the displacement durations do not depend on the impulse magnitude and there is more scatter than in the corresponding deflection data. These trends are retained because the load impulse does not appear in the denominator of Equation (3.3), which thus is constant for a given plate configuration. Furthermore, the good correlation between the data of Bodner & Symonds and Nurick *et al.* supports the conclusions based the vibrating membrane analogy, *i.e.* that the displacement duration is independent of the plate thickness while being proportional to the plate radius and to the root of the quotient of its density and yield stress.

[2]A comparative study of the dimensionless deformation duration of plates of different shapes, but identical in all other respects, including area, is in progress, but outside the scope of this thesis.

From Figure 3.4 an additional trend is evident, namely that most of the dimensionless duration data points are less than unity. The probable reason for this is that the flow stress during deformation is greater that the quasi-static yield stress. The denominator of Equation (3.3) does not account for strain or strain rate hardening, both of which would tend to increase the flow stress. Hence, using the yield stress in the denominator would tend to decrease the dimensionless duration. For example, the dimensionless duration values of 0.816 and 0.707, highlighted in Figure 3.4, correspond to α values of 1.5 and 2 respectively, as would apply to Equation (2.32). The interpretation of the α values are considered in more detail in Section 3.3.4.2.

It was noted in Section 2.2.2 that, in comparison with the corresponding deflection results, the deformation duration data set has a greater amount of scatter and appears to have a distinct lower limit. This trend is even more evident in Figure 3.4, in that the two mild steel data sets appear to have the same lower limit of 0.816, even though the mild steel data due to Nurick *et al.* has the greater scatter. To accommodate the lower limit, a lognormal distribution fit [152] was applied to the combined mild steel data, resulting in mean, median an mode[3] values of 0.908, 0.887 and 0.855 respectively, as shown in Figure 3.4. In this thesis, the mode value will be taken to be representative of the mild steel response. The titanium data is insufficient for a similar analysis, hence the mean of 0.777 will be used.

A possible reason for the scatter is the variable and non-ideal characteristics of the blast loads. While the charge configurations of Bodner & Symonds and Nurick *et al.* would both tend to produce short duration impulsive loads, their time histories would differ. As mentioned previously, attenuators were used to prevent spalling of the plates by reducing the peak pressure applied to the plate. Nurick *et al.* used a 16 mm thick polystyrene attenuator to ensure that the impulse from the concentric rings of explosive was evenly spread, whereas Bodner & Symonds used a sheet explosive and hence a 6.35 mm thick polystyrene attenuator was sufficient. Consequently, for a given impulse, any variation in the attenuator thickness would tend to result is a slightly less intense blast load of a longer duration, which would tend to increase the dimensionless duration. The effect of finite duration loads will be considered theoretically in Section 4.3.

Another possible cause of scatter in the data may be the small charge sizes. Bodner & Symonds used machine rolled sheet explosive and found that it could sustain a detonation at a thicknesses as low as 0.42 mm. It is well known that the specific yield of an explosive charge decreases as the charge thickness tends to a critical value, below which a detonation cannot be sustained [150, 153]. This could explain the increased deformation duration at the low impulse end of the Bodner & Symonds data. By contrast, the scatter in the data of Nurick & Martin does not appear to be depend on the charge mass. Nurick *et al.* found that their sheet explosive would not detonate below a thickness of 3 mm [151]. To achieve lower impulse loadings, the explosive was configured in concentric annular rings so as to spread the load over the plate[4]. In other words, the charges used by Nurick *et al.* were always close to the critical thickness, which may explain the wider band of scatter.

Finally, the scatter may include some experimental error. Unlike the total impulse and final deflection, which are measured *a posteriori*, the plate response must be captured *in situ*, which was technically challenging at the time. Furthermore, neither Bodner & Symonds nor Nurick *et al.* report a synchronized

[3] In this context the term 'mode' refers to the location of the peak of the lognormal duration distribution, and is not to confused with displacement and/or failure modes.

[4] This approach was suggested by Bodner, who was a visiting researcher at the University of Cape Town at the time.

measurement of the detonation signal or a method to account for the elastic component of the plate response, with the result that the start and end times had to be obtained by inspection. With regard to the data presented as part of this thesis, an experimental approach by which these parameters can be captured will be presented in Chapter 5.

3.2.4 Shock Tube Loaded Plate Deflection Histories

In Section 2.2.3, experimental results for the dynamic shock loading of metal plates were reviewed. In particular, Figure 2.8 shows deflection histories recorded by Munday & Newitt [34] and Stoffel [98]. As mentioned previously, the light occlusion technique used by Munday & Newitt to measure the deflection of the centre of the plate was partially obscured by the specimen clamping fixture and the initial plate response was not captured. Furthermore, the arrival time of the shock relative to the plate response was not reported. These two shortcomings in the data of Munday & Newitt lead to uncertainty regarding the precise moment when a plate began to move. According to the guidelines of Krauthammer *et al.* [1], as discussed in Section 1.1.2, this would constitute a lack of precision reporting. By contrast, Stoffel measured the complete displacement history of the centre of a plate specimen and captured the pressure history at a short distance before the clamped boundary of the plate, as shown in Figure 2.7.

In lieu of a measured value, the temporal offset of the Munday & Newitt curves must be estimated theoretically. The simplest approach is to compare the measured deflection history to that predicted for a free plate, of the same density and dimensions, subjected to a constant pressure. This approach is motivated by the observation that the motion of the plate centre is not initially affected by the presence of the plate boundaries, as shown in Figure 2.1, and accelerates as a free disk. Hence, the early displacement history is parabolic with the form,

$$\tilde{w} = \frac{1}{2} a_0 t^2 \quad \text{where} \quad a_0 = \frac{P}{\rho H} \quad \text{and} \quad \dot{\tilde{w}} = a_0 t \tag{3.4}$$

where P is the initial reflected shock pressure less the initial test pressure, *i.e.* the initial gauge pressure driving the plate. The result of this approach is shown in Figure 3.5. It is noticeable that the data due to Stoffel lie significantly closer the constant pressure curve than that of Munday & Newitt, despite the greater shock pressure. In Section 3.2.5 it will be shown that this is primarily due to the greater inertia of the specimens used by Stoffel, whereas the specimens used by Munday & Newitt, though of higher density, were substantially thinner.

Munday & Newitt argued that the divergence shown in Figure 3.5 results from a decrease in the reflected pressure due to the rapid response of the plates. The argument is based on the work of Meyer [154], who investigated the response of 0.043 mm thick cellulose acetate sheets to low Mach number shock loads using approximate series solutions. A constant pressure assumption is sufficiently accurate if the velocity of the plate is small in comparison the shocked air particle velocity, *i.e.* the shock 'wind'. However, the assumption begins to break down when the plate velocity is not small, in which case the shocked air particles are no longer brought to rest by the reflected shock and the full stagnation pressure is not reached. With modern desktop computing power, Meyer's approach is not necessarily the most convenient. In this section a similar but simpler approach than that of Meyer will be pursued. In

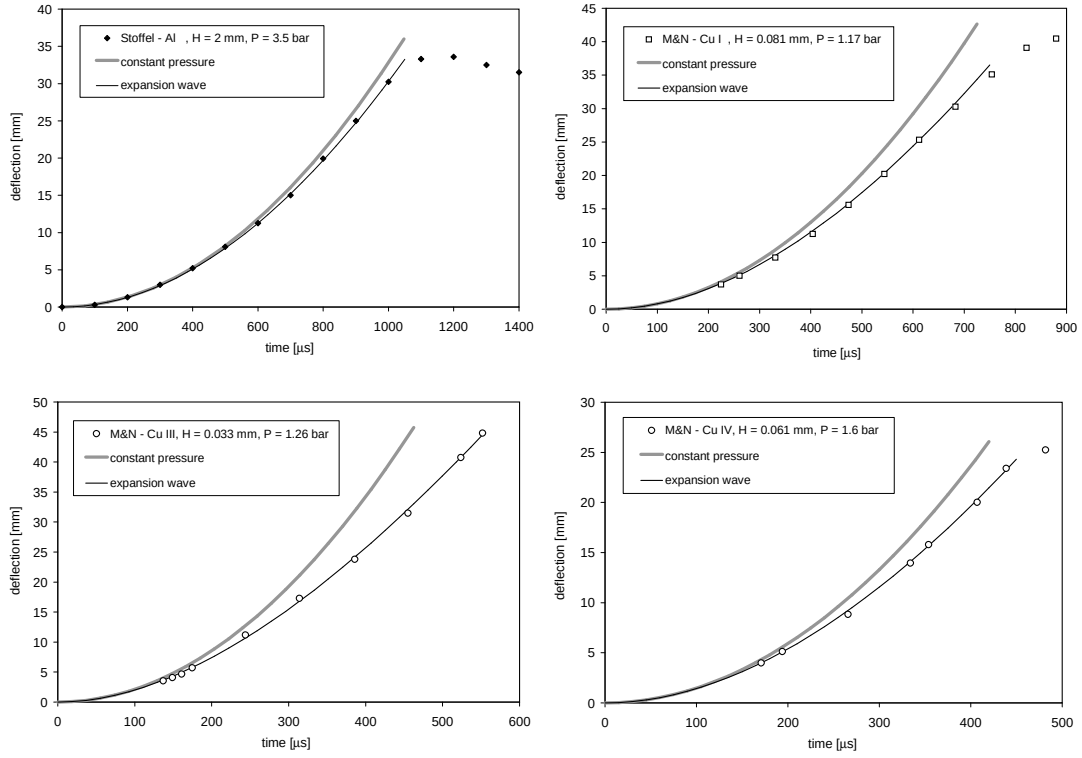

Figure 3.5: Deflection history data for shock tube loaded circular plates due to Munday & Newitt [34] and Stoffel [98] compared to equivalent free plate predictions based on constant pressure or expansion wave assumptions.

particular, only shock-structure interaction on the proximal specimen face will be considered and pressure waves emanating from the distal face are assumed to be negligible.

Consider a spatially and temporally uniform shock impinging on a homogeneous plate of uniform thickness that is free to move. Initially the plate is stationary and causes a reflected shock that brings the shocked particles to rest at stagnation pressure. Initially, the reflected shock velocity is much greater than the plate velocity and therefore travels a significant distance before the plate moves appreciably. Under these conditions the free plate can be viewed as a projectile acted upon by a uniform column of gas at the initial reflected shock pressure and temperature. This process is well understood and discussed in internal ballistics texts such as that by Seigel [155]. As the plate begins to accelerate under the action of the gas pressure, expansion waves will propagate from the plate surface into the gas column, decreasing the pressure exerted on the plate, according to the equation,

$$\frac{P_{abs}}{P_r} = \left[1 - \frac{\gamma_c - 1}{2}\frac{v}{a_r}\right]^{\frac{2\gamma_c}{\gamma_c - 1}} \quad \text{where} \quad a_r = \sqrt{\gamma_c \Re T_r} \tag{3.5}$$

where v is the velocity of the plate and P_{abs} the absolute pressure acting on the plate. The absolute initial pressure, temperature and speed of sound, due to the reflected shock, are denoted by P_r, T_r and a_r respectively, while γ_c is the ratio of specific heats and $\Re$ is the universal gas constant. Furthermore,

for a given pressure the plate acceleration is,

$$a = \frac{P}{\rho H} = \frac{P_{abs} - P_0}{\rho H} \tag{3.6}$$

where P_0 is the unshocked absolute gas pressure, which is the same as the gas pressure on the distal plate face. The combination of Equations (3.5) and (3.6) is not convenient for exact analytical integration[5], but a simple Euler type numerical integration scheme [156] provides sufficient accuracy. The plate motion predicted using this approach correlates well with data due to Stoffel up to the point of inflection, as shown in Figure 3.5. Since Stoffel reported all the relevant experimental parameters, such that no temporal shifting is required, this result is regarded as a validation of expansion wave approach.

The calculations based on the data of Stoffel indicate that incident shock gas particle velocity and maximum plate velocity are approximately 214 m/s and 56 m/s respectively. Therefore, at the instant of maximum plate velocity, the shocked gas particles are not brought to rest resulting in a reflected gauge pressure of 2.75 bar, as opposed to the stagnation gauge pressure of 3.5 bar, *i.e.* a drop of 21.3 %. In other words, a relatively modest plate velocity can lead to a significant drop in pressure and a consequent drop in the impulse transferred. However, this pressure drop will only occur at the centre of the plate while the pressure drop nearer to the clamped boundary will be less severe, as is indicated by the experimental measurements in Figure 2.7. The end result is that, despite the pressure drop, the plate motion up to the inflection point only deviates slightly from the free plate motion, which suggests that a plate deformation model using a constant pressure assumption may yield useful results. A model of this type will be presented in Section 4.3.

As mention in Section 2.2.3, the data of Munday & Newitt is incomplete. In particular, the initial motion of the plate centre as well the shock intensity, shock velocity and shock arrival time were not reported. Hence, where the measured value of P_r was used to correlate the data of Stoffel, 'best fit' values for P_r have to be inferred from the deflection data of Munday & Newitt. For the majority of the their tests, Munday & Newitt report a pressure ratio of 2.88 between the driver and test sections of their shock tube, which, according to ideal shock tube theory [157], should produce a peak reflected shock gauge pressure of 1.67 bar. However, when using this value, satisfactory agreement between the predicted and measured curves could not be obtained. Typically, shock tubes do not attain the predicted performance due to practical limitations, such the finite duration and insufficient repeatability of the diaphragm bursting process [157]. Therefore, the driver pressures used in the calculations were varied until satisfactory correlations were obtained, as shown in Figure 3.5. For the same nominal driver pressure, the resulting reflected shock gauge pressures vary from 1.6 bar, which is close to theoretical prediction, to 1.17 bar, *i.e.* a absolute pressure variation of 16.5 %. This performance is reasonable considering the size of the diaphragm. Given the above, it is concluded the expansion approach produces acceptable correlations for data of Munday & Newitt and Stoffel. Furthermore, it confirms that shock-structure interaction (SSI) effects must be considered during shock loading events of finite duration. The effect of SSI on blast loading experiments will be discussed in Section 3.2.5.

In Section 2.2.3 it was shown that dimensionless time parameter of Munday & Newitt, given in Equation (2.4), is not able to adequately correlate the data of Munday & Newitt and Stoffel. Furthermore, the form of Equation (2.4) does not appear to have any theoretical motivation. Hence, the following

[5]Two approximate solutions are discussed in Section 3.2.5

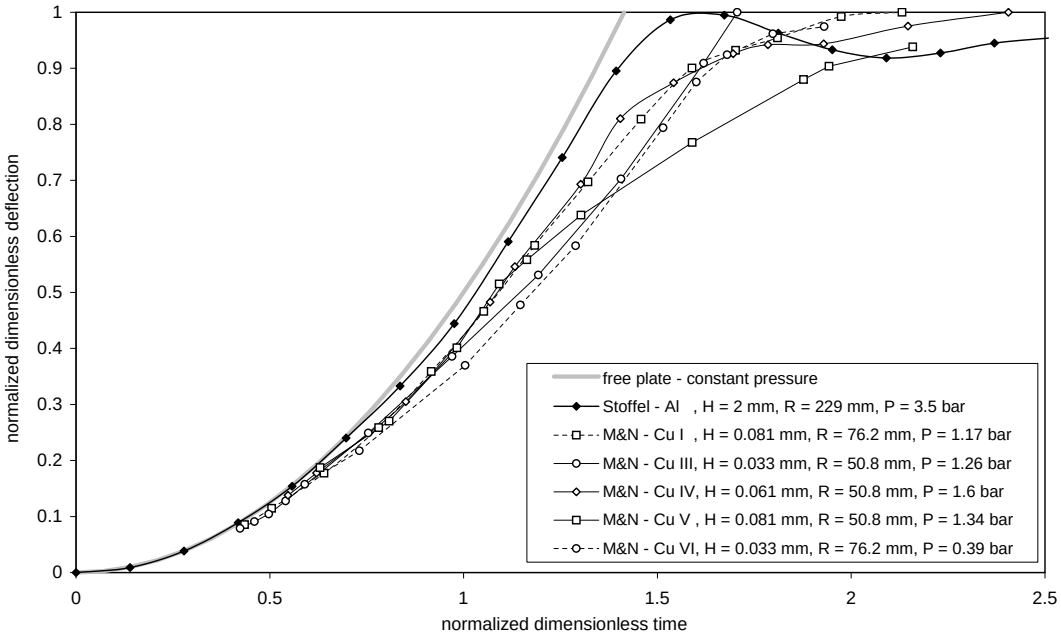

Figure 3.6: Normalized dimensionless deflection history data due to Munday & Newitt [34] and Stoffel [98] for dynamically shock loaded circular plates using Equation (3.9).

dimensionless time parameter is proposed,

$$\tau_{IDS} = t\sqrt{\frac{a_0}{H}} \tag{3.7}$$

where the subscript *IDS* stands for 'ideal dynamic shock' loading. Equation (3.7) is motivated by the parabolic motion of a free plate subjected to a constant pressure and obtained by substituting Equation (3.4) into the definition of dimensionless deflection given in Equation (2.2), which gives,

$$\delta = \frac{\tilde{w}}{H} = \frac{1}{2}\frac{a_0}{H}t^2 = \frac{1}{2}\left(t\sqrt{\frac{a_0}{H}}\right)^2 = \frac{1}{2}\tau_{IDS}^2 \tag{3.8}$$

where the proposed expression for dimensionless time appears in parenthesis. Hence, since all the plates in Figure 2.8 should initially behave as free plates, Equations(3.7) and (3.8) should cause the initial portions of all the curves to correlate to the same simple quadratic curve. However, a large variation in plate thickness will not provide a conveniently legible graph. This can be remedied by normalizing Equation (3.8) with respect to the maximum dimensionless deflection, leading to the expression,

$$\delta_{norm} = \frac{\delta}{\delta_{max}} = \frac{1}{2}\left(\frac{\tau_{IDS}}{\sqrt{\delta_{max}}}\right)^2 \tag{3.9}$$

which is the normalized dimensionless deflection, while the expression in parenthesis is the normalized dimensionless time. Figure 3.6 shows the result of the application of Equation (3.9).

From Figure 3.6 it can be seen that Equation (3.9) provides an improved basis for correlating shock tube loaded plate data than the dimensionless time parameter of Munday & Newitt. In particular, the four

Munday & Newitt tests with a similar nominal pressure are tightly grouped. At small values of δ_{norm} (<0.2) the curves remain close to the constant pressure curve, *i.e.* the low plate velocities do not greatly affect the reflected pressure, while at large values of δ_{norm} (>0.8), the curves diverge strongly due to membrane stresses arresting the plate motion. At intermediate deflections, the curves display noticeable divergence due to the influence of the plate velocities on the reflected pressures, with the thinner plates showing greater effects.

Similar effects can be expected for blast loading, such as published data reviewed in Section 2.2, where the pressures produced are two orders of magnitude greater than those considered in this section. To address this issue, closed form estimates for the influence of plate motion during shock-structure interaction will be derived in Section 3.2.5. Furthermore, the total plate motion for configurations where the influence of SSI is negligible will be considered in Section 4.3.

3.2.5 Shock-Structure Interaction

In analytical models, such as those reviewed in Section 2.3, and numerical models [158] it is often assumed that the pressure exerted on the target plate is not affected by the movement of the plate. However, as discussed in Section 2.5.3 and shown in Section 3.2.4, this may not always be correct. In particular, if the magnitude of the plate velocity is a significant fraction of the shocked air particle velocity, *i.e.* the shock 'wind', then the shocked air particles are no longer brought to rest by the reflected shock and the full stagnation pressure is not reached. The aim of this section is to present approximate closed form solutions for shock-structure interaction (SSI), which establishes upper and lower bounds to the decrease in reflected shock pressure due to plate motion[6]

In Section 3.2.4, a homogeneous free plate of uniform thickness was considered as a projectile acted upon by a uniform column of gas created by the impinging of uniform shock. The accelerating plate would cause expansion waves propagate into the gas column, decreasing the reflected shock pressure. The relation between the plate velocity and shock pressure is given by Equation (3.5), while the plate acceleration is given by Equation (3.6).

A typical result obtained by numerical integration of Equations (3.5) and (3.6) using an Euler type scheme [156] is shown in Figure 3.7, where a 1.6 mm thick steel plate subjected to a 10 MPa shock load is considered. For load durations approaching 1 ms, the SSI effects are clear and cause the plate velocity to deviate substantially from the prediction based on a constant pressure approach, *i.e.* Equation (3.4). By contrast, the deviation after a short duration is negligible. Therefore, to justify the assumption that the plate motion does not significantly affect the reflected pressure, a convenient means of estimating the velocity error due to SSI is required. This, in turn, requires the development of closed form approximate solutions to Equations (3.5) and (3.6).

In the case of a strong shock, Equation (3.6) can be simplified by taking the value of P to be equal to P_{abs}, since P_0 is negligible in comparison to both, and the resulting expression for the acceleration is,

$$a = \frac{dv}{dt} = \frac{P}{\rho H} \approx \frac{P_r}{\rho H}\left[1 - \frac{\gamma_c - 1}{2}\frac{v}{a_r}\right]^{\frac{2\gamma_c}{\gamma_c - 1}} \tag{3.10}$$

[6]The work contained in this section has been published by Cloete & Nurick [159].

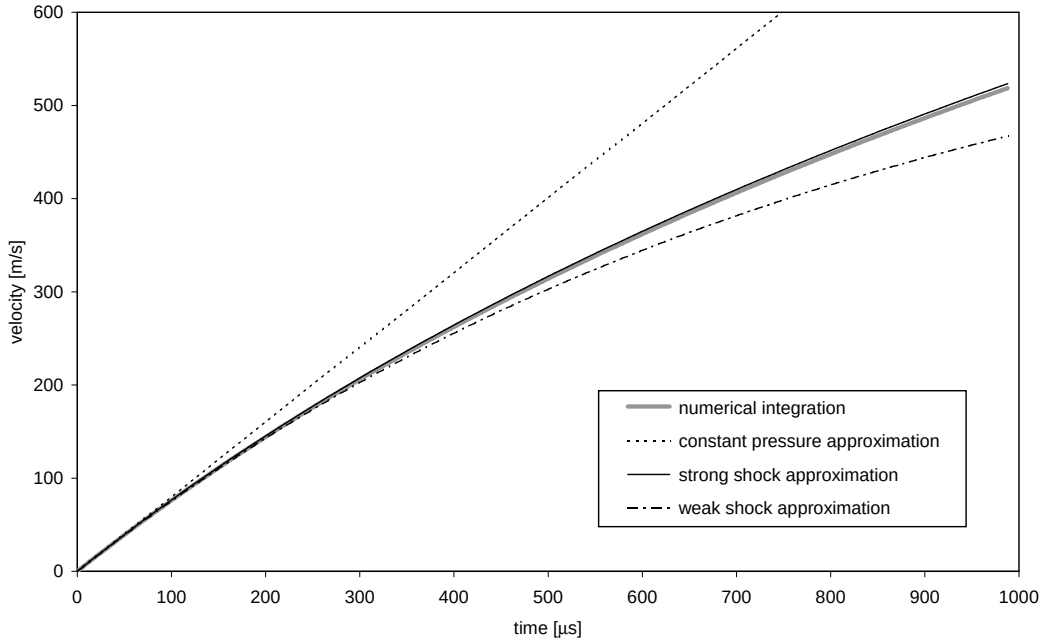

Figure 3.7: Velocity history for a 1.6 mm thick steel free plate dynamically shock loaded in air with an initial pressure of 10 MPa.

Integration by separation of variables, noting that $v = 0$ when $t = 0$, gives the velocity history as,

$$v(t) = \frac{2a_r}{\gamma_c - 1}\left[1 - \left[1 + \frac{\gamma_c + 1}{2a_r}\frac{P_r}{\rho H}t\right]^{\frac{1-\gamma_c}{1+\gamma_c}}\right] \tag{3.11}$$

The velocity history obtained using Equation (3.11) is compared to a numerical integration result in Figure 3.7. The strong shock approximation breaks down when the plate velocity v becomes a large fraction of the initial speed of sound of the gas particles processed by the reflected shock a_r. For the case shown in Figure 3.7, a_r is approximately 958 m/s and P_r is in the order of 100 times greater that P_0, and therefore the strong shock approach provides a good approximation[7].

For weak shock loading, such as the experiments by Munday & Newitt [34] and Stoffel [98] discussed in Section 3.2.4, the effect of P_0 cannot be ignored. In other words, Equation (3.11) does not provide an accurate approximation at low shock pressures, as shown in Figure 3.8, where the data from Plate III of Munday & Newitt is considered.

An approximate solution for weak shock is obtained by expanding Equation (3.5) as a Taylor series of the form [160],

$$(1 + Bt)^n \approx 1 + nBt + \frac{1}{2}n(n-1)(Bt)^2 + ... \tag{3.12}$$

[7]A formula for the displacement history can be obtained by a second integration, but will not be presented here since the velocity is of primary interest for energy methods.

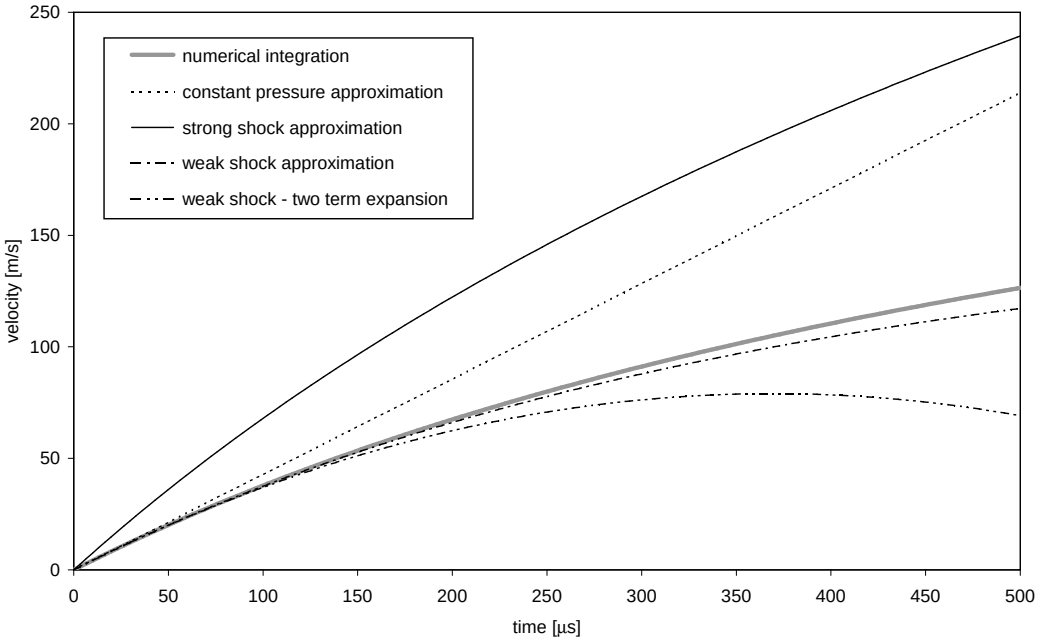

Figure 3.8: Velocity history for a 0.033 mm thick copper free plate dynamically shock loaded in air with an initial pressure of 1.26 bar.

where B and n are constants. Using the first two terms, the resulting expression for the acceleration is,

$$a = \frac{dv}{dt} \approx \frac{P_r}{\rho H}\left[1 - \frac{\gamma_c}{a_r}v\right] - \frac{P_0}{\rho H} \tag{3.13}$$

Integration by separation of variables, noting that $v = 0$ when $t = 0$, gives the velocity history as,

$$v(t) = \frac{a_r}{\gamma_c}\left(1 - \frac{P_0}{P_r}\right)\left[1 - e^{-\frac{\gamma_c}{a_r}\left(\frac{P_r}{\rho H}t\right)}\right] \tag{3.14}$$

Velocity histories obtained using Equation (3.14) are compared to the previous results in Figures 3.7 and 3.8. In both cases the weak shock approach consistently underpredicts the velocity. The reason for this is the two term expansion used in Equation (3.13), which causes the acceleration to be consistently underestimated. This effect becomes more severe as the plate velocity v becomes a large fraction of the initial speed of sound of the gas particles processed by the reflected shock a_r. In this case of Figure 3.8, a_r is approximately 397 m/s. Nevertheless, Equation (3.14) provides an accurate approximation at short durations for both high and low shock pressures.

The form of Equation (3.14) is not convenient for developing an estimate for the velocity deviation from constant pressure behaviour due to SSI. A more convenient form is obtained by expanding the exponential term using the first three terms of the Taylor series [160],

$$e^x \approx 1 + x + \frac{x^2}{2!} + \frac{x^3}{3!} + ... \tag{3.15}$$

Table 3.1: Comparison of experimental plate velocity deviations from the constant pressure response, as shown in Figure 3.5, with first order estimates of shock-structure interaction effects obtained using Equation (3.17). In all cases a γ_c value of 1.4 is assumed.

test	P_r [bar]	T_s [K]	a_r [m/s]	ρ [kg/m^3]	H [mm]	t [μs]	τ_{IDS}	Δv_{exp} [%]	Δv [%]
Stoffel - Al	4.5	473	443	2800	2	1015	5.7	10.9	12.9
M&N - Cu I	2.17	375	395	8890	0.081	675	30.2	26.1	35.9
M&N - Cu III	2.26	380	397	8890	0.033	500	56.9	40.3	67.6
M&N - Cu IV	2.6	396	406	8890	0.061	435	30.3	25.9	36.0

which, when applied to Equation (3.14), gives,

$$v(t) \approx \frac{P_r - P_0}{\rho H} t \left[1 - \frac{\gamma_c}{2a_r}\left(\frac{P_r}{\rho H} t\right)\right] \tag{3.16}$$

Note that, unlike Equation (3.14), the term outside the parenthesis is the plate velocity due to a constant pressure, which implies that at short durations Equation (3.16) will tend to the constant acceleration solution given in Equation (3.4). Hence, the second term in the parenthesis is, effectively, a first order approximation for the deviation from constant pressure behaviour due to SSI. When expressed as a percentage, the difference is,

$$\Delta v = \frac{a_{const} t - v(t)}{a_{const} t} \times 100\% \approx \frac{\gamma_c}{2a_r}\left(\frac{P_r}{\rho H} t\right) \times 100\% \tag{3.17}$$

As shown in Table 3.1, Equation (3.17) is not valid for long dimensionless durations where Equation (3.16) begins to deviate significantly below the weak shock approximation, which itself would underpredict the exact solution. However, at short durations the difference between Equations (3.14) and (3.16) is significantly smaller than their mutual deviation from the constant pressure solution. In other words, if the error indicated by Equation (3.17) is small, then the difference between Equation (3.16) and the weak shock approximation is negligible and the velocity deviation estimate may be considered to be trustworthy. Therefore, for short dimensionless durations (< 10), Equation (3.16) is considered to provide a useful upper estimate for the velocity deviation from constant pressure behaviour due to SSI.

In the application of Equation (3.17), the role of the gas temperature is crucial. The ability of a given column of gas to maintain a near constant base pressure on a projectile is strongly dependent on the temperature of the gas. An increase in temperature results in an increased speed of sound in the gas, which reduces the time required for the gas to respond to pressure perturbations due to the moving plate. Thus, double shocked gas particles, *i.e.* particles processed by both the incidence and reflected shocks, have significantly elevated temperatures and are less likely to be attenuated due to plate motion. This is especially important for strong shocks resulting from explosive loading, where the plate experiences a large acceleration and can attain velocities that are a large fraction of the ambient speed of sound.

As will be shown in Section 5.3, a typical short stand-off blast load can cause a reflected shock of 100 MPa, which will produce a temperature in the order of 15000 K giving a speed of sound in the order of 2500 m/s [157]. Assuming the shock load delivers an impulse of 10 Ns to a 100 mm diameter steel plate of 1.6 mm thickness, the pressure duration would be 12.7 μs. Hence, Equation (3.17) predicts an

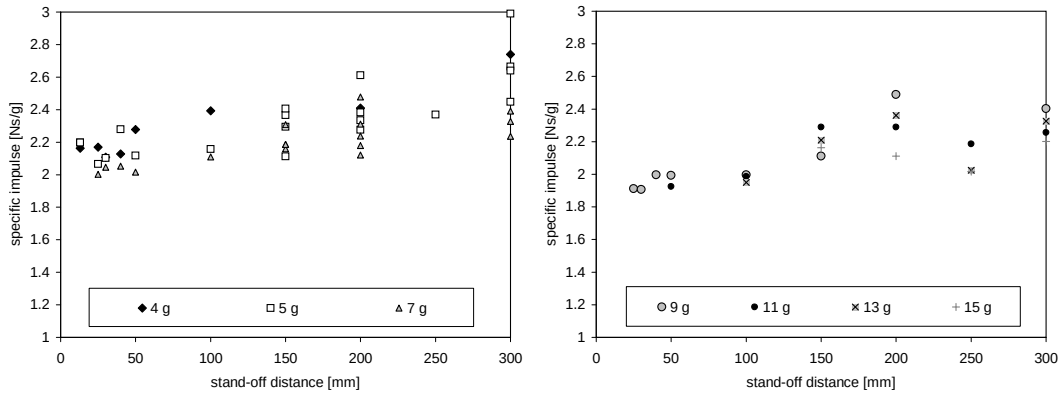

Figure 3.9: Effect of charge stand-off distance on the impulse measured for blast tube loading of mild steel plates according to Jacob *et al.* [107].

upper limit difference of 2.84%. A difference of this magnitude is regarded as acceptable in the context of results reviewed and reported in this thesis.

3.2.6 Blast Tube Data and Stand-off Effect Analysis

The data of Jacob *et al.*, who used a blast tube to load circular plates, was discussed in Section 2.2.4. An interesting aspect of the data is that for a given charge mass, the plate deflection is reasonably constant from a stand-off, *i.e.* tube length, of 75 mm to 300 mm. However, the constant deflection is not associated with a constant impulse, as shown in Figure 3.9, which was generated using the data of Jacob *et al.* and shows the specific impulse, *i.e.* impulse divided charge mass, as a function of stand-off distance. The data shows that, for a given charge mass, the recorded impulse increases with blast tube length. The net effect is that the midpoint deflection for a given impulse appears to decreases with an increase in stand-off distance. Furthermore, note that for the shorter stand-off distances and larger explosive masses, the specific impulse tends to a value of 1.9 Ns/g, which correlates with the data in Section 3.2.2.

The increase in measured impulse with blast tube length was not highlighted or discussed by Jacob *et al.*, nor does it appear to be dealt with in the literature. An investigation of this effect using numerical shock wave simulations and will be discussed in Section 5.3.3. However, Jacob *et al.* have subtly incorporated the effect into their modification of the dimensionless damage number proposed by Nurick & Martin [6] to account for stand-off effects. The damage number is given in Equation (2.5) and incorporates a loading parameter given in Equation (2.6) and repeated here for convenience,

$$\gamma_S = \frac{1 + ln\frac{R}{R_c}}{1 + ln\frac{S}{R_c}} \quad \text{for} \quad (S \geq R_c) \tag{3.18}$$

where S is the stand-off distance and R_c is the charge radius. As mentioned previously, the numerator accounts for the fact that a localized load produces a greater central displacement than a uniform load of equivalent impulse, while the denominator, added by Jacob *et al.*, has the effect of cancelling out the effect of the numerator when the stand-off distance is equal to the plate radius. In other words, Equation (3.18) states that, with respect to Mode I response, a localized load at a stand-off distance of

one plate radius will produce that same effect as a uniform ideal impulsive load of the same total impulse. Furthermore, as the stand-off increases, the loading parameter becomes less than unity and reduces the final damage number for a given measured impulse. In this way, the loading parameter compensates for the fact that, for a given plate displacement, a greater impulse is measured for longer blast tubes.

The preceding discussion implies that when developing theoretical models for blast tube loaded plates, the meaning of the total measured impulse must be carefully considered. The damage number modified by Jacob *et al.* was originally developed for impulsively loaded structures. However, Jacob *et al.* did not report pressure or plate displacement histories, and it is therefore unclear whether the load is impulsive or dynamic. Furthermore, it is not known whether a given plate specimen had ceased deforming before the blast load had decayed to a negligible level. Bearing in mind that a persistent residual pressure, even if weak, can contribute substantially to the total impulse without causing any further damage, the use of the total measured impulse in theoretical models and correlations may lead to erroneous conclusions. An experimental rig is presented in Chapter 5 with which the pressure history during blast tube loading is measured. This data, along with analytical models of the displacement duration, will be used to evaluate what fraction of the total impulse is effective in deforming the plate specimens.

3.3 Analytical models of Circular Plates

Several analytical models for the impulsive loading of circular plates were reviewed in Section 2.3. Some of the models [38,45,66,122] share common features, such as the ideal impulsive loading (IIL) assumption and a constant deformation profile, *i.e.* mode shape. These common features, though derived or defined from distinct perspectives, allow for the construction of a unified approach, through which the published models to be compared and evaluated. The purpose of this section is to present a unified approach, which can be viewed as a generalization of the energy method of Duffey [38]. This generalized energy method will also provide the basis for further model development in Chapters 4 and 7.

3.3.1 Generalized Energy Method for Ideal Impulsive Loading

The energy method of Duffey, outlined in Section 2.3.4.1, provides an expression for the final deflection of a circular plate, subjected to an ideal impulsive load, by equating the energy dissipated through plastic work as the plate deforms to the initial kinetic energy, given by Equation (2.19).

Duffey's method is beguilingly simple in that only the initial and final deformation states need to be considered. However, it conceals some mathematical sleight of hand, in that the initial and final displacement profiles are different, but yet no mechanism is postulated to cause the change. The unstated assumption is that any intermediate deformation profiles is considered not to alter the monotonic nature of the strain history and hence not to affect the estimate of the plastic dissipation and, consequently, the final displacement.

While the above mentioned assumption, inherent in Duffey's approach, is reasonable, it does not allow for the deformation duration to be calculated since the intermediate configurations are unknown. One possible solution, as used in the membrane approach, is to assume the plate has a constant mode shape,

Table 3.2: Results for various assumed deformation profiles obtained using the generalized energy method, *i.e.* the plastic stiffness and effective mass coefficients, normalized expressions for the non-dimensional central deflection, initial central velocity and displacement response time under ideal impulsive loading conditions and the correlated hardening parameter.

Profile	λ		μ		$\frac{\delta}{\sqrt{\frac{1}{\alpha}}\,\phi}$	$\frac{\dot{\tilde{w}}_0}{V_0}$	$\frac{T}{R_o\sqrt{\frac{\rho}{\alpha\sigma_y}}}$	$\alpha_{\exp}$
	exact	approx.	exact	approx.				
parabolic	2	2	$\frac{1}{3}$	0.3333	0.7071	1.7321	0.6413	2.2160
Bessel	$\Lambda^2 J_1^2(\Lambda)$	1.5586	$J_1^2(\Lambda)$	0.2695	0.8009	1.9263	0.6532	2.8430
conical	1	1	$\frac{1}{6}$	0.1666	1	2.4495	0.6413	4.4321

as given in Equation (2.28). This implies that an expression for the kinetic energy of a given plate shape is required.

In the sections to follow, Duffey's method will be generalized by defining generic forms for the plastic dissipation and kinetic energy, and it will be shown that this approach can be used to confirm and compare various published theoretical displacement results. Furthermore, in Chapter 4 it will be shown that the energy method can be extended to include intermediate profiles, which will allow non-ideal impulsive and dynamic loads to be considered.

3.3.1.1 Plastic Stiffness

Duffey [38] considered several plate shapes, among which only the quadratic will be considered in this thesis, in addition to the conical and Bessel function shapes. Expressions for plastic work based on parabolic and Bessel type displacement functions were given in Equations (2.25) and (2.27) respectively. To facilitate subsequent comparison and manipulation, it is proposed that these, and other, expressions for plastic work can all be written in the form,

$$W_P = \frac{1}{2}\tilde{K}\tilde{w}^2 \tag{3.19}$$

The quantity $\tilde{K}$ will be referred to as the 'plastic stiffness' since the form of plastic work is reminiscent of the expression for the strain energy in a spring. Admittedly, $\tilde{K}$ characterizes energy dissipation as opposed to storage and thus referring to it as 'plastic stiffness' is, strictly speaking, an oxymoron, nevertheless it is considered useful for discussion purposes. It will be shown that $\tilde{K}$ has, essentially, the same form for all the plate configurations considered in this thesis [8]. For circular plates, $\tilde{K}$ has the form,

$$\tilde{K} = \lambda\pi H\alpha\sigma_y \tag{3.20}$$

where λ is the plastic dissipation parameter that is characteristic of a given displacement profile. The λ values for the plate profiles considered in this section are given in Table 3.2. The derivations for the various λ values are discussed in Section 3.3.2.

[8] In fact, $\tilde{K}$ may be applicable to all plate configurations for which a closed form expressions for the equivalent membrane vibration problem is known. However, pursuit of this proposition is beyond the scope of this thesis.

3.3.1.2 Final Central Deflection

Following Duffey, the general form of the plastic work, given in Equations (3.19) and (3.20), is equated to the initial kinetic energy, given in equations (2.19), leading to a general expression for the final central deflection as a function of the total impulse of the load,

$$E_{k,0} = W_P \quad \Rightarrow \quad \tilde{w} = \sqrt{\frac{2E_{k,0}}{\tilde{K}}} = \sqrt{\frac{I^2/\pi R_o^2 H\rho}{\lambda\pi H\alpha\sigma_y}} \tag{3.21}$$

Dividing both sides by H to render the relation non-dimensional and rearranging results in,

$$\delta = \frac{1}{\sqrt{\lambda\alpha}}\phi \quad \text{where} \quad \delta = \frac{\tilde{w}}{H} \quad \text{and} \quad \phi = \frac{I}{\pi R_o H^2\sqrt{\rho\sigma_y}} \tag{3.22}$$

where δ is the dimensionless deflection of the centre of the plate and ϕ is the dimensionless impulse. The dimensionless deflection can be normalized as,

$$\frac{\delta}{\sqrt{\frac{1}{\alpha}}\,\phi} = \frac{1}{\sqrt{\lambda}} \tag{3.23}$$

Values of $\lambda^{-\frac{1}{2}}$ for various plate profiles are given in Table 3.2, and will be derived in Section 3.3.2.

Note that the energy method leads to a simple closed form solution for circular plates that agrees with the linear relationship between impulse and deflection observed in experiments. Furthermore, the expression for the dimensionless impulse is identical to Equation (2.1), which was developed by Nurick and co-workers, using dimensionless analysis, to correlate experimental blast test data. These observations, and the simplicity of the derivation, serve as the motivation to extend the energy method to other plate configurations in Chapter 7.

3.3.1.3 Effective Mass

As mentioned previously, an expression for the kinetic energy of a circular plate with a given displacement profile is required to facilitate the comparison of various published models. Following a procedure similar to that in the previous section, it is proposed that a general form for the kinetic energy can be written as,

$$E_k = \frac{1}{2}\tilde{M}\dot{\tilde{w}}^2 \tag{3.24}$$

where $\tilde{M}$ is the effective mass and $\dot{\tilde{w}}$ is the central velocity. For circular plates the form of $\tilde{M}$ is[9],

$$\tilde{M} = \mu m \quad \text{where} \quad m = \rho\pi R_o^2 H \tag{3.25}$$

where m is the total plate mass and μ is the effective mass parameter that is characteristic of a given displacement profile. Note that an arbitrary point on the plate will have a velocity that is smaller than

[9]The expression for $\tilde{M}$ may be applicable to any plate configuration with a closed form solution for the equivalent membrane vibration problem. However, pursuit of this is beyond the scope of this thesis.

$\dot{\tilde{w}}$, which implies that μ will typically be less than unity. In other words, a μ value of unity implies a uniform velocity distribution. The μ values for the circular plate profiles considered in this thesis are given in Table 3.2 and will be derived in Section 3.3.2. In Sections 7.4, the expression for $\tilde{M}$ will be altered slightly to accommodate annular and centrally supported plates, where $\dot{\tilde{w}}$ will represent the maximum profile velocity but not the central velocity.

3.3.1.4 Initial Central Velocity

To remain consistent with the energy method, the initial central velocity $\dot{\tilde{w}}_0$ must be chosen such that the initial energy of the assumed velocity distribution is the same that calculated for a plate subjected to a uniform impulsive load. Hence, from Equations (2.17) and (3.24) follows,

$$E_{k,0} = \frac{1}{2} m V_0^2 = \frac{1}{2} \tilde{M} \dot{\tilde{w}}_0^2 \tag{3.26}$$

From which, using Equation (3.25), the normalized initial central velocity can be written as,

$$\frac{\dot{\tilde{w}}_0}{V_0} = \frac{1}{\sqrt{\mu}} \tag{3.27}$$

Values of $\mu^{-\frac{1}{2}}$ for various plate profiles are given in Table 3.2, and are discussed in Section 3.3.2.

Given that μ is typically less than unity, the implication is that $\dot{\tilde{w}}$ is typically greater than V_0. This stands to reason, since the only way a nonuniform velocity distribution can have the same total kinetic energy as a uniform distribution is if the maximum velocity of the former is greater that the velocity of the latter. However, this also represents an inherent contradiction in the constant deformation profile, *i.e.* mode shape, approach in that the initial energy is calculated based on the assumption of a uniform initial velocity, while the deformation is analyzed based on an assumed non-uniform velocity distribution. A method to resolve the contradiction will be proposed in Section 4.2.

3.3.2 Maximum Displacement

In this section, the three distinct PCS deformation profiles considered in this thesis will be considered from the perspective of the generalized energy method. literature results obtained using an energy approach will be recast in the form of Equation (3.22). Furthermore, where required, the literature result will be re-derived using the generalized energy method and the effective mass will be determined.

3.3.2.1 Parabolic Displacement Profile

The plastic work obtained by integrating the strain energy of a parabolic displacement profile was discussed in the context of the work of Duffey and given in Equation (2.25), which, when cast in the form of Equations (3.19) and (3.20), has the form,

$$W_P = \pi H \alpha \sigma_y \tilde{w}^2 = \frac{1}{2} \tilde{K} \tilde{w}^2 \quad \text{where} \quad \tilde{K} = \lambda \pi H \alpha \sigma_y \quad \text{and} \quad \lambda = 2 \tag{3.28}$$

This value of λ leads to a normalized non-dimensional deflection of 0.7071, as reported in Table 3.2.

It is interesting to note that R_o appears in the limits and argument of the integral in Equation (2.25), but does not appear in the final expression. The physical implication is that for a given plate thickness and maximum transverse displacement, the same amount of energy will be dissipated regardless of the diameter of the plate. This is, of course, provided that the deflections and material behaviour remain within the limits imposed by the approximations used in the analysis. It will be seen that the other plate configurations exhibit similar results.

The total kinetic energy of a plate is obtained from the integral,

$$E_k = \int_V \frac{1}{2}\dot{w}^2 dm \quad \text{where} \quad dm = \rho\, dV \quad \text{and} \quad dV = 2\pi r H\, dr \tag{3.29}$$

where ρ is the density and $\dot{w}$ is the transverse velocity of the plate at radius r. As before, the integration subscript V signifies integration over the volume of the plate. The velocity distribution is obtained by taking the temporal derivative of Equation (2.20),

$$\dot{w}(r) = \dot{\tilde{w}}\left[1 - \left(\frac{r}{R_o}\right)^2\right] \tag{3.30}$$

Substituting Equation (3.30) into Equation (3.29), the expression for the kinetic energy becomes,

$$E_k = \rho\pi H\dot{\tilde{w}}^2 \int_0^{R_o} r\left[1 - \left(\frac{r}{R_o}\right)^2\right]^2 dr = \frac{1}{6}\rho\pi R_o^2 H\,\dot{\tilde{w}}^2 \tag{3.31}$$

Casting this result in the form of Equations (3.24) and (3.25) gives,

$$E_k = \frac{1}{2}\mu m\,\dot{\tilde{w}}^2 \quad \text{where} \quad m = \rho\pi R_o^2 H \quad \text{and} \quad \mu = \frac{1}{3} \tag{3.32}$$

This value of μ leads to a normalized initial central velocity of 1.7321, as reported in Table 3.2. In other words, the initial central velocity $\dot{\tilde{w}}_0$ of a parabolic deformation profile must be 73% greater than the initial velocity V_0 of a uniform distribution with the same initial energy.

3.3.2.2 Bessel Displacement Profile

The expression for the plastic work reported by Lippmann [45] for a Bessel function displacement profile, given in Equation (2.27), can also be obtained using the energy method. The appropriate form for the displacement profile is given in Equation (2.16) and is repeated here for convenience,

$$w(r) = \tilde{w} J_0\left(\Lambda\frac{r}{R_o}\right) \quad \text{where} \quad \Lambda = 2.4048 \tag{3.33}$$

Using Equation (2.21) the expression for the radial strain is,

$$\epsilon_r = \frac{1}{2}\,\tilde{w}^2\left(\frac{\Lambda}{R_o}\right)^2 J_1^2\left(\frac{\Lambda}{R_o}r\right) \tag{3.34}$$

Using Equation (2.23) the expression for the plastic work is,

$$W_P = \int_0^{R_o} \alpha\sigma_y\epsilon_r 2\pi r H\, dr = \pi H\alpha\sigma_y\tilde{w}^2 \left(\frac{\Lambda}{R_o}\right)^2 \int_0^{R_o} rJ_1^2\left(\frac{\Lambda}{R_o}r\right)\, dr \tag{3.35}$$

Using the transformation,

$$x = \frac{\Lambda}{R_o}r \tag{3.36}$$

and the integration formula [160, 161],

$$\int xJ_1^2(x)\, dx = \frac{x^2}{2}\left[J_1^2(x) - J_0(x)J_2(x)\right] \tag{3.37}$$

Equation (3.35) can be rewritten as,

$$W_P = \pi H\alpha\sigma_y\tilde{w}^2 \int_0^{\Lambda} xJ_1^2(x)\, dx = \pi H\alpha\sigma_y\tilde{w}^2 \left(\frac{\Lambda^2}{2}J_1^2\left(\Lambda\right)\right) \tag{3.38}$$

Note that, as with the parabolic profile, R_o does not appear explicitly in the expression for the plastic work, with the implication that, for a given plate material and thickness, the amount of dissipated energy depends only on deflection and not on the size of the plate, which is somewhat counter intuitive. Finally, casting the result in the form of Equations (3.19) and (3.20), the expression for the total plastic work is,

$$W_P = \frac{1}{2}\tilde{K}\tilde{w}^2 \quad \text{where} \quad \tilde{K} = \lambda\pi H\alpha\sigma_y \quad \text{and} \quad \lambda = \Lambda^2 J_1^2\left(\Lambda\right) = 1.5589 \tag{3.39}$$

Note that this expression for the plastic work is identical to that reported by Lippmann [45], as given in Equation (2.27). However, the resulting value for the normalized non-dimensional deflection of 0.8009, as reported in Table 3.2, differs from that reported by Symonds & Wierzbicki [122], and given in Equation (2.31), which has the value of 0.6661. The reason for this discrepancy will be discussed in Section 3.3.3.1.

To find an expression for the total kinetic energy, the velocity distribution is obtained by taking the temporal derivative of Equation (3.33),

$$\dot{w} = \dot{\tilde{w}}J_0\left(\Lambda\frac{r}{R_o}\right) \quad \text{where} \quad \Lambda = 2.4048 \tag{3.40}$$

Substituting Equation (3.40) into Equation (3.29) and integrating gives,

$$E_k = \rho\pi H\dot{\tilde{w}}^2 \int_0^{R_o} rJ_0^2\left(\Lambda\frac{r}{R_o}\right)\, dr = \frac{1}{2}J_1^2(\Lambda)m\,\dot{\tilde{w}}^2 \quad \text{where} \quad m = \rho\pi R_o^2 H \tag{3.41}$$

Rearranging Equation (3.41) in the form of Equations (3.24) and (3.25) gives,

$$E_k = \frac{1}{2}\mu m\,\dot{\tilde{w}}^2 \quad \text{where} \quad m = \rho\pi R_o^2 H \quad \text{and} \quad \mu = J_1^2(\Lambda) = 0.2695 \tag{3.42}$$

This value of μ leads to a normalized initial central velocity of 1.9263, as reported in Table 3.2. In other words, the initial central velocity of a Bessel function deformation profile is be 93% greater than the equivalent energy uniform velocity. This μ value differs from that value of 1.602 reported by Symonds & Wierzbicki [122], and given in Equation (2.29). This discrepancy will also be discussed in Section 3.3.3.1.

3.3.2.3 Conical Displacement Profile

The travelling hinge solution for the ideal impulsive loading of a circular plate due to Taylor [15] was reviewed in Section 2.3.6. The predicted final plate shape is conical and the expression for the final central deflection, given in Equation (2.35), can be written in dimensionless form as,

$$\delta = \frac{1}{\sqrt{\lambda\alpha}}\phi \qquad \text{where} \qquad \phi = \frac{I}{\pi R_o H^2 \sqrt{\rho\sigma_y}} \qquad \text{and} \qquad \lambda = 1 \tag{3.43}$$

Even though the travelling hinge approach is distinct from the constant displacement profile approach, an identical expression for the final central displacement can be obtained using the generalized energy analysis. The appropriate expression for the conical displacement profile is,

$$w = \tilde{w}\left[1 - \frac{r}{R_o}\right] \tag{3.44}$$

Using Equation (2.21) the expression for the radial strain is,

$$\epsilon_r = \frac{1}{2}\left(\frac{\tilde{w}}{R_o}\right)^2 \tag{3.45}$$

Substituting Equation (3.45) into Equation (2.23), the expression for the plastic work is,

$$W_P = \int_0^{R_o} \alpha\sigma_y\epsilon_r 2\pi r H\, dr = \pi H\alpha\sigma_y\left(\frac{\tilde{w}}{R_o}\right)^2 \int_0^{R_o} r\, dr \tag{3.46}$$

Upon integration, the dissipated plastic work is,

$$W_P = \frac{1}{2}\pi H\alpha\sigma_y\tilde{w}^2 \tag{3.47}$$

Equation (3.47) can be rewritten as,

$$W_P = \frac{1}{2}\tilde{K}\tilde{w}^2 \quad \text{where} \quad \tilde{K} = \lambda\pi H\alpha\sigma_y \quad \text{and} \quad \lambda = 1 \tag{3.48}$$

Finally, Equation (3.43) can be obtained by equating the plastic work to the initial kinetic energy using Equation (3.21) and rearranging the answer according to Equation (3.22). The λ value of unity implies a normalized non-dimensional deflection of unity, as reported in Table 3.2.

To find an expression for the total kinetic energy, the velocity distribution is obtained by taking the temporal derivative of Equation (3.44)

$$\dot{w}(r) = \dot{\tilde{w}}\left[1 - \frac{r}{R_o}\right] \tag{3.49}$$

Substituting Equation (3.49) into Equation (3.29), the expression for the kinetic energy becomes,

$$E_k = \rho\pi H\dot{\tilde{w}}^2 \int_0^{R_o} r\left[1-\frac{r}{R_o}\right]^2 dr = \frac{1}{12}\rho\pi R_o^2 H\,\dot{\tilde{w}}^2 \tag{3.50}$$

Casting this result in the form of Equations (3.24) and (3.25) gives,

$$E_k = \frac{1}{2}\mu m\,\dot{\tilde{w}}^2 \quad \text{where} \quad m = \rho\pi R_o^2 H \quad \text{and} \quad \mu = \frac{1}{6} \tag{3.51}$$

This value of μ leads to a normalized initial central velocity of 2.4495, as reported in Table 3.2, implying that $\dot{\tilde{w}}_0$ of a conical profile must be 145% greater than V_0 of an energy equivalent uniform distribution.

3.3.2.4 Comparison with Experimental Deflection Results

In the literature, it is common practice to compare analytical predictions directly to raw experimental data [5, 66, 122]. However, as mentioned in Section 3.2.1, individual experimental data sets all display a positive x-intercept, which is interpreted as the portion of the total impulse taken up by recoverable elastic deformation and implies that a minimum impulse is required to cause permanent plastic deformation. Further experimental evidence supporting this interpretation will be provided in Section 6.3.3.1. By contrast, elastic effects were not considered in the solutions discussed in the previous sections. In other words, a direct comparison with the experimental data is inappropriate since the analytical solutions will not reproduce the observed offset in the x-direction. Therefore, in this thesis, only the slope of the correlation obtained from the experimental data will be used, or the x-direction offset of the correlation will be subtracted from the experimental data when comparisons are made with analytical solutions.

Table 3.2 records a wide range for the normalized dimensionless deflection predictions, ranging from 0.7071 to unity. These predictions are all significantly greater than the experimental correlation of 0.475, which relates δ to ϕ, as given in Equation (3.1). The experimental data is considered reliable since it is based on a wealth of data, from a number of individual researchers, working over the span of several decades. Hence, the implication is that strain rate and strain hardening effects must be taken into account. The hardening parameter values required to correlate the experimental and theoretical results can be estimated by rearranging Equation (3.23) in the form,

$$\alpha_{\text{exp}} = \frac{1}{\lambda}\left(\frac{\phi}{\delta}\right)^2_{\text{exp}} \tag{3.52}$$

The resulting α_{exp} estimates are given in Table 3.2. When compared to the measured rate sensitivity of mild steel, as shown in Figure 2.13, the α_{exp} value required for the conical profile is unrealistically high, which casts doubt on its validity. This is not an unexpected result, since, as was shown in Figure 2.12, the conical profile does not correlate with measured deformation profiles. By contrast, the α_{exp} values for the parabolic and Bessel function profiles are realistic, although the Bessel function shape provides the best fit to the final deformed shape.

3.3.3 Comparison of Non-Energy based Analytical Solutions

As proposed in Section 3.3.1.1, Equation (3.20) provides a general form for the 'plastic stiffness' of a PCS plate, with the only difference being the value of λ. However, other solutions, not based on an energy approach, do not conform to the generalized solution. The similarities and differences between these alternative solutions and the generalized solution as discussed in this section.

3.3.3.1 Membrane Mode Methods

The membrane mode solution for the ideal impulsive loading of a circular plate due to Symonds & Wierzbicki [122] was reviewed in Section 2.3.5. Their expression for the final plate deflection, given in Equation (2.31), can be written in dimensionless form as,

$$\delta = \left(\frac{2}{\Lambda}\right)\frac{\phi}{\sqrt{\lambda\alpha}} \qquad \text{where} \qquad \phi = \frac{I}{\pi R_o H^2\sqrt{\rho\sigma_y}} \qquad \text{and} \qquad \lambda = \Lambda^2 J_1^2\left(\Lambda\right) = 1.5589 \tag{3.53}$$

where that expression for λ is the same as that given in Equation (3.39) since both analyses use a Bessel function to describe the plate shape. The value of the factor $2/\Lambda$ in Equation (3.53) is 0.8317, which implies that the deflection predicted by Symonds & Wierzbicki is 16.8 % less than that obtained using the generalized energy method for the same plate shape and loading scenario. This difference can be explained by considering the distinct methods by which the initial central velocity is obtained.

As shown in Section 3.3.2.2 and Table 3.2, for the initial kinetic energy of a plate with a Bessel function deformation profile to be equal to that of an impulsively loaded plate with a uniform initial velocity V_0, the initial central velocity $\dot{\tilde{w}}_0$ must be 1.9263 times greater than V_0. By contrast, Symonds & Wierzbicki, who used the minimization procedure of Martin & Symonds [42], as given in Equation (2.29), found that $\dot{\tilde{w}}_0$ must be 1.6018 times greater than V_0. Note that the ratio of the $\dot{\tilde{w}}_0$ values 0.8317, *i.e.* the same as the deflection ratio. This stand to reason since Equation (3.22) implies that deflection is proportional to impulse, which, in turn, is proportional to the initial velocity. In other words, the initial central velocity obtained using the method of Symonds & Wierzbicki is smaller than that obtained using the energy method, which leads to correspondingly smaller final displacements.

The preceding discussion raises the issue of whether the generalized energy approach or the method of Symonds & Wierzbicki is more accurate. Symonds & Wierzbicki noted that Equation (2.29) was derived for small deflection problems, but argued that it would still provide a 'best' approximation for large deflection problems. While a full review of minimization procedure of Martin & Symonds [42], as implemented by Symonds & Wierzbicki, is beyond the scope of this work, some insight can be gained by considering the physical interpretation of the consequence of the minimization criterion.

Considering the ratio of the initial momentum and kinetic energy of a uniform velocity distribution and invoking Equation (2.29), the following sequence of equivalent expressions can be written,

$$\frac{I_0}{E_{k,0}} = \frac{mV_0}{\frac{1}{2}mV_0^2} = \frac{1}{\frac{1}{2}V_0} = \frac{1}{\frac{1}{2}\dot{\tilde{w}}_0}\frac{\int_0^{R_o}\phi r\,dr}{\int_0^{R_o}\phi^2 r\,dr} = \frac{\int_0^{R_o}\rho(\dot{\tilde{w}}_0\phi)2\pi r H\,dr}{\int_0^{R_o}\frac{1}{2}\rho(\dot{\tilde{w}}_0\phi)^2 2\pi r H\,dr} = \frac{\tilde{I}_0}{\tilde{E}_{k,0}} \tag{3.54}$$

where I_0 and $\tilde{I}_0$ represent the initial momenta of the uniform and modal velocity distributions respectively, while $E_{k,0}$ and $\tilde{E}_{k,0}$ represent the corresponding initial kinetic energies.

Equation (3.54) shows that the minimization procedure of Martin & Symonds causes the ratio of momenta to be the same as that of the energies. In other words, the criterion minimizes the percentage difference between the initial momenta and kinetic energies of the actual and assumed distributions, such that one is never greater than the other. Hence, it is the 'best' approximation in the sense that it is the closest simultaneous match for both the momentum and energy. By contrast, the energy method ensures energy equivalence and simply abandons momentum equivalence. The implied argument is that the deformation process is governed by plastic work and that once the total impulse has been used to obtain the initial energy, momentum conservation can be ignored.

In essence, the distinction between the energy approach and the minimization procedure of Symonds & Wierzbicki arises due to the alternative strategy employed to overcome their common inconsistency, *i.e.* a Bessel function velocity distribution cannot have the same energy and momentum as a uniform distribution. This, in turn, is a result of ignoring the travelling hinge phase of motion. An analysis will be presented in Section 4.2.1 to address this issue.

3.3.3.2 Travelling Hinge Methods

From the preceding section it is evident that methods based on assumed constant deformation profiles or mode shapes provide good estimates for the final plate shape and deflection, but cannot consistently accommodate a uniform initial velocity distribution. The reason for this is that, per definition, transient plate shapes incorporating moving plastic hinges are not considered. By contrast, the travelling hinge methods of Taylor [15], Hudson [18] and Frederick [19], which accommodated a uniform initial velocity distribution in a consistent manner, do not capture the final plate shape, as shown in Figure 2.12. The reason for this is that the radial hinge velocity is taken to be constant and hence the final plate profile is, in effect, assumed to be conical.

Despite the fundamental difference between the two methods, it was shown in Section 3.3.2.3 that, if a conical deflection profile is assumed, the energy approach can give an identical result to that obtained using the travelling hinge assumption. As mentioned in Section 3.3.2.4, the conical assumption does not correlate with measured deformation profiles, and leads to unrealistically high α_{exp} values. Furthermore, this agreement requires the flow stress to be constant, which is not the case with the materials used to generate the experimental data reviewed in Section 2.2. These materials are typically strain and strain rate sensitive, as briefly reviewed in Section 2.3.7, which implies that the deformation history needs to be considered. The topic of strain rate sensitivity will be considered in Section 3.3.5 while an approximate energy model incorporating transient deformation profiles will be presented in Section 4.2.1.

3.3.4 Displacement Duration

Solutions for the displacement duration based on the membrane mode and travelling hinge models were reviewed in Sections 2.3.5 and 2.3.6 respectively. To the authors knowledge, the literature contains no duration solutions that are based on energy methods. In this section, it will be shown that the energy

method can be used to obtain the same result as the membrane mode method and, thereafter, the results will compared to published experimental results.

3.3.4.1 Energy Method Displacement Duration

The aim of this section is to obtain an estimate of the displacement duration T of a circular plate subjected to an ideal impulsive load using the generalized energy method applied to an assumed constant deformation profile. In this analysis, the magnitude of the initial kinetic energy $E_{k,0}$ is not specified, although, typically, the initial central velocity $\dot{\tilde{w}}_0$ would be chosen such that the initial kinetic energy is the same as it would be for an identical plate subjected to an equivalent uniform impulsive load.

As the plate deforms, energy is dissipated through plastic work and the kinetic energy decreases. Hence, since the initial energy is known and the total plastic work is a function of the central deflection, $\tilde{w}$, the residual kinetic energy can be written as,

$$E_k(\dot{\tilde{w}}) = E_{k,0} - W_P(\tilde{w}) \tag{3.55}$$

Using Equations (3.19) and (3.24), Equation (3.55) can be written as,

$$\frac{1}{2}\tilde{M}\dot{\tilde{w}}^2 = E_{k,0} - \frac{1}{2}\tilde{K}\tilde{w}^2 \tag{3.56}$$

Rearranging Equation (3.56) in terms of the central velocity gives,

$$\dot{\tilde{w}} = \frac{d\tilde{w}}{dt} = \sqrt{2\frac{E_{k,0}}{\tilde{M}} - \frac{\tilde{K}}{\tilde{M}}\tilde{w}^2} \tag{3.57}$$

which, by separating the variables, leads to the integrals,

$$\int_0^t dt = \int_0^{\tilde{w}} \frac{d\tilde{w}}{\sqrt{2\frac{E_{k,0}}{\tilde{M}} - \frac{\tilde{K}}{\tilde{M}}\tilde{w}^2}} \tag{3.58}$$

Upon integration the result is,

$$t = \sqrt{\frac{\tilde{M}}{\tilde{K}}}\ sin^{-1}\left(\sqrt{\frac{\tilde{K}}{2E_{k,0}}}\tilde{w}\right)$$

Noting that the argument of the arcsine contains the inverse of the expression for the maximum central deflection for an ideal impulsive loading given in equation (3.21), the time t taken to reach a central deflection $\tilde{w}$ may be written as,

$$t = \sqrt{\frac{\tilde{M}}{\tilde{K}}}\ sin^{-1}\left(\frac{\tilde{w}}{\tilde{w}_{max}}\right) \tag{3.59}$$

Hence, the deformation duration T is the value of t when $\tilde{w}$ is equal to $\tilde{w}_{max}$,

$$T = t_{max} = \frac{\pi}{2}\sqrt{\frac{\tilde{M}}{\tilde{K}}} = \frac{\pi}{2}\sqrt{\frac{\mu}{\lambda}}\,R_0\sqrt{\frac{\rho}{\alpha\sigma_y}} \tag{3.60}$$

The normalized values of T for three constant deformation profiles are given in Table 3.2.

For a Bessel function profile, the values of μ and λ, as given in Table 3.2, result in a coefficient identical to that reported by [122], as given in Equation (2.32). Furthermore, when inverted, Equation (3.59) gives the same expression for the central displacement history as given in Equation (2.30). In other words, except for the estimate of the initial central velocity and, hence, the final deflection, the generalized energy approach results in the same solution as the membrane mode approach of Symonds & Wierzbicki. This is possible because, as noted in Section 2.3.5, the initial kinetic energy does not appear in equation (3.60), with the result that, for a given plate configuration, the deformation duration is constant and independent of the size of the impulse.

As an aside, it is interesting to note that the normalized values for T given in Table 3.2 are very similar, with the Bessel function profile providing the highest value. That this should be the case can be confirmed through Rayleigh's minimum theorem [124,162]. Rayleigh's method is a well known technique for obtaining estimates for the lowest natural frequency of elastic structures. It involves choosing an arbitrary displacement profile and finding the associated expressions for the maximum total elastic strain energy and maximum total kinetic energy in a structure. At the point of maximum strain energy, *i.e.* maximum displacement, the kinetic energy vanishes, since it is a turning point. Conversely, at the point of maximum kinetic energy, *i.e.* maximum displacement, the strain energy vanishes, since it is the initial configuration. Equating these maxima and assuming a sinusoidal displacement history, an expression for the natural frequency can be obtained for the chosen profile. Rayleigh's method provides surprisingly accurate estimates even when using profiles that are relatively poor approximations. However, Rayleigh's minimum theorem shows that the predicted frequencies will always be greater than the exact solution, *i.e.* the exact solution always has the greatest period.

When applied to circular stretched elastic membranes, Rayleigh's method is analogous to Duffey's energy method [38]. This is, in essence, the motivation for Taylor's [15] approach of considering the deformation duration of a thin plastic fully plastic plate to be identical to the first quarter period of a vibrating membrane with a tension equal to the product of the dynamic flow stress and thickness of the plate. Furthermore, as shown in Section 2.3.1, the equation of motion of a thin plastic fully plastic plate is identical to that of a vibrating membrane. The consequence of this analogous behaviour is that conclusions drawn from Rayleigh's minimum theorem are directly applicable to the study of impulsively loaded circular plates when cast as a constant deformation profile problem. In other words, an arbitrary assumed profile will result in a deformation duration solution that is reasonably accurate but smaller that obtained with a Bessel function profile, which is the exact solution for a vibrating circular membrane.

The preceding discussion explains the good correlation of the theoretical deformation duration results given in Table 3.2. However, the implication that the response duration is insensitive to the choice of deformation profile is not true in general, as will be shown in Section 4.2. Nevertheless, in the next section, only the Bessel function solution will be considered since the parabolic and conical results are almost identical.

Table 3.3: Comparison of experimental and theoretical non-dimensional response duration results for impulsively loaded PCS plates. The final two columns are based on $\alpha = 2.843$.

Material	τ_{min}	τ_{mode}	α_{exp}	τ_{mem}	τ_{hinge}
steel	0.818	0.855	1.368	0.593	0.908
titanium	0.729	0.777	1.656	0.593	0.908

3.3.4.2 Comparison with Experimental Duration Results

Experimental deformation duration results for PCS plates subjected to a near uniform ideal impulsive load, due to Bodner & Symonds [56] and Nurick *et al.* [60], are presented in a non-dimensional form in Figure 3.4. The results are summarized in Table 3.3, where τ_{min} and τ_{mode} represent, respectively, the minimum and mode values of the response duration distributions[10].

Also shown in Table 3.3 are the hardening parameters values, denoted by α_{exp}, required to correlate the experimental results with the theoretical prediction based on a constant Bessel function displacement profile, *i.e.* Equation (3.60). The α_{exp} values for both the mild steel and titanium result are unrealistically low when compared to the strain rate sensitivity data reviewed in Section 2.3.7. In Section 3.3.2.4, an α_{exp} value of 2.843 was obtained from the displacement results. Substituting this value into Equation (3.60), and assuming a Bessel function displacement profile, results in a dimensionless duration number of 0.593, as given in the τ_{mem} column of Table 3.3. By contrast, using the α value of 2.843 in the travelling hinge model, *i.e.* Equation (2.34), results in a dimensionless duration number of 0.908, as given in the τ_{hinge} column of Table 3.3. In other words, models based on an assumed constant displacement profile tend to significantly underpredict the displacement duration, while travelling hinge models with a constant radial hinge velocity tend to overpredict.

The tendency of τ_{mem} to underpredict the displacement duration is an artifact of the modelling approximation. As mentioned previously, the predicted response history is sinusoidal, whereas the experimental displacement histories are linear [60], and the predicted initial central velocity is significantly greater than that expected based on the ideal impulsive assumption. The combination of these two features leads to the underprediction of the displacement duration.

The tendency of τ_{hinge} to overpredict the displacement duration is also an artifact of the modelling approximation. While the travelling hinge approach correctly describes the initial velocity distribution, it does not provide a good description of the final plate shape. Consequently, the predicted final central deflection is the greatest among the profiles considered, as shown in Table 3.2. This combination of the greatest deflection with the lowest initial velocity leads to the overprediction of the displacement duration.

From the above, it is evident that both the constant displacement profile model and the travelling hinge model rest on assumptions that experiments have shown to be incorrect. The former method provides an accurate description of the final plate shape, but neglects the initial travelling hinge phase of the motion, while the latter includes only the first phase of motion, but results in a poor description of the final plate shape. However, despite these differences, both methods predict that the magnitude of the initial velocity does not affect the deformation duration. Furthermore, it in interesting to note that the

[10]In this context the term 'mode' refers to the most frequently occurring non-dimensional deflection duration value, *i.e.* the 'peak' of the distribution, and not a mode of failure.

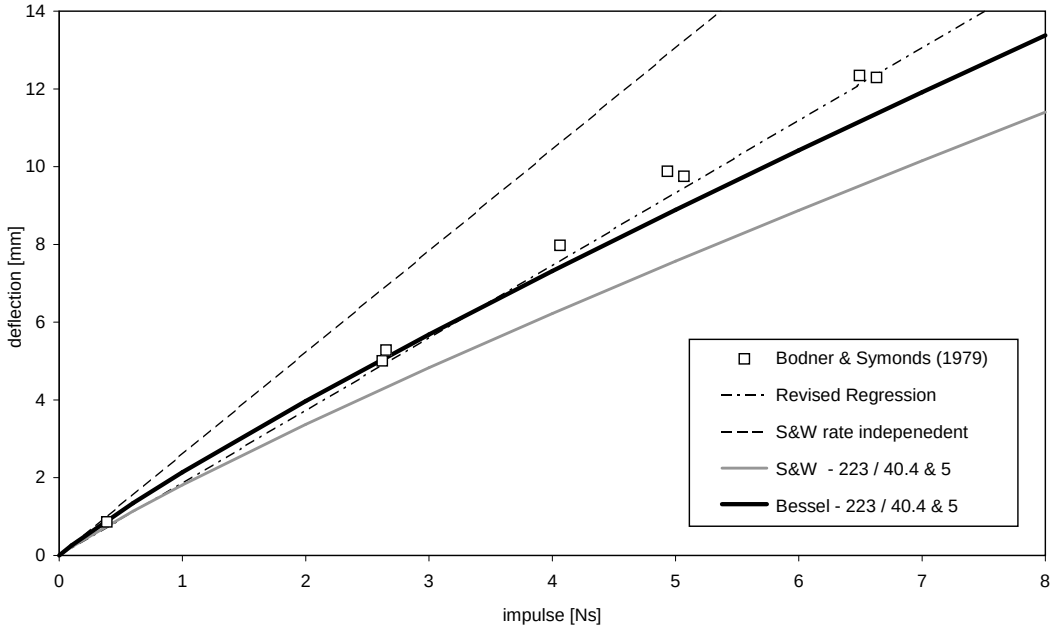

Figure 3.10: Comparison of experimental data due to Bodner & Symonds [56] for a circular mild steel plate subjected to a uniform impulsive load with predictions of Symonds & Wierzbicki (S&W) [122], which incorporate averaged strain rate effects. The numbers in the legend indicate the yield stress and Cowper-Symonds hardening coefficients.

measured deflection duration falls between these two extremes. These results motivated the development of a combined model for impulsive PCS plate motion, *i.e.* an approximate approach that incorporates travelling hinges within the generalized energy method, which will be presented in Section 4.2.1.

3.3.5 Strain Hardening and Strain Rate Sensitivity

The significance of strain hardening and strain rate effects is evident in the experimental results for maximum displacement and deformation duration discussed in Sections 3.3.2.4 and 3.3.4.2, respectively. Published analytical approaches accounting for these effects, were briefly reviewed and discussed in Section 2.3.7, with emphasis given to the average strain rate estimate of Symonds & Wierzbicki [122].

In general, the iterative solution of Symonds & Wierzbicki, incorporating strain rate effects, showed an improved correlation with the raw experimental data of Bodner & Symonds [56]. However, as argued in Section 3.3.2.4, a direct comparison with the raw experimental data is inappropriate since the analytical solutions do not considered elastic effects. Figure 3.10 shows a comparison of the Symonds & Wierzbicki solution with the experimental data of Bodner & Symonds that has been offset in the x-direction such that the associated regression passes through the origin.

Figure 3.10 also shows a solution obtained by using the same iterative approach as Symonds & Wierzbicki, except that the maximum deflection is calculated using Equations (3.22) and (3.39) instead of Equations (3.53), *i.e.* an energy approach instead of a membrane mode solution. The comparison shows that the energy approach results in a better correlation with the experimental data and provides some confirmation of the limitations of the membrane mode solution, as discussed in Section 3.3.3.1.

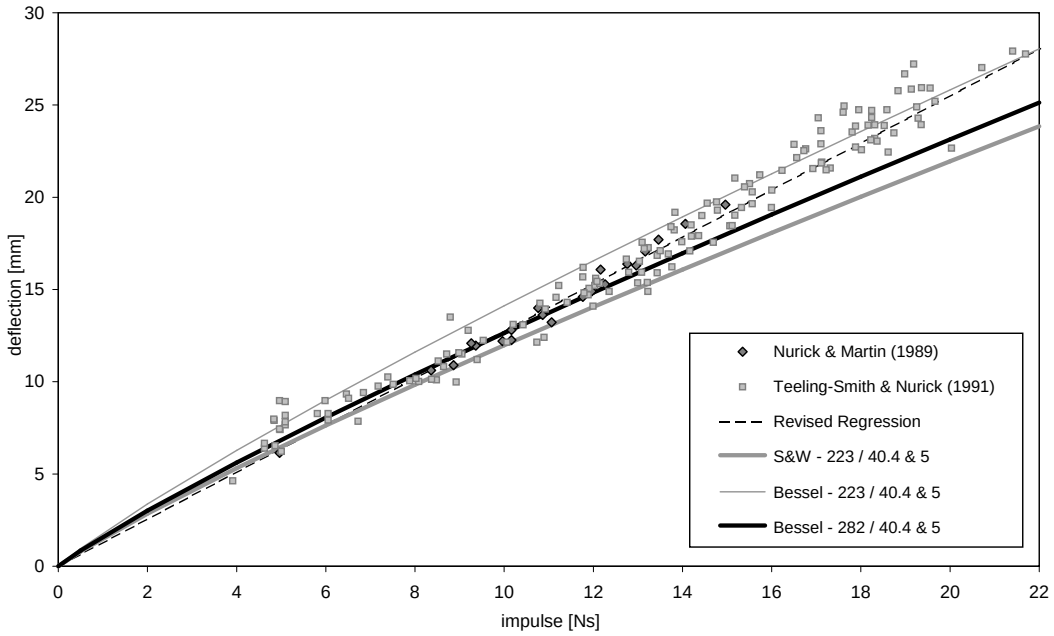

Figure 3.11: Comparison of experimental data for impulsively loaded circular mild steel plates due to Nurick *et al.* [60] with predictions that incorporate averaged strain rate effects. The regression fit is given in Equation (2.3), while the numbers in the legend indicate the yield stress and Cowper-Symonds hardening coefficients.

Jones [4] noted that the addition of strain rate effects removes the non-dimensional character of the solutions. Hence, the experimental results of Bodner & Symonds and Nurick *et al.* have to be considered separately. The impulsively loaded mild steel plate data of Nurick *et al.* [60,67] is shown in Figure 3.11. As before, the data has been offset to ensure that the associated linear regression passes through the origin. Also shown are the solutions predicted using both an iterative energy and membrane mode approach. Furthermore, energy solutions based on the yield stress values reported by both Bodner & Symonds and Nurick *et al.*, as given in Table 2.3, are considered. As before, the energy approach provides the best correlation with the experimental data.

The preceding deflection predictions show that the iterative average strain rate approach is remarkably accurate, especially when considering the relative simplicity of the model. By contrast, the deflection duration predictions do not show a good correlation with the experimental results. The experimental data of Bodner & Symonds [56] record durations of between 100 μs and 120 μs, while the iterative approach of Symonds & Wierzbicki predict durations of between 68 μs and 80 μs for the same impulse range. Similarly, from Figures 2.5 and 3.4, the data of Nurick *et al.* [60] shows a modal[11] duration of 146 μs for impulses greater than 10 Ns, while the predicted durations are less than 102 μs for the same impulse range. As discussed in Section 3.3.4, these results stem from the tendency of constant displacement profile models to underpredict the deformation duration. These results will be reconsidered in Section 4.2.3.

In addition to the underpredicted duration results, and notwithstanding the accurate deflection results, the iterative average strain rate approach, as applied to a constant displacement profile model, has other potential shortcomings that do not appear to have been conclusively addressed the literature.

[11] In this context, the term 'modal' refers to the peak of the lognormal duration distribution.

For example, the analysis ignores the effect of radial displacements and bending strains, which will be addressed in Sections 3.3.6 and 3.3.7 respectively. In particular, a consequence of neglecting radial displacements is that the radial strain distribution is incorrect, which could influence the average strain rate estimate. Lastly, the deflection results do not account for strain hardening effects. This issue will be addressed in Appendix B, where it will be shown that mild steel does not strain harden appreciably at high strain rates.

3.3.6 Radial Displacement Effects

The analyses discussed in the preceding sections all include the assumption that the effect of radial displacements on the dynamic deformation of plates is negligible. As discussed in Section 2.3.8, this is a standard approach for modelling impulsively loaded plates with large deflection behaviour. However, the magnitude of the error induced by this approach, while assumed to be small, does not appear to have been analytically quantified in the literature[12]. Therefore, the purpose of this section is to consider the effect of radial displacements on the prediction of the maximum deflection and strain distribution. Firstly, a general consideration of the interaction of radial and circumferential strains will be presented. Thereafter, some particular solutions, incorporating specific assumptions, will be presented. Finally, the limitations imposed by some of the assumptions and their physical interpretations will be discussed.

Consider an axisymmetric plate that experiences both transverse and radial displacements. Membrane strains are assumed to dominate and therefore, ignoring higher order terms, the strain distribution is given by equation (2.57), which is repeated here for convenience,

$$\epsilon_r = \frac{1}{2}\left(\frac{dw}{dr}\right)^2 + \frac{du}{dr} \quad \text{and} \quad \epsilon_\theta = \frac{u}{r} \tag{3.61}$$

Extending equation (2.23) to include circumferential strains, the general expression for plastic work has the form,

$$W_P = \int_V \left(\sigma_d \epsilon_r + \sigma_d \epsilon_\theta\right) dV \quad \text{where} \quad dV = 2\pi r H\, dr \tag{3.62}$$

Whether both of the terms in the integrand of equation (3.62) are required depends on the choice of yield criterion and flow rule.

For analytical convenience, the material is assumed to be perfectly plastic and obey a Tresca yield criterion with an associated flow rule, as given by Hopkins & Prager [21,22] and Onat & Haythornthwaite [28] and graphically depicted in Figure 3.12. Point A represents the case where both the radial and circumferential strains are tensile and hence, in accordance to the associated flow rule, the corresponding stresses are also tensile. In other words, the plate is stretching is both the radial and circumferential directions. This condition is satisfied if every point on the plate, excluding the fixed boundary, is displacing upwards and outwards, which is the case for the PCS and PCA deformation profiles reviewed in Sections 2.3.8 and 2.4. In particular, experimental results reviewed in Section 2.3.8.2 show that this situation is representative

[12] During the course of completing this thesis, the work contained in Sections 3.3.6, 3.3.7 and 3.3.8 was published by Cloete & Nurick [133].

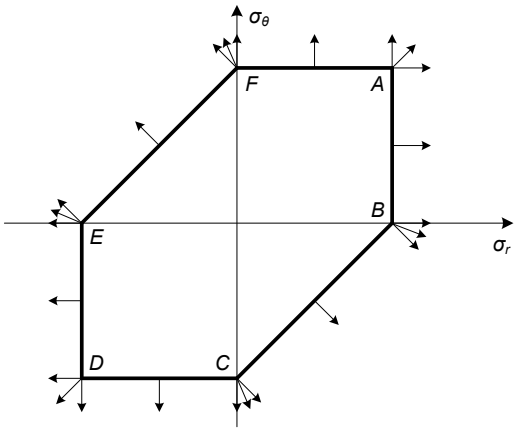

Figure 3.12: Tresca yield locus and associated flow rule for an axisymmetric plastic membrane according to Hopkins & Prager [21, 22] and Onat & Haythornthwaite [28].

of several impulsive loading configurations where the maximum transverse displacement occurs at the centre of the plate.

Under these conditions the flow stress in equation (3.62) can be taken out as a common factor and for a plate with inner and outer boundaries the expression becomes,

$$\begin{aligned} W_P &= \sigma_d \int_{R_i}^{R_o} \left[\frac{1}{2} \left(\frac{dw}{dr} \right)^2 + \frac{du}{dr} + \frac{u}{r} \right] 2\pi r H \, dr \\ &= 2\pi H \sigma_d \left[\int_{R_i}^{R_o} \frac{1}{2} \left(\frac{dw}{dr} \right)^2 r \, dr + \int_{R_i}^{R_o} \left(r \frac{du}{dr} + u \right) dr \right] \end{aligned} \tag{3.63}$$

The first integral of equation (3.63) represents the plastic work due to transverse displacement, while the second accounts for the contribution of the radial displacement. Using integration by parts, the second integral can be written as,

$$\int_{R_i}^{R_o} r \frac{du}{dr} \, dr + \int_{R_i}^{R_o} u \, dr = [ru]_{R_i}^{R_o} - \int_{R_i}^{R_o} u \, dr + \int_{R_i}^{R_o} u \, dr = R_o u(R_o) - R_i u(R_i) \tag{3.64}$$

The physical interpretation of Equation (3.64) has great significance for the analytical modelling of impulsively loaded plates. In particular, when Equation (3.64) is applied to any form of $u(r)$ that satisfies the yield condition and has no radial displacement at the inner and outer boundaries, the plastic strain associated with radial displacement makes no net contribution to the overall plastic dissipation. The reason for this is that the additional plastic work due to circumferential strain is canceled by the reduction in plastic work in the radial direction. The implication of this analysis is that radial displacements may be ignored when using an energy method to determine the maximum deflection of shock loaded PCS plates, provided that the boundary conditions are satisfied. In other words, Equation (3.64) provides sufficient justification for the displacement profiles used is all the PCS models reviewed in Section 2.3.

The final expression in equation (3.64) provides two interesting additional results. Any slippage or 'pull-in' at the outer boundary would result in the $u(R_o)$ term having a negative value. In other words, 'pull-in'

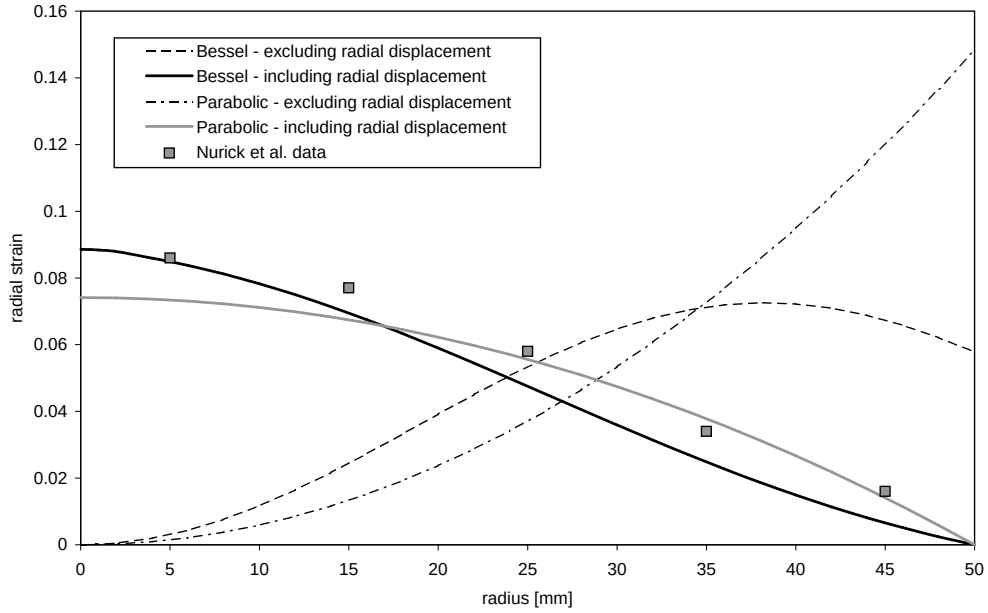

Figure 3.13: Comparison of the published radial strain results by Nurick *et al.* [62] with parabolic and Bessel displacement profiles that include or exclude the effects of radial displacements.

results in less plastic dissipation for a given maximum displacement, and hence, greater displacement for a given impulse. This agrees with the remarks of Jones [44] with regard to the blast experiments performed by Florence [36] that showed a significant amount of 'pull-in' as discussed in Sections 2.2.1 and 3.2.1. Similarly, in the case of annular plates, an outward displacement at the inner boundary would result in less plastic work for a given displacement. Hence, invoking the principle that structures tend to deform along the path of least work, this explains the observed behaviour of annular plates and justifies the analyses reviewed in Section 2.4.

It must be emphasized that, while radial displacements do not affect the maximum displacement, they will affect the strain distribution. Nurick *et al.* [62] pointed out that the strain distribution obtained by ignoring radial displacements is the inverse of that observed experimentally, as shown in Figure 3.13. Also shown are the strain distributions obtained by implementing Taylors analysis, as reviewed in Section 2.3.8 The radial strain distribution may have significant implications for failure prediction, especially with regard to Mode II, and should be accounted for in such an analysis.

The preceding analyses serve as a justification for the analytical techniques pursued in this thesis and most of the publications reviewed in Chapter 2. However, the result must be used with caution since the simplifying assumptions used with regarding to the flow stress and yield criterion are unlikely to provide a complete description of real material behaviour. Nevertheless, the good correlations with experimental results suggests that the assumptions provide acceptable approximations.

3.3.7 Bending Effects

Theoretical approaches for dealing with combined bending and membrane deformation in circular plates were reviewed in Section 2.3.8. Of particular interest is the solution due to Wen [66], who assumed a parabolic displacement profile and used an energy approach. Wen considered plastic work due to simultaneous bending and membrane strains, but in a summative sense without coupling. This was found to be representative of the literature, *i.e.* there appear to be no dynamic studies that treat bending and membrane strain in a coupled sense, although Onat & Haythornthwaite [28] reported a coupled solution for quasi-static deformations. Furthermore, the effect of radial displacements on bending deformations are not accounted for. While it was shown in the previous section that radial displacements do not affect the total plastic dissipation for plastic membranes with radially constrained boundaries, the same effect will not occur in the presence of bending strains. In this section the approach of Wen is extended to include the coupling between bending and membrane deformations and account for the effect of radial displacements.

Following the approach of Wen, a circular plate is assumed to be subjected to an ideal impulsive load and deform with a parabolic profile[13], as give in Equation (2.20) and repeated here,

$$w(r) = \tilde{w}\left[1 - \left(\frac{r}{R_o}\right)^2\right] \tag{3.65}$$

However, unlike Wen, it is assumed that the radial displacements of the mid-plane of the plate are described by Taylor's formula given in Equation (2.59) and repeated here,

$$u(r) = \frac{\bar{w}^2}{R_o}\left[\frac{r}{R_o} - \left(\frac{r}{R_o}\right)^3\right] \tag{3.66}$$

In this case, the expressions for the radial and circumferential strains, ϵ_r and ϵ_θ, are,

$$\epsilon_r = \frac{1}{2}\left(\frac{dw}{dr}\right)^2 + \frac{du}{dr} - z\frac{d^2w}{dr^2} \quad \text{and} \quad \epsilon_\theta = \frac{u}{r} - \frac{z}{r}\frac{dw}{dr} \tag{3.67}$$

where z is the height above the midplane of the plate. The first two terms in the expression for the radial strain and the first term in the expression for the circumferential strain are identical to Equation (2.57) and are thus identified as the membrane contributions $\epsilon_{r,m}$ and $\epsilon_{\theta,m}$ respectively. The remaining term in each equation represents the bending contributions $\epsilon_{r,b}$ and $\epsilon_{\theta,b}$.

Substituting Equations (3.65) and (3.66) into equation (3.67) gives the result,

$$\epsilon = \epsilon_r = \epsilon_\theta = \left(\frac{\tilde{w}}{R_o}\right)^2\left[1 - \left(\frac{r}{R_o}\right)^2\right] + 2\left(\frac{\tilde{w}}{R_o}\right)\left(\frac{z}{R_o}\right) \tag{3.68}$$

In other words, at any given point in the plate, the magnitude of the strains in the radial and circumferential directions are identical throughout the plate. This feature of the model is very convenient for analytical work, but unlikely to be valid for arbitrary displacement profiles. Nevertheless, the insights

[13] In addition to being mathematically tractable, the use of a parabolic profile is justified by its reasonable correlation with experimental results, as shown in Figure 2.12 and Table 3.2.

gained by Taylor, Duffey & Key and Wen, when using the same profile, support the present approach and suggests that the result will be representative of general plate behaviour.

As in Wen's model, Equation (3.68) indicates that both the membrane and bending strains, in both the radial and circumferential direction, are tensile above the midplane. This implies that the flow stress will be tensile in both the radial and circumferential directions, *i.e.* point A in Figure 3.12. However, below the mid-plane the membrane and bending strains are opposed, due to the sense of z, and the sense of the flow stress will depend on which deformation mechanism dominates. Wen ignores this interaction, which implies a simplified yield criterion equivalent to that of Hodge [29], resulting in an overestimate of the plastic dissipation. In this section the coupling between membrane and bending deformation is accounted for using an approach similar to that of Onat & Haythornthwaite [28].

The boundary between the tensile and compressive regions, which will be referred to as the neutral line, corresponds to the locus of points where the strains vanish. An expression for the position of the neutral line $\bar{z}(r)$ is obtained by setting equation (3.68) equal to zero, which gives,

$$\bar{z}(r) = -\frac{\tilde{w}}{2}\left[1 - \left(\frac{r}{R_o}\right)^2\right] \tag{3.69}$$

Equation (3.69) indicates that $\bar{z}$ is always negative, *i.e.* the neutral line lies on or below the midplane of the plate. Furthermore, the magnitude of $\bar{z}$ is zero at the outer boundary and increases toward the centre. The neutral radius $\bar{R}$, where the neutral line crosses the lower plate surface, is obtained by setting $\bar{z}$ equal to $-\frac{1}{2}H$, which gives,

$$\bar{R} = R_o\sqrt{1 - \frac{H}{\tilde{w}}} = R_o\sqrt{1 - \frac{1}{\delta}} \tag{3.70}$$

Equation (3.70) shows that the neutral radius coincides with the centre of the lower surface of the plate when $\delta = 1$, *i.e.* when the plate centre displacement is equal to its thickness. For displacements of less than a plate thickness the value of $\bar{R}$ is imaginary, *i.e.* the neutral line never crosses the plate surface. By contrast, for displacements of more than a plate thickness the value of $\bar{R}$ is real and the plate is divided into a region inside the neutral radius, where tensile stresses dominate, and an outer region where both tensile and compressive stresses are considered. These three strain distributions are depicted schematically in Figure 3.14. Note that these diagrams depict a simply supported plate, whereas typical blast loaded plates have clamped or built in boundaries where bending moments will occur. While these bending moments will alter the strain distribution, they will not be considered since the effect is localized and does not affect the conclusion reached in this analysis.

Assuming perfect plasticity, the stress state in the tensile and compressive regions are, respectively, represented by points A or D in Figure 3.12. Furthermore, Equation (3.68) indicates that the energy dissipation in the radial and circumferential directions is identical. Hence, from Equation (3.62), the

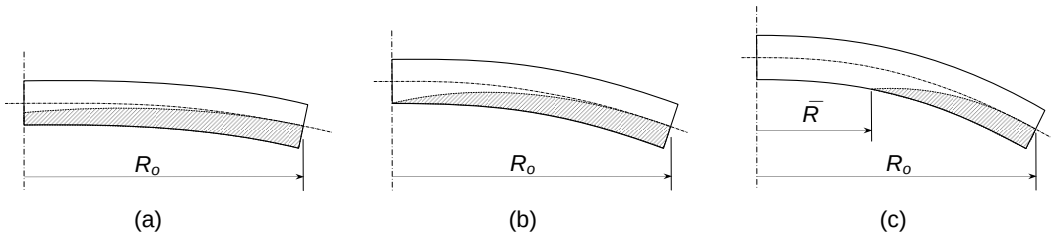

Figure 3.14: Schematic diagram of the position of the neutral line separating tensile and compressive regions (shaded area) when (a) $\frac{\tilde{w}}{H} < 1$, (b) $\frac{\tilde{w}}{H} = 1$ and (c) $\frac{\tilde{w}}{H} > 1$.

general expression for the total plastic work is,

$$\begin{aligned} W_P &= \int_V (\sigma_d \epsilon_r + \sigma_d \epsilon_\theta)\, dV = 2\int_V \sigma_d \epsilon\, dV \\ &= 2\int_0^{\bar{R}} \int_{-\frac{H}{2}}^{\frac{H}{2}} \sigma_d \epsilon\, dz\, 2\pi r\, dr + 2\int_{\bar{R}}^{R_o} \int_{\bar{z}}^{\frac{H}{2}} \sigma_d \epsilon\, dz\, 2\pi r\, dr + 2\int_{\bar{R}}^{R_o} \int_{-\frac{H}{2}}^{\bar{z}} (-\sigma_d) \epsilon\, dz\, 2\pi r\, dr \end{aligned} \tag{3.71}$$

Note that the flow stress is indicated to be negative in the final integral term to account for compressive strain below the neutral line. For deflections greater than a plate thickness, *i.e.* $\frac{\tilde{w}}{H} > 1$, the expression for the neutral radius is given in Equation (3.70). However, for central deflection of less than a plate thickness, *i.e.* $\frac{\tilde{w}}{H} < 1$, $\bar{R}$ is imaginary and must be set to zero, which also effectively results in the removal of the first integral term. Subsequent integration, though lengthy and tedious, is straightforward and is omitted. The final form of the plastic work is,

$$W_P = \begin{cases} \left[1 + \frac{1}{3}\left(\frac{\tilde{w}}{H}\right)^2\right] \pi \sigma_d H^2 \tilde{w} & \text{if} \quad \frac{\tilde{w}}{H} < 1 \\ \left[1 + \frac{1}{3}\left(\frac{H}{\tilde{w}}\right)^2\right] \pi \sigma_d H \tilde{w}^2 & \text{if} \quad \frac{\tilde{w}}{H} \geq 1 \end{cases} \tag{3.72}$$

Assuming an ideal impulsive loading case, equating the plastic work with the initial kinetic energy, *i.e.* Equation (2.19), and considering only real positive roots gives,

$$\delta = \begin{cases} \left[\frac{3}{4}\phi^2 + \sqrt{1 + \left(\frac{3}{4}\phi^2\right)^2}\right]^{\frac{1}{3}} + \left[\frac{3}{4}\phi^2 - \sqrt{1 + \left(\frac{3}{4}\phi^2\right)^2}\right]^{\frac{1}{3}} & \text{if} \quad \delta < 1 \\ \sqrt{\dfrac{\phi^2}{2\alpha} - \dfrac{1}{3}} & \text{if} \quad \delta \geq 1 \end{cases} \tag{3.73}$$

where δ and ϕ are the dimensionless deflection and impulse as defined by Nurick & Martin [6] and given in Equations (2.1) and (2.2). Note that while Equations (3.72) are superficially similar, their final results are distinct. This is due to the final solutions being quadratic for $\delta \geq 1$ and cubic for $\delta < 1$. Equation (3.73) is depicted in Figure 3.15, where it is compared to the solutions of Duffey & Key and Wen, as given in Equations (3.22) and (2.55).

Also shown in Figure 3.15 is the result obtained by including coupled yielding, but excluding radial displacements. The analysis is very similar to that presented in this section except for the fact that membrane strains never occur in the circumferential direction. Hence, an additional term due to bending

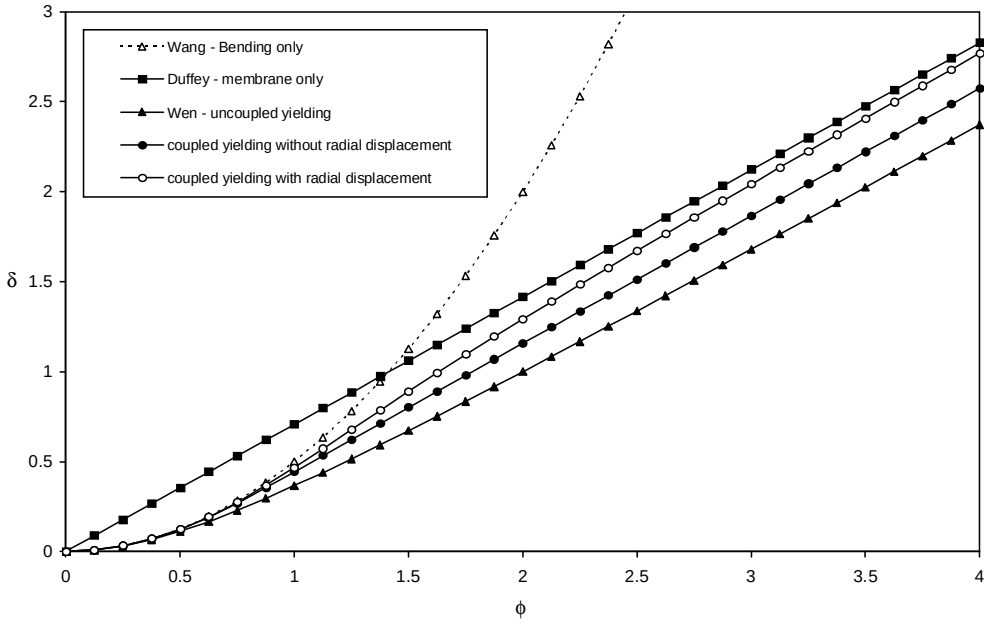

Figure 3.15: Comparison of the results of Wang [24] (bending only), Duffey & Key [38, 39] (membrane only) and Wen [66] (uncoupled membrane and bending) with the result of Equation (3.73) (coupled membrane and bending with radial displacement) and a coupled membrane and bending solution where radial displacements are ignored. The value of α is unity.

persists in the expression for plastic work, even at large displacements, leading to an under prediction of displacement.

Figure 3.15 shows that membrane strains tend to dominate at larger deflections for all the models considered, and the essential difference between the models that include bending effects is how soon the membrane strains begin to dominate. For displacements greater than half a plate thickness, Wen's uncoupled model predicts that bending effects will result in a constant negative offset in comparison with the pure membrane solution of Duffey & Key. In other words, Wen's approach implies that bending effects are still significant in lower portion of the large deflection regime, as defined in Section 2.3.1. By contrast, the model including coupled yielding predicts that membrane strains are not only larger, but also tend to suppress the contribution of bending strains, though not completely. This effect is enhanced when radial displacement effects are included in the model, with the result that for dimensionless displacements greater than unity, the behaviour rapidly asymptotes to the pure membrane solution of Duffey & Key.

The conclusion of this analysis is that, at large deflections, membrane strains tend to suppress bending effects and are therefore the dominant energy dissipation mechanism. This conclusion concurs with that of Jones [44], who considered annular plates, as discussed in Section 2.4. Furthermore, it justifies the general approach used in this thesis, *i.e.* the use of an energy method, while ignoring the contribution of bending and radial displacements, to describe and predict the shock response of thin circular plates.

3.3.8 Non-Monotonic Strain Effects

Hitherto, all the combined membrane and bending strain solutions reviewed or presented in this thesis have been based on the assumption of a monotonic strain history, *i.e.* the magnitude of the strain at any point in the plate never decreases. This assumption is incorrect, as can be seen by inspection of Equation (3.68). As noted previously, below the midplane of the plate, *i.e.* $z < 0$, the second term in Equation (3.68), *i.e.* the bending term, is negative. Furthermore, the bending term is linearly dependent on $\tilde{w}$, while the membrane term depends on $\tilde{w}^2$. The implication is that all points below the midplane will initially be in compression but will eventually experience tensile strains at larger deflections. In other words, the strain history is non-monotonic and, therefore, plastic work estimates based on the final strain distribution will underestimate the total energy dissipation. The purpose of this section is to estimate the plastic work contribution of the initial compression strains, by extended to model developed in Section 3.3.7.

The maximum compressive strain of any point in the plate is represented by the local minimum of Equation (3.68) with respect to $\tilde{w}$. Hence, causing the derivative of Equation (3.68) to vanish gives,

$$\tilde{w}_c = \frac{-z}{1 - \left(\frac{r}{R_o}\right)^2} \tag{3.74}$$

where $\tilde{w}_c$ is the value of the central displacement at which the particle at position (r, z) experiences its maximum compressive strain. Substituting this result into Equation (3.68) gives,

$$\epsilon_c = \frac{-\left(\frac{z}{R_o}\right)^2}{1 - \left(\frac{r}{R_o}\right)^2} \tag{3.75}$$

where ϵ_c is the maximum compressive strain a particle at position (r, z) will experience.

The locus of points that are at their maximum compressive strain for a given central deflection is obtained by rewriting Equation (3.74) with z as the subject of the formula,

$$\bar{\bar{z}}(r) = -\tilde{w}\left[1 - \left(\frac{r}{R_o}\right)^2\right] \tag{3.76}$$

The line defined by $\bar{\bar{z}}$ lies below $\bar{z}$, as given in Equation (3.69), and separates regions of increasing compressive strain from those of decreasing compressive strain or increasing tensile strain. The radius $\bar{\bar{R}}$ at which $\bar{\bar{z}}$ intersects with the lower plate surface is obtained by setting $\bar{\bar{z}}$ equal to $-\frac{1}{2}H$, which gives,

$$\bar{\bar{R}} = R_o\sqrt{1 - \frac{H}{2\tilde{w}}} = R_o\sqrt{1 - \frac{1}{2\delta}} \tag{3.77}$$

Equation (3.77) implies that $\bar{\bar{z}}$ coincides with the centre of the lower surface of the plate when $\delta = \frac{1}{2}$, *i.e.* for displacements of less than half a plate thickness $\bar{\bar{z}}$ never crosses the plate surface.

A general expression for the total plastic work can be obtained by using the same assumptions and a similar procedure as that followed in Section 3.3.7 to obtain Equation (3.71). However, in this case the

additional plastic work due to the imposing and removing of plastic compressive strain must be included. This is accomplished by integrating the product of the flow stress and the maximum compressive strain for every point between the midplane and $\bar{\bar{z}}$, *i.e.* every point where the strain history has progressed beyond the point of maximum compressive strain. The form of the total plastic work is thus,

$$W_P = 2\int_0^{\bar{\bar{R}}}\int_{-\frac{H}{2}}^{\frac{H}{2}} \sigma_d\epsilon\, dz\, 2\pi r\, dr + 2\int_{\bar{\bar{R}}}^{R_o}\int_{\bar{\bar{z}}}^{\frac{H}{2}} \sigma_d\epsilon\, dz\, 2\pi r\, dr + 2\int_{\bar{\bar{R}}}^{R_o}\int_{-\frac{H}{2}}^{\bar{\bar{z}}} (-\sigma_d)\epsilon\, dz\, 2\pi r\, dr$$
$$+ 4\int_0^{\bar{\bar{R}}}\int_{-\frac{H}{2}}^{0} \sigma_d\left|\epsilon_c\right|\, dz\, 2\pi r\, dr + 4\int_{\bar{\bar{R}}}^{R_o}\int_{\bar{\bar{z}}}^{0} \sigma_d\left|\epsilon_c\right|\, dz\, 2\pi r\, dr \tag{3.78}$$

The factor of 4 preceding the last two terms accounts for plastic work in the radial and circumferential directions and for the fact that work is done during both the imposition and the reversal of the compressive plastic strain. A subtle point to note is that in the region between $\bar{z}$ and $\bar{\bar{z}}$ the compressive strain will not have been completely reversed. A consequence is that the last two terms overstate the plastic work in this region. This approach is taken for mathematical convenience, and the effect is corrected by the fact that the argument of the second integral term will result negative work in this region.

For deflections greater than half a plate thickness $\bar{\bar{z}}(r)$ never crosses the lower plate surface and $\bar{\bar{R}}$ must be set to zero. In other words, the first and third integral terms vanish and the lower radial limit of the remaining integrals is zero. Upon integration, which is lengthy but straightforward and therefore omitted, the final form of the plastic work is,

$$W_P = \begin{cases} \left[\frac{4}{9}\left(\frac{\tilde{w}}{H}\right)^3 + \frac{\tilde{w}}{H}\right]\pi\sigma_d H^3 & \text{if} \quad \frac{\tilde{w}}{H} < \frac{1}{2} \\ \left[\left(\frac{\tilde{w}}{H}\right)^2 + \frac{11}{36} + \frac{1}{6}ln\left[2\frac{\tilde{w}}{H}\right]\right]\pi\sigma_d H^3 & \text{if} \quad \frac{\tilde{w}}{H} \geq \frac{1}{2} \end{cases} \tag{3.79}$$

Assuming an ideal impulsive loading case, equating the plastic work with the initial kinetic energy, *i.e.* Equation (2.19), gives the relationship between the dimensionless impulse and deflection as,

$$\frac{\phi}{\sqrt{2\alpha}} = \begin{cases} \sqrt{\frac{4}{9}\delta^3 + \delta} & \text{if} \quad \delta < \frac{1}{2} \\ \sqrt{\delta^2 + \frac{11}{36} + \frac{1}{6}ln\left[2\delta\right]} & \text{if} \quad \delta \geq \frac{1}{2} \end{cases} \tag{3.80}$$

where δ and ϕ are the dimensionless deflection and impulse as defined by Nurick & Martin [6] and given in Equations (2.1) and (2.2). Equation (3.80) is depicted in Figure 3.16, where it is compared to Equation (3.73) and the solutions of Duffey & Key and Wen, as given in Equations (3.22) and (2.55).

Figure 3.16 shows that the inclusion of non-monotonic strain effects has a minor effect on the total plastic dissipation. In Section 4.3.7 it will be shown that the effect is more significant in the case of ideal dynamic loading. This result supports the conclusions of Section 3.3.7, *i.e.* membrane strains tend to dominate at larger deflections, and further justifies the general approach used in this thesis.

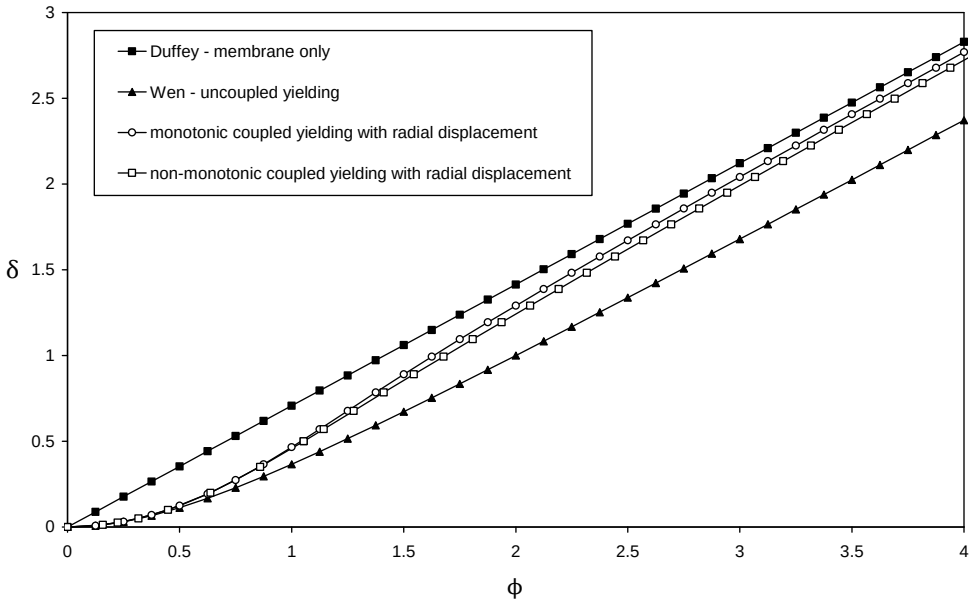

Figure 3.16: Comparison of the results of Duffey & Key [38,39] (membrane only) and Wen [66] (uncoupled membrane and bending) with the result of Equation (3.73) (monotonic coupled membrane and bending with radial displacement) and Equation (3.80) (non-monotonic coupled membrane and bending with radial displacement). The value of α is unity.

3.4 Evaluation of Published Data using Precision Test Requirements

This chapter and the preceding chapter have presented a general review and critique of literature pertaining to the experimental shock loading of metal plates with a specific detailed emphasis on laboratory scale blast loading of circular plates and the associated analytical models. It is, therefore, instructive to evaluate this body of work with respect to the precision test requirements set out in Section 1.1.2.

1. The structural behaviour must be accurately described and highly repeatable.

   As shown in Sections 2.2, shock loading research has produced an extensive literature and yet suitable code validation data are surprisingly sparse. Not only are papers with experimental data relatively rare in comparison theoretical studies, but amongst these papers only a small subset contain sufficient data for the assessment of repeatability. This is evident in the published data for circular plates subjected to uniform impulsive loads where a few specific papers are regularly cited by theoretical studies, principal amongst these being the studies of Bodner & Symonds [56] and Nurick & co-workers [60,68–70]. Nevertheless, these studies show that, under laboratory conditions, the response of blast loaded structures can be highly repeatable and accurately measured, thus meeting this requirement of a precision test.

The data of Bodner & Symonds and Nurick *et al.* [60] is not only repeatable in terms of final deflection and failure, but also provides consistent time resolved deflection data. This aspect experimental diagnostics shows great potential for improvement based on the application of new diagnostic techniques to laboratory scale blast loading, such as digital image correlation (DIC) [77, 86, 88] to capture plate motion. In particular, the further steady improvement of high resolution high speed digital cameras appears likely to make detailed time resolved full field strain measurement a standard feature of laboratory scale blast loading experiments.

2. Failure modes must be individually observable and experimentally decoupled from other effects.

   As shown in Section 2.1.4, the identification and description of failure modes is one of the traditional strengths of laboratory scale blast testing. Furthermore, the load intensities at which the transitions between the failure modes occur are well established. However, the experimental decoupling of a given failure mechanism from other competing mechanisms and response effects has not been reported. It was noted in the Trondheim workshop that this is a difficult problem for dynamic tests in general due to inertia and strain rate issues. Furthermore, the temporal resolution of failure events does not appear to have received attention.

   Addressing this aspect of laboratory scale blast testing is the primary motivation for the work that has culminated in this thesis, some of which has been published [51–53], and is presented in detail in Section 5.2.

3. The applied load must be controlled and highly repeatable in terms of magnitude and both spatial and temporal distribution.

   As discussed in Section 1.1.3, this aspect of laboratory scale blast loading has received strong criticism. Strictly speaking, this criticism is justified in that few, if any, of the studies reviewed in Chapters 2 and 3 meet all the applied load requirements given above. Many of the requirements appear to have been met in isolation by individual studies. For example, the data of Bodner & Symonds and Nurick *et al.* show a high degree of control and repeatability with regard to the total impulse, as shown in Section 3.2.2. However, even these excellent studies do not report any experimental data for the peak pressure or spatiotemporal distribution. Hence, none of the reviewed studies meet all the requirements of a precision test[14].

   Addressing this aspect of laboratory scale blast testing is the second significant motivation for the work that has culminated in this thesis, some of which has been published [51–53, 90], and is presented in detail in Section 5.3.

4. Boundary conditions must be fully defined, including parameters such as stiffness and friction.

   It is generally acknowledged that support conditions are difficult to fully define [1]. However, certain aspects, such as the boundary geometry are relatively trivial to define. For example, Nurick*et al.* [70] investigated the effect of clamp edge radii on the tearing failure of clamped circular blast loaded plates. Similarly, Bonorchis & Nurick [163] investigated the effect of a clamped or welded boundary in comparison to a fully built-in boundary. In other words, while the boundary geometry effect

[14] While this thesis is focused on circular plates, some related work on square plates should be noted. Bonorchis & Nurick inferred the impulse distribution for short stand-off blast tests using a variety of target configurations [158], which will be discussed in the context of a short review of the ballistic pendulum technique in Section 5.2.1. More recent studies have shown that spatiotemporal features such as the blast duration, profile, distribution and peak pressure can be measured using robust techniques such as Hopkinson pressure bars or digital image correlation [91–93].

is significant, it can be defined with sufficient precision such that distinct and consistent failure behaviour is evident in the experimental results.

In contrast to geometry, other aspects, such as boundary stiffness and friction are notoriously difficult to define with precision. There do not appear to be any published laboratory scale blast loading studies that report the friction parameters of clamped boundary conditions. This is despite the observation that the effect of insufficient friction can be significant, as discussed in Section 3.2.1 with regard to the effect of pull-in in the data of Florence [36]. While seldom specifically stated, the apparent standard approach for clamped plates is to ensure that clamped area is large in comparison to the area exposed to the blast and supported by thick clamp plates. In essence, this approach ensures that the plastic work required to draw in the clamped portion of the plate greatly exceeds the plastic work required to deform the exposed portion, thus limiting pull-in to a negligible level. This approach is typically enhanced by ensuring that the clamped area includes the clamping bolts and alignment pins such that the absence of deformation about these features is indicative of sufficient clamping.

Unlike boundary geometry and friction, the issue of boundary stiffness does not appear to have received any attention in the laboratory scale blast loading literature. Boundary stiffness has a significant effect on the vibration response of complex structures loaded dynamically, but mostly within the elastic limit. This is, presumably, the reason for the inclusion of this precision test requirement. However, for simple beam and plate structures undergoing large plastic deformation with relatively massive supports there is no experimental evidence that the boundary stiffness significantly affects the results. Nevertheless, it is good practice to consider the overall stiffness response of an experimental configuration with the aim of dynamically isolating a specimen clamp assembly from any sensor mounts and other support structures, as discussed in Section 2.1.1 with regard to the work of Bodner & Symonds [56]. This principle of dynamic isolation has been used to developed the apparatus used in this thesis [51, 53] and is described in detail in Section 5.2.4.

5. Suitable transducers must be selected.

   As discussed in Section 2.1.3, the majority of the literature data pertaining to laboratory scale blast loading has focuses on measuring the total impulse and final deflection using a ballistic pendulum. Hence, there has been relatively sparse use of diagnostic techniques such as capacitive sensors [56] and light occlusion for deformation history [61], trip wires for fragment velocity [67] or strain gauges for stress history [39]. The new millennium has seen a marked increase in the use of diagnostics such as digital image correlation (DIC) [72, 77, 79, 86–88] to capture plate motion and pressure history characterization using piezoelectric transducers [79,87,89] or Hopkinson pressure bars [52,53,90–93]. These measuring technique are accurate, non-invasive and, when suitable mounted and isolated, are unaffected by specimen or fixture motion. In other words, this work has shown that laboratory scale blast tests can meet precision tests transducer requirements. The only significant parameter for code validation that is not routinely measured is boundary reaction forces, which, along with blast load and failure characterization, is one of the primary motivations for this thesis.

6. The data collected from the experiments must have some redundancy.

   Some instances of experimental redundancy are evident in the blast loading studies reviewed in Chapter 2, although it is not a common feature. For example, there is some redundancy in blast tests

that measure both the transient target displacement and the final deformed shape, *i.e.* following the plastic deformation phase the data typically captures elastic vibrations about the final deformed shape.

7. Precision reporting must be provided for all test parameters that could influence the results.

   In general, the level of precision reporting in the blast loading studies reviewed in Chapter 2 is poor, *i.e.* the information is often insufficient to allow for correlations with other studies. However, there are also several studies that meet many of precision test requirements, for example the blast pendulum work of Bodner & Symonds [56] and the shock tube work of Stoffel [98], to mention only two. These studies typically contain adequate descriptions of equipment, sensor, instrumentation, data acquisition, load characterization, *etc.*, for meaningful for theoretical model validation.

8. The material properties must be well defined, especially with regard to strain rate sensitivity.

   In general, the blast loading studies reviewed in Chapter 2 seldom report the constitutive relations of the specimen materials in sufficient detail, with strain rate sensitivity data taken from the literature for nominally similar materials. Over the last two decades some researchers have begun to address this issue, with studies focused on material characterization closely followed by blast loading studies using material from the same stock and not merely the same type of material [79, 158, 164]. These positive developments show that laboratory blast tests can meet precision reporting requirements.

9. Analyses should be included in the development of the experimental apparatus to ensure usable results.

   As mentioned in Section 2.1.1, the work of Bodner & Symonds [56] is the first instance of the laboratory scale blast test intended as a validation experiment. In particular, the use of thin sheet explosive was specifically motivated by the existence of impulse based analytical solutions. Similarly, Nurick & Martin [5,6] emphasized the large number of analytical solutions available when compared to experimental studies at the time. In other words, there is a strong tradition of the inclusion of analyses in the planning and interpretation of laboratory scale blast tests.

   Addressing this aspect of laboratory scale blast testing is the third significant motivation for the work that has culminated in this thesis, some of which has been published [52, 133, 159], and is presented in detail in Chapters 4 and 7.

10. The validation process must involve predictions and not 'postdictions'.

    The literature reviewed in Chapter 2 show little evidence that data from blast loading experiments are used to 'massage' analytical or numerical model parameters to improve correlations.

The preceding discussion shows that a significant number of classical and modern laboratory scale blast loading studies satisfy the majority of the precision test criteria. However, one conspicuous exception is the measurement of boundary reaction forces and, consequently, a lack of data regarding the timing and force magnitudes involved in various failure modes and their associated transitions. Therefore, boundary reaction force measurement forms the central theme of this thesis. Furthermore, secondary themes focused on blast load characterization and extensions to classical analytical models are presented to support and evaluate the primary theme.

Chapter 4

Transient Behaviour of PCS Plates

"Everything should be made as simple as possible, but not simpler."

Albert Einstein (1879-1955)

4.1 Introduction

In Section 3.3 a generalized energy method was developed as a basis for discussing and comparing various published analytical models. The analytical predictions were shown to compare well with published experimental data for impulsively loaded plates, with good correlations obtained for final central deflections. Furthermore, the results showed that strain and strain rate hardening effects are significant and correspond to the known properties of the plate materials. However, the published models were found to have some shortcomings. In particular, when using the same set of material properties that provide good deflection estimates, the constant deformation profile approach tends to underpredict the deformation duration, while the travelling hinge approach tends to overpredict. Furthermore, it appears that no closed form analytical solutions have been published for the large deflection two phase response of circular plates, where the first phase persists into the large deflection regime[1]. This assessment applies to both impulsive loads and finite duration shock loads, despite the increased use of finite duration shock loading techniques, as reviewed in Sections 2.1.2, 2.2.3 and 2.2.4.

Given the above, the focus of this chapter is to develop approximate closed form solutions for the finite duration response of shock loaded peripherally clamped solid (PCS) circular plates that exhibit large deflection behaviour with transient deformation effects. The purpose of the analysis is to provide a basis for comparing and correlating experimental results obtained using non-ideal loading conditions. In addition, it will serve as a template for the analytical approach pursued in Section 7.5. The generalized energy method is extended to provide solutions that include the concept of travelling hinges, while the ideal impulsive load assumption is relaxed to consider the effect of finite duration loads.

[1] The solution due to Jones [43] considers only bending hinges in Phase I, implying a small displacements restriction.

4.2 Ideal Impulsive Loading

The majority of the analytical models for the large deflection of impulsively loaded circular plates make use of the ideal impulsive loading (IIL) assumption, as reviewed and critiqued in Sections 2.3 and 3.3. However, most of these models are based on the constant deformation profile, *i.e.* mode shape, approach and, therefore, cannot capture the initial uniform velocity condition of the IIL assumption. As shown in Section 3.3.1.4, an equivalent energy velocity distribution must be used which leads to an increased value for the initial central velocity. This approach will provide acceptable estimates for the final deformation, provided that the deformation process is monotonic and the final shape is accurate. However, the modal approach predicts an unrealistic sinusoidal deformation history and consistently under predicts the deformation duration. By contrast, the travelling hinge approach can accommodate the exact IIL initial velocity distribution and gives improved deformation duration estimates, though it overestimates that final deflection[2].

In this section, a solution is presented that incorporates the essential elements of the travelling hinge approach into the generalized energy method. The intention is to improve the description of the initial velocity condition and the deformation history, while not affecting the final deflection estimates.

4.2.1 Transient Deformation Profiles

An extension of the generalized energy method to include a description of a travelling hinge requires that the assumption of a constant deformation profile be abandoned in favour of a transient deformation profile. Following the travelling hinge approach, it is proposed that the displacement field be divided into two regions separated by the travelling hinge, as shown in Figure 4.1. However, unlike the travelling hinge approach of Taylor [15], the outer region is not assumed to have been brought to rest. The inner region of the plate is assumed to be rigid with a uniform transverse velocity field, while the outer region is assumed to deform according to a prescribed profile. For the sake of consistency, the displacement field of the outer region of the plate is assumed to have the same form as the three profiles considered in Sections 2.3 and 3.3. In the case of the conical profile, this assumed velocity field is identical to that used in the classical bending solution proposed by Wang [24]. However, only the parabolic profile provides a convenient closed form solution for the complete displacement history of the hinge. Therefore, only the parabolic profile will be considered in this section, while the central displacement history of all three profiles will be considered in the next section.

The form of the transient plate profile can be defined as,

$$w(r) = \begin{cases} w_h & \text{if } r < R_h \\ \tilde{w}_h \left[1 - \left(\frac{r}{R_o}\right)^2\right] & \text{if } r \geq R_h \end{cases} \tag{4.1}$$

[2]As discussed in Section 3.3.3.1, Symonds & Wierzbicki [122] proposed to solve this paradox using the minimization procedure of Martin & Symonds [42], which effectively ensures equal errors for both energy and momentum.

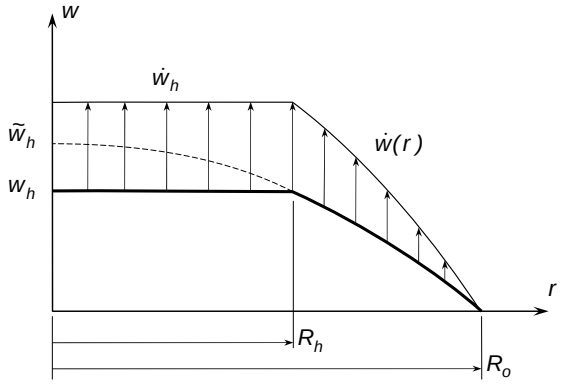

Figure 4.1: Transient Profile

where w_h is the transverse displacement at the radial position R_h of the travelling hinge, and $\tilde{w}_h$ is the hypothetical central displacement of the parabolic profile, which is related to w_h by,

$$w_h = \tilde{w}_h \left[1 - \left(\frac{R_h}{R_o}\right)^2\right] \tag{4.2}$$

Following the energy method as set out in Section 2.3.4, radial displacement is ignored[3] and the strain is found according to Equation (2.21). Per definition, no strain occurs in the rigid inner region of the plate and, therefore, only strain in the outer region is considered. Using Equation (2.23), the expression for the plastic work in terms of $\tilde{w}_h$ is thus,

$$W_P = \int_V \sigma_d \epsilon_r \, dV = \int_{R_h}^{R_o} \alpha\sigma_y \left(2\tilde{w}_h^2 \frac{r^2}{R_o^4}\right) 2\pi r H \, dr = \pi H \alpha \sigma_y \tilde{w}_h^2 \left[1 - \left(\frac{R_h}{R_o}\right)^4\right] \tag{4.3}$$

When expressed in terms of w_h, the plastic work has the form,

$$W_P = \pi H \alpha \sigma_y \frac{R_o^2 + R_h^2}{R_o^2 - R_h^2} \, w_h^2 \tag{4.4}$$

Note that Equation (4.4) reduces to Equation (2.25) when R_h vanishes.

An expression for the kinetic energy can be found using a similar approach. The velocity distribution is obtained by differentiating Equation (4.1) with respect to time. The entire inner region has a uniform velocity of $\dot{w}_h$, *i.e.* the transverse velocity of the hinge, while the velocity distribution for the outer region is given by,

$$\dot{w}(r) = \dot{\tilde{w}}_h \left[1 - \left(\frac{r}{R_o}\right)^2\right] \quad \text{where} \quad \dot{w}_h = \dot{\tilde{w}}_h \left[1 - \left(\frac{R_h}{R_o}\right)^2\right] \quad \text{if} \quad r \geq R_h \tag{4.5}$$

[3]This approach is justified by the radial displacement analysis presented in Section 3.3.6.

Using this velocity distribution, the total kinetic energy of the plate is,

$$E_k = \int_V \frac{1}{2}\dot{w}^2 dm = \frac{1}{2}\rho\pi R_h^2 H\dot{w}_h^2 + \rho\pi H \int_{R_h}^{R_o} \dot{\tilde{w}}_h^2 \left[1 - \left(\frac{r}{R_o}\right)^2\right]^2 r\, dr \tag{4.6}$$

The solution to the integral in the second term is,

$$\int_{R_h}^{R_o} \dot{\tilde{w}}_h^2 \left[1 - \left(\frac{r}{R_o}\right)^2\right]^2 r\, dr = \frac{1}{6}\dot{\tilde{w}}_h^2 R_o^2 \left[1 - \left(\frac{R_h}{R_o}\right)^2\right]^3 = \frac{1}{6}\dot{w}_h^2 (R_o^2 - R_h^2) \tag{4.7}$$

The final expression for the kinetic energy in terms of $\dot{w}_h$ is thus,

$$E_k = \frac{1}{2}\rho\pi R_h^2 H\dot{w}_h^2 + \frac{1}{6}\rho\pi (R_o^2 - R_h^2) H\dot{w}_h^2 \tag{4.8}$$

Note that Equation (4.8) reduces to Equation (3.31) when R_h vanishes.

Following the same reasoning as outlined in Section 3.3.4, the instantaneous kinetic energy of the plate must be equal to the difference between the initial kinetic energy and the accumulated plastic work,

$$E_k(\dot{w}_h) = E_{k,0} - W_P(w_h) \tag{4.9}$$

Hence, substituting Equations (2.17), (4.4) and (4.8) into Equation (4.9) gives,

$$\frac{1}{2}\rho\pi R_h^2 H\dot{w}_h^2 + \frac{1}{6}\rho\pi (R_o^2 - R_h^2) H\dot{w}_h^2 = \frac{1}{2}\rho\pi R_o^2 H V_0^2 - \pi H\alpha\sigma_y \frac{R_o^2 + R_h^2}{R_o^2 - R_h^2}\, w_h^2 \tag{4.10}$$

However, unlike the constant displacement profile assumption, which contains an inherent contradiction regarding the central velocity history, the use of a transient displacement profile allows for the inner region of the plate to be treated as a free plate, for which the velocity, under IIL conditions, is equal to the initial velocity V_0. Hence, for continuity, the transverse velocity of travelling hinge $\dot{w}_h$, which forms the inner edge of the deforming region of the plate, must also be equal to V_0. Furthermore, this implies that at a given time t the transverse displacement of the travelling hinge w_h is $V_0 t$.

Given the preceding arguments, Equation (4.10) can be simplified, by eliminating V_0, and rearranged as,

$$\frac{t}{T_{_T}} = \frac{1}{\sqrt{3}} \frac{1 - (\frac{R_h}{R_o})^2}{\sqrt{1 + (\frac{R_h}{R_o})^2}} \quad \text{where} \quad T_{_T} = R_o\sqrt{\frac{\rho}{\alpha\sigma_y}} \tag{4.11}$$

The quantity $T_{_T}$ is the deformation duration according to Taylor's travelling hinge model, as given in Equation (2.34). Alternatively, t could be eliminated to give,

$$\frac{w_h}{V_0 T_{_T}} = \frac{\delta_h}{\sqrt{\frac{1}{\alpha}}\phi} = \frac{1}{\sqrt{3}} \frac{1 - (\frac{R_h}{R_o})^2}{\sqrt{1 + (\frac{R_h}{R_o})^2}} \tag{4.12}$$

where the dimensionless impulse and displacement were introduced using,

$$V_0 T_{_T} = \frac{I}{\rho\pi R_o^2 H} R_o\sqrt{\frac{\rho}{\alpha\sigma_y}} = \frac{I}{\pi R_o H\sqrt{\rho\alpha\sigma_y}} = \frac{H}{\sqrt{\alpha}}\phi \tag{4.13}$$

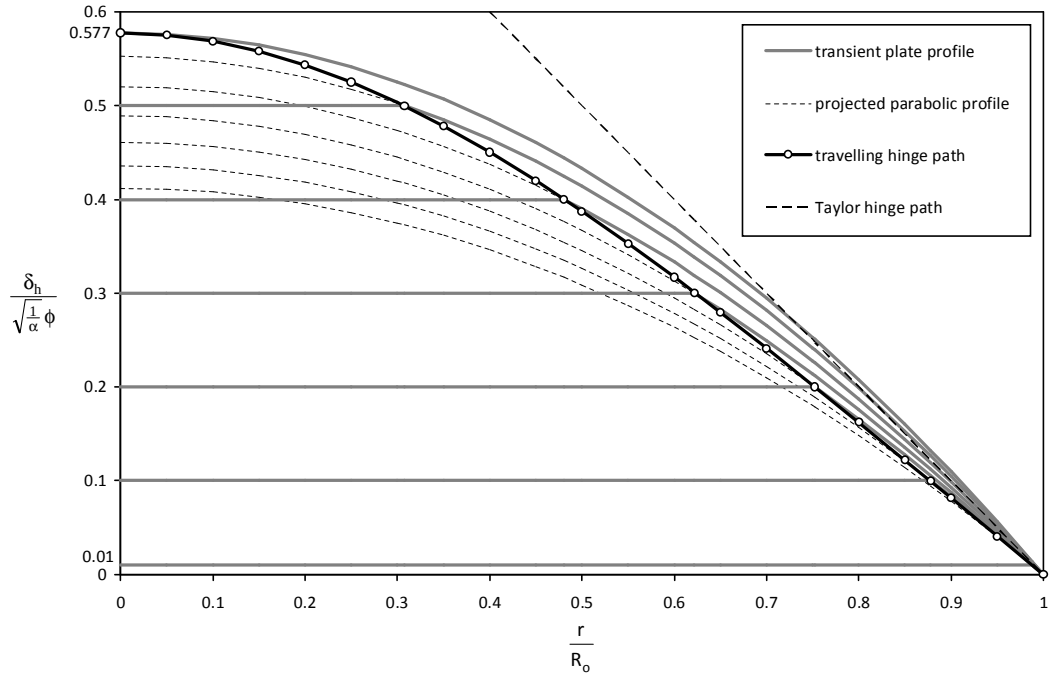

Figure 4.2: Normalized transient plate profiles and hinge path for a cicular plate subjected to an ideal impulsive load.

Equation (4.12) provides a relationship between the normalized position of the travelling hinge and the normalized displacement or time. The locus of the normalized hinge position, *i.e.* the hinge path, is shown in Figure 4.2, along with the transient plate shape at several instants.

In addition to the normalized dimensionless hinge path, Figure 4.2 also shows the hinge path according to the constant hinge velocity model of Taylor [15]. Furthermore, Figure 4.2 shows the projected parabolic profile for the various transient plate shapes. Note that the value of $\tilde{w}_h$ does not tend to vanish if the travelling hinge is at the outer edge of the plate. Substituting Equation (4.2) into Equation (4.11) and setting R_h equal to R_o results in a limit value of 0.408. The physical implication is that a significant deflection gradient, and consequently a reaction force, is immediately present at the plate boundary from the moment an ideal impulsive load is applied[4]. This effect is not captured by the constant mode shape approach.

4.2.2 Deflection Duration

It is conventional, in the impulsive loading literature [4], to subdivide the plate response behaviour into phases. Typically, Phase I is defined as the initial transient part of the response, *i.e.* when a travelling hinge is present. In the context of this thesis, Phase I lasts from the initial application of the load, when a travelling hinge initiates at the plate boundary, up to the point in time where the hinge reaches that

[4]Calculation of the boundary reaction force is possible using this approach, but is beyond the scope of this thesis and will be a topic of future research.

Table 4.1: Normalized values of T_I and T_{II} and for an ideal impulsive load. Note that the normalized values of δ_I and T_I are identical, while those of δ_{II} are given in Table 3.2.

Profile	$\frac{T_I}{R_o\sqrt{\frac{\rho}{\alpha\sigma_y}}}$		$\frac{\delta_I}{\delta_{II}}$		$\frac{T_{II}}{R_o\sqrt{\frac{\rho}{\alpha\sigma_y}}}$
	exact	approx.	exact	approx.	approx.
parabolic	$\sqrt{\frac{1}{3}}$	0.5774	$\sqrt{\frac{2}{3}}$	0.8165	0.8286
Bessel	$\sqrt{\frac{1-J_1^2(\Lambda)}{\Lambda^2 J_1^2(\Lambda)}}$	0.6846	$\sqrt{1-J_1^2(\Lambda)}$	0.8547	0.9114
conical	$\sqrt{\frac{5}{6}}$	0.9129	$\sqrt{\frac{5}{6}}$	0.9129	1.0846

centre of the plate and annihilates, which is designated as time T_I. Consequently, Phase II is defined as the rest of the response from time T_I until the plate motion is arrested, which is designated as time T_{II}.

Section 4.2.1 dealt specifically with Phase I motion. In particular, the outer portion of the transient deformation profile was assumed to have a parabolic shape, which resulted in a normalized value for T_I of 0.577. In this section, both Phase I and II motion will be considered using a generalized approach that is applicable to the three axisymmetric configurations[5] considered in Section 3.3.4. The aim is to find a general expression for the deformation history of the centre of the plate. In other words, details of hinge motion will not be considered, but can be reconstructed once the central deformation history is known.

From the argument set out in the previous section, at time T_I, when the travelling hinge arrives at the centre of the plate, the plate shape can be described by the deformation profiles discussed in Section 3.3.4. Therefore, at time T_I, the central velocity $\dot{\tilde{w}}$ would be equal to the initial velocity V_0. Furthermore, up to this point the centre of the plate would have behaved as a rigid body with a constant velocity V_0 and the central displacement $\tilde{w}$ would be equal to the product of V_0 and T_I. Hence, substituting the aforementioned and the expression for the initial kinetic energy, *i.e.* Equation (2.17), into the conservation of energy expression, given in Equation (3.56), results in,

$$\frac{1}{2}\tilde{M}V_0^2 = \frac{1}{2}mV_0^2 - \frac{1}{2}\tilde{K}(V_0T_I)^2 \quad \Rightarrow \quad T_I = \sqrt{\frac{m-\tilde{M}}{\tilde{K}}} \tag{4.14}$$

Thereafter, substituting the definition for $\tilde{M}$ and $\tilde{K}$, from Equations (3.20) and (3.25) respectively, and simplifying, gives a general expression for T_I, which can be normalized, using the approach given in Equation (4.11), to give,

$$\frac{T_I}{T_T} = \frac{\delta_I}{\sqrt{\frac{1}{\alpha}}\,\phi} = \sqrt{\frac{1-\mu}{\lambda}} \tag{4.15}$$

The normalized values of T_I for three mode shapes are given in Table 4.1.

From time T_I to T_{II} the plate is assumed to behave as deforming membrane with a constant deformation profile. In other words, for displacements greater than δ_I, all the results obtained in Section 3.3.4, using

[5]In principle, this approach should also be applicable to non-axisymmetric plate shapes, but consideration of this was beyond the scope of this thesis.

the constant mode shape approach, are valid provided that the appropriate temporal offset is accounted for. In this case, the temporal offset is the difference between the deformation duration predicted using the two phase approach and that obtained using the constant deformation profile assumption, *i.e.* the difference between T_{II} and T, as given by Equation (3.60). Hence, from Equation (2.30), the expression for the Phase II displacement history of the centre of the plate is,

$$\frac{\tilde{w}}{\tilde{w}_{II}} = sin\left[\left(\frac{\pi}{2}\right)\frac{t-(T_{II}-T)}{T}\right] \quad \text{where} \quad t \geq T_I \quad \text{and} \quad T = \frac{\pi}{2}\sqrt{\frac{\mu}{\lambda}}\,R_0\sqrt{\frac{\rho}{\alpha\sigma_y}} \tag{4.16}$$

Furthermore, the expression for the final deflection δ_{II} is identical to that given for δ in Equation (3.22), while the normalized values of δ_{II} are given in Table 3.2. Comparing Equations (4.15) and (3.23) gives the ratio of δ_I to δ_{II}, and hence $\tilde{w}_I$ to $\tilde{w}_{II}$, as simply,

$$\frac{\tilde{w}_I}{\tilde{w}_{II}} = \frac{\delta_I}{\delta_{II}} = \sqrt{1-\mu} \tag{4.17}$$

Consequently, substituting Equation (4.17) into Equation(4.16) gives,

$$T_{II} = T_I + \left[1 - \frac{2}{\pi}sin^{-1}\sqrt{1-\mu}\right]T \quad \text{where} \quad T = \frac{\pi}{2}\sqrt{\frac{\mu}{\lambda}}\,R_0\sqrt{\frac{\rho}{\alpha\sigma_y}} \tag{4.18}$$

or, when normalized,

$$\frac{T_{II}}{T_T} = \sqrt{\frac{1-\mu}{\lambda}} + \sqrt{\frac{\mu}{\lambda}}\left(\frac{\pi}{2} - sin^{-1}\sqrt{1-\mu}\right) \tag{4.19}$$

Using the normalized values of T_I, δ_I, T_{II} and δ_{II}, given in Equations (3.23), (4.15) and (4.19), while using a linear function for the first phase and Equation (4.16) for the second phase, the two phase displacement history of the centre of the plate can be constructed, as shown in Figure 4.3. Also shown, for the sake of comparison, are the equivalent single phase constant deformation profile solutions and Taylor's travelling hinge solution.

Some general conclusions can be drawn from the preceding analysis. Firstly, since the two phase model is an extension of the energy method, the inclusion of the travelling hinge phase does not alter the maximum displacement predictions obtained using the constant displacement profile approach. However, it significantly increases the deformation duration, *i.e.* the membrane duration solution will always give a lower bound to the actual solution, as mentioned in Section 3.2.3. Secondly, the two phase model predicts distinct deformation durations for each profile shape, whereas those obtained using the constant displacement profile assumption show negligible variation. Thirdly, the normalized value of T_I is less than unity, implying that the two phase model predicts a greater average radial hinge velocity than that assumed by Taylor, as given in Equation (2.33). This result applies to each of the assumed deformation shapes discussed above, including the conical case, even though the assumed deformation shape and predicted final displacement are identical the those of Taylor.

While a detailed discussion of published travelling hinge models [15, 18, 19] is beyond the scope of this thesis, certain features of the models are relevant to the present discussion. In particular, the travelling hinge models all assume that any given point on the plate is instantaneously brought to rest upon the arrival of the hinge. This implies a velocity discontinuity between the 'rigid' portion of the plate just inside

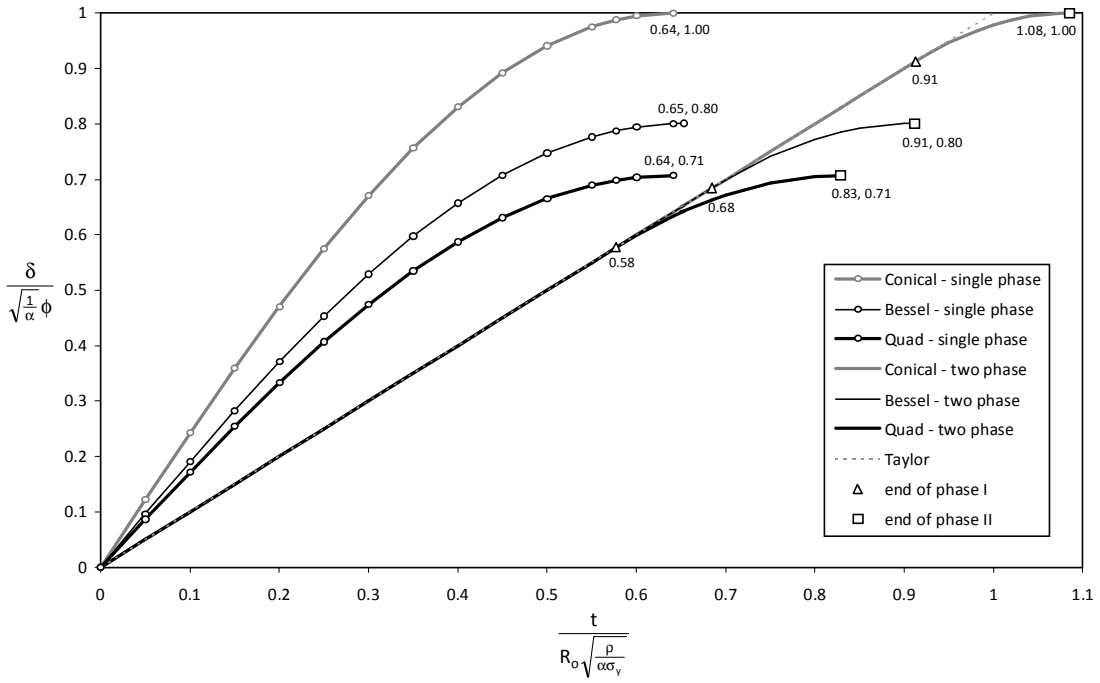

Figure 4.3: Comparison of the normalized two phase deflection history prediction with that obtained using the single phase constant deformation profile approach and Taylor's travelling hinge approach.

the hinge, which is still moving at the initial velocity, and the deformed portion of the plate just outside the hinge, which is at rest. This velocity discontinuity, which is not physically realistic, does not occur in the two phase model as shown in Figure 4.1. However, though it avoids infinite accelerations, the two phase model still implies a sudden change of curvature at the hinge, which would involve infinite strain rates. Hence, the strain rates can only be estimated in an average sense, as discussed in Section 2.3.7.

4.2.3 Comparison with Experimental Results

As shown in Table 3.3, the constant displacement profile approach predicts deformation durations that are too short compared to experimental results, while the predictions of Taylor's travelling hinge approach are too long. By contrast, using a Bessel function, which best describes the final plate shape, and substituting Equation (4.19) into Equation (3.3), with $\alpha = 2.843$, gives a dimensionless duration of 0.828. In other words, the two phase model gives a τ value in between the experimental τ_{min} and τ_{mode} values for mild steel of 0.818 and 0.855 respectively, as shown in Figure 3.4. This is an acceptable result, given the simplicity of the analysis, and sufficient justification for the use of an energy based two phase model.

Further evidence of the validity of the two phase model is obtained by modifying the iterative average strain rate approach of Symonds & Wierzbicki [122], to include the energy based two phase model. This is accomplished by simply using Equations (3.22) and (3.39) to calculate the maximum deflection instead of Equations (3.53), while using Equation (4.19) to calculate the deformation duration instead of Equation (2.32), *i.e.* a two phase energy approach instead of a membrane mode solution. The result of

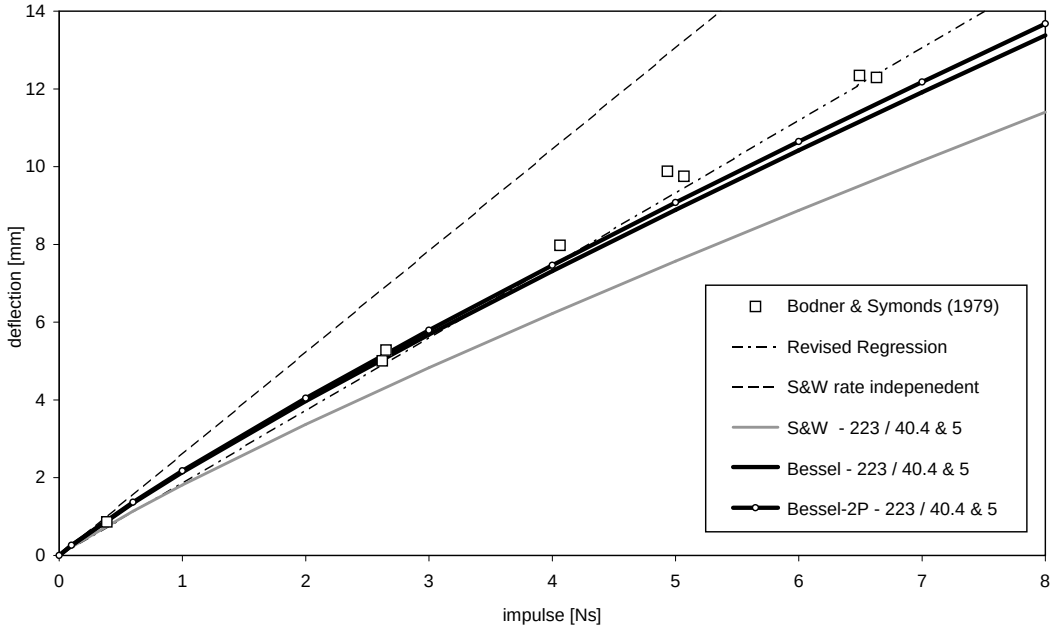

Figure 4.4: Comparison of experimental deflection data due to Bodner & Symonds [56] for circular mild steel plates subjected to uniform impulsive loads with predictions based on an iterative rate sensitive solution incorporating the two phase (2P) deflection approach. The numbers in the legend indicate the yield stress and Cowper-Symonds hardening coefficients.

this modification is shown in Figures 4.4 and 4.5, which compare the iterative two phase approach to the experimental data and previous solutions discussed in Section 3.3.5.

Figure 4.4 shows that the two phase approach results in a deflection prediction that is virtually identical to the single phase solution. The reason for this is that the two solutions use the same expression for the maximum deflection and have durations that differ by a factor of 1.4, which only slightly alters the hardening parameter α due to its logarithmic dependence on strain rate, as given in Equation (2.36). By contrast, the factor of 1.4 has a significant effect on the duration prediction, as shown in Figure 4.5 where a good correlation between the two phase solution and the experimental data is evident. In particular, the model appears to capture the experimental trend where the displacement duration shows a gradual decrease with an increase in impulse.

Finally, Figure 4.6 shows a comparison of the two phase model displacement duration predictions with the duration data of Nurick *et al.* [60] and the predictions of the single phase model. For completeness, predictions based on the quasi-static flow stress reported by Nurick *et al.* (282 MPa) and Bodner & Symonds (223 MPa) are presented. Unfortunately, the scatter in the data of Nurick *et al.* is too great to confirm the aforementioned decreasing duration trend. Nevertheless, the two phase model also provides an improved agreement with the modal duration[6].

[6]In this context, the term 'modal' refers to the peak of the lognormal duration distribution.

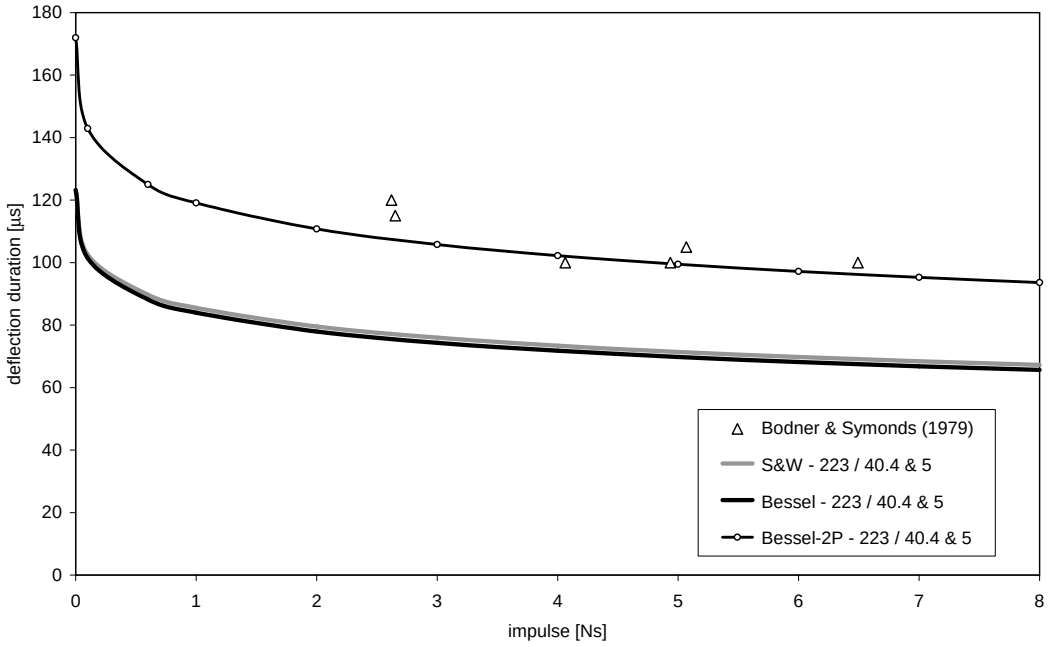

Figure 4.5: Comparison of experimental duration data due to Bodner & Symonds [56] for circular mild steel plates subjected to uniform impulsive loads with predictions based on an iterative rate sensitive solution incorporating the two phase (2P) deflection approach. The numbers in the legend indicate the yield stress and Cowper-Symonds hardening coefficients.

4.2.4 Discussion of Hinge Velocity Predictions

In the preceding section, the two phase model was found to give an improved correlation with the experimental deformation duration data when compared with predictions obtained using the single phase approach or the constant hinge velocity approach. In particular, the results imply that the plastic hinge must be travelling faster than would be predicted using the standard expression for the velocity of a disturbance in a plastic membrane, as given in Equation (2.33). However, the theory regarding a constant hinge velocity in a plastic membrane is well established [15,18,19,63,165], and hence, the results of the Section 4.2.3 present an apparent contradiction. To the author's knowledge, this contradiction has not been noted or discussed in the literature.

The analysis presented in Sections 4.2.1 and 4.2.2 does not resolve the hinge velocity contradiction. As mentioned in the preamble of Section 4.2, the intention of the two phase model is to retain the simplicity and accurate final deflection estimates of the generalized energy method, while incorporating a consistent initial velocity distribution and improving the deformation duration estimate. Hence, following the energy approach, the plate displacement shape is chosen *a priori* and the resulting hinge velocity is a consequence of this choice, rather than depending solely on the plate properties.

As reviewed in Sections 2.1.1 and 2.3.6, moving hinge solutions exist for the large deflection of membranes [15, 18, 19] and result in a constant hinge velocity that has been shown to over estimate the deformation duration of impulsively loaded thin plates. By contrast, bending dominated solutions for the small deflection of plates [4, 24] result in non-constant hinge velocities that are load dependent and result in deformation duration estimates that are shorter than those measured in the large displacement

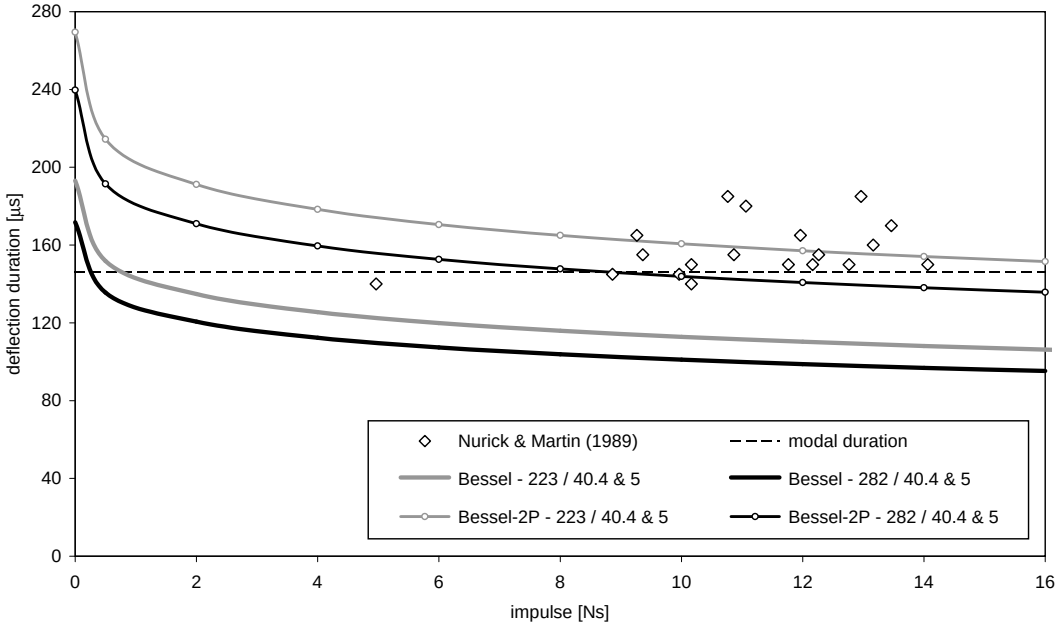

Figure 4.6: Comparison of experimental duration data due to Nurick *et al.* [60] for circular mild steel plates subjected to uniform impulsive loads with predictions based on an iterative rate sensitive solution incorporating the two phase (2P) deflection approach. The numbers in the legend indicate the yield stress and Cowper-Symonds hardening coefficients.

regime. These observations suggest that a model that includes both bending and membrane effects could resolve the hinge velocity contradiction. This suggestion is notwithstanding the analysis in Section 3.3.7, which showed that bending effects are negligible at large displacements for a typical final displacement shape, and does not preclude the possibility that bending effects could alter the hinge velocity during the transient displacement phase. Unfortunately, there does not appear to be a published solution for the plastic hinge velocity during the large deflection of a plate that is thin, but not thin enough to be considered a membrane. Further consideration of this problem was deemed to be beyond the scope of this thesis, but is a topic for future consideration.

4.3 Finite Duration Loading

The literature concerning the analytical treatment of circular plates subjected to shock loads of finite duration was reviewed in Section 2.5.1. It was found that, in contrast to ideal impulsive loads, relatively few closed form solutions exist for large deflection under finite load durations In particular, there do not appear to be any closed form analytical solutions for the case where a finite duration load persists into the large deflection regime where deformations are dominated by membrane effects. However, in several experimental configurations, such as shock or blast tubes, finite duration loads are of great importance. Furthermore, even short stand-off explosive charges, which are typically regarded as ideal impulsive loads, may have non-ideal characteristics, as will be discussed in Section 5.3.1.2.

In this section, the generalized energy method is extended to accommodate uniform loads of 'rectangular' shape, *i.e.* loads of finite duration and constant intensity. Firstly, the transient profile approach, presented in Section 4.2.1, will be extended to obtain a solution for the hinge path under a constant intensity load with a duration less that is less than the Phase I duration. As before, only the Phase I solution corresponding to the parabolic displacement profile assumption will be presented. Thereafter, the Phase I solution will be used to obtain the final Phase II deflection based on the parabolic and Bessel displacement profiles. Secondly, a simplified Phase I analysis of the central deflection that can be applied to an arbitrary plate shape will be presented. Finally, the simplified approach will be extended to provide a solution for the central displacement history for a constant intensity load of arbitrary duration.

4.3.1 Transient Deformation Profiles

Experimental results, such as those depicted in Figure 2.1, show that travelling hinge phenomena are significant during shock loading events of finite duration. Therefore, the transient deformation profile approach of Section 4.2.1 will be extended to accommodate finite duration loads.

Consider the transient circular plate profile, as depicted in Figure 4.1 and defined by Equations (4.1) and (4.2), which is subjected to a shock load with a constant uniformly distributed pressure P. Assuming only transverse displacements and a uniform load, the total work done by a pressure P acting on a deforming axisymmetric plate is,

$$W_L = \int_A Pw \, dA \tag{4.20}$$

where the subscript L denotes the work done by the load and A is the area that the pressure is acting on. Furthermore, if the pressure is constant and uniform, *i.e.* if P does not depend on w, the double integral reduces to a single integral and, using the expression for w given in Equation (4.1), has the form,

$$W_L = \int_0^{R_o} Pw(r) 2\pi r \, dr = \int_0^{R_h} Pw_h 2\pi r \, dr + \int_{R_h}^{R_o} P\tilde{w}_h \left[1 - \left(\frac{r}{R_o}\right)^2\right] 2\pi r \, dr \tag{4.21}$$

which, upon integration and substitution of Equation (4.2), gives,

$$W_L = \pi R_h^2 P w_h + \frac{1}{2}\pi \left(R_o^2 - R_h^2\right) P w_h = \pi R_h^2 P w_h + \frac{1}{2}\pi R_o^2 P w_h \left[1 - \left(\frac{R_h}{R_o}\right)^2\right] \tag{4.22}$$

In Equations (4.21) and (4.22), the first term represents the work done on the inner region of the plate, *i.e.* inside the hinge radius, while the second term represents that of the outer region.

Following similar reasoning as outlined in Section 3.3.4, the instantaneous kinetic energy of the plate must be equal to the difference between the work done up to that instant and the accumulated plastic work,

$$E_k(\dot{w}_h) = W_L(w_h) - W_P(w_h) \tag{4.23}$$

Since the inner region of the plate is moving as a rigid body, it may be considered in isolation. Substituting the first term of Equations (4.8) and (4.22) into Equation (4.23), while noting that there is no plastic dissipation, gives,

$$\frac{1}{2}\rho\pi R_h^2 H\dot{w}_h^2 = \pi R_o^2 P w_h \tag{4.24}$$

Hence, the expression for the transverse hinge velocity as a function of its transverse displacement is,

$$\dot{w}_h = \sqrt{\frac{2Pw_h}{\rho H}} \tag{4.25}$$

For the outer region, substituting Equation (4.4) and the second term of Equations (4.8) and (4.22) into Equation (4.23), gives,

$$\frac{1}{6}\rho\pi(R_o^2 - R_h^2)H\dot{w}_h^2 = \frac{1}{2}\pi\left(R_o^2 - R_h^2\right)Pw_h - \pi H\alpha\sigma_y\frac{R_o^2 + R_h^2}{R_o^2 - R_h^2}\,w_h^2 \tag{4.26}$$

To satisfy continuity, the values of $\dot{w}_h$ and w_h must be identical in Equations (4.25) and (4.26). Therefore, substituting the former into the latter, to eliminate $\dot{w}_h$, gives the spatial hinge path as,

$$\frac{w_h}{\frac{1}{2}\frac{P}{\rho H}{R_o}^2\left(\frac{\rho}{\alpha\sigma_y}\right)} = \left(\frac{t}{T_T}\right)^2 = \frac{1}{3}\frac{\left[1-(\frac{R_h}{R_o})^2\right]^2}{1+(\frac{R_h}{R_o})^2} \tag{4.27}$$

where the middle expression is obtained by invoking Equation (3.4) to eliminate w_h.

Taking the square root of Equation (4.27) gives an identical time history for the radial hinge position as Equation (4.11). In other words, the value of T_I is the same for an ideal impulsive load and a constant pressure shock load, which represent the extremes of the uniform shock loading regime. This result, while only strictly applicable to a parabolic deformation profile, suggests that T_I is relatively insensitive to temporal load characteristics, and provides the basis for an approximation to deal with loads with variable pressure histories that will be discussed in Section 4.3.5.

For the case where the load duration T_L is equal to T_I, Equation (4.27) can be rewritten in a normalized dimensionless form as,

$$\frac{\delta_h}{\sqrt{\frac{1}{\alpha}\phi}} = \sqrt{\frac{1}{12}}\frac{\left[1-(\frac{R_h}{R_o})^2\right]^2}{1+(\frac{R_h}{R_o})^2} \tag{4.28}$$

In Figure 4.7 the resulting hinge path is compared to the hinge path for and ideal impulsive load.

4.3.2 Impulsive vs Dynamic Loading

As discussed in Section 2.1, the literature contains a variety of definitions for the term 'impulsive loading', including some that imply a load of short, but necessarily negligible, duration. Hence, in this thesis, the qualifier 'ideal impulsive' was introduced to refer specifically to loads with a negligible duration such

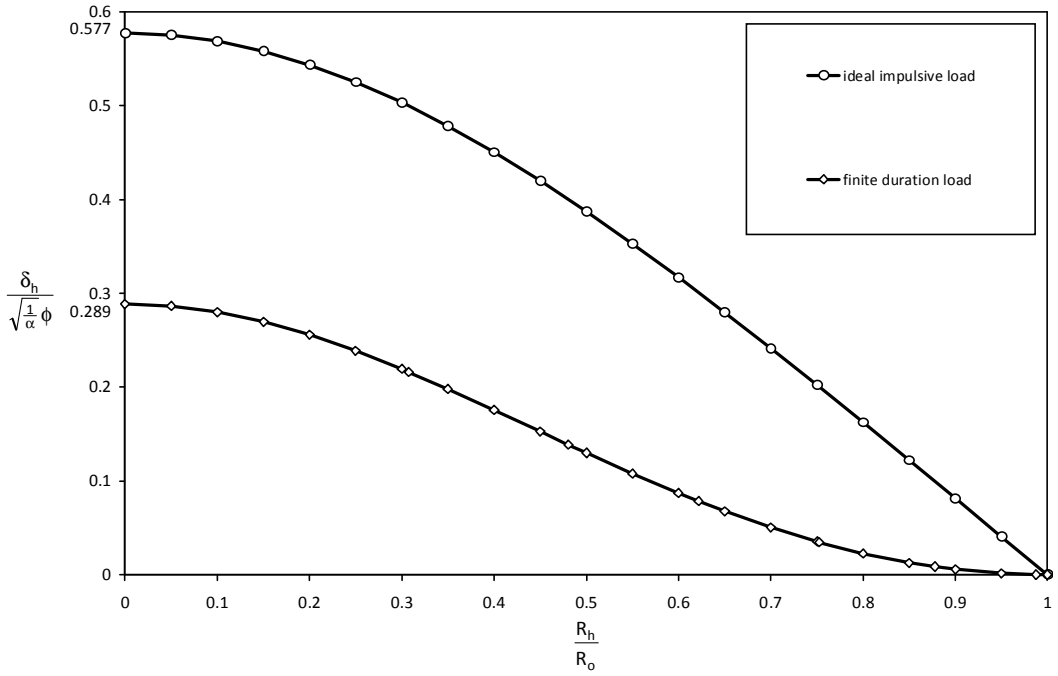

Figure 4.7: Comparison of normalized dimensionless hinge paths for a circular plate subjected to an ideal impulsive load and a finite duration load where $T_L = T_I$.

that details of load history are irrelevant and only the total impulse is of concern. In Section 2.5.2, some definitions of what constitutes an impulsive or dynamic load were reviewed and discussed. In particular, it was argued that criteria based on the asymptotes of pressure-impulse diagrams were somewhat vague and require the subjected choice of an asymptotic threshold. Hence, for the purposes of this thesis, an unambiguous and physically meaningful criterion for the transition from impulsive to dynamic loading needs to be defined.

From the previous section, it is apparent that the value of T_I is characteristic of a given plate configuration and marks the transition from a transient deformation profile to one that is constant. Therefore, it is proposed that T_I be used to distinguish between impulsive and dynamic loads, *i.e.* an impulsive load (IL) has a duration T_L that is finite and less than T_I, while a dynamic load (DL) persists beyond T_I[7]. Consequently, an ideal impulsive load (IIL) has a duration that tends to vanish, while an ideal dynamic load (IDL) has a constant intensity and a duration equal to, or greater than, the total plate response time[8].

4.3.3 Impulsive Loading - Parabolic Phase I Profile

The final central deflection of a circular plate subjected to an ideal impulsive load is presented in Section 3.3.1.2, where the plastic work was equated with the initial kinetic energy. This approach can

[7]For general blast profiles, such as an exponential decaying blast wave, the 'effective load' approach of Youngdahl [46] can be used to define an equivalent square wave.

[8]This terminology differs from that used in the pressure-impulse literature, where a constant intensity load is referred to as a 'qausi-static' load, as discussed in Section 2.5.2.

be adapted for a constant intensity impulsive load by replacing the initial kinetic energy term with an expression for the total work done by the load,

$$W_L = W_P \tag{4.29}$$

where the general form of the plastic work W_P is given in Equations (3.19) and (3.20).

The expression for the work done by the impulsive load as a function of the transverse hinge deflection is given in Equation (4.22). Furthermore, the transverse hinge deflection is the same as that of the inner region of the plate, which moves as a rigid body according to Equation (3.4). The transverse hinge deflection at $T_{\scriptscriptstyle L}$ is thus,

$$w_{\scriptscriptstyle L} = \frac{1}{2}\frac{P}{\rho H}\,T_{\scriptscriptstyle L}^2 \tag{4.30}$$

which, upon substitution into Equation (4.22), gives,

$$W_L = \frac{1}{4}\frac{\pi R_o^2}{\rho H}\left(P\,T_{\scriptscriptstyle L}\right)^2\left[1+\left(\frac{R_{\scriptscriptstyle L}}{R_o}\right)^2\right] = \frac{1}{4}\frac{I^2}{\pi R_o^2 \rho H}\left[1+\left(\frac{R_{\scriptscriptstyle L}}{R_o}\right)^2\right] \tag{4.31}$$

where I is the total impulse of the load, *i.e.* the product of P, $T_{\scriptscriptstyle L}$ and the exposed plate area, while $R_{\scriptscriptstyle L}$ is the hinge radius at the end of the loading phase $T_{\scriptscriptstyle L}$.

Substituting Equations (4.31), (3.19) and (3.20) into Equation (4.29) and rearranging gives,

$$\delta_{\scriptscriptstyle II}^2 = \frac{\tilde{w}_{\scriptscriptstyle II}^2}{H^2} = \frac{1}{2}\left(\frac{1}{\alpha\lambda}\right)\frac{I^2}{\pi^2 R_o^2 H^4 \rho\sigma_y}\left[1+\left(\frac{R_{\scriptscriptstyle L}}{R_o}\right)^2\right] \quad \Rightarrow \quad \delta_{\scriptscriptstyle II} = \frac{\phi}{\sqrt{\alpha}}\sqrt{\frac{1}{2\lambda}\left[1+\left(\frac{R_{\scriptscriptstyle L}}{R_o}\right)^2\right]} \tag{4.32}$$

Note that Equation (4.32) tends to Equation (3.22) as $R_{\scriptscriptstyle L}$ tends to R_o, *i.e.* the ideal impulsive solution is recovered as the radial position of the hinge at time $T_{\scriptscriptstyle L}$ tends to the outer boundary of the plate. Conversely, if the load persists until $T_{\scriptscriptstyle I}$, *i.e.* until the hinge is annihilated, the final deflection is only 70.7 % of what it would be for an equivalent ideal impulsive load.

The normalized final deflection can be expressed in terms of the load duration by making the quotient of $R_{\scriptscriptstyle L}$ and R_o the subject of Equation (4.27), and substituting it into Equation (4.32), with the result,

$$\frac{\delta_{\scriptscriptstyle II}}{\sqrt{\frac{1}{\alpha}}\phi} = \sqrt{\frac{1}{\lambda}}\sqrt{1+\frac{3}{4}\left(\frac{T_{\scriptscriptstyle L}}{T_{\scriptscriptstyle T}}\right)^2-\left(\frac{T_{\scriptscriptstyle L}}{T_{\scriptscriptstyle T}}\right)\sqrt{\frac{3}{2}+\frac{9}{16}\left(\frac{T_{\scriptscriptstyle L}}{T_{\scriptscriptstyle T}}\right)^2}} \tag{4.33}$$

The parameter λ appears in Equation (4.33) because the general form of the plastic dissipation, given in Equations (3.19) and (3.20), was introduced into Equation (4.29). In other words, the choice of the final deformation profile is arbitrary, even though a quadratic profile was used to obtain W_L.

A similar approach is used to determine the deflection at the end of Phase I, with the difference being the inclusion of the kinetic energy term, which gives,

$$E_k = W_L - W_P \tag{4.34}$$

Since the hinge has reaches the plate centre at the end of Phase I, a constant displacement profile is assumed from this point on and the general expression for the kinetic energy is given in Equations (3.24) and (3.25). Upon substitution this gives,

$$\frac{1}{2}\mu\rho\pi R_o^2 H\dot{\tilde{w}}_I^2 = \frac{1}{4}\frac{\pi R_o^2}{\rho H}\left(P\,T_L\right)^2\left[1+\left(\frac{R_L}{R_o}\right)^2\right]+\frac{1}{2}\lambda\pi H\alpha\sigma_y\tilde{w}_I^2 \tag{4.35}$$

The transverse hinge velocity is constant between times T_L and T_I, since it is the same as that of the inner region of the plate which moves as a rigid body. Hence, the central velocity at the end of Phase I is the same as the transverse hinge velocity at T_L, which gives,

$$\dot{\tilde{w}}_I = \dot{\tilde{w}}_L = \frac{P}{\rho H}\,T_L \tag{4.36}$$

Substituting Equation (4.36) into Equation (4.35), rearranging and invoking the definition of dimensionless impulse gives,

$$\frac{\mu}{\lambda}\left(\frac{\phi^2}{\alpha}\right) = \frac{1}{2\lambda}\left(\frac{\phi^2}{\alpha}\right)\left[1+\left(\frac{R_L}{R_o}\right)^2\right]-\left(\frac{\tilde{w}_I}{H}\right)^2 \tag{4.37}$$

Consequently, substituting Equation (4.32) into Equation (4.37) and invoking the definition of the normalized dimensionless deflection, provides the expression,

$$\frac{\delta_I}{\sqrt{\frac{1}{\alpha}}\phi} = \sqrt{\left(\frac{\delta_{II}}{\sqrt{\frac{1}{\alpha}}\phi}\right)^2-\frac{\mu}{\lambda}} \tag{4.38}$$

Finally, the normalized form of the deflection δ_L at the end of the loading phase T_L, as given in Equation (4.30), is,

$$\frac{w_L}{H} = \frac{1}{2}\left(\frac{PT_L}{\rho H^2}\right)\frac{T_L}{T_T}R_o\sqrt{\frac{\rho}{\alpha\sigma_y}} = \frac{1}{\sqrt{\alpha}}\left[\frac{\pi R_o^2 PT_L}{\pi R_o H^2\sqrt{\rho\sigma_y}}\right]\frac{1}{2}\left(\frac{T_L}{T_T}\right) \quad\Rightarrow\quad \frac{\delta_L}{\sqrt{\frac{1}{\alpha}}\phi} = \frac{1}{2}\left(\frac{T_L}{T_T}\right) \tag{4.39}$$

The effect of the load duration T_L on the central deflections δ_L, δ_I and δ_{II}, as predicted by Equations (4.33), (4.38) and (4.39), is shown in a normalized dimensionless form in Figures 4.8 and 4.9 for the parabolic and Bessel type final displacement profile respectively.

4.3.4 Critical Impulsive Loading

The Phase I model presented in Section 4.3.1 is restricted to the use of a parabolic displacement profile so as to provide a convenient closed form solution for the transient hinge position. However, a more general solution can be found for the specific case where the load duration is equal to the Phase I duration, *i.e.* $T_L = T_I$. In this thesis, this loading case will be referred to as the critical impulsive load (CIL) since it represents the transition from the impulsive to the dynamic loading regime.

At time T_I, the transient phase of motion is complete and the plate shape can be described using the displacement profiles considered in Section 3.3. Since the pressure is assumed to be constant during

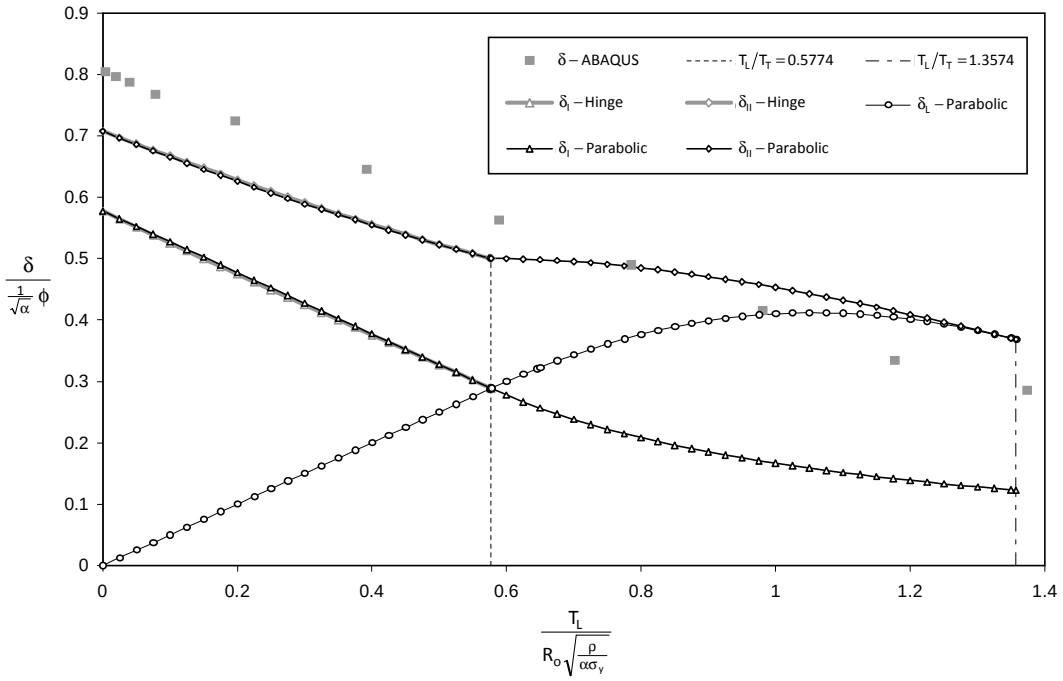

Figure 4.8: Comparison of numerical and theoretical predictions for the normalized dimensionless central deflections of a shock loaded circular plate as a function of the dimensionless load duration. The theoretical models are based on a parabolic final deflection profile, where the thick grey curves represent the model presented in Sections 4.3.3, while the thin black curves represent the models presented in Sections 4.3.5 and 4.3.6.

Phase I, a complete description of the deflection history is not required and description of the plate shape at T_I is sufficient to determine the work performed by the pressure load, which is referred to as the 'pressure work' in this thesis. Hence, for a parabolic displacement profile, the pressure work is determined by substituting Equation (2.20) into Equation (4.20) and integrating. The result is identical to Equation (4.22) when R_h vanishes and w_h can be replaced by $\tilde{w}$, and can be written in the form,

$$W_L = \tilde{P}\tilde{w} \quad \text{where} \quad \tilde{P} = \beta\pi R_o^2 P \quad \text{and} \quad \beta = \frac{1}{2} \tag{4.40}$$

where $\tilde{P}$ is the effective pressure and β is the effective pressure parameter[9]. In essence, β specifies the work done by the pressure P in comparison to the work done if P had acted on a rigid that deflected by an amount $\tilde{w}$. In other words, β captures the effect of the plate which restricts the motion of the plate and, consequently, the work that can be done by the pressure P.

For the case of a Bessel function displacement distribution, as given in Equation (3.33), the integration of Equation (4.20) gives,

$$W_L = 2\pi P\tilde{w}\int_0^{R_o} rJ_0(\Lambda\frac{r}{R_0})\,dr = \frac{2J_1(\Lambda)}{\Lambda}\pi R_0^2 P\tilde{w} \quad \Rightarrow \quad \beta = \frac{2J_1(\Lambda)}{\Lambda} = 0.4318 \tag{4.41}$$

[9]This term must not be confused with the effective pressure load as defined by Youngdahl [46].

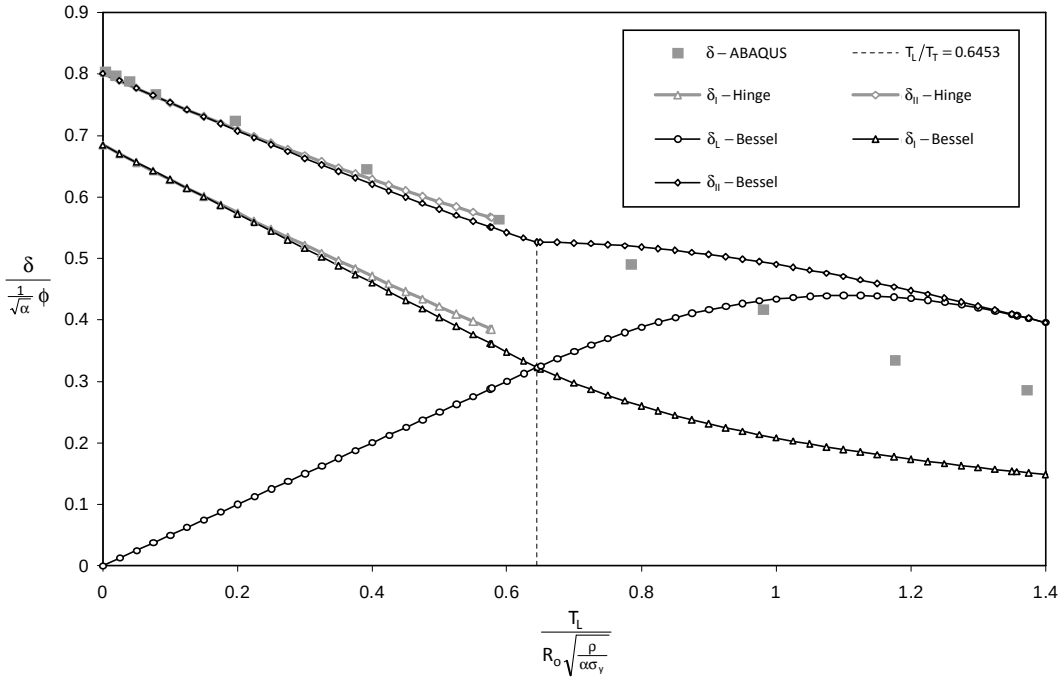

Figure 4.9: Comparison of numerical and theoretical predictions for the normalized dimensionless central deflections of a shock loaded circular plate as a function of the dimensionless load duration. The theoretical models are based on a Bessel type final deflection profile, where the thick grey curves represent the model presented in Sections 4.3.3, while the thin black curves represent the models presented in Sections 4.3.5 and 4.3.6.

For the case of a conical displacement distribution, as given in Equation (3.44), the integration of Equation (4.20) gives,

$$W_L = 2\pi P\tilde{w}\int_0^{R_o} r\left[1-\frac{r}{R_0}\right]dr = \frac{1}{3}\pi R_0^2 P\tilde{w} \quad \Rightarrow \quad \beta = \frac{1}{3} \tag{4.42}$$

Following the energy approach of the previous section, the duration of Phase I is obtained by equating the kinetic energy of the plate with the difference between the pressure work and the plastic dissipation. Hence, substituting Equations (3.24), (4.40) and (3.19) into Equation (4.34) gives,

$$\frac{1}{2}\mu\rho\pi R_o^2 H\dot{\tilde{w}}_I^2 = \beta\pi R_o^2 P\tilde{w}_I - \frac{1}{2}\lambda\pi H\alpha\sigma_y\tilde{w}_I^2 \tag{4.43}$$

Rewriting Equations (4.30) and (4.36) in terms of T_I, $\tilde{w}_I$ and $\dot{\tilde{w}}_I$, substituting the result into Equation (4.43), introducing the Taylor duration T_T and simplifying gives the dimensionless Phase I duration under critical impulsive loading as,

$$\frac{T_I}{T_T} = 2\sqrt{\frac{\beta-\mu}{\lambda}} \tag{4.44}$$

Values for the critical dimensionless Phase I duration for the three deformation profiles considered in this thesis are given in Table 4.2. In the case of the parabolic profile, the value is identical to the corresponding values in Table 4.1, *i.e.* the result obtained in Section 4.3.1 is recovered. However, in case of the Bessel

Table 4.2: Normalized values of δ_I, δ_{II}, T_I and T_{II} and for a critical impulsive load, *i.e.* $T_L = T_I$.

Profile	β		$\frac{\delta_I}{\sqrt{\frac{1}{\alpha}}\phi}$		$\frac{T_I}{R_o\sqrt{\frac{\rho}{\alpha\sigma_y}}}$	$\frac{\delta_{II}}{\sqrt{\frac{1}{\alpha}}\phi}$		$\frac{T_{II}}{R_o\sqrt{\frac{\rho}{\alpha\sigma_y}}}$
	exact	approx.	exact	approx.	approx.	exact	approx.	approx.
parabolic	$\frac{1}{2}$	0.5	$\sqrt{\frac{1}{12}}$	0.2887	0.5774	$\sqrt{\frac{1}{4}}$	0.5	0.9674
Bessel	$\frac{2J_1(\Lambda)}{\Lambda}$	0.4318	$\sqrt{\frac{2-\Lambda J_1(\Lambda)}{\Lambda^3 J_1(\Lambda)}}$	0.3226	0.6453	$\sqrt{\frac{2}{\Lambda^3 J_1(\Lambda)}}$	0.5263	1.0241
conical	$\frac{1}{3}$	0.3333	$\sqrt{\frac{1}{6}}$	0.4082	0.8165	$\sqrt{\frac{1}{3}}$	0.3333	1.1371

and conical profiles, the CIL Phase I durations are approximately 6% and 10% smaller, respectively, than under IIL conditions. This observation suggests that the Phase I duration is near constant and forms the basis for the impulsive duration analysis presented in Section 4.3.5.

The Phase I deflection under critical impulsive loading is obtained by substituting Equation (4.44) into Equation (4.30) and invoking the definition of dimensionless impulse, which gives,

$$\frac{\delta_I}{\sqrt{\frac{1}{\alpha}}\phi} = \frac{1}{2}\left(\frac{T_I}{T_T}\right) = \sqrt{\frac{\beta-\mu}{\lambda}} \tag{4.45}$$

This expression is identical to Equation (4.39), *i.e.* the deflection at the end of an impulsive loading phase, which is consistent since $T_L = T_I$ under CIL conditions.

The Phase II deflection under critical impulsive loading is obtained using Equation (4.43), except that the plastic dissipation is expressed in terms of $\tilde{w}_{II}$ and the kinetic energy term vanishes. As before, expressing the pressure work term using Equation (4.30) and invoking the definition of dimensionless impulse, gives,

$$\frac{\delta_{II}}{\sqrt{\frac{1}{\alpha}}\phi} = \sqrt{\frac{\beta}{\lambda}} \tag{4.46}$$

A summary of the values for the normalized Phase I and II dimensionless deflections under CIL conditions is given in Table 4.2.

It is interesting to note that the IIL deflection estimates are recovered from Equations (4.45) and (4.46) when β is set to unity. The reason for this is that $\beta = 1$ implies a uniform displacement profile which, for a given impulsive load, results in the same uniform plate velocity as that assumed in the IIL approach.

4.3.5 Impulsive Loading - General Profile

In this section, an approximate approach to estimate the deflection history of thin plates subjected to finite duration impulsive loads is presented. This approach is required because the detailed hinge path analysis, as described in Section 4.3.1, proved to be mathematically intractable for a general displacement profile, and a general expression for the Phase I duration T_I could not be found. However, it was shown in Section 4.3.4 that the values of T_I predicted under IIL and CIL conditions do not differ significantly.

Hence, for the sake of simplicity, it is assumed that under impulsive loading conditions the Phase I duration is near constant and can be approximated using a linear interpolation of the form,

$$T_I = \left(1 - \frac{T_L}{(T_I)_{CIL}}\right)(T_I)_{IIL} + T_L \tag{4.47}$$

where $(T_I)_{IIL}$ and $(T_I)_{CIL}$ are the Phase I durations under IIL and CIL conditions, as given in Equations (4.15) and (4.44), respectively.

Once a value for T_I is known, the central deflection at the end of Phase I can be obtained treating the central portion of the plate as a rigid mass moving at a constant velocity between times T_L and T_I, which gives,

$$\tilde{w}_I = w_L + \dot{w}_L\,(T_I - T_L) \tag{4.48}$$

where w_L and $\dot{w}_L$ are given by Equations (4.30) and (4.36), respectively. This approach is reasonable since there will be no deceleration force at the centre of the plate before the arrival of the travelling hinge, *i.e.* the end of Phase I. Substituting the aforementioned equations into Equation (4.48) and introducing the dimensionless deflection and Taylor duration gives,

$$\delta_I = \frac{\tilde{w}_I}{H} = \frac{PT_L}{\rho H^2} R_o \sqrt{\frac{\rho}{\alpha\sigma_y}} \left[\frac{T_I}{T_T} - \frac{1}{2}\frac{T_L}{T_T}\right] = \frac{\phi}{\sqrt{\alpha}} \left[\frac{T_I}{T_T} - \frac{1}{2}\frac{T_L}{T_T}\right] \tag{4.49}$$

The normalized dimensionless deflection at the end of Phase I is thus,

$$\frac{\delta_I}{\sqrt{\frac{1}{\alpha}}\phi} = \frac{T_I}{T_T} - \frac{1}{2}\frac{T_L}{T_T} \tag{4.50}$$

From time T_I to T_{II} the deformation behaviour is essentially identical to the IIL response analyzed in Section 4.2.2. In other words, the deformation is described using a constant displacement profile, which results in a sinusoidal displacement history. Hence, using the same approach as that followed in Equation (4.16), setting the time equal to T_I and comparing the result to Equation (4.49) gives,

$$\frac{\tilde{w}_I}{\tilde{w}_{II}} = sin\left[\left(\frac{\pi}{2}\right)\frac{T_I - (T_{II} - T)}{T}\right] = \frac{1}{\tilde{w}_{II}}\left(\frac{PT_L}{\rho H}\right)\left[T_I - \frac{1}{2}T_L\right] \tag{4.51}$$

Differentiating Equation (4.16) gives the central velocity history from T_I to T_{II} as,

$$\frac{\dot{\tilde{w}}}{\tilde{w}_{II}} = \frac{\pi}{2T}\,cos\left[\left(\frac{\pi}{2}\right)\frac{t - (T_{II} - T)}{T}\right] \tag{4.52}$$

Setting the time equal to T_I and comparing the result to Equation (4.36) gives,

$$\frac{\dot{\tilde{w}}_I}{\tilde{w}_{II}} = \frac{\pi}{2T}\,cos\left[\left(\frac{\pi}{2}\right)\frac{T_I - (T_{II} - T)}{T}\right] = \frac{1}{\tilde{w}_{II}}\left(\frac{PT_L}{\rho H}\right) \tag{4.53}$$

The quotient of Equations (4.51) and (4.53) gives,

$$\frac{2T}{\pi}\,tan\left[\left(\frac{\pi}{2}\right)\frac{T_I - (T_{II} - T)}{T}\right] = T_I - \tfrac{1}{2}T_L \tag{4.54}$$

Introducing the Taylor duration and rearranging gives the total dimensionless deformation duration as,

$$\frac{T_{II}}{T_T} = \frac{\pi}{2}\sqrt{\frac{\mu}{\lambda}} + \frac{T_I}{T_T} - \sqrt{\frac{\mu}{\lambda}}\, tan^{-1}\left[\sqrt{\tfrac{\lambda}{\mu}}\left(\frac{T_I}{T_T} - \tfrac{1}{2}\frac{T_L}{T_T}\right)\right] \tag{4.55}$$

Under CIL conditions the expression reduces to,

$$\frac{T_{II}}{T_T} = 2\sqrt{\frac{\beta-\mu}{\lambda}} + \sqrt{\frac{\mu}{\lambda}}\left[\frac{\pi}{2} - sin^{-1}\sqrt{1-\frac{\mu}{\beta}}\right] \tag{4.56}$$

The dimensionless T_{II} values for the three PCS deformation profiles considered in this thesis are given in Table 4.2.

Finally the deflection at the end of Phase II can be obtained by rewriting Equation (4.53) as,

$$\tilde{w}_{II} = \left(\frac{PT_L}{\rho H}\right)\frac{2T}{\pi}\Big/ cos\left[\left(\frac{\pi}{2}\right)\frac{T_I - (T_{II}-T)}{T}\right] \tag{4.57}$$

Expressing the numerator in terms of the dimensionless impulse, modifying the argument of the cosine term using Equation (4.54) and rearranging gives the normalized dimensionless deflection as,

$$\frac{\delta_{II}}{\sqrt{\frac{1}{\alpha}}\phi} = \sqrt{\frac{\mu}{\lambda}}\Big/ cos\left[tan^{-1}\left[\sqrt{\frac{\lambda}{\mu}}\left(\frac{T_I}{T_T} - \tfrac{1}{2}\frac{T_L}{T_T}\right)\right]\right] \tag{4.58}$$

Under CIL conditions, where $T_I = T_L$ and has the dimensionless form given in Equation (4.44), the expression reduces to,

$$\frac{\delta_{II}}{\sqrt{\frac{1}{\alpha}}\phi} = \sqrt{\frac{\mu}{\lambda}}\Big/ cos\left[tan^{-1}\sqrt{\frac{\beta-\mu}{\mu}}\right] = \sqrt{\frac{\mu}{\lambda}}\Big/ cos\left[cos^{-1}\sqrt{\frac{\mu}{\beta}}\right] = \sqrt{\frac{\beta}{\lambda}} \tag{4.59}$$

In other words, Equation (4.46) is recovered, as would be expected.

The predictions of Equations (4.50), (4.58) and (4.55) for the parabolic and Bessel function type displacement profiles are shown in a normalized dimensionless form in Figures 4.8, 4.9 and 4.10 respectively. Note that for the case of a parabolic profile, Figure 4.8 shows that the displacements are virtually identical to those obtained in Section 4.3.3 indicating that the assumption of a constant T_I is acceptable. Likewise, for the case of a Bessel type profile, Figure 4.9 shows that the displacements correlate well with those obtained in Section 4.3.3 and are virtually identical at small values of T_I, indicating that the assumption of a linearly varying T_I is acceptable.

4.3.6 Dynamic Loading

In this section, a general approach to estimate the deflection history of thin plates subjected to dynamic loading (DL) conditions, *i.e.* loads of constant intensity and finite duration where $T_L > T_I$, is presented. Phase I under DL conditions is identical to that under a CIL condition in that the load is applied throughout T_I. Hence, the expression for T_I obtained for the CIL condition is valid for all DL conditions. In other words, for a given plate configuration and assumed deformation profile, T_I is constant under DL

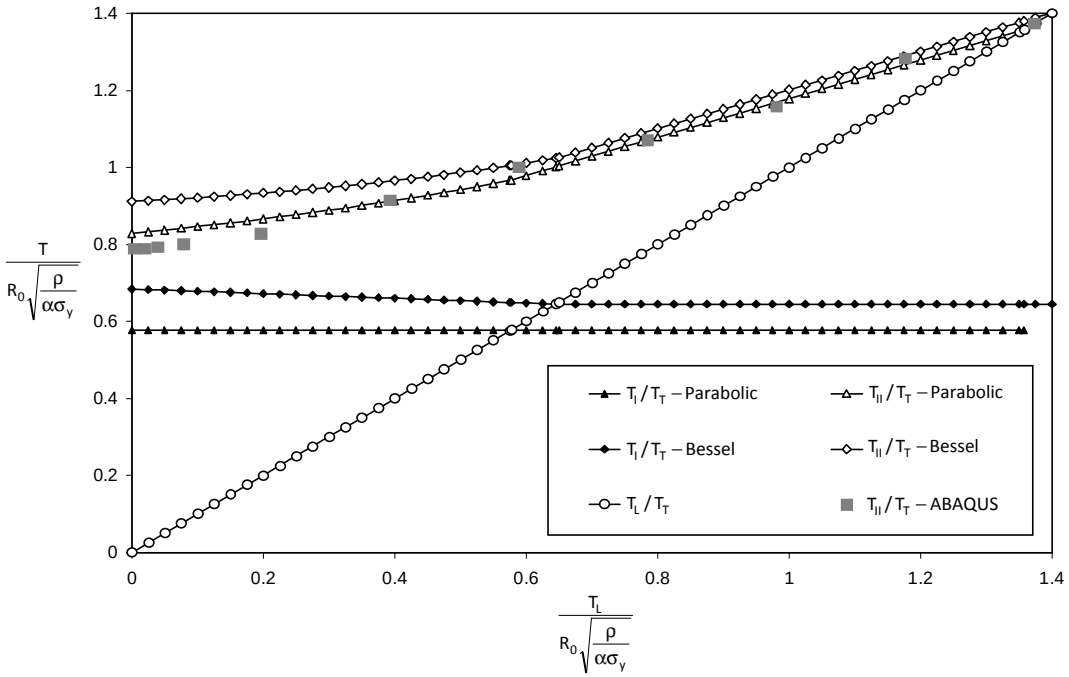

Figure 4.10: Comparison of numerical and theoretical predictions for the normalized dimensionless deflection duration of a shock loaded circular plate as a function of the dimensionless load duration. Theoretical predictions based on both a parabolic and Bessel function final deflection profile are shown. The impulsive loading $T_{_L} \leq T_{_I}$ and dynamic loading $T_{_L} > T_{_I}$ curves represent the model presented in Sections 4.3.5 and 4.3.6 respectively.

conditions and given by Equation (4.44). Consequently, Equation (4.30) can be rewritten as,

$$\tilde{w}_{_I} = \frac{1}{2}\frac{P}{\rho H}\,T_{_I}^2 = \frac{1}{2}\frac{P}{\rho H}\left[2\sqrt{\frac{\beta-\mu}{\lambda}}\,T_{_T}\right]^2 \tag{4.60}$$

Expressing the pressure in terms of the total impulse and $T_{_L}$, while invoking the definitions of the dimensionless deflection and Taylor duration gives,

$$\delta_{_I} = \frac{2}{\rho H^2}\left(\frac{I}{\pi R_o^2 T_{_L}}\right)\left(\frac{\beta-\mu}{\lambda}\right)T_{_T}^2 = 2\left(\frac{\beta-\mu}{\lambda}\right)\sqrt{\frac{1}{\alpha}}\,\frac{I}{\pi R_o H^2\sqrt{\rho\sigma_y}}\left(\frac{T_{_T}}{T_{_L}}\right) \tag{4.61}$$

Consequently, invoking the definitions of the dimensionless impulse and changing the subject of the formula gives the normalized dimensionless deflection at the end of Phase I as,

$$\frac{\delta_{_I}}{\sqrt{\frac{1}{\alpha}}\phi} = 2\left(\frac{\beta-\mu}{\lambda}\right)\Big/\left(\frac{T_{_L}}{T_{_T}}\right) \tag{4.62}$$

The plate behaviour during the loading phase subsequent to Phase I, *i.e.* $T_{_I} < t < T_{_L}$, can be treated as an extension of the generalized energy method as applied to an arbitrary constant displacement profile,

$$E_k(\dot{\tilde{w}}) = W_L(\tilde{w}) - W_P(\tilde{w}) \tag{4.63}$$

Hence, substituting Equations (3.24), (4.40) and (3.19) into Equation (4.63) gives,

$$\frac{1}{2}\tilde{M}\dot{\tilde{w}}^2 = \tilde{P}\tilde{w} - \frac{1}{2}\tilde{K}\tilde{w}^2 \quad \Rightarrow \quad \dot{\tilde{w}} = \frac{d\tilde{w}}{dt} = \sqrt{\tfrac{2\tilde{P}}{\tilde{M}}\tilde{w} - \tfrac{\tilde{K}}{\tilde{M}}\tilde{w}^2} \tag{4.64}$$

Integrating using separation of variables gives,

$$\int_{T_I}^{t} dt = \int_{\tilde{w}_I}^{\tilde{w}} \frac{d\tilde{w}}{\sqrt{\frac{2\tilde{P}}{\tilde{M}}\tilde{w} - \frac{\tilde{K}}{\tilde{M}}\tilde{w}^2}} \quad \Rightarrow \quad t - T_I = 2\sqrt{\tfrac{\tilde{M}}{\tilde{K}}}\left[sin^{-1}\sqrt{\tfrac{\tilde{K}}{2\tilde{P}}\,\tilde{w}} - sin^{-1}\sqrt{\tfrac{\tilde{K}}{2\tilde{P}}\,\tilde{w}_I}\right] \tag{4.65}$$

Rearranging gives the displacement as,

$$\tilde{w} = \tfrac{2\tilde{P}}{\tilde{K}}\, sin^2\left[\tfrac{1}{2}\sqrt{\tfrac{\tilde{K}}{\tilde{M}}}\,(t - T_I) + sin^{-1}\sqrt{\tfrac{\tilde{K}}{2\tilde{P}}\,\tilde{w}_I}\right] \quad , \quad T_I < t < T_L \tag{4.66}$$

The quotients of the plastic stiffness, effective mass and effective pressure can be written as,

$$\frac{\tilde{P}}{\tilde{K}} = \frac{\beta\pi R_o^2 P}{\lambda\pi H\alpha\sigma_y} = \left(\frac{\beta}{\lambda}\right)\frac{\pi R_o^2 P T_L}{\pi R_o H^2\sqrt{\rho\sigma_y}}\sqrt{\frac{1}{\alpha}}\left(\frac{H}{T_L}\right)R_o\sqrt{\frac{\rho}{\alpha\sigma_y}} = H\left(\frac{\beta}{\lambda}\right)\frac{\phi}{\sqrt{\alpha}}\Big/\frac{T_L}{T_T} \tag{4.67}$$

and

$$\frac{\tilde{K}}{\tilde{M}} = \frac{\lambda\pi H\alpha\sigma_y}{\mu\rho\pi R_o^2 H} = \frac{\lambda}{\mu}\Big/R_o^2\left(\frac{\rho}{\alpha\sigma_y}\right) = \frac{\lambda}{\mu}\left(\frac{1}{T_T^2}\right) \quad \Rightarrow \quad \sqrt{\frac{\tilde{K}}{\tilde{M}}} = \frac{1}{T_T}\sqrt{\frac{\lambda}{\mu}} \tag{4.68}$$

From the above, and incorporating the normalized form of δ_I given in Equation (4.62), the argument of the arcsine term in Equation (4.66) becomes,

$$\frac{\tilde{K}}{2\tilde{P}}\tilde{w}_I = \frac{\tilde{w}_I}{2}\Big/H\left(\frac{\beta}{\lambda}\right)\frac{\phi}{\sqrt{\alpha}}\left(\frac{T_T}{T_L}\right) = \frac{1}{2}\left(\frac{\lambda}{\beta}\right)\frac{T_L}{T_T}\frac{\delta_I}{\sqrt{\frac{1}{\alpha}}\phi} = 1 - \frac{\mu}{\beta} \tag{4.69}$$

Substituting Equations (4.67), (4.68) and (4.69) into Equation (4.66), introducing the normalized form of T_I given in Equation (4.44) and rearranging gives,

$$\frac{\delta(t)}{\sqrt{\frac{1}{\alpha}}\phi} = 2\,\frac{\beta}{\lambda}\left(\frac{T_T}{T_L}\right)sin^2\left[\frac{1}{2}\sqrt{\frac{\lambda}{\mu}}\left(\frac{t}{T_T}\right) - \sqrt{\frac{\beta}{\mu} - 1} + sin^{-1}\sqrt{1 - \frac{\mu}{\beta}}\right] \quad , \quad T_I < t < T_L \tag{4.70}$$

Hence the normalized deflection at the end of the loading phase is,

$$\frac{\delta_L}{\sqrt{\frac{1}{\alpha}}\phi} = 2\,\frac{\beta}{\lambda}\left(\frac{T_T}{T_L}\right)sin^2\left[\frac{1}{2}\sqrt{\frac{\lambda}{\mu}}\left(\frac{T_L}{T_T}\right) - \sqrt{\frac{\beta}{\mu} - 1} + sin^{-1}\sqrt{1 - \frac{\mu}{\beta}}\right] \tag{4.71}$$

The energy expression required to obtain the final deflection δ_{II} at the end of Phase II is similar to Equation (4.63), except that the kinetic energy term vanishes, giving,

$$W_L(\tilde{w}_L) = W_P(\tilde{w}_{II}) \quad \Rightarrow \quad \tilde{P}\tilde{w}_L = \frac{1}{2}\tilde{K}\tilde{w}_{II}^2 \quad \Rightarrow \quad \tilde{w}_{II} = \sqrt{2\,\frac{\tilde{P}}{\tilde{K}}\,\tilde{w}_L} \tag{4.72}$$

Substituting Equation (4.67) into Equation (4.72) and introducing the normalized form of the dimensionless deflection gives,

$$\frac{\delta_{II}}{\sqrt{\frac{1}{\alpha}\phi}} = \sqrt{\frac{2\tilde{P}}{H\tilde{K}} \Big/ \sqrt{\tfrac{1}{\alpha}\phi}} \sqrt{\frac{\tilde{w}_L}{H} \Big/ \sqrt{\tfrac{1}{\alpha}\phi}} = \sqrt{2\,\frac{\beta}{\lambda}\left(\frac{T_L}{T_T}\right)} \sqrt{\frac{\delta_L}{\sqrt{\frac{1}{\alpha}\phi}}} \tag{4.73}$$

finally, substituting Equation (4.71) into Equation (4.73) and rearranging gives the normalized dimensionless deflection at the end of Phase II as,

$$\frac{\delta_{II}}{\sqrt{\frac{1}{\alpha}\phi}} = 2\,\frac{\beta}{\lambda}\left(\frac{T_T}{T_L}\right) sin\left[\frac{1}{2}\sqrt{\frac{\lambda}{\mu}}\left(\frac{T_L}{T_T}\right) - \sqrt{\frac{\beta}{\mu} - 1} + sin^{-1}\sqrt{1 - \frac{\mu}{\beta}}\right] \tag{4.74}$$

The predictions of Equations (4.62), (4.71) and (4.74) for the parabolic and Bessel type displacement profiles are shown in Figures 4.8 and 4.9 respectively.

Finally, the deflection duration at the end of Phase II is obtained by recognizing that from time T_L to T_{II} the deformation behaviour is essentially identical to the IIL response of a constant displacement profile, *i.e.* a sinusoidal displacement history. Hence, substituting T_L into Equation (4.16) gives,

$$\frac{\tilde{w}_L}{\tilde{w}_{II}} = \frac{\delta_L}{\delta_{II}} = sin\left[\left(\frac{\pi}{2}\right)\frac{T_L - (T_{II} - T)}{T}\right] \quad \text{where} \quad T = \frac{\pi}{2}\sqrt{\frac{\mu}{\lambda}}\,T_T \tag{4.75}$$

However, the quotient of Equations (4.71) and (4.74) has the form,

$$\frac{\delta_L}{\delta_{II}} = sin\left[\frac{1}{2}\sqrt{\frac{\lambda}{\mu}}\left(\frac{T_L}{T_T}\right) - \sqrt{\frac{\beta}{\mu} - 1} + sin^{-1}\sqrt{1 - \frac{\mu}{\beta}}\right] \tag{4.76}$$

Consequently, equating the arguments in Equations (4.75) and (4.76) and rearranging gives to total dimensionless deformation duration under DL conditions as,

$$\frac{T_{II}}{T_T} = \frac{1}{2}\left(\frac{T_L}{T_T}\right) + \sqrt{\frac{\beta - \mu}{\lambda}} + \sqrt{\frac{\mu}{\lambda}}\left[\frac{\pi}{2} - sin^{-1}\sqrt{1 - \frac{\mu}{\beta}}\right] \tag{4.77}$$

The predictions of Equation (4.77) for the parabolic and Bessel function type displacement profiles are shown in Figure 4.10.

4.3.7 Ideal Dynamic Load

A special case of the dynamic loading considered in Section 4.3.6 is where the load duration is equal to the Phase II duration, *i.e.* $T_L = T_{II}$. In this thesis, this loading case will be referred to as the ideal dynamic load (IDL), as briefly discussed in Section 2.5.2.

Following the argument in Section 4.3.6, the expression for the Phase I dimensionless duration is the same as that given in Equations (4.44) with values identical to those given in Table 4.2. Furthermore, the expressions for the Phase I dimensionless deflection is given in Equation (4.62), except that $T_L = T_{II}$.

Table 4.3: Normalized values of δ_I, δ_{II} and T_{II} and for an ideal dynamic load, *i.e.* $T_L = T_{II}$. Note that the normalized value of T_I are identical to those given in Table 4.2.

Profile	$\frac{\delta_I}{\sqrt{\frac{1}{\alpha}}\phi}$ approx.	$\frac{T_I}{R_o\sqrt{\frac{\rho}{\alpha\sigma_y}}}$ approx.	$\frac{\delta_{II}}{\sqrt{\frac{1}{\alpha}}\phi}$ approx.	$\frac{T_{II}}{R_o\sqrt{\frac{\rho}{\alpha\sigma_y}}}$ approx.
parabolic	0.1228	0.5774	0.3684	1.3574
Bessel	0.1484	0.6453	0.3949	1.4029
conical	0.4082	0.8165	0.4573	1.4578

The total dimensionless deformation duration under IDL conditions is obtained by simply replacing T_L with T_{II} in Equation (4.77) and rearranging, which gives,

$$\frac{T_{II}}{T_T} = 2\sqrt{\frac{\beta-\mu}{\lambda}} + 2\sqrt{\frac{\mu}{\lambda}}\left[\frac{\pi}{2} - sin^{-1}\sqrt{1-\frac{\mu}{\beta}}\right] \tag{4.78}$$

The final deflection δ_{II} is obtained using the energy approach, where in this case $\tilde{w}_L = \tilde{w}_{II}$ at the end of Phase II and Equation (4.72) and reduces to,

$$W_L(\tilde{w}_L) = W_L(\tilde{w}_{II}) = W_P(\tilde{w}_{II}) \quad \Rightarrow \quad \tilde{P}\tilde{w}_{II} = \frac{1}{2}\tilde{K}\tilde{w}_{II}^2 \quad \Rightarrow \quad \tilde{w}_{II} = \frac{2\tilde{P}}{\tilde{K}} \tag{4.79}$$

Hence, substituting Equations (4.67) and (4.78) into Equation (4.79) and rearranging gives the expression for the normalized dimensionless deflection at the end of Phase II as,

$$\frac{\delta_{II}}{\sqrt{\frac{1}{\alpha}}\phi} = 2\left(\frac{\beta}{\lambda}\right)\Big/\frac{T_{II}}{T_T} = \frac{\beta}{\lambda}\Big/\sqrt{\frac{\mu}{\lambda}}\left[\frac{\pi}{2} + \sqrt{\frac{\beta}{\mu}-1} - sin^{-1}\sqrt{1-\frac{\mu}{\beta}}\right] \tag{4.80}$$

The dimensionless δ_{II} and T_{II} values under IDL conditions for the three PCS deformation profiles considered in this thesis are given in Table 4.3.

4.3.8 Comparison with Numerical and Experimental Results

As discussed in Chapter 2 and Section 4.1, there appears to be no published analytical solutions or experimental data for the large deformation of circular plates subjected to finite duration uniform impulsive loads. The lack of experimental data is due to the practical difficulties encountered when attempting to generate a 'square' loading, *i.e.* a uniform load of constant intensity and finite duration. Experiments conducted using explosives produce typical blast load pressure histories [51,52], *i.e.* a sudden pressure rise followed by an exponential decay, with short stand-off configurations tending toward an ideal impulsive load condition. At the other extreme of the finite duration regime, an ideal dynamic load can be achieved using shock tube techniques, which will be considered later in this section.

In lieu of the above, numerical simulations of impulsively loaded circular plates were used to provide appropriate data with which to compare the general models presented in Sections 4.3.5 and 4.3.6. A series

Table 4.4: Material constant for the PCS Abaqus SE model.

ρ [kg/m^3]	E_y [GPa]	σ_y [MPa]	R_o [mm]	H [mm]	I [Ns]
7800	200	300	50	1.6	4.712

of simple numerical simulations were conducted using the explicit finite element code Abaqus SE (Version 6.7). Each simulation employed an axisymmetric mesh which consisted of 100×4 four node elements and was fully constrained along the outer radial periphery. In each individual simulation run, the mesh was subjected to a uniform pressure load of constant intensity and finite duration. In particular, the intensity and duration were varied between simulations such that the total impulse remained constant. The element properties and simulation parameters are given in Table 4.4. No strain hardening or strain rate effects were included.

The simulation results are compared to the analytical predictions in Figures 4.8, 4.9 and 4.10. The analytical and numerical solutions show good agreement in the impulsive loading regime. In particular, Figure 4.9 shows that the solution based on a Bessel type displacement profile provides the best deflection correlation, which is to be expected given the IIL results discussed in section 4.2. These results tend to support the validity of the assumptions regarding the estimate of T_I used to develop the analytical model. However, Figures 4.10 shows that the dynamic deformation duration solution based on a parabolic displacement profile provides a better deflection duration correlation.

The analytical and numerical results show reasonable agreement in the dynamic loading regime, but not to the same degree as the impulsive regime. In particular, for the analytical curves there is a distinct change of gradient at the CIL transition between the impulsive and dynamic regimes, which is absent in the numerical results. However, Figures 4.10 shows that the analytical dynamic deformation duration predictions for both the parabolic and Bessel type displacement profiles are in good agreement with the numerical results.

It is interesting to note that the dimensionless impulse ϕ does not appear in Equations (4.55) or (4.77). In other words, for a given load duration T_L, the deformation duration T_{II} is independent of the total impulse of the load. Furthermore, Figure 4.10 indicates that the slope of the deformation duration curves tend to 'level off' as the load duration T_L approaches the IIL limit. In other words, in the region close to the impulsive limit, the deformation duration T_{II} is near to constant, *i.e.* it is practically independent of the load duration T_L. These two observations imply that, for a given plate configuration, short stand-off blast loading experiments that merely tend toward an IIL condition should produce deformation duration results that are consistent with the IIL prediction. This results is broadly in agreement with the data discussed in Section 3.2.3.

In contrast with the previous observation, Figures 4.8 and 4.9 indicate that the slope of the dimensionless deflection curves do not tend to 'level off' but remain steep as the load duration T_L approaches the IIL limit. This implies that, short stand-off blast loads, even if tending toward the IIL condition, cannot be viewed as equivalent to an IIL condition. In other words, an impulsive load with a finite duration, even if small relative to T_{II}, will produce a final deflection that is smaller than the IIL prediction. This result is of particular relevance to experimental configurations intended to approach the IIL condition,

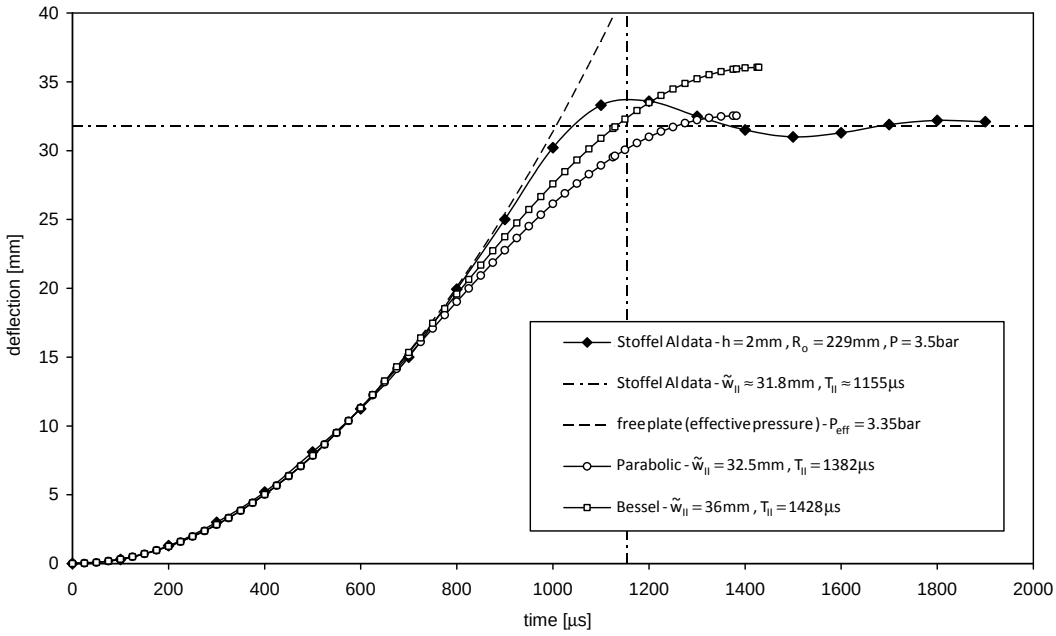

Figure 4.11: Comparison of theoretical predictions for an ideal dynamic load with the experimental data due to Stoffel [98] for a shock loaded circular plate.

such as that discussed in Section 5.3.1. Impact arrested tests may provide a closer approximation to the IIL condition, but deformation duration measurements for these tests are not available in the literature.

Finally, a comparison of the IDL solution with the experimental data of Stoffel [98] is shown in Figure 4.11. As previously reviewed in Sections 2.2.3, Stoffel used a shock tube to impose a near ideal dynamic load on a 2 mm thick aluminium plate with a clamped radius of 229 mm. The experimental load history is shown Figure 2.7, while the strength properties are shown in Figure 4.12.

Figure 2.7 shows incident and initial reflected shock overpressures of approximately 1.2 bar and 3.5 bar, respectively. However, according to the shock-structure interaction analysis in Section 3.2.4, the reflected pressure is affected by the movement of the plate. This effect is evident in Figure 2.7 where the pressure drops to approximately 3.35 bar while the plate is deforming. This pressure drop is less than what would be predicted for a free plate since the periphery of the plate is clamped. Hence, for the IDL analysis, which is based on the assumption of a constant pressure load, a mean effective pressure P_{eff} equal to the lower measured value of 3.35 bar is used.

Figure 4.12 shows that the flow stress of the plate material displays strain hardening with slight rate sensitivity, as is typical of aluminium. Hence, the equations presented in Section 4.3.7 have to be applied iteratively. Following the iterative procedure for a Bessel function displacement profile, as discussed in Section 2.3.7, results in maximum and average final strains of 0.024 and 0.019, respectively. A similar analysis using a Parabolic displacement profile results in values of 0.04 and 0.02. In other words, while the maximum strain varies greatly, depending on the displacement profile, the average strain is similar. The reason for this is that the definition of the average strain is such that it gives the correct total plastic work when multiplied with the flow stress and volume of the plate. Hence, for a given initial

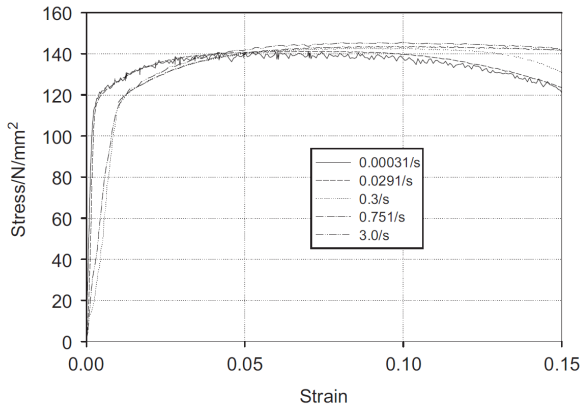

Figure 4.12: Material properties for the aluminium plate shock tube experiments reported by Stoffel [98].

kinetic energy or pressure work, the final average strain must be similar, regardless of the displacement profile. Furthermore, the two profiles have a similar displacement histories and T_{II} values, which result in average strain and strain rate values over the entire deformation history of approximately, 0.01 and 14s^{-1}, respectively. In Figure 4.12, a strain of 0.01 corresponds to a stress of less than 130 MPa. However, the reported strength properties appear to be incomplete in that the strain rate range does not cover that expected in the shock tests. Furthermore, the strength curves appear to be expressed in terms of the engineering strain, as opposed to the true strain, and the elastic compliance has not been removed. While these factors cannot be fully accounted for without further experimental details, a dynamic flow stress of 135 MPa at a plastic strain of 0.01 appears to be reasonable. The density of the plate material is given by Stoffel as 2669 kg/m^3.

Stoffel does not report the numerical value of the final deflection. However, the experimental deflection history provides $\tilde{w}_{II}$ and T_{II} estimates of 31.8 mm and 1155 μs respectively and are indicated in Figure 4.11. The final plastic central deflection is considered to be the residual deflection after the elastic oscillations have damped, while the plastic deflection duration is considered to coincide with the point of maximum deflection.

Figure 4.11 shows that the free plate and IDL curves initially fall marginally below the experimental results, which is due to fact that $P_{\text{eff}} < P$. The Parabolic and Bessel function solutions have Phase I durations of 588 μs and 657 μs respectively. These T_I values correspond to the inflection point of the curves, where they begin to diverge from the free plate curve. It is noticeable that the inflection point occurs considerably earlier in the IDL curves than in the experimental curve, which suggests that the IDL model overestimates the hinge velocity and, hence, under predicts the Phase I duration. Furthermore, Figure 4.11 indicates that both the IDL solutions over predicted the final deflection and Phase II duration. The $\tilde{w}_{II}$ and T_{II} predictions for the parabolic displacement profile are 32.5 mm and 1382 μs respectively, which represent errors of 2.2 % and 19.7 %. The corresponding predictions for the Bessel function displacement profile are 36 mm and 1428 μs with errors of 13.2 % and 23.6 %.

These results are regarded to be acceptable, considering the relative simplicity of the model in comparison to the complexity of the shock loading and plate response behaviour. However, there is a subtle difference

between these results and the previous comparison of the general dynamic loading predictions with numerical results, where the displacement duration predictions showed better correlations than the deflection predictions. The reason for this is unclear, but it is noted that the plates used by Stoffel had a diameter to thickness ratio (553:2) that is more than double that used in the numerical model (100:1.6), which was based on the experimental configuration of Nurick & co-workers [60, 68–70]. Furthermore, it is interesting to note that the Taylor duration, as given in Equation (2.34), for the test parameters given above is 1038 μs, which is close to the inflection point on experimental curve in Figure 4.11. Resolution of these issues is beyond the scope of this thesis and is a subject of future research.

Chapter 5

Experimental Method using the Instrumented Pendulum

"If your experiment needs statistics, you ought to have done a better experiment."

Ernest Rutherford (1871-1937)

5.1 Introduction

The last three decades have witnessed an exponential growth in the sophistication of commercial simulation codes and the processing power of work stations, which has lead to the application of these tools to a broad spectrum of engineering practice. These tools allow problems to be analyzed at a level of detail that surpasses the level of experimental detail generally available in the literature, and this has lead to a growing recognition of the need for reliable and detailed experimental data for the purpose of code validation. Such experiments have been termed precision tests, the definition and characteristics of which are discussed in Chapter 1.

The purpose of this chapter is to present a novel experimental apparatus, developed specifically to produce data for the validation of numerical codes intended to study of the deformation and fracture of blast loaded plates. The experimental configuration is described along with the techniques for capturing and processing the experimental data. Furthermore, experimental and numerical results relating to the characterization of the loading technique are presented and analyzed to evaluate the performance of the blast testing configuration.

5.2 The Instrumented Ballistic Pendulum

The basic platform for all experiments reported in this thesis is an instrumented ballistic pendulum. In this section a short motivation for the development of the instrumented pendulum is given followed by a description of the apparatus and the associated data capturing and processing techniques.

5.2.1 Conventional Ballistic Pendulum Techniques

The essential concept of the ballistic pendulum is over 300 years old [3] and it has been used extensively to study blast and impact events, as discussed in Sections 2.1.1 and B.3. The ballistic pendulum technique is simple, robust, reliable and repeatable and thus ideal for the harsh environment of experimental blast loading.

According to Nurick & Martin [6], the first blast loaded ballistic pendulum experiments were intended to generate experimental results to confirm the predictions of analytical studies of the behaviour of impulsively loaded plates. In this application, it was deemed sufficient to measure the total blast impulse and the final deflection of plate, as discussed in Section 2.2.1. However, this approach relies on four crucial independent assumptions. Firstly, it is assumed that the load application is effectively instantaneous over the loading region. Secondly, the load duration is assumed to be small compared to the deformation duration of the structural specimen, *i.e.* it closely approximates an ideal impulsive loading (IIL) condition. Thirdly, all the impulse is assumed to be transmitted to the pendulum through the test specimen. In other words, no other part of the pendulum, such as the specimen clamps, are considered to be loaded directly by the blast. Finally, it is assumed that the specimen deformation duration is small compared to the natural period of the pendulum, so that an initial velocity condition can be assumed for the pendulum motion analysis.

Of the four assumptions listed above, typically only the first and fourth are explicitly motivated in the literature. Florence [36] argued that the first assumption is reasonable because the detonation velocity of an explosive charge is greater than the speed of sound in a plate specimen. In other words, the requirement of an instantaneous load application is sufficiently met because any arbitrary point on the plate experiences the blast pressure prior to the arrival of any disturbance propagating through the plate itself. The last assumption is closely approximated by using a ballistic pendulum with an appropriately large mass and radius of gyration. The theory required for this is well known and summarized in Appendix C.

Unlike the first and fourth assumption, motivations for the second and third assumptions are less common in the literature. For example, with regard to the second assumption, some researchers appear to simply take for granted that a short stand-off explosive charge will produce a load that is essentially ideally impulsive [36, 56]. However, as alluded to in Section 3.2.3, the use of attenuators to prevent spalling indicates that the load intensity is reduced, which implies that the load duration has been extended. Furthermore, the first and second assumptions are not always clearly distinguished, leading to a load duration estimate based on the so-called 'burn time' of the explosive charge, *i.e.* the time required for the detonation front to reach the furthest extremity of the charge [70]. This approach does not consider the finite time required for the high pressure gas, produced by the detonation, to dissipate, *i.e.* expand into

the surrounding volume. In other words, the 'burn time' effectively sets a lower limit for the load duration, which could be significantly longer. Consequently, estimating the mean blast pressure by dividing the impulse intensity by the 'burn time' leads to an overestimate of the mean peak blast load pressure. It is shown in Section 4.3 that, for a given impulse, a finite load duration, even when a small fraction of the deformation duration, can affect the final displacement. The implication is that the blast load history, or at least the blast duration, should be measured.

The third assumption does not appear to be addressed directly in the literature for uniformly loaded plates. However, the case of localized loading has been considered by, Bonorchis & Nurick [158], who conducted a series of blast test on rigid and deformable targets of varying exposed areas using clamping fixtures of different heights that provide various degrees of blast confinement. To assess the impulse applied to the exposed area of the specimen plate without the influence of clamp fixtures, a rigid[1] target of the same dimensions as the exposed specimen area was constructed. The supports connecting the rigid target to the pendulum were mounted so as to be shrouded from the blast by the rigid target. In other words, no significant component of the blast could act directly on the pendulum. The effect of clamping fixtures could then be discerned by comparing the impulse measured in this way to that obtained from rigid targets with clamping fixtures.

With regard to the third assumption, the results of Bonorchis & Nurick indicate that the area of the clamps can affect the measured impulse. Having passed over the specimen plate, the blast wave can move over the clamping fixtures, thereby contributing to the overall impulse measurement. Bonorchis & Nurick report that this effect is not large, but nevertheless detectable. Deformable targets were also tested with identical clamping configurations. The results showed strong correlation with the rigid target data, implying that measured impulse was not affected by specimen plate deformation. This result indicates that adequate shrouding of the exposed specimen area may be required.

Bonorchis & Nurick also report a second clamp fixture effect. Using numerical simulations, it was shown that the shock front, after traversing the plate, reflects off the clamps causing a significant pressure increase at the clamping boundary. This effect was confirmed experimentally by conducting a series of nominally identical blast tests with increasing clamp heights. An interesting aspect of this is that the peripheral high pressure was significantly delayed relative to the main loading event. In fact, the simulations suggested that it only acted once the plate had ceased deforming. In other words, a portion of the impulse acts on the plate after it has reached its maximum deflection and hence the total impulse should not be used for experimental correlation. The simulations also showed that the pressure decays exponentially with all the deformation inducing impulse transferred within $30\,\mu$s. In other words, the blast duration is a significant proportion of the plate deformation duration, which is typically in the order of $100\,\mu$s, indicating that the ideal impulsive assumption may not be appropriate.

The rigid target approach of Bonorchis & Nurick is analogous to the uniformly loaded free plate tests conducted by Florence & Wierzbicki [36, 37], as reviewed in Section 3.2.2. In both instances the effect of the clamping fixture was experimentally eliminated. However, Bodner & Symonds [56], using the explosive configuration but including clamps, achieved identical impulse results. This appears to imply that uniform loading is not as susceptible to clamping effects as localized loading. Nevertheless, from the above, it is clear that an accurate assessment of the load distribution and duration is important.

[1] In this context the term 'rigid' implies a target that is not expected to deform plastically to a significant degree.

While the preceding discussion has focused on the load history, the plate response history is equally important and is also not captured in standard ballistic pendulum testing. Instrumented versions of the ballistic pendulum have been developed that allow for the deflection history of the plate to be recorded [56, 61, 86], as discussed in Section 2.2.3. However, there remain some experimental parameters that would be useful in code validation that have not been successfully captured.

One phenomenon that has proven difficult to investigate experimentally is fracture at the boundaries of blast loaded plates [67, 68, 70]. Although the energy dissipated through fracture has been estimated [67], the timing of boundary fracture events and the magnitude of the associated forces have not been recorded during conventional ballistic pendulum tests. The reason for this is that the contribution that shearing makes to the overall deflection of the plate is small and difficult to discern [68]. Furthermore, any attempt to measure the shear forces at a clamped (or built-in) boundary is obscured by the inertia of the clamps and/or the dynamic interaction between the load transducers and their support structures.

The experimental focus of this thesis is an instrumented ballistic pendulum apparatus and associated specimen configuration that has been developed specifically to address the above mentioned issues. The primary aim has been to develop a technique to measure boundary reaction force histories during a blast loading event. To the authors knowledge, data of this nature has not been published prior the work associated with this thesis [51–53, 90]. This primary aim implies the need for well defined boundary conditions and the use of a sensor that is robust, has a rapid response, a sufficient recording duration and does not influence the specimen/boundary interaction. A Secondary aim has been to develop a technique to measure the blast load history and assess the blast load distribution in space and time. The configuration of the instrumented pendulum and specimen plate will be described and motivated in the next section.

5.2.2 Peripherally Clamped Centrally Supported Circular Plates

The principal blast loading configuration used in this thesis is the peripherally clamped centrally supported (PCCS) circular plate. As the designation suggests, this configuration consists of a thin specimen plate clamped between two thick plates with circular cutouts, while also being centrally supported by a cylindrical bar. In other words, the PCCS configuration is essentially the same as that used for clamped circular plates, as discussed in Section 2.2, except for the additional central support. Two variations of the PCCS configuration are shown schematically in Figure 5.1(a) and (b).

The primary purpose of traditional ballistic pendulum tests is to generate data to evaluate theoretical models of the impulsive behaviour of plate structures [56]. Hence, the traditional experimental plate configurations are, essentially, scale models of plate structures found in engineering practice, so as to be representative of the intended application. By contrast, the PCCS configuration is not intended to be representative of any practical structure. Rather, it is specifically intended to provide precision data in a convenient form for the purpose of model validation. In particular, this configuration has been designed to capture the shear force history at a plate support so as to provide insight into the timing and magnitude of boundary failure events.

Three specific features make the PCCS configuration well suited to the study of boundary failure during blast loading events. Firstly, introducing a central support creates an additional boundary where failure

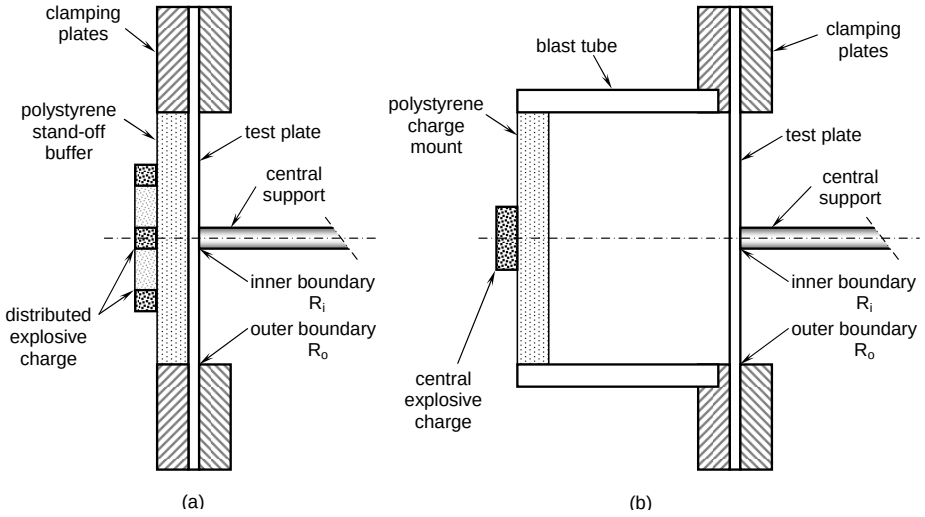

Figure 5.1: The peripherally clamped centrally supported (PCCS) plate configuration with a short stand-off distributed charge (a) and a large stand-off central charge using a blast tube (b).

will occur preferentially. A theoretical model explaining this preferential behaviour will be presented in Chapter 7. Secondly, the central support can take the form of a Hopkinson pressure bar (HPB). In other words, the central support also acts as a high speed load transducer, allowing the reaction force history between the plate specimen and the central support to be deduced from the stress waves captured in the central support during a blast test. Finally, the PCCS configuration is axisymmetric which simplifies the theoretical treatment.

The use of a Hopkinson bar as a central support allows the problems associated with clamp inertia and dynamic sensor/structure interaction to be circumvented. Typical clamp fixture geometries are large and relatively complex, leading to multiple stress wave reflections that would obscure any attempt to measure the reaction forces. By contrast, the use of a Hopkinson bar, provided it is long enough, allows the entire reaction force history to be captured prior to the arrival of any stress wave reflections. Details of the analysis and interpretation of the central support signals will be discussed in Sections 5.2.6 and 5.3 and in Chapters 6 and 8.

The two primary variations of the PCCS configuration shown schematically in Figures 5.1(a) and (b) correspond to two distinct blast loading regimes, namely short stand-off and large stand-off, respectively. Both charge configurations are intended to deliver near uniform blast loads, the former by means of a distributed charge and the latter by means of a blast tube. These charge configurations were used in two distinct series of tests conducted as part of this thesis, both of which have been published in part [51–53]. In both configurations the explosive charge is positioned by means of a polystyrene disk and the entire assembly is mounted on a ballistic pendulum as shown in Figures 5.2 and 5.3. The two charge configurations are discussed in detail in Sections 5.2.5.1 and 5.2.5.2.

In Chapter 6, blast test results are reported for mild steel plates with nominal thicknesses of 1.6 mm, 2 mm and 3 mm. The material properties for these specimens are reported in Appendix B. The majority of the plate specimens had a clamped boundary of 100 mm diameter, while a small number of the 1.6 mm thick plates had a clamped boundary of 130 mm and 160 mm diameter. The inner boundary of the plates

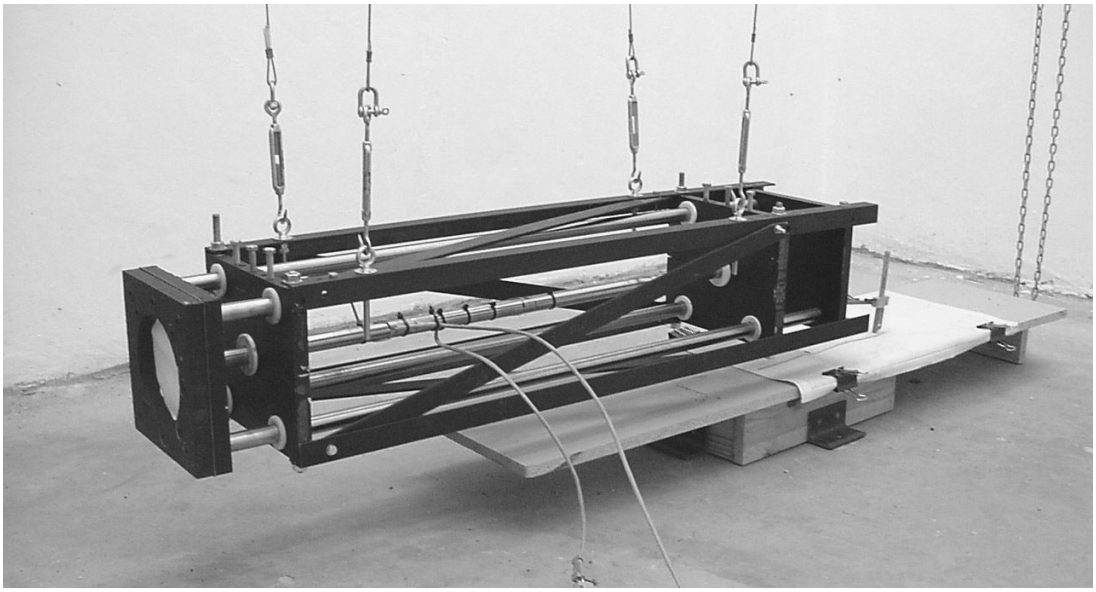

Figure 5.2: The short Stand-off PCCS plate configuration mounted on the instrumented ballistic pendulum in a blast chamber.

was 22 mm for the short stand-off plates and 20 mm for the blast tube configuration. Bars with square and 2 mm radius front face edge conditions were used in the blast tube test series, while only square edges were used for the short stand-off tests.

5.2.3 Peripherally Clamped Annular Plates

A secondary blast test configuration used in this thesis is the peripherally clamped annular (PCA) plate. The PCA plates were machined from the same metal sheets as the PCCS plates and were almost identical to the PCCS plates, the only difference being a central hole with a diameter slightly larger the central bar[2]. Hence, when mounted in the same clamps as the PCCS plates, the PCA plate deformation is such that the central hole never makes contact with the central bar during a test.

The PCA plate tests were conducted for two reasons. Firstly, blast loaded PCA plate deflection data is useful for comparison with PCCS data, especially at large impulses. While the PCCS configuration is intended to study failure at the central support, the PCA configuration avoids all interaction with the central bar, but is otherwise identical. Hence, under similar loading conditions, the difference between the PCCS and PCA plate responses can only be due to the central support boundary condition. This provides an opportunity to experimentally isolate the failure behaviour at the central support. In particular, under intense blast loads the PCCS configuration is expected to exhibit early failure at the central support and, thereafter, to deform as an annular plate. In effect, the PCA plate configuration represents the limit response of PCCS plate with negligible through thickness shear strength.

The second motivation for the PCA plate tests is the measurement of blast loads. The presence of the central hole allows the central bar to record the blast load without being affected by the plate response.

[2]The term 'central bar', as opposed to 'central support', will be used in the context of the annular plate tests since the annular plate was not in contact with, and hence not supported by, the central bar.

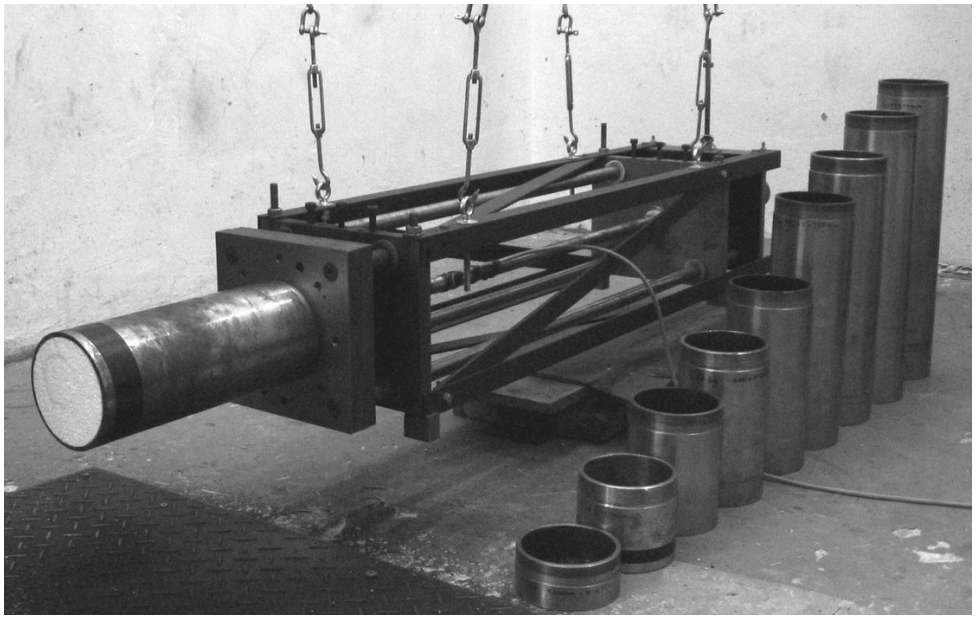

Figure 5.3: The large Stand-off PCCS plate configuration mounted on the instrumented ballistic pendulum in a blast chamber, along with blast tubes of a various lengths.

In other words, PCA plate tests results can be used to characterize the blast load, as will be discussed in Section 5.3. Furthermore, as with the deflection data, comparing the central blast pressure history from a PCA plate test to the central support stress history from a PCCS plate, subjected to nominally the same load, allows the failure response to be discerned.

The initial central hole size for the short stand-off tests was 24 mm, *i.e.* there was an initial gap of 1 mm between the plate and the central Hopkinson bar. For the subsequent large stand-off blast tube tests, the specimen and Hopkinson bar alignment procedures were improved such that the initial central hole size could be reduced to 21 mm, *i.e.* there was an initial gap of 0.5 mm between the plate and the central Hopkinson bar.

5.2.4 The Central Hopkinson Bar

The distinguishing feature of the ballistic pendulum configuration used in this thesis is the central Hopkinson bar. As mentioned previously, the primary function of the bar is that of an instrumented central support in the PCCS plate configuration, with a secondary function as a blast pressure transducer during PCA plate tests. While the former application is novel, the latter is not. In fact, Hopkinson originally conceived the device that bears his name as a means of measuring the peak pressure obtained from gun cotton detonations [110]. It was over three decades after Hopkinson's work that Kolsky [58] introduced the split Hopkinson bar (SHB) configuration for material characterization, as discussed in Appendix B.

While the SHB is now more common than the Hopkinson pressure bar (HPB), there are a small number of papers that deal with its use as a high speed pressure transducer. Edwards *et al.* [113] describe the measurement of reflected blast pressures using a HPB that was instrumented with foil strain gauges and

give a short survey of similar work by Wenzel & Esparza [111] and Delderk [112]. More recently, in addition to the work published from this thesis [52], the HPB technique as been used by Piehler *et al.* [114], for air blasts, and Taylor *et al.* [115], for buried charges. It is noteworthy that in all six of the above mentioned studies the aim was to measure short stand-off blast histories, which require a robust sensor with a rapid response. In particular, the performance criteria sought by Edwards *et al.* were a temporal resolution of 1 μs with a reflected pressure of up to 1500 MPa, which is difficult to achieve with conventional pressure transducers.

The limiting factor of conventional high speed pressure transducers is their inherent natural frequencies and associated settling times. The rapid pressure rise associated with a blast load tends to excite these natural frequencies and the transient response of the sensor and its mounting is often noticeable on the pressure traces. This transient response is due to internal stress wave reflections prior to the sensor achieving quasi-static equilibrium with the applied load.

The essential difference between conventional pressure transducers and the HPB is that, while capturing a dynamic signal, the HPB is never intended to be in equilibrium. Rather, the HPB technique relies on the bar being long enough to ensure that stress wave reflections do not return before the entire duration of the load signal has been captured. In other words, unlike conventional pressure transducers, the transient response of a HPB, rather than being an impediment, is the means by which a signal is captured. For similar reasons the HPB signal will not be influenced by its mountings, provided that they are far enough removed or do not impede the HPB motion. Therefore, in principle, there is no frequency limit to the data that can be captured with a Hopkinson bar. However, practical limits are imposed by the associated electronic data capture equipment and theoretical difficulties in accounting for the phenomenon of wave dispersion. These aspects will be discussed in Section 5.2.6.

The length of a HPB effectively isolates the desired signal from other influences. This is similar to the principle used by Bodner & Symonds [56] when measuring the deflection history of blast loaded plates. As mentioned in Section 2.1.1, Bodner & Symonds isolate their capacitive deflection sensor by mounting it and the clamped plate specimens on separate cantilever arms, the ends of which were secured to a ballistic pendulum. Thus, to adversely affect the deflection sensor, the stress waves induced in the clamps have to travel the combined length of these cantilever arms, by which time the entire deformation history had already been captured. The same technique is employed in the ballistic pendulum shown in Figures 5.2 and 5.3, where the clamp plates are supported by steel bars that run the entire length of the ballistic pendulum. These bars, and the central HPB, slide freely in PTFE bushings and abut against a rubber pad at the rear of the pendulum. In this way the primary axial loads transmitted through the outer plate boundary are isolated from those transmitted to the HPB through the inner boundary.

The central Hopkinson bars used in this thesis were all made from silver steel (1%C, 0.3%Si, 0.4%Cr, 0.35%Mn), the front end of which was hardened. For the short stand-off test series, the bar was 1 m in length and 22 mm in diameter, while for blast tube test series the bars were 1.25 m in length and 20 mm in diameter. In both test series, strain gauges were placed at a distance of 250 mm from the front bar face, with the short stand-off tests having additional gauges in the middle of the bars. Details of the strain gauge instrumentation will be given in Section 5.2.6.

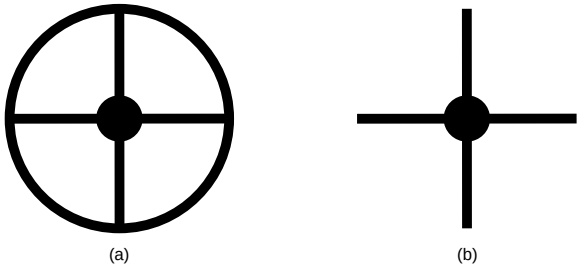

Figure 5.4: General layout of the short stand-off explosive charges with (a) and without (b) an outer ring charge.

5.2.5 Charge Configurations

In this thesis, the primary motivation for choosing high explosive (HE) blast loading is that more realistic impulse intensities and pressure histories can be achieved than is the case with shock tubes. However, for the purpose of precision experiments, applied loads must be well defined and repeatable in terms of magnitude and both spatial and temporal distribution. Furthermore, to render the experimental results amenable to analytical treatment, and more convenient for numerical simulations, it is preferable that the impulse intensity and temporal history are uniform. In this section, the explosive charge configurations used in this thesis are described, while the degree to which a uniform blast load was achieved is discussed in Section 5.3.

In particular, this section is a response to the strenuous debate described in the Trondheim workshop proceedings, as discussed in Section 1.1.3, regarding the advantages and disadvantages of both blast and shock tube experiments. Some delegates argued that shock tubes provide precision shock load control, while others noted that shock tubes cannot generate impulse intensities produced by high explosive (HE) charges. Furthermore, it was argued that HE charges may introduce inaccuracies, in that explosive loads are difficult to define and reproduce. It will be shown in this section that these concerns are addressed through careful design and validation.

5.2.5.1 Short Stand-Off Charge Configuration

The use of short stand-off charge configurations is well established in the blast loading literature [6, 11], as discussed in Sections 2.1.1 and 3.2.2. Initial experiments were conducted with a central charge, but the results were unsatisfactory in that significant deformation prior to shear failure at the inner boundary could not be induced. It was concluded that the central load was too localized. Therefore, all the short stand-off blast test results reported in this thesis were obtained using the ring charge technique of Nurick & co-workers [6, 61, 67]. The charge configuration is shown schematically in Figure 5.4.

The explosive used for all the results reported in thesis is PE4[3], which is equivalent to Composition C4. Following an established practice [52,158], in this thesis the properties of PE4 are assumed to be the same as those of Composition C4 [149,153]. The stand-off distance was achieved by mounting the explosive on a 30 mm thick polystyrene attenuator. Detonation was initiated through a detonator and leader charge of

[3]The designation 'PE4' stands for 'plastic explosive 4'.

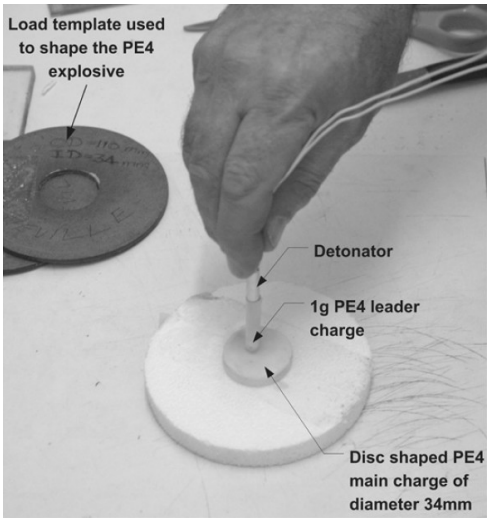

Figure 5.5: Layout of the blast tube explosive charge used by Jacob *et al.* [107], which is identical to that used in this thesis.

1 g placed in the centre of two cross-leaders attached to the outer ring charge. For the 100 mm diameter plates, the cross leaders had a mass of 1 g and the outer ring charge had a 60 mm diameter with a mass ranging between 2 and 7 g. For the 130 mm and 160 mm diameter plates, respectively, the cross leader masses were 1.25 g and 1.5 g, while the ring charge diameters were 75 mm and 90 mm.

5.2.5.2 Blast Tube

The use of a blast tube, *i.e.* an explosively driven shock tube, is well established in the blast loading literature [104–107], as discussed in Sections 2.1.2 and 2.2.4. In essence, a blast tube aims to combine the ability of HE charges to produce blast loads with large impulse intensities and short durations with the tendency of a shock tube to produce uniform loads. When mounted on a ballistic pendulum a blast tube provides an additional benefit in that it prevents any other portion of the pendulum from being loaded. Furthermore, unlike a closed shock tube, the open end ensured that no subsequent pressure pulses large enough to deform the plate can form and hence the specimens can be recovered after a single loading event.

The blast tube configuration used in this thesis is very similar to that of Jacob *et al.* [107] and is shown in Figures 5.1(b) and 5.3. The tubes have an inner diameter of 100 mm and range in length from 50mm to 500 mm in 50 mm increments. The PE4 charge layout comprises a 35 mm main charge that is initiated through a 1 g leader charge as shown in Figure 5.5. The charge is mounted on a polystyrene disk and placed at the open end of the blast tube.

5.2.6 Data Processing and Analysis

The instrumented ballistic pendulum facilitates the measurement of three distinct types of experimental data, namely the total impulse, the recovered plate shape and the central Hopkinson bar stress history.

The former two data types are those of the traditional ballistic pendulum and will be briefly discussed, while the latter is unique to the instrumented ballistic pendulum and will be discussed in detail.

The total impulse imparted to the plate was obtained from the recorded motion of the pendulum. The ballistic pendulum is a simple, reliable and repeatable instrument, the mechanics of which have been well documented for close on 300 years and will, therefore, not be discussed in detail. However, for completeness the motion analysis is summarized in appendix C.

All residual deflection data were obtained *a posteriori*, by physically measuring the deformed plates. The recovered plates were reclamped and the clamped assembly was placed on a flat table where the deformed shape was measured using a height gauge.

The stress wave induced in the central Hopkinson bar by the plate response and/or blast pressure were recorded via pairs of strain gauges, diametrically mounted in a half bridge configuration, using a 1 MHz bandwidth amplifier and data logging card sampling at 10MHz with 12-bit resolution. For the short stand-off configuration, the gauges were initially bonded in the middle of the central Hopkinson bar, *i.e.* 500 mm from the front end. However, this lead to a capture duration of only 200 μs. Therefore, a subsequent gauge pair were bonded at 250 mm, a practice that was continued in the blast tube configuration. The Hopkinson bars used in the instrumented pendulum were calibrated dynamically using standard techniques [166]. The reaction force history of the central support is obtained by multiplying the stress signal by the cross-sectional area of the support bar. Integrating the resulting reaction force history provides a measure of the impulse transferred through the central support.

In the remainder of these sections, the signal processing applied to the captured signals will be described. In particular, the phenomenon of dispersion and the correction techniques applied to some of the signals are discussed in Sections 5.2.6.1 and 5.2.6.2. Furthermore, the smoothing algorithm used to remove the spurious oscillations, *i.e.* those not arising as a result of dispersion, is presented in Section 5.2.6.3. Finally, the procedure used to synchronize a blast wave history relative to the moment of initiation of the detonation of the explosive charge is described in Section 5.2.6.4.

5.2.6.1 Dispersion Correction

The requirement of a practically sized inner boundary for the PCCS plates necessitated the use of relatively large Hopkinson bar diameters. This, coupled with the high frequency content of typical blast waves, lead to noticeable dispersion in some of the Hopkinson bar signals, especially in the short stand-off configuration. The dispersive behaviour of elastic cylindrical bars has been studied for many years [167–174]. Therefore, the mathematical details of the phenomenon will not be discussed in depth and the reader is referred to the work of Marais *et al.* [166] and Govender *et al.* [175] for details concerning the specific technique used in this thesis.

Dispersion is a phenomenon whereby a stress wave travelling along a Hopkinson bar changes shape due to the various frequency components that make up the stress wave travel at different velocities. Pochammer [167] and Chree [168], in the late 19^{th} century, were the first to analyse the vibration modes of infinite bars and, therefore, the oscillations that appear in dispersed signals are referred to as Pochammer-Chree oscillations. Despite this early work, more than half a century would pass before the Pochammer-Chree solution would be used by Bancroft [169] to calculate the velocities of elastic

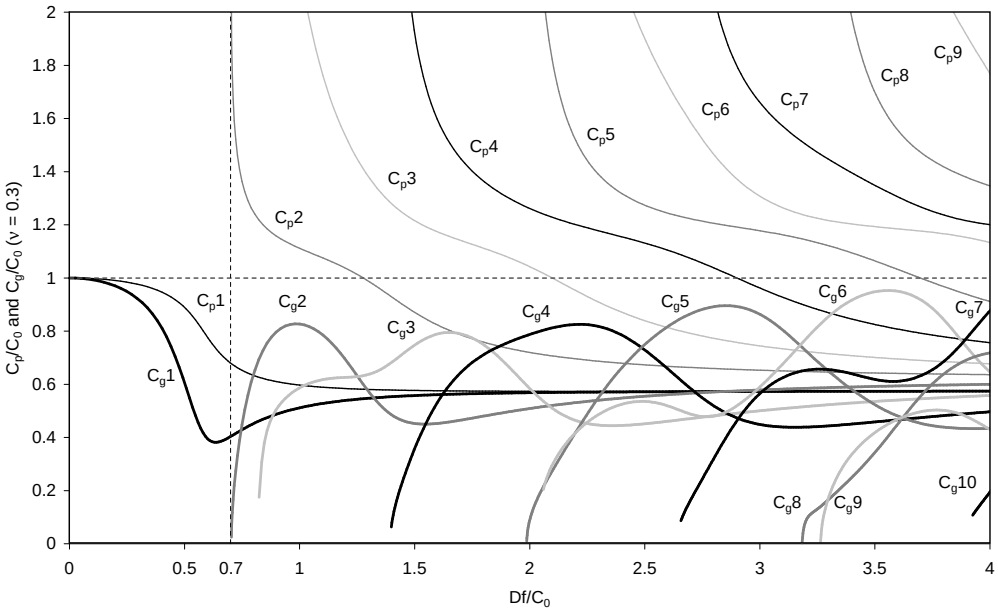

Figure 5.6: The non-dimensional phase and group velocities of the Pochammer-Chree modes with respect to the non-dimensional frequency, for an infinitely long round bar with a Poisson's ratio of 0.3.

waves, and by Davies [170] to study the propagation of elastic waves in a Hopkinson bar. Part of the delay was presumably due to the tedious calculations required to evaluate the solution. This impediment was removed by the availability of digital computers in the late 20^{th} century and lead to a renewed interest in stress wave propagation.

While the mathematical details will be omitted, an understanding of the meaning of the Pochammer-Chree solution is required when evaluating the performance of the central Hopkinson bar in the instrumented pendulum. It is well known that standing waves, *e.g.* the Pochammer-Chree vibration solutions, can be represented as the superposition of identical travelling waves of constant amplitude but propagating in opposite directions [14]. The speed of propagation of these travelling waves is referred to as their phase velocity c_p which, for a given vibration frequency, is equal to the quotient of the spatial wavelength and period of the vibration. It is convenient to plot the Pochammer-Chree solutions in a non-dimensional form using the expressions,

$$\frac{c_p}{c_0} \quad \text{and} \quad \frac{Df}{c_0} \tag{5.1}$$

which are referred to as the dimensionless phase velocity and dimensionless frequency respectively, and where D is the bar diameter, f is the component frequency and c_0 is the fundamental wave velocity, *i.e.* the limit velocity of a very low frequency wave or, alternatively, the wave speed of a very thin bar. The dimensionless phase velocity curves, up to a dimensionless frequency of 4, for a bar with a Poisson's ratio of 0.3 are shown in Figure 5.6.

Each phase velocity curve represents a distinct mode of vibration, each of which are characterized by the number of inflection points in the mode shape of a bar cross-section. Mode I has one inflection, two for

Mode II, and so forth[4]. Note that the 2^{nd} mode phase velocity curve has an asymptote at a dimensionless frequency of approximately 0.7. This is significant because it implies that only the fundamental mode can exist below that frequency. In the case of a 20 mm diameter steel bar this translates to a frequency of 175 kHz. A limit of 100 kHz is typically sufficient to resolve the stress waves generated during split Hopkinson bar material tests and, hence, it is standard practice in to use only the 1^{st} mode for dispersion correction [171, 172].

Dispersion correction seeks to 'undo' the effect of dispersion by processing the wave components individually. This is accomplished by breaking the recorded signal down into its components using a fast Fourier transform (FFT), and then shifted them in time according to the quotient of the distance travelled and their individual phase velocities[5]. The dispersion corrected signal is obtained by applying an inverse FFT to the shifted components. This approach has proved to be very successful with the 1^{st} Pochameer-Chree mode [166, 171, 172].

To fully resolve the peak pressure detail of a short duration reflected shock wave, frequencies up to 1 MHz, or more, may be required. Some researchers have attempted to improve their signal resolution by using thinner bars. Delderk [112] used a 13 mm bar, giving a cut-off frequency of 270 kHz, while Edwards *et al.* [113] used 6 mm and 3 mm bars giving cut-off frequencies of approximately 500 kHz and 1 MHz respectively An alternative approach was followed by Lee *et al.* [174], who used a 12.7 mm bar and employed a multi-mode dispersion correction approach. Lee *et al.* used a Gaussian window filter to investigate the time of arrival of various frequency components. They found that the time of arrival corresponded closely with the time predicted when using the highest group velocity c_g of the Pochammer-Chree modes for a given frequency. Davies [170] was the first to point out the importance of the group velocity by noting that it is the rate at which energy is transmitted down the bar. In other words, even though the phase velocity is used for dispersion correction, the group velocity represent the speed with which physical wave packets of a given frequency will travel down a bar. An example of this is given in Section 5.2.6.2. Achenbach [176] gives the formula for obtaining the group velocity from the phase velocity curves as,

$$\frac{1}{c_g} = \frac{1}{c_p} - \frac{f}{c_p^2}\frac{dc_p}{df} \tag{5.2}$$

The group velocities for the various Pochammer-Chree modes are shown in Figure 5.6.

Lee *et al.* proposed that when correcting a given frequency component, the phase velocity used should correspond to the mode with the highest group velocity. In essence, Lee *et al.* assumed that all the energy associated with a particular frequency component will propagate according to a single mode. This approach has been implemented with some success by Cloete *et al.* [51], although it was noticeable that a significant portion of the high frequency content was not correctly shifted. More recent work by Govender *et al.* [175] suggests that the single mode assumption of Lee *et al.* may not be correct in that, while the mode with the highest group velocity has a dominant effect, a non-negligible portion of the energy may be carried by other modes.

To the author's knowledge, the approach of Lee *et al.* is the only multi-mode dispersion correction technique in the open literature. Therefore, it is tentatively applied to some of the signal discussed in

[4]These modes are not to be confused with the failure Modes of PCCS plates.
[5]Computationally, the shifting is executed as a phase shift in the frequency domain.

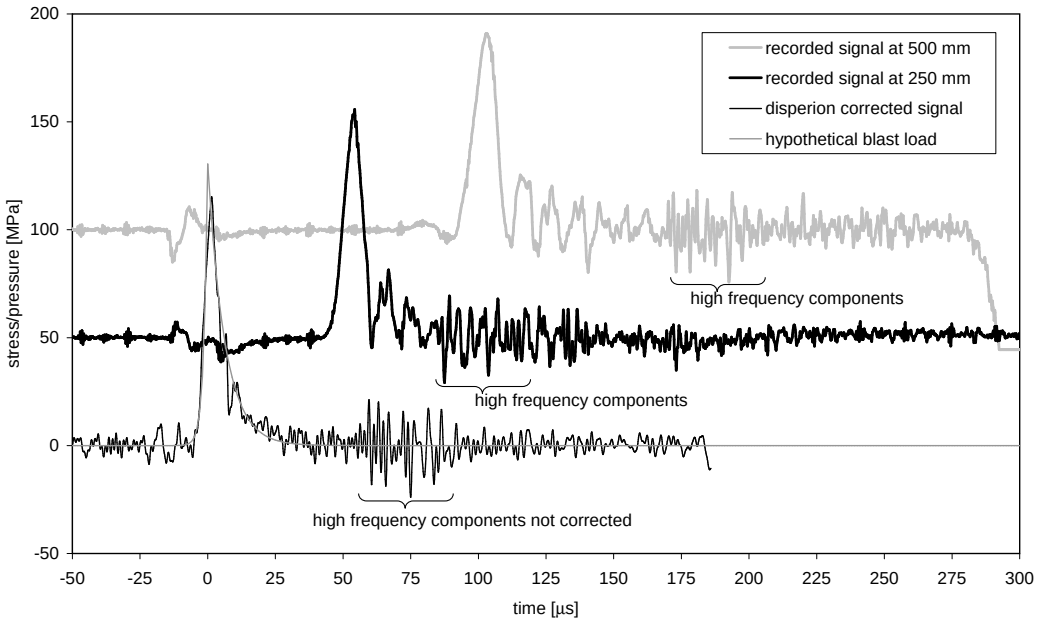

Figure 5.7: Recorded and dispersion corrected signals for a short stand-off PCA plate test using the charge configuration depicted in Figure 5.4b. The signals have been offset by 50 MPa or clarity.

this thesis, the results of which are discussed in the next section. However, the topic of higher mode dispersion correction is yet to be conclusively resolved and is an ongoing area of research, but further development is deemed to be beyond the scope of this thesis.

5.2.6.2 Dispersion Effects

Typical central Hopkinson bar signals, captured during a short stand-off PCA plate test using the charge configuration depicted in Figure 5.4b, is shown in Figure 5.7. Both the recorded signals feature a large initial pulse followed by relatively low frequency oscillations and a distinct portion of high frequency oscillations. The high frequency oscillations clearly do not represent noise since they do not occur simultaneously in the recorded signals, unlike the noise that is apparent in the early portion of the signals. Furthermore, the high frequency oscillations can be seen to be receding from the head of the wave as the it travels further down the bar, *i.e.* they are subject to dispersion. Also shown in Figure 5.7 is the dispersion corrected signal for the front face of the bar according to the multi-mode technique of Lee *et al.* [174]. Note that the low frequency oscillations, that immediately followed the head of the pulse in the recorded signals, are almost completely accounted for, and the characteristic exponential decay of a blast wave is evident. However, it is apparent that the high frequency oscillations have not been shifted correctly.

The significant high frequency components are assumed to be a result of a sharp pressure peak that is expected to be at the head of a blast wave. Hence, the consequence of incomplete dispersion correction is an inability to resolve the head of the wave. To test this conjecture, a hypothetical blast wave was generated such that it has the same rise and decay features of the dispersion corrected signal but with a sharp peak. This hypothetical signal is shown superimposed upon the dispersion corrected signal in

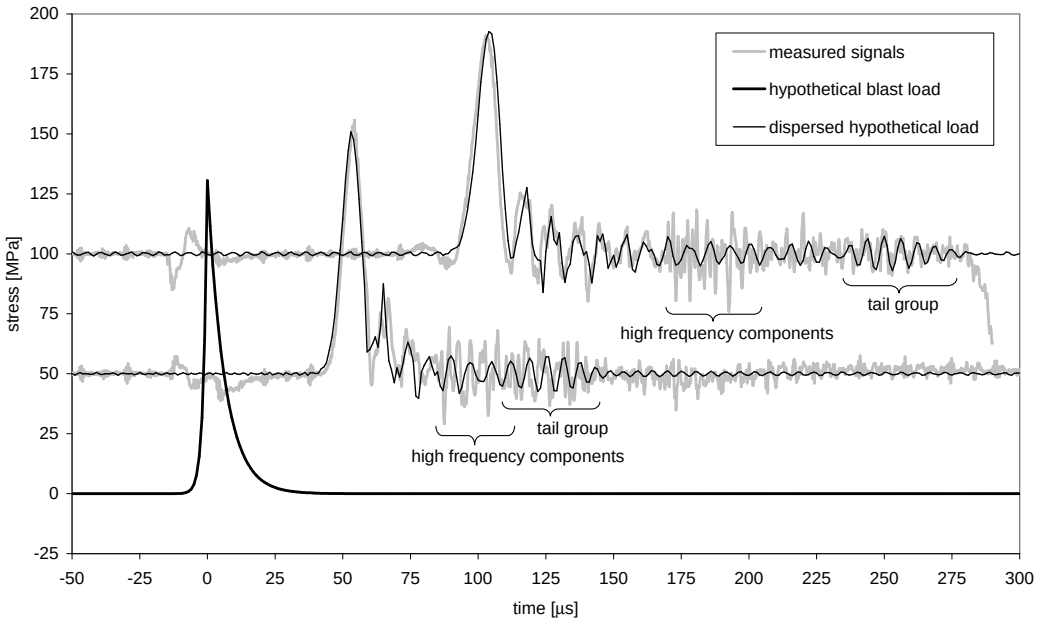

Figure 5.8: Recorded and dispersed hypothetical signals for a short stand-off PCA plate test using the charge configuration depicted in Figure 5.4b. The signals have been offset by 50 MPa or clarity.

Figure 5.7. The hypothetical signal was then dispersed according to the method of the Lee *et al.* using frequency components up to 1 MHz, the results of which are shown in Figure 5.8 superimposed upon the recorded signals. It is evident that all the major features of the recorded signals are predicted, except for the high frequency oscillations.

Consider, for example, the 'tail group' wave packet that is evident in both the recorded signals. By inspection, this wave packet is approximately 50 μs in duration and contains seven oscillations, *i.e.* its carrier frequency is approximately 140 kHz. For a 22 mm bar this equates to a dimensionless frequency of 0.61, which is shown in Figure 5.6 to corresponds to a local minimum of 0.4 in the group velocity of the 1^{st} Pochammer-Chree mode. This implies that, given a typical fundamental wave speed for steel of 5000 m/s, the 'tail group' will propagate at only 2000 m/s. Therefore, after propagating for 250 mm and 500 mm, the 'tail group' should trail the head of the wave by approximately 75 μs and 150 μs respectively, which is in agreement with the recorded signals. While this cannot be considered as proof, it nevertheless shows the general coherence of the dispersion correction methodology.

The effect of the incomplete dispersion correction is to reduce the frequency component available to resolve the peak pressure. This is demonstrated in Figure 5.9 where the dispersion corrected and hypothetical signals are compared to two Fourier approximations limited to frequency components up to 1 MHz and 180 kHz respectively. Note that the 1 MHz Fourier approximation successfully resolves the hypothetical signal, while the 180 kHz approximation corresponds closely to the dispersion corrected signal. In other words, the dispersion correction algorithm effectively acts as a low-pass filter. A frequency of 180 kHz corresponds to a dimensionless frequency of 0.79, *i.e.* the method of Lee *et al.* appears to correctly deal with the 1^{st} and 2^{nd} Pochammer-Chree modes, but not the higher modes.

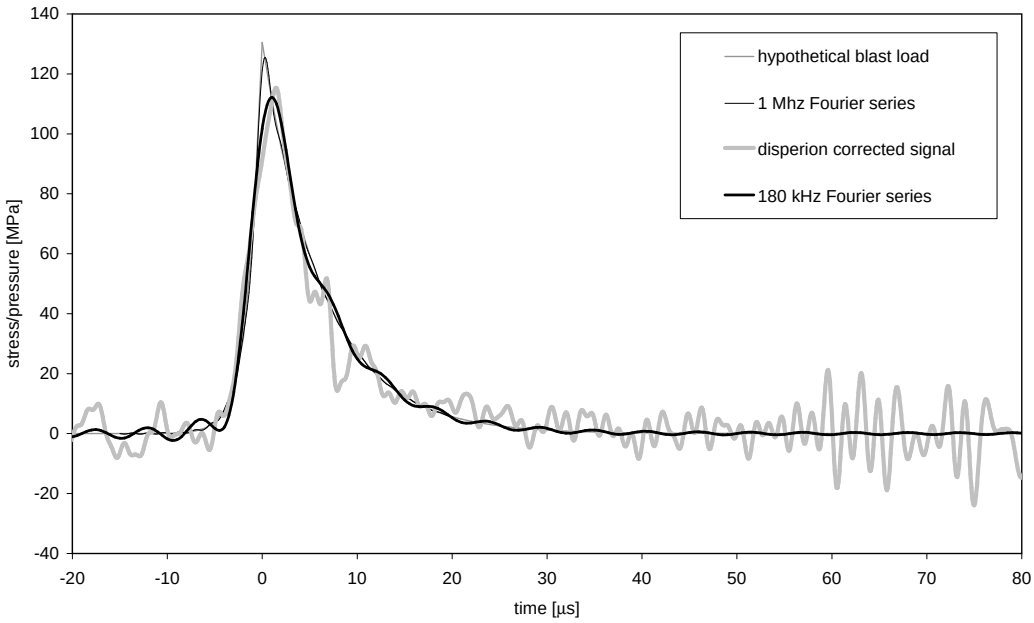

Figure 5.9: Comparison of the dispersion corrected and hypothetical signals with two Fourier approximations of the hypothetical signal for a short stand-off PCA plate test using the charge configuration depicted in Figure 5.4b.

The signals generated using the blast tube were of a longer duration and significantly less affected by dispersion, as shown in Figure 5.10, where a recorded signal is compared to a dispersed hypothetical signal with the original hypothetical signal superimposed for comparison. In fact, applying dispersion correction did not appreciably alter the shape or reduce the oscillations in the signal. Therefore, for tests conducted with the blast tube, the recorded signals were not dispersion corrected, but merely shifted in time according to the fundamental wave velocity.

5.2.6.3 Signal Smoothing

In general, the signals captured in the central Hopkinson bar contained dispersed high frequency oscillations that could not be corrected with currently available methods. These oscillations are clearly an artifact of the measurement technique and do not represent any physical behaviour of the plate specimens or blast waves. Therefore, the oscillations need to be removed through a filtering or smoothing algorithm so that the signals can be compared and interpreted.

Traditional filtering and moving average smoothing proved to be inappropriate. The degree of filtering or averaging required to smooth high frequency oscillations (periods of less than 4 μs) also tended to reduce the magnitude of the longer duration stress spikes (durations greater than 10 μs). This is problematic because the existence of long duration yet sharp signal spikes are expected since the primary loading is due to the blast waves, which have a characteristic sharp wave form featuring a pressure rise followed by an exponential decay. The effect of blunting these is therefore unacceptable. Furthermore, it was found that averaging tended to reduce the temporal integral of the signal. This too is unacceptable because the integral is proportional to the momentum carried in the stress wave which should not be affected by dispersion, though noise spikes may have a small effect. Figure 5.11 shows the effect of a simple moving

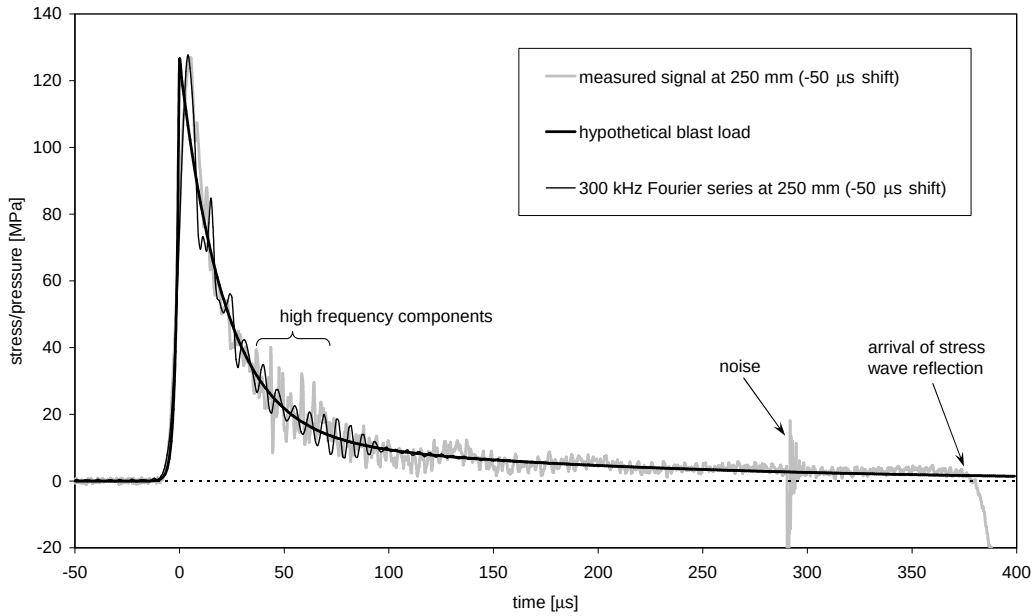

Figure 5.10: Comparison of measured signal with an original and dispersed hypothetical signals for a blast tube PCA plate test using a 16 g charge.

average smoothing algorithm on the signals from a blast tube test on a 2 mm thick PCCS plate using a 10 g charge. The signal was sampled at 10 MHz and averaged over 81 samples, *i.e.* a 8 μs averaging window.

To address the aforementioned issues, a weighted smoothing algorithm was developed that is able to effectively eliminate the high frequency oscillations, while maintaining the sharp character of the long duration signal spikes and preserve the integral. The algorithm follows a three-step procedure. In the first step, the signal is smoothed by means of a moving least-squares fit over an 8 μs sampling window. This step suppresses high-frequency oscillations in the order of 125 kHz and above, but also blunts the long duration signal spikes, as shown in Figure 5.11. The moving least-squares fit also provides a smoothed 1^{st} derivative of the signal. The second step involves evaluating the 2^{nd} derivative of the smoothed signal, which is then normalized and rectified, as shown in Figure 5.11. The significance of the magnitude of the 2^{nd} derivative is that it is indicative of the rate of change of the slope of the original signal. In other words, features such as the sudden rise, signal peak and sudden drop off, which are of great relevance to this study, are all associated with a rapid changes in the signal gradient, *i.e.* large absolute values of the 2^{nd} derivative. With this in mind, the third step in the algorithm involves evaluating a weighted sum of the original and smoothed signals, using the normalized absolute value of the 2^{nd} derivative as the weighting factor. In other words, the amount of effective smoothing applied to a fluctuating portion of the signal is weighted according to the duration and severity of the fluctuation. High frequency oscillation of short duration remain suppressed, while features such as signal spikes resulting from the blast loading, which are of relatively long duration, are restored. An example of the resultant weighted smoothing is also is shown in Figure 5.12 where it is superimposed upon the measured signal.

It is evident that the high-frequency components oscillations have essentially been eliminated, while the overall character of the signal has been preserved. Furthermore, the weighting algorithm did not alter

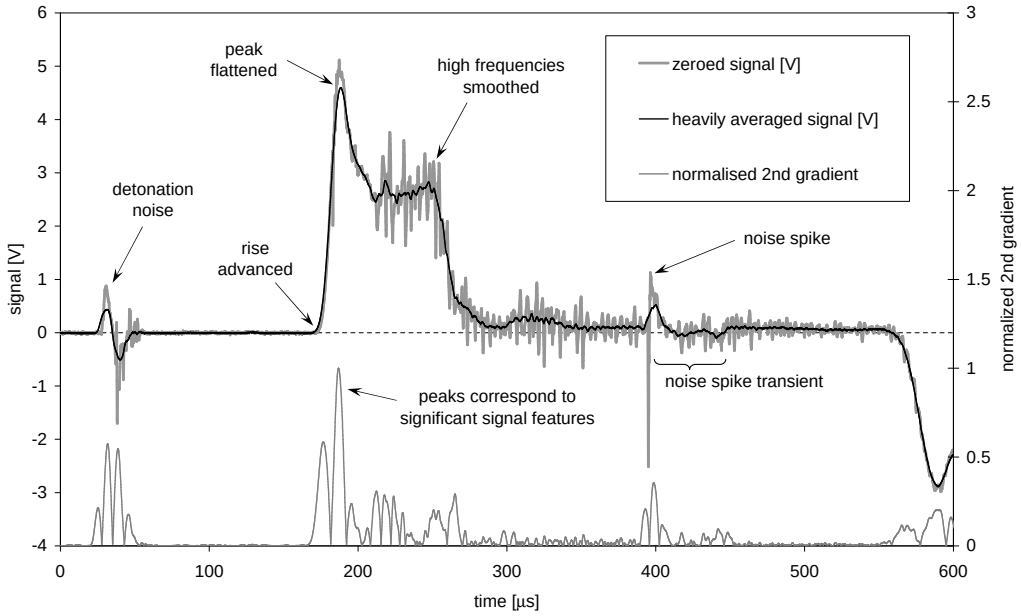

Figure 5.11: Effect of a simple moving average smoothing algorithm on the signals from a blast tube test on a 2 mm thick PCCS plate using a 10 g charge.

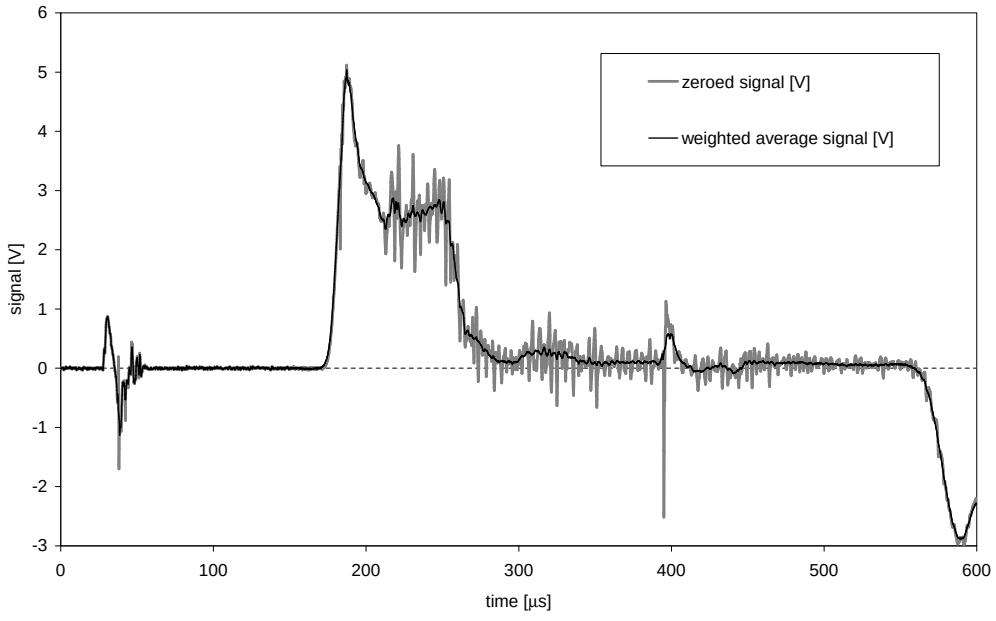

Figure 5.12: Effect of the weighted smoothing algorithm on the signals from a blast tube test on a 2 mm thick PCCS plate using a 10 g charge.

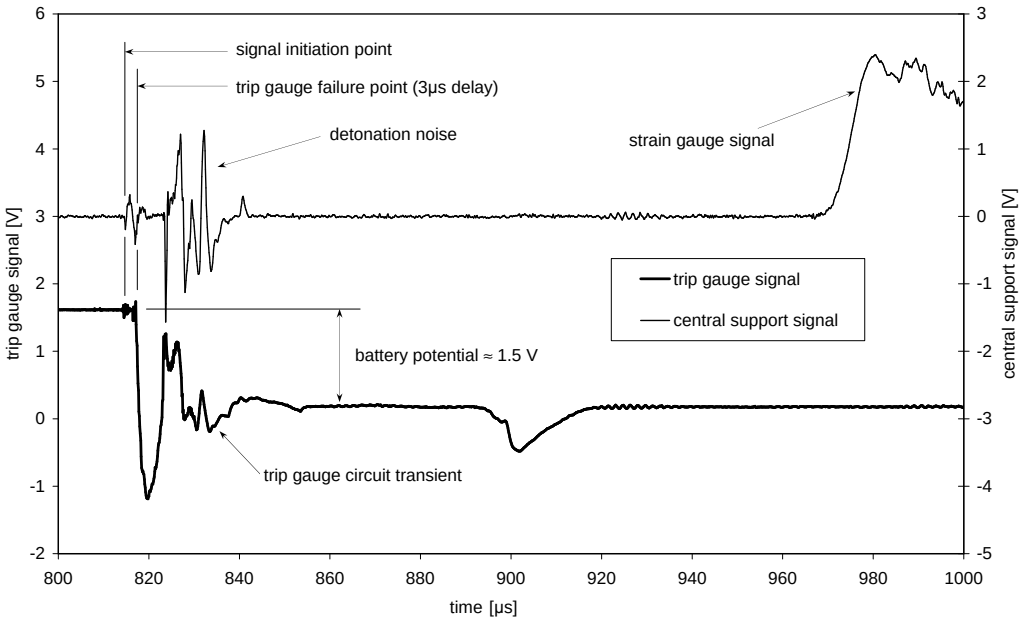

Figure 5.13: Comparison of the trip gauge signal to central Hopkinson bar signal.

the integral of the signal and hence the evaluation of the momentum contained in the stress wave is unaffected. The particular signal shown in Figure 5.12 is representative of a worst case with respect to noise. Generally, the recorded signals contained less severe oscillations.

5.2.6.4 Blast Load Synchronization

Aspects of the interpretation of the signals discussed in this thesis depend on the timing of the recorded signal relative to the moment of detonation of the explosive charge. The majority of the signals were captured using delayed self triggering of the data recorder. Consequently, the exact moment of triggering could be affected by random noise spikes in the recorded signal. However, all the captured signals showed that the detonation event produced a short interference pulse, examples of which can be seen in Figures 5.7 and 5.11. Therefore, in this thesis, the beginning of the interference pulse was taken to signify the moment of detonation. To confirm this, a few tests were conducted with a trip gauge, in the form of a thin strip of aluminium foil, placed beneath the explosive charge and connected in series to a simple circuit incorporating a 1.5 V battery and a resistor. The voltage across the resistor was captured on the same data recorder as the Hopkinson bar signal, a typical example of which is shown in Figure 5.13.

As the name suggests, the trip gauge is cut by the blast wave as it emerges from the explosive charge, which causes a sudden drop in the voltage over the resistor. Figure 5.13 shows a delay of 3 μs between the start of the detonation pulse and drop in the trip gauge signal. Furthermore, during this delay a small but distinct amount of noise appears in the trip gauge signal. The reason for the delay and the associated noise is unclear. The time required for the detonation wave to pass through the explosive charge would be a small fraction of a microsecond and cannot be a significant factor in the delay. The delay could represent the response time of the detonator, or the time required for the trip gauge to be severed. In this thesis, the start of the detonation pulse is viewed as the moment of detonation and is used for signal

synchronization when time of flight data is required. From the preceding discussion it is concluded that any timing error incurred by this assumption is at most 3 μs. The transient behaviour of the signal after the sudden drop, which may represent electromagnetic oscillations in the circuit or subsequent contact of the severed trip gauge with the steel walls of the blast tube, was not considered to be important and not investigated further.

5.3 Blast Load Characteristics

In this section, the blast load characteristics of the two load configurations presented in Section 5.2.5 are discussed[6]. From the perspective of precision testing, the important features are the blast load history, distribution and repeatability. The peak pressure and blast duration are required to assess whether a blast test may be analysed using the ideal impulsive assumption or a finite load duration model. Of particular importance for this thesis is whether the blast load, or at least the impulse intensity, is uniform. The term 'impulse intensity', which has units of Pas, refers to the impulse transferred per unit area of the target plate and is used to describe the impulse distribution over the plate[7]. An additional blast loading feature of secondary importance is to assess whether the blast loads are self-similar, *i.e.* for a given experimental configuration, can the peak blast pressure simply be scaled up to account for large impulses or do the shape and duration of the blast wave change as the charge mass increases.

5.3.1 Short Stand-Off Blast Characteristics

As reviewed in Sections 2.1.1 and 3.2.2, the use of thin sheet or concentric ring explosive charges, placed at short stand-off distances using neoprene or polystyrene attenuators, are intended to experimentally create near ideal impulsive loading conditions. Based on the high detonation velocity and large detonation pressure of the explosive, it was assumed that these charge configurations provide a pressure load that is effectively uniform, instantaneous and of negligible duration. However, as discussed in Section 5.2.1, the blast duration estimates based on the 'burn time' of the explosive charge do not account for the effect of the attenuators and the finite time required for the high pressure detonation products to dissipate. The purpose of this section is to assess the extent of these effects for the short stand-off explosive charges used in this thesis.

5.3.1.1 Short Stand-Off Blast Impulse

The tabulated experimental results for the short stand-off blast tests are given in Appendix E.2. The total impulses obtained from charges of varying mass are shown in Figure 5.14. The majority of the data points represent tests conducted using the ring-charge configuration shown in Figure 5.4a. Only the two 4 g data points did not have a ring charge and consisted of a 1 g leader charge and two 1.5 g cross-leader charges.

[6] The work contained in this section has been published by Cloete & Nurick [90].
[7] Other authors use the term 'specific impulse' or 'impulse density' [158].

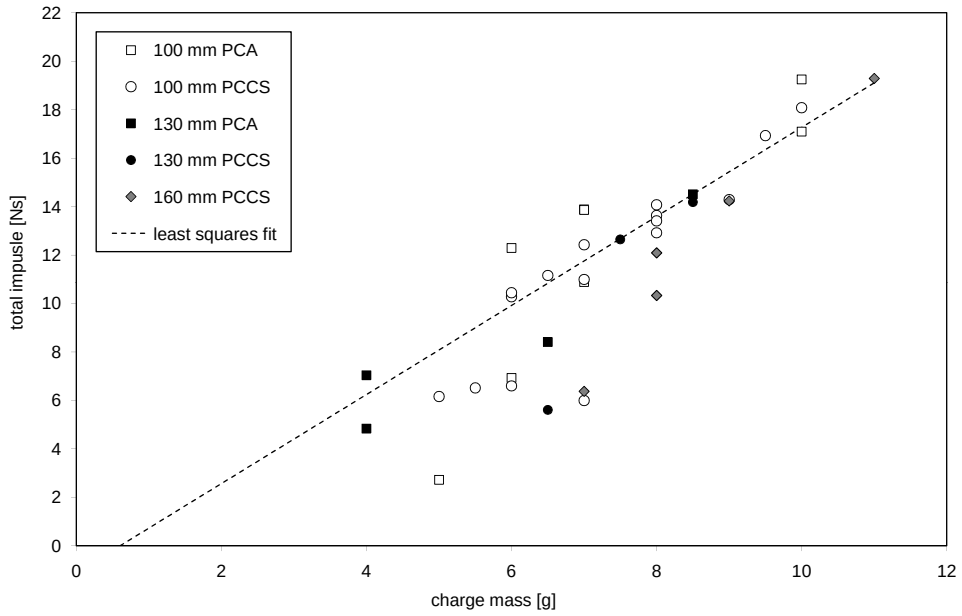

Figure 5.14: Experimental charge mass vs impulse data for the short stand-off charge configuration.

From Figure 5.14 it is evident that several of the explosive charges with a total mass between 5 g and 7 g did not deliver an impulse greater than that obtained without a ring charge, *i.e.* the two 4 g charges, which implies that the ring charge did not always detonate. In particular, the charges that produced an impulse of less than 10 Ns appear to suffer ring charge deflagration.

As discussed in Section 3.2.2, an explosive charge will deflagrate when rolled below a certain thickness. The average thickness of a cross-leaders and ring charges can be estimates using the formulae,

$$d_{cl} = \sqrt{\frac{4m_{cl}}{\pi \rho_e L_{cl}}} \quad \text{and} \quad d_{rc} = \frac{1}{\pi}\sqrt{\frac{4m_{rc}}{\rho_e D_{rc}}} \tag{5.3}$$

where ρ_e is the density of the explosive charge, while d_{cl} and L_{cl} are the thickness and length of a cross-leader charge and d_{rc} and D_{rc} are the thickness and diameter of a ring charge, respectively. From the charge geometry given in Section 5.2.5.1 and using a density of 1600 kg/m^3 for PE4, Equations (5.3) estimate the average thickness of the cross-leaders to be 3.64 mm, while the ring charge thicknesses range from 2.91 mm to 5.44 mm, as summarized Table 5.1.

The results show that the transition from deflagration to detonation occur at a critical thickness of approximately 3.36 mm. This conclusion is strengthened by the consistent value of the critical thickness for each ring charge diameter and the reliable performance of the leader charges, which are only slightly thicker than the critical thickness. Though marginally lower, the inferred critical thickness of PE4 is consistent with that of composition C-4, which is between 3.81 mm and 5.08 mm [149,153]. These results indicate that the PE-4 may not be entirely equivalent to C-4 and that simulations based on the assumed equivalence should be treated with caution.

Table 5.1: Average thickness and performance of the PE4 ring charge component of the three short stand-off charge configurations.

ring charge mass [g]	60 mm diameter charge thickness [mm]	detonation	75 mm diameter charge thickness [mm]	detonation	90 mm diameter charge thickness [mm]	detonation
2	2.91	no	no rec.		no rec.	
2.5	3.25	no	no rec.		no rec.	
3	3.56	yes	3.18	no	2.91	no
3.5	3.84	yes	no rec.		no rec.	
4	4.11	yes	3.68	yes	3.36	yes
5	4.59	yes	4.11	yes	3.75	yes
6	5.03	yes	no rec.		no rec.	
6.5	5.24	yes	no rec.		no rec.	
7	5.44	yes	no rec.		4.44	yes

Note: The entry 'no rec.' indicates that the charge configuration was not tested.

Considering only the data points that represent detonation, a linear regression provides a gradient of 1.838 Ns/g and an x-intercept of 0.603 g, as shown in Figure 5.14. This result is in good agreement with the data of Bodner & Symonds [56] and Nurick *et al.* [60], as shown in Figure 3.3, although the data shows more scatter with an r^2 correlation coefficient of 0.848. However, given that this data includes several distinct plate and charge configurations, the degree of scatter is acceptable. Furthermore, in the isolated case of the PCCS configuration, the scatter compares well with that of Bodner & Symonds and Nurick *et al.*

5.3.1.2 Short Stand-Off Blast Pressure History

The blast pressure history captured by the central Hopkinson bar for a PCA plate loaded by a charge configuration without a ring charge, *i.e.* Figure 5.4b, is shown in Figure 5.15. The pressure history shows the typical blast wave features of a steep initial pressure rise followed by a relatively gradual exponential decay. However, the negative pressure phase of a typical blast wave [108,153] cannot be discerned because it amounts to pressure variation of less than 0.1 MPa, which is negligible when compared to the peak pressure of over 100 MPa. For this reason, the negative pressure phase will not be considered in this thesis. Incidentally, this is also one of the reasons why the oscillations in the signal are known to be noise, *i.e.* a negative pressure of greater than 0.1 MPa is not physically meaningful.

The blast pressure history for a PCA plate loaded by a charge configuration including a ring charge, *i.e.* Figure 5.4a, is shown in Figure 5.16. The signal contains two distinct pressure spikes, with the first spike being practically identical to the signal in Figure 5.15. This observation suggests that the first pressure spike is due to the leader and cross-leader charges while the second spike is due to the ring charge. This conclusion is discussed further in Section 6.2 where Figure 6.5 shows that the magnitude of the second pressure spike increases with an increase in the mass of the ring charge.

The pressure history results have three important implications. Firstly, from Figures 5.15 and 5.16 it is evident that the blast load durations are approximately 30 μs and 50 μs respectively. Hence, given the analyses presented in Section 4.3, this implies that the short stand-off charge configuration does not provide an ideal impulsive loading, although it is a reasonable experimental approximation. In other words, an analysis based on the IIL assumption is likely to provide a slight overprediction of the final

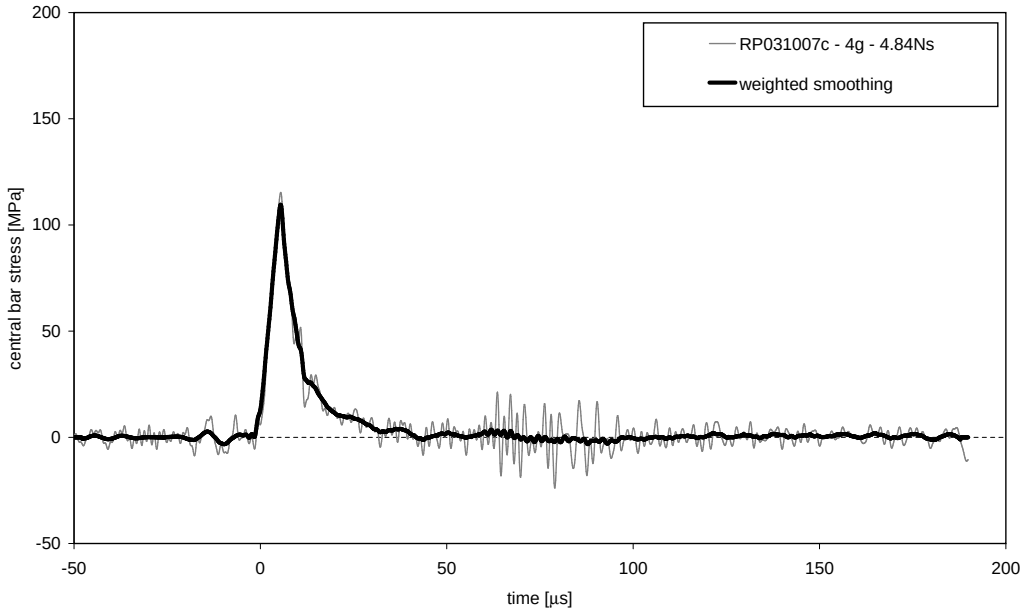

Figure 5.15: Graph of the central support reaction force history for an annular plate without the outer ring charge.

displacement when compared to experimental results. Nevertheless, given the good impulse correlations presented in Section 5.3.1.1, the experimental results reported in this thesis should still correlate with published PCS blast testing results, as will be shown in Section 8.3.

Secondly, assuming a detonation velocity for PE4 of approximately 8190 m/s [149,153], the 'burn time' for the charge configurations corresponding to Figures 5.15 and 5.16 are approximately 4.58 μs and 6.54 μs respectively. It is evident that the 'burn time' is almost an order of magnitude shorter that the blast duration, which supports the argument presented in Section 5.2.1 that the 'burn time' effectively sets a lower limit for the load duration.

Thirdly, the time difference between the pressure spikes in Figure 5.16 is almost a factor of three greater that the 'burn time', which indicates that the pressure waves due to detonation take a considerable amount of time to travel across the plate. Therefore, at any given time the blast pressure will not be uniform over the plate and the form of the pressure history will change as a function of radius. However, despite this, the impulse distribution may still be uniform, as will be discussed next in Section 5.3.1.3.

5.3.1.3 Short Stand-Off Blast Impulse Distribution

An indication of the uniformity of the impulse distribution produced by the short stand-off charge configuration can be obtained from the fraction of the total impulse transmitted through the central Hopkinson bar during a PCA plate test. The Hopkinson bar impulse is obtained by integrating the pressure history over the cross-sectional area of the bar, while the total impulse is obtained using the ballistic pendulum. The measured impulse fractions for short stand-off 100 mm and 130 mm PCA plate tests are given in Tables E.1 and E.3. The measured impulse fractions range from 12.02 % to 7.16 % for the 100 mm plates and from 6.13 % to 4.64 % for the 130 mm plates. However, for a uniform impulse

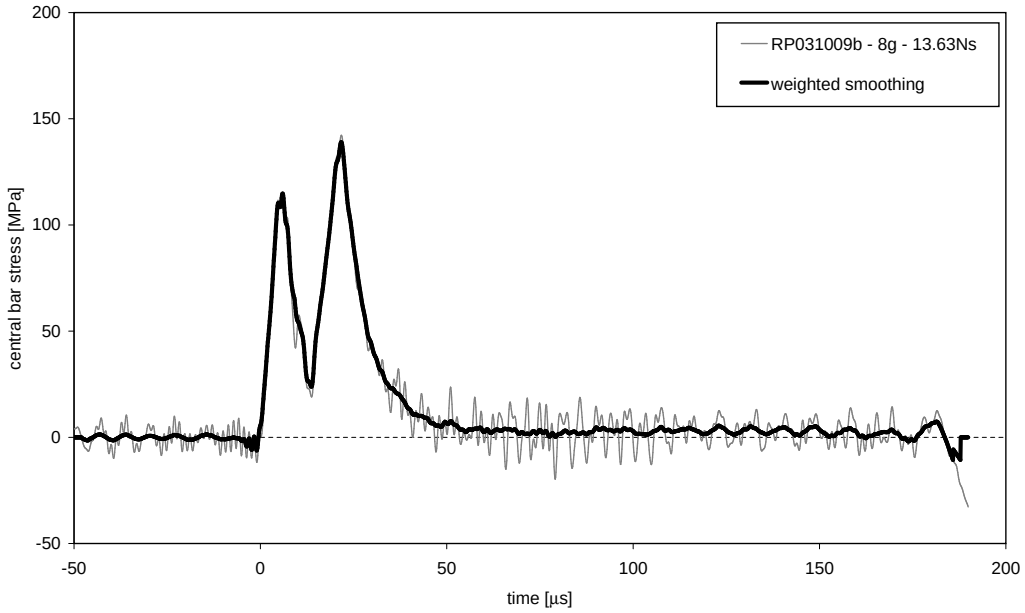

Figure 5.16: Graph of the central support reaction force history for an annular plate with an 8g charge.

distribution, the Hopkinson bar impulse fraction should be proportional to the area ratio between the bar cross-section and the specimen plate, *i.e.* 4.84 % for the 100 mm plate and 2.86 % for the 130 mm plate. All the measured impulse fractions are greater than the theoretical uniform impulse value, but appear to asymptote toward the theoretical value as the charge mass increases, as shown in Figure 5.17[8], where the measured data have been normalized using the impulse fraction prediction based on the area ratios.

It is proposed that the asymptotic behaviour is due to the localized contribution of the 1 g leader charge. A first order estimate of this effect can be obtained by assuming that the impulse contribution of the leader charge is proportional to its weight but only distributed over an inner portion of the plate while the impulse due to the cross-leader and ring charges are evenly spread. Using this approach, with the leader charge acting on a diameter of 55 mm, leads to the two theoretical predictions shown in Figure 5.17. The correlation is sufficient to suggest that the theoretical interpretation of the experimental data is correct.

The preceding analysis suggests that the impulse distribution was near uniform, with only a small ring around the central support experiencing an impulse intensity approximately 50 % greater than the average value. Therefore, this data is considered to be adequate for the purpose of comparison with theoretical predictions based a uniform impulse assumption.

Finally, this result confirms that, as originally intended [62,151], the ring charge configuration can provide a uniform impulsive load, despite having a non-uniform pressure history. Therefore, caution should be exercised to distinguish between uniform blast pressure and uniform impulse distribution when using the term ‘uniform blast load’.

[8]The 100 mm test with a 5 g charge has been treated as a 3 g charge since the ring charge appears to have deflagrated.

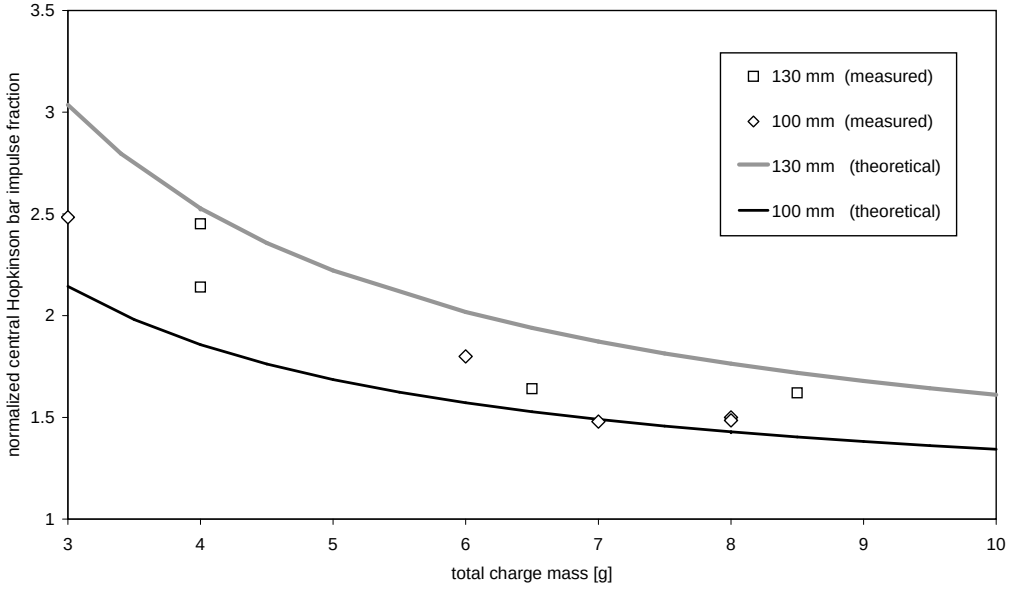

Figure 5.17: Normalized fraction of the total impulse transmitted through central Hopkinson bar as a function of the total charge mass for short stand-off blast tests of 100 mm and 130 mm diameter PCA plates.

5.3.1.4 Short Stand-Off Blast Repeatability

The data presented in the preceding sections show that the short stand-off ring charge configuration displays good repeatability. In particular, Figure 5.14 shows that the ring charge configuration delivers a consistent impulse. Furthermore, Figures 5.15 and 5.16 show that distinguishing features of pressure history, such as the initial pressure spike, are consistent between tests. Additional examples of repeatability are given in Figures 6.5 and 6.6, which are discussed in Section 6.2 in the context of the response behaviour of PCCS plates to the short stand-off charge configuration.

5.3.2 Blast Tube Load Characteristics

In this thesis, the blast tube technique is intended to address some of the shortcomings of the short stand-off charge configuration, as discussed in Sections 5.3.1.2 and 5.3.1.3. In particular, the literature reviewed in Sections 2.1.2 and 2.2.4 suggest that a blast tube can provide impulsive shock loads with a similar intensity to that obtained from the short stand-off charge configuration, but with a uniform pressure history and, consequently, a uniform impulse distribution [105, 107]. However, it is known that the intensity of a blast wave decreases with stand-off distance, while the duration increases [108, 153, 177], *i.e.* the blast wave may become less impulsive and more dynamic[9]. The purpose of this section is to assess the extent of these effects for the blast tube configuration used in this thesis.

[9]The distinction between an impulsive and dynamic load is discussed in Section 4.3.2.

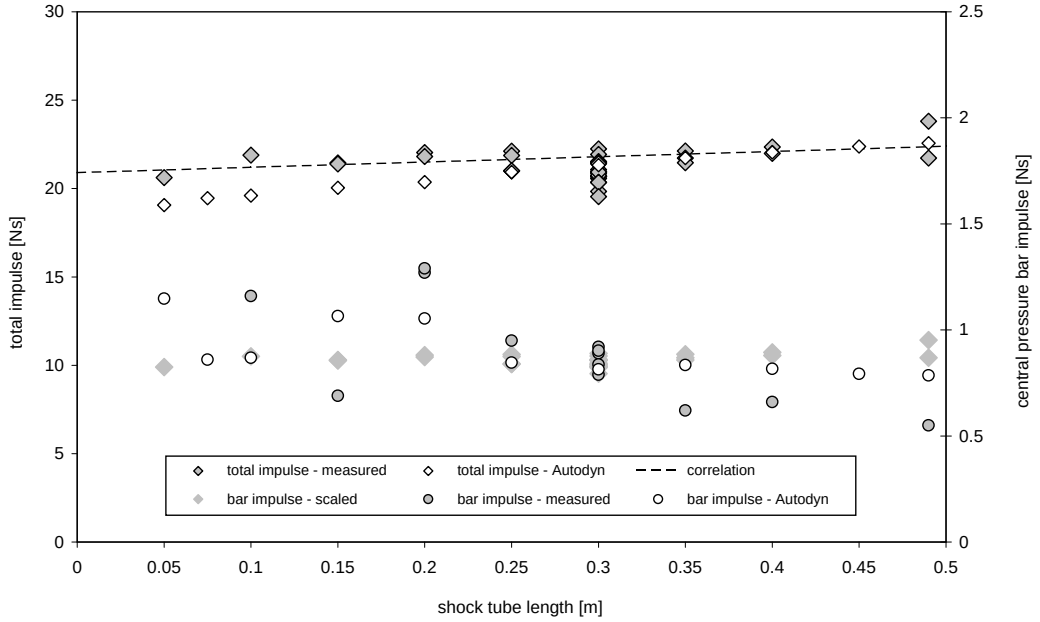

Figure 5.18: Effect of the blast tube length on the transferred impulse for a 10 g charge mass.

5.3.2.1 Blast Tube Impulse Length Effect and Impulse Distribution

The effect of the blast tube length on the impulse transferred to the plate specimen was assessed by conducting an initial series of PCA plate tests where the tube length varied but the charge mass was fixed. The purpose of this initial test series was to determine the shortest tube length that would provide a uniform blast pressure history. The charges had a mass of 10 g, *i.e.* a 1 g leader charge and a 9 g main charge, and were mounted in the manner depicted in Figure 5.1(b). The experimental data from the initial test series and all subsequent PCA tests with a charge mass of 10 g are given in Tables E.7, E.8, E.12, E.15, E.19 and E.20.

The experimental results for the total impulse and the impulse transferred through the central Hopkinson bar, referred to simply as the bar impulse, are shown in Figure 5.18. Also shown are the predictions obtained from a series of numerical simulations that are discussed in Section 5.3.3. The total impulse shows a steady gradual increase with an increase in tube length, which is similar to the data due to Jacob *et al.* [107] discussed in Section 3.2.6. By contrast, the bar impulse appears to decrease with an increase in tube length, although there is no clear trend below tube lengths of 200 mm. An explanation for some of these observations is proposed in Section 5.3.3.2.

Given the outer plate and Hopkinson bar diameters of 100 mm and 20 mm respectively, an ideally uniform blast pressure distribution should result in a bar impulse that is 4 % of the total impulse when scaled according to the area ratio. For comparison, the ideal scaled bar impulse is plotted in Figure 5.18. The results suggest that a near uniform impulse distribution is achieved for a blast tube length of 300 mm, which was therefore used for all subsequent blast tube tests. Figure 5.19 shows the bar impulse results for PCA tests for which a pressure history was captured. The majority of the data are close to 4 % or slightly above, which indicates that good impulse uniformity was attained. However, the bar impulse fraction appears to increase with an increase in the total. In particular, the bar impulse falls below 4%

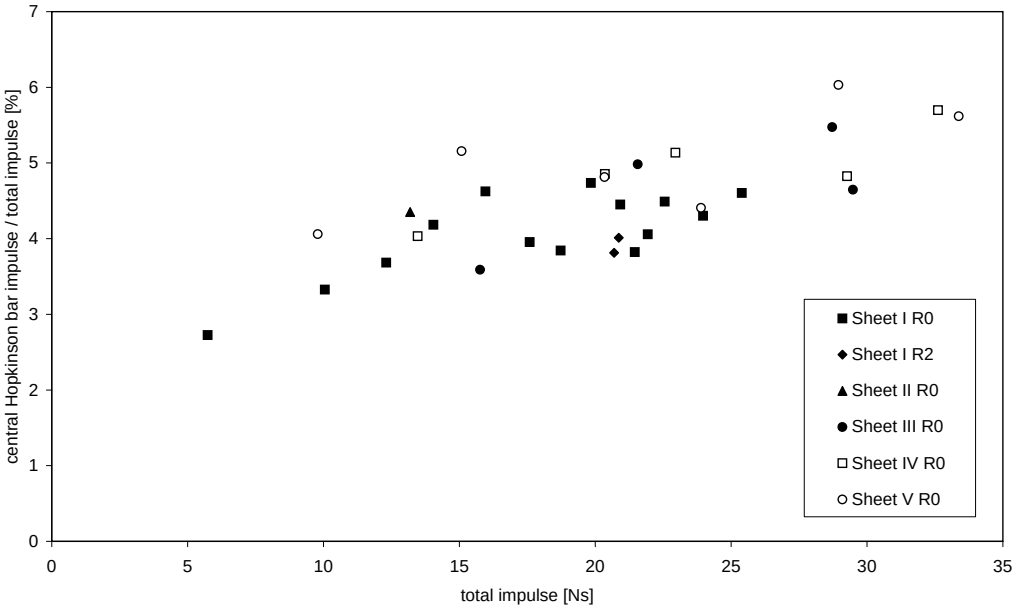

Figure 5.19: Fraction of the total impulse transmitted through the central Hopkinson bar for PCA plate tests using a 300 mm blast tube.

for impulses smaller than 10 Ns, while fractions greater than 5% are obtained for total impulses greater than 28 Ns. The impulse distribution is discussed further in Sections 5.3.2.3 and 5.3.3.2.

5.3.2.2 Blast Tube Impulse and Repeatability

The total impulses obtained using a 300 mm blast tube with charges of varying mass are shown in Figure 5.20. The data points represent tests conducted on both PCA and PCCS plate specimens cut from three different thickness sheets.

Unlike the ring-charge configuration, the impulse data does not appear to have a linear dependence on the charge mass. To assess the repeatability of the blast tube loading technique a nonlinear regression was performed using a function of the form,

$$I = B(m_e - m_0)^m \tag{5.4}$$

Where I is the total impulse, m_e is the charge mass, B and m are constants and m_0 is the x-intercept. Taking the natural logarithm of Equation (5.4) gives,

$$y = mx + b \quad \text{where} \quad y = ln(I) \;\; , \;\; m = ln(x_e - x_0) \;\; \text{and} \;\; b = ln(B) \tag{5.5}$$

A standard linear regression was performed using Equation (5.5), while the value of x-intercept was iteratively adjusted to maximize the value of the r^2 correlation coefficient. The best fit is shown in Figure 5.20 and has parameter values of $m = 0.619$, $b = 1.709$ and $x_0 = 1.549$ g. The optimized r^2 value is 0.993, which implies that the blast tube loading technique is highly repeatable and thus meets the criteria for precision testing.

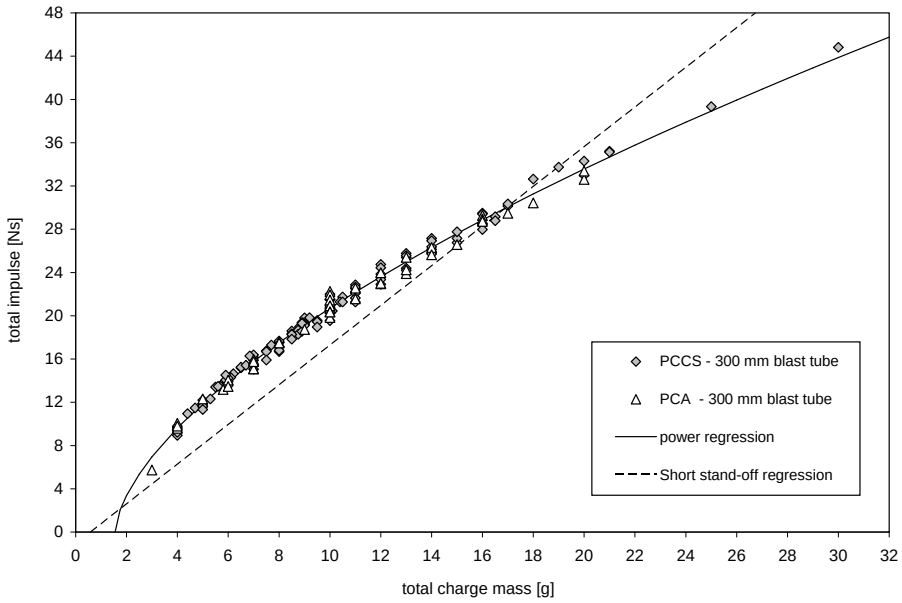

Figure 5.20: Experimental charge mass vs total impulse data for the 300 mm blast tube configuration.

Figure 5.20 also shows the regression curve corresponding to the short stand-off charge configuration. For charge masses smaller than 10 g, the blast tube data is above and approximately parallel to the short stand-off. This result was expected since the blast tube confines the explosive event to a certain extent. However, for charge masses greater than 10 g, the blast tube data tends toward the short stand-off trend while for masses greater than 18 g it falls below the short stand-off trend. The precise cause of this non-linearity was not investigated further as it was considered to be beyond the scope of this thesis, but is a topic of future research.

5.3.2.3 Blast Tube Pressure History and Repeatability

Typical blast pressure histories captured during PCA plate tests using a 300 mm blast tube with charge masses of 10 g and 20 g are shown in Figures 5.21 and 5.22 respectively. In both figures, the pressure histories of two or three nominally identical blast tests are superimposed and temporally synchronized using the start of the detonation noise, as discussed in Section 5.2.6.4. The pressure histories show the classical blast wave features of a sudden initial pressure spike followed by an exponential decay. It is evident that the blast tube loading technique provides a high degree of repeatability. In particular, the temporal position of the pulse and the shape of the pressure decay show good consistency, and as a result, non-repeating random noise spikes stand out clearly and can be ignored during subsequent analysis.

Notwithstanding their general repeatability, three features of the recorded pressure pulse show some variability or non-ideal behaviour. Firstly, the peak magnitude of the initial pressure spike can differ significantly between otherwise near identical pulses. Secondly, the blast pressure does not decay smoothly but contains minor low frequency undulations. Lastly, the blast pressure does not immediately decay down to atmospheric conditions and displays a residual pressure that persists for a considerable time after

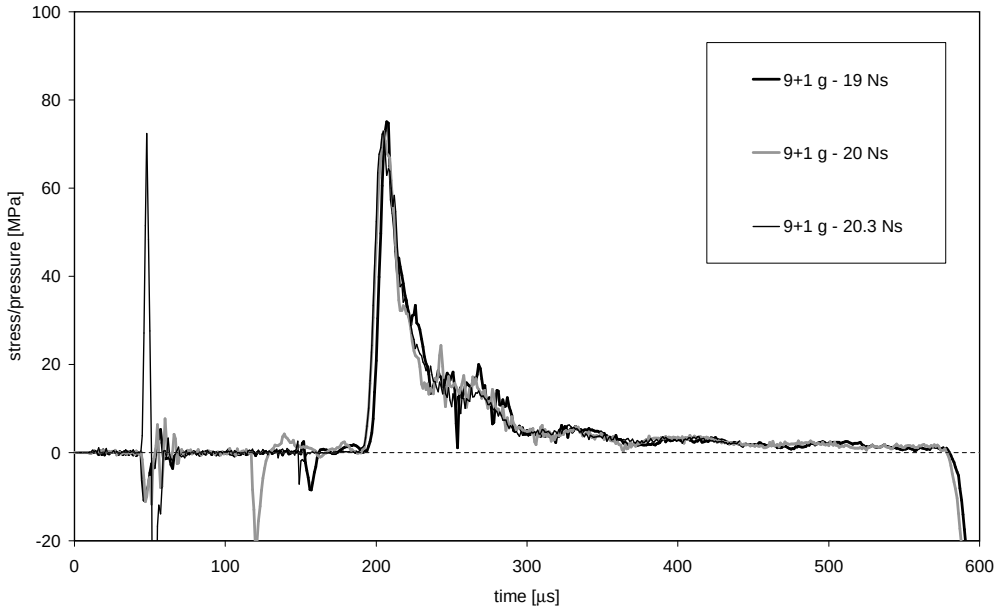

Figure 5.21: Pressure history repeatability for 10 g charge mass in a 300 mm blast tube configuration.

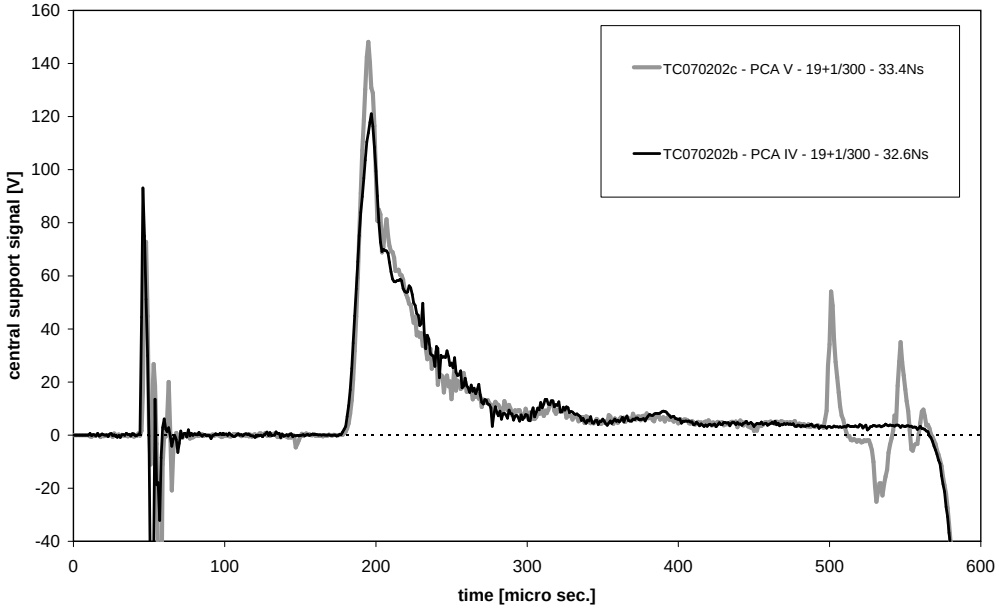

Figure 5.22: Pressure history repeatability for 20 g charge mass in a 300 mm blast tube configuration.

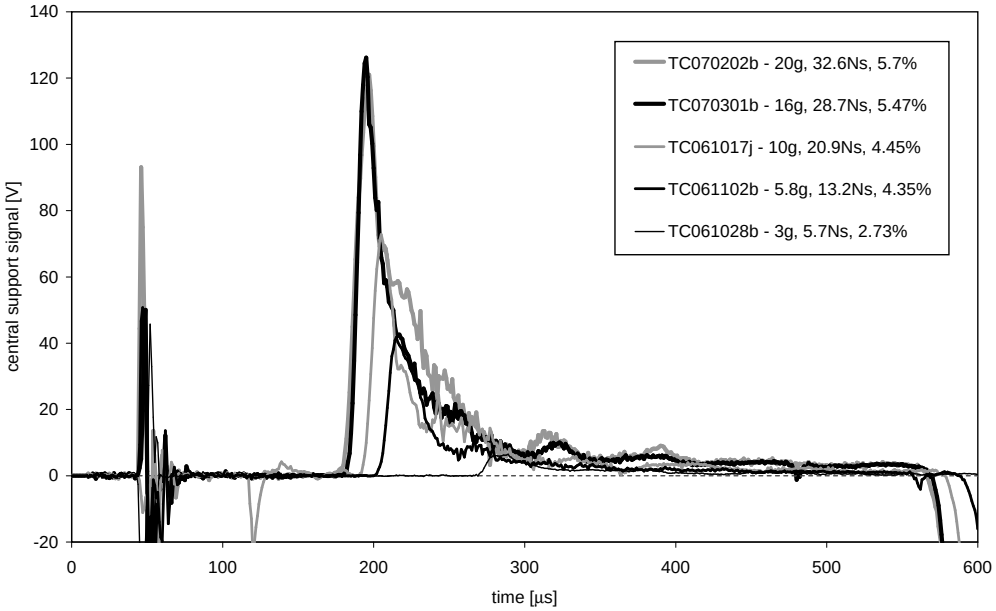

Figure 5.23: Pressure histories for various charge masses in a 300 mm blast tube configuration. The legend gives the test number, charges mass, total impulse and bar impulse fraction.

the main portion of the pressure pulse has dissipated. These three features are absent from the blast wave produced by the short stand-off charge configuration, which suggests that they may be attributed to the effect of the blast tube. The blast pressure appears to be sensitive to experimental variables such as the axial symmetry of the initial shock wave in the blast tube, the reflections of shocks in the blast tube and semi-confinement of the residual blast pressure. A detailed examination of these effects was deemed to be beyond the scope of this thesis, although some further considerations will be presented in Section 5.3.3.

It is noticeable that the time of arrival (TOA) of the blast wave front is slightly sooner in Figure 5.22 than in Figure 5.21. This observation is consistent with fact that shock wave velocity increases with an increase in shock pressure. This behaviour is also evident in Figure 5.23, which shows five blast pressure histories from the range of charge masses used in this thesis.

The pressure histories shown in Figure 5.23 cover a wide range of peak blast pressures with a corresponding variation in the residual pressures, although the pressure decay characteristics appear to be reasonably similar. Figure 5.24 shows the result of dividing an individual pressure history by its corresponding total impulse, as measured using the instrumented ballistic pendulum, and then aligning the curve such that an extension of the initial pressure rise would intersect with the origin. This approach shows that the blast waves have similar characteristics. In particular, the pressure decay behaviour is highly repeatable and the magnitude of the residual pressure appear to scale with the total impulse. However, some features, such as the peak pressure and initial decay rate, show some inconsistencies which will be considered later in this section. Note that this impulse scaling approach must not be confused with the well known Hopkinson-Cranz scaling laws [108, 109].

The scaled pressure histories shown in Figure 5.24 provide a basis for a generic blast wave model that can be used in future numerical analyses. It is assumed that the scaled blast pressure history $P(t)/I$ can

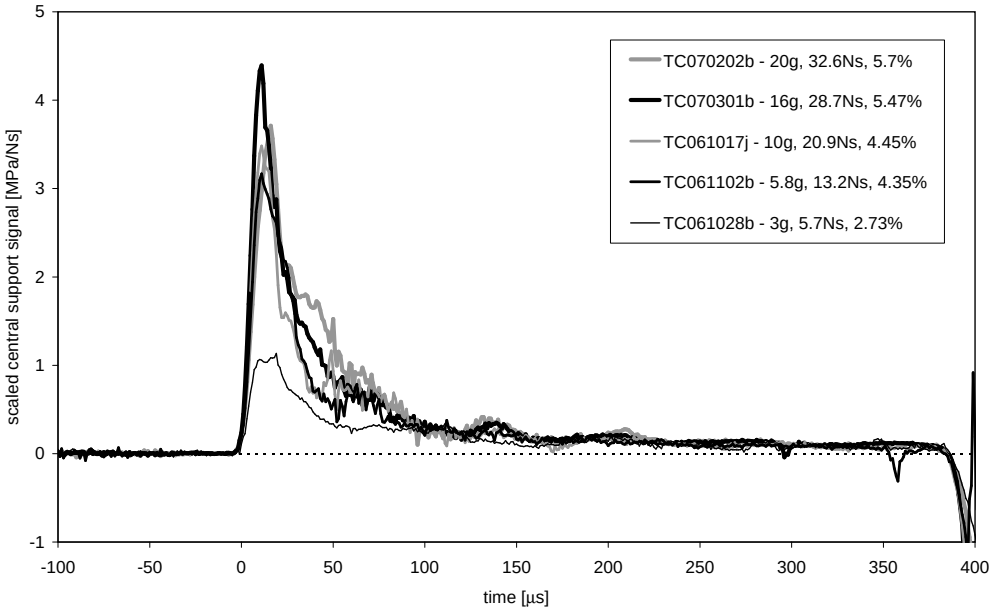

Figure 5.24: Impulse scaled pressure histories for various charge masses in a 300 mm blast tube configuration. The legend gives the test number, charge mass, total impulse and bar impulse fraction.

be approximated as an initial linear rise followed by a double exponential decay of the form,

$$\frac{P(t)}{I} = \begin{cases} \left(\frac{P_0}{I}\right)\frac{t}{t_0} & \text{if} \quad 0 \le t < t_0 \\ \left(\frac{P_0}{I} - \frac{P_l}{I}\right) e^{-\gamma_s (t-t_0)} + \left(\frac{P_l}{I}\right) e^{-\gamma_l (t-t_0)} & \text{if} \quad t \ge t_0 \end{cases} \tag{5.6}$$

where P_0/I is the scaled peak blast pressure which occurs at time t_0, while γ_s and γ_l are the decay constants for the short and long duration exponential terms respectively and P_l/I is the scaled peak pressure of the long duration exponential term. Note that the subscript '0' has been retained to denote parameters associated with the peak blast pressure, *i.e.* t_0 is the start of the decay phase and not the start of the pulse as a whole.

The double exponential form of Equation (5.6) was chosen after initial calculations showed that the pressure history could not be adequately described by a single exponential term. The short duration exponential term is required to capture the initial steep pressure decay, which is similar to that observed for unconfined blast loads, such as that shown in Figure 5.15. Conversely, the long duration exponential term is required to capture the relatively slow decay of the residual pressure, which is not observed for unconfined blast loads and is therefore postulated to be a result of semi-confinement due to the blast tube.

From Equation (5.6), the expression for the scaled impulse intensity for $t \ge t_0$ is,

$$\frac{1}{\pi R_o^2}\left(\frac{I(t)}{I}\right) = \tfrac{1}{2}\left(\frac{P_0}{I}\right) t_0 + \frac{1}{\gamma_s}\left(\frac{P_0}{I} - \frac{P_l}{I}\right)\left[1 - e^{-\gamma_s (t-t_0)}\right] + \frac{1}{\gamma_l}\left(\frac{P_l}{I}\right)\left[1 - e^{-\gamma_l (t-t_0)}\right] \tag{5.7}$$

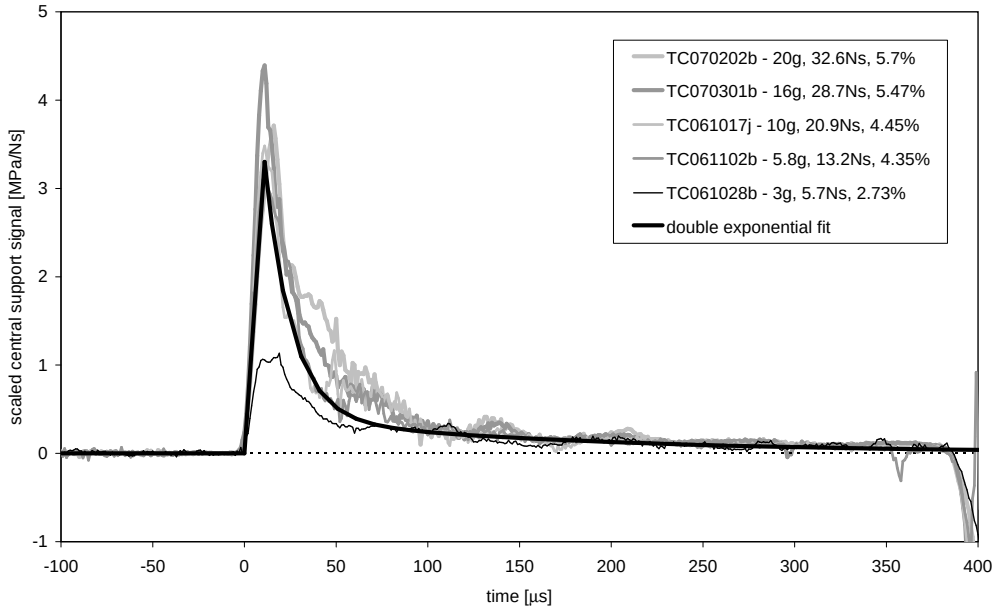

Figure 5.25: Pressure history similarity for various charge masses in a 300 mm blast tube configuration.

The quotient $I(t)/I$ is an expression of the fraction of the total impulse I that has been applied to the target plate at time t. Hence, for large values of t the value of $I(t)/I$ approaches unity as the exponential terms vanish and Equation (5.7) can be rewritten as,

$$\gamma_s = \frac{\frac{P_0}{I} - \frac{P_l}{I}}{\frac{1}{\pi R_o^2} - \frac{1}{2}\left(\frac{P_0}{I}\right) t_0 - \frac{1}{\gamma_l}\left(\frac{P_l}{I}\right)} \tag{5.8}$$

The form of Equation (5.8), with γ_s as the subject of the formula, allows the parameters of Equation (5.6) to be determined by a simple heuristic procedure. Firstly, the most consistent features of the scaled pressure histories shown in Figure 5.24 are timing of the peak blast pressure and the residual pressure, and hence the parameters t_0, P_l/I and γ_l are determined first. The scaled pressure history fit shown in Figure 5.25 was obtained by inspection and uses the parameter values $t_0 = 10\,\mu$s, $P_l/I = 0.4\,$MPa/Ns and $\gamma_l = 6000\,\mathrm{s}^{-1}$. The remaining two parameters, P_0/I and γ_s, display more variation than the preceding parameters and obtaining reasonable values requires some physical interpretation. Since the aim is to formulate a generic model for a uniform blast wave, a value of $P_0/I = 3.3\,$MPa/Ns was chosen, which is the average of the two peak pressures for which the experimental bar impulse fraction is close to 4 %, *i.e.* those produced by the 5.8 g and 10 g charges. Thereafter, Equation (5.8) gives the value $\gamma_s = 65674\,\mathrm{s}^{-1}$.

Figure 5.25 shows that Equation (5.6), using the above mentioned parameter values, provides a good fit to the pressure histories with a bar impulse fraction close to 4 %. This is to be expected, since Equation (5.8) ensures that the pressure history fit provides the correct average impulse intensity, and consequently a bar impulse fraction of exactly 4 %. Using the same approach, good fits to the other pressure histories can be obtained if the impulse intensity is modified to reflect the measured bar impulse fractions.

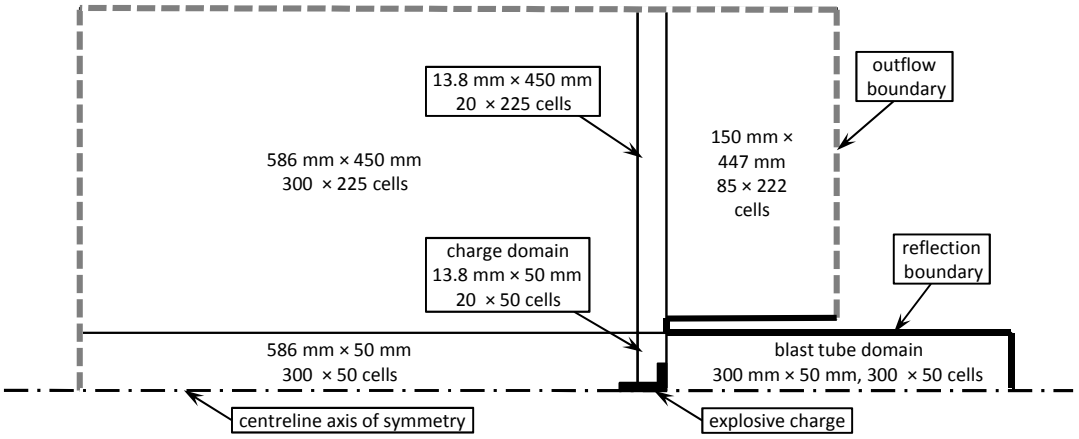

Figure 5.26: Computational Grid for the numerical simulation of a 10 g charge mass in a 300 mm blast tube configuration.

5.3.3 Blast Tube Simulations

In this section, the results of a small series of numerical simulations of the blast tube are presented. In particular, the aim is to investigate the blast pressure history, impulse uniformity and blast tube length effect. The simulations were conducted using the hydrocode ANSYS AUTODYN-2D V11.0 [85, 158, 178, 179]. The numerical domain consists of six interconnected axisymmetric Eulerian sub-domains according to the schematic diagram shown in Figure 5.26. The bottom right subdomain represents the blast tube and can be modified to represent different tube lengths without affecting the other domains. The walls of the blast tube are represented by reflective boundary conditions. The dimensions and grid pattern of bottom centre domain were chosen such that the simulated charge mass can be altered in 1 g increments without having to create a new grid. The size of the other domains were chosen such that the reflected blast wave in the blast tube would reach the open end of the tube before the head of the unconfined shock wave reached the boundary of the other domains. Thereafter, outflow boundary conditions are used while the pressure in the blast tube drops to far field conditions.

The majority of the cells were filled with air, while the explosive was modelled as C4. PE4 and C4 have similar compositions and densities since both are RDX based plastic explosives and only differ in terms of the plasticisers used. The C4 explosive model is based on the Jones-Wilkins-Lee (JWL) equation of state [180], for which the parameters were taken from the AUTODYN material library [178] and are given in Table 5.2. The air is modelled using the ideal gas law with the properties given in Table 5.3. The AUTODYN code requires the initial internal energy E_0 to be specified when filling the air cells. Typical pressure contours and velocity vectors are shown in Figure 5.27.

5.3.3.1 Simulated Blast Tube Pressure History

A typical simulation result for a 300 mm long blast tube with a 10 g charge is shown in Figure 5.28. In general the simulated pressure history was not uniform across the end of the blast tube. Hence, to allow for comparison with the experimental results, the numerical results were averaged over portions of the

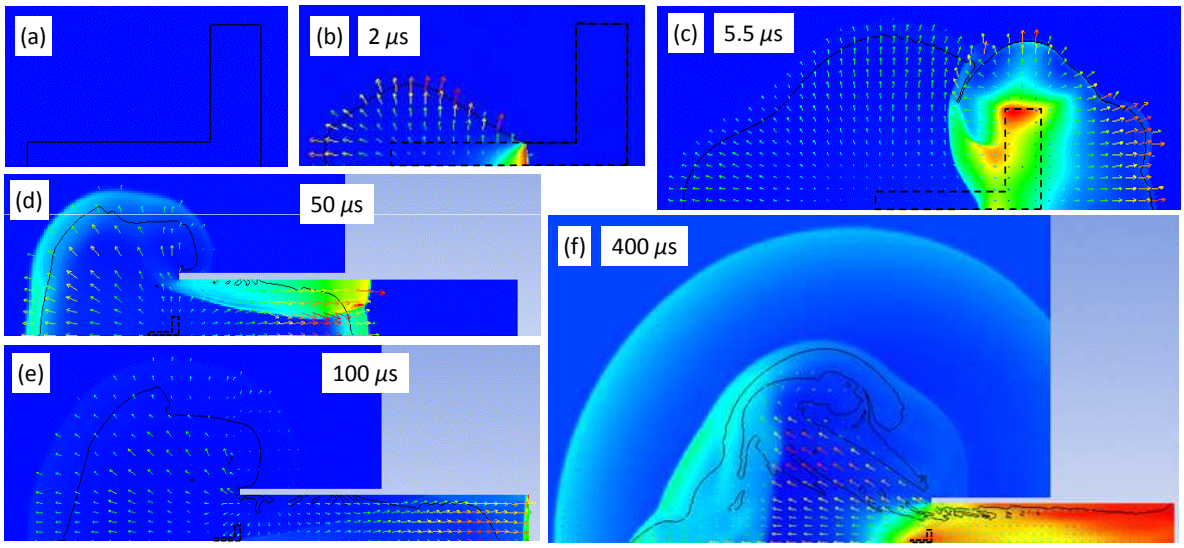

Figure 5.27: Pressure contours and velocity vector plots for the numerical simulation of a 10 g charge mass in a 300 mm blast tube configuration.

Table 5.2: JWL Equation of state parameters for C4 (PE4) obtained from the AUTODYN material library [178].

ρ_0 [g/cm^3]	A [kPa]	B [kPa]	R_1	R_2	ω	CJ detonation velocity [m/s]	CJ energy/ volume [$kJpmc$]	CJ Pressure [kPa]	Auto-convert to ideal gas
1.601	6.0977×10^8	1.295×10^7	4.5	1.4	0.25	8193	9.0×10^6	28.0×10^6	yes

Table 5.3: Equation of state parameters for air (ideal gas) obtained from the AUTODYN material library [178].

ρ_0 [g/cm^3]	γ	T_0 [K]	c_p [J/kgK]	E_0 [J/kg]
1.225×10^{-3}	1.4	288.2	7.476×10^2	2.068×10^5

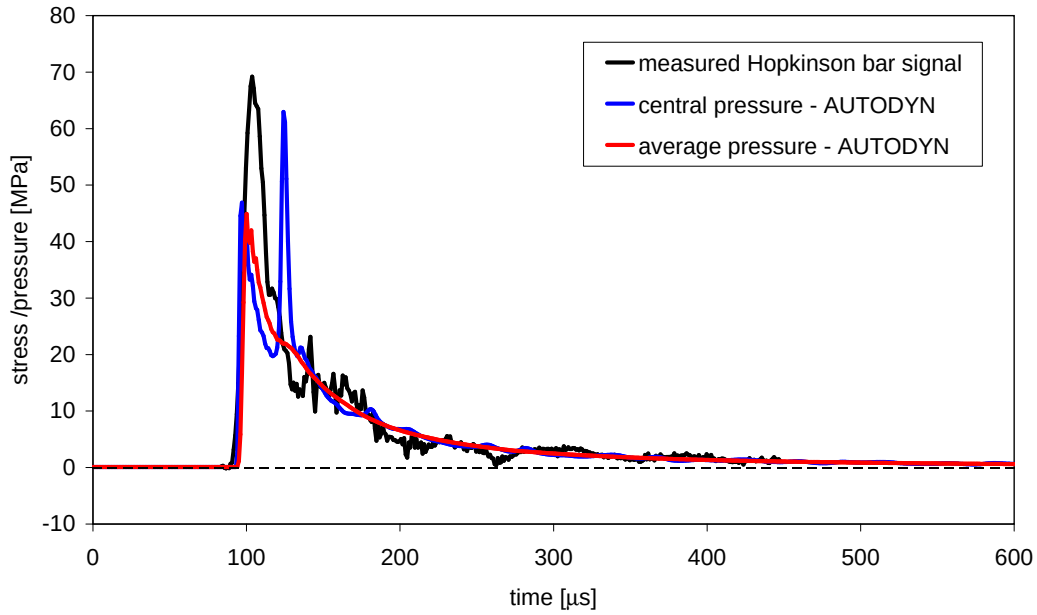

Figure 5.28: Comparison of experimental and averaged numerical pressure histories for a 10 g charge mass in a 300 mm blast tube configuration.

tube end that correspond to the central Hopkinson bar area and total plate area, which are respectively referred to as the central pressure and average pressure in Figure 5.28.

The results show that there is good agreement between the experimental and numerical pressure histories, even though they differ with regard to certain detailed features. In particular, the time of arrival of the blast wave and the long term pressure decay show good agreement. Furthermore, the predicted total impulse correlates well with the experimental measurements, as will be discussed in Section 5.3.3.2. The most significant differences between the numerical and experimental results are peak pressure values and the corresponding initial pressure decay rate. Both the central and average pressure curves show an initial peak pressure that is lower than the experimental value. However, the central pressure curve shows a distinct secondary pressure spike that has a similar intensity to that of the experimental peak value. The simulated pressure contours suggest that the pressure spike is due to converging shock waves that have reflected off the tube walls. In general it was found that such detailed features of the blast pressure histories were sensitive to variations in the model parameters. Therefore, it is plausible that the differences in the detailed blast wave features may be due to experimental factors that are not captured in the simulations, such as the presence of the polystyrene attenuator or slight imperfections in the shape and placement of the explosive charge. Therefore, it is postulated that in the experimental blast tube tests the converging reflected shock waves coincide with the initial blast front to produce the large initial pressure. These phenomena appear to be a rich subject for future research involving further detailed experimental and numerical studies, but were considered to be beyond the scope of this thesis and not pursued further.

5.3.3.2 Simulated Blast Tube Impulse Distribution and Tube Length Effect

Primary purpose of the numerical study presented in this section was to investigate the uniformity of the impulse distribution provided by the blast tube technique. A typical simulation result for the impulse distribution at the closed end of a 300 mm blast tube for a 10 g charge mass is shown in Figure 5.29. A slight increase in the impulse intensity is predicted at the outer boundary of the target plate. This is due to the pressure increase at the clamped boundary where multiple reflections occur between the plate and tube wall. This phenomenon is discussed in detail by Bonorchis & Nurick [158], for whom the boundary effect was more severe. A similar effect occurs at the centre of the plate where the axis of symmetry acts as a reflective boundary condition. Notwithstanding these two effects, the results suggest that the impulse distribution is essentially uniform, with the boundary and symmetry conditions only leading to a slight increase in the impulse intensity. Based on this result, the uniform impulse assumption is considered to be an acceptable approximation and is used in the theoretical models developed in Chapter 7.

The analysis reported above was repeated in a series of simulations where the length of the blast tube was varied while all the other model parameters were left unchanged. The total impulse and central impulse results are summarized in Figure 5.18 and compared to experimental results. The total impulse results show good agreement, especially for the longer tube lengths. In particular, the numerical results show that the total impulse for a given charge mass increases with an increase in the length of the blast tube, which is in keeping with data produced during this thesis and the results of Jacob *et al.* [107] discussed in Section 3.2.6 and shown in Figure 3.9. Furthermore, the numerical results support the conclusion that a 300 mm long blast tube is required to obtain a near uniform impulse distribution. For tube lengths below 250 mm the experimental and numerical values for the central bar impulse show a similar degree of variation although they do not follow precisely the same trend. These results support the previous conclusion that while the numerical model can capture the effects of shock wave reflections and interactions, further refinement of the model is required to bring the detailed features of the pressure histories into agreement.

Finally, the numerical results suggest a possible reason for the tube length effect on the total impulse. Figure 5.27(f) shows a secondary shock wave generated by the reflected blast wave exiting the blast tube followed by a stream of high pressure gas. This suggests that the total impulse is composed of two components. Firstly, the majority of the impulse is transferred by the reflection of the blast wave at the closed end of the blast tube, *i.e.* the target plate. This impulse transfer should not be affected by the length of the blast tube because the total momentum of the gas particles comprising blast wave is conserved even though the shape of the blast wave may change. However, a secondary effect of the passage of the initial and reflected blast waves is that they leave the blast tube filled with gas at an elevated pressure and temperature. Subsequently, this gas escapes from the open end of the blast tube which, in effect, acts as rocket motor, as shown in Figure 5.27(f), and increases the total impulse transfer. This secondary effect explains why a persistent residual pressure is observed in the blast tube results but is not present in the short stand-off pressure histories. Furthermore, it is evident that a longer blast tube would contain a greater volume of gas, which explains why, for a given charge mass, the total impulse gradual increases with an increase in the blast tube length.

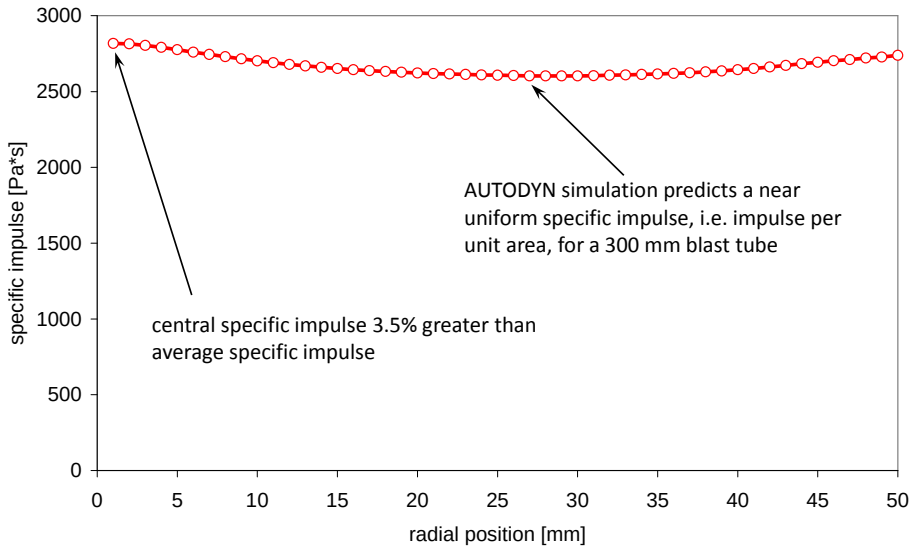

Figure 5.29: Numerical impulse intensity distribution for a 10 g charge mass in a 300 mm blast tube configuration.

Chapter 6

Experimental Results using the Instrumented Pendulum

> "It doesn't matter how beautiful your theory is,... If it doesn't agree with experiment, it's wrong."
>
> Richard Feynman (1918-1988)

6.1 Introduction

This chapter presents novel experimental results obtained for the peripherally clamped centrally supported (PCCS) and peripherally clamped annular (PCA) plate configurations using the instrumented pendulum in both the short stand-off and blast tube configurations. This experimental configuration has been developed specifically to produce data with a level of detail not generally available in the literature for the validation of theoretical models intended to study of the deformation and fracture of blast loaded plates. Some of the data presented in this chapter have been published during the course of this thesis [51–53].

The experimental configuration and the techniques for capturing and processing the experimental data are described in detail in Chapter 5. Nevertheless, some aspects of the experimental method, such as the repeatability of the blast test results, are revisited to evaluate the performance of the blast testing configuration in the context of the notion of precision tests, as defined in Chapter 1.

A detailed theoretical analysis and discussion of the results in this chapter are presented in Chapters 7 and 8, where it is shown that some of the terminology and parameter definitions used for peripherally clamped solid (PCS) plates are not suitable for the PCCS or PCA configurations. Hence, in the two subsections to follow, modified terms and definitions are presented, with limited initial justification, to allow for the concise presentation of the experimental results contained in this chapter. The validity of these modifications will become apparent upon presentation of the experimental results and the formal mathematical derivations in Chapter 7.

6.1.1 PCCS failure Modes

The distinct modes of failure that occur in blast loaded PCS plates were reviewed in Section 2.1.4. These failure mode definitions include the three distinct modes proposed by Teeling-Smith & Nurick [67], who followed the definitions of Menkes & Opat [48], and the subsequent refinements by Nurick *et al.* [70, 181] to include subcategories that distinguish between observed responses such as necking and tearing or complete and partial failure.

In the context of this thesis the relevant PCS failure modes are:

Mode I	Large inelastic deformation.
Mode II*	Partial tearing along the clamped boundary with large inelastic deformation.
Mode II	Complete tearing along the clamped boundary with large inelastic deformation.
Mode III	Complete transverse shearing along the clamped boundary without large inelastic deformation.

Through the course of this thesis it became apparent that the general behaviour of the PCCS circular plates did not conform to the conventional definitions. For example, under large blast loads it is possible for complete transverse shear failure to occur along the inner boundary with large inelastic deformation, which does not conform to any of the failure mode definitions given above. The implication of this contradiction, is that the distinction between the failure modes should not primarily be based on the appearance of the failure, *i.e.* tearing or shearing, or on whether large inelastic deformations occurred or not. Rather, it is proposed that the distinction should be based on the sequence in which the various failure mechanisms occur, which results in the following modifications to the failure modes definitions:

Mode I	Large inelastic deformation.
Mode II*	Partial failure (tearing or shearing) along a boundary subsequent to large inelastic deformation.
Mode II	Complete failure (tearing or shearing) along a boundary subsequent to large inelastic deformation.
Mode III	Complete failure (typically shearing) along a boundary prior to large inelastic deformation.

Illustrations of the revised definitions are given in Figure 6.1. The revised definitions adequately describe the behaviour of both PCS and PCCS plates. In effect, the proposed revisions extend the definitions of failure modes so as to make them more generally applicable. Hereafter, the results presented in this chapter will be discussed within the context of the revised failure mode definitions.

6.1.2 PCCS Dimensionless Impulse and Deflection

Following the blast data presentation format reviewed in Section 2.2.1 and critiqued in Section 3.2.1, the experimental results generated as part of this thesis will be presented in a dimensionless form. However, the definition of dimensionless impulse and deflection given in Section 2.2.1 is only suitable for PCS plates and is not applicable to PCCS or PCA plates. In blast tests on PCS plates, the plate geometry ensures that the maximum deflection will occur at a single point in the centre of the plate, even if the loading is slightly asymmetric. No such unique point exists for PCCS or PCA plates.

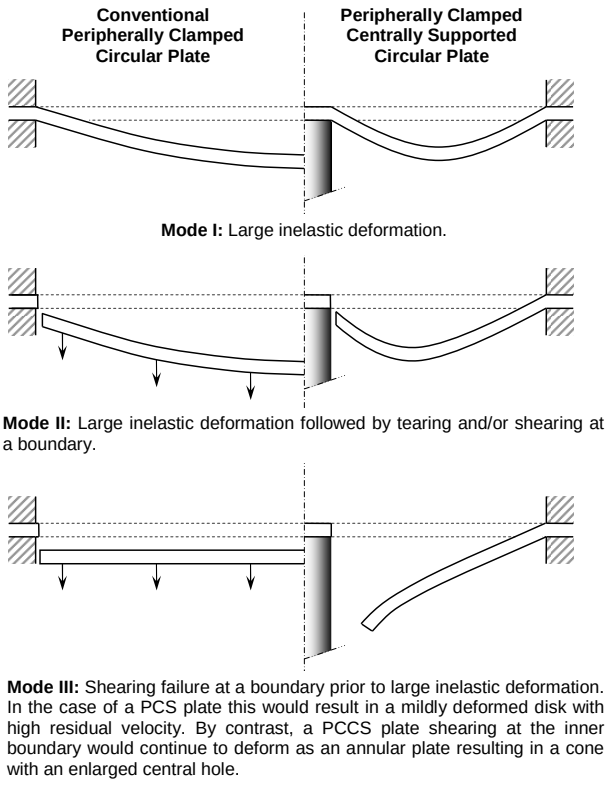

Figure 6.1: Modes of failure for a PCCS plate (right) compared with a PCS plate (left).

In an ideal blast test on a PCCS or PCA plate, the response will be axisymmetric and the maximum deflection will occur along a circumferential line as opposed to a single point. In other words, each infinitesimal segment of the plate will have one point that experienced that maximum displacement. It is difficult to experimentally achieve a perfectly symmetric blast load and the maximum displacement along an infinitesimal segment will typically differ from segment to segment. For the data presented in this thesis, the resulting asymmetry was quantified by firstly measuring the absolute maximum displacement of the plate, which is referred to as the max-max displacement. Secondly, the smallest value of all the maximum segment displacements was measured. This point is referred to as the min-max displacement and is a saddle point since it constitutes a local minimum with respect to the circumferential direction, but a local maximum with respect to the radial direction. The measured max-max and min-max displacement values for all the blast tests conducted as part of this thesis are recorded in Tables E.1 to E.21 in Appendix E. In this thesis, all deflection vs impulse data points will represent the mean of the max-max and min-max displacements, which is referred to as the ave-max displacement, with the extent of the variation between the max-max and min-max values indicated by error bars.

It is shown in Section 7.3 that the appropriate expression for the dimensionless impulse and deflection for PCCS and PCA plates is,

$$\delta = \frac{\tilde{w}}{H} \qquad \text{and} \qquad \phi = \frac{I}{\pi(R_o + R_i)H^2\sqrt{\rho\sigma_y}} \tag{6.1}$$

The form of Equation (6.1) is virtually identical the expressions given in Equations (2.1) and (2.2), except for the additional term R_i which is the inner radius of the PCCS or PCA specimen plate[1]. However, note that in this case $\tilde{w}$ refers to the ave-max deflection, as defined above, and not to the central deflection, as is the case for PCS plates. As an aside, it is interesting to note that Equation (2.1) is recovered when Equation (6.1) is applied to a PCS plate, for which inner radius vanishes.

6.2 Short Stand-Off Blast Test Results

In this section, the results of a series of blast test using the short stand-off configuration of the instrumented ballistic pendulum, as shown in Figures 5.1(a) and 5.2, are presented. In all, 31 blast tests were conducted on 1.6 mm thick mild steel plates with diameters of 100 mm, 130 mm or 160 mm, in addition to which the PCA plates had an inner diameter of 24 mm. The blast test results are summarized in Tables E.1 to E.5 while the material properties are presented in Appendix B.4. The data reported here regarding the 100 mm plates has been published by Cloete *et al.* [52], while the additional data concerning the 130 mm and 160 mm plates was reported by Palmer [182].

6.2.1 Impulse and Deflection

The dimensionless deflection vs dimensionless impulse results for the short stand-off PCCS and PCA blast tests are shown in Figure 6.2. As mentioned previously, the error bars on the data points indicate the difference between the absolute maximum and saddle point deflections and give an indication of the asymmetry of the permanent displacements observed in the deformed plates. In general, the deformed 100 mm plates displayed better symmetry than the 130 mm and 160 mm plates.

The four distinct deformation modes defined in Section 6.1.1 were observed in the PCCS plate deformation results, while only Mode I behaviour was observed in the PCA plate results. The failure mode classification was primarily conducted by visual inspection of the recovered plate and correlated with specific features of both the Impulse vs deflection data and the central support force history, as will be shown in Section 6.2.3. Figure 6.2 shows that the PCCS plate test data for all three plate diameters can be grouped into distinct mode response regions, although some overlap of the regions can occur.

The dotted lines represent least-squares regression fits for the Mode I responses of the PCCS and PCA plates. The regression formula for the Mode I responses of the PCCS plates is,

$$\delta = 0.2198\phi - 0.4495 \tag{6.2}$$

with a r^2 correlation coefficient of 0.9141, while that for the PCA plates is,

$$\delta = 0.6673\phi - 0.8529 \tag{6.3}$$

with a r^2 correlation coefficient of 0.9681.

[1]The use of $(R_o + R_i)$ in Equation (6.1) is somewhat counter intuitive since $(R_o - R_i)$ represents the radial width of a PCCS or PCS plate. The reason for this is discussed in Section 7.3.1.

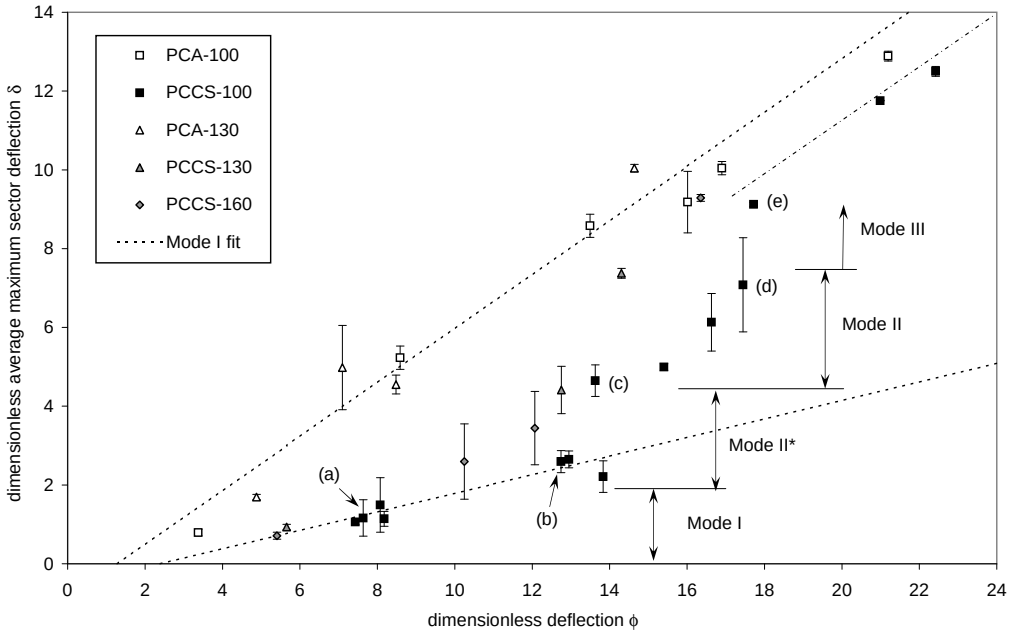

Figure 6.2: Dimensionless deflection vs impulse data for the short stand-off blast tests. The annotations (a) to (e) relate to the specific tests considered in Sections 6.2.2 and 6.2.3.

The majority of the ave-max data points lie within a half plate thickness of the regression line, the exception being a pair of PCA data points for the 130 mm plates that are within a plate thickness. From Figure 6.2 it appears that Equation (6.1) provides a valid correlation for the Mode I behaviour of plates of varying diameter in both the PCCS and PCS plate configurations. Similar results for plates of varying thickness are given in Section 6.3.1.

The Mode I to II* transition is not clearly distinguishable in Figure 6.2 since some of the Mode II* data points tend to lie close to the Mode I correlation. By contrast, the transition to Mode II behaviour is characterized by a strong deviation from the Mode I correlation, where a small increase in impulse leads to a large increasing trend in the dimensionless deflection. Similarly, the Mode III data points are distinguished by a transition to a third trend which tends toward the PCA Mode I correlation These trends are discussed in greater detail in Section 6.2.3.

In addition to the final deflection vs impulse results, which is the traditional data obtained from ballistic pendulum tests, the PCCS and PCA plate configurations allow for two complementary global response measurements, namely the final central hole diameter and the fraction of the total impulse transferred through the central support.

Figure 6.3 shows the final hole diameter in relation to the total impulse. In the case of the PCA plates, the final hole size increases steadily with an increase in the total impulse. By contrast, for the PCCS plates, hole formation and enlargement shows three distinct regions that correlate with specific deformation modes. The first region corresponds to Mode I and II* behaviour, to which a value of zero is assigned since complete holes were not formed. The second region corresponds to Mode II behaviour, where a complete hole was formed but the final hole size showed only a slight increase with increasing total impulse. Finally, the transition to Mode III behaviour is characterized by a marked increase in the final

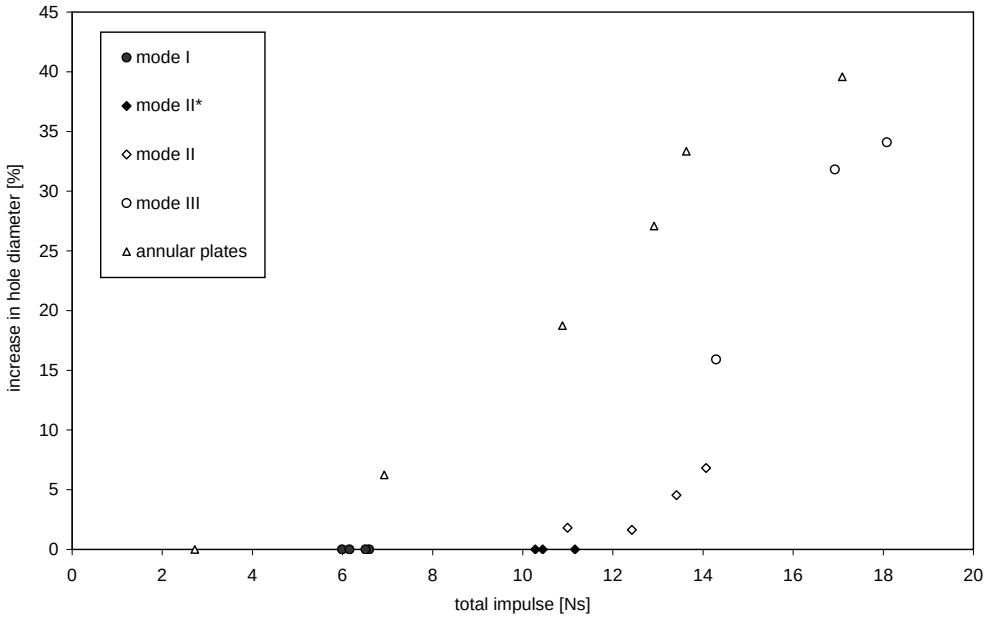

Figure 6.3: Increase in the final hole diameter vs the total impulse for the 100 mm PCA and PCCS plates. Data points corresponding to Mode I and Mode II* behaviour, where no hole was formed, are included for the sake of comparison.

hole size with increasing total impulse. Furthermore, as with the dimensionless impulse, at larger impulses the Mode III data tends toward the PCA Mode I data.

The transitions between the failure modes is also evident in the fraction of the total impulse transferred through the central support, as shown in Figure 6.4, where the data is depicted as a function of the total impulse for the 100 mm PCA and PCCS plates. The central support impulse fraction is obtained by integrating the central support signal as discussed in Section 5.3.1.3, where the PCA data is used to assess the impulse distribution during short stand-off blast loading and its slight decreasing trend is discussed. The PCA data is included in Figure 6.4 for comparison with the PCCS data, for which it essentially serves as a lower limit.

In the case of the PCCS Mode I results, the data is clustered about an impulse of 6 Ns and no clear trend can be obtained. However, there is a clear downward trend from Mode I to II* behaviour. This trend appears to become steeper during the transition to Mode II behaviour, where a distinct drop is evident at a load of approximately 11 Ns, *i.e.* $\phi = 13.6$, which correlates well with Mode II* to II transition in Figure 6.2. After this, the central support impulse fraction decreases steadily as the total impulse increases. The transition to Mode III behaviour appears to be marked by a slight drop in the impulse fraction, but this may simply be an artifact of the sparse data set. Nevertheless, as the total impulse is increased, the combined Mode II and III data points appear to approach an asymptote that is similar to, but greater than, the PCA Mode I trend.

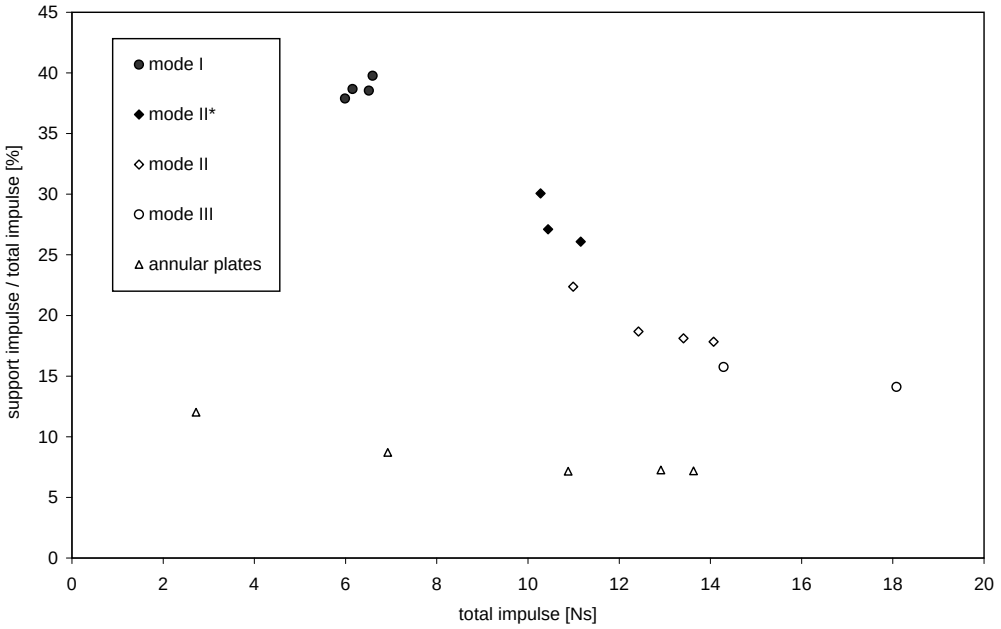

Figure 6.4: Fraction of the total impulse transferred through the central support vs the total impulse for the 100 mm PCA and PCCS plates.

6.2.2 Central Support Force Histories

A selection of central support force histories from five blast tests on 100 mm PCCS plates are shown in Figure 6.5. The curve numbers (a) to (e) correspond to the annotations in Figure 6.2 where the corresponding dimensionless impulse vs deflection data points are indicated. Note that these curves represent the combined effect of the blast pressure and the shear force at the inner boundary of the plate. Hence, the curves will be referred to as force histories even though the units of MPa have been retained to allow for a direct comparison with Figures 5.15 and 5.16. The curves depicted in Figure 6.5 are representative of the typical central support force histories obtained for different failure modes and are discussed in detail in Section 6.2.3.

Some general observations regarding the repeatability of the PCCS plate configuration can be drawn from Figure 6.5. Firstly, all the curves in Figure 6.5 show consistent initial spikes that are also consistent with the initial pressure spikes observed in the curves in PCA test, as shown in Figures 5.15 and 5.16. This implies that the initial spike is primarily due to the blast pressure propagating through the plate specimen and directly into the central support, *i.e.* there is no significant contribution due to plate deformation. Secondly, other than curve (a), the force histories all show a clear secondary spike that increases in magnitude with an increase in the mass of the ring charge. These results support the conclusion in Section 5.3.1.2 that the secondary spike is a result of the ring charge and, consequently, that the initial spike is due to the leader charge. Furthermore, the lack of a clear secondary spike in curve (a) suggests that the small ring charge mass of 2 g has deflagrated, which supports the conclusion in Section 5.3.1.1 regarding the critical explosive thickness required for detonation.

A further example of the repeatability of the PCCS plate configuration is shown in Figure 6.6 where the central support force history for two nominally identical PCCS plate tests with 7 g charges are compared.

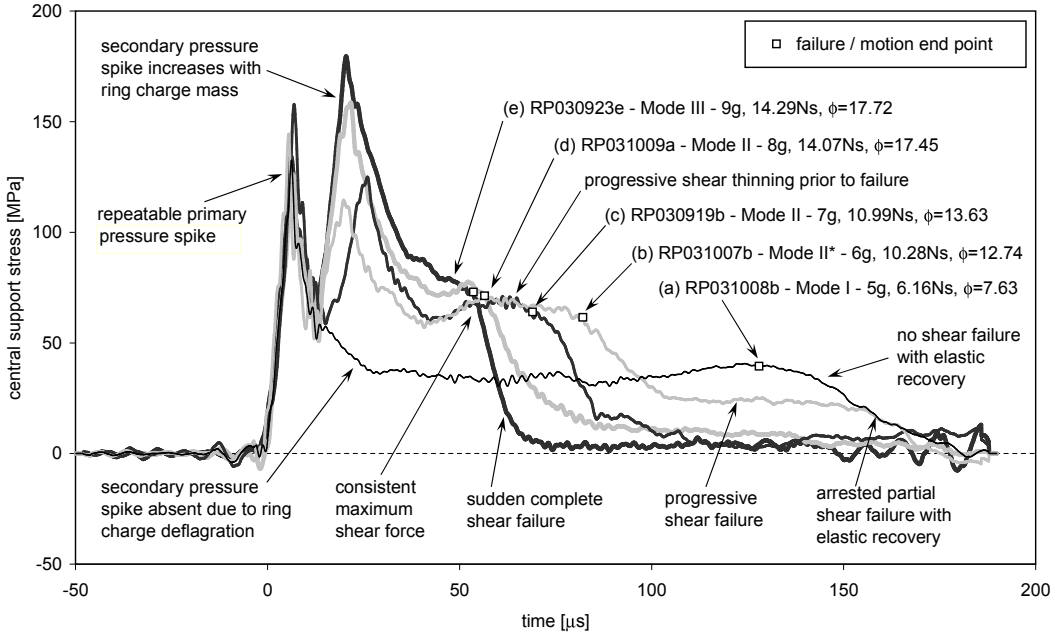

Figure 6.5: Comparison of the central support force histories of five short stand-off blast test on 100 mm diameter PCCS plates.

The two curves show good repeatability, even though the total impulse values are slightly different. Furthermore, the displacements, as recorded in Table E.2, were also similar with the larger impulse resulting in a slightly larger deflection.

The demonstrated repeatability and consistency of the PCCS and PCA plate configurations allows for the comparison of their force histories so as to isolate the shear force contribution in the PCCS plate tests. For example, PCCS plate test number RP031009a (see Figure 6.5) was loaded with a nominally identical 8 g charge to that used in PCA test RP031009b (see Figure 5.16). A comparison between these two test is shown in Figure 6.7. The force histories both exhibit two spikes of similar magnitude and timing within the first 30 μs. However, after the second spike the signals differ considerably, with the pressure history for the PCA plate test decaying exponentially to zero, while for the PCCS plate test a local maximum is observed after approximately 50 μs. Since the two tests differ only with respect to their inner boundary conditions, the force difference is attributed to the interaction of the PCCS plate with the central support through shear forces along the inner boundary. Based on this observation, an estimate of the contribution of the plate response to the force history is obtained by subtracting the force history of the PCA plate test from the that of the PCCS plate test. The resulting estimate for the force history due to the plate response is depicted by the thick grey curve in Figure 6.7.

The plate response curve in Figure 6.7 is referred to as an estimate in the sense that the original curves are obtained from two different tests and thus the blast pressure histories are unlikely to be identical. Hence, some portions of the curve may not accurately represent the exact plate response. In particular, the dip in the plate response curve between 20 μs and 25 μs is not considered to represent the plate behaviour. Nevertheless, from approximately 30 μs onward the plate response appears to dominate. Hence, an estimate of the nominal transverse shear stress in the specimen plate along the inner boundary

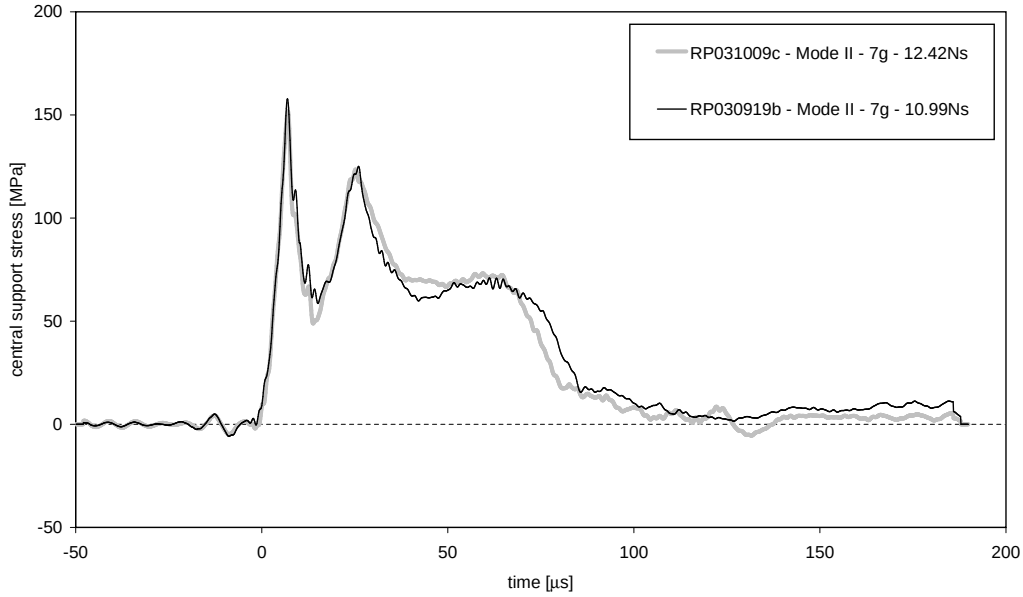

Figure 6.6: Repeatability of the central support force history for two nominally identical PCCS plate tests.

can be obtained by multiplying the recorded signal by the cross-sectional area of the central support bar and dividing by the transverse shear area, *i.e.* the product of the plate thickness and the inner boundary perimeter. For example, the force history in Figure 6.7 has a maximum of 77 MPa at 53 μs, which implies a peak nominal shear stress of approximately 265 MPa.

The features discussed above appeared, to varying degrees, in the support bar signals for all the PCCS plate tests. Based on the above observations, stress spikes that appear in the support bar signals were taken to be a result of the blast wave propagating through the plate and directly in the central support, while features that appear after approximately 50 μs were taken to be representative of the shear forces at the inner boundary due to the plate response. The implications of nominal shear stress results are discussed in Section 6.2.3.

6.2.3 Detailed Experimental Observations

In this section, the complete response behaviour of the five of the short stand-off blast tests on 100 mm diameter PCCS plates considered in Section 6.2.2 are discussed in detail. Photographs of the five recovered plate specimens that are representative of the observed failure modes are shown in Figure 6.8, where the plate specimen numbers (a) to (e) correspond to the annotated impulse vs deflection data points in Figure 6.2 and the curve numbers in Figure 6.5.

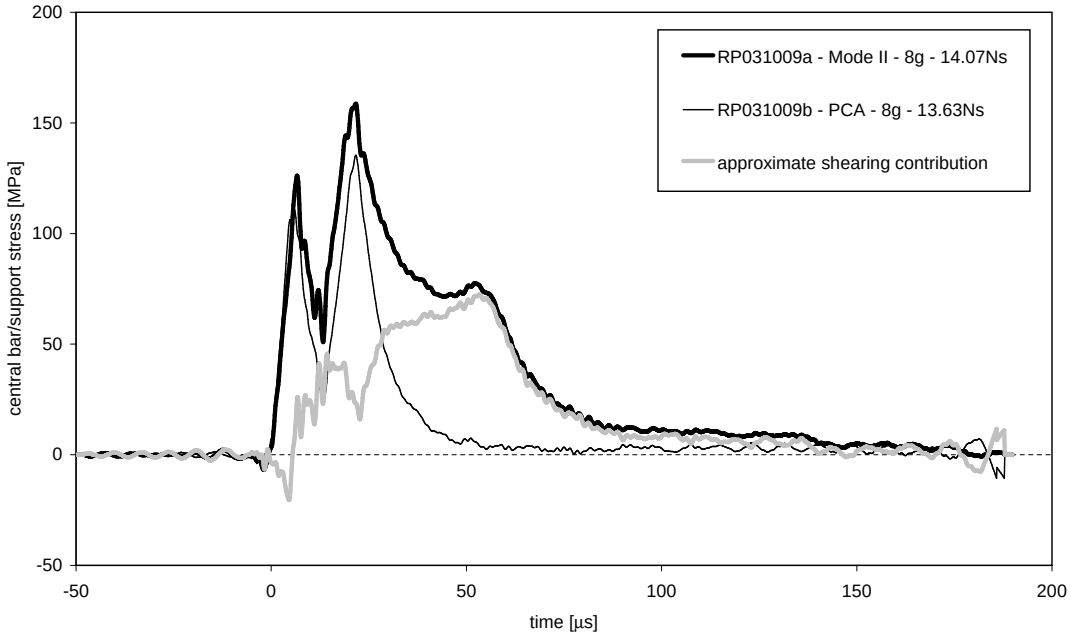

Figure 6.7: Estimate of shear force history at the central support boundary by comparison of PCA and PCCS results from short stand-off blast tests.

6.2.3.1 Mode I

Figure 6.8(a) shows the recovered plate specimen from test number RP031008b, for which the total charge mass was 5 g and resulted in a total impulse of 6.16 Ns ($\phi = 7.63$). The recovered plate exhibits large plastic deformation but no shear or tensile failure at the boundaries, *i.e.* a Mode I response.

In addition to test number RP031008b, three other 100 mm diameter PCCS plates displayed a similar Mode I response. As shown in Figure 5.14, all four tests have impulse values clustered between 6 Ns and 6.6 Ns, *i.e.* $\phi = 7$ and $\phi = 8.5$, even though the corresponding charge masses vary between 5 g and 7 g. The reason for this is sporadic deflagration of the ring charge when the total charge mass was below 7 g, as shown in Section 5.3.1.1. Conversely, when ring charge detonation did occur, the impulse was considerably higher and resulted in shear failure. Hence, it proved difficult to achieve a broad range of Mode I behaviour, which is one of the reasons for the development of the blast tube configuration.

In Figure 6.4, the data points corresponding to Mode I failure indicate that approximately 37 % to 40 % of the total impulse passed through the central support. In other words, the reaction force required to arrest the plate motion is divided between the inner and outer boundaries, with the outer boundary making a slightly larger contribution. However, given the greater extent of the outer boundary, the stress at the inner boundary is expected to be higher than at the outer boundary, which explains why initial failure occurs at the inner boundary.

Test number RP031008b corresponds to curve (a) in Figure 6.5, which shows the characteristic initial spike, but no clear secondary spike. Following the conclusions in Section 6.2.2, the initial spike is due to detonation of the leader charge, while the lack of a clear secondary spike is further evidence of the deflagration of the 2 g ring charge. After the initial spike, the signal maintains a level of approximately

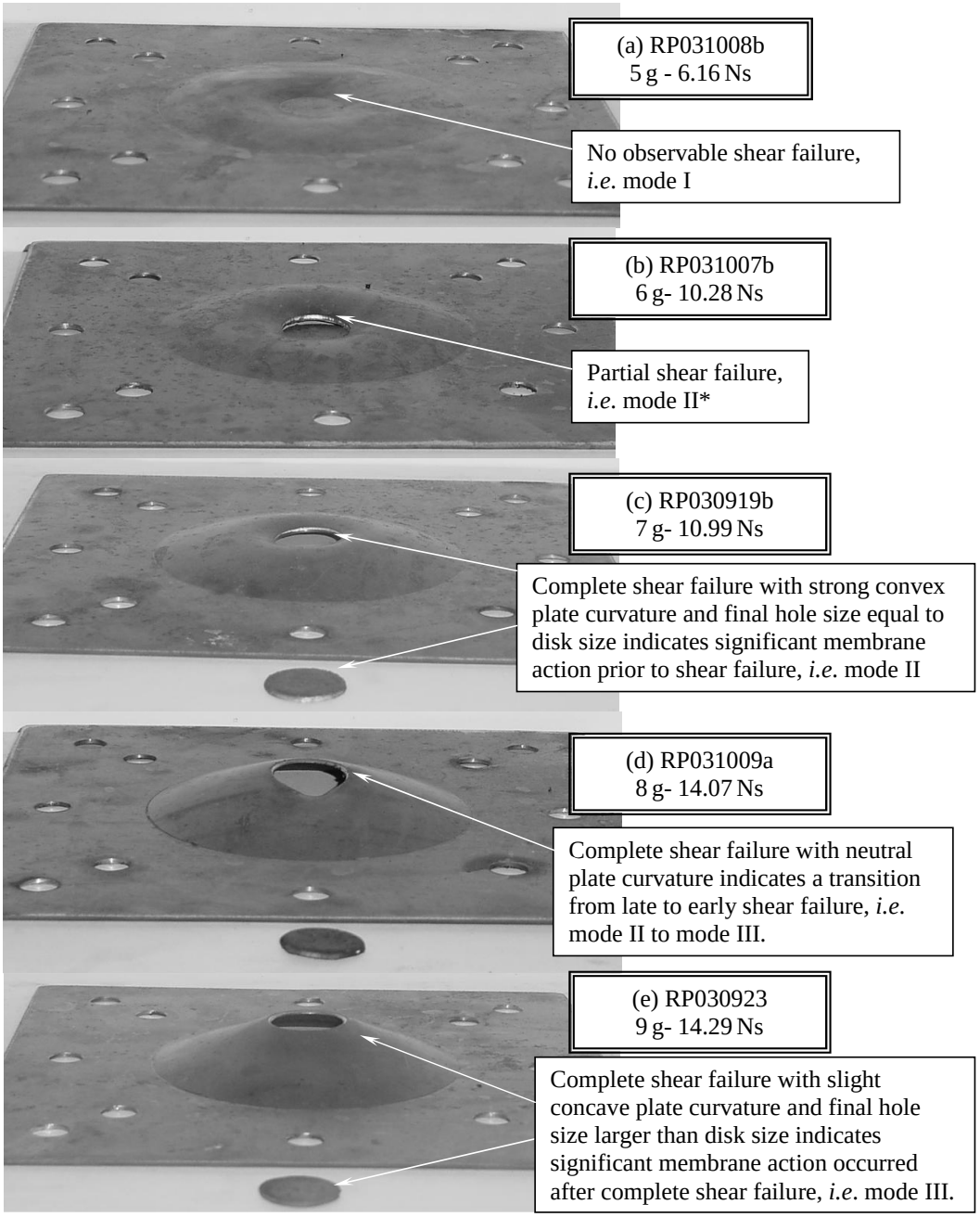

Figure 6.8: Photographs of short stand-off blast tested 100 mm PCCS plate specimens. The plate numbering (a) to (e) corresponds to those in Figures 6.2 and 6.5.

35 MPa until it begins to rise again at 100 μs and reaches a maximum of 40 MPa after approximately 130 μs, which implies a peak nominal shear stress of approximately 138 MPa. This is equivalent to a Mises stress of 238 MPa, which is well below the quasi static yield strength of the material, as shown in Figure B.1 in Appendix B, and is therefore consistent with the observed Mode I response.

Following the peak at 130 μs, the signal gradually decreases to zero at approximately 180 μs. The shape of this portion of the force history resembles a quarter period of a cosine curve, which can be interpreted in terms of the elastic rebound of the plate. Blast loaded plates are known to experience residual elastic vibrations after the plastic deformation is complete [56, 61]. In essence, the plastic deformation process terminates at the point of maximum deflection, after which the residual elastic strain energy in the plate causes the plate to rebound, initiating a vibration about the final static equilibrium position. In the PCCS configuration, the rebounding plate continues to exert a force on the central support. However, the interface between the plate specimen and the central support cannot sustain a tensile stress and hence the plate separates from the central support after the first quarter of the vibration period, which explains the cosine shape of the final portion of signal. Note that this interpretation draws an important distinction between the duration of the recorded central support bar signal and the deformation duration of the plate. In this thesis, the Mode I deformation duration is defined as the time to reach maximum displacement, which excludes the elastic rebound portion of the force history. In other words, the deformation duration coincides with the point of peak nominal shear stress at 130 μs, which signifies the end of the plastic deformation response.

6.2.3.2 Mode II*

Figure 6.8(b) shows the recovered plate specimen from test number RP031007b, for which the total charge mass was 6 g and resulted in a total impulse of 10.28 Ns ($\phi = 12.74$). The recovered plate exhibits large plastic deformation with partial shear failure at the inner boundary, *i.e.* a Mode II* response.

The corresponding data point (b) in Figure 6.2 lies close to the Mode I correlation, as noted in Section 6.2.1. The reason for this is that the partial fracture around a small portion of the inner diameter does not significantly increase the general plate deformation. Nevertheless, the partial shear fracture is sufficient to cause some unloading of the inner boundary, which is reflected in the decrease in the fraction of the total impulse transferred through the central support, as shown in Figure 6.4.

The corresponding curve (b) in Figure 6.5 shows the characteristic initial and secondary spike of the short stand-off charge configuration. After the secondary spike, the force history drops slightly as the blast pressure decays and then rises to a peak value of approximately 70 MPa at 57 μs as the plate response begins to dominate. Assuming that the blast pressure is negligible at this point, the peak force implies a peak nominal shear stress of approximately 240 MPa, *i.e.* a Mises equivalent of 417 MPa. This value is considerably above the quasi-static yield strength of the material and is therefore consistent with the observed Mode II* response. However, the fact that such a large shear stress lead only to partial failure suggests that strain rate effects are significant.

Curve (b) displays two plateau like features. The first plateau begins at the point of peak nominal shear stress at 57 μs, after which the support stress drops slightly to 60 MPa at 82 μs, which equates to a nominal transverse shear stress of 206 MPa. At this point a sudden drop occurs indicating that shear

failure has taken place. The fact that shear failure does not occur at the point of maximum shear stress suggests that a finite amount of shear sliding occurs at the boundary prior to shear failure [183]. Shear sliding decreases the effective shear area while the associated plastic work increases the temperature in the shearing region. A combination of these factors can explain the slight drop in the shear strength prior to a point where the shear stress can no longer be sustained resulting in the initiation of shear fracture via unstable thermoplastic shear. Evidence of some shear sliding is observed in the deformed plate along portions of the inner boundary that did not fracture.

The second plateau occurs after the initiation shear where the signal does not drop to zero, but levels off at 25 MPa at 105 μs, indicating that the shear failure did not occur simultaneously around the entire inner boundary. This result is consistent with the partial shear failure observed along the inner boundary of the deformed specimen, which is characteristic of Mode II*. The stress plateau of 25 MPa persists for a considerable time before the signal drops to zero after 170 μs. This could be indicative of the stress level required in the support bar to sustain the shear process zone as it moves along the inner support boundary.

6.2.3.3 Mode II

Figure 6.8(c) shows the recovered plate specimen from test number RP030919b, for which the total charge mass was 7 g and resulted in a total impulse of 10.99 Ns ($\phi = 13.63$). The recovered plate exhibits large plastic deformation with complete shear failure at the inner boundary. In addition, the plate shows strong convex curvature adjacent to the inner boundary with no significant hole enlargement, which indicates that a large portion of the plastic deformation occurred prior to shear failure, *i.e.* a Mode II response.

In addition to test number RP030919b, three other 100 mm diameter PCCS plates displayed a similar Mode II response. As noted in Section 6.2.1, the Mode II data points form a trend that deviates strongly from the Mode I correlation, *i.e.* a small increase in impulse leads to a large increase in the dimensionless deflection. Furthermore, all the Mode II plate specimens experienced limited hole enlargement, as shown in Figure 6.3, where an increasing impulse results in only a small increase in the final hole diameter. These two observations show that the portion of the plastic deformation occurring after shear fracture steadily increases with an increasing impulse, which suggests that the fracture event begins to occur earlier in the deformation history. The effect of complete shear failure along the inner boundary is also evident in Figure 6.4, where the transition to a Mode II response is associated with a distinct drop in the central support impulse fraction. This reflects the fact that plate separation from the central support has occurred before the plate motion has been fully arrested, with the result that less of the total impulse is transferred through the central support.

Test number RP030919b corresponds to curve (c) in Figure 6.5, which has several features that are similar to those in test RP031007b, such as the two characteristic force spikes and the subsequent slight drop in the force history prior to a rise to a practically identical peak value of approximately 70 MPa at 57 μs. However, the subsequent plateau is only half the length of that in test RP031007b, with initial shear fracture occurring at 72 μs, even though the stress levels were virtually identical. This behaviour suggests that the maximum shear stress is an inherent material property of the plate while the shear force duration depends on the test parameters, *i.e.* the plate velocity induced by the blast wave.

After fracture initiation, the force history drops rapidly to zero, with only a small plateau occurring between 87 μs and 95 μs, indicating that shear failure had occurred simultaneously along most of the inner boundary. This interpretation is confirmed by the observation that the plate had separated from the central support and a shear disk had formed on the central support. Separation occurred after approximately 110 μs, which is significantly earlier than in test number RP031007b.

6.2.3.4 Mode II to Mode III

Figure 6.8(d) shows the recovered plate specimen from test number RP031009a, for which the total charge mass was 8 g and resulted in a total impulse of 14.07 Ns ($\phi = 17.45$). The recovered plate exhibits large plastic deformation with complete shear failure at the inner boundary. However, unlike test RP030919b, the plate shows only a slight convex curvature near the inner boundary, which indicates that a relatively small amount of deformation still occurred prior to failure, *i.e.* a plate response is close to the transition between Mode II and Mode III. This conclusion is supported by the final hole size of 23.5 mm, which indicates that a small but noticeable amount of hole enlargement has occurred.

The corresponding curve (d) in Figure 6.5 is only superficially similar to those for tests RP031007b and RP030919b. For example, while curve (d) shows two force spikes, the secondary spike is greater in magnitude than the initial spike, indicating the dominant contribution of the ring charge to the total impulse. The force history shows a slight rise following the decay of the blast pressure and reaches a maximum of 77 MPa after 53 μs, which is higher and earlier than the corresponding point in the preceding tests. However, the most significant difference is the lack of a force plateau after the peak value. In this case, the force history shows a short drop to a value of 71 MPa after 57 μs, after which the initiation of shear fracture occurs. The force values equate to a maximum nominal shear stress of 265 MPa, while at fracture initiation it is 244 MPa. The shear fracture occurs approximately 16 μs earlier than in test RP030919b. It is shown in Section 7.4 that this is a significant period in the context of the overall plate response time and indicates that the plate fails early in the deformation process. Nevertheless, the slight delay from the peak force value and the shear fracture suggest a brief period of deformation and shear sliding, which correlates with the Mode II behaviour.

In addition to the force history, the earlier separation is reflected in the central support impulse fraction, which deceases steadily as the total impulse increases, because the time available to transfer momentum to the central support is reduced. The earlier fracture is also consistent with the increased deformation and hole enlargement since more time and residual kinetic energy is available for post fracture deformation.

6.2.3.5 Mode III

Figure 6.8(e) shows the recovered plate specimen from test number RP030923e, for which the total charge mass was 9 g and resulted in a total impulse of 14.29 Ns ($\phi = 17.72$). The recovered plate exhibits large plastic deformation with complete shear failure at the inner boundary. Furthermore, the plate has a final hole size of 25.5 mm, *i.e.* a substantial amount of hole enlargement has occurred, and shows a distinct concave curvature adjacent the inner boundary. Both of these features suggests that the majority of the plastic deformation occurred after the shear failure, *i.e.* a Mode III response.

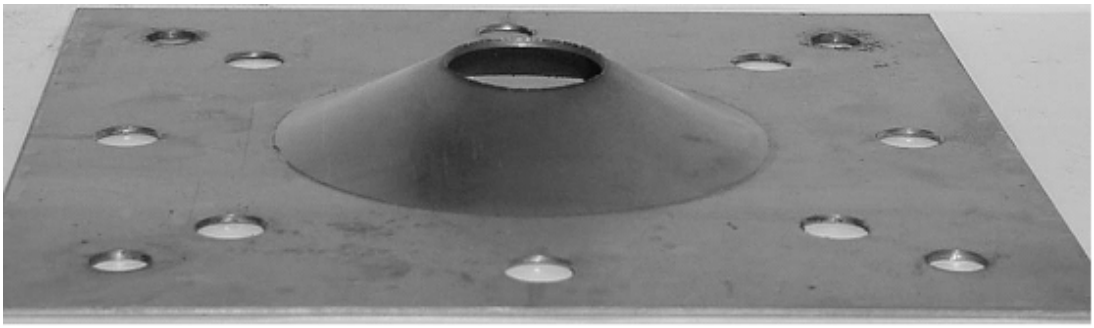

Figure 6.9: Photograph of the deformed PCA plate for test number RP031009b.

While the preceding observations are sufficient to categorize the plate response as Mode III, the diagnostic features of the recovered plate can be subtle when compared to the upper range of the Mode II response and supplemental diagnostics are preferable for precision testing. The most characteristic feature of a PCCS Mode III response is the early and complete shear fracture around the inner boundary, subsequent to which large plastic deformation occurs. In other words, after fracture, a PCCS plate essentially behaves as a PCA plate. As discussed in Section 5.2.3, this was the original motivation for conducting PCA tests, *i.e.* the Mode III response of a PCCS plates is expected to be similar to a PCA plates, which provides a basis for identifying the transition from Mode II to Mode III response.

Figure 6.9 shows the recovered plate specimen from PCA plate test number RP031009b, for which the total charge mass was 8 g and resulted in a total impulse of 13.63 Ns ($\phi = 16.90$). Other than the central hole, the initial geometry and material properties of the PCA plate specimen were nominally identical to preceding PCCS plates. It is evident that the final shape of the PCA plate is essentially identical to that of PCCS plate test RP030923e, which supports the Mode III classification of the latter.

In addition to a visual comparison with PCA plates, the Mode III response of the PCCS plates is also evident in the impulse vs deflection results. Table E.2 indicates that two other 100 mm diameter PCCS plates displayed the characteristic features of a Mode III response. Figure 6.2 shows that these Mode III data points all have large dimensionless impulse values above $\phi = 17.5$. Furthermore, as noted in Section 6.2.1, the Mode III data points clearly deviate from the Mode II trend. In particular, they appear to asymptote toward a trend line that is parallel to that of the PCA Mode I data, but offset by a dimensionless impulse of approximately $\phi = 2$, *i.e.* an impulse offset of 1.65 Ns. This observation of asymptotic behaviour is somewhat tentative due to the sparse data and forms part of the motivation for the larger blast tube test series reported in Section 6.3. Nevertheless, the results confirm that the PCA data can be used, as intended, to distinguish the onset of Mode III behaviour and correlates well with the visual assessment of the recovered plate specimens. The impulse offset between the PCCS Mode III and PCA Mode I trends is interpreted as the impulse transferred to the central support through the shear force at the inner boundary of the PCCS plate, since the configurations are essentially identical in all other respects.

The distinct Mode III behaviour is also evident in Figure 6.3 where significantly larger final hole diameters are observed for all the plates specimens displaying a Mode III response, as compared to the Mode II data. This result supports the mode definitions proposed in Section 6.1.1, *i.e.* that shear failure occurs earlier during Mode III, after which the plate behaves as a PCA plate. Furthermore, the degree of hole

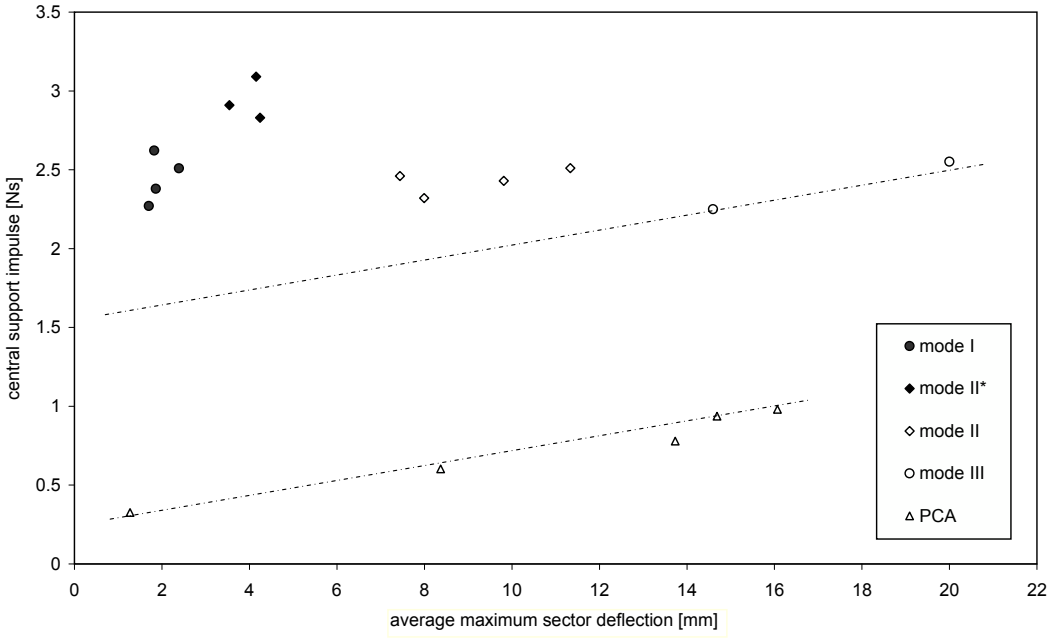

Figure 6.10: The central support impulse as a function of the average maximum sector deflection.

enlargement increases with an increasing impulse, which forms a trend that is approximately parallel to the PCA Mode I data, and has a similar impulse offset as observed in the dimensionless deflection data.

Unlike the deflection data, distinctive Mode III behaviour is not as apparent in Figure 6.4, where, as the impulse increases, the central support impulse fraction decreases steadily from Mode II to Mode III. Nevertheless, the impulse offset is still evident. A clearer indication of the impulse offset is given in Figure 6.10, where the central support impulse is depicted in relation to the average maximum sector deflection. The Mode III data is too sparse to obtain a reliable trend line, in lieu of which, two parallel chain lines are included in Figure 6.10 as visual aids. The results indicate that the impulse offset between the PCA Mode I and PCCS Mode III data is approximately 1.6 Ns. Given that the impulse values are obtained by integrating the central support force histories, this results confirms the interpretation of the impulse offset as due to the shear forces at the inner PCCS plate boundary. Furthermore, since both the ballistic pendulum analysis and integration of the central support signals provide close to identical values for the impulse offset, these results indicate that the instrumented ballistic pendulum fulfills the measurement redundancy requirement of a precision experiment, as described in Section 1.1.2, *i.e.* certain important experimental parameters can be inferred by independent measurements.

The central support signal from which the impulse fraction was determined for test RP030923e is depicted as curve (e) in Figure 6.5. The force history is similar to curve (d) of test RP031009a, but has some distinct features. For example, curve (e) shows two force spikes, with a dominant secondary spike. However, unlike curve (d), there is no slight rise following the decay of the blast pressure. This suggests that complete shear fracture occurs before the blast load has dissipated. Nevertheless, the point of fracture initiation can still be discerned by the sudden drop in the force history after 53 μs, which is a short interval in the context in the overall plate response. The stress level in the support at the time of failure is 73 MPa and equates to a nominal transverse shear stress of 251 MPa. This is slightly lower than the corresponding point in the

test RP031009a, and suggests a more intense shear banding event. The absence of significant deformation prior to the shear failure implies that bending and membrane stresses would have been relatively small and that the Von Mises equivalent failure stress can be estimated based on the shear stress alone, which gives a result of 435 MPa. These force history results confirm the defining characteristic of a PCCS Mode III response, *i.e.* the early and complete shear fracture around the inner boundary prior to extensive plastic deformation, and are consistent with other features such as the large final hole diameters.

6.2.4 Summary of General Observations

From the foregoing analyses, a number of general observations can be made. Firstly, the short stand-off configuration of the instrumented ballistic pendulum provides consistent and repeatable results. This is particularly evident in the good r^2 values of 0.9141 and 0.9681 obtained in Section 6.2.1 for the Mode I correlations of the dimensionless deflection and impulse data of both the PCCS and PCA plate configurations, respectively. The repeatability is also evident in the magnitude and shape of the initial force spike in Figure 6.5, which is consistent with the fact that nominally identical leader charges were used in every test. Furthermore, the increases in the magnitude of the second stress spike corresponded to an increase in the mass of the ring charge, confirming the link between them.

The four failure modes defined in Section 6.1.1 and shown in Figure 6.1 are observed in the recovered PCCS plates shown in Figure 6.8. Furthermore, the transition behaviour is evident in plots of the global experimental data, such as the dimensionless impulse and deflection, the degree of central hole expansion and the central support impulse fraction, *i.e.* Figures 6.2, 6.3 and 6.4. The identification of the Mode II to III transition is aided by the comparison of PCCS data to the PCA results, which also provides a basis for estimating the shear force history at the inner boundary, as shown in Figure 6.7.

The mode response transition point correlated well with recorded force history signals, where each response regime is associated with specific signal features. The time to failure decreases with increasing impulse, while the nominal transverse shear stress at failure increases slightly from 206 MPa in test number RP031007b to 251 MPa in test RP030923e, indicating a certain amount of rate sensitivity in the failure behaviour.

A particularly interesting observation is that in every test that exhibited shear fracture the maximum plate response occurs at approximately the same time (53 μs - 57 μs) with virtually identical magnitudes (70 MPa - 77 MPa). In other words, the maximum nominal transverse shear stress that the specimen plates can sustain along the inner boundary is relatively consistent and fracture initiation at this point marks the transition from Mode II to Mode III failure. This experimental result lends support to the maximum shear stress criterion used by Olson *et al.* [184, 185] for the prediction of Mode III failure.

6.2.5 The Short Stand-Off PCCS Configuration as a Precision Blast Test

In the preceding sections, the blast test results obtained using the instrumented ballistic pendulum with the PCCS and PCA plate test configurations are shown to address all of the precision test criteria in outlined in Section 1.1.2. This is particularly evident in the high level of repeatability of the blast load and plate response, especially considering that the tests were conducted by two different researchers

over a period of 7 months. Furthermore, other requirements are also addressed, such as the well defined boundary conditions and measurement redundancy. This topic is considered in greater detail in Chapter 9.

Notwithstanding these results, certain aspects of the short stand-off configuration are considered to be sub-optimal from the perspective of analytical and numerical analysis. In particular, the blast pressure and impulse intensity, though repeatable, is not uniform in space and time. Furthermore, the small charge masses required for low impulse values are difficult to control. These considerations, in conjunction the desire for a larger set of data are the primary motivation for the blast tube configuration, the results of which are presented in the next section.

6.3 Blast Tube Test Results

In this section, the results of a series of blast tests using the 300 mm blast tube configuration of the instrumented ballistic pendulum, as shown in Figures 5.1(b) and 5.3, are presented. In all, 155 blast tests were conducted on PCCS and PCA mild steel plate specimens machined from five separate sheets of material[2]. Material sheets I, II and III all had a nominal thickness of 1.6 mm, while sheets IV and V had nominal thicknesses of 2 mm and 3 mm respectively. In this thesis, groups of plates are referred to in terms of their nominal thickness, but all calculations are based on the measured thicknesses of the individual plates. The individual plates thicknesses are reported as part of the blast test results summarized in Tables E.7 to E.21, while the material properties are presented in Appendix B.5. All the plates had a clamped outer diameter of 100 mm, in addition to which the PCA plates had an inner diameter of 21 mm to ensure that no contact was made with the central support. The majority of the blast tests were conducted using a central support bar with square front face edge condition. However, an additional series of 1.6 mm PCCS plate tests were conducted using a central support bar with a 2 mm radius front face edge condition. The squared and radiused edge conditions are indicated using the designations R0 and R2 respectively. A portion of the data reported here regarding the 1.6 mm and 2 mm plates has been published by Cloete & Nurick [53].

6.3.1 Impulse and Deflection

The dimensionless deflection vs impulse results for the blast tube test on PCCS and PCA plates are shown in Figure 6.11. As before, the error bars indicate the difference between the absolute maximum and saddle point deflections, giving an indication of the asymmetry of the permanent deformation observed in the recovered plates. The legend indicates from which sheet the specimen were machined, the corresponding average sheet thickness, the specimen configuration and the edge radius of the central support. It is evident in Figure 6.11 that the error bars are smaller on average than those in Figure 6.2, which suggests that a more consistently uniform load was achieved with the blast tube configuration.

The four distinct deformation modes defined in Section 6.1.1 were observed in the recovered PCCS plates, while the PCA plate exhibited only Mode I behaviour. The modes were classified by visual inspection and correlated with specific features of the both the Impulse vs deflection data and the central support force history, as will be discussed in Section 6.3.3. Figure 6.11 shows that the dimensionless PCCS plate

[2]Tests conducted using other blast tube lengths are not considered in this section.

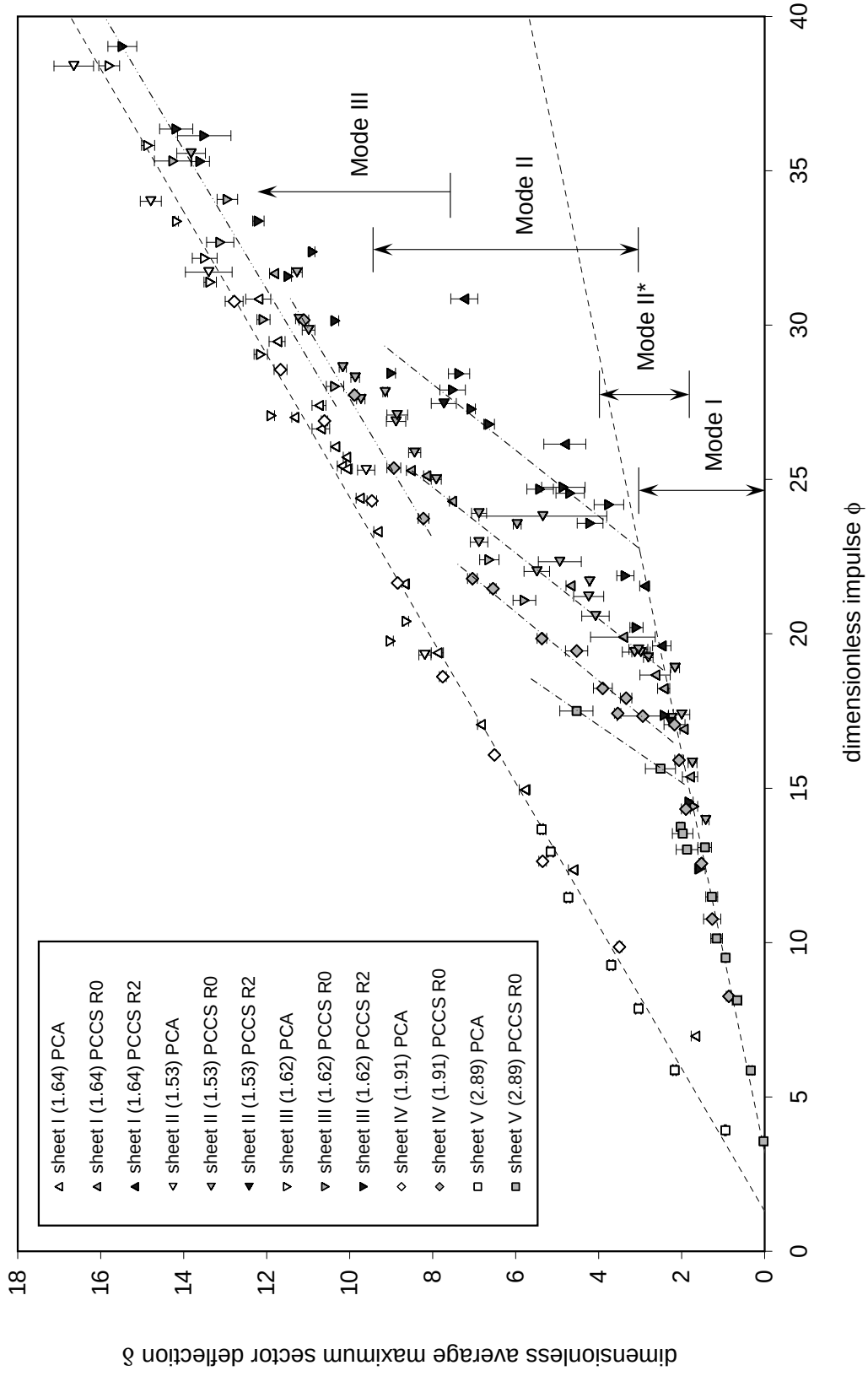

Figure 6.11: Dimensionless deflection vs impulse data for blast tests on 100 mm diameter PCCS and PCA plates using a 300 mm blast tube. The dashed lines represent linear regression fits to the ModeI response of both the PCA and PCCS data. The single dot chain lines delineate the distinct PCCS ModeII responses of the four combinations of plate thickness and central support edge condition, while the double dot chain lines indicate the approximate PCCS ModeIII asymptotes. The legend indicates the specimen source sheet, the average sheet thickness, the specimen configuration and the edge radius of the central support.

test data can only be grouped into approximate mode response regions due to the influence of the plate thickness and central support boundary conditions on the failure response. This is particularly evident in transition from Mode I to Mode II* behaviour and is discussed further in Section 6.3.4.

The dashed lines in Figure 6.11 represent least-squares regression fits for the mode I responses of the PCCS and PCA plates. The regression formula for the Mode I responses of the PCCS plates is,

$$\delta = 0.1544\phi - 0.4949 \tag{6.4}$$

with a r^2 correlation coefficient of 0.9678, while that for the PCA plates is,

$$\delta = 0.4324\phi - 0.561 \tag{6.5}$$

with a r^2 correlation coefficient of 0.99.

The correlation coefficients represent a slight improvement over those obtained from the short stand-off data. As with the reduced size of the error bars, this suggests that the blast tube configuration provides a more repeatable blast load. Furthermore, it is evident that the vast majority of the ave-max data points lie within a half plate thickness of the regression line, the exception being a few of the PCA data points that are within a plate thickness. From Figure 6.11 it is evident that Equation (6.1) provides a valid correlation for the Mode I behaviour of plates of varying thickness in both the PCCS and PCS plate configurations. These results, along with those presented in Section 6.2.1 for plates of varying diameter, confirm the validity of the analyses presented in Chapter 7, from which Equation (6.1) is obtained. Subsequent to the theoretical model development in Chapter 7, the detailed comparison of the experimental and theoretical results is discussed further in Section 8.3.

The slope of the PCCS regression is 30% smaller than that for the short stand-off data, while the PCA regression is 35% smaller. This is indicative of the fact that the short stand-off test is impulsive, while the blast tube test is dynamic, with the resultant effect on the dimensionless displacements, as discussed in the context of PCS plates in Section 4.3. These effects are considered further in Section 7.5.

In addition to the Mode I regression fits, the other data points in Figure 6.11 follow similar trends to those observed in the short stand-off data. In particular, the Mode I to II* transition is indistinct since some of the the Mode II* data points lie close to the Mode I correlation, which contrasts with the Mode II trend that deviates strongly from the Mode I correlation, while the Mode III data points asymptote to a trend that is approximately parallel to the PCA Mode I correlation. For clarity, single and double dot chain lines are included in Figure 6.11 to delineate, respectively, the distinct PCCS Mode II and Mode III responses of the four combinations of plate thickness and central support edge condition. These chain lines do not represent regression fits, but are intended as visual aids in the detailed discussion of the results in Section 6.3.3.

Figure 6.12 shows the final hole diameter in relation to the total impulse for the 2 mm thick blast tube loaded PCA and PCCS plates. The results closely resemble those of the short stand-off tests. For example, the final hole size of a PCA plate increases monotonically with an increase in the total impulse. However, due to the size of the data set, some subtle features become evident, such as non-linear trend of the PCA data, which will be discussed further in Section 6.3.3.5. For PCCS plates, as before, a value of zero is assigned to the Mode I and II* data points to represent incomplete hole formation. Thereafter, the

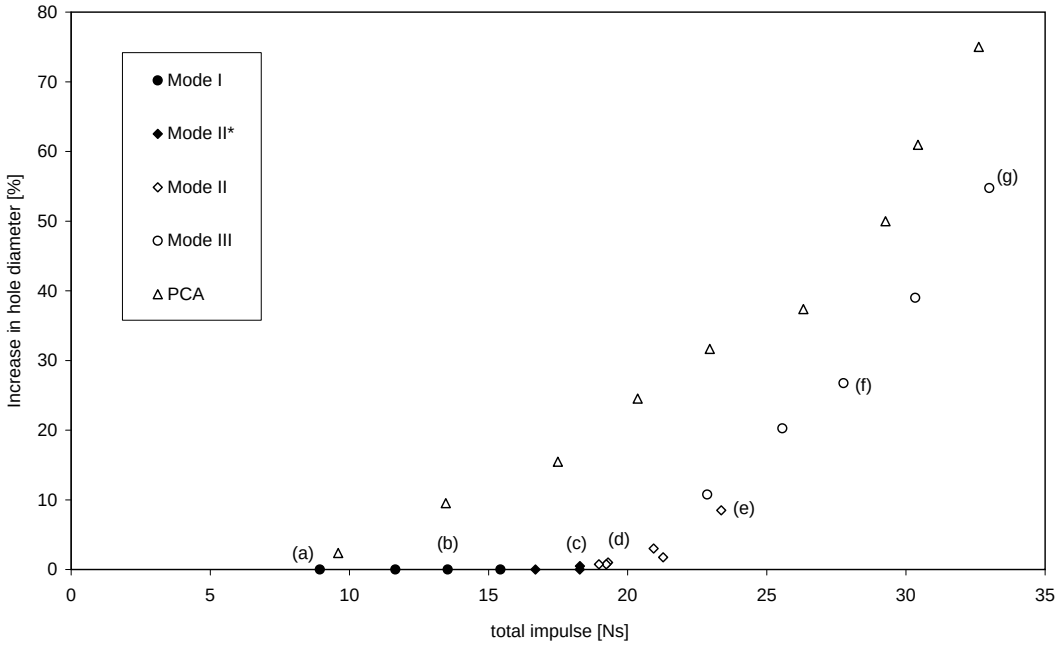

Figure 6.12: Increase in the final hole diameter vs the total impulse for 2 mm thick blast tube loaded PCA and PCCS plates, *i.e.* sheet IV. Data points corresponding to Mode I and Mode II* behaviour, where no hole was formed, are included for the sake of comparison.

onset of Mode II behaviour is characterized by a slight increase in the final hole size, which contrasts with Mode III where an increasing total impulse leads to a substantial increase in the final hole size. However, unlike the short stand-off data, the size and impulse range of the data set is sufficient to show that the transition points between the failure modes are smooth and would be difficult to discern on the basis of the final hole size alone. Nevertheless, it is again evident that at larger impulses the Mode III data tends toward the PCA Mode I data, but with a distinct impulse offset.

The fraction of the total impulse transferred through the central support for the 2 mm thick blast loaded PCA and PCCS plates is shown in Figure 6.13. As with the hole enlargement results, the data suggests that the transitions between the failure modes are smooth, which is not apparent for the short stand-off data. For example, the Mode I to II* transition forms a continuous downward trend. Nevertheless, a distinct drop occurs in the Mode II* trend at a load of approximately 18.5 Ns, *i.e.* $\phi = 16.8$, which correlates well with Mode II* to II transition in Figure 6.11, and will be discussed further in Section 6.3.3.2. After this, the data points of Modes II and III form a continuous trend with the central support impulse fraction deceasing steadily as the total impulse increases. In particular, there is no evidence of a distinct drop in the impulse fraction during the transition to Mode III behaviour, as suggested by the short stand-off data. At large impulses, the Mode III data points appear to approach an asymptote that is similar to, but greater than, the PCA Mode I trend. As before, the PCA data is included in Figure 6.13 for comparison with the PCCS data, for which it serves as a lower limit.

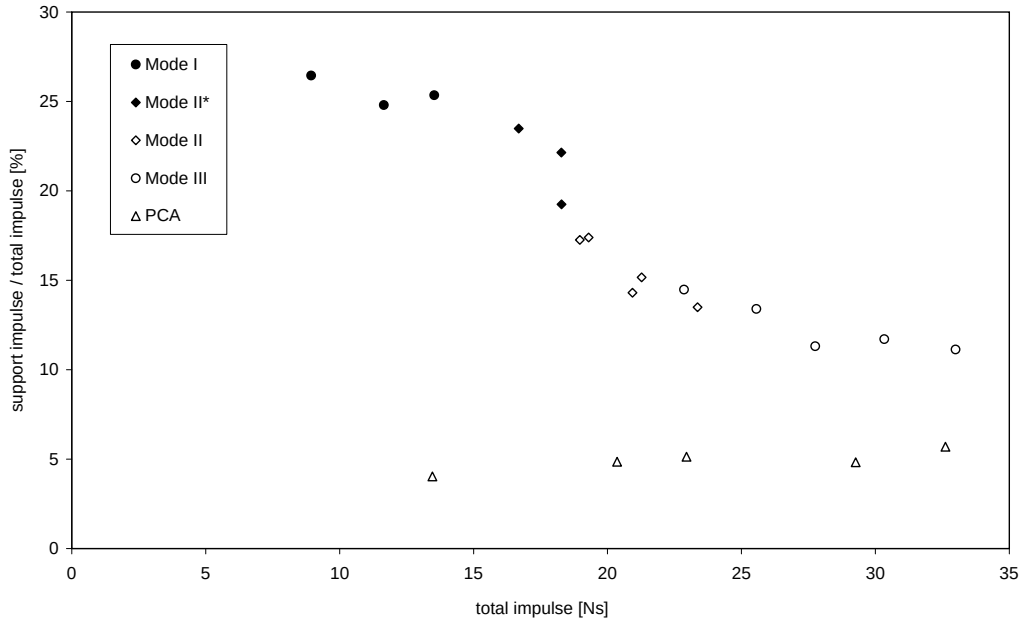

Figure 6.13: Fraction of the total impulse transferred through the central support vs the total impulse for the 100 mm Sheet IV PCA and PCCS plates.

6.3.2 Central Support Force Histories

A selection of central support force histories from blast tube tests on PCCS plates are shown in Figures 6.14, 6.15 and 6.16, with some additional results presented in Section 6.3.3. These results are representative of typical results obtained from the instrumented central support bar. The curves numbered (a) to (g) in Figure 6.14 correspond to specific blast tests that will be discussed in detail in Section 6.3.3. As before, these curves will be referred to as force histories even though the units of MPa have been retained so as to allow for a direct comparison with Figures 5.21 to 5.25.

Some general observations regarding the repeatability of the blast tube loaded PCCS plate configuration can be drawn from the aforementioned figures. It is noticeable that, unlike the short stand-off tests, there is no initial 'spike' in the force histories, which is consistent with absence of a leader charge in the blast tube configuration. Rather, all the curves show a steep initial rise to a peak value that increases in magnitude with an increase in the mass of the explosive charge, which is similar to the secondary 'spike' due to the ring charge in the short stand-off tests. However, the initial peak value is frequently not as distinct and sharply defined as the secondary 'spike' in the short stand-off tests, even though the blast wave produced in the blast tube typically has such a feature, as shown in Figures 5.21 to 5.25. This implies that, unlike the short stand-off tests, the initial rise is not primarily due to the blast pressure propagating through the plate specimen and directly into the central support, but already contains a significant contribution due to localized plate deformation around the central support. The influence of this localized deformation is considered in more detail in Section 6.3.3. Nevertheless, the initial force history features are consistent across all the blast tube tests, which indicates the repeatability of the loading technique and PCCS plate response.

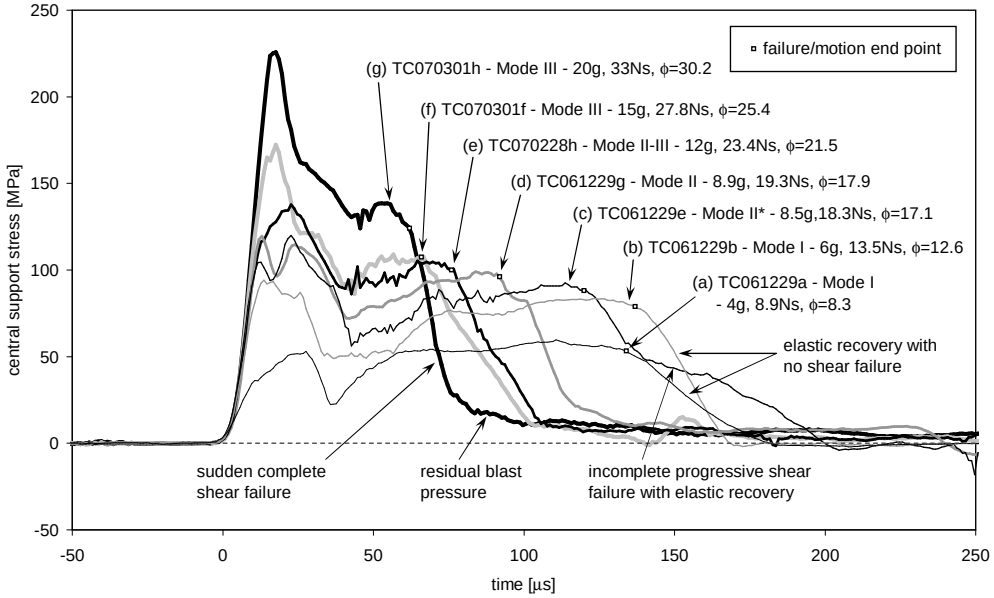

Figure 6.14: Comparison of the R0 central support force histories of seven blast test on 2 mm thick PCCS plates, *i.e.* sheet IV. Note that curves (a) and (c) appear to touch at 140 μs, but do not cross.

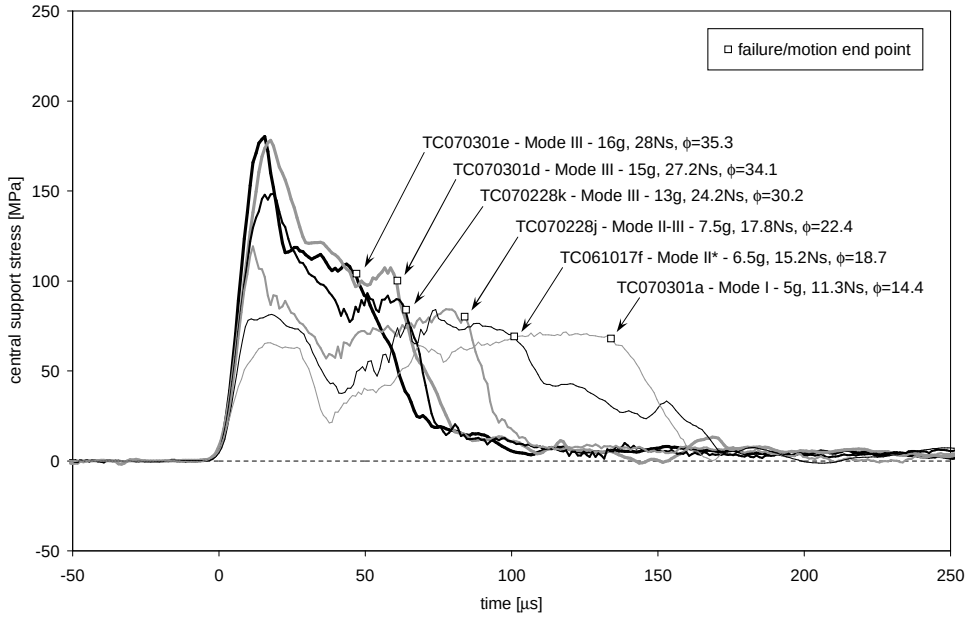

Figure 6.15: Comparison of the R0 central support force histories for blast test on 1.6 mm thick PCCS plates, *i.e.* sheets I to III.

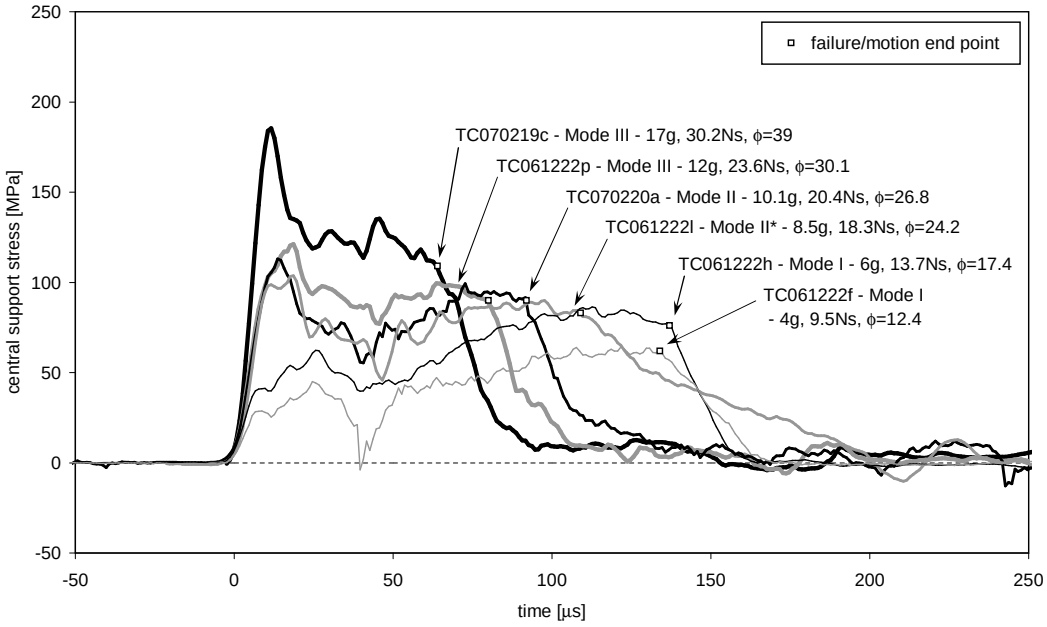

Figure 6.16: Comparison of the R2 central support force histories for blast test on 1.6 mm thick PCCS plates, *i.e.* sheets I to III.

Subsequent to the initial peak values, there is a consistent drop in all the force histories as the blast load decays. This is especially evident with the relatively steep decay in Figures 6.14 and 6.15, for which the curves were obtained with the R0 central support. By contrast, the decay is relatively gradual in the data obtained with an R2 central support, as shown in Figure 6.16, which suggests greater localized deformation effects due to the rounded inner edge condition. The effect of the R2 edge condition is discussed in more detail in Section 6.3.4.

The rapid drop in the force history after the initial peak has a short duration after which there is a transition to a steady rise, the gradient of which is reasonably consistent across all the force histories. The transition point is at approximately 40 μs for the majority of the tests, while tending toward 50 μs for the larger blast loads. The interpretation of this characteristic transition is that it represents the point where the global membrane type deformation of the plate under its own inertia begins to the dominate plate response. In general, this leads to a steady rise in the force signal and terminates at a local maximum value which represents either the point of fracture or the end point of plastic deformation. A detailed discussion of these features in representative individual mode response curves is given in Section 6.3.3.

Some specific examples of the repeatability of the PCCS plate configuration are shown in Figures 6.17 and 6.18 where the central support force histories for nominally identical PCCS plates subjected to similar explosive charges are compared. The curves show good repeatability, even though the total impulse values are slightly different. Furthermore, the permanent displacements, as recorded in Tables E.7 to E.21, are also similar, with the slightly larger impulses typically resulting in a slightly larger deflections. As discussed in Section 6.2.2, this consistency and repeatability allows an estimate of the shear force contribution in the PCCS plate tests to be isolate by comparing the force histories from PCCS and PCA

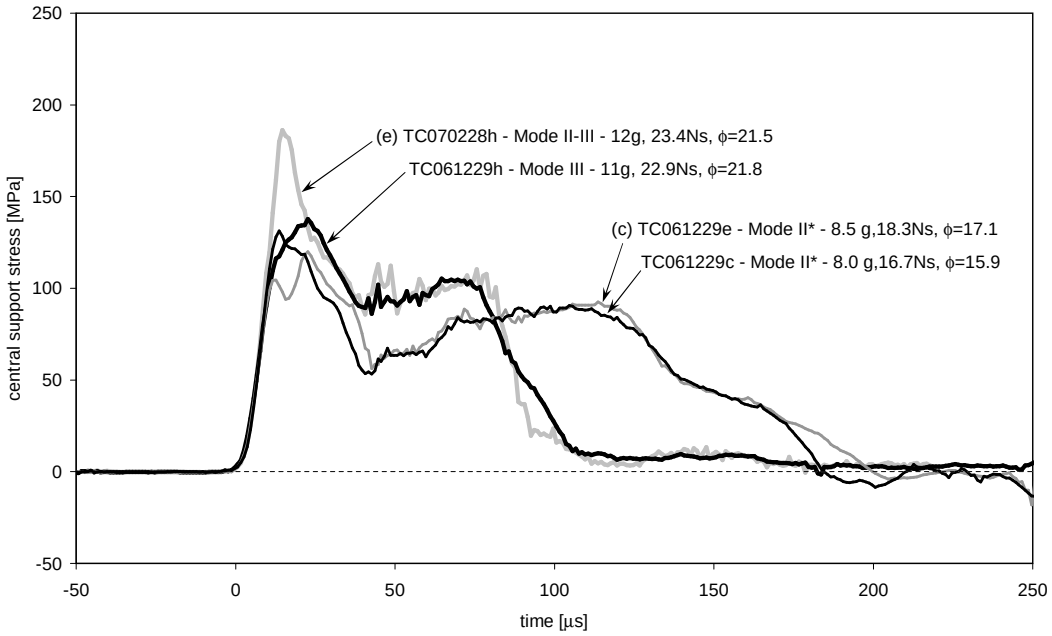

Figure 6.17: Repeatability of the R0 central support force histories for blast test on 2 mm thick PCCS plates, *i.e.* sheet IV.

plate tests with nominally identical charges. Typical examples of these for each type of mode response are discussed in Section 6.3.3.

6.3.3 Detailed Experimental Observations

In this section, the detailed response behaviour of a selection of the plate tests considered in Section 6.3.2 are discussed. These specific results are representative of the general response behaviour observed during all the plate tests. Particular attention is given to the blast tube loaded 2 mm thick 100 mm diameter PCCS plates, although examples from other plate thicknesses will be presented as required.

The dimensionless impulse vs deflection results for the 2 mm thick plates presented in Figure 6.11 are shown in isolation on Figure 6.19, where the annotated data points (a) to (g) correspond to the central support force histories shown in Figure 6.14. Photographs of five of the recovered 2 mm thick PCCS plate specimens, which are representative of the observed failure modes, are shown in Figure 6.20, where the plate specimen numbers (b) to (g) correspond to the annotated dimensionless impulse vs deflection data points in Figure 6.19 and the curve numbers in Figure 6.14.

6.3.3.1 Mode I

Figure 6.20(b) shows the recovered plate specimen from test number TC061229b, for which the total charge mass was 6 g and resulted in a total impulse of 13.53 Ns ($\phi = 12.6$). The recovered plate specimen exhibits large plastic deformation with no visual indication of shear or tensile failure at the inner or outer

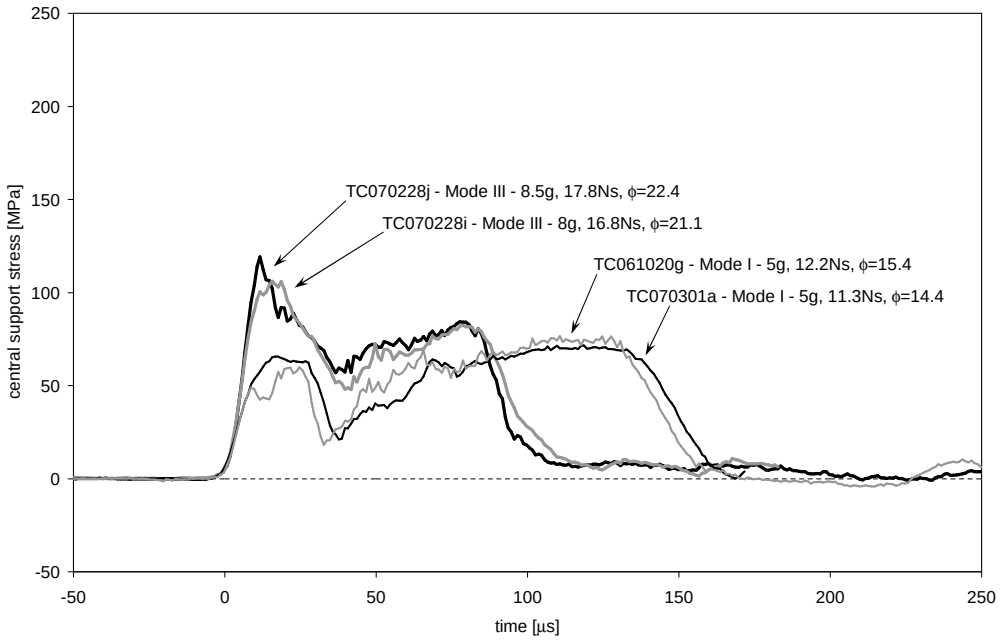

Figure 6.18: Repeatability of the R0 central support force histories for blast test on 1.6 mm thick PCCS plates, *i.e.* sheets I to III.

boundary, *i.e.* a Mode I response. This classification is consistent with the Figure 6.19, where the test (b) data point lies on the Mode I correlation.

In addition to plate number TC061229b, three other 2 mm PCCS plates displayed a similar Mode I response. The four Mode I test results all have a dimensionless impulse of less than $\phi = 15$ and lie on the Mode I correlation, as shown in Figure 6.19. In addition, the Mode I classification is evident in the central support force histories, as shown by the consistent response duration of curves (a) and (b) in Figure 6.14. This observation is in agreement with Bodner & Symonds [56] and Nurick & Martin [6] who found that, for a given PCS plate configuration, the Mode I duration is independent of impulse, as discussed in Sections 3.2.3 and 4.2.3.

The consistent Mode I response duration is also evident in the force histories of the other test series shown in Figures 6.15 and 6.16. In fact, the maximum Mode I response duration was found to be consistent for all the PCCS plates tested as part of this thesis. For example, Figure 6.21 compares the force histories of three PCCS plates of varying thickness, but made from nominally the same material. Across all the Mode I PCCS plate tests, the maximum plate response showed little variation and typically occurred between 125 μs and 130 μs. The total Mode I response duration showed slightly more variation with values between 155 μs and 180 μs, where the longer durations are associated with smaller residual deformations. These values compare well with the short stand-off results reported in Section 6.2.3.1.

As argued in Section 6.2.3.1, the point of maximum Mode I response corresponds to the end of the plastic deformation, after which the plate rebounds and unloads elastically. In other words, the rigid plastic Mode I analysis considered in Chapter 7 is only valid up to the point of maximum plate response. Furthermore, the elastic unloading curves have a distinct quarter cosine wave shape, which represents

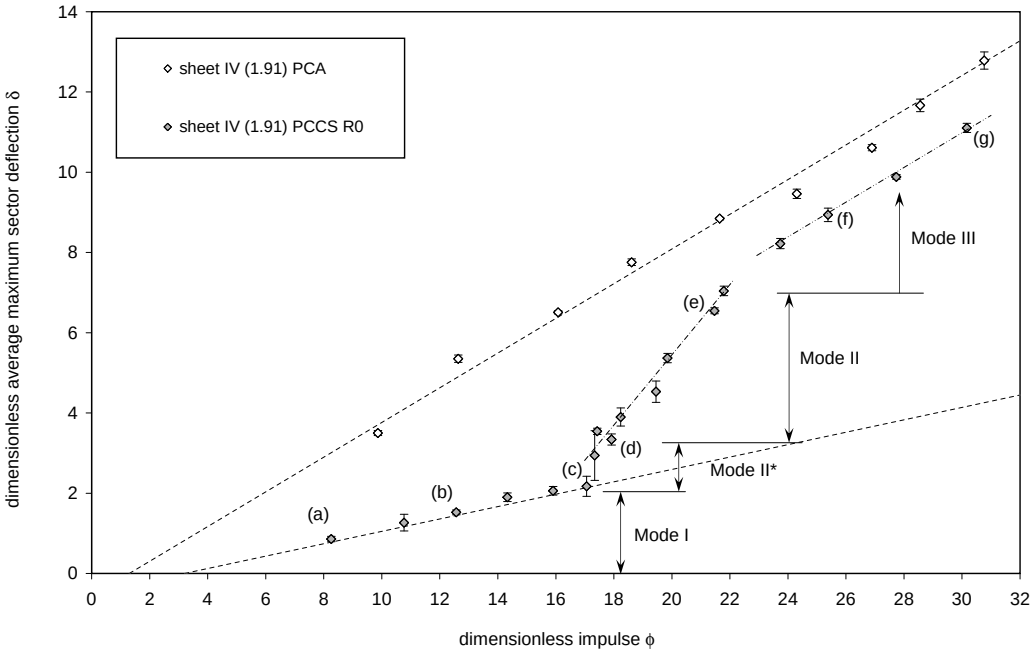

Figure 6.19: Dimensionless deflection vs impulse data for sheet IV.

the first quarter period of an elastic vibration, *i.e.* an elastic rebound from the maximum displacement to the new equilibrium position, at which point the plate separates form the central support.

An analysis of the rebound duration would require a solution for the vibration of a shallow annular elastic shell, potentially incorporating both bending and membrane behaviour. A convenient solution to this problem does not appear in the literature and was considered beyond the scope of this thesis. However, tabulated solutions have been published for the vibration of annular plates, such as that by Han & Liew [186]. This solution is directly applicable to test TC070228b, where a 2.91 mm thick PCCS plate was loaded with a 4 g charge resulting in a final residual deflection of only 0.09 mm[3]. The central support force history for test TC070228b is shown in Figure 6.22, along with the results from two other sheet V PCCS specimens that showed a Mode I response with increasing charge masses. Figure 6.22 shows that the rebound duration decreases with an increase in the final deflection, with tests TC070228b and TC070228d resulting in rebound durations of approximately 53 μs and 45 μs respectively. For comparison, the solution of Han & Liew for a simply supported annular plate of the same dimensions provides a quarter period estimate of 51.95 μs. In other words, the bending solution of Han & Liew shows reasonable agreement with the experimental result and provides a justification for interpretation of elastic rebound. Furthermore, the solution provides a lower limit estimate for the rebound duration since a shallow annular shell can be expected to be stiffer than an annular plate, which leads to shorter rebound duration, as shown in Figure 6.22.

In addition to the above, test TC070228b also supports the argument, presented in Section 3.2.1, that the Mode I regression should have a positive x-axis intercept, *i.e.* the impulse must exceed a certain threshold before permanent deformation occurs. This is most evident in Figure 6.11 where the data point

[3]Deflections of less than half a plate thickness are typically considered to fall in the regime where bending effects dominate.

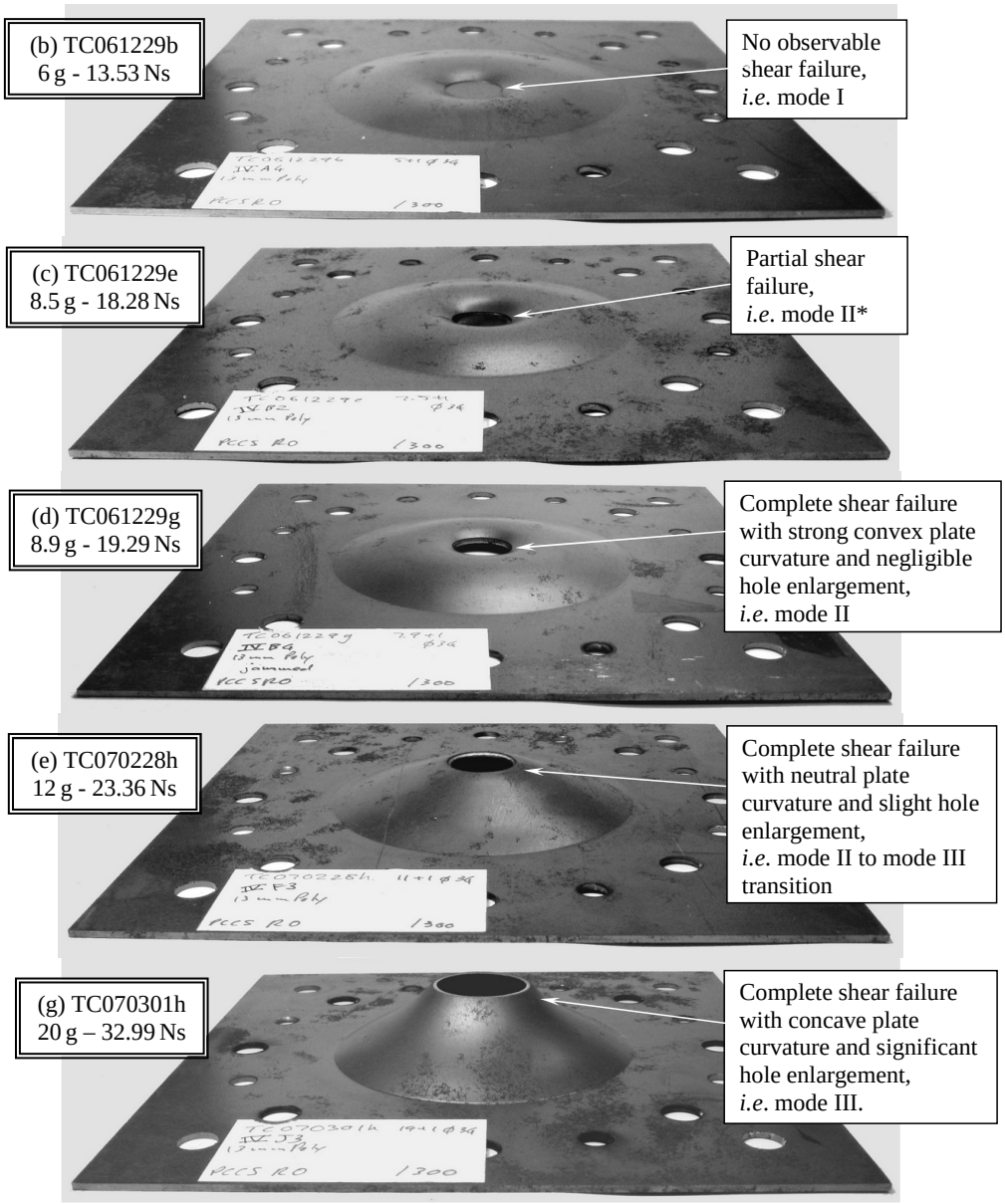

Figure 6.20: Photographs of blast tube blast loaded 2 mm thick 100 mm PCCS plate specimens. The plate numbering (b) to (g) corresponds to those in Figures 6.14 and 6.19.

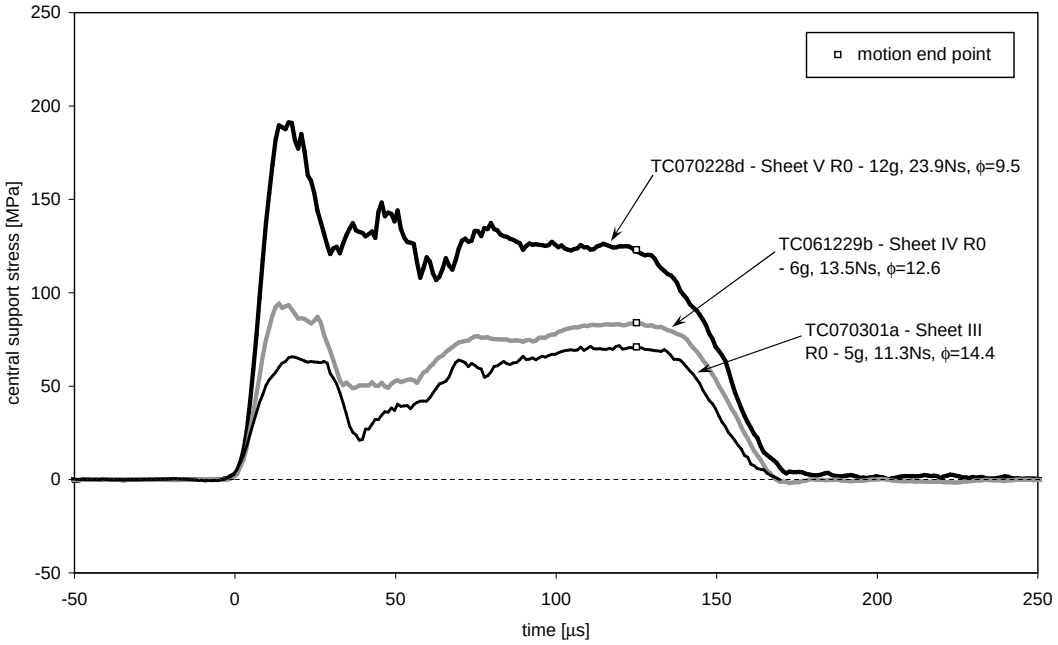

Figure 6.21: Repeatability of the Mode I deformation duration as shown in the central support force histories for blast test on various thickness PCCS plates.

corresponding to test TC070228b lies close to the x-axis intercept of the PCCS Mode I regression at a dimensionless impulse of just less than 4.

An estimate of the shear force history is obtained by comparing test TC061229b to the force history of test TC061017h, as shown in Figure 6.23. In test TC061017h, a PCA plate from Sheet I with a R0 central support was subjected to a 6 g charge which produced a blast load of 14.05 Ns, which is consistent with test TC061229b. The curves have been temporally aligned according to the start of the detonation noise signal.

The resulting Mode I shear force history has several distinct features. Unlike the short stand-off result shown in Figure 6.7, a large shear force is evident shortly after the arrival of the blast wave. In fact, after 12 μs the initial peak of the shear force contribution is approximately 56 MPa, which is slightly larger than the peak PCA blast load pressure of 42 MPa. As shown in Section 4.3, a blast load is not ideally impulsive and will cause a plate to go through an acceleration phase where the early plate velocity and displacement is small. Hence, it is unlikely that significant membrane forces would be generated at an early point in the deformation response, and, consequently, the large shear force evident in Figure 6.23 must be due to localized deformation of the plate in the region of the central support.

An estimate of the extent of the localized response can be inferred from the relative magnitudes of the blast and shear force signals. In this case, the results suggest that the initial blast load is being transferred to the support bar via a central portion of the plate that is slightly larger than twice the area of the support bar end face. This is equivalent to adding a ring of material to the end of the support bar that is just over 5 mm wide. Given the nominal sheet IV plate thickness of 2 mm, this force transfer most

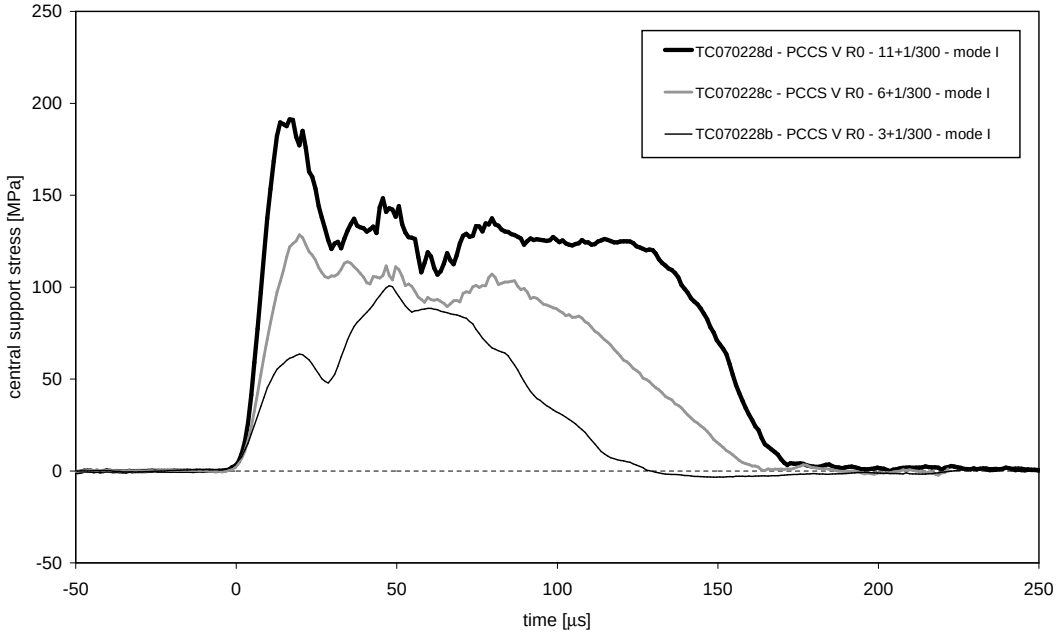

Figure 6.22: Central support force histories for Mode I behaviour of 3 mm thick blast loaded PCCS plates, *i.e.* sheet V.

likely occurs through localized shear and bending as opposed to membrane strain[4]. Furthermore, it is noticeable that the temporal position of the initial peak of the shear force corresponds with that of the blast wave and subsequently decreases as the blast wave decays, even though the global plate deflection would be increasing at this point, which supports the interpretation that the initial portion of the shear force history is due to localized plate deformation.

After the initial peak at 12 μs the blast wave begins to decay. However, the shear force rises slightly to a second local maximum of 65 MPa after approximately 26 μs. It is interesting to note that the secondary shear force peak is only evident after the blast pressure contribution is removed from the central support signal. This increase in the shear force, despite the drop in the blast pressure, suggests a progressive enlargement in the size of the effective ring of material that the blast wave is acting on, which is most likely related to the action of a moving bending hinge[5]. The plate used in test TC061229b had a thickness of 1.92 mm and, therefore, the shear force corresponds to a nominal shear stress of 169 MPa. This, in turn, represents a Mises equivalent stress of 293 MPa, which is distinctly larger than the average quasi-static yield stress for Sheet IV of 260 MPa, as reported in Appendix B.

Subsequent to the secondary stress peak, the signal drops rapidly to a local minimum after 35 μs, after which it begins to rise at a relatively gradual rate. This rise cannot be due to renewed localized deformation since the blast wave continues to decay. Hence, the local minimum represents the point in the response where global membrane type deformation begin to make a larger contribution to the support bar reaction force than localized bending. The signal increases to a value of 81 MPa after approximately

[4]It is likely that this initial force transfer can be analyzed using a classical small strain bending wave analysis. However, this is considered to be beyond the scope of this thesis and will only be pursued subsequent to this work.

[5]A detailed bending hinge solution is beyond the scope of this thesis, for which the focus is on large strain membrane type behaviour.

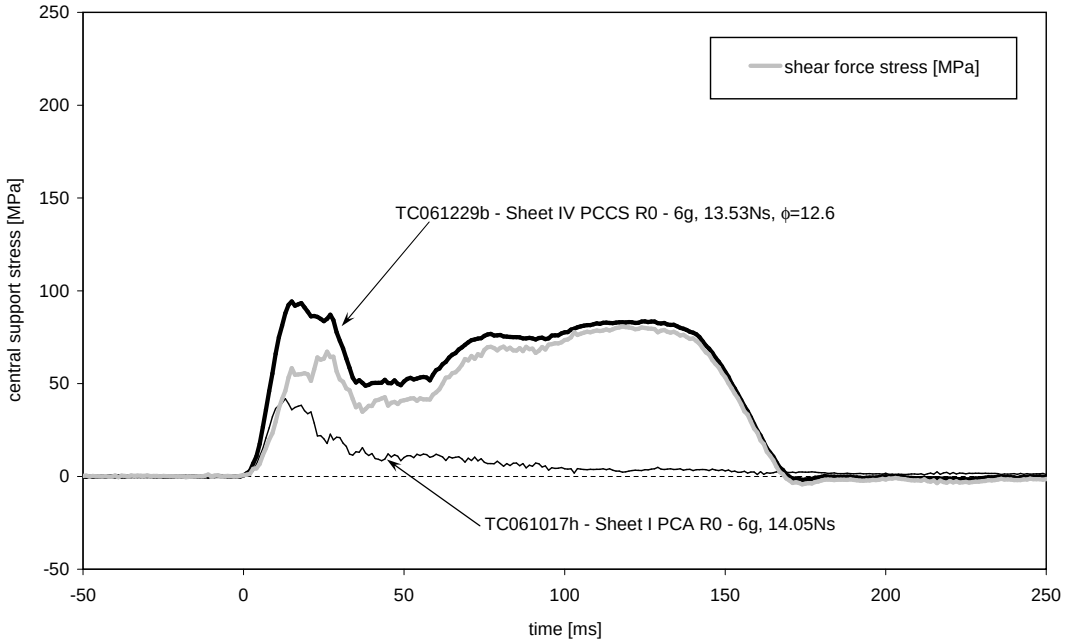

Figure 6.23: Central support shear force history for Mode I behaviour of 2 mm thick blast loaded PCCS plates, *i.e.* sheet IV.

130 μs, which signifies the maximum membrane response, *i.e.* the point at which plastic deformation ceases. At this point the contribution of the blast pressure is small and the central support stress essentially represents the boundary reaction force due to global membrane type plate deformation. The maximum values corresponds to a nominal shear stress of 211 MPa, *i.e.* a Mises equivalent of 365 MPa. This value is approximately 100 MPa greater than the average quasi-static yield stress for Sheet IV. Notwithstanding the effect of strain hardening, these results imply that strain rate effects are significant throughout the deformation response.

Similar behaviour is evident in the 1.6 mm plates cut from Sheets I to III. For example, test TC070301a in Figure 6.15 displays a maximum membrane response of 70 MPa, for which the Mises equivalent is 372 MPa. Even when allowance is made for the residual blast pressure, this value is significantly higher than the average quasi-static yield stress for this Sheet III of 290 MPa.

Following the maximum membrane response, the signal decreases in the quarter cosine shape that is characteristic of elastic plate rebound, as discussed previously in this section. Note that the recorded PCCS signal drop zero after approximately 170 μs, while the PCA signal does not. The reason for this is that, after rebounding, the PCCS plate separates from the central support, which is, therefore, shielded from the residual blast pressure. Consequently, when subtracting the PCA signal from the PCCS signal at this point, the resulting shear force signal appears drops below zero, which does not represent the actual plate behaviour. Finally, note that the shear stress produced during the maximum membrane response is greater than that generated during the initial localized deformation. These results are consistent with the observation Mode I response of test TC061229b.

6.3.3.2 Mode II*

Figure 6.20(c) shows the recovered plate specimen from test number TC061229e, for which the total charge mass was 8.5 g and resulted in a total impulse of 18.28 Ns ($\phi = 17.1$). The recovered plate exhibits large plastic deformation with partial shear failure at the inner boundary, *i.e.* a Mode II* response.

Despite the shear failure, Figure 6.19 shows that the dimensionless deflection data point of test (c) lies on the Mode I correlation. This suggests that the shear fracture occurred relatively late in the deformation process, by which time most of the kinetic energy had been dissipated such that no significant post fracture plastic deformation was possible. Similar behaviour is evident in Figure 6.13 where the central support impulse fractions for both Mode I and II* appear to form a continuous slightly decreasing trend However, as discussed in Section 6.3.1, a distinct drop in the Mode II* trend is evident at a load of approximately 18.5 Ns, *i.e.* $\phi = 16.8$, which correlates well with Mode II* to II transition in Figure 6.11. The general smoothness of data in Figure 6.13 suggests that this is not an artifact of the test method and appears to provide the clearest indication of a transition point, which shows the value of being able to capture the central support impulse.

The late shear fracture conclusion is supported by the central support force history for test (c), as shown in Figure 6.14, where the form of the force history is similar to a Mode I response, but the peak membrane response is slightly greater and occurs approximately 10 μs earlier. Given the consistency of the Mode I duration, the early peak implies that shear failure has interrupted the Mode I type deformation, resulting in the unloading of the central support. Furthermore, the force history does not drop to zero, which is consistent with a Mode II* response, *i.e.* the shear failure was arrested and did not extend along the entire central support boundary.

The Mode II* behaviour of the 2 mm PCCS plates was found to be highly consistent and repeatable, as can be seen in Figure 6.17. Similar behaviour is observed in blast tube tests results for 1.6 mm thick PCCS plates with both square and round central support edge conditions, as shown in Figures 6.15 and 6.16. This behaviour is also similar to that observed for short stand-off blast test, as shown in Figure 6.5 and discussed in Section 6.2.3.2.

The consistent Mode II* response allows an estimate of the shear force history to be obtained by comparing test TC061229e to the force history of test TC061017l, as shown in Figure 6.24. In test TC061017h, a PCA plate from Sheet I with a R0 central support was subjected to a 9 g charge which produced a blast load of 18.73 Ns, which is similar to that of test TC061229e. The curves have been temporally aligned according to the start of the detonation noise signal.

The initial Mode II* shear force history is similar to that of Mode I. After approximately 12 μs an initial peak shear load of 60 MPa occurs that is 25 % larger than the peak PCA blast load pressure of 45 MPa. These initial peak values are only 7 % larger that those for the Mode I response, which is somewhat surprising given the 35 % increase in the total impulse. However, their relative magnitude is similar to that of Mode I result. By contrast, the secondary shear load peak of 93 MPa after 23 μs is 42 % larger than the corresponding Mode I value. Given the plate thickness of 1.91 mm, the peak load corresponds to a nominal shear stress of 243 MPa, *i.e.* a Mises equivalent of 421 MPa, which is higher than the any peak load in the Mode I response. Furthermore, it is well above the average quasi-static yield stress for Sheet IV of 260 MPa, which suggests that some shear sliding type failure, if not shear fracture, may have

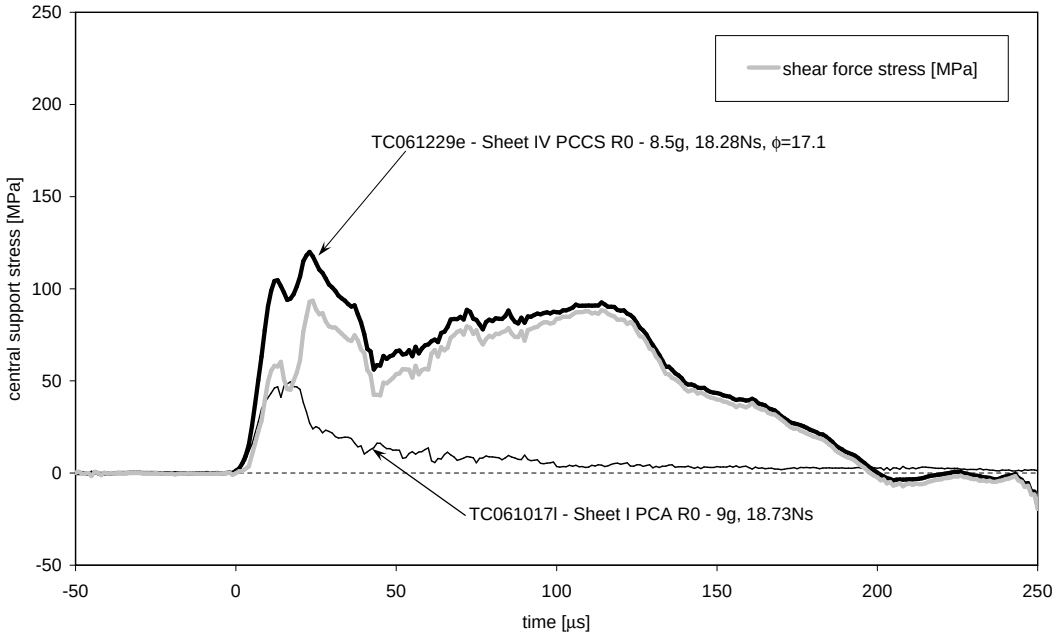

Figure 6.24: Central support shear force history for the Mode II* behaviour of a 2 mm thick blast loaded PCCS plates, *i.e.* sheet IV.

occurred at this point. This interpretation will be elaborated upon as related results are presented in subsequent sections.

The intensity of the initial portion of the shear load history supports the interpretation that the load transfer occurs through localized shear and bending deformation as opposed to membrane strain, as discussed in Section 6.3.3.1. Likewise, the rapid decrease in the shear load signal subsequent to the secondary stress peak reflects the decay of the blast pressure rather that membrane strain, which would be increasing at this point. A local signal minimum occurs after 44 μs, which is approximately 10 μs later than the equivalent feature in the Mode I response and is consistent with the increase intensity of the shear load. Thereafter, the signal rises gradually, which is consistent with an increase in the global membrane type deformation.

The shear load history shows a maximum membrane response of 89 MPa after approximately 116 μs, which corresponds to a nominal shear stress of 233 MPa, *i.e.* a Mises equivalent of 404 MPa. This value is noticeably higher that the peak Mode I membrane response, for which the Mises equivalent is 365 MPa, but is marginally lower than the secondary shear load peak of 93 MPa. These results suggest that that some early shear sliding is likely to have been induced during the secondary peak shear load, only to be subsequently arrested as the blast load died away.

Subsequent to the maximum membrane response the shear load begins to drop-off gradually in a manner that is similar to the Mode I response, except for its earlier occurrence. This is consistent with a progressive partial shear failure, whereas a complete shear failure would be expected to result in a sudden drop in the shear load signal. As mentioned previously, the partial shear failure is also reflected in the fact that the trend does not continue to zero but levels off after 140 μs, which is interpreted as the point where the progressive shear failure was arrested. Since the shear failure is driven by plastic

membrane type deformation, this point also represents the deformation response duration. This result is consistent with the Mode I deflection duration of 130 μs since the shear failure would slightly weaken the inner boundary condition and allow a small amount of additional time for deformation.

In the final phase of the Mode II* response, the shear load history gradually drops to zero after 200 μs in a shallow quarter cosine shape that is indicative of elastic plate rebound, as discussed previously. In comparison to the total Mode I response duration, the Mode II* is significantly longer, while the maximum gradient of the elastic recovery is less than half. Both these features are consistent with the weakened inner boundary condition due to partial shear failure, which leads to a reduction in the plate stiffness and extends the elastic rebound behaviour.

Finally, as with the Mode I response, the shear load history drop below zero while the PCA signal does not, indicating that the central support is shielded from the residual blast pressure by the rebounding PCCS plate. However, in this case, unlike the Mode I response, the total central support signal also drops below zero. Though the effect is small, it may indicate that, through partial shear failure, the deformed plate forms a reasonably tight fit around the end of the central support which causes in a small tensile stress to be exerted on the central support when the plate separates from it during the elastic rebound.

6.3.3.3 Mode II

Figure 6.20(d) shows the recovered plate specimen from test number TC061229g, for which the total charge mass was 8.9 g and resulted in a total impulse of 19.29 Ns ($\phi = 17.9$). The recovered plate exhibits large plastic deformation with strong convex curvature adjacent to the central support and complete shear failure along the entire inner boundary with negligible hole enlargement, *i.e.* a Mode II response.

The Mode II behaviour is reflected in Figure 6.19 where the test (d) data point has a distinctly greater dimensionless deflection than the points on the Mode I correlation, even though the dimensionless impulse is only slightly larger than the Mode II* response considered in Section 6.3.3.2. In all, five of the recovered 2 mm thick PCCS plates showed clear Mode II behaviour. These tests correspond to data point (d) and the next four data point with increasing deflections shown in Figure 6.19. Data point (e) corresponds to a plate specimen that displayed both Mode II and Mode III features, *i.e.* it marks the transitions between the two response regimes and will be discussed in Section 6.3.3.4. Figure 6.19 shows that these six data points form a steeply rising trend of increasing dimensionless deflection that is distinct from that of Mode I. Similar trends are evident for all the other plate configurations in Figure 6.11, although it is apparent that shear failure does not scale with dimensionless impulse.

For test TC061229g, the convex plate curvature indicates that a considerable amount of deformation occurred prior to shear failure along the inner boundary, while the negligible hole enlargement suggests that the shear fracture occurred relatively late in the deformation process, though not as late as Mode II* shear failure. In other words, there was still sufficient residual kinetic energy to complete the shear fracture process and induce a small amount of post fracture plastic deformation.

As the impulse increases, the recovered plates display a decrease in the extent of the region with strong convex curvature. This behaviour is accompanied by a relatively small, but distinct, increase in the final hole diameter, as shown in Figure 6.12. These results suggests that an increasing impulse causes progressively earlier failure, which allows more time for the observed increase in both the final deflection

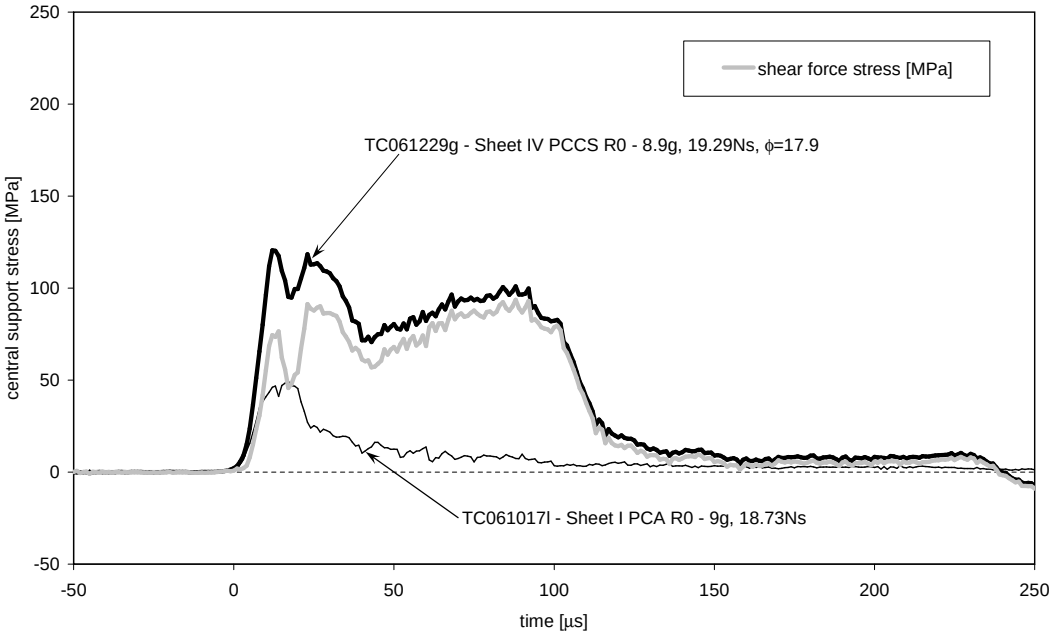

Figure 6.25: Central support shear force history for the Mode II behaviour of a 2 mm thick blast loaded PCCS plates, *i.e.* sheet IV.

and hole size. Furthermore, the early shear fracture interpretation is consistent with the central support impulse fraction data shown in Figure 6.13. As discussed in Sections 6.3.1 and 6.3.3.3, the distinct drop in the trend at approximately 18.5 Ns correlates well with Mode II* to II transition, after which the Mode II data points continue to show a decreasing trend. In other words, the progressively earlier failure leads to a decreasing fraction of the total impulse being transmitted through the central support.

The early shear fracture interpretation is also supported by the form of the force history for test TC061229g, *i.e.* curve (d), in Figure 6.14, which is similar to the Mode II* response in Section 6.3.3.2, but has a peak membrane response that occurs approximately 20 μs earlier. Furthermore, the subsequent drop-off in the stress signal is more sudden, which is indicative of shear failure along the entire central support boundary. Note, however, that at this point the stress history does not drop to zero, which is not consistent with a Mode II response, the cause of which will be discussed later in this section.

The Mode II behaviour of the 2 mm PCCS plates was found to be consistent and repeatable, as can be seen in the dimensionless deflection results in Figure 6.19. Furthermore, similar Mode II force histories are observed in blast tube tests results for the 1.6 mm thick PCCS plates with both square and round central support edge conditions, as shown in Figures 6.15 and 6.16. This behaviour is also similar to that observed for short stand-off blast test, as shown in Figure 6.5 and discussed in Section 6.2.3.3.

An estimate of the Mode II shear force history to be obtained by comparing test TC061229g to the force history of test TC061017l, as shown in Figure 6.25. Note that this is the same PCA signal as used in the Mode II* analysis and, as before, the curves have been temporally aligned according to the start of the detonation noise signal.

The initial Mode II shear load history has several features in common with that of the Mode II* response. A clear initial shear load peak of 75 MPa occurs after 14 μs with a secondary peak of 90 MPa after 23 μs.

The magnitude and timing of the secondary peak is nearly identical to the Mode II* response. However, in this case, the shear load appears to form a small plateau that persists for just over 8 μs. Given that partial shear failure occurred in the Mode II* response at a shear load of 89 MPa, the small plateau suggests that some shear sliding may be taking place due to localized deformation. After the plateau, the shear load falls rapidly to a local minimum after 43 μs, which is marginally earlier than the equivalent Mode II* feature. However, in this case, the magnitude of the local minimum is 57 MPa, which is approximately 10 MPa larger than that for Mode II*. This suggests that the portion of the shear load due to membrane type deformation is rising more rapidly than during the Mode II* response, which is consistent with the increasing blast load.

Subsequent to the local minimum, the shear load rises to a value of 89 MPa after 71 μs. As mentioned previously, this is the same load at which Mode II* shear failure was initiated, but only after 116 μs, which further emphasizes the increased membrane response. At this point, the shear load history enters a second plateau, with the signal rising marginally to 90 MPa after 92 μs. Based on a plate thickness for test TC061229g of 1.92 mm, this equates to a nominal shear stress of approximately 232 MPa, *i.e.* a Mises stress of 401MPa, persisting for 21 μs, which suggest further shear sliding along the inner boundary. After the second plateau there is a distinct drop in the shear load to 81 MPa after 102 μs, indicating the possible initiation of shear failure, followed by sudden large drop in the shear load, which is consistent with complete, near simultaneous shear failure around the entire inner plate boundary.

Given the complete shear failure at the inner boundary, it would be reasonable to expect the shear load to drop to zero since the plate would have separated from the central support. However, this does not occur and instead a low load, with an average magnitude of approximately 9 MPa, persists for over 100 μs until eventually vanishing after a total duration of 240 μs. When the specimen plate was recovered after the blast test it was found to have 'jammed' onto the central support, which could only be removed using a mallet. In essence, it appears that the shear failure had created a central hole that was marginally smaller than the bar diameter[6], resulting in the equivalent of a light press-fit between the central support and perforated PCCS plate. Hence, the low load represents a shear force of approximately 7 kN a the inner boundary as it scraped along the central support during the final stage of plate deformation. In other words, test TC061229g happens to record the total duration of the plate deformation after shear separation, which may be a useful parameter for future analysis. Finally, at the end of the plastic deformation, the elastic rebound of the plate would cause a small tensile stress in the central support, which is consistent with the shear load dropping below zero after 240 μs.

6.3.3.4 Mode II to Mode III

Figure 6.20(e) shows the recovered plate specimen from test number TC070228h, for which the total charge mass was 12 g and resulted in a total impulse of 23.36 Ns ($\phi = 21.5$). The recovered plate exhibits large plastic deformation with a neutral curvature, *i.e.* the deformation profile is near linear but contains both slightly convex and concave portions, and complete shear failure along the entire inner boundary with a relatively small amount of hole enlargement, *i.e.* a transition between Mode II to Mode III behaviour.

[6]The final hole diameter recorded in Table E.18 represents the state of the plate specimen after separation from the central support.

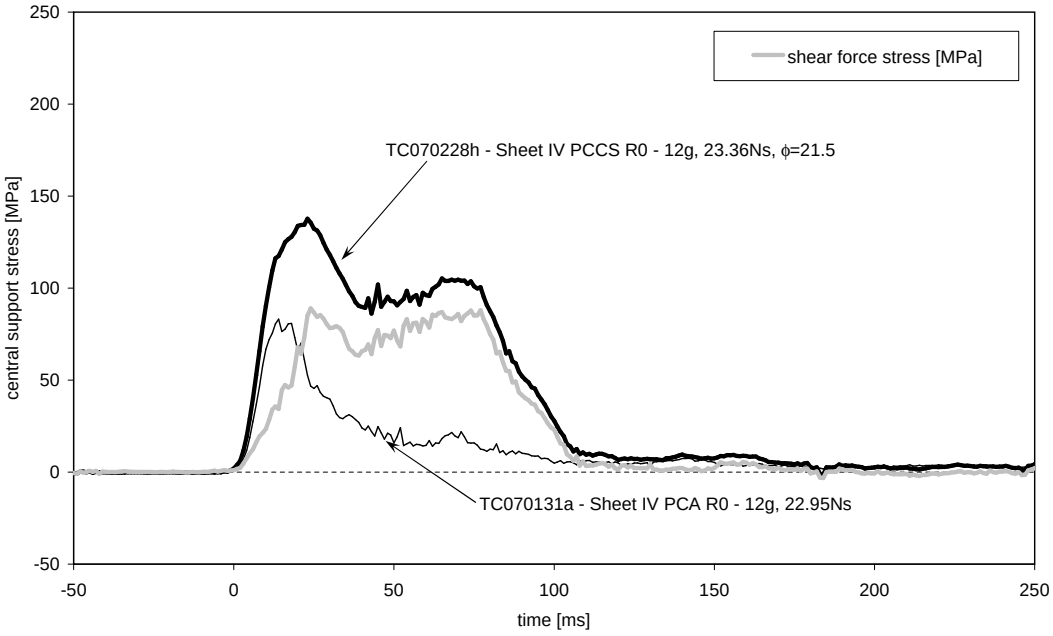

Figure 6.26: Central support shear force history for the Mode II to III behaviour of a 2 mm thick blast loaded PCCS plates, *i.e.* sheet IV.

The transition from Mode II to Mode III type response is readily identified by comparing the recovered plate to clear examples of Mode II and Mode III behaviour. As mentioned in Section 6.3.3.3, for plates showing a Mode II response, the amount of convex curvature adjacent to the central hole decreases with an increasing blast load. Hence, the transition point corresponds to the minimum dimensionless impulse at which no significant membrane type plastic deformation, *i.e.* clear convex curvature, occurs prior to shear failure at the inner boundary. It is evident in Figure 6.20 that this is the case for test TC070228h, *i.e.* test (e). The transition point is also evident in Figure 6.19, where the test (e) data point lies at the intersection of the Mode II trend and that of Mode III, which runs parallel to the PCA correlation, which will be discussed in Section 6.3.3.5. Furthermore, Figure 6.12 shows a distinct increase in the final hole size in comparison to that of the Mode II data point, which suggests that the shear fracture occurred relatively early in the deformation process.

From the above, the Mode II to III transition behaviour of the 2 mm PCCS plates is considered to be consistent and repeatable. The repeatability is apparent in Figure 6.17 where the central support force history for test (e) is compared to that of test TC061229h. Furthermore, similar force histories are observed in blast tube tests results for the 1.6 mm thick PCCS plates, such as shown in Figures 6.15. This behaviour is also similar to that observed for short stand-off blast test, as shown in Figures 6.5 and 6.8 and discussed in Section 6.2.3.3.

An estimate of the Mode II to III shear force history to be obtained by comparing test TC070228h to the force history of test TC070131a, as shown in Figure 6.26. In test TC070131a, a 2 mm thick PCA plate with an R0 central support was subjected to a 12 g charge which produced a blast load of 22.95 Ns, which is similar to that of test TC070228h.

Unlike the shear load histories considered in Sections 6.3.3.1 to 6.3.3.3, no clear initial shear load peak is evident in the Mode II-III response. This may simply be due to a difference in the peak pressure of test TC070131a and the actual blast load peak for test TC070228h, which is not known and is the least repeatable of the blast load features. However, other that for the peak pressure, the general repeatability of the blast loads allows several features of the shear load history to be resolved that are similar to the Mode II response. Hence, a shear load peak 89 MPa occurs after 24 μs, which is essentially identical to the secondary peak of the Mode II response, although the small plateau is absent. After this, the shear load falls to a local minimum of 64 MPa after 38 μs, which is marginally larger and earlier than the equivalent Mode II feature. Recalling that corresponding local minimum of the Mode II response was also marginally larger and earlier than that of the Mode II* response, this provides additional support that this feature is a result of the shear load contribution due to membrane type deformation is rising more rapidly with an increasing blast load.

Following the local minimum, the shear load rises to a value of 88 MPa after 64 μs, and then enters a second plateau that persists for 13 μs. This behaviour closely resembles that of the Mode II response, except that the plateau occurs earlier and has a shorter duration. Based on a plate thickness for test TC070228h of 1.93 mm, this equates to a nominal shear stress of approximately 228 MPa, *i.e.* a Mises stress of 395MPa. This is marginally lower than that of the Mode II response but well within the experimental scatter and may not be significant. Nevertheless, this result supports the interpretation that the shear load plateau represents shear sliding along the inner boundary. In this case, the shorter plateau duration suggests a greater shear velocity, which is consistent with the greater blast impulse that would result in a higher initial plate velocity.

After 77 μs the shear exhibits a sudden drop, which suggests near simultaneous shear failure around the entire inner plate boundary. As with the Mode II response, the shear load does not immediately drop to zero, indicating that some scraping along the central support. However, this effect is significantly smaller and of shorter duration than the corresponding feature in the Mode II response. Finally, the shear load gradually tapers off, which is consistent with the greater expansion of the central hole, such that the plate eventually looses contact with the central support somewhere between 150 μs and 180 μs.

6.3.3.5 Mode III

Figure 6.20(g) shows the recovered plate specimen from test number TC070301h, for which the total charge mass was 20 g and resulted in a total impulse of 32.99 Ns ($\phi = 30.2$). The recovered plate exhibits large plastic deformation and complete shear failure along the entire inner boundary with strong concave curvature adjacent to the resulting central hole, which is substantially enlarged, *i.e.* a Mode III response.

In all, five of the recovered 2 mm thick PCCS plates showed clear Mode III behaviour. These tests correspond to the five data points in Figure 6.19 with greater deflections than data point (e) and include data points (f) and (g). The data points lie on a rising trend, with a near linear relationship between the dimensionless impulse and the corresponding dimensionless deflection, that runs essentially parallel to the PCA correlation with a dimensionless impulse offset of approximately $\phi = 3.4$, *i.e.* an impulse

offset of 3.7 Ns. Figure 6.11 shows that the 1.6 mm thick PCCS plate behaviour approaches a similar asymptotic trend, with the R0 response converging earlier that R2 results[7].

The asymptotic impulse offset between the PCA Mode I and PCCS Mode III behaviour is analogous to test results for blunt projectile penetration of steel plates in the range of 100 m/s to 400 m/s [187, 188]. In particular, for tests beyond the ballistic limit the residual projectile velocity appears to approach an asymptote that is offset from the initial impact velocity. A detailed comparison of these analogous shear failure processes is considered to be beyond the scope of this these, but will be a topic of continuing research.

Similar asymptotic behaviour with an impulse offset is evident in Figure 6.12, which shows a large increase in the final hole diameters of both PCA and PCCS plates at large impulses. The asymptotic behaviour even more clearly evident in Figure 6.27, where the final hole diameter is plotted in relation to the average maximum sector deflection. This amounts to a comparison of purely geometric features and, therefore, if a PCCS Mode III response is truly equivalent to PCA behaviour, the result should be identical. Furthermore, if it is assumed that no radial strain occurs in the plate, the expected hole enlargement is obtained from a simple geometric analysis, which is represented by the dotted line in Figure 6.27 and has the form,

$$\frac{R_{if} - R_i}{R_i} \times 100\% = \frac{R_o - R_i}{R_i} \left[1 - \sqrt{1 - \left(\frac{\tilde{w}}{R_o - R_i} \right)^2} \right] \times 100\% \tag{6.6}$$

where R_i and R_o are the initial inner and outer radii of the PCA plate, while $\tilde{w}$ and R_{if} are the final maximum deflection and inner radius of the plate. It is evident that the final hole size in the PCA plates is slightly smaller than that described by Equation (6.6), which implies that a small amount of radial strain has occurred. Furthermore, the results show that the PCCS Mode III response is only equivalent to PCA behaviour above hole size increase of approximately 40%, which, according to Figure 6.12, correlates to impulse values above 30Ns.

These results correspond closely to the short stand-off PCCS Mode III results discussed in Section 6.2.3.5, and lead to similar conclusions. Hence, a large increase in the diameter of the central hole is indicative of early shear fracture prior to any significant membrane type deformation, after which a specimen behaves like a PCA plate. Indeed, as mentioned previously, the PCA configuration was intended for this purpose, *i.e.* to serve as a reference to identify Mode III response, with the offset interpreted as the impulse required to complete the shear fracture along the inner boundary.

Figure 6.28 shows the central support impulse as a function of the average maximum sector deflection for both the 2 *mm* thick PCA and PCCS plates. While the data is less sparse than that in Figure 6.10, a reliable asymptotic trend line can still not be obtained for the PCCS data and, hence, two parallel chain lines are included in as visual aids. It is noticeable that the PCA data appears to have a positive x-intercept, which is not physically meaningful. This corresponds to the observation that the percentage impulse transferred through the central support increases with an increase in the total impulse, as shown in Figure 5.19. The reason for this effect is unclear, but is suspected to involve pressure concentration effects due to shock wave reflections in the blast tube which lead to pressure oscillation being superimposed

[7] A Mode III response was not achieved in the 3 mm thick PCCS plates.

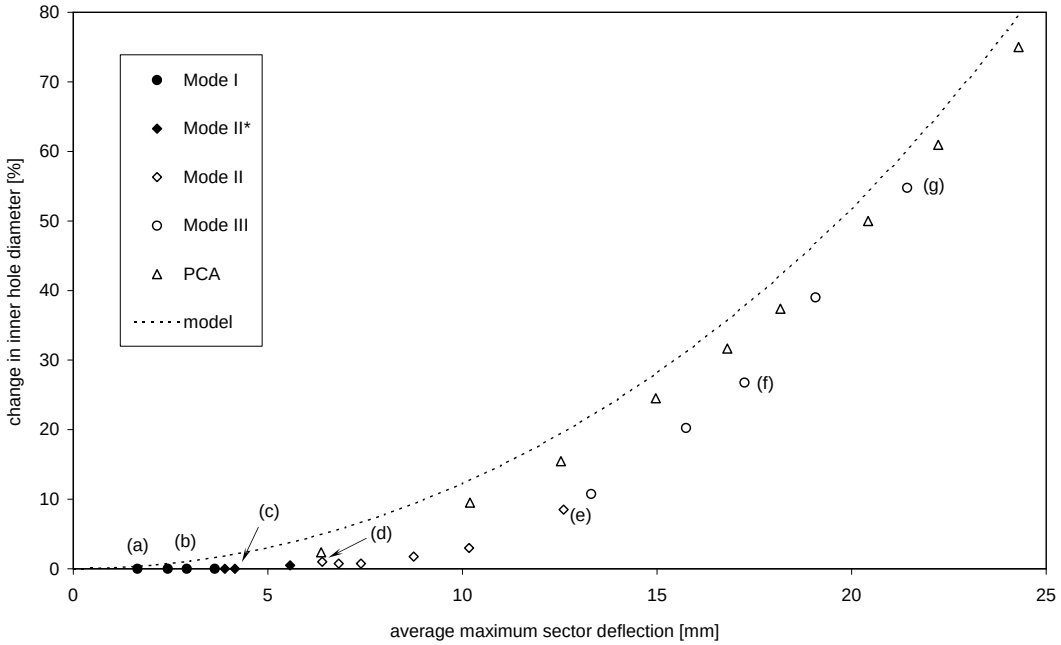

Figure 6.27: Increase in the final hole diameter vs the average maximum sector deflection for 2 mm thick blast loaded PCA and PCCS plates, *i.e.* sheet IV. The model (dotted line) is the expected hole enlargement assuming zero radial strain. Data points corresponding to Mode I and Mode II* behaviour, where no hole was formed, are included for the sake of comparison.

upon the exponential decay of the blast pressure, as can be seen in Figure 5.24[8]. Nevertheless, the effect is expected to be nominally identical for both PCA and PCCA plate configurations and, therefore, a valid impulse offset estimate can still be obtained.

Figure 6.28 shows that the impulse offset between the PCA Mode I and PCCS Mode III data tends to an asymptote of approximately 2 Ns. As argued in Section 6.2.3.5, the impulse values in Figure 6.28 are obtained by integrating the central support force histories and the impulse offset can only be due to the shear forces at the inner PCCS plate boundary. The central support impulse offset is approximately 40% smaller than that obtained from the ballistic pendulum analysis, as shown in Figure 6.19. While this difference is larger than that obtained in the short stand-off results, the results are still consistent and show potential for further refinement of the technique.

The Mode III behaviour of both the 2 mm and 1.6 mm PCCS plates is considered to be consistent and repeatable. In addition to the repeatability evident in the preceding discussion, *e.g.* Figures 6.19 and 6.27, it is also apparent in the central support force histories for similarly loaded plates, as shown in Figures 6.17 and 6.18. Furthermore, the similar progression in the force histories for the different plate configurations is evident, not only when comparing Figures 6.14, 6.15 and 6.16, but also for the short stand-off blast tests, as shown in Figures 6.5.

An estimate of the Mode III shear force history is obtained by comparing test TC070301h to the pressure history of test TC070202b, as shown in Figure 6.29. In test TC070202b, a 2 mm thick PCA plate with an R0 central support was subjected to a 20 g charge which produced a blast load of 32.61 Ns, which is

[8] Establishing the definitive reason for this effect was considered to be could not be beyond the scope of this these and is a topic of future research.

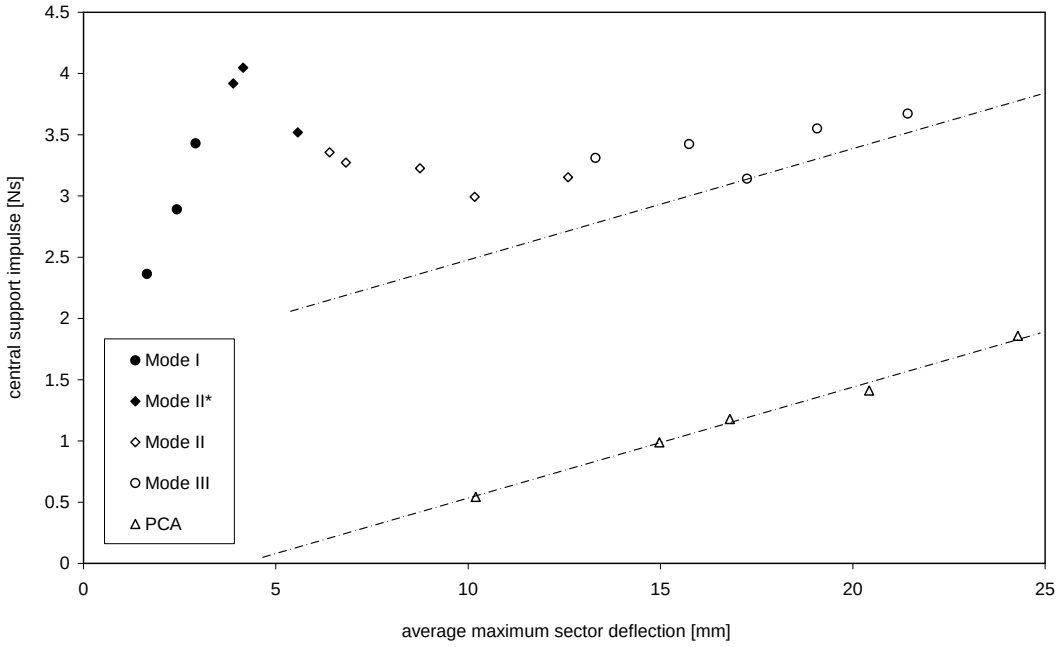

Figure 6.28: The central support impulse as a function of the average maximum sector deflection. The parallel chain line are included as visual aids.

similar to that of test TC070301h. As before, the curves are temporally aligned according to the start of the detonation noise signal.

The first distinctive feature of the resulting Mode III shear force history is the initial peak of 112 MPa that occurs after 16 μs. Given the plate thickness of 1.93 mm, the peak corresponds to a nominal shear stress of 290 MPa, *i.e.* a Mises equivalent of 503 MPa, which is greater than the stress at which shear sliding appears to have occurred in plates displaying a Mode II response, and may indicate elevated strain rate effects. However, this conclusion is tentative since it relies on the repeatability of the peak value of the blast load, which is subject to more variation than the rest of the pressure history, which is highly repeatable, as shown in Figure 5.22. Nevertheless, even allowing for such variation, the initial peak is still significantly greater than that observed during a Mode II response. At worst, accounting for the variation would bring the load level down to that of the shear load plateau of 91 MPa which follows the initial peak after 22 μs. This represents a nominal shear stress of 236 MPa, *i.e.* Mises stress of 408 MPa, which corresponds to the plateaus observed during Mode II response and suggests that Mode III shear failure initiates at the inner boundary immediately upon application of the blast load. In other words, it appears that the transition to Mode III occurs when the blast load is sufficiently intense to cause incipient failure through highly localized shear loading prior to the development of a localized bending response. Furthermore, the loading intensity is such that the transition to localized bending is not clear, *i.e.* there is no distinct secondary peak.

The load plateau that follows the initial load peak has a duration of 11 μs, which is significantly longer that that observed during Mode II behaviour. After 33 μs the shear load history decreases to a local minimum of 74 MPa after 45 μs. This value is greater than the Mode II local minima but occurs later, which corresponds to the extended duration of the plateau.

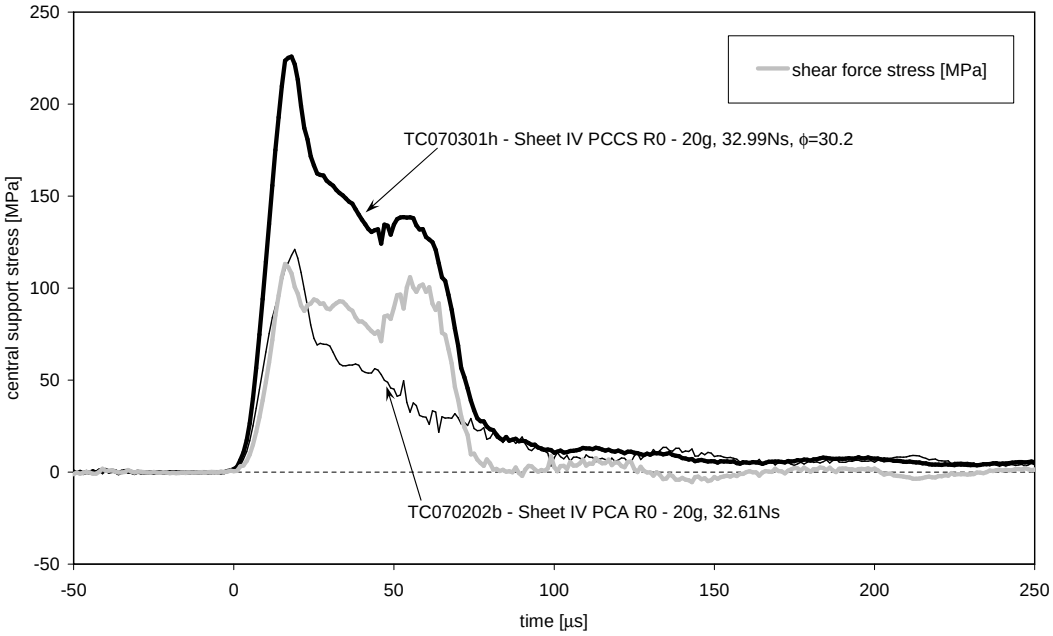

Figure 6.29: Central support shear force history for the Mode III behaviour of a 2 mm thick blast loaded PCCS plates, *i.e.* sheet IV.

Subsequent to the local minimum the shear load history rises rapidly to a 101 MPa after 55 μs. This feature suggests that at least a small amount of membrane deformation does occur prior to shear failure. However, this is somewhat at odds with the definition of a Mode III behaviour and does not correspond to the lack of convex curvature observed in the recovered plate specimens. A possible scenario is that the apparent membrane response corresponds to an early Phase I membrane hinge response with limited convex curvature which subsequently convex curvature 'snaps through' to concave curvature during the post failure deformation. A definitive analysis of this behaviour is beyond the scope of the analytical models pursued in this thesis and will likely require numerical analysis, which is a topic of future research.

The peak membrane response corresponds to a nominal shear stress of 261 MPa, *i.e.* a Mises equivalent of 453 MPa, which, as with the initial peak, is significantly greater than the shear load at which shear failure occurred during the Mode II response. However, unlike the blast pressure peak, this feature corresponds to a portion of the blast load signal that is highly repeatable, *i.e.* it is unlikely that the elevated shear load is an artifact of uncertainties in the data processing. Furthermore, this elevated response at approximately 55 μs is also evident in the central support signals for all the plate configurations, as shown in Figures 6.14, 6.15 and 6.16. Hence, this feature is considered to be an accurate representation of the actual plate response and is, presumably, the result of strain rate effects.

After the peak membrane response, the shear load history appears to enter a second plateau, although this is a tentative observation given the noise in the signal. Nevertheless, after 61 μs there is a distinct drop in the shear load, indicating complete shear failure around the entire inner plate boundary. Furthermore, unlike the Mode II behaviour, the shear load clearly drops immediately to zero, *i.e.* there is no hint of scraping of the resulting hole along the central support. In other words, upon shear failure, the hole immediately begins to enlarge as the plate separates from the central support, *i.e.* PCA like behaviour.

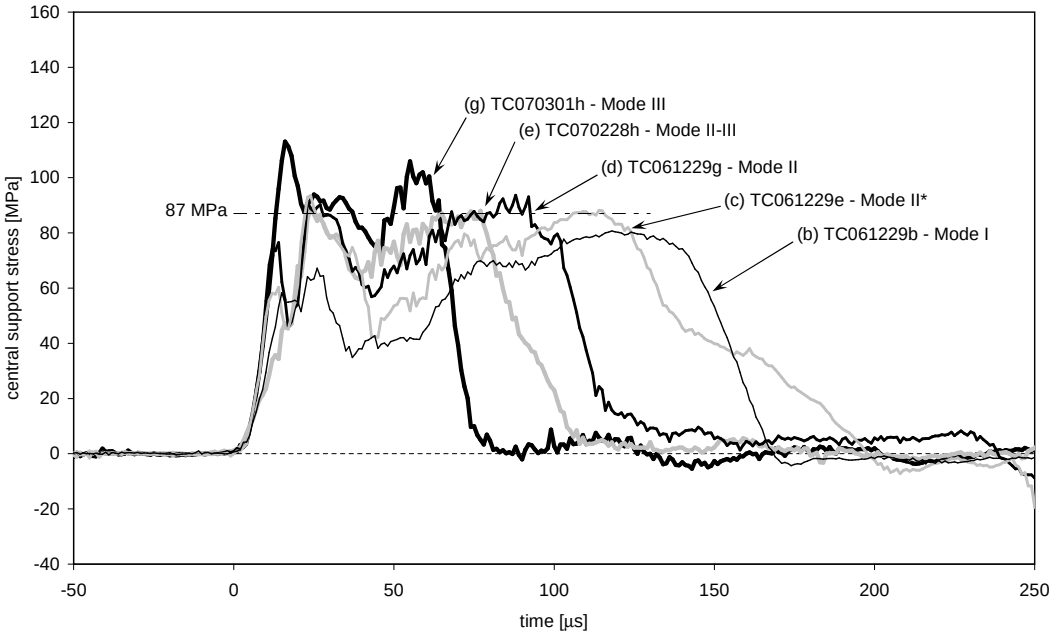

Figure 6.30: Shear force history comparison for the five Sheet IV plate specimens shown in Figure 6.20.

6.3.3.6 Shear Response Comparison

In the preceding sections it is shown that several distinct features of the shear force histories inferred from the central support signals can be related to corresponding features in the summative data plots, such as the dimensionless impulse and deflection. Further insight can be a gained by a direct comparison of the inferred shear force histories, as shown in Figure 6.30, where the curves obtained from the central support signals of the five PCCS plates shown in Figure 6.20 are superimposed.

Figure 6.30 shows that certain features of the shear force histories exhibit a strong correlation between the various failure modes. For example, consistent primary and secondary force spikes are evident, with the time lag between the spikes being particularly repeatable. This suggests that the time lag is not dependent on the blast pressure, which varies considerably. By contrast, the localized deformation response of the plate is likely to be more consistent since it involves plastic bending waves with repeatable wave speeds. Hence, the consistent time lag supports the interpretation that the secondary force spike is due to localized bending type plate deformation.

A second notable feature of Figure 6.30 is the consistent maximum force level in the signals associated with shear failure. As a visual aid, a horizontal chain line has been added that corresponds to a signal level of 87 MPa, *i.e.* a nominal shear stress and Mises equivalent of 225 MPa and 390 MPa, respectively. Figure 6.30 shows that for a Mode II* response, *i.e.* partial shear failure at the inner boundary, the corresponding shear force history briefly touches this signal level. By contrast, for the Mode II and Mode II-III, *i.e.* complete shear failure at the inner boundary, the curves maintain the signal level for considerable durations. This supports the conclusion that the indicated signal level represents a consistent dynamic flow stress throughout the Mode II* and Mode II response regimes, which shows strong strain rate effects, *i.e.* the Mises equivalent of 390 MPa falls in the mid-range of the material properties for

Sheet IV.The signal level of 87 MPa also corresponds to the secondary stress spike peak values during a Mode II* or Mode II response, which is consistent with the conclusion that shear sliding initiates during the secondary shear stress spike. By contrast, the initial Mode III signal shows a plateau at the same signal level with an absence of distinct primary and secondary shear force spikes[9], which supports the interpretation Mode III shear failure is initiated from the primary pressure spike. Lastly, in Sections 6.3.3.3 to 6.3.3.5, where the shear force histories are considered in isolation, the appearance of stress plateaus are regarded as tentative due the relatively noisy signals. However, the apparent consistent shear sliding at the signal level of 87 MPa in Figure 6.30 strengthens the stress plateau interpretation.

In addition to the specific features mentioned above, Figure 6.30 generally support the observations presented in the preceding sections since certain features are easier to appreciate when the shear force signals are superimposed. For example, the consistent timing, *i.e.* between 40 μs and 50 μs, and increasing value of the local minimum is apparent, as is the consistent gradient, but increased value, of the subsequent rise in the signal prior to the stress plateau. Similarly, the progressive decrease in the time to failure with an increasing impulse is clearly illustrated.

6.3.4 Central Support Radius Effect

The results for 2 mm thick plates discussed the preceding sections are broadly representative of similar features observed in the other plate configurations. For example, Figure 6.11 shows that the dimensionless deflection vs impulse results for the PCA and PCCS Mode I response of all the plate configurations are identical. In addition, the Mode I deformation response times appear to be independent of plate thickness, as shown in Figure 6.21. However, Figure 6.11 also shows that the transition to Mode II behaviour is strongly dependent on both the plate thickness and the edge condition of the central support at the inner plate boundary. The aim of this section is to briefly consider the effect of the central support edge condition.

Figures 6.31(a) and (b) show comparisons of typical central support force histories for blast loaded 1.6 mm thick PCCS plates with R0 and R2 central support edge conditions. Figure 6.31(a) shows the force histories for tests TC061020g and TC070210c, where the plate specimens were subjected to nominally identical 5 g charges that resulted in a Mode I response. It is evident that the initial force spikes and maximum plate response are essentially identical, while the Mode I response durations show a difference of 5 μs. This amounts to a difference of less than 4%, which is within the experimental scatter. For example, a similar variation in the deformation duration of two nominally identical blast tests with R0 edge conditions is shown in Figure 6.18. In other words, the central support edge condition has no perceptible influence on the Mode I response.

Figure 6.31(b) shows the force histories for tests TC070301e and TC070210i, where the plate specimens were subjected to nominally identical 16 g charges that resulted in a Mode III response. As before, it is evident that the initial force spikes and maximum plate response are essentially identical. However, in contrast to the Mode I behaviour, the Mode III results show that the time to failure of the R2 edge condition is delayed by 11μs relative to the time to failure of the R0 edge condition. This amounts to a difference of close to 25%, which is outside the range of the experimental scatter. For example, the

[9] As discussed in Section 6.3.3.5, the initial force spike is not considered to be reliable.

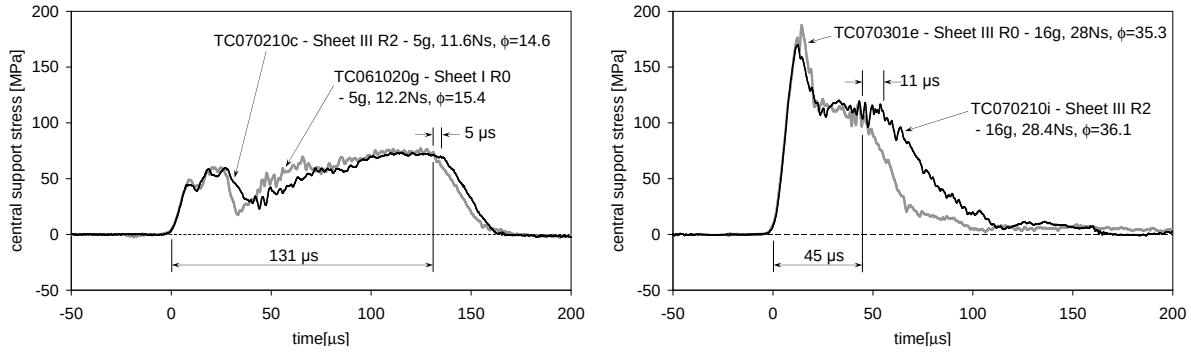

(a) Mode I (b) Mode III

Figure 6.31: Comparison of the central support force histories for blast tests on 1.6 mm thick PCCS plates, *i.e.* sheets I to III, with R0 and R2 central supports during Mode I (a) and Mode III (b) behaviour.

typical repeatability of the Mode III behaviour is shown in Figure 6.18, which shows the near identical force histories of two nominally identical blast tests with R0 edge conditions. Hence, experimental scatter can be eliminated as the cause of the observed difference in time to failure. In other words, the central support edge condition has significant influence on the failure behaviour during a Mode III response.

Estimates of the Mode III shear force history are obtained by comparing the force histories for tests TC070301e and TC070210i to the pressure history of PCA test TC070301b, shown in Figure 5.23, which has a nominally identical charge mass. The resulting Mode III shear force history estimates at the R0 and R2 central support boundaries are shown separately, in Figures 6.32 (a) and (b), respectively, and juxtaposed in Figure 6.33.

In addition to the previously mentioned difference in the time to failure, other characteristic features are evident in Figure 6.33. The shear force histories are similar to that in Figure 6.26. Neither of the curves show a distinct initial shear load peak but rise steadily to a value of 55 MPa after 14 μs. At this point the R2 curve shows the a stress plateau while the R0 curve shows an apparent secondary shear load peak, although both of these features are tentative since they correspond to the portion of the shear force history that has displays some variability.

After approximately 32 μs, both the R0 and R2 histories display distinct shear force plateaus. These plateaus are considered to be reliable and representative of the plate behaviour since they correspond to a portion of the shear force history that is highly repeatable. In the case of the R0 curve the plateau value of the shear force is 71 MPa. Given the plate thickness of 1.63 mm, this is equivalent to a nominal shear stress of 218 MPa, which is consistent with the value of 225 MPa at which shear sliding occurs in the 2 mm thick plates, as reported in Section 6.3.3.6. By contrast, the plateau shear force for the R2 curve is 78 MPa, *i.e.* a nominal shear stress of 239 MPa, which is distinctly higher than that of the R0 curve. Furthermore, the duration of the R2 plateau is 28 μs while for the R0 curve is only 17 μs. Finally, it is evident that, after failure, the shear force drop is more gradual in the case of the R2 edge condition.

Taken together, the results show that the support bar edge condition has a negligible effect on the global plastic deformation of the plate specimen, but a large influence on the localized failure response at the inner boundary. The shear failure induced by the R0 edge condition is consistent with that observed in

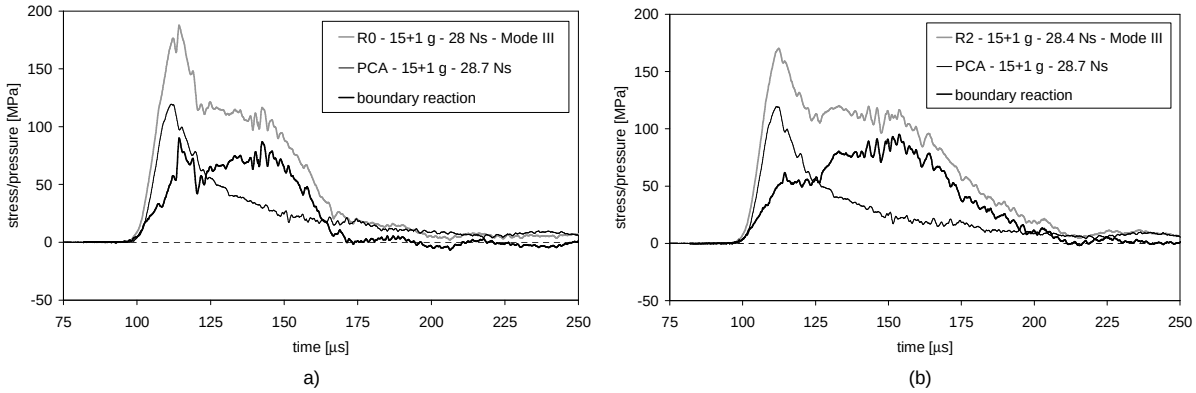

Figure 6.32: Estimates of Mode III shear force history at the (a) R0 and (b) R2 central support boundaries by comparing the force histories of PCCS tests TC070301e and TC070210i to that of PCA test TC070301b.

the 2 mm plates, as reported in Section 6.3.3. By contrast, the rounded R2 edge condition appears to reduce the severity of the induced shear response such the a larger shear force is required over a longer duration to produce failure. These interpretations of the Mode I and Mode III force history results are consistent with the Mode II transition behaviour observed in Figure 6.11.

6.3.5 Summary of General Observations

From the preceding sections, a number of general observations can be made regarding the blast tube configuration of the instrumented ballistic pendulum.

6.3.5.1 Repeatability

The first, and most general, observation is that the blast tube configuration provides consistent and repeatable results. This is most evident in the r^2 values presented in Section 6.3.1 for the Mode I dimensionless deflection vs impulse data, which show a high degree of correlation for both the PCCS (0.9678) and PCA (0.99) plate configurations. These r^2 values constitute a marginal improvement on the data obtained using the short stand-off configuration reported in Section 6.2.1, which suggests that the blast tube configuration is slightly more reliable. This slight improvement is most likely due to the near uniform nature of the blast load produced using a blast tube.

Considering that the correlations are based on data from several different plate thicknesses and span a wide range of impulse values, these results provide strong support for the form of the dimensionless impulse given in Equation (6.1). Furthermore, the correlations provide definitive evidence of a positive x-axis intercept for Mode I regressions, *i.e.* an impulse threshold must be exceed for permanent deformation to occur. In particular, the x-axis intercept of the PCCS Mode I regression in Figure 6.11 is virtually coincident with the data point corresponding to test TC070228b, which showed only marginal residual plastic deformation.

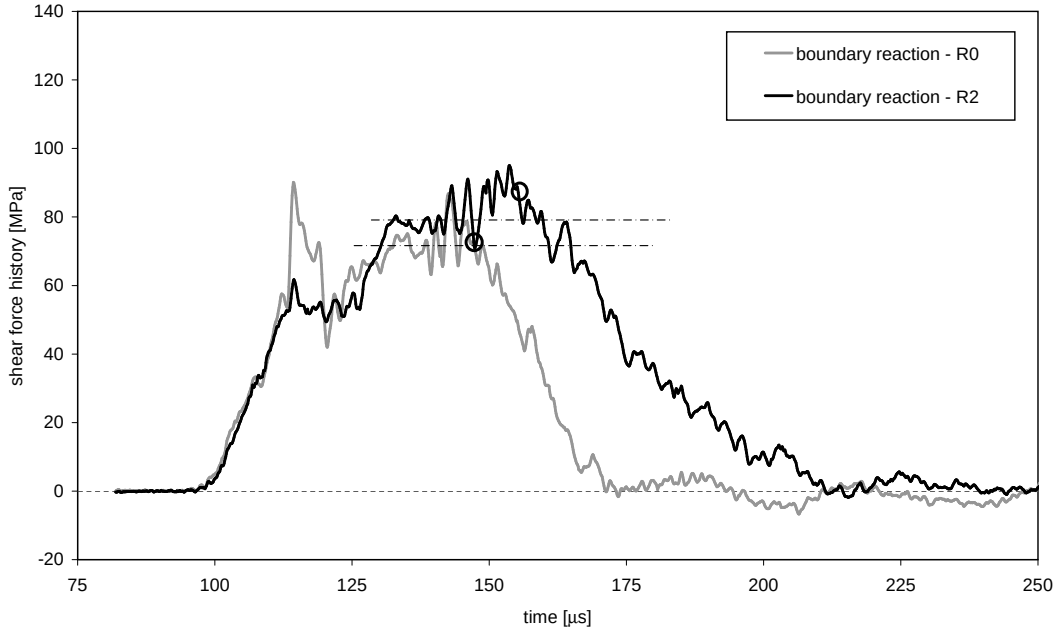

Figure 6.33: Comparison of the Mode III PCCS shear force history estimates shown in Figure 6.32 for R0 and R2 central support boundaries.

The high degree of correlation for the Mode I data of both the blast tube and short stand-off configurations, suggests that the difference between the gradients is significant. From Equations (6.2), (6.3), (6.4) and (6.5), it can be seen that, for a given impulse, the short stand-off PCCS and PCA data, respectively, are approximately 42 % and 54 % higher that the corresponding blast tube data. This may be attributed to the slight attenuating effect of a blast tube, which results in a blast wave that is closer to a critical impulsive load and dynamic in character, as opposed to the near ideal impulsive load produced by a short stand-off charge[10].

Furthermore, the consistent quality of the blast tube data allows for the repeatability of the force history to be considered. For example, Figures 6.17 and 6.18 show that nominally identical plates subjected to similar blast loads display virtually identical response histories. These results are significant because the response histories include phenomena such as tensile necking and shear failure, which are deformation instabilities and, therefore, inherently sensitive to variability in the test conditions. Consequently, the consistent force histories allow reliable failure data to be extracted for comparison with numerical simulations.

6.3.5.2 Failure Modes

The four failure modes defined in Section 6.1.1 were observed in the recovered plates of all the test series, with one exception for the 3 mm thick plates where Mode III could not be achieved without damaging the blast tube. Typical recovered 2 mm thick PCCS plates are shown in Figure 6.20. Furthermore, while the mode transitions do not scale with dimensionless impulse, they are consistent for each individual plate thickness, as is evident in the dimensionless impulse and deflection plots of Figure 6.11. In particular,

[10] This interpretation is considered further in Section 8.3.3.

the Mode II transitions were distinct and highly repeatable for each plate thickness and support edge condition, which may be a useful feature to test scaling effects in numerical codes.

The mode response transition points correlated well with recorded force history signals, where each response regime could be associated with specific signal features. As in the short stand-off test, the time to failure decreases with increasing impulse, while the nominal transverse shear stress at failure increases slightly indicating a certain amount of rate sensitivity in the failure behaviour. Additional evidence of the failure mode transition is shown in the degree of central hole expansion and the central support impulse fraction, *i.e.* Figures 6.12 and 6.13. In all the above, the identification of the Mode II to III transition is aided by the comparison of PCCS data to the PCA results, such as in Figure 6.19.

6.3.5.3 Shear Fracture Forces

The blast tube configuration shows similar fracture behaviour to that observed in the short stand-off tests. In particular, it was noted in Section 6.2.4 that the short stand-off tests exhibited shear fracture at a maximum plate response of approximately 73 MPa, which implies a nominal shear stress in the order of 250 MPa. The less impulsive nature of the blast tube loading means that more nuance is evident in the central support for histories. For example, Figure 6.14 shows an increase in the shear failure response after the transition from Mode II to Mode III, where the short stand-off tests do not. In this case the transition occurs at a plate response of approximately 100 MPa, which implies a nominal shear stress in the order of 250 MPa, *i.e.* virtually identical to the short stand-off result and indicative of the consistency of the blast tests.

In addition to the above, the higher repeatability of the blast tube configuration, both in terms of the blast load and mode response, allows for more estimates the shear force history at the inner boundary, as shown in Figure 6.30. The notable feature is the consistent maximum response 87 MPa, which implies a nominal shear stress in the order of 225 MPa. This shows the importance of being able to remove the contribution of the blast load and lends further support to the maximum shear stress criterion used by Olson *et al.* [184, 185] for the prediction of Mode III failure, although a finite time to allow for shear sliding may need to be incorporated.

6.3.6 The Blast Tube PCCS Configuration as a Precision Blast Test

In the preceding sections, the blast test results obtained using the blast tube configuration of the instrumented ballistic pendulum with the PCCS and PCA plate test configurations have been shown to be an improvement on the short stand-off configuration. The high level of repeatability of the blast load and plate response was further improved, while the well defined boundary conditions and measurement redundancy. Furthermore, the aspects of the short stand-off configuration considered to be sub-optimal from the perspective of analytical and numerical analysis were addressed. The use of a blast tube resulted in repeatable pressure and impulse intensities that are uniform in space and time, while small charge masses required for low impulse values detonate reliably. As a consequence of these improvements, it is possible to capture subtle effects such as the difference in the failure mechanism between square and rounded boundary edge conditions. These results suggest that the blast tube configuration of the

instrumented pendulum in conjunction with the PCCS and PCA plate configurations provide superior data to the PCS configuration in terms of a precision test, and will be discussed in detail in Chapter 9.

Chapter 7

Analytical Modelling of PCCS and PCA Plates

"There is nothing more practical than a good theory."

James C. Maxwell (1831-1879)

7.1 Introduction

This chapter presents the development of approximate closed form solutions for blast loaded peripherally clamped centrally supported (PCCS) and peripherally clamped annular (PCA) circular plates. The purpose is to provide a basis for comparing, correlating and interpreting the experimental results presented in Chapter 6. The particular focus is on the large deflection regime, *i.e.* maximum deflections of more than a plate thickness and less that a plate radius, as defined in Section 2.3.1, since this accounts for the majority of the experimental results. The models are developed in the general tradition of the assumed displacement solutions reviewed in Section 2.3. In particular, the models can be viewed as extension of the generalized energy method, as presented in Section 3.3 and Chapter 4 for PCS plates, to the PCCS and PCA configurations.

In the sections to follow, the first introduces and motivates the assumed displacement profiles chosen for the analysis of PCCS and PCA plates, following similar reasoning as reviewed in Section 2.3.1. In particular, the chosen profiles are discussed with reference to measured PCCS and PCA plate profiles. Thereafter, the next two sections of this chapter are devoted to ideal impulsive loading. Expressions for the plastic stiffness and the plastic dissipation parameter λ are developed in accordance with Section 3.3, and used to obtain solutions for the final deflection of PCCS and PCA plates subjected to an ideal impulsive load. These solutions provide the form of the dimensionless impulse used to analyse the experimental data in Chapter 6. Furthermore, expressions for the deformation duration are developed based on single phase and two phase descriptions. The two phase description incorporates aspects of the transient behaviour analysis presented in Chapter 4 and includes the concept of moving plastic hinges in an approximate

sense. In other words, details of the plastic hinge motion are not considered, although the influence of Phase I motion will be accounted for. In the final section, the transient analysis is extended to loads of finite duration where two special cases, namely a critical impulsive load (CIL) and an ideal dynamic load (IDL), are considered. Comparisons of these theoretical results with the experimental results are discussed in Chapter 8.

7.2 Assumed Displacement Profile

In the context of the generalized energy method, the displaced shapes of the plates are assumed *a priori* and then used in the analyses. Hence, the choice of plate shape will have a large bearing on the accuracy of the results. Throughout this chapter, the plate deformation profiles will be chosen to match the plate shapes obtained from the blast loading experiments as closely as possible, while maintaining a reasonably compact mathematical form. Nevertheless, it will also be shown that in many cases the chosen plate shape also has a sound physical interpretation.

7.2.1 Peripherally Clamped Centrally Supported Plates

As mentioned in Section 6.1, the PCCS plate configuration has been developed to study the boundary reaction forces of blast loaded plates. By implication, this configuration is novel and does not have an associated body of literature dealing with the analysis of its behaviour, except for the paper published in the course of this work [52]. Hitherto, only a simple parabolic deflection shape has been considered,

$$w(r) = 4\tilde{w}\left[\frac{r - R_i}{R_o - R_i} - \left(\frac{r - R_i}{R_o - R_i}\right)^2\right] \tag{7.1}$$

where R_i and R_o are the inner and outer radius respectively and $\tilde{w}$ is the maximum plate deflection, which in this case occurs at the mid-radius and not the middle of the plate. The choice of this equation was initially motivated by the success achieved using a parabolic shape for PCS plates. Furthermore, it has a simple and convenient mathematical form and automatically satisfies the kinematic boundary conditions. However, unlike the PCS case, a simple parabolic deflection shape does not represent the general quasi-static solution of Equation (2.8) for a PCCS plate. Nevertheless, it will be shown below, that Equation (7.1) does represent the quasi-static solution for the case where R_i tends to R_o. This is, in fact, the basis for the membrane analogy, first proposed by Prandtl [189], used in the study of the pure elastic torsion of open thin walled sections. In other words, the parabolic assumption is not without physical meaning and can be expected to provide a useful first estimate for comparison with the more accurate displacement shapes. Furthermore, it provides a useful proxy for problems where more exact profiles may prove to be mathematically intractable, an example being the analysis presented in Section 2.3.8.

Figure 7.1 shows the parabolic profile compared to typical experimental data from recovered plates of the three plate thicknesses studied in this work. While the parabolic profile provides a reasonably accurate description of the final plate shape, there are distinct discrepancies. In particular, the experimental

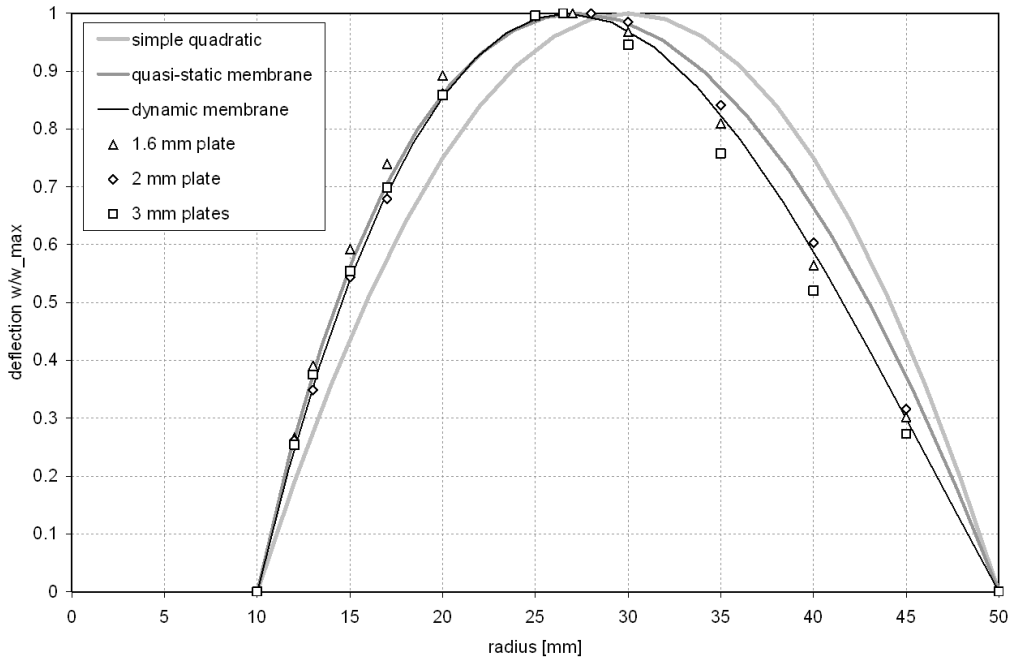

Figure 7.1: Various assumed displacement shapes for PCCS plates compared with experimental data.

evidence indicates that the maximum deflection should occur at a radius of between 26.5 mm and 28 mm, whereas the parabolic assumption places the maximum at 30 mm.

An improved shape is obtained using the procedure outlined in Sections 2.3.1 and 2.3.2. Taylor [15], in his seminal work, argued that if the plates are relatively thin, suffer large deformations and can be viewed as rigid-plastic, then they are likely to behave in an analogous manner to dynamically deforming membranes. Hence, solutions of Equation (2.7) for the PCCS configuration under both the static loading and vibrating conditions are considered.

The procedure for the static solution of Equation (2.8) for the PCCS configuration is the same as for the PCS configuration, except that the position of the maximum deflection is not known *a priori*. The solution for the case of a quasi-static load is[1],

$$w = \frac{P}{2\sigma_0 H}\left[\tilde{R}^2 ln\left(\frac{r}{R_i}\right) - \frac{1}{2}\left(r^2 - R_i^2\right)\right] \quad \text{with} \quad \tilde{R} = \sqrt{\frac{R_o^2 - R_i^2}{2\,ln\left(\frac{R_o}{R_i}\right)}} \tag{7.2}$$

where $\tilde{R}$ is the radius at which the maximum deflection occurs.

[1]This solution was obtained by invoking the analogy between laminar pipe flow and static membrane deflection [189] to make use of the solution for the velocity distribution of laminar viscous flow in an annular pipe, as given by White [120].

Note that in the case where R_i tends to R_o, the logarithmic terms can be approximated by the first term of the Taylor expansion,

$$ln\left(\frac{r}{R_i}\right) \approx \left(\frac{r}{R_i} - 1\right) \quad \text{and} \quad ln\left(\frac{R_o}{R_i}\right) \approx \left(\frac{R_o}{R_i} - 1\right)$$

Using these approximations, Equation (7.2) reduces to the form of Equation (7.1), as mentioned previously.

For the plates used in this work, Equation (7.2) gives a prediction of $\tilde{R} = 27.31$ mm, which is well within the experimental data. Furthermore, Figure 7.1 shows that Equation (7.2) gives a good estimate of the inner portion of the plate, *i.e.* for radii less than $\tilde{R}$. However, the deflections are over predicted for the outer portion of the plate.

The dynamic case, *i.e.* a vibrating PCCS membrane, is governed by Equation (2.10) for which the spatial component of the general solution is given in Equation (2.15) and repeated here for convenience.

$$w(r) = \tilde{w}A\left[J_0\left(\Lambda\frac{r}{R_o}\right) + BY_0\left(\Lambda\frac{r}{R_o}\right)\right] \tag{7.3}$$

At the inner and outer boundary the displacement vanishes, hence,

$$w(R_i) = w(R_o) = 0 \quad \Rightarrow \quad J_0(\Lambda) + BY_0(\Lambda) = J_0\left(\Lambda\frac{R_i}{R_o}\right) + BY_0\left(\Lambda\frac{R_i}{R_o}\right) = 0 \tag{7.4}$$

Eliminating the constant B results in,

$$\frac{J_0\left(\Lambda\frac{R_i}{R_o}\right)}{J_0(\Lambda)} = \frac{Y_0\left(\Lambda\frac{R_i}{R_o}\right)}{Y_0(\Lambda)} \tag{7.5}$$

from which Λ can be solved numerically for a given ratio of R_i to R_o. For the results presented in Chapter 6, the ratio is equal to 0.2 for which $\Lambda = 3.816$, and consequently $B = 6.955$ by back substitution. The values of the constants for other ratio of R_i to R_o are given in Appendix D.

To solve for the value of A, the radial position $\tilde{R}$ of the maximum displacement $\tilde{w}$ is required. The gradient of Equation (7.3) is,

$$\frac{dw}{dr} = \tilde{w}A\left(-\frac{\Lambda}{R_o}\right)\left[J_1\left(\Lambda\frac{r}{R_o}\right) + BY_1\left(\Lambda\frac{r}{R_o}\right)\right] \tag{7.6}$$

Setting the gradient to zero and solving for r gives the value of $\tilde{R} = 26.78$ mm. Thereafter, back substituting into Equation (7.3) and solving gives $A = 0.2647$. The value $\tilde{R}$ is well within the experimental data and very similar to the static result. Figure 7.1 shows that Equation (7.3) gives the most accurate correlation with the experimental results. In particular, the experimental results for the 1.6 mm and 2 mm plates are well described.

The only data that is not well described is the deflection of the outer portion of the 3 mm plates. A possible reason for this is that the 3 mm plates are thick enough for bending effects to make significant contribution. The role of bending effect in the deflection of PCS plates was presented in Section 3.3.7. While the results are not strictly applicable to the PCCS configuration, the effect of bending strain in the

outer portion of the plates should be similar. Figure 3.15 indicates that bending effects are negligible for displacements greater than twice the plate thickness, which corresponds to the largest Mode I deflections for the 1.6 mm and 2mm plates, as shown in Figure 6.11. By contrast, the largest Mode I deflections for the 3 mm plates are in the order of a plate thickness, where Figure 3.15 indicates that bending effects would be noticeable. Nevertheless, even in this case, the correlation is considered to be adequate for the analyses presented in this chapter.

The results indicate that the Bessel function deflection profile correlates best with the experimental results and is thus the best choice for the PCCS plate shape. Solutions based on the static plate shape will not be pursued since it is similar to the Bessel profile and does not simplify further mathematical manipulations.

7.2.2 Peripherally Clamped Annular Plates

Published analytical solutions for impulsively loaded peripherally clamped annular plates were briefly reviewed in Section 2.4. In particular, the work of Jones [44] showed that membrane strains were the dominant deformation mechanism at relatively small finite displacements and suggested that at larger deflections a pure membrane solution would provide an accurate approximation. Jones proposed the linear displacement profile given in Equation (2.62), which can be rewritten as,

$$w(r) = \tilde{w}\left[1 - \left(\frac{r - R_i}{R_o - R_i}\right)\right] \tag{7.7}$$

Furthermore, Jones assumed that there are no radial strains, as opposed to the typical assumption that there are no radial displacements. This is equivalent to viewing a radial cross-section as hinging at the outer clamped edge while maintaining a constant length. While this assumption may not be appropriate for all plate shapes, especially if the central radius is small, Figure 7.2 shows that it is an accurate assumption for the PCA plate experiments reported in Chapter 6. Note that the radial displacement is significantly smaller than the transverse deflection, which, in turn, is less than half the radial length of the cross-section. Hence, the approximate expression proposed by Jones for the radial displacement given in Equation (2.63) can be used,

$$u(r) \approx \frac{w^2}{2(R_o - r)} \tag{7.8}$$

where u is the radial displacement. A scaled plot of experimental deflections for the three plate thicknesses is shown in Figure 7.3. It is clear that the linear assumption adequately describes that plate shape.

7.3 Ideal Impulsive Loading

In this section, the ideal impulsive loading (IIL) approach is extended to the PCCS and PCA plate configurations. As described in Section 2.3.3, the load is assumed to be uniformly distributed and of such a short duration that the plate is considered to have a simple uniform initial velocity distribution. Under these conditions, the initial kinetic energy is given by Equation (2.19), which is repeated here for

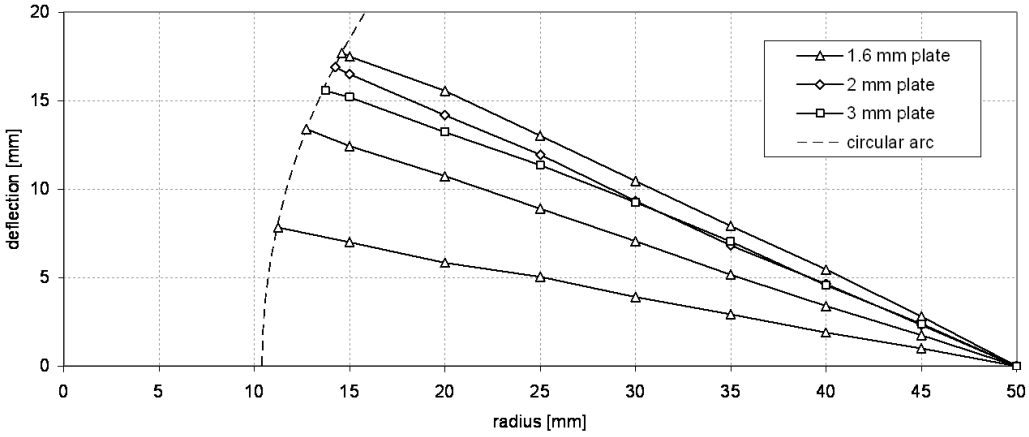

Figure 7.2: Typical experimental displacement profile for PCA plates.

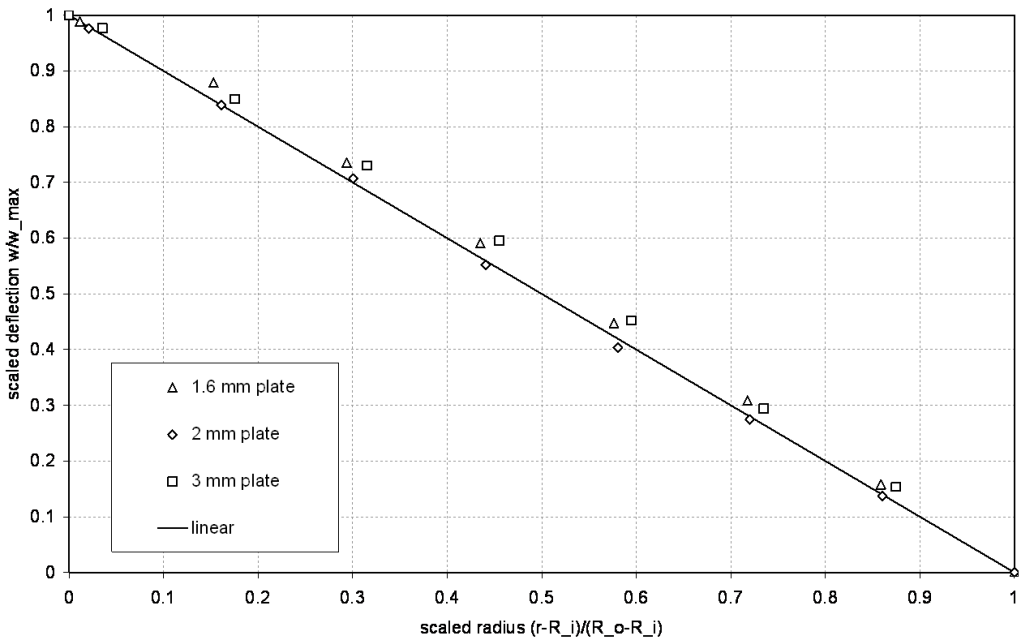

Figure 7.3: Typical experimental displacement profile for PCA plates.

convenience,

$$E_{k,0} = \frac{I^2}{2m} \tag{7.9}$$

In this case, the mass of both a PCCS or PCA plate is,

$$m = \rho\pi(R_o^2 - R_i^2)H \tag{7.10}$$

where R_o and R_i are the outer and inner radii of the plate, respectively, while the other variables retain their previous definitions. Note that in the case of a PCS plate the inner diameter vanishes and Equation (2.18) is recovered. Furthermore, note that in this case I is not the total measured experimental impulse since some of it will have been transferred directly to the central support. Only the impulse applied to the deforming portion of the plate is considered, *i.e.* the impulse applied within the R_i boundary does not contribute to Equation (2.19). In other words, since the impulse is assumed to be uniform, I is obtained by scaling the measured impulse according to the ratio of the annular area of the plate, *i.e.* between R_i and R_o, and the total exposed area of the plate.

As discussed in Section 3.3.1, the IIL approach assumes distinct initial and final deformation shapes without considering the intermediate configurations. Strictly speaking, this approach is only correct if the material is rate insensitive and the strain is monotonic, which is not generally the case. Nevertheless, the iterative analysis reviewed in Section 2.3.7 showed that reasonable predictions are achieved when rate effects and the deformation duration are considered in an approximate sense. Further improvements are obtained by considering the intermediate states, as shown in Section 4.2.3. The deformation duration for the PCCS configuration will be considered in Section 7.4.

7.3.1 Plastic stiffness of PCCS Circular Plates

In this section the generalized energy method is use to obtain the plastic stiffness parameter λ for PCCS circular plates, which is then used to predict the IIL response. Two assumed deformation shapes are considered, namely a parabolic and Bessel form, as discussed in Section 7.2.1. Noting that for a PCCS plate both the inner and outer boundaries do not experience significant radial motion, the analysis performed in Section 3.3.6 is applicable and, therefore, the effect of radial displacements will not be considered. Furthermore, the PCCS response is considered to be sufficiently similar to that of the PCS configuration that the conclusions reached in Sections 3.3.7 and 3.3.8 are applicable, and hence bending and non-monotonic strain effects will not be considered.

7.3.1.1 Parabolic Displacement Distribution

From Equation (7.1) a parabolic axial displacement for a PCCS plates has the form,

$$w = 4\tilde{w}\left[\frac{r - R_i}{R_o - R_i} - \left(\frac{r - R_i}{R_o - R_i}\right)^2\right] \tag{7.11}$$

Neglecting radial displacements and using Equation (2.21), the expression for the radial strain is,

$$\epsilon_r = \frac{8\tilde{w}^2}{(R_o - R_i)^2}\left[1 - 2\frac{r - R_i}{R_o - R_i}\right]^2 \tag{7.12}$$

Upon integration, the dissipated plastic work is,

$$W_P = \frac{1}{2}\lambda\pi H\alpha\sigma_y\frac{R_o + R_i}{R_o - R_i}\tilde{w}^2 \tag{7.13}$$

where

$$\lambda = \int_{R_i}^{R_o}\frac{32}{(R_o + R_i)(R_o - R_i)}\left[1 - 2\frac{r - R_i}{R_o - R_i}\right]^2 r dr = \frac{16}{3}$$

Note that the value of λ is independent of the choice of R_i and R_o.

Writing Equation (7.13) in the form of Equation (3.19) gives,

$$W_P = \frac{1}{2}\tilde{K}\tilde{w}^2 \quad \text{where} \quad \tilde{K} = \lambda\pi H\alpha\sigma_y\frac{R_o + R_i}{R_o - R_i} \quad \text{and} \quad \lambda = \frac{16}{3} \tag{7.14}$$

where $\tilde{K}$ is the plastic stiffness. Note that the expression for $\tilde{K}$ is a generalized form of the expression for the plastic stiffness of PCS plates given in Equation (3.20), which reduces to the PCS form as R_i vanishes. Furthermore, as with the PCS plates, $\tilde{K}$ is independent of the size of the plate, provided that the ratio of R_i to R_o remains constant.

Equating the plastic work to the initial kinetic energy using Equations (2.19), (7.10) and (7.13) gives,

$$E_{k,0} = W_P \quad \Rightarrow \quad \tilde{w} = \sqrt{\frac{2E_{k,0}}{\tilde{K}}} = \sqrt{\frac{I^2/\pi(R_o^2 - R_i^2)H\rho}{\lambda\pi H\alpha\sigma_y\frac{R_o+R_i}{R_o-R_i}}} \tag{7.15}$$

Dividing both sides by H, to render the relation non-dimensional, and rearranging, results in,

$$\delta = \frac{1}{\sqrt{\lambda\alpha}}\phi \quad \text{where} \quad \delta = \frac{\tilde{w}}{H} \quad \text{and} \quad \phi = \frac{I}{\pi(R_o + R_i)H^2\sqrt{\rho\sigma_y}} \tag{7.16}$$

Note that the expression for the dimensionless impulse is identical to equation (3.22) except for the R_i term. Equation (7.16) is essentially a generalization of equation (3.22), where the latter can be regained by allowing the R_i term to vanish. Furthermore, the geometry of the plate only appears in the ϕ expression, *i.e.* this analysis predicts that all PCCS plate results should fall on the same dimensionless trend line, regardless of the R_i to R_o ratio since λ is a constant. A summary of the values for the PCCS plate profile parameters considered in this thesis are given in Table 7.1.

7.3.1.2 Bessel Function Displacement Distribution

From equation (7.3) a Bessel function axial displacement for a PCCS plates has the form,

$$w(r) = \tilde{w}A\left[J_0\left(\Lambda\frac{r}{R_o}\right) + BY_0\left(\Lambda\frac{r}{R_o}\right)\right] \tag{7.17}$$

Table 7.1: Summary of IIL results for PCCS and PCA deformation profiles using the generalized energy method, *i.e.* the plastic stiffness and effective mass coefficients, normalized non-dimensional central deflection, single phase initial central velocity, single phase displacement duration and two phase displacement durations.

Profile	λ		μ		$\frac{\delta}{\sqrt{\frac{1}{\alpha}}\,\phi}$	$\frac{\dot{\tilde{w}}_0}{V_0}$	$\frac{T}{T_T}$	$\frac{T_{II}}{T_T}$
	exact	approx.	exact	approx.				
parabolic	$\frac{16}{3}$	5.3333	$\frac{8}{15}$	0.5333	0.4330	1.3693	0.9953	1.1094
Bessel	Eq (7.19)	4.4088	Eq (7.43)	0.4731	0.4763	1.4539	1.0291	1.1883
Hinge	4	4	-	-	0.5	1	1	-
PCA ($u_r = 0$)	1	1	-	-	1	-	-	-
PCA ($\epsilon_r = 0$)	$\frac{2}{3}$	0.6667	-	-	1.2247	-	-	-

where, for a R_i to R_o ratio of 0.2 the constants are $\Lambda = 3.816$, $B = 6.955$ and $A = 0.2647$. Neglecting radial displacement and using Equation (2.21), the expression for the radial strain is,

$$\epsilon_r = \frac{1}{2}\left(\frac{A\Lambda}{R_o}\right)^2 \tilde{w}^2 \left[-J_1\left(\Lambda\frac{r}{R_o}\right) - BY_1\left(\Lambda\frac{r}{R_o}\right)\right]^2 \tag{7.18}$$

From equation (2.23), the expression for dissipated plastic work is,

$$W_P = \pi H\alpha\sigma_y\tilde{w}^2\left(\frac{A\Lambda}{R_o}\right)^2 \int_{R_i}^{R_o} r\left[-J_1\left(\Lambda\frac{r}{R_o}\right) - BY_1\left(\Lambda\frac{r}{R_o}\right)\right]^2 dr$$

Introducing the dummy variable $x = \Lambda r/R_o$ and rewriting to have a form that corresponds with the previous sections, the plastic work can be expressed as,

$$W_P = \frac{1}{2}\lambda\pi H\alpha\sigma_y\frac{R_o + R_i}{R_o - R_i}\tilde{w}^2 \quad \text{where} \quad \lambda = 2A^2\frac{R_o - R_i}{R_o + R_i}\int_{\frac{R_i}{R_o}\Lambda}^{\Lambda} x\left[-J_1(x) - BY_1(x)\right]^2 dx \tag{7.19}$$

The expansion of the integral takes the form,

$$\int_{\frac{R_i}{R_o}\Lambda}^{\Lambda} x\left[-J_1(x) - BY_1(x)\right]^2 dx = \int_{\frac{R_i}{R_o}\Lambda}^{\Lambda} xJ_1^2(x)dx + 2B\int_{\frac{R_i}{R_o}\Lambda}^{\Lambda} xJ_1(x)Y_1(x)dx + B^2\int_{\frac{R_i}{R_o}\Lambda}^{\Lambda} xY_1^2(x)dx$$

These are Lommel integrals for which the solutions are well known [161] and give the result,

$$\begin{aligned}\int_{\frac{R_i}{R_o}\Lambda}^{\Lambda} x\left[-J_1(x) - BY_1(x)\right]^2 dx = &\left[\frac{x^2}{2}\left\{J_1^2(x) - J_0(x)J_2(x)\right\}\right]_{\frac{R_i}{R_o}\Lambda}^{\Lambda} \\ &+ 2B\left[\frac{x^2}{4}\left\{2J_1(x)Y_1(x) - J_0(x)Y_2(x) - J_2(x)Y_0(x)\right\}\right]_{\frac{R_i}{R_o}\Lambda}^{\Lambda} \\ &+ B^2\left[\frac{x^2}{2}\left\{Y_1^2(x) - Y_0(x)Y_2(x)\right\}\right]_{\frac{R_i}{R_o}\Lambda}^{\Lambda}\end{aligned} \tag{7.20}$$

At this point the analysis reveals a feature that is not present in the previous analyses, namely that the value of λ depends on the geometry of the plate. Values for λ ranging from 3.683 to 4.932 are evaluated in Appendix D for R_i to R_o ratios ranging from 0.05 to 0.9 respectively. Note that the latter value is approaching the value of 5.333 derived in the previous section. This is expected since a parabolic shape assumption should become more accurate as R_i tends to R_o, as discussed previously. For a R_i to R_o ratio of 0.2, equation (7.19) can be rewritten as,

$$W_P = \frac{1}{2}\tilde{K}\tilde{w}^2 \quad \text{where} \quad \tilde{K} = \lambda\pi H\alpha\sigma_y\frac{R_o + R_i}{R_o - R_i} \quad \text{and} \quad \lambda = 4.4088 \tag{7.21}$$

Equating the plastic work to the initial kinetic energy using Equations (2.19) and (7.19) gives,

$$\delta = \frac{1}{\sqrt{\lambda\alpha}}\phi \qquad \text{where} \qquad \delta = \frac{\tilde{w}}{H} \qquad \text{and} \qquad \phi = \frac{I}{\pi(R_o + R_i)H^2\sqrt{\rho\sigma_y}} \tag{7.22}$$

Note that the expression for the dimensionless impulse is identical to equation (7.16), with the exception that λ is not a constant. Hence, this analysis predicts that all PCCS plate results should not fall on the same dimensionless trend line, but will depend on the R_i to R_o ratio. However, this dependence is not strong as shown in appendix D, where, for R_i to R_o ratios of 0.05 to 0.9, the values of $1/\sqrt{\lambda}$ vary from 0.521 to 0.45 respectively. Hence, this effect may be difficult to observe experimentally due to masking of the inherent scatter in blast test results. Experimental correlation based on this analysis are presented in Section 8.3.

7.3.2 Plastic stiffness of PCA Circular Plates

In this section the generalized energy method is use to obtain the plastic stiffness parameter λ for PCA circular plates, which is then used to predict the IIL response. As shown in Section 7.2.2, the measured displaced shape of an impulsively loaded PCA plate is essentially a straight sided cone. Hence, for analysis purposes, the linear axial displacement profile given in Equation (7.7) is assumed. In addition, two distinct assumptions, namely zero radial displacement and zero radial strain, are considered. The zero radial displacement assumption is consistent with the analyses in the previous section and is included for the sake of completeness. By contrast, the deformation shape described in Section 7.2.2 suggests that the zero radial strain assumption is more applicable. In other words, the contribution of radial displacements are accounted for using Equation (7.8). Lastly, the PCA response is considered to be sufficiently similar to that of the PCS configuration that the conclusions reached in Sections 3.3.7 and 3.3.8 are applicable, and hence bending and non-monotonic strain effects will not be considered.

7.3.2.1 Zero Radial Displacement Assumption

Using Equation 2.21 the expression for the radial strain is,

$$\epsilon_r = \frac{1}{2}\frac{\tilde{w}^2}{(R_o - R_i)^2} \tag{7.23}$$

Upon integration, the dissipated plastic work is,

$$W_P = \frac{1}{2}\pi H \alpha \sigma_y \frac{R_o + R_i}{R_o - R_i}\tilde{w}^2 \tag{7.24}$$

Equation (7.24) can be rewritten as,

$$W_P = \frac{1}{2}\tilde{K}\tilde{w}^2 \quad \text{where} \quad \tilde{K} = \lambda \pi H \alpha \sigma_y \frac{R_o + R_i}{R_o - R_i} \quad \text{and} \quad \lambda = 1 \tag{7.25}$$

Note that the expression for $\tilde{K}$ reduces to the form in Equations (2.25) and (2.27) as R_i vanishes and the resulting deformation shape is a solid cone. Furthermore, as with the PCS plates, the diameter of the plate does not alter $\tilde{K}$, although in this case the ratio of R_i to R_o has an effect.

Equating the plastic work to the initial kinetic energy using equations 2.19 and 7.24 gives,

$$\delta = \frac{1}{\sqrt{\lambda\alpha}}\phi \qquad \text{where} \qquad \delta = \frac{\tilde{w}}{H} \qquad \text{and} \qquad \phi = \frac{I}{\pi(R_o + R_i)H^2\sqrt{\rho\sigma_y}} \tag{7.26}$$

Note that the expression for the dimensionless impulse is identical to equation 3.22 except for the R_i term. Equation 7.26 is essentially a generalization of equation 3.22, where the latter can be regained by allowing the R_i term to vanish.

7.3.2.2 Zero Radial Strain Assumption

As mentioned in Section 7.2.2, PCA plates deform in a conical shape with the inner diameter increasing significantly such that the radial length of the cross-section of the cone remains unchanged. As before, the axial displacement is assumed to have the form described by equation (7.7), while the expression for the radial displacement is given in equation (7.8). Following Section 2.3.8, the expression for the radial strain that includes both axial and radial displacements is given by Equation (2.57) and repeated here for convenience,

$$\epsilon_r = \frac{1}{2}\left(\frac{dw}{dr}\right)^2 + \frac{du}{dr} \tag{7.27}$$

Differentiating Equations (7.7) and (7.8) and substituting into equation (7.27) results in ϵ_r vanishing, *i.e.* no radial strain occurs in the plate. Hence, strains occur only in the transverse 'hoop' direction, the expression for which is also given by Equation (2.57) and repeated here for convenience,

$$\epsilon_\theta = \frac{u}{r} \tag{7.28}$$

Substituting equation (7.8) into equation (7.28) gives,

$$\epsilon_\theta = \frac{1}{2}\left(\frac{\tilde{w}}{R_o - r}\right)^2 \left(\frac{R_o}{r} - 1\right) \tag{7.29}$$

Upon integration, the dissipated plastic work is,

$$W_P = \frac{1}{2}\pi H \alpha \sigma_y \tilde{w}^2 \tag{7.30}$$

Keeping with the form of previous results, Equation (7.30) can be rewritten as,

$$W_P = \frac{1}{2}\tilde{K}\tilde{w}^2 \quad \text{where} \quad \tilde{K} = \lambda \pi H \alpha \sigma_y \frac{R_o + R_i}{R_o - R_i} \quad \text{and} \quad \lambda = \frac{R_o - R_i}{R_o + R_i} \tag{7.31}$$

Equating the plastic work to the initial kinetic energy using Equations (2.19) and (7.30) gives,

$$\delta = \frac{1}{\sqrt{\lambda \alpha}}\phi \qquad \text{where} \qquad \delta = \frac{\tilde{w}}{H} \qquad \text{and} \qquad \phi = \frac{I}{\pi (R_o + R_i) H^2 \sqrt{\rho \sigma_y}} \tag{7.32}$$

The expression for the dimensionless impulse and deflection are the same as that given in Equation (7.26), but in this case λ is not a constant. In other words, the effect of the plate geometry is not captured by ϕ alone and the dimensionless data from PCA tests with various R_i to R_o ratios cannot be expected to collapse onto the same trend line.

7.4 IIL PCCS Deformation Duration

In this section, the response duration of a PCCS plate subjected to an ideal impulsive loading condition is considered[2]. Three distinct approaches are considered. The first approach is the travelling hinge method of Taylor as outlined in Section 2.3.6. The second approach is the single phase energy approach presented in Section 3.3.4.1, which is closely related to the membrane mode method of Symonds & Wierzbicki, as reviewed in Section 2.3.5. Lastly, the two phase energy approach outlined in Section 4.2.2 will be adapted to the PCCS configuration. The last approach is, essentially, an amalgam of the first two methods that seeks to combine their distinct advantages to overcome their individual weaknesses.

7.4.1 Travelling Hinge Approach for PCCS Plates

As discussed in Section 2.3.6, the travelling hinge approach assumes that an IIL condition will result in a plate with a uniform initial velocity according to Equation (7.9). As with the PCS configuration, a plastic hinge will initiate at the outer boundary R_o and propagate inward at a speed given by Equation (2.33). However, unlike the PCS configuration, a plastic hinge will also initiate at the inner boundary R_i and propagate outward with the same velocity. Consequent, the plastic hinges will annihilate at the mid radius between the R_i and R_o, and, assuming that a given region of a plate is brought to rest by the passage of a plastic hinge, the deformation duration is simply the quotient of the distance to the mid radius and the wave speed,

$$T_{\scriptscriptstyle T} = \frac{R_o - R_i}{2}\sqrt{\frac{\rho}{\alpha \sigma_y}} \tag{7.33}$$

[2]The response duration of a PCA plate will not be considered since it is not primary focus of this work and there is no experimental data with which to compare the solution.

Note that the subscript T is used to denote the Taylor duration for both the PCS and PCCS configurations and which equation is applicable is implied by the context. The final deflection is the product of the Taylor duration and the intial velocity V_0, which is obtained as the quotient of the impulse I and the mass m as defined in Equation (7.10). Upon manipulation and simplification, the final expression has the form,

$$\delta = \frac{1}{\sqrt{\lambda\alpha}}\phi \qquad \text{where} \qquad \delta = \frac{\tilde{w}}{H} \qquad , \qquad \lambda = 4 \qquad \text{and} \qquad \phi = \frac{I}{\pi(R_o + R_i)H^2\sqrt{\rho\sigma_y}} \tag{7.34}$$

Finally, note that this approach would predict that the maximum deflection occurs at the mid radius, which is in agreement with the parabolic displacement profile, but at odds with both the Bessel and measure displacement profiles, as shown in Figure 7.1. The results of this analysis are discussed in Section 8.4

7.4.2 Membrane Approach and Effective Mass of PCCS Circular Plates

The single phase membrane solution for the deformation duration of an ideal impulse loaded plate presented in section 3.3.4.1 does not assume a plate shape and is therefore equally valid for the PCCS configuration. Hence, all that remains is for the effective mass and the corresponding parameter μ to be determined according to the assumed displacement profiles. In this section the expressions are derived for the effective mass of a PCCS plate with a parabolic or Bessel function velocity distribution.

For the PCCS circular plate configuration, it will be shown in this section that the effective plate mass $\tilde{M}$ can be written as a fraction of the total plate mass, *i.e.*,

$$\tilde{M} = \mu\rho\pi\left(R_o^2 - R_i^2\right)H \tag{7.35}$$

where μ is the effective mass parameter that must be determined for a given plate configuration. Taking Equation (7.35) and the most general expression for $\tilde{K}$ given in Equation (7.14), and substituting into Equation (3.60) gives,

$$T = \pi\sqrt{\frac{\mu}{\lambda}}\,\frac{(R_o - R_i)}{2}\sqrt{\frac{\rho}{\alpha\sigma_y}} = \pi\sqrt{\frac{\mu}{\lambda}}\,T_T \tag{7.36}$$

Note that this expression differs by a factor of 2 from that obtained for the PCS configuration, as given in Equation (3.60), due to the modified form of the Taylor duration.

7.4.2.1 PCCS Parabolic Displacement distribution

Assuming that the plate shape is parabolic throughout the plate motion, the form of the velocity distribution can be obtained from equation (7.1),

$$\dot{w} = 4\dot{\tilde{w}}\left[\frac{r - R_i}{R_o - R_i} - \left(\frac{r - R_i}{R_o - R_i}\right)^2\right] \tag{7.37}$$

As in the previous derivations, the kinetic energy of the plate is described by equation (3.29). Substituting equation (7.37) into equation (3.29) gives,

$$E_k = 16\rho\pi H\dot{\tilde{w}}^2 \int_{R_i}^{R_o} r\left[\frac{r-R_i}{R_o-R_i} - \left(\frac{r-R_i}{R_o-R_i}\right)^2\right]^2 dr = \frac{4}{15}\rho\pi\left(R_o^2-R_i^2\right)H\dot{\tilde{w}}^2 \tag{7.38}$$

A more convenient way to write the equation is,

$$E_k = \frac{1}{2}\tilde{M}\dot{\tilde{w}}^2 \quad \text{where} \quad \tilde{M} = \mu\rho\pi\left(R_o^2-R_i^2\right)H \quad \text{and} \quad \mu = \frac{8}{15} = 0.5333 \tag{7.39}$$

where the form of $\tilde{M}$ is the same as that given in Equation (7.35).

Note that μ is less than unity, which is in agreement with the general argument given in Section 3.3.1.3. Furthermore, to remain consistent with the single phase membrane solution, the initial central sector velocity is obtained using Equation (3.27) as,

$$\dot{\tilde{w}}_0 = \sqrt{\frac{1}{\mu}}\,V_0 = 1.3693\,V_0$$

where V_0 is the initial IIL uniform plate velocity as defined in Section 7.4.1, *i.e.* a greater initial maximum velocity is required for the assumed deformation profile to have the same initial kinetic energy as a uniform velocity plate.

In this case the estimate for the response duration is,

$$\pi\sqrt{\frac{\mu}{\lambda}} = \pi\sqrt{\frac{8/15}{16/3}} = \pi\sqrt{\frac{1}{10}} \quad \Rightarrow \quad T_{IIL} = 0.9935\,\frac{R_o-R_i}{2}\sqrt{\frac{\rho}{\alpha\sigma_y}} = 0.9935\,T_T \tag{7.40}$$

7.4.2.2 PCCS Bessel Function Displacement Distribution

Assuming that the plate has a Bessel function shape throughout the plate motion, the form of the velocity distribution can be obtained from equation (7.3),

$$\dot{w} = \dot{\tilde{w}}A\left[J_0\left(\Lambda\frac{r}{R_o}\right) + BY_0\left(\Lambda\frac{r}{R_o}\right)\right] \tag{7.41}$$

where, for a R_i to R_o ratio of 0.2 the constants are $\Lambda = 3.816$, $B = 6.955$ and $A = 0.2647$. Substituting equation (7.41) into equation (3.29) gives,

$$E_k = \rho\pi H\dot{\tilde{w}}^2 \int_{R_i}^{R_o} rA^2\left[J_0\left(\Lambda\frac{r}{R_o}\right) + BY_0\left(\Lambda\frac{r}{R_o}\right)\right]^2 dr \tag{7.42}$$

Introducing the dummy variable $x = \Lambda r/R_o$ and rewriting to have a form that corresponds with the previous sections, the kinetic energy can be expressed as,

$$E_k = \frac{1}{2}\tilde{M}\dot{\tilde{w}}^2 \quad \text{where} \quad \tilde{M} = \mu\rho\pi\left(R_o^2 - R_i^2\right)H$$
$$\text{and} \quad \mu = \frac{2}{1-(R_i/R_o)^2}\left(\frac{A}{\Lambda}\right)^2 \int_{\frac{R_i}{R_o}\Lambda}^{\Lambda} x\left[J_0(x) + BY_0(x)\right]^2 dx \tag{7.43}$$

The expansion of the integral takes the form of Lommel integrals for which the solutions are well known [161] and give the result,

$$\begin{aligned}\int_{\frac{R_i}{R_o}\Lambda}^{\Lambda} x\left[J_0(x) + BY_0(x)\right]^2 dx = &\left[\frac{x^2}{2}\left\{J_0^2(x) + J_1^2(x)\right\}\right]_{\frac{R_i}{R_o}\Lambda}^{\Lambda} \\ &+ 2B\left[\frac{x^2}{2}\left\{J_0(x)Y_0(x) + J_1(x)Y_1(x)\right\}\right]_{\frac{R_i}{R_o}\Lambda}^{\Lambda} \\ &+ B^2\left[\frac{x^2}{2}\left\{Y_0^2(x) + Y_1^2(x)\right\}\right]_{\frac{R_i}{R_o}\Lambda}^{\Lambda}\end{aligned} \tag{7.44}$$

Using the radius ratio and constants stated at the start of this section, the Equation (7.43) gives an effective mass parameter value of $\mu = 0.4731$.

As before, μ is less than unity and marginally smaller than that obtained for the parabolic profile. This implies that Bessel profile provides a velocity distribution that is slightly less uniform than the parabolic profile and/or the velocity distribution is skewed toward the inner radius where less mass is present. Both of these implications are consistent with the displacement profiles shown in Figure 7.1.

Furthermore, the initial central sector velocity is obtained using Equation (3.27) as,

$$\dot{\tilde{w}}_0 = \sqrt{\frac{1}{\mu}}\,V_0 = 1.4539\,V_0$$

where V_0 is the initial IIL uniform plate velocity as defined in Section 7.4.1. Note that this value is slightly larger than that of the parabolic profile, which is consistent with the preceding observations, *i.e.* a higher initial velocity is required to provide the same initial kinetic energy.

Finally, the corresponding estimate for the response duration is,

$$\pi\sqrt{\frac{\mu}{\lambda}} = \pi\sqrt{\frac{0.4731}{4.4088}} \quad \Rightarrow \quad T_{IIL} = 1.0291\,\frac{R_o - R_i}{2}\sqrt{\frac{\rho}{\alpha\sigma_y}} = 1.0291\,T_T \tag{7.45}$$

7.4.3 Two Phase Approach for PCCS Circular Plates

The preceding subsections have considered two single phase deformation assumptions, namely the travelling hinge method of Taylor and the membrane mode method of Symonds & Wierzbicki. As argued in Section 4.2, in the context of PCS plates, both these methods capture certain aspects of observed plate behaviour but ignore others. In particular, the travelling hinge model captures the initial phase of motion, while the membrane mode method captures the latter phase of plate behaviour. In this section, the two

phase response model developed in Section 4.2.2 for PCS plates is adapted to PCCS plates subjected an ideal impulsive loading condition. The aim is to find a general expression for the deformation history of the radius at which the maximum deflection occurs, *i.e.* details of hinge motion will not be considered.

Phase I is defined as the initial transient response, where travelling hinges initiate at the inner and outer radii and propagate toward the mid-radius of the PCCS plate. Phase I ends at time T_I, when the hinges mutually annihilate. Up to this point the mid-radius portion of the plate would have behaved as a rigid body moving at the initial velocity V_0, as defined in Equation (7.10). Therefore, at time T_I, the maximum velocity $\dot{\tilde{w}}$ would be equal to the initial velocity V_0 and the maximum displacement $\tilde{w}$ would be equal to the product of V_0 and T_I. Hence, an expression for T_I can be obtained by equating the kinetic energy at the end of Phase I to difference between the initial kinetic energy and the plastic work during Phase I. When expressed in terms of the effective mass and plastic stiffness, the energy equation has the form given in Equation (4.14) and repeated here for convenience,

$$\frac{1}{2}\tilde{M}V_0^2 = \frac{1}{2}mV_0^2 - \frac{1}{2}\tilde{K}(V_0T_I)^2 \quad \Rightarrow \quad T_I = \sqrt{\frac{m-\tilde{M}}{\tilde{K}}} \tag{7.46}$$

Consequently, substituting in the expressions for mass, effective mass and plastic stiffness given in Equations (7.10), (7.35) and (7.14) respectively, and simplifying, gives,

$$T_I = \sqrt{\frac{1-\mu}{\lambda}}\,(R_o - R_i)\sqrt{\frac{\rho}{\alpha\sigma_y}} \quad \Rightarrow \quad \frac{T_I}{T_T} = 2\sqrt{\frac{1-\mu}{\lambda}} \tag{7.47}$$

Using the values for μ and λ given in Table 7.1, the non-dimensional Phase I deformation durations T_I/T_T for the parabolic and Bessel displacement profiles are 0.5916 and 0.6914 respectively.

Note that while Equations (7.46) and(4.14) are identical, Equations (7.47) and (4.15) differ by a factor of 2. In other words, the expression for T_I in terms of effective mass, plastic stiffness, *etc.*, applies to different plate configurations, but is configuration specific when expressed in terms of parameters such as μ and λ.

Phase II is defined as the rest of the response from time T_I until the plate motion is arrested, which is designated as time T_{II}. Continuing with the approach developed in Section 4.2.2, the plate is assumed to behave as a deforming membrane with a constant displacement profile. Hence, all the results obtained in Section 7.4.2, are valid provided that the appropriate temporal offset is accounted for, *i.e.* the difference between the two phase duration T_{II} and the single phase duration T, as given by Equation (7.36). Hence, from Equation (2.30), the expression for the Phase II displacement history of the radius at which the maximum deflection occurs is,

$$\frac{\tilde{w}}{\tilde{w}_{II}} = sin\left[\left(\frac{\pi}{2}\right)\frac{t-(T_{II}-T)}{T}\right] \quad \text{where} \quad t \geq T_I \quad \text{and} \quad T = \pi\sqrt{\frac{\mu}{\lambda}}\,T_T \tag{7.48}$$

where the form of T_T is given in Equation (7.33).

An expression for T_{II} is obtained by noting that at the start of Phase II, *i.e.* $t = T_I$, $\tilde{w}_I$ is the product of V_0 and T_I, while the value of $\tilde{w}_{II}$ is given by the IIL deflection solution given in Equations (7.16) or (7.22). Upon substitution of the appropriate definitions given above and elsewhere in this section, the majority

of the terms cancel such that the quotient of $\tilde{w}_I$ and $\tilde{w}_{II}$ simplifies to the expression,

$$\frac{\tilde{w}_I}{\tilde{w}_{II}} = \frac{V_0 T_I}{H\frac{\phi}{\sqrt{\lambda\alpha}}} = \sqrt{1-\mu} \tag{7.49}$$

Note that this result is identical to Equation (4.17). Substituting Equation (7.49) into Equation(7.48) gives,

$$T_{II} = T_I + \left[1 - \frac{2}{\pi} sin^{-1}\sqrt{1-\mu}\right] T \quad \text{where} \quad T = \frac{\pi}{2}\sqrt{\frac{\mu}{\lambda}}\, T_T \tag{7.50}$$

which is identical in form to Equation (4.18), but differs in the definition of T_T. Consequently, when normalized with respect to T_T, the expression for T_{II} is,

$$\frac{T_{II}}{T_T} = 2\sqrt{\frac{1-\mu}{\lambda}} + 2\sqrt{\frac{\mu}{\lambda}}\left(\frac{\pi}{2} - sin^{-1}\sqrt{1-\mu}\right) \tag{7.51}$$

which differs from the PCS solution, given in Equation (4.19), by a factor of 2.

Equation (7.51) gives non-dimensional deformation duration results for the parabolic and Bessel displacement profiles of 1.1094 and 1.1883, respectively. These results and those of the preceding sections are summarised in Table 7.1. Several of the general observations drawn from the two phase analysis of PCS plates in Section 4.2.2 are equally valid in this case and are discussed further in Section 8.4.3.

7.5 Finite Duration Loading

In this section, the response duration of a PCCS plate subjected to a finite duration 'rectangular'[3] pressure load is considered. Two special cases are considered, namely a critical impulsive load (CIL), where the load persists for the duration of Phase I, and an ideal dynamic load (IDL) where the load persists for the entire plate response duration. Throughout this section, the extension of the two phase energy approach developed in Section 4.3, and the associated definitions, will be adapted to the PCCS configuration.

7.5.1 Effective Pressure

The general expression for the work done by a pressure load of constant intensity of given in Section 4.3.1. Assuming only transverse displacements and a uniform load, the total work done by a pressure P acting on a deforming axisymmetric plate is given in Equation (4.20) and repeated here for convenience,

$$W_L = \int_A Pw\, dA \tag{7.52}$$

where the subscript L denotes the work done by the pressure load and A the area that the pressure is acting on. Note that the assumption of a constant and uniform pressure implies that P is independent of w. In other words, integration through the deformation history is not required and only the shape of the plate at given point in time needs to be considered. Consequently, for the CIL and IDL loading cases,

[3]The term 'rectangular' implies a pressure load of finite duration and constant intensity.

where the pressure load persists throughout Phase I, the details of the transient travelling hinge motion may be ignored and only the fully developed deformation profiles are of interest. It will be shown in this section that the aforementioned restrictions result in an expression of the form,

$$W_L = \tilde{P}\tilde{w} \quad \text{where} \quad \tilde{P} = \beta\pi(R_o^2 - R_i^2)P \tag{7.53}$$

where $\tilde{P}$ is the effective pressure load and β is the effective pressure parameter, which must be determined for each plate configuration. Note that the use of $\tilde{P}$, in conjunction with the plastic stiffness $\tilde{K}$ and effective mass $\tilde{M}$, reduces a three dimensional problem to a single dimension expressed in terms of $\tilde{w}$ and renders the problem mathematically tractable. In particular, β specifies the amount of work done on the plate relative to the work that would be done if the entire plate had a uniform displacement of $\tilde{w}$.

7.5.1.1 PCCS Parabolic Displacement distribution

Assuming that the PCCS plate has a parabolic displacement profile, the expression for w is given in Equation (7.1), which, when substituted into Equation (7.52), gives,

$$W_L = \int_{R_i}^{R_o} Pw(r)2\pi r\,dr = P\tilde{w}\int_{R_i}^{R_o} 4\left[\frac{r-R_i}{R_o-R_i} - \left(\frac{r-R_i}{R_o-R_i}\right)^2\right]2\pi r\,dr \tag{7.54}$$

Upon integration, the work done by pressure P can be written as,

$$W_L = \tilde{P}\tilde{w} \quad \text{where} \quad \tilde{P} = \beta\pi(R_o^2 - R_i^2)P \quad \text{and} \quad \beta = \frac{2}{3} \tag{7.55}$$

7.5.1.2 PCCS Bessel Displacement distribution

Assuming that the PCCS plate has a Bessel displacement profile, the expression for w is given in Equation (7.3), which, when substituted into Equation (7.52), gives,

$$W_L = \int_{R_i}^{R_o} Pw(r)2\pi r\,dr = P\tilde{w}\int_{R_i}^{R_o} A\left[J_0\left(\Lambda\frac{r}{R_o}\right) + BY_0\left(\Lambda\frac{r}{R_o}\right)\right]2\pi r\,dr \tag{7.56}$$

where, for a R_i to R_o ratio of 0.2 the constants are $\Lambda = 3.816$, $B = 6.955$ and $A = 0.2647$.

Introducing the dummy variable $x = \Lambda r/R_o$ results in Bessel integrals for which the solutions are well known [161] and give the result,

$$\begin{aligned}\int_{R_i}^{R_o} A\left[J_0\left(\Lambda\frac{r}{R_o}\right) + BY_0\left(\Lambda\frac{r}{R_o}\right)\right]2\pi r\,dr &= 2\pi A\left(\frac{R_0}{\Lambda}\right)^2\int_{\frac{R_i}{R_o}\Lambda}^{\Lambda} x\left[J_0(x) + BY_0(x)\right]dx \\ &= 2\pi A\left(\frac{R_0}{\Lambda}\right)^2\left[xJ_1(x) + BxY_1(x)\right]_{\frac{R_i}{R_o}\Lambda}^{\Lambda}\end{aligned} \tag{7.57}$$

Rewriting to have a form that corresponds with the previous sections and using the radius ratio and constants stated above, the work done by pressure P can be expressed as,

$$W_L = \tilde{P}\tilde{w} \quad \text{where} \quad \tilde{P} = \beta\pi(R_o^2 - R_i^2)P$$
$$\text{and} \quad \beta = \frac{2}{1-(R_i/R_o)^2}\left(\frac{A}{\Lambda}^2\right)\left[xJ_1(x) + BxY_1(x)\right]_{\frac{R_i}{R_o}\Lambda}^{\Lambda} = 0.6116 \tag{7.58}$$

7.5.2 Critical Impulsive Loading

In Section 4.3.4 it was noted that, in general, a convenient closed form solution for the transient hinge position during Phase I motion of an arbitrary displacement profile is mathematically intractable. In lieu of this, a general solution is sought for the critical impulsive load (CIL) case where the load duration is equal to the Phase I duration, *i.e.* $T_L = T_I$, which represents the transition from the impulsive to the dynamic loading regime.

At time T_I, the transient phase of motion is complete and the plate shape can be described using the displacement profiles given in Equations (7.1) and (7.3). Furthermore, as argued above, the pressure is assumed to be constant during Phase I, which implies that the plate shape at T_I is sufficient to determine the pressure work as given in Equations (7.55) and (7.58). Consequently, at T_I the generalized energy method results in the expression,

$$\frac{1}{2}\tilde{M}\dot{\tilde{w}}_I^2 = \tilde{P}\tilde{w}_I - \frac{1}{2}\tilde{K}\tilde{w}_I^2 \tag{7.59}$$

where $\tilde{M}$, $\tilde{P}$ and $\tilde{K}$ are given by Equations (7.35), (7.53) and (7.14) respectively.

Time T_I is introduced by noting that the mid-radius of the plate would behave as a rigid body under a constant acceleration, which, following Equations (4.30) and (4.36), gives,

$$\tilde{w}_I = \frac{1}{2}\frac{P}{\rho H}T_I^2 \quad \text{and} \quad \dot{\tilde{w}}_I = \frac{P}{\rho H}T_I \tag{7.60}$$

Substituting this results into Equation (7.59), expanding, simplifying and invoking the Taylor during gives the expression for the CIL Phase I duration as,

$$\frac{T_I}{T_T} = 4\sqrt{\frac{\beta-\mu}{\lambda}} \tag{7.61}$$

This result differs from that for the PCS configuration, given in Equation (4.44), by a factor of 2, which is due to the presence of two travelling hinges, as discussed previously.

Equation (7.61) gives non-dimensional Phase I duration values for the Parabolic and Bessel displacement profiles of $\sqrt{2/5} = 0.6325$ and 0.7090 respectively, as summarized in Table 7.2. These durations are marginally longer that the equivalent Phase I results for the IIL case of 0.5916 and 0.6914, *i.e.* a difference of 6.5% and 1.5% respectively. In other words, the loading history does not appear to have a large effect on the Phase I duration.

Table 7.2: Summary of CIL results for PCCS deformation profiles using the generalized energy method, *i.e.* the effective pressure coefficients, normalized non-dimensional mid-radius Phase I and Phase II deflections, non-dimensional Phase I and Phase II displacement durations.

Profile	β		$\frac{\delta_I}{\sqrt{\frac{1}{\alpha}\,\phi}}$	$\frac{\delta_{II}}{\sqrt{\frac{1}{\alpha}\,\phi}}$	$\frac{T_I}{T_T}$	$\frac{T_{II}}{T_T}$
	exact	approx.				
parabolic	$\frac{2}{3}$	0.6667	0.1581	0.3536	0.6325	1.3328
Bessel	Eq (7.58)	0.6116	0.1772	0.3725	0.7090	1.4132

The total axial impulse experienced by a PCCS plate during a CIL event is,

$$I_{CIL} = \pi \left(R_o^2 - R_i^2\right) P\, T_I \tag{7.62}$$

Consequently, an expression for the mid-radius Phase I deflection is obtained by substituting Equation (7.61) back into Equation (7.60) while invoking the definition of the Taylor duration, given in Equation (7.33), and the CIL impulse, given above, which, upon simplification, gives,

$$\delta_I = \sqrt{\frac{\beta-\mu}{\lambda}}\,\frac{\phi}{\sqrt{\alpha}} \qquad \text{where} \qquad \delta_I = \frac{\tilde{w}_I}{H} \quad , \quad \phi = \frac{I}{\pi(R_o+R_i)H^2\sqrt{\rho\sigma_y}} \tag{7.63}$$

Note that this expression is identical to the corresponding PCS result given in Equation (4.45). Equation (7.63) gives non-dimensional Phase I displacement values for the Parabolic and Bessel displacement profiles of $\sqrt{1/40} = 0.1581$ and 0.1772 respectively, as summarized in Table 7.2.

At time T_{II}, the plate motion is complete. Hence, the kinetic energy vanishes and the plastic dissipation is described in terms of $\tilde{w}_{II}$. However, the pressure is still assumed to only act during Phase I, *i.e.* the pressure work is described in terms of $\tilde{w}_I$. Consequently, at T_{II} the generalized energy method results in the expression,

$$\tilde{P}\tilde{w}_I - \frac{1}{2}\tilde{K}\tilde{w}_{II}^2 = 0 \tag{7.64}$$

Proceeding from the above, an expression for the final Phase II deflection is obtained by leaving $\tilde{w}_{II}$ in the second term unchanged, while substituting $\tilde{w}_I$ in the first term with Equation (7.60) and invoking the expressions for T_T and I given in Equations (7.33) and (7.62). Upon simplification, this result is,

$$\delta_{II} = \sqrt{\frac{\beta}{\lambda}}\,\frac{\phi}{\sqrt{\alpha}} \qquad \text{where} \qquad \delta_{II} = \frac{\tilde{w}_{II}}{H} \quad , \quad \phi = \frac{I}{\pi(R_o+R_i)H^2\sqrt{\rho\sigma_y}} \tag{7.65}$$

Note that this expression is identical to the corresponding PCS result given in Equation (4.46). Equation (7.65) gives non-dimensional Phase I displacement values for the Parabolic and Bessel displacement profiles of $\sqrt{1/8} = 0.3536$ and 0.3725 respectively, as summarized in Table 7.2.

The Phase II duration is obtained by following the same procedure as that for the two phase IIL case in Section 7.4.3. In other words, the plate is assumed to behave as an ideal plastic membrane with a constant displacement profile deforming under zero external load until motion is arrested at time T_{II}. Consequently, the Phase II deformation will be identical to the single phase IIL solution, but with a

temporal offset amounting to the difference between the two phase CIL duration T_{II} and the single phase IIL duration T, as given by Equation (7.36). Hence, from Equation (7.48), the expression for the Phase II displacement of the centre of the plate at time T_I, *i.e.* the start of the phase, is given by,

$$\frac{\tilde{w}_I}{\tilde{w}_{II}} = sin\left[\left(\frac{\pi}{2}\right)\frac{T_I - (T_{II} - T)}{T}\right] \quad \text{where} \quad T = \pi\sqrt{\frac{\mu}{\lambda}}\,T_T \tag{7.66}$$

where the form of T_T is given in Equation (7.33).

While Equations (7.66) and (7.48) are identical in form, the implementation differs between loading cases based on the expressions for $\tilde{w}_I$, $\tilde{w}_{II}$ and T_{II}. In the CIL case, Equations (7.63) and (7.65) give,

$$\frac{\tilde{w}_I}{\tilde{w}_{II}} = \frac{\delta_I}{\delta_{II}} = \sqrt{1 - \frac{\mu}{\beta}} \tag{7.67}$$

Consequently, substituting Equations (7.67) and (7.61) into Equation(7.66) and rearranging gives,

$$\frac{T_{II}}{T_T} = 4\sqrt{\frac{\beta - \mu}{\lambda}} + 2\sqrt{\frac{\mu}{\lambda}}\left[\frac{\pi}{2} - sin^{-1}\sqrt{1 - \frac{\mu}{\beta}}\right] \tag{7.68}$$

As observed previously, this result differs from that of the PCS solution, given in Equation (4.56), by a factor of 2, due to the dual travelling hinges discussed previously.

Equation (7.68) results in non-dimensional Phase II duration values for the parabolic and Bessel displacement profiles of 1.3328 and 1.4132, as summarized in Table 7.2. These duration results are significantly longer than the equivalent Phase II values for the IIL case of 1.1094 and 1.1883, *i.e.* a difference of 20.1% and 18.9% respectively In other words, unlike the Phase I results, the loading history does appear to have a large effect on the Phase II duration. These results are discussed further in Section 8.5.1.

7.5.3 Ideal Dynamic Loading

In this section, a solution for the deflection history of thin PCCS plates subjected to ideal dynamic loading (IDL) conditions, *i.e.* a load of constant intensity and finite duration $T_L = T_{II}$, is developed from the general approach presented in Sections 4.3.6 and 4.3.7 for PCS plates.

The IDL Phase I response is identical to that under a CIL conditions, *i.e.* the load is applied throughout T_I. Hence, the expression for T_I given in Equation (7.61) is also valid under IDL conditions.

The total axial impulse experienced by a PCCS plate under IDL conditions is also similar to the CIL case except that the duration is T_{II} and opposed to T_I, which gives,

$$I_{IDL} = \pi\left(R_o^2 - R_i^2\right) P\, T_{II} \tag{7.69}$$

Given the equivalent Phase I behaviour under IDL and CIL conditions, an expression for the IDL Phase I displacement can obtained from Equation (7.63) by noting that the deflection is proportional to the impulse delivered during Phase I. In other words, in the IDL case, the ratio of the Phase I impulse to the total impulse is equal to the quotient of T_I and T_{II}. Applying this reasoning to Equations (7.63)

Table 7.3: Summary of IDL results for PCCS deformation profiles using the generalized energy method, *i.e.* the normalized non-dimensional mid-radius Phase I and Phase II deflections, non-dimensional Phase I and Phase II displacement durations.

Profile	$\frac{\delta_I}{\sqrt{\frac{1}{\alpha}}\,\phi}$	$\frac{\delta_{II}}{\sqrt{\frac{1}{\alpha}}\,\phi}$	$\frac{T_I}{T_T}$	$\frac{T_{II}}{T_T}$
parabolic	0.0492	0.2459	0.6325	2.0330
Bessel	0.0593	0.2621	0.7090	2.1174

and (7.61) gives [4],

$$\delta_I = \sqrt{\frac{\beta-\mu}{\lambda}}\,\frac{\phi}{\sqrt{\alpha}}\left(\frac{T_I}{T_{II}}\right) \quad \Rightarrow \quad \frac{\delta_I}{\sqrt{\frac{1}{\alpha}}\,\phi} = 4\left(\frac{\beta-\mu}{\lambda}\right)\Big/\frac{T_{II}}{T_T} \tag{7.70}$$

Unlike previous deflection solutions, this expression differs by a factor of two from that for a PCS plate, given in Equation (4.62). The reason for this is the inclusion of the Taylor duration in the expression and, as a consequence, the dual hinge effect. Furthermore, the evaluation of Equation (7.70) requires the expression for T_{II} to be known since it is included in the impulse. Therefore, the normalized values for δ_I are given at the end of this section in Table 7.3.

An expression for the deflection at time T_{II}, *i.e.* when the plate motion is complete, is obtained using same energy argument as employed in the CIL case. However, in the IDL case, both the pressure work and the plastic dissipation is described in terms of $\tilde{w}_{II}$, since the pressure is assumed to act during the entire motion. Consequently, the generalized energy method for the IDL case at T_{II} gives,

$$\tilde{P}\tilde{w}_{II} - \frac{1}{2}\tilde{K}\tilde{w}_{II}^2 = 0 \qquad \Rightarrow \qquad \tilde{w}_{II} = 2\,\frac{\tilde{P}}{\tilde{K}} \tag{7.71}$$

Substituting the expressions $\tilde{P}$ and $\tilde{K}$, given in Equations (7.53) and (7.14) respectively, while invoking the expressions for T_T and I given in Equations (7.33) and (7.69) and simplifying gives,

$$\delta_{II} = 4\left(\frac{\beta}{\lambda}\right)\frac{\phi}{\sqrt{\alpha}}\Big/\frac{T_{II}}{T_T} \qquad \text{where} \qquad \delta_{II} = \frac{\tilde{w}_{II}}{H} \quad , \quad \phi = \frac{I}{\pi(R_o+R_i)H^2\sqrt{\rho\sigma_y}} \tag{7.72}$$

Like the δ_I solution, this expression differs by a factor of two from that for a PCS plate, given in Equation (4.80), due to the inclusion of the Taylor duration. Furthermore, the evaluation of Equation (7.72) requires the expression for T_{II} and is, therefore, given at the end of this section in Table 7.3.

The application of the generalized energy method to obtain an expression for the deflection duration T_{II} under IDL conditions differs substantially from the Phase II analysis of the IIL and CIL cases. The continued application of the pressure load implies that the single phase IIL analysis is not applicable. Rather, a solution is required for the full generalized energy equation, as given in Equation (4.64) for the

[4] This result can also be obtained using the procedure in Section 7.5.2 but is omitted here for brevity.

PCS case, and repeated here for convenience,

$$\frac{1}{2}\tilde{M}\dot{\tilde{w}}^2 = \tilde{P}\tilde{w} - \frac{1}{2}\tilde{K}\tilde{w}^2 \quad \Rightarrow \quad \dot{\tilde{w}} = \frac{d\tilde{w}}{dt} = \sqrt{\tfrac{2\tilde{P}}{\tilde{M}}\tilde{w} - \tfrac{\tilde{K}}{\tilde{M}}\tilde{w}^2} \tag{7.73}$$

for which the general solution is,

$$\tilde{w} = \tfrac{2\tilde{P}}{\tilde{K}}\, sin^2\left[\tfrac{1}{2}\sqrt{\tfrac{\tilde{K}}{\tilde{M}}}\,(t - T_I) + sin^{-1}\sqrt{\tfrac{\tilde{K}}{2\tilde{P}}}\,\tilde{w}_I\right] \quad , \quad T_I < t < T_L \tag{7.74}$$

A thorough exposition of Equation (7.74) in the context of PCS plate behaviour is given in Section 4.3.6, which will not be repeated here. Rather, by inspection it is evident that the maximum deflection occurs when then the sine function is unity, *i.e.* the expression in parenthesis is equal to $\pi/2$. Furthermore, Equation (7.71) implies that the argument of the second term in parenthesis in Equation (7.74) is the quotient of the final Phase I and II deflections. Hence, using Equations (7.70) and (7.72), the argument is,

$$\frac{\tilde{K}}{2\tilde{P}}\,\tilde{w}_I = \frac{\tilde{w}_I}{\tilde{w}_{II}} = \frac{\delta_I}{\delta_{II}} = 1 - \frac{\mu}{\beta} \tag{7.75}$$

Consequently, for the maximum deflection, *i.e.* $t = T_{II}$, the expression in parenthesis in Equation (7.74), can be rewritten as,

$$T_{II} = T_I + 2\sqrt{\tfrac{\tilde{M}}{\tilde{K}}}\left[\frac{\pi}{2} - sin^{-1}\sqrt{1 - \frac{\mu}{\beta}}\right] \tag{7.76}$$

From Equations (7.35), (7.14) and (7.33) the square root of the quotient of the effective mass and plastic stiffness is,

$$\sqrt{\frac{\tilde{M}}{\tilde{K}}} = 2\sqrt{\frac{\mu}{\lambda}}\,T_T \tag{7.77}$$

Finally, substituting Equations (7.61) and (7.77) into Equation (7.76) gives,

$$\frac{T_{II}}{T_T} = 4\sqrt{\frac{\beta - \mu}{\lambda}} + 4\sqrt{\frac{\mu}{\lambda}}\left[\frac{\pi}{2} - sin^{-1}\sqrt{1 - \frac{\mu}{\beta}}\right] \tag{7.78}$$

As noted for all the PCCS duration solutions, this result differs from that of the PCS solution, given in Equation (4.78), by a factor of 2, due to the dual travelling hinges discussed previously.

Equation (7.78) results in non-dimensional Phase II duration values for the parabolic and Bessel displacement profiles of 2.033 and 2.1174 respectively, as summarized in Table 7.3. These duration results are close to double that of the equivalent Phase II values for the IIL case, with a difference of differences of 83.3% and 78.2% for the parabolic and Bessel displacement profiles respectively. Even more than the ICL case, these results show that, for a given impulse, the duration of the load has a profound effect on the Phase II duration. Comparisons of these results with experimental data are discussion in Section 8.5.2.

Chapter 8

Discussion of Experimental and Analytical Results

"Facts do not 'speak for themselves'; they are read in the light of theory."

Stephen Jay Gould (1941-2002)

8.1 Introduction

In this chapter, the ability of the generalized energy method to describe and predict the observed behaviour of blast loaded peripherally clamped centrally supported (PCCS) and peripherally clamped annular (PCA) plates, is assessed[1].

As shown in Section 2.1.1, the published experimental data for PCCS and PCA are sparse. Apart from the work published as part of this thesis [51–53], only Ghosh *et al.* [49, 50] appear to have considered these two experimental configurations. However, Ghosh *et al.* restricted their work to lead plates and did not publish a complete set of results such that a detailed comparison is not possible.

Given the above, the PCCS and PCA data presented in this work is novel, *i.e.* there is no data set in the literature with which it can directly be compared. Consequently, the primary focus will be to show that the data reported in Chapter 6 is internally consistent and in agreement with the theory presented in Chapter 7. However, the non-dimensional parameters suggested by the theory reviewed and developed in Chapters 2, 3, 4 and 7 will allow some indirect comparisons to be made between the experimental results reported in this work with that for peripherally clamped solid (PCS) plates reviewed and critiqued in Chapters 2 and 3.

[1] The consideration of non-circular plates is beyond the scope of this thesis

8.2 Assumed Displacement Profile

The assumed deformation profiles developed in Section 7.2 provide good approximations to the measured final plate profiles as shown previously in Figures 7.1 and 7.3. While some of the profiles were motivated by physical analogies, none were derived from first principles, but were chosen specifically to match the measured profiles. Consequently, it is prudent to show that the assumed profiles are consistent with other measurements, such as the fraction of the total impulse transferred trough the central support.

For a PCCS plate, assuming that transverse shear forces are negligible, the in-plane membrane forces are horizontal at $\tilde{R}$, *i.e.* there is no axial component. Hence, during Mode I deformation, the radius $\tilde{R}$ separates the plate into two regions. Since membrane forces only act in tension, this implies that the outer clamped boundary can only resist the axial motion of the portion of a PCCS plate outside $\tilde{R}$. Likewise, all the impulse applied to the portion of the plate inside $\tilde{R}$ must be transferred through the central support during a Mode I response. In other words, for a uniformly distributed load, the fraction of the total impulse transferred through the central support during a PCCS plate test is proportional the fraction of the exposed plate area within $\tilde{R}$.

This argument is not adversely affected by the initial transient plate shape since the region between $\tilde{R}$ and the mid-radius would be the last to be processed by the plastic hinges emanating from the fixes boundaries and would experience only horizontal in-plane membrane forces up to that point. Consequently, the accumulated momentum would still be divided according to the position of $\tilde{R}$. The only possible exception is the short time between the moment that the plastic hinges annihilate, presumably at the mid-radius, and the transition to the deformation profile with maximum displacement at $\tilde{R}$. In other words, it is assumed that the duration of the transition is negligible is comparison to the deformation duration.

In Section 7.2.1 it is shown that for the Bessel function deflection profile the value of $\tilde{R}$ is 26.78 mm, which gives an inner area fractions of 28.6 %. This value compares well with the Mode I blast tube results shown in Figure 6.13, where the central support impulse fraction varies between from 25 % and 26 %, which strengthens the conclusion that a uniform impulse was achieved. By contrast, the Mode I values in Figure 6.4 vary from 38 % to 40 %, which is consistent with the conclusion in Section 5.3.1.3 that the short stand-off blast configuration produces a slightly non-uniform impulse distribution.

Finally, while the inner boundary deals with between $\frac{1}{3}$ and $\frac{1}{4}$ of the total impulse, the length of the inner boundary only amounts to 20 % of the outer boundary. Hence, given the greater extent of the outer boundary, the stress at the inner boundary is expected to be higher than at the outer boundary, which explains why initial failure occurs at the inner boundary.

8.3 Ideal Impulsive Loading

In this section the predictions of the ideal impulse load (IIL) models developed in Sections 7.3 and 7.4 are compared to the experimental results reported in Section 6.2. A close correlation would not be expected since the measured blast load characteristics presented in Section 5.3, show that neither the short stand-off nor the blast tube loading configurations provide IIL conditions. Nevertheless, of the two, the short stand-off tests as closer to the IIL condition and are, therefore, the focus of this section.

Table 8.1: Dimensionless deflection vs impulse gradient predictions for PCCS plates under IIL conditions.

α	Parabolic	Bessel
1	0.433	0.476
2	0.306	0.337
2.8	0.259	0.284

8.3.1 PCCS Experimental Results

The short stand-off PCCS blast test results are summarized in Figure 6.2, where the dimensionless deflection vs impulse gradient of the Mode I response is 0.2198. Under IIL conditions, the general form of the final deflection is given by Equation (7.16) and repeated here for convenience,

$$\delta = \frac{1}{\sqrt{\lambda\alpha}}\phi \qquad \text{where} \qquad \delta = \frac{\tilde{w}}{H} \qquad \text{and} \qquad \phi = \frac{I}{\pi(R_o + R_i)H^2\sqrt{\rho\sigma_y}} \tag{8.1}$$

Hence the predicted gradient is,

$$\frac{\delta}{\phi} = \frac{1}{\sqrt{\lambda\alpha}} \tag{8.2}$$

where the values for plastic stiffness parameter λ are 5.3333 and 4.4088 for the parabolic and Bessel displacement shapes respectively, as given in Table 7.1.

The gradient predictions for various values of the strain rate sensitivity factor α are shown in Table 8.1, which shows that all the results are significantly larger that the experimental value for both deformation profiles. Even for a large value of $\alpha = 2.8$, which provides a good correlation for the PCS configuration according to Table 3.2, the predictions are 18.3% and 29.2% greater for the parabolic and Bessel shapes respectively.

These results may appear to suggest that the parabolic displacement profile is the better assumption since it gives more accurate results. However, it is clear from Figure 7.1 that the Bessel function provides are better fit to the measured profiles of recovered plates and is, therefore, the more appropriate choice.

Given the material properties reported in appendix B, the use of larger values for the rate sensitivity parameter are unrealistic. Hence, the aforementioned results indicate that the IIL assumption is insufficient to predict the deformation behaviour of PCCS circular plates subjected to a short stand-off blast. In every case the IIL prediction overestimates that gradient, which suggests that incorporating non-ideal factors, such as finite duration loading, may bring the results into closer agreement. These, and other, factors are considered in Section 8.5.

8.3.2 PCA Experimental Results

The short stand-off PCA blast test results are also summarized in Figure 6.2, where the dimensionless deflection vs impulse gradient is 0.6673. The general form of the predicted gradient under IIL conditions given in Equation (8.2) is also applicable in this case.

Table 8.2: Comparison of simple IIL deflection predictions for PCA plates with experimental data

α	$u = 0$	$\epsilon_r = 0$
1	1	1.225
2	0.707	0.866
2.8	0.598	0.732

Two analytical models for PCA plates have been developed, as presented in Section 7.3.2. Both models are based on a linear displacement profile but differ with regard to the radial displacement assumption. The zero radial displacement assumption, *i.e.* $u = 0$, is convenient in that it is consistent with the axial motion assumption used for the PCCS configuration, as shown in Section 7.3.2.1, and leads a single value of the plastic stiffness parameter λ of unity, as given by Equation (7.25). Conversely, the zero radial strain assumption, developed in Section 7.3.2.2, is motivated by measurements of final deformed shape of the recovered PCA plates, as shown in Figure 7.2. Under the zero radial strain assumption, *i.e.* $\epsilon_r = 0$, the definition of λ is given by Equation (7.31), which, for a R_i to R_o ratio of 0.2, gives a value of $\lambda = 0.6667$.

The gradient predictions for various values of the strain rate sensitivity factor α are shown in Table 8.2 In general, the results are larger than the experimental value for both deformation profiles, but not to the same degree as with the PCCS configuration. In fact, for the large value of $\alpha = 2.8$, the zero radial motion assumption gives a prediction that lower that than the experimental value, *i.e.* a difference of -10.8%, while the zero radial strain assumption still overpredicts by 9.7%.

Similar to the preceding section, these results may appear to suggest that the zero radial displacement assumption is correct as it gives more accurate results. However, as discussed above, the zero radial strain assumption provides the better fit to the measured profiles of recovered plates and is, therefore, the more appropriate choice.

From the greater displacement of a PCA plate relative to a dimensionally identical PCCS plate, it is reasonable to assume that, all else being equal, the deformation duration of the PCA plate would be longer. Consequently, a given short stand-off load can be expected to be close to the IIL assumption for a PCA plate for a dimensionally identical PCCS plate. This argument is consistent with the smaller differences apparent in the PCA prediction relative to those of the PCCS configuration. Nevertheless, considering the non-ideal experimental loading, the IIL assumption is still expected to provide an upper limit to the deformation prediction. Hence, the aforementioned results are encouraging and lend support to the zero radial strain assumption.

Finally, the contrast between the zero radial displacement and zero radial strain assumptions provides support for the model developed in Section 3.3.6. The greater deflection predicted by the zero radial strain assumption is in agreement with Equation (3.64), which predicts that an increase in the inner radius will decrease the plastic work for the given axial deflection. In other words, more deflection is required to dissipate the initial kinetic energy.

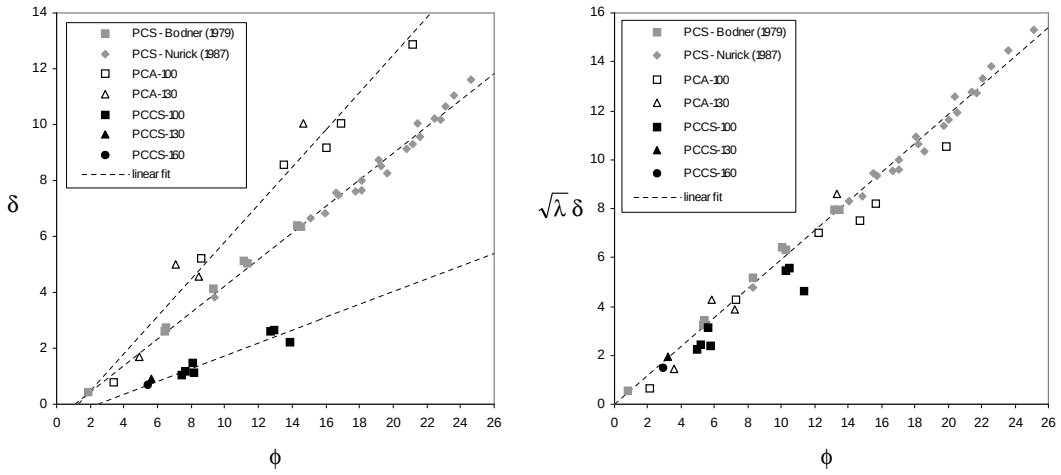

Figure 8.1: Comparison of standard δ and normalized $\sqrt{\lambda}\,\delta$ dimensionless deflection data as a function of dimensionless impulse ϕ for PCS, PCCS and PCA mild steel plates under short stand-off blast loading conditions. In (b) the ϕ offset, due to elastic behaviour, has been removed such that the individual correlations pass through the origin.

8.3.3 Plastic Stiffness Parameter Correlation

The review of published blast loading analyses presented in Chapter 2 found that the majority of the large deflection PCS plate models are based on the IIL assumption. Furthermore, the published experimental studies intended to validate these models were typically conducted using short stand-off explosive charges, similar to that described in Section 5.2.5.1, in an attempt to create loading conditions approaching that of the IIL assumption. However, Section 5.3 and the results of the preceding section show that the short stand-off configuration does not provide a loading condition that closely approaches that of the IIL assumption. Nevertheless, while falling short of their intended purpose, these efforts resulted in a collection of published experimental PCS data that is a relatively rich and, in combination with the data in Section 6.2, provides a basis for evaluating certain aspects of the generalized energy method.

The resistance of a plate to plastic deformation can be expressed in terms of the plastic stiffness $\tilde{K}$. From Sections 3.3.1.1 and 7.3, the plastic stiffness of the three plate configurations considered in this work can be characterized using the general form[2],

$$\tilde{K} = \lambda \pi H \alpha \sigma_y \frac{R_o + R_i}{R_o - R_i} \tag{8.3}$$

where only the plastic stiffness parameter λ distinguishes between the plate configurations. Furthermore, the general form of dimensionless deflection vs impulse gradient, given in Equation (8.2), indicates that, for materials with a nominally consistent strain rate parameter α, non-dimensionalized results for the three plate configurations should fall on three distinct response curves. This result is supported by the data shown in Figure 8.1(a), where the deflection data for mild steel PCS plates, due to Bodner & Symonds [56] and Nurick *et al.* [60], are compared with the data for mild steel PCCS and PCA plates, due to Cloete *et al.* [52] and Palmer [182].

[2]The form of $\tilde{K}$ for PCS plates, as given in Equation (3.20), is recovered as R_i vanishes.

The effect of the plastic stiffness parameter λ can be assessed by using it to normalize the dimensionless deflection vs impulse gradient, *i.e.* rewriting Equation (8.2) as,

$$\frac{\sqrt{\lambda}\,\delta}{\phi} = \frac{1}{\sqrt{\alpha}} \tag{8.4}$$

This result suggests that if the IIL approach is consistent and the assumed displacement profiles are well chosen, then, for a given rate parameter α, the normalized non-dimensionalized results for the three plate configurations should collapse onto a single response curves. The result is supported by the data shown in Figure 8.1(b), where the mild steel plate deflection data, due to Bodner & Symonds, Nurick *et al.*, Cloete *et al.* and Palmer, essentially collapse onto a single curve.

As alluded to above, the choice of displacement profile, and hence λ, has a strong influence on the correlations shown in Figure 8.1. In the case of the PCS and PCCS plates, Bessel function displacement profiles were used. For all PCS plates the value of λ is 1.5589, as given in Equation (2.27), but for PCCS plates the λ value depends on the ratio of R_i to R_o, albeit weakly, as given in Equation (7.19) and Appendix D. For the data in Figure 8.1, the value of R_i was 10 mm, while the values of R_o were 50 mm, 65 mm or 80 mm, giving λ values of 4.4088, 4.2672 or 4.1540 respectively. For the PCA plates, the displacement profile that includes radial displacements was used, which implies that the value of λ also depends on the ratio of R_i to R_o, as given in Equation (7.31). In all cases the value of R_i was 10 mm, while the value of R_o was 50 mm or 65 mm, giving λ values of 0.6667 and 0.7333 respectively.

For each plate configurations, the displacement profile that most closely corresponds to the final experimental plate shape was chosen. In other words, the displacement profiles were not specifically selected to provide the best deflection correlation[3]. Hence, given the wide range of plate configurations, the good correlation in Figure 8.1 is considered sufficient to validate the plastic stiffness parameters derived in this work.

Notwithstanding, the preceding result, it is evident that the PCA and PCCS data deviates slightly below the linear fit to the PCS data. This may be be due to several factors, such as differing rate effects, *i.e.* α values. A significant factor may be the slight difference in the loading configuration. The PCS data were obtained using either sheet explosive or multiple concentric rings of explosive at a small stand-off. By contrast the PCCS and PCA data were obtained using a single explosive ring configuration at a stand-off of 30 mm, which is approximately double the 16 mm stand-off used by Nurick *et al.* [60]. As shown in Section 5.3, the peak intensity of a blast wave drops dramatically with an increase in stand-off distance, while the blast duration increases. Consequently, the loading experienced by the PCA and PCCS plates is likely to have been marginally less impulsive than that experienced by the PCS plates. This observation is one of the motivations for investigating the effects of finite load durations.

8.4 IIL PCCS Deformation Duration

In Sections 6.2.3.1 and 6.3.3.1 it is argued that the Mode I deformation duration can be inferred from the secondary peak of the central support force history of a PCCS blast test. In other words, this point

[3]The parabolic PCCS profile provides a marginally improved correlation, but the remaining profile shapes for PCS and PCA plates all resulted in inferior correlations

is interpreted to be where plastic deformation of the plate ceases and elastic rebound begins. Using this interpretation, the force history results for 100 mm diameter PCCS plates reported in Chapter 6 show remarkably consistent deformation duration results of between 125 μs and 130 μs. Provided that Mode I behaviour was maintained, this behaviour appears to be independent of impulse magnitude and plate thickness, as shown in Figure 6.21. Hence, in this section, the aforementioned narrow range of values is used to evaluate the Mode I deformation duration predictions for PCCS plates subjected to an ideal impulsive load.

8.4.1 PCCS Taylor Duration

The travelling hinge model of Taylor, as reviewed in Section 2.3.6, was adapted to the PCCS configuration in Section 7.4.1 and resulted in the expression for the deformation duration given in Equation (7.33), and repeated here for convenience,

$$T_{\scriptscriptstyle T} = \frac{R_o - R_i}{2}\sqrt{\frac{\rho}{\alpha\sigma_y}} \tag{8.5}$$

As shown in Chapter 7, this is a characteristic quantity that appears in several solutions and is, therefore, denoted by the subscript T, *i.e.* the Taylor duration.

As previously noted in regard to the Taylor duration for PCS plates, Equation (8.5) is independent of the plate thickness. This is in broad agreement with results presented in Chapter 6. For example, Figure 6.21 shows that the durations of the Mode I central support force history for three PCCS plates of different thicknesses are essentially identical.

Using values of $R_o = 50$ mm, $R_i = 10$ mm, $\rho = 7800$ kg/m^3 and $\sigma_y = 300$ MPa, values of $\alpha = 2$ and $\alpha = 2.8$ give deflection duration estimates of $T_{\scriptscriptstyle T} = 72.11\,\mu$s and $T_{\scriptscriptstyle T} = 60.94\,\mu$s. In other words, the predicted deformation duration based on the Taylor duration is approximately half the measured value. This result is to be expected since two of the fundamental assumptions are not satisfied by the experiments, namely the blast load does not meet the IIL condition and a travelling hinge model does not capture the complete plate response. Nevertheless, it will be shown that the Taylor duration provides a convenient basis for non-dimensional comparison of experimental data and theoretical models.

8.4.2 PCCS Membrane Duration

The single phase energy approach presented in Section 3.3.4.1, which is closely related to the membrane mode method of Symonds & Wierzbicki reviewed in Section 2.3.5, was adapted to the PCCS configuration in Section 7.4.2. The resulting expression for the deformation duration is given in Equation (7.36), and repeated here for convenience,

$$T = \pi\sqrt{\frac{\mu}{\lambda}}\,T_{\scriptscriptstyle T} \tag{8.6}$$

where μ is the effective mass parameter and $T_{\scriptscriptstyle T}$ is the Taylor duration as repeated above in Equation (8.5).

Both a parabolic and a Bessel displacement profile were considered in Sections 7.4.2.1 and 7.4.2.2 respectively. The effective mass parameter μ, the corresponding non-dimensional initial mid-radius velocity $\dot{\tilde{w}}_0/V_0$ and the non-dimensional single phase deformation duration $T/T_{_T}$ were determined for each profile and summarized in Table 7.1.

The μ values for the parabolic and Bessel PCCS profiles are 0.5333 and 0.4731 respectively. Both these values are less than unity, as would be expected, but are significantly larger than the corresponding PCS values of 0.3333 and 0.2695 respectively, as given in Table 3.2. As discussed in Section 3.3.1.3, the effective mass parameter indicates what fraction of the total mass must be considered when calculating the kinetic energy using the maximum profile velocity $\dot{\tilde{w}}$. Hence, the μ value for the parabolic profile is slightly larger than the Bessel profile, since the parabolic profile is more rounded, *i.e.* a greater portion of the plate has a velocity close to $\dot{\tilde{w}}$. Similarly reasoning can explain why the the PCCS μ values are greater than the corresponding PCS values. For the PCS configuration, the highest velocities occur at the centre of the plate, which represents a small portion of the total mass. By contrast, for the PCCS configuration, the highest velocities occur along a mid-radius strip of the plate, which represents a larger portion of the total mass than the central region.

The initial non-dimensional mid-radius velocities $\dot{\tilde{w}}_0/V_0$ for the parabolic and Bessel PCCS profiles are 1.3693 and 1.4539 respectively, which are both significantly smaller than the corresponding central PCS values of 1.7321 and 1.9263 respectively. These values are consistent with the preceding discussion, *i.e.* a smaller μ value implies that less of the plate is at an initial velocity close to $\dot{\tilde{w}}_0$ and, therefore, a higher $\dot{\tilde{w}}_0$ value is required for the initial kinetic energy to be equivalent to a uniform plate moving at V_0.

Tables 7.1 and 3.2 show that the non-dimensional displacement duration values for the PCCS profiles differ significantly from those of the PCS profiles. The significance of this difference between the $T/T_{_T}$ values is difficult to assess since the respective Taylor durations are based on distinct plastic hinge configurations. By contrast, it is interesting to note that for a given plate configurations the $T/T_{_T}$ values are remarkably consistent. The $T/T_{_T}$ values for the parabolic and Bessel PCCS profiles are 0.9953 and 1.0291 respectively, *i.e.* a difference of just over 3%, while the corresponding PCS values are 0.6413 and 0.6532 respectively, *i.e.* a difference of less than 2%. This result is to be expected since the single phase energy analysis is analogous to Rayleigh's method for vibration, as discussed at length in Section 3.3.4.1.

The $T/T_{_T}$ values in Table 7.1 are close to unity, which implies that the PCCS single phase deflection duration will be similar to the Taylor duration. Using the Taylor duration values determined in Section 8.4.1, the single phase deflection duration estimates for the parabolic profile are $T = 71.77\,\mu$s and $T = 60.65\,\mu$s, for $\alpha = 2$ and $\alpha = 2.8$ respectively, while the corresponding Bessel profile durations estimates are $T = 74.21\,\mu$s and $T = 62.71\,\mu$s. As mentioned previously, these duration estimates are approximately half the measured value reported in Section 6.3.3.1. Furthermore, comments regarding the Taylor duration are also applicable in this case, *i.e.* the IIL condition is not satisfied in the experiments and the single phase model does not capture the complete plate response.

8.4.3 PCCS Two Phase Duration

The two phase IIL energy approach for PCS plates presented in Section 4.2.2, was adapted to the PCCS configuration in Section 7.4.3. The resulting expressions for the Phase I and II deformation durations are

given in Equations (7.47) and (7.51) respectively, and repeated here for convenience,

$$\frac{T_I}{T_T} = 2\sqrt{\frac{1-\mu}{\lambda}} \quad \text{and} \quad \frac{T_{II}}{T_T} = \frac{T_I}{T_T} + 2\sqrt{\frac{\mu}{\lambda}}\left(\frac{\pi}{2} - sin^{-1}\sqrt{1-\mu}\right) \tag{8.7}$$

where all the parameters are as defined in the preceding sections and summarized in Table 7.1.

As shown in Section 7.4.3, the T_I/T_T values for the parabolic and Bessel displacement profiles are 0.5916 and 0.6914 respectively. These values are remarkably similar to those obtained for the PCS configuration, as shown in Figure 4.3, and carry the same implications, *i.e.* the two phase model predicts a greater average radial hinge velocity than that assumed by Taylor, as given in Equation (8.5).

As discussed in Section 4.2.2, Taylor's travelling hinge model assumes that any given point on the plate is instantaneously brought to rest upon the arrival of the hinge. This is not physically realistic since it implies a velocity discontinuity between the 'rigid' portion of the plate, which is still moving at the initial velocity, and the deformed portion of the plate, which is at rest. By contrast, the two phase model is explicitly based on the notion of velocity continuity between the 'rigid' and the deforming portion of the plate[4].

As noted in Section 4.2.2, the two phase model is an extension of the constant displacement profile energy method, where the inclusion of the travelling hinge phase allows the correct initial conditions to be captured without altering the maximum displacement predictions. The two phase displacement history at radius $\tilde{R}$ has a similar form to that shown in Figure 4.3 A consequence of the additional phase is the extension of the deformation duration in comparison to the single phase membrane approach. However, unlike the PCS case where the duration increase for the parabolic and Bessel profiles are 43% and 34% respectively, the increase for the PCCS configuration is only 11% and 15% respectively.

The T_{II}/T_T values in Table 7.1 are close to unity, which implies that the PCCS two phase deflection duration will be similar to the Taylor duration. Using the Taylor duration values determined in Section 8.4.1, the two phase deflection duration estimates for the parabolic profile are $T_{II} = 80\,\mu$s and $T_{II} = 67.61\,\mu$s, for $\alpha = 2$ and $\alpha = 2.8$ respectively, while the corresponding Bessel profile durations estimates are $T_{II} = 85.69\,\mu$s and $T_{II} = 72.42\,\mu$s.

While slightly longer than the single phase predictions, the aforementioned deformation duration estimates are still just over half the measured values of between $125\,\mu$s and $130\,\mu$s reported in Sections 6.2.3.1 and 6.3.3.1 for both the short stand-off and blast tube loading configurations. Furthermore, unlike the single phase models, the two phase model does capture the complete plate response, *i.e.* the initial uniform velocity due to the IIL condition, the transient hinge motion and the latter membrane response. Hence, the IIL assumption is the most likely source for the discrepancy and is, therefore, the focus of the next section.

[4] A detailed discussion of published travelling hinge models [15, 18, 19] is beyond the scope of this thesis. However, it is noted that it may be possible to relax the assumptions related to the membrane hinge so as to avoiding features such as infinite accelerations and sudden changes of curvature. An example of this is the classical bending analysis of Wang [24] which avoids discontinuities and leads to a variable hinge velocity.

Table 8.3: Dimensionless deflection vs impulse gradient predictions for PCCS plates under CIL and IDL conditions.

α	CIL-Parabolic	CIL-Bessel	IDL-Parabolic	IDL-Bessel
1	0.3536	0.3725	0.2459	0.2621
2	0.2500	0.2634	0.1739	0.1853
2.5	0.2236	0.2356	0.1555	0.1657
2.8	0.2113	0.2226	0.1470	0.1566

8.5 Finite Duration Loading

In this section the effect of finite duration loading on the response of PCCS plates is discussed. In particular, the predictions of the critical impulsive load (CIL) and ideal dynamic load (IDL) models developed in Sections 7.5.2 and 7.5.3, respectively, are compared to the experimental results for short stand-off and blast tube tests reported in Sections 6.2 and 6.3 respectively.

8.5.1 Critical Impulsive Loading

The critical impulsive load (CIL) approach for PCS plates presented in Section 4.3.4 was adapted to the PCCS configuration in Section 7.5.2. A critical impulsive load is defined in Section 4.3.4 as a uniform pressure load of constant intensity, *i.e.* a 'square' load, with a duration T_L equal to T_I, *i.e.* the duration of Phase I involving transient plastic hinge motion. This loading case is regarded as 'critical' in the sense that it marks the transition from impulsive loading, *i.e.* $T_L < T_I$, to dynamic loading, *i.e.* $T_L > T_I$, as defined in Section 4.3.2.

The expression for the Phase I and II deflections under CIL conditions are given in Equations (7.63) and (7.65) respectively and can be rewritten in terms of a dimensionless deflection vs impulse gradient in the form,

$$\frac{\delta_I}{\phi} = \sqrt{\frac{\beta - \mu}{\alpha\lambda}} \quad \text{and} \quad \frac{\delta_{II}}{\phi} = \sqrt{\frac{\beta}{\alpha\lambda}} \tag{8.8}$$

where β is the effective pressure parameter as defined in Section 7.5.1. The values for β are 0.6667 and 0.6116 for the parabolic and Bessel displacement shapes respectively, as given in Table 7.2.

The Phase II gradient predictions for various values of the strain rate sensitivity factor α are shown in Table 8.3. As before, the parabolic profile assumption results in lower deflection predictions but the Bessel function profile is considered to be more appropriate as it matches the measured plate profiles. Recalling that the measured short stand-off gradient is 0.2198, Table 8.3 shows that the CIL results are significantly closer to the experimental value than the IIL case, as given in Table 8.1. In particular, for a value of $\alpha = 2.8$ the prediction based on the Bessel shape is within 1.3% of the measured gradient. In other words, a good correlation is achieved using the same α value that provides a good correlation for the PCS configuration under an IIL assumption.

The resulting expressions for the Phase I and II deformation durations are given in Equations (7.61) and (7.68) respectively, and repeated here for convenience,

$$\frac{T_I}{T_T} = 4\sqrt{\frac{\beta-\mu}{\lambda}} \quad \text{and} \quad \frac{T_{II}}{T_T} = \frac{T_I}{T_T} + 2\sqrt{\frac{\mu}{\lambda}}\left[\frac{\pi}{2} - sin^{-1}\sqrt{1-\frac{\mu}{\beta}}\right] \tag{8.9}$$

The non-dimensional Phase I duration values for the Parabolic and Bessel displacement profiles are 0.6325 and 0.7090 respectively, as summarized in Table 7.2. As discussed in Section 7.5.2, these durations are virtually identical to the equivalent IIL Phase I values, *e.g.* the Bessel result differs by only 1.5%, which implies that the loading history appears to have no significant effect on the Phase I duration. From the Taylor duration given in Section 8.4.1, the Phase I durations are 45.61 μs and 43.21 μs for the parabolic and Bessel profiles respectively. According to the CIL condition, these values also represent the assumed duration of the pressure load.

For comparison with the above, the duration of the short stand-off blast loads can be inferred from the pressure histories shown in Figures 5.15 and 5.16. The pressure histories show that the loading has effectively dissipated after 50 μs and, when a ring charge is present, the bulk of the load occurs between 20 μs and 40 μs. Therefore, the theoretical CIL pressure load duration T_I is considered to be a reasonable approximation to the measured short stand-off blast load duration. This observation in conjunction with the good agreement for δ_{II}/ϕ using $\alpha = 2.8$ suggests that the generalized energy approach using a CIL assumption provides an appropriate model for short stand-off blast loading of PCCS plates.

Notwithstanding the aforementioned, some aspects of the CIL model for could not be correlated with experimental data. In particular, the non-dimensional Phase II duration values for the parabolic and Bessel displacement profiles are 1.3328 and 1.4132 respectively, as summarized in Table 7.2. From the Taylor duration given in Section 8.4.1, the Phase II durations are 96.11 μs and 86.12 μs for the parabolic and Bessel profiles respectively. These values are significantly smaller than the apparent Mode I duration of approximately 125 μs shown in Figure 6.5. However, there are several reasons for caution regarding the experimental result. Firstly, trace (a) in Figure 6.5 is the only successful recording of a Mode I response to a short stand-off test in the data set due to Palmer [182], *i.e.* the degree of repeatability is not known. Secondly, the lack of repeatability is due to the difficulty experienced in avoiding deflagration at charge masses small enough not to cause a Mode II* response. Indeed, Figure 5.14 suggests that all four of the Mode I data points for the 100 mm diameter PCCS plates are a result of ring charge deflagration. Hence, the pressure load duration is unknown and, given that deflagration is a slower process than detonation, is likely to have extended beyond Phase I, *i.e.* the CIL assumption would no longer apply. Thirdly, in the case of PCS plates, Figure 4.10 shows that the CIL duration is much shorter than the IDL duration. Tables 7.2 and 7.3 predict a similar response for the PCCS plate configuration. However, the short stand-off and blast tube Mode I durations, in Figures 6.5 and 6.21 respectively, all appear to be in the region of 125 μs. Considering the distinct characters of the short stand-off and blast tube pressure histories, this result should not occur. Given the above, the short stand-off Mode I duration is not considered to be insufficient to invalidate the CIL model.

Finally, the ability of the CIL assumption to accurately reproduce the salient features of the short stand-off blast test results confirms that only capturing the total impulse of an experimental blast load is insufficient for a precision blast test. Other load parameters, such as the duration, average pressure

or pressure history, must be captured for sufficient information to be available for accurate analysis and interpretation. In other words, the IIL assumption, at best, provides only an upper limit for the behaviour of blast loaded plates, since it can lead to a significant overestimate of the final deflection.

8.5.2 Ideal Dynamic Loading

The ideal dynamic load (IDL) approach for PCS plates presented in Section 4.3.7 was adapted to the PCCS configuration in Section 7.5.3. An ideal dynamic load is defined in Section 4.3.7 as a uniform pressure load of constant intensity with a duration T_L equal to T_{II}, *i.e.* the full duration of the plate motion marked by the end of Phase II.

The expression for the Phase I and II deflections under IDL conditions are given in Equations (7.70) and (7.72) respectively and can be rewritten in terms of a dimensionless deflection vs impulse gradient in the form,

$$\frac{\delta_I}{\phi} = 4\left(\frac{\beta-\mu}{\lambda\sqrt{\alpha}}\right)\Big/\frac{T_{II}}{T_T} \quad \text{and} \quad \frac{\delta_{II}}{\phi} = 4\left(\frac{\beta}{\lambda\sqrt{\alpha}}\right)\Big/\frac{T_{II}}{T_T} \tag{8.10}$$

where the definitions and values of the parameters are as defined in the preceding sections of this chapter.

Note that, unlike CIL case, Equations (8.10) contain T_{II}/T_T explicitly. The reason for this is that in the CIL case the expression for the load duration, *i.e.* T_I, has a convenient form that allows for significant simplification one substituted into the expression for δ_I and δ_{II}. However, this is not the case for T_{II} and, therefore, it is computationally simpler to first compute T_{II}/T_T and, thereafter, δ_I and δ_{II} [5].

The Phase II gradient predictions for various values of the strain rate sensitivity factor α are shown in Table 8.3. As before, the parabolic profile deflection predictions are lower but the Bessel function results are considered to be more appropriate. Recalling that the measured blast tube gradient is 0.1544, Table 8.3 shows that the IDL results are significantly closer to the experimental value than the either the IIL or CIL case, *i.e.* Tables 8.1 and 8.3. In particular, for a value of $\alpha = 2.8$ the prediction based on the Bessel shape is only 1.4% greater than the measured gradient. In other words, a good correlation is achieved using the same α value that provides a good correlation for the PCS configuration under an IIL assumption and the short stand-off PCCS configuration under the CIL assumption.

The IDL condition implies that the pressure is constant during Phase I and, consequently, that the Phase I deformation duration is identical to the CIL case, *i.e.* Equation (7.61). However, the IDL expression for the Phase II deformation duration differs significantly from the CIL case and is given in Equation (7.78) respectively. The aforementioned expressions are repeated here for convenience,

$$\frac{T_I}{T_T} = 4\sqrt{\frac{\beta-\mu}{\lambda}} \quad \text{and} \quad \frac{T_{II}}{T_T} = \frac{T_I}{T_T} + 4\sqrt{\frac{\mu}{\lambda}}\left[\frac{\pi}{2} - sin^{-1}\sqrt{1-\frac{\mu}{\beta}}\right] \tag{8.11}$$

The non-dimensional Phase I and II duration values are summarized in Table 7.3. As discussed in previous section, the Phase I durations are virtually identical to the equivalent IIL Phase I values, *i.e.* the loading

[5] Notwithstanding this dependency, the solutions for δ_I and δ_{II} are presented before that for T_{II} to maintain a consistent sequence of presentation with prior sections.

history appears to have no significant effect on the Phase I duration. As before, the Phase I durations are 38.54 μs and 43.21 μs for the parabolic and Bessel profiles respectively.

From Table 7.3, the non-dimensional Phase II duration values for the Parabolic and Bessel displacement profiles are 2.033 and 2.1174 respectively. Unlike the Phase I durations, the IDL Phase II durations are significantly longer than those of both the IIL and CIL assumptions, *e.g.* the Bessel results differ by 78% and 50% respectively. From the Taylor duration given in Section 8.4.1, the Phase II durations using a value of $\alpha = 2.8$ are 123.9 μs and 129 μs for the parabolic and Bessel profiles respectively. Both these results correlate well with the PCCS Mode I response from the blast tube experiments shown in Figure 6.21, where the maximum plastic plate response varied between 125 μs and 130 μs.

From the preceding results it is apparent that the IDL assumption provides reasonably accurate estimates of both the final maximum displacement and deformation duration of blast tube loaded PCCS plates. These results, encouraging though they are, should be treated with some caution for a few reasons. Firstly, Figure 4.9 shows that for the PCS configuration the IDL assumption significantly overpredicts the final deflection in comparison with an FEA solution. Conversely, Figure 4.10 shows that for the PCS configuration the IDL assumption provides a good estimate deflection duration when comparison to the FEA solution. In other words, a good temporal solution does not necessarily imply a good deflection solution. Secondly, Figure 5.24 shows that the typical pressure histories produces by the blast tube configuration has a characteristic 'blast wave' profile, *i.e.* it's shape differs significantly from the IDL assumption. Thirdly, Figure 5.24 also shows that while the blast wave persists beyond Phase I, *i.e.* it is clearly a dynamic rather than impulsive load, it also persists beyond the end of Phase II, which also differs significantly from the IDL assumption. Furthermore, this implies that a portion of the measured total impulse may have been transfered to the ballistic pendulum after plate deformation has ceased, *i.e.* the total measured impulse is greater than the impulse that contributed to the deformation.

Notwithstanding the aforementioned reservations, the performance of the IDL based model is encouraging and suggests that it could be useful for first estimate predictions of a plate response to large stand-off long duration blast loads. Furthermore, the good correlations achieved with a value of $\alpha = 2.8$ when using the appropriate loading assumption suggests that the generalized energy method is consistent and a valid approach for simplified blast loading analysis.

Chapter 9

Conclusions and Recommendations

> "Knowledge is a process of piling up facts; wisdom lies in their simplification."
>
> Martin H. Fischer (1879-1962)

9.1 Introduction

The central purpose of this thesis is to present a novel laboratory scale blast loading experimental apparatus, and the associated plate configurations, developed specifically to produce data for the validation of simulation codes intended for the study of the deformation and fracture of blast loaded plates. In addition, this required the development of novel analytical solutions to provide a theoretical framework for the presentation of experimental data and lay a foundation for future validation work.

For this endeavour, the notion of a 'precision test' was adopted as a central guiding philosophy. A set of ten requirements were adopted from the 1996 Trondheim workshop entitled 'Precision testing in support of computer code validation and verification' [1], as set out in Section 1.1.2.

The following four objectives were identified and set out in Section 1.2 as follows:

1. Review published blast loading studies, with a particular emphasis on laboratory scale blast testing of structures, and evaluate whether they can be considered as precision tests.
2. Review published theoretical models used to interpret blast loading studies, with particular emphasis on closed form solutions for large displacements, and evaluate whether they are coherent and sufficient to provide basis for the interpretation of precision tests results.
3. Present a novel experimental apparatus for the blast loading of plates, and demonstrate that it meets the requirements of a precision test.
4. Present a unified theory for the blast loading of axisymmetric plates which subsumes previous closed form solutions and extends the theory to include the novel specimen configuration presented in this thesis.

The first two objectives were achieved in Chapters 2 and 3, and summarized relative to the precision test requirements in Section 3.4.

With regard to experimental techniques, it was found that the majority of the precision testing requirements were met using classical techniques, such as the ballistic pendulum, although a few crucial requirements were not met. This was the motivation for the third objective that culminated in the development of the instrumented ballistic pendulum, incorporating a central support in the form of a Hopkinson bar, and the associated peripherally clamped centrally supported (PCCS) and peripherally clamped annular (PCA) plate specimen configuration, as discussed in Chapter 5, with the experimental results presented in Chapter 6. Therefore, the purpose of Section 9.2 in this chapter is to show that the instrumented ballistic pendulum, incorporating a central support in the form of a Hopkinson bar, and the associated PCCS and PCA plate specimen configuration meets the requirements of a precision test.

With regard to analytical solutions, it was found that the literature contained several classical closed form solutions for the large deflection of impulsively loaded peripherally clamped solid (PCS) circular plates. These solutions successfully described the linear relationship between dimensionless impulse and deflection typically observed in laboratory scale blast loading experiments. Furthermore, additional manipulations of the analytical solutions showed that expression for the dimensionless impulse can be obtained that are in agreement with those of Nurick & Martin [5,6]. Hence, the prospect of obtaining dimensionless impulse expressions for the PCCS and PCA plate configurations was the initial motivation for the analytical work pursued in this thesis. However, during these theoretical investigations, it was found that several crucial aspects of the published analytical solutions for PCS plates were contradictory and/or incomplete in the literature. In particular, for the large deflections of impulsively loaded PCS plates, there did not appear to be any two phase solutions nor any models that incorporate non-impulsive loads. This was the motivation for the fourth objective that culminated in the analytical models presented in Section 3.3 and Chapters 4 and 7. Conclusions regarding the fourth objective are discussed in Section 9.3.

Finally, recommendations for future work are discussed in Section 9.4.

9.2 The Instrumented ballistic Pendulum as a Precision Test

According to the Trondheim workshop report, reviewed in Chapter 1, there are ten criteria that a test apparatus and testing protocol must satisfy to be considered a precision experiment. In this section, the performance of the instrumented ballistic pendulum, the PCCS and PCA plate configuration and associated analytical solutions will be evaluated with respect to the precision test requirements set out in Section 1.1.2. This evaluation will mirror that conducted in Section 3.4 for published studies.

9.2.1 Structural Behaviour

Requirement: The structural behaviour must be accurately described and highly repeatable.

As noted in Section 3.4, amongst the extensive literature devoted to shock loading experiments, studies with suitable code validation data are surprisingly sparse as only a small subset contain sufficient data for the assessment of repeatability. This is most evident when observing that a few specific papers are

regularly cited by theoretical studies, principal amongst these being the studies of Bodner & Symonds [56] and Nurick & co-workers [60,68–70]. These studies show that, under laboratory conditions, the response of blast loaded structures can be highly repeatable and accurately measured, thus meeting this requirement of a precision test.

The common feature of these aforementioned tests was the use of the ballistic pendulum pendulum and a short stand-off charge. Hence, the use of a ballistic pendulum as the basic experimental platform along with the blast loading protocols used by Nurick & co-workers ensured that the proven accuracy and repeatability associated with these techniques was carried over to the new apparatus. This is evident in the dimensionless deflection vs impulse results for short stand-off PCCS and PCA blast tests shown in Figure 6.2. The least-squares regression fits for the Mode I responses of the PCCS and PCA plates resulted in r^2 correlation coefficient of 0.9141 and 0.9681, respectively, while the majority of the ave-max data points lie within a half plate thickness of the regression line. Given that this data spans 31 blast tests conducted on 1.6 mm thick mild steel plates with diameters of 100 mm, 130 mm or 160 mm, this represents a high degree of correlation.

Further enhancement of repeatability was achieved through the use of a blast tube and the reasons for this will be elaborated upon in Section 9.2.3. For this subsection it is sufficient to observe the repeatability evident in the dimensionless deflection vs impulse results for blast tube loaded PCCS and PCA tests shown in Figure 6.11. The least-squares regression fits for the Mode I responses of the PCCS and PCA plates resulted in r^2 correlation coefficient of 0.9678 and 0.99, respectively, while the majority of the ave-max data points lie within a half plate thickness of the regression line[1]. Given that this data spans 155 blast tests conducted on 100 mm diameter mild steel plates with thicknesses of 1.6 mm, 2 mm and 3 mm, this represents a high degree of correlation. Hence, both the short stand-off and blast tube data are in keeping with the data reported by Bodner & Symonds and Nurick & co-workers shown in Figures 3.1 and 3.2.

Lastly, it is evident that the results from both the short stand-off and blast tube tests, which together span a variety of plate thicknesses and diameters, prove the validity of the theoretically derived dimensionless impulse expressions that will be discussed further in Section 9.2.9. In addition to the above, there is further evidence of measurement accuracy and highly repeatability, which will be discussed in the context of more specific precision test requirement in subsequent sections.

9.2.2 Failure modes

Requirement: Failure modes must be individually observable and experimentally decoupled from other effects.

The identification, observation and individual description of failure modes is one of the strengths of traditional laboratory scale blast testing. This is exemplified by the failure modes for beams by Menkes & Opat [48], as given in Table 2.1, and for plates by Nurick & Co-workers [67, 70], as given in Table 2.2. In particular, the impulses values at which the transitions between the failure modes occur have been well established. Hence, persisting with the ballistic pendulum ensured that this feature was retained in the new apparatus.

[1] Part of these data have been published by Cloete *et al.* [52, 53] with over 60 citations to date on Google Scholar.

Notwithstanding the above, the latter part of the criterion, *i.e.* the experimental decoupling of failure modes from other effects, does not appear to have been addressed. The precise meaning of 'decoupling' was not clearly defined, although it was noted in the Trondheim workshop that this is a difficult problem for dynamics tests in general due to inertia and strain rate issues. In other words, a dynamic test cannot be interrupted at the moment of failure due to the excess inertia of the plate and, therefore, the progression of the failure cannot be captured. Furthermore, a series of test on nominally identical plates with increasing impulsive loading, while a valid set of data in itself, will also not provide evidence of the progression of the failure. For example, the final state of a Mode II* response cannot be assumed to represent the failure initiation stage of during a Mode II response due to the higher deformation rate.

Addressing the 'decoupling' aspect of laboratory scale blast testing so as to meet the precision test requirement is one of the primary motivations for the work in this thesis. From the literature it became evident that the temporal resolution of failure events had not received attention, but that this is crucial if competing failure mechanism are to be distinguished, *i.e.* 'decoupled', from other response effects. This observation inspired the introduction of the instrumented central support and, hence, the development of the PCCS plate configuration, as discussed in detail in Chapter 5.

The introduction of the PCCS configuration marks a subtle shift in emphasis with regards to blast testing. Previous test had mostly focused on plate configurations that correspond to those encountered in practice. By contrast, the PCCS configuration is intended specifically to generate data for code validation.

The PCCS configuration retains the feature of distinct failure modes, as is evident in Figures 6.8 and 6.20, although the failure mode definitions had to be generalized as given in Section 6.1.1 and Figure 6.1. In this way the primary requirement of the second precision test criterion is met. The latter 'decoupling' requirement of the precision test criterion is satisfied by the reaction force captured from the central support, which allows the timing of a mode transitions and magnitude of failure event can be captured. In addition, integrating the force history to obtain the fraction of the total impulse transferred through the central support increased the clarity with which the mode transitions can be distinguished. Finally, the ability to contrast the PCCS plate response with the PCA plate response, especially with regard to Mode III, provides additional information regarding boundary fracture process that is not available from the traditional plate configurations. These and other advantages of the central support are discussed further in the context of subsequent precision test criterion.

9.2.3 Load Control and Repeatability

Requirement: The applied load must be controlled and highly repeatable in terms of magnitude and both spatial and temporal distribution.

The issue of load control and repeatability during laboratory scale blast loading elicited one of the more strenuous debates during the Trondheim workshop proceedings, as reviewed in Section 1.1.3. Critics noted that shock tubes cannot generate the impulse intensities that are typically of interest, while high explosive (HE) charges are difficult to reproduce and define with respect to the peak pressure or spatiotemporal distribution.

While this criticism was justified for many of the studies reviewed in Chapter 2 and 3, it was also overly pessimistic since studies by Bodner & Symonds and Nurick *et al.* had demonstrated a high degree of

control and repeatability with regard to the total impulse, as shown in Section 3.2.2. Furthermore, more recent studies have shown that spatiotemporal blast features such as duration, rate of application and removal, peak pressure and impulse distribution can routinely and reliably be inferred using robust techniques such as Hopkinson pressure bars or digital image correlation (DIC) [51–53, 90–93]. In other words, the combination of the blasting techniques developed by Bodner & Symonds and Nurick *et al.* sufficiently addresses the criticism mentioned above, thus meeting this requirement of a precision test. For the case of the short stand-off tests, this is most evident in the pressure histories shown in Figures 5.15 and 5.16.

The addition of a blast tube, as described in Section 5.2.5.2, enabled further improvement of the control and repeatability of the blast loading. In essence, a blast tube combined spatial uniformity of a load produced by a shock tube with the impulse intensity produced by an HE charge. In particular, the blast tube expanded control over the lower range of the blast loading domain, which is restricted in short stand-off testing due to the minimum thickness requirement of the charge. This capability is most evident in Figure 6.22 where the response signal to the 4 g charge represents a purely elastic response, *i.e.* the plate showed no residual elastic deformation and allowed the horizontal intercept in Figure 6.11 to be confirmed. The high degree of repeatability is evident in Figure 5.21 where three 10 g produce near identical pressure traces. Lastly, the spatial uniformity of the blast tube loading was confirmed via the good correspondence between the total impulse and impulse obtained by integrating central support signal. In addition, the axial symmetry of the load is evident in the reduced error bars in Figure 6.11. This is significant because, unlike the PCS plate configuration, the PCCS plate configuration is sensitive to load non-uniformity.

9.2.4 Boundary Conditions

Requirement: Boundary conditions must be fully defined, including parameters such as stiffness and friction.

As noted in Section 3.4, support conditions are acknowledged to be difficult to fully define [1]. Certain aspects, such as the boundary geometry are relatively trivial to define. For example, the nature of a boundary, *i.e.* whether a boundary is clamped, welded or fully built-in [163], and its geometry, *e.g.* size, fillet radii, clamp edge radii, *etc.* Nurick*et al.* [70], can be clearly defined.

Unlike the boundary geometry, other aspects, such as boundary stiffness and friction are notoriously difficult to define with precision. Boundary stiffness has a significant effect on the vibration response of complex structures loaded dynamically with a response within the elastic limit. This is, presumably, the reason for the inclusion of this precision test requirement. However, for the impulsive loading of simple beam and plate structures undergoing large plastic deformation with relatively massive supports, there is no experimental evidence that the boundary stiffness significantly affects the results and is, therefore, not required for precision testing.

In contrast to boundary stiffness, boundary friction can have a significant effect as is evident in Figure 2.3 where significant boundary pull-in is evident in the data of Florence [36] due to insufficient clamp friction. From the literature, the standard approach for clamped plates is to ensure that clamped area is large in comparison to the area exposed to the blast and supported by thick clamp plates. This approach ensures

that the plastic work required to draw in the clamped portion of the plate greatly exceeds the plastic work required to deform the exposed portion, thus limiting pull-in to a negligible level and obviating the need for a large clamping force. Under these circumstances the clamping friction is assumed not to have a large effect and therefore its exact value is not required for precision testing.

While the preceding discussion shows that the boundary condition definitions of traditional blast tests, such as those of Bodner & Symonds and Nurick *et al.*, are adequate for precision testing, the aims of this thesis introduced additional requirements. In particular, as previously mentioned, the PCCS configuration is intended generate data for code validation with a particular emphasis on boundary reaction forces. Given the size and inertia of the clamping plates, along with the unknown stiffness properties, it was evident that measuring reaction forces at the outer boundary would not be possible. As discussed in Section 5.2.2, the addition of a central support creates a new inner boundary where failure would occur preferentially, while maintaining axial symmetry. Furthermore, since the central support is in the form of a Hopkinson bar, its stiffness properties are well known and can be dynamically isolating from the specimen clamp assembly and support structures. In other words, while incorporating all the precision features of traditional blast tests, the PCCS plate configuration and central support incorporates additional features to satisfy the boundary condition requirement of a precision blast test.

9.2.5 Transducer selection

Requirement: Suitable transducers must be selected.

As discussed in Section 3.4, the primary data obtained from traditional laboratory scale blast tests using a ballistic pendulum is the total impulse and final deflection. Prior to the new millennium, the use of transducers had been relatively rare, *e.g.* capacitive sensors [56] and light occlusion for deformation history [61], trip wires for fragment velocity [67] or strain gauges for stress history [39]. More recently there has been an increased use of diagnostics, *e.g.* DIC to capture plate motion [72, 77, 79, 86–88] and piezoelectric transducers [79,87,89] or Hopkinson pressure bars [52,53,90–93] to capture pressure history[2].

A particular focus of this thesis has been the introduction[3] of the Hopkinson pressure bar (HPB) as a force and pressure transducer for laboratory scale blast testing. Considering the blast test on PCA plates, the central Hopkinson bar satisfies all the requirements of a pressure transducer for a precision test. Firstly, the central HPB is non-invasive, *i.e.* it does not interfere with the specimen behaviour as PCA plate deflects away from the central bar during its motion. Secondly, it is a robust sensor, as is evident from the Figure 5.22 where peak pressures of over 140 MPa were recorded[4]. Thirdly, the sensor has a rapid response as discussed in detail in Section 5.2.6. In particular, the multi-mode dispersion cut-off frequency of 180 kHz is sufficient for the dispersion correction to reconstitute the blast signal for the short stand-off blast tests. Furthermore, it was shown that the blast tube signal does not disperse appreciably. Fourthly, the sensor has a sufficient recording duration as the central HPB was designed to be long enough to capture a full blast load prior to the return of the reflected pulse. Fifthly, the central HPB length

[2] Work published as part of this thesis has been at the forefront of these developments [51–53, 90] with over 70 citations to date on Google Scholar.

[3] It could be argued that 're-introduction' is a more accurate term as blast characterization was the original purpose for which Bertram Hopkinson invented the device that bears his name, as discussed in Section 2.1.3.

[4] In fact, this technique is limited by the bond strength of strain gauge glue rather than the strength of the Hopkinson bar.

also means that the sensor is dynamically isolated from the specimen clamp assembly and any sensor mounts or other support structures. Finally, the HPB can be dynamically calibrated, as demonstrated in Appendix B. These features and the high degree of repeatability, as shown in Figures 5.21 and 5.22, satisfy all the requirements of a pressure transducer for a precision test.

All the above mentioned characteristics carry over to blast test using the PCCS plate configuration where the Hopkinson bar acts as a central support. As previously mentioned, the intent was to create a well defined inner boundary condition where failures occur preferentially and the boundary reaction forces could be measured during a blast test[5]. The reaction force results proved to be highly repeatable in both the short stand-off and blast tube configurations, as shown in Figures 6.6, 6.17 and 6.18. Data of this nature is valuable for code validation as it enhances the precision and richness of data obtained with a ballistic pendulum. For example, failure mode transitions can be more clearly identified by considering the portion of the impulse transfered through the central support, as shown in Figure 6.13. Furthermore, the total duration of motion and the precise timing of failure events can be clearly discerned, as shown, for example, in Figure 6.14. Finally, given the high degree of repeatability of the blast test and resulting signals, the nominal shear stress during shear fracture events could be inferred by subtracting the blast signal obtained during PCA plate tests from the force signal obtained from PCCS plate tests with nominally identical HE charges. From the above it is apparent that the central boundary condition is well defined and the results obtained from the instrumented central support are non-invasive, accurate and highly repeatable, *i.e.* the requirements of a precision test are satisfied.

9.2.6 Data Redundancy

Requirement: The data collected from the experiments must have some redundancy[6]

The greater the amount and variety of experimental data, the more stringent a code validation process will be. Furthermore, it is preferable that some important experimental parameters have some degree of redundancy, *i.e.* be measured or inferred from more than one sensor or observation. In other words, there should be some way to cross-check a given experimental reading. For instance, if a pressure transducer is used to measure the pressure history of a particular blast loading event and the blast loading technique is known to produce a uniform load, the resulting pressure history could be integrated to yield the impulse delivered to the target, which could be compared to the actual impulse obtained by mounting the target on a ballistic pendulum.

In this thesis, the testing of both PCCS and PCA plate configurations leads to some data redundancy. Most significant is the comparison of PCA plate response to the Mode III response of the PCCS plates at higher impulses. At higher impulses complete shear failure occurs at the inner boundary of the PCCS plate before significant plastic displacement has occurred. From then on, the sheared PCCS plate is, essentially, a PCA plate and responds accordingly. However, there tends to be a consistent offset between the dimensionless displacement vs impulse results for PCA plates and the Mode III trend of PCCS plates, as shown in Figures 6.2 and 6.11. This impulse offset is due to the fraction of the total impulse required

[5] To the authors knowledge, data of this nature has not been published prior the work associated with this thesis [51–53, 90].

[6] From the Trondheim report it is not clear whether data redundancy is regarded as essential or merely beneficial, but it is included here for the sake of completeness.

to shear the PCCS plate at the inner boundary. This impulse offset should be equal to the difference between the impulse measured by the central HPB during PCA and PCCS plate tests. This, in turn, would be equal to the impulse transfered from the deforming PCCS plate to the central support, *i.e.* the temporal integral isolated shear force history. In other words, there are multiple features of the blast test data that must cross-correlate for the data set to be regarded as coherent. In addition, there are further redundancies such as the ability to detect the impulse at which failure mode transitions occur from both the dimensionless deflection vs impulse curves and the central support impulse fraction curves. From the above it is apparent that the experimental configurations pursued in this thesis permit a considerable degree of data redundancy as required by a precision blast test.

9.2.7 Precision Reporting

Requirement: Precision reporting must be provided for all test parameters that could influence the results.

Precision reporting implies the comprehensive and accurate documentation of all specifications and measurements along with an unambiguous description of the observed behavior. The specifications should include data acquisition, *e.g.* sensor and instrumentation characteristics, the initial conditions of the specimen, interface definitions, support geometry and material test data or constitutive relations for all materials involved. Measurements should include tabulated global data, such as deflection and impulse, and accessible curated electronic files of sensor data including load characterization. In other words, reported studies must contain adequate detailed information for to allow for meaningful theoretical model validation and correlations with other studies.

A small number of classical laboratory scale studies meet many of these requirements, such as the blast pendulum work of Bodner & Symonds [56] and Nurick & co-workers [60, 68–70]. Therefore, the practices established in those studies are continued in this thesis as can be seen in the comprehensive tabulated data in Appendix E and the unambiguous description of the observed damage modes which are refined and generalized in this thesis. In addition, all the necessary specifications for the specimens, pendulum, data acquisition, *etc.* are given in Chapter 5 and Appendices B, C and F. Finally, detailed load characterization and central support force histories are given in Section 5.3 and Chapter 6 respectively. From the above it is apparent that the experimental reporting pursued in this thesis meets the requirements of a precision blast test.

9.2.8 Material Properties

Requirement: The material properties must be well defined, especially with regard to strain rate sensitivity.

As mentioned in Section 3.4, the blast loading studies reviewed in Chapter 2 seldom report the constitutive relations of the specimen materials in sufficient detail, with strain rate sensitivity data typically taken from the literature for nominally similar materials. More recently, some researchers have begun to address this by publishing studies focused on material characterization closely followed by blast loading studies using material from the same stock and not merely the same type of material [79, 158, 164]. The same approach has been followed in this thesis with detailed quasi-static and dynamic material data reported

in Appendix B. Therefore it is evident that the material properties requirements of a precision blast test have been addressed in this thesis.

9.2.9 Concurrent Analyses

Requirement: Analyses should be included in the development of the experimental apparatus to ensure usable results

As discussed in point 9 of Section 1.1.2, the proceedings of the Trondheim workshop highlight the need for stronger interaction between testing and analysis. In particular, it was noted that researchers developing analytical or numerical solutions typically do not carry out experimental work and have little practical experience in high strain rate testing. This is confirmed by the review presented in Chapter 2 showing that the literature contains several closed form solutions for the large deflection of impulsively loaded PCS circular plates, but none that were developed concurrently with experimentation. This is also the case for many researchers developing numerical solutions, although the rise of powerful and affordable commercial codes and workstation has made concurrent analysis more commonplace [164, 179].

Notwithstanding the absence of concurrent analysis, it would be incorrect to suggest that extant solutions were not considered. As mentioned in Section 2.1.1, the work of Bodner & Symonds [56] may be viewed as the first instance of the laboratory scale blast test intended as a validation experiment, *i.e.* thin sheet explosive was specifically employed to closely approximate the impulsive loads assumed by analytical solutions. Similarly, Nurick & Martin [5, 6] compared a large number of analytical solutions to their experimental results. In other words, there is a clear tradition of the including analyses in the planning and interpretation of laboratory scale blast tests.

A particular advantage of analytical solutions is revealed in Section 3.3.1.2 where it is shown that the energy method based analytical solution of Duffey [38] provides an identical expression for the dimensionless impulse as that obtained from experimental data by Nurick & Martin [5, 6] using dimensionless analysis. In this thesis, following a generalized energy method, a dimensionless impulse expression was obtained for the PCCS and PCA plate configurations, as shown in Sections 7.3.1 and 7.3.2. In addition, the analytical solutions developed in Chapters 4 and 7 resulted in useful criteria with which to distinguish between impulsive and dynamic loadings, while providing good correlations with the experimental data, as shown in Chapter 8.

Finally, familiarity with the development and validation of analytical solutions provided an appreciation for the importance of including certain features in their experimental design. For example, the PCCS and PCA plate configurations maintain an axisymmetric character which is amenable to theoretical models and results in a strong interaction between testing and analysis. In addition to maintain axial symmetry, the pursuit of other features such as preferential failure at inner boundary for PCCS plates, dynamic isolation of the clamped plates, blast uniformity and load characterization where all motivated by knowledge of the challenges involved in the validation of analytical or numerical solutions. From the aforementioned, it can be concluded that the concurrent analyses requirement of a precision blast testing has been addressed in this thesis.

9.2.10 Validation Predictions not 'Postdictions'

Requirement: The validation process must involve predictions and not 'postdictions'.

In this thesis there is a clear distinction between material characterization tests, as discussed in Appendix B, load characterization test, as described in Section 5.3 and dynamic structural tests, *i.e.* blast loading of plates, as reported in Chapter 6. All the data required to setup and 'calibrate' a numerical code and/or material model is provided in by the characterization test. Hence, no code validation based on the data provided in this thesis should require any additional data, such a material data from the literature, the parameters of which may require 'massaging' to ensure correlation. In other words, no 'postdictions' are required, which satisfies this precision test requirement.

9.2.11 Overall Assessment

From the preceding subsections it is evident that all the features of the classical laboratory scale blast loading studies that satisfied the majority of the precision test criteria have been retained and refined. More significantly, the one experimental parameter that remained to be addressed, namely the measurement of boundary reaction forces, has been addressed by incorporating the instrumented central support in conjunction with the PCCS specimen plate configuration. The central Hopkinson bar also fulfills a secondary purpose of blast load characterization when used in conjunction with the PCA plate configuration. Consequently, the lack of data regarding the timing and force magnitudes involved in various failure modes and their associated transitions has been addressed and shows the potential to provide a wealth of code validation data. In addition extensions to classical analytical models were presented to support and evaluate the experimental work. Therefore, it is concluded that the instrumented ballistic pendulum incorporating a central support in the form of a Hopkinson bar in conjunction with the PCCS and PCA plate configurations satisfies all the requirement of a precision test as set out in the Trondheim workshop proceedings as discussed in Section 1.1.2. Thus the third thesis objective, as set forth in Section 1.2, is satisfied.

9.3 Analytical Modelling of PCS, PCCS and PCA Plates

In the literature review presented in Sections 2.3 and 2.4 several classical closed form solutions for the large deflection of impulsively loaded PCS and PCA circular plates are considered. While these models produced useful results, such as good final deflection predictions, it was evident that several aspects of the solutions were inconsistent and/or contradictory and that the justifications for crucial assumptions were incomplete. Hence, prior to extending these analytical models to the PCCS plate configuration in fulfillment of the concurrent analyses requirement, a unified analytical approach for blast loaded axisymmetric plates with large deflections was required that subsumes previous closed form solutions, resolves inconsistent and/or contradictory, provides justifications for crucial assumptions and allows for extensions to novel specimen configurations. This requirement motivated the fourth objective of this thesis, the results of which are evaluated in this section.

In Section 3.3.1 the generalized energy method based on the analytical approach of Duffey [38] was introduced. This approach was chosen as it was found that a constant flow stress gives a linear relationship between dimensionless impulse and deflection and provides an identical expression for the dimensionless impulse as that obtained from experimental data by Nurick & Martin [5,6] using dimensionless analysis[7]. In Section 3.3.2 it was shown that this approach was amenable to the typical displacement profiles used in the literature, while Section 7.2 showed the same for the profiles developed for this thesis. Moreover, the choice was validated when a dimensionless impulse expressions for the PCCS and PCA plate configurations was obtained, as reported in Section 7.2. In particular, the analysis provided a novel plastic stiffness parameter λ with which the dimensionless deflection vs impulse data for variety of axisymmetric plates, with distinct configurations, dimensions and material composition, would collapse onto a single curve.

In Section 3.3.3 the generalized energy method was extended to subsume the membrane mode solution of Symonds & Wierzbicki [122] and the travelling hinge model of Taylor [15], which required the introduction of a uniform notation. Unlike the original energy approach of Duffey, these solutions provided displacement duration estimates, although both underpredicted experimental results and provided final displacement results were inferior to those of Duffey. It was shown that the discrepancies in both the membrane mode and travelling hinge solutions were due to the assumption that the entire deformation history could be described by a single phase. Since, at least, the pioneering photographic work of Munday & Newitt [34], shown in Figure 2.1, it has been known that the response of a thin metal plates to an impulsive load involves two distinct phases, *i.e.* an initial transient Phase I involving plastic hinge motion and a latter Phase II where a near constant deformation profile with in-plane stretching predominates. Hence, Taylor's travelling hinge model, *i.e.* purely Phase I, captures the transient phase with the correct initial energy but assumes that a given point on the plate comes to rest as the hinge passes, thus restricting the final plate shape to that of a cone, which is not realistic. By contrast, in the case of the membrane mode solution, *i.e.* purely Phase II, the assumed deformation profile, *i.e.* a Bessel function, closely matches the final shape of recovered plate specimens but neglects the transient phase, which results in an incorrect value for the initial energy. To address the aforementioned discrepancies, the generalized energy method was extended to include a two phase model for PCS circular plates, as presented in Section 4.2, which incorporates salient features of both the travelling hinge and membrane mode solutions[8]. The two phase model retained the good deflection results of Duffey while significantly improving the displacement duration predictions, as shown in Section 4.2.2.

In Sections 3.3.6 and 3.3.7, the influence of radial displacements and bending strains on the final deflection of impulsively loaded plates was investigated. In published analytical models it is often assumed that these effects are negligible, but thorough justifications for these assumptions are seldom, if ever, provided. The results in Section 3.3.6 show that radial displacements are, in fact, not negligible, have a significant effect on the strain distribution and must be accounted for if a strain based failure criterion is to be used. However, when calculating the total plastic work, the reduction in radial plastic work due to the presence of radial displacements is balanced by the increase in circumferential plastic work such that the effects cancel out. Hence, if only the prediction of axial deflections is of concern, then radial displacements need

[7] To the authors knowledge, this relationship had not been noted in the literature prior the work published in association with this thesis [52].

[8] To the authors knowledge, this is the first closed form two phase solution for the large deflection of impulsively loaded plates.

not be considered. Similarly, the results in Section 3.3.7 show that the contribution of bending strain are not negligible at small displacements but that membrane strains become dominant above a dimensionless deflection of unity[9].

The aforementioned results shows that generalized energy method was able to deal with all the discrepancies observed in published analytical solutions for impulsively loaded axisymmetric plates. However, for the purposes of this thesis, solutions for finite duration loads were also required. In Section 4.3 it was shown that the generalized energy method and two phase model could be extended to include finite duration loads for plates exhibiting a large displacement response[10]. Subsequently, in Section 7.5 these solutions were extended to the PCCS and PCA plate configurations. These models have provided promising results when compared to experimental data, as discussed in Section 8.5. Furthermore, the models have suggested improved definitions to distinguish between impulsive and dynamic loads.

From the preceding discussion it is apparent that the generalized energy method provides a consistent and unified analytical approach for impulsively and dynamically loaded axisymmetric plates with large deflections. Furthermore, it subsumes published closed form solutions and provides models for the PCCS and PCA specimen configurations developed in this thesis. Thus the fourth thesis objective, as set forth in Section 1.2, has been satisfied.

9.4 Recommendations for future work

It is a common refrain that researcher projects tend to unearth more questions than they answer. The same is true for this thesis, for even tough all four thesis objectives were achieved, several potential avenues of inquiry became evident that were beyond the scope of this thesis, but are regarded are worthy of pursuit.

9.4.1 Blast Loading Experiments

While the data presented in this thesis represents a substantial and coherent set of data, there are some areas where the experimental approach could be enhanced and extended. Possible enhancements include additional sensors and/or refinement of existing sensors, while extensions imply further variations of the plate configurations and/or testing domains.

With regard to additional sensors, the first to consider would be the use of a laser displacement sensor to more accurately capture the movement or even directly measure the initial velocity of the ballistic pendulum [88]. Similarly, laser displacement sensors could also be used to capture the transient motion of the plate, although the rapidly improving capabilities are DIC systems are more likely to be used as they provide full field measurements [77, 86, 88]. This aspect experimental diagnostics, in particular, shows great potential for improvement, although in the case of a PCCS plate configuration with a central support, a three camera system may be required. Indeed, further improvements of high resolution high

[9] This work has been published [133] and has received ten citations to date on Google Scholar.

[10] To the authors knowledge, this is the first closed form solution for the large deflection of plates subjected to finite duration loads.

speed digital cameras may cause detailed time resolved full field strain measurement to be a standard feature of laboratory scale blast loading experiments.

Sensor refinement would focus on improving the analysis of central HPB data. In particular, the aim would be to develop higher mode Pochammer-Chree dispersion correction techniques so that more accurate central support force histories can be obtained. This could result in improved blast load characterization and allow finer details of inner boundary fracture process to be discerned. However, this is a challenging problem [175] and other areas of possible improvement may be more fruitful in the near term.

Additional plate configuration and boundary conditions could enhance the variety of data available for code validation. Of particular interest would be a fully built-in variation of a PCCS plate, *i.e.* a specimen machined from thicker plate stock such that the annular portion of the specimen is thinned down but the inner and outer boundaries retain the full thickness and match the geometry of the clamps and central support. This would avoid friction issues by eliminate pull-in in the clamped region as well as sliding at the central boundary. furthermore, a variety of machined fillet radii could be investigated and used to refine fracture models.

In addition to the above, it could be potential to investigate means to extend the blast test domain with respect to the blast load profile. For example, extending the length of the blast tube could lower and extend the duration of the blast load, *i.e.* tending toward dynamic loading. At the other extreme, it may be useful to consider the possibility of returning to thin sheet explosives to better approximate ideal impulsive loads.

9.4.2 Analytical Solutions

While the generalized energy method and associated analytical solutions developed in this thesis satisfied the fourth objective, there are clear avenues for further analytical model development. The following should are recommended for future work.

Firstly, none of the existing models of a means to deal with fracture. This phenomenon is challenging because it is highly localized and typically exhibits a non-axisymmetric progression. Nevertheless, models that can capture this, even if only in an approximate sense, may provide useful correlations and dimensionless numbers.

Secondly, extending the generalized energy method to accommodate realistic blast load profiles, *i.e.* a sudden pressure rise followed by an exponential decay, would be valuable. However, this would significantly complicate the integration of the pressure work and an alternative or approximate approach may be required.

Thirdly, the generalized energy method shows promise to be extend to including non-axisymmetric plate shapes, such an ellipse, equilateral triangle, square and rectangle. The reason to be optimistic is that solutions for quasi-static membrane inflation and membrane vibration exist for all these shapes and thus repurposing these solutions for a blast response models may be possible.

Finally, one last significant blast loaded plate response remains to be explained. It is evident in Appendix B that the materials used in this thesis for the plate specimens are strain rate sensitive, *i.e.* non-linear. Nevertheless, blast load tests with these materials consistently produce noticeable linear

relationships between dimensionless impulse and deflection, as observed in the experimental data reviewed in Section 2.2.1 and presented in Sections 6.2.1 and 6.3.1. By contrast, the analytical solutions reviewed and presented in this thesis all predict a linear relationship between dimensionless impulse and deflection only when a constant flow stress is assumed, *i.e.* when rate sensitivity is included, as discussed in Section 2.3.7 and 3.3.5, the general linear relationship is lost. The essence of the problem lies in the fact that both experimental data and theoretical solutions tend to show that the displacement duration is relatively constant and independent of impulse. This implies that larger impulses, which lead to greater deflections and strains, will induce greater strain rates. This, in turn, implies that the plates should offer greater resistance to deformation at larger impulses, which should then result in a non-linear relationship between impulse and deflection. This is a rather vexing problem that does not appear to have been raised in the literature, let alone addressed, and is a worthy problem to consider for further research.

References

[1] Krauthammer, T., Jensen, A., and Langseth, M. Precision testing in support of computer code validation and verification. workshop report NR 234/96, Norwegian Defence Construction Service, 1996.

[2] Thacker, B., Doebling, S., Hemez, F., Anderson, M., Pepin, J., and Rodriquez, E. Concepts of model verification and validation,. Technical Report LA-14167-MS, Los Alamos National Laboratory, 2004.

[3] Johnson, W. The origins of the ballistic pendulum: the claims of Jacques Cassini (1677-1756) and Benjamin Robins (1707-1751). *International Journal of Mechanical Sciences*, 32(4):345–374, 1990.

[4] Jones, N. *Structural Impact*. Cambridge, 1989.

[5] Nurick, G. N. and Martin, J. B. Deformation of thin plates subjected to impulsive loading - a review, Part I: Theoretical considerations. *International Journal of Impact Engineering*, 8(2):159–170, 1989.

[6] Nurick, G. N. and Martin, J. B. Deformation of thin plates subjected to impulsive loads - a review, Part II: Experimental studies. *International Journal of Impact Engineering*, 8(2):171–186, 1989.

[7] Corbett, G. G., Reid, S. R., and Johnson, W. Impact loading of plates and shells by free-flying projectiles - a review. *International Journal of Impact Engineering*, 18(2):141–230, 1996.

[8] Florek, J. R. and Benaroya, H. Pulse-pressure loading effects on aviation and general engineering structures - review. *Journal of Sound and Vibration*, 284:421–453, 2005.

[9] Rajendran, R. and Narasimhan, K. Deformation and fracture behaviour of plate specimens subjected to underwater explosion a review. *International Journal of Impact Engineering*, 32:1945–1963, 2006.

[10] Zhu, F. and Lu, G. A review of blast and impact of metallic and sandwich structures. *EJSE Special Issue: Loading on Structures*, 2007.

[11] Rajendran, R. and Lee, J. M. Blast loaded plates (review). *Marine Structures*, 22:99–127, 2009.

[12] Tse, F. S., Morse, I. E., and Hinkle, R. T. *Mechanical Vibrations: Theory and Applications*. Allyn & Bacon, 2^{nd} edition, 1979.

[13] Thomson, W. T. *Theory of Vibration with applications*. Chapman & Hall, 4^{th} edition, 1993.

[14] Meirovitch, L. *Fundamentals of Vibrations*. McGraw-Hill, 2001.

[15] Taylor, G. I. The distortion under pressure of a diaphragm which is clamped along its edge and stressed beyond the elastic limit. In *Underwater Explosion Research*, volume 3, The Damage Process, pages 107–121. Office of Naval Research, 1950 (originally written 1942).

[16] Richardson, J. M. and Kirkwood, J. G. Theory of the plastic deformation of thin plates by underwater explosions. In *Underwater Explosion Research*, volume 3, The Damage Process, pages 305–421. Office of Naval Research, 1950 (originally work 1944).

[17] Cole, R. H. *Underwater Explosions*. Dover, New York, 1948.

[18] Hudson, G. E. A theory of the dynamic plastic deformation of a thin diaphragm. *Journal of Applied Physics*, 22(1):1–11, 1951.

[19] Frederick, D. A simplified analysis of circular mambranes subjected to an impulsive loading producing large plastic deformations. In *Proceedings of the 4^{th} Midwestern Conference on Solid Mechanics*, pages 18–35, University of Texas, 1959.

[20] Symonds, P. S. Dynamic characteristics in plastic bending of beams. *Journal of Applied Mechanics*, 20 (Trans. A.S.M.E. 75):475–481, 1953.

[21] Hopkins, H. G. and Prager, W. The load carrying capacity of circular plates. *Journal of the Mechanics and Physics of Solids*, 2:1–13, 1953.

[22] Hopkins, H. G. and Prager, W. On the dynamics of plastic circular plates. *ZAMP (J. Appl. Math. and Phys.)*, 5:317–330, 1954.

[23] Wang, A. J. and Hopkins, H. G. The plastic deformation of built-in circular plates under impulsive loads. *Journal of the Mechanics and Physics of Solids*, 3:22–37, 1954.

[24] Wang, A. J. The permanent deflection of a plastic plate under blast loading. *Journal of Applied Mechanics*, 22:375–376, 1955.

[25] Perzyna, P. Dynamic load carrying capacity of a circular plate. *Archivum Mechaniki Stosowanej*, 10:635–647, 1958.

[26] Prager, W. On the use of singular yield conditions and associated flow rules. *Journal of Applied Mechanics, Transactions of A.S.M.E.*, 75:317–320, 1953.

[27] Onat, E. T. and Prager, W. Limit analysis of shells of revolution I&II. *Proceedings of the Royal Netherlands Academy of Sciences, Series B*, 57:534–548, 1954.

[28] Onat, E. T. and Haythornthwaite, R. M. The load-carrying capacity of circular plates at large deflections. *Journal of Applied Mechanics*, 23 (Trans. ASME 78):49–55, 1956.

[29] Hodge, P. G. Yield conditions for rotationally symmetric shells under axisymmetric loading. *journal of applied mechanics*, 27(2):323–331, June 1960. Trans. ASME Vol. 82, Series E.

[30] Weil, N. A. and Newmark, N. M. Large plastic deformation of circular membranes. *Journal of Applied Mechanics*, 22:533–538, 1955.

[31] Hoffman, A. J. The plastic response of circular plates to air blasts. Master's thesis, University of Delaware, 1955.

[32] Gerard, G. A new experimental technique for applying impulsive loads. In *Proceedings of the Symposium on Impact Testing, number 176 in ASTM Special Technical Publication*, pages 94–109, Atlantic City, NY, 1956.

[33] Witmer, E. A., Balmer, N. A., Leech, J. W., and Pian, T. N. N. Large dynamic deformations of beams, rings, plates and shells. *AIAA*, 1:1848–1857, 1963.

[34] Munday, G. and Newitt, D. M. The defromation of transversely loaded disks under dynamic loads. *Philosophical Transactions of the Royal Society of London*, A256:1–30, 1963.

[35] Humphreys, J. S. Plastic deformation of impulsively loaded straight clamped beams. *Journal of Applied Mechanics*, 32:7–10, 1965.

[36] Florence, A. L. Circular plates under a uniformly distributed impulse. *International Journal of Solids and Structures*, 2:37–47, 1966.

[37] Wierzbicki, T. and Florence, A. L. A theoretical and experimental investigation of impulsively loaded clamped circular viscoplastic plates. *International Journal of Solids and Structures*, 6:553–568, 1970.

[38] Duffey, T. A. The large deflection dynamic response of clamped circular plates subjected to explosive loading. research report SC-RR-67-532, Sandia National Laboratories, 1967.

[39] Duffey, T. A. and Key, S. W. Experimental-theoretical correlations of impulsively loaded clamped circular plates. *Experimental Mechanics*, 9(6):241–249, 1969.

[40] Jones, N., Uran, T., and Tekin, S. A. The dynamic plastic behaviour of fully clamped rectangular plates. *International Journal of Solids and Structures*, 6:1499–1512, 1970.

[41] Boyd, D. E. Dynamic deformations of circular membranes. *Journal of the Engineering Mechanics Division, Proceedings of ASCE*, 92(EM3):1–16, June 1966.

[42] Martin, J. B. and Symonds, P. S. Mode approximations for impulsively-loaded rigid-plastic structures. *Journal of the Engineering Mechanics Division, Proceedings, ASCE*, 92(EM5):43–66, 1966.

[43] Jones, N. Impulsive loading of a simply supported circular rigid plastic plate. *Journal of Applied Mechanics*, 35:59–65, 1968.

[44] Jones, N. Finite deflections of a rigid-viscoplastic strain-hardening annular plate loaded impulsively. *Journal of Applied Mechanics*, 35:349–356, 1968.

[45] Lippmann, H. Kinetics of the axisymmetric rigid-plastic membrane subject to initial impact. *International Journal of Mechanical Sciences*, 16:297–303, 1974.

[46] Youngdahl, C. Correlation parameters for eliminating the effect of pulse shape on dynamic plastic deformation. *Journal of Applied Mechanics*, 37:744–752, 1970.

[47] Krauthammer, T., Astarlioglu, S., Blasko, J., Soh, T., and Ng, P. Pressure-impulse diagrams for the behavior assessment of structural components. *International Journal of Impact Engineering*, 35:771–783, 2008.

[48] Menkes, S. B. and Opat, H. J. Tearing and shear failure in explosively loaded clamped beams. *Experimental Mechanics*, 13:480–486, 1973.

[49] Ghosh, S. K., Balendra, R., and Travis, F. W. Inertial forming of circular and annular diaphragms. In *Proceedings of the 18th International Machine Tool Design and Research Conference*, pages 845–855, London, 1978. MacMillan.

[50] Ghosh, S. K. and Travis, F. W. A unique experimental high-rate forming machine. *International Journal of Mechanical Engineering Education*, 7:69–74, 1979.

[51] Cloete, T. J., Ahmed, R., and Nurick, G. N. Peripherally clamped centrally supported blast loaded circular plates: a precision test for code validation. *Journal de Physique IV France*, 110:507–512, 2003.

[52] Cloete, T. J., Nurick, G. N., and Palmer, R. N. The deformation and shear failure of peripherally clamped centrally supported blast loaded circular plates. *International Journal of Impact Engineering*, 32:92–117, 2005.

[53] Cloete, T. J. and Nurick, G. N. Blast tube loading of plates using an instrumented ballistic pendulum. In *Proceedings of IMPLAST 2010*, Providence, Rhode Island, USA, 12-14 October 2010. SEM Society for Experimental Mechanics Inc. ISBN 9781935116066.

[54] Johnson, W. *Impact Strength of Materials*. Edward Arnold, 1972.

[55] Li, Q. M. and Jones, N. On dimensionless numbers for dynamic plastic response of structural members. *Archive of Applied Mechanics*, 70:245–254, 2000.

[56] Bodner, S. R. and Symonds, P. S. Experiments of viscoplastic response of circular plates to impulsive loading. *Journal of the Mechanics and Physics of Solids*, 27:91–113, 1979.

[57] Clifton, R. Obituary - Paul Southworth Symonds, August 20, 1916 - March 28, 2005. *International Journal of Impact Engineering*, 32:4–5, 2005.

[58] Kolsky, H. An investigation of the mechanical properties of materials at very high rates of loading. *Proceedings of the Physical Society of London*, 62B:676–700, 1949.

[59] Wegener, R. B. and Martin, J. B. Predictions of permanent deformation of impulsively loaded simply supported square tube steel beams. *International Journal of Mechanical Sciences*, 27(1-2):55–69, 1985.

[60] Nurick, G. N., Pearce, H. T., and Martin, J. B. The deformation of thin plates subjected to impulsive loading. In Bevilacqua, L., Feijoo, R., and Valid, R., editors, *Inelastic Behaviour of Plates and Shells, IUTAM Symposium*, pages 597–616, Rio de Janiero, 1986. Springer.

[61] Nurick, G. N. A new technique to measure the deflection-time history of a structure subjected to high strain rates. *International Journal of Impact Engineering*, 3:17–26, 1985.

[62] Nurick, G. N., Pearce, H. T., and Martin, J. B. Predictions of transverse deflections and in-plane strains in impulsively loaded thin plates. *International Journal of Mechanical Sciences*, 29(6):435–442, 1987.

[63] Wierzbicki, T. and Nurick, G. N. Large deformation of thin plates under localised impulsive loading. *International Journal of Impact Engineering*, 18:899–918, 1996.

[64] Mihailescu-Suliciu, M. and Wierzbicki, T. Wave solution for an impulsively loaded rigid-plastic circular membrane. *Archives of Mechanics*, 54(5-6):737–759., 2002.

[65] Wierzbicki, T. Petalling of plates under explosive and impact loading. *International Journal of Impact Engineering*, 22:935–954, 1999.

[66] Wen, H. M. Deformation and tearing of clamped circular work-hardening plates under impulsive loading. *International Journal of Pressure Vessels and Piping*, 75:67–73, 1998.

[67] Teeling-Smith, R. G. and Nurick, G. N. The deformation and tearing of thin circular plates subjected to impulsive loads. *International Journal of Impact Engineering*, 11:77–91, 1991.

[68] Nurick, G. N. and Teeling-Smith, R. G. Predicting the onset of necking and hence rupture of thin plates loaded impulsively - an experimental view. In *2^{nd} International Conference on Structures Under Shock and Impact*, pages 431–445, 1992.

[69] Thomas, B. and Nurick, G. N. The effect of boundary conditions on thin plates subjected to impulsive loads. In *The 5^{th} International Symposium on Plasticity and its Current Application - PLASTICITY 95*, pages 85–88, Osaka, Japan, July 17-21 1995.

[70] Nurick, G. N., Gelman, M. E., and Marshall, N. S. Tearing of blast loaded plates with clamped boundary conditions. *International Journal of Impact Engineering*, 18(7-8):803–827, 1996.

[71] Zhu, F., Zhao, L., Lu, G., and Wang, Z. Deformation and failure of blast-loaded metallic sandwich panelsexperimental investigations. *International Journal of Impact Engineering*, 35:937–951, 2008.

[72] Hargather, M. J. and Settles, G. S. Laboratory-scale techniques for the measurement of a material response to an explosive blast. *International Journal of Impact Engineering*, 36:940–947, 2009.

[73] Bambach, M. R. Behaviour and design of aluminium hollow sections subjected to transverse blast loads. *Thin-Walled Structures*, 46:1370–1381, 2008.

[74] Bambach, M., Zhao, X., and Jama, H. Energy absorbing characteristics of aluminium beams strengthened with CFRP subjected to transverse blast load. *International Journal of Impact Engineering*, 37:37–49, 2010.

[75] Cui, X., Zhao, L., Wang, Z., Zhao, H., and Fang, D. Dynamic response of metallic lattice sandwich structures to impulsive loading. *International Journal of Impact Engineering*, 43:1–5, 2012.

[76] Kakogiannis, D., Hemelrijck, D. V., Palanivelu, S., Paepegem, W. V., Ackeren, J. V., Wastiels, J., Reymen, B., and Vantomme, J. Measurement of the transmitted impulse from hemispherical charges. In *9th National Congress on Theoretical and Applied Mechanics*, Brussels, 9-11 May 2012.

[77] Zhao, X., Tiwari, V., Sutton, M. A., Deng, X., Fourney, W. L., and Leiste, U. Scaling of the deformation histories for clamped circular plates subjected to blast loading by buried charges. *International Journal of Impact Engineering*, 54:31–50, 2013.

[78] Jing, L., Wang, Z., Shim, V. P. W., and Zhao, L. An experimental study of the dynamic response of cylindrical sandwich shells with metallic foam cores subjected to blast loading. *International Journal of Impact Engineering*, 71:60–72, 2014.

[79] Aune, V., Fagerholt, E., Hauge, K. O., Langseth, M., and Børvik, T. Experimental study on the response of thin aluminium and steel plates subjected to airblast loading. *International Journal of Impact Engineering*, 90:106–121, 2016.

[80] Hanssen, A. G., Enstock, L., and Langseth, M. Close-range blast loading of aluminium foam panels. *International Journal of Impact Engineering*, 27:593–618, 2002.

[81] Enstock, L. K. and Smith, P. D. Measurement of impulse from the close-in explosion of doped charges using a pendulum. *International Journal of Impact Engineering*, 34:487–494, 2007.

[82] Martin, L. and Link, R. Numerical characterization of mine blast loading final report,. Contract Report CR 2006-016, Defence Research and Development Canada, DRDC Suffield, August 2003.

[83] Taylor, L. C., Skaggs, R. R., and Gault, W. Vertical impulse measurement on mines buried in saturated sand. *Fragblast*, 9(1):19–28, 2005.

[84] Turner, G. R. An alternative method for the measurement of the mechanical impulse of a vertically directed blast,. *Review of Scientific Instruments,*, 70:075102, 2008.

[85] Pickering, E., Yuen, S. C. K., Nurick, G., and Haw, P. The response of quadrangular plates to buried charges. *International Journal of Impact Engineering*, 49:103–114, 2012.

[86] Tiwari, V., Sutton, M. A., McNeill, S. R., Xu, S., Deng, X., Fourney, W. L., and Bretall, D. Application of 3D image correlation for full-field transient plate deformation measurements during blast loading. *International Journal of Impact Engineering*, 36:862–874, 2009.

[87] Spranghers, K., Kakogiannis, D., Ndambi, J.-M., Lecompte, D., and Sol, H. Deformation measurements of blast loaded plates using digital image correlation and high-speed photography. In *14th International Conference on Experimental Mechanics*, volume 6, page 12006. EPJ Web of Conferences, 2010.

[88] Curry, R. J. and Langdon, G. S. Transient response of steel plates subjected to close proximity explosive detonations in air. *International Journal of Impact Engineering*, 102:102–116, 2017.

[89] Hargather, M. J. and Settles, G. S. Optical measurement and scaling of blasts from gram-range explosive charges. *Shock Waves*, 17:215–223, 2007.

[90] Cloete, T. J. and Nurick, G. N. Blast characterization using a ballistic pendulum with a centrally mounted hopkinson bar. *International Journal of Protective Structures*, 7(3):367–388, 2016.

[91] Tyas, A., Reay, J. J., Fay, S. D., Clarke, S. D., Rigby, S. E., Warren, J. A., and Pope, D. J. Experimental studies of the effect of rapid afterburn on shock development of near-field explosions. *International Journal of Protective Structures*, 7(3):452–465, 2016.

[92] Rigby, S. E., Tyas, A., Curry, R. J., and Langdon, G. S. Experimental measurement of specific impulse distribution and transient deformation of plates subjected to near-field explosive blasts. *Experimental Mechanics*, 59:163–178, 2019.

[93] Rigby, S. E., Akintaro, O. I., Fuller, B. J., Tyas, A., Curry, R. J., Langdon, G. S., and Pope, D. J. Predicting the response of plates subjected to near-field explosions using an energy equivalent impulse. *International Journal of Impact Engineering*, 128:24–36, 2019.

[94] Nemat-Nasser, S., Kang, W., McGee, J., Guo, W.-G., and Isaacs, J. Experimental investigation of energy-absorption characteristics of components of sandwich structures. *International Journal of Impact Engineering*, 34:1119–1146, 2007.

[95] Schleyer, G. K., Hsu, S. S., White, M. D., and Birch, R. S. Pulse pressure loading of clamped mild steel plates. *International Journal of Impact Engineering*, 28:223–247, 2003.

[96] Toutelmonde, F., Rossi, P., Oulay, C., Gourraud, C., and Guedon, D. Dynamic behaviour of concrete: tests of slabs with a shock tube. *Materials and Structures*, 28,:293–298, 1995.

[97] Klosowski, P., Woznica, K., and Weichert, D. Comparison of numerical modelling and experiments for the dynamic response of circular elasto-viscoplastic plates. *European Journal of Mechanics A/Solids*, 19(2):343–359, 2000.

[98] Stoffel, M. Phenomenological and micromechanical viscoplastic laws applied to high strain rate deformations of plates. *Thin-Walled Structures*, 47:39–43, 2009.

[99] Schleyer, G. K., Lowak, M. J., Polcyn, M. A., and Langdon, G. S. Experimental investigation of blast wall panels under shock pressure loading. *International Journal of Impact Engineering*, 34:1095–1118, 2007.

[100] Børvik, T., Hanssen, A., Langseth, M., and Olovsson, L. Response of structures to planar blast loads - a finite element engineering approach. *Computers and Structures*, 87:507–520, 2009.

[101] LeBlanc, J., Shukla, A., Rousseau, C., and Bogdanovich, A. Shock loading of three-dimensional woven composite materials. *Composite Structures*, 79:344–355, 2007.

[102] Tekalur, S. A., Bogdanovich, A. E., and Shukla, A. Shock loading response of sandwich panels with 3-D woven E-glass composite skins and stitched foam core. *Composites Science and Technology*, 69:736–753, 2009.

[103] Herzler, J., Fikri, M., Hitzbleck, K., Starke, R., Schulz, C., Roth, P., and Kalghatgi, G. Shock-tube study of the autoignition of n-heptane/toluene/air mixtures at intermediate temperatures and high pressures. *Combustion and Flame*, 149:25–31, 2007.

[104] Duff, R. E. and Blackwell, A. N. Explosive driven shock tubes. *Review of Scientific Instruments*, 37(5):579–586, 1966.

[105] Ågårdh, L. FE-modeling of fibre reinforced concrete slabs subjected to blast loads. *Journal de Physique IV France*, 7(C3):723–728, 1997.

[106] Robey, R. Blast tubes and tunnels: facilities, instrumentation, and techniques. blast tubes. In Ben-Dor, G., Igra, O., and Elperin, T., editors, *Handbook of Shock Waves*, volume 1, pages 623–650. Academic Press, San Diego, 2001.

[107] Jacob, N., Nurick, G. N., and Langdon, G. S. The effect of stand-off distance on the failure of fully clamped circular mils steel plates subjected to blast loads. *Engneering Structures*, 29:2723–2736, 2007.

[108] Baker, W. E. *Explosions in Air*. University of Texas Press, Austin, 1973.

[109] Esparza, E. D. Blast measurement and equivalency for spherical charges at small scaled distances. *International Journal of Impact Engineering*, 4(1):23–40, 1986.

[110] Hopkinson, B. A method of measuring the pressure in the deformation of high explosives by the impact of bullets. *Philosophical Transactions of the Royal Society of London*, A213:437–452., 1914.

[111] Wenzel, A. B. and Esparza, E. D. Measurement of pressures and impulses at dose distances from explosive charges buried and in air. Report SNRI-02-3132 (AD-903534), South West Research Institute, San Antonio, Texas, 1972. for U.S. Army R & D Centre, Fort Belvoir, Virginia 22660.

[112] Delderk, A. Measurement of near-field blast effects in fluidically encased explosives. Report NWC-TP-5857 (AD-BOII 646L), Denver Research Institute, Colorado 93555, 1976.

[113] Edwards, D. H., Thomas, G. O., Miln, A., Hooper, G., and Tasker, D. Blast wave measurements close to explosive charges. *Shock Waves*, 2:237–243, 1992.

[114] Piehler, T., Birk, A., Benjamin, R., Summers, E., and Aubert, S. Near-field impulse loading measurement techniques for evaluating explosive blast. Technical Report ARL-RP-235, Army Research Laboratory, Aberdeen Proving Ground, Maryland, January 2009.

[115] Taylor, L. C., Fourney, W. L., and Leiste, H. U. Pressures on targets from buried explosions. In *Proceedings of the IMPLAST 2010 Conference*, Providence, Rhode Island, USA, October 12-14 2010.

[116] Stoffel, M. Evolution of plastic zones in dynamically loaded plates using different elastic-viscoplastic laws. *International Journal of Solids and Structures*, 41:6813–6830, 2004.

[117] Strand, O. T., Goosman, D. R., Martinez, C., Whitworth, T. L., and Kuhlow, W. W. Compact system for high-speed velocimetry using heterodyne techniques. *REVIEW OF SCIENTIFIC INSTRUMENTS*, 77:083108, 2006.

[118] Langdon, G. S. and Schleyer, G. K. Inelastic deformation and failure of clamped aluminium plates under pulse pressure loading. *International Journal of Impact Engineering*, 28:1107–1127, 2003.

[119] Reissner, E. On finite deflections of circular plates. In *Proceedings of the Symposium of Applied Mathematics*, volume 1, pages 213–219, New York, 1949. American Mathematical Society.

[120] White, F. M. *Viscous Fluid Flow*. McGraw-Hill, 2^{nd} ISE edition, 1991.

[121] Kreyszig, E. *Advanced Engineering Mathematics*. John Wiley & Sons, Inc., 9 edition, 2006.

[122] Symonds, P. S. and Wierzbicki, T. Membrane mode solutions for impulsively loaded circular plates. *Journal of Applied Mechanics*, 46:58–64, 1979.

[123] Perrone, N. and Bhadra, P. Simplified large deflection mode solutions for impulsively loaded viscoplastic circular membranes. *Journal of Applied Mechanics*, 51:505–509, 1984.

[124] Strutt, J. W., Baron Rayleigh. *The Theory of Sound*, volume 1. Dover, New York, 2^{nd} revised edition, 1945 (1^{st} ed. 1877).

[125] Lee, Y.-W. and Wierzbicki, T. Fracture prediction of thin plates under localized impulsive loading. Part I: dishing. *International Journal of Impact Engineering*, 31:1253–1276, 2005.

[126] Cowper, G. R. and Symonds, P. S. Strain-hardening and strain-rate effects in the impact loading of cantilever beams. Contract Nonr-562(10) NR-064-406, Office of Naval Research, 1957.

[127] Manjoine, M. J. Influence of rate of strain and temperature on yield stress of mild steel. *Journal of Applied Mechanics*, 11:211–218, 1944.

[128] Campbell, J. D. and Cooper, R. H. Yield and flow of low-carbon steel at medium strain rates. In *Proceedings of Conference on Physical Basis of Yield and Fracture*, pages 77–87. Institute of Physics and Physical Society, 1966.

[129] Zhao, H. A constitutive model for metals over a large range of strain rates identification for mild-steel and aluminium sheets. *Materials Science and Engineering*, A230:95–99, 1997.

[130] Griffith, J. and Vanzant, H. Large deformation of circular membranes under static and dynamic loading, Paper No. 702. In *1^{st} International Congress on Experimental Mechanics*, New York, 1961.

[131] Karunes, B. and Onat, E. T. Plastic-wave propagation effects in transverse impact of membranes. *Journal of Applied Mechanics*, 27:172–176, 1960.

[132] Kosing, O. E. and Skews, B. W. An investigation of high-speed forming of circular plates in a liquid shock tube. *International Journal of Impact Engineering*, 21(9):801–816, 1998.

[133] Cloete, T. J. and Nurick, G. N. On the influence of radial displacements and bending strains on the large deflections of impulsively loaded circular plates. *International Journal of Mechanical Sciences*, 82:140–148, 2014.

[134] Aggarwal, H. R. and Ablow, C. M. Plastic bending of an annular plate by uniform impulse international. *Journal of Non-Linear Mechanics*, 6:69–80, 1971.

[135] Lellep, J. and Torn, K. Dynamic plastic deformation of annular plates with transverse shear effects international. *Journal of Impact Engineering*, 34:1061–1080, 2007.

[136] Hodge, P. G. The influence of blast characteristics on the final deformation of circular cylindrical shells. *Journal of Applied Mechanics*, 23:617–624, 1956.

[137] Biggs, J. *Introduction to structural dynamics*. McGraw-Hill, New York, 1964.

[138] Abrahamson, G. R. and Lindberg, H. E. Peak load-impulse characterization of critical pulse loads in structural dynamic,. *Nuclear Engineering and Design*, 37:35–46, 1976.

[139] Li, Q. M. and Meng, H. Pressure-impulse diagram for blast loads based on dimensional analysis and single-degree-of-freedom model. *Journal of Engineering Mechanics*, 128(1):87–92, January 2002.

[140] Li, Q. and Meng, H. Pulse loading shape effects on pressure-impulse diagram of an elastic-plastic, single-degree-of-freedom structural model. *International Journal of Mechanical Sciences*, 44:1985–1998, 2002.

[141] Abedini, M., Mutalib, A. A., Raman, S. N., Alipour, R., and Akhlaghi, E. Pressure-impulse (P-I) diagrams for reinforced concrete (RC) structures: A review. *Archives of Computational Methods in Engineering*, 26:733–767, 2019.

[142] Young, W. C. and Budynas, R. G. *Roark's formulas for stress and strain*. McGraw-Hill, 7 edition, 2002.

[143] Zhao, Y. P., Yu, T. X., and Fang, J. Large dynamic plastic deflection of a simply supported beam subjected to rectangular pressure pulse. *Archive of Applied Mechanics*, 64:223–232, 1994.

[144] Zhu, L. and Yu, T. X. Saturated impulse for pulse-loaded elastic-plastic square plates. *International Journal of Solids and Structures*, 34(14):1709–1718, 1997.

[145] Taylor, G. I. Aerodynamics and the mechanics of projectiles and explosions. In Batchelor, G. K., editor, *The Scientific Papers of Sir Geoffrey Ingram Taylor*, volume III, pages 287–303. Cambridge University Press, Cambridge, England, 1963.

[146] Kambouchev, N., Noels, L., and Radovitzky, R. Nonlinear compressibility effects in fluid-structure interaction and their implications on the air-blast loading of structures. *Journal of Applied Physics*, 100:063519, 2006.

[147] Kambouchev, N., Noels, L., and Radovitzky, R. Numerical simulation of the fluid-structure interaction between air blast waves and free-standing plates. *Computers and Structures*, 85:923–931, 2007.

[148] Peng, W., Zhang, Z., Gogos, G., and Gazonas, G. Fluid structure interactions for blast wave mitigation. *Journal of Applied Mechanics*, 78:031016, 2011.

[149] Dobratz, B. M. and Crawford, P. C. LLNL explosives handbook. Technical report, Lawrence Livermore National Laboratory, January 1985.

[150] Cooper, P. W. and Kurowski, S. R. *Introduction to the Technology of Explosives*. Wiley-VCH, New York, 1996.

[151] Nurick, G. N. *Large Deformations of Thin Plates Subjected to Impulsive Loading*. PhD thesis, University of Cape Town, 1987.

[152] Aitchison, J. and Brown, J. A. C. *The Lognormal Distribution*. Cabridge University Press, 1957.

[153] Zukas, J. A. and Walters, W. P., editors. *Explosive Effects and Applications*. Springer, 1998.

[154] Meyer, R. F. The impact of a shock wave on a movable wall. *Journal of Fluid Mechanics*, 3(3):309–323, 1957.

[155] Seigel, A. E. The theory of high speed guns. Technical Report AGARDograph 91, North Atlantic Treaty Organization - Advisory Group for Aerospace Research & Development, May 1965.

[156] Gerald, C. F. and Wheatley, P. O. *Applied Numerical Analysis*. Addison-Wesley Publishing Company, 4 edition, 1989.

[157] Bradley, J. N. *Shock Waves in Chemistry and Physics*. John Wiley & Sons Inc., 1962.

[158] Bonorchis, D. and Nurick, G. N. The influence of boundary conditions on the loading of rectangular plates subjected to localised blast loading - importance in numerical simulations. *International Journal of Impact Engineering*, 36:40–52, 2009.

[159] Cloete, T. J. and Nurick, G. N. A dimensionless number for shock-structure interaction. In Zingoni, editor, *Advances in Engineering Materials, Structures and Systems: Innovations, Mechanics and Applications*. Taylor & Francis, 2019.

[160] Spiegel, M. R. and Liu, J. *Mathematical Handbook of Formulas and Tables*. Schaum's Outlines Series. McGraw-Hill, 2^{nd} edition, 1999.

[161] McLachlan, N. W. *Bessel Functions for Engineers*. Oxford University Press, 1934.

[162] Den Hartog, J. P. *Mechanical Vibrations*. McGraw-Hill, 4^{th} edition, 1956 (1^{st} ed. 1934).

[163] Bonorchis, D. and Nurick, G. N. The effect of welded boundaries on the response of rectangular hot-rolled mild steel plates subjected to localised blast loading. *International Journal of Impact Engineering*, 34:1729–1738, 2007.

[164] Bonorchis, D. and Nurick, G. N. The analysis and simulation of welded stiffener plates subjected to localised blast loading. *International Journal of Impact Engineering*, 37:260–273, 2010.

[165] Teng, X. and Wierzbicki, T. Dynamic shear plugging of beams and plates with an advancing crack. *International Journal of Impact Engineering*, 31:667–698, 2005.

[166] Marais, S. T., Tait, R. B., Cloete, T. J., and Nurick, G. N. Material testing at high strain rate using the split Hopkinson pressure bar. *Latin American Journal of Solids and Structures*, 1:319–339, 2004.

[167] Pochhammer, L. Ueber die fortpflanzungsgeschwindigkeiten kleiner schwinungen in einem unbegrenzten isotropen kreiscylinder (On the propagation velocities of small oscillations in an unlimited isotropic circular cylinder). *Journal für die Reine und Angewandte Mathematik (Journal de Crelle. Berlin)*, 81:324–336, 1876.

[168] Chree, C. The equations of an isotropic elastic solid in polar and cylindrical coordinates, their solutions and applications. *Transactions of the Cambridge Philosophical Society A*, 14:250–369, 1889.

[169] Bancroft, D. The velocity of longitudinal waves in cylindrical bars. *Physical Review*, 59:588–593, 1941.

[170] Davies, R. M. A critical study of the Hopkinson pressure bar. *Philosophical Transactions of the Royal Society of London, Series A*, 240:375–457, 1948.

[171] Follansbee, P. S. and Frantz, C. E. Wave propagation in the split Hopkinson pressure bar. *Journal of Engineering Materials and Technology*, 105:61–66, 1983.

[172] Gorham, D. A. A numerical method for the correction of dispersion in pressure bar signals. *Journal of Physics E: Scientific Instruments*, 16:477–479, 1983.

[173] Lee, C. K. B. and Crawford, R. C. A new method for analysing dispersed bar gauge data. *Measurement Science and Technology*, 4:931–937, 1993.

[174] Lee, C. K. B., Crawford, R. C., Mann, K. A., Colemen, P., and Petersen, C. Evidence of higher Pochhammer-Chree modes in an unsplit Hopkinson bar. *Measurement Science and Technology*, 6:853–859, 1995.

[175] Govender, R. A., Cloete, T. J., and Nurick, G. N. A numerical investigation of dispersion in Hopkinson pressure bar experiments,. *Journal de Physique IV France, Vol.*, 134:521–526, 2006.

[176] Achenbach, J. D. *Wave Propagation in Elastic Solids*. North-Holland series in Applied Mathematic and Mechanics. North-Holland, 1973.

[177] Kinney, G. F. *Explosive Shocks in Air*. Macmillan, 1962.

[178] *ANSYS Inc. ANSYS AUTODYN material library R12.1a; 2009.*

[179] Balden, V. and Nurick, G. Numerical simulation of the post-failure motion of steel plates subjected to blast loading. *International Journal of Impact Engineering*, 32:14–34, 2005.

[180] Lee, E. L., Hornig, H. C., and Kury, J. W. Adiabatic expansion of high explosive detonation products. Technical report UCRL-50422., Lawrence Radiation Laboratory, University of California, 1968.

[181] Nurick, G. N. and Shave, G. C. The deformation and tearing of thin square plates subjected to impulsive loads - an experimental study. *International Journal of Impact Engineering*, 18(1):99–116, 1996.

[182] Palmer, R. N. Experimental investigation of the response of peripherally clamped centrally supported blast loaded plates. Final year project, University of Cape Town, 2003.

[183] Li, Q. M. and Jones, N. Formation of shear localization in structural elements under transverse dynamic loads. *International Journal of Solids and Structures*, 37:6683–66704, 2000.

[184] Olson, M. D., Nurick, G. N., and Fagnan, J. R. Deformation and rupture of blast loaded plates - predictions and experiments. *International Journal of Impact Engineering*, 13:279–291, 1993.

[185] Rudrapatna, N. S., Varizi, R., and Olson, M. D. Deformation and failure of blast loaded square plates. *International Journal of Impact Engineering*, 22:449–467, 1999.

[186] Han, J. B. and Liew, K. M. Axisymmetric free vibration of thick annular plates. *International Journal of Mechanical Sciences*, 41:1089–1109, 1999.

[187] Børvik, T., Hopperstad, O. S., Langseth, M., and Malo, K. A. Effect of target thickness in blunt projectile penetration of Weldox 460 E steel plates. *International Journal of Impact Engineering*, 28:413–464, 2003.

[188] Forrestal, M. J. and Hanchak, S. J. Perforation experiments on HY-100 steel plates with 4340 R_c 38 and maraging T-250 steel rod projectiles. *International Journal of Impact Engineering*, 22:923–933, 1999.

[189] Timoshenko, S. P. and Goodier, J. N. *Theory of Elasticity*. McGraw-Hill, 3^{rd} edition, 1970.

[190] Gilat, A. and Wu, X. Plastic deformation of 1020 steel over a wide range of strain rates and temperatures. *International Journal of Plasticity*, 12(6-7):611–32, 1997.

[191] Tanimura, S., Mimura, K., and Zhu, W. A dynamic constitutive equation and its experimental verification. *Journal de Physique IV*, 10(9):33–38, 2000.

[192] Johnson, G. R. and Cook, W. H. A constitutive model and data for metals subjected to large strains, high strain rates and high temperatures. In *Proceedings of the 7^{th} International Symposium on Ballistics*, pages 541–547, the Hague, Netherlands, 1983.

Appendix A

List of Publications

A.1 Introduction

This appendix contains a list of the published journal papers and conference proceedings that stem from the work reported in this thesis.

A.2 Journal Papers

1. Cloete, T. J., Ahmed, R., and Nurick, G. N., Peripherally clamped centrally supported blast loaded circular plates: a precision test for code validation. *Journal de Physique IV France*, 110:507512, 2003 [51].

   This paper represents the first publication of the instrumented ballistic pendulum and the peripherally clamped centrally supported (PCCS) plate configuration. In addition, this paper presents an application of multi-mode dispersion correction for a Hopkinson pressure bar signal, as discussed in Section 5.2.6.1.

2. Cloete, T. J., Nurick, G. N., and Palmer, R. N., The deformation and shear failure of peripherally clamped centrally supported blast loaded circular plates. *International Journal of Impact Engineering*, 32:92117, 2005 [52].

   This paper represents the first publication of a series of blast tests using the instrumented ballistic pendulum, a short stand-off charge and the PCCS plate configuration, as discussed in Sections 6.2. In addition, this paper represents the first publication of the peripherally clamped annular (PCA) plate configuration and the derivation of the dimensionless impulse number for the PCCS and PCA plate configurations, as discussed in Sections 2.2.1.

3. Cloete, T. J. and Nurick, G. N., On the influence of radial displacements and bending strains on the large deflections of impulsively loaded circular plates. *International Journal of Mechanical Sciences*, 82:140148, 2014 [133].

   This paper represents a study of the effects of a radial displacements and bending on the plastic work in deforming axisymmetric plates, as discussed in Sections 3.3.6, 3.3.7 and 3.3.8.

4. Cloete, T. J. and Nurick, G. N., Blast characterization using a ballistic pendulum with a centrally mounted hopkinson bar. *International Journal of Protective Structures*, 7(3):367388, 2016 [90].

   This paper represents a study of blast load characterization using the instrumented ballistic pendulum, as discussed in Section 5.3.

A.3 Conference Proceedings

1. Cloete, T. J. and Nurick, G. N., Blast tube loading of plates using an instrumented ballistic pendulum. In *Proceedings of IMPLAST 2010*, Providence, Rhode Island, USA, 12-14 October 2010. SEM Society for Experimental Mechanics Inc. ISBN 9781935116066 [53].

   This paper represents the first publication of a series of blast tests using a blast tube in conjunction with the instrumented ballistic pendulum and the PCCS plate configuration, as discussed in Section 6.3.

2. Cloete, T. J. and Nurick, G. N., A dimensionless number for shock-structure interaction. In Zingoni, editor, *Advances in Engineering Materials, Structures and Systems: Innovations, Mechanics and Applications*. Taylor & Francis, 2019 [159].

   This paper represents a study of the effect of a moving plate on the intensity of a reflected shock wave, as discussed in Sections 3.2.4 and 3.2.5.

Appendix B

Material Characterization

B.1 Introduction

This appendix contains the results of the material characterization tests conducted on samples machined from the same sheet stock as the plate specimens used in the blast tests in this thesis. The purpose of this appendix is to satisfy the eighth precision test requirement set out in Section 1.1.2, *i.e.* the material properties must be well defined, especially with regard to strain rate sensitivity. Hence, the aim of this appendix is to outline the testing methodology, present the resulting material properties and provide the corresponding coefficients for typical phenomenological material models. The results are intended for use in future code validation and for the analytical work presented in Chapter 7, which cannot accommodate intricate material models.

B.2 Quasi-Static Tests

The quasi-static material Characterization test were performed on a Zwick universal tensile test machine in the Centre for Materials Engineering (CME) at the University of Cape Town (UCT). The specimen dimensions are given in Figure F.1. For the sheet material used in the short stand-off blast tests, the quasi-static strain rates were $5 \times 10^{-4}\,\mathrm{s}^{-1}$. For the sheet material used in the blast tube tests, the quasi-static feed rates were 2.4 mm/min and 200 mm/min, which translate to strain rates of $0.86 \times 10^{-3}\,\mathrm{s}^{-1}$ and $0.54 \times 10^{-1}\,\mathrm{s}^{-1}$ respectively.

B.3 Dynamic Tests

The dynamic tests were carried out on a compressive split Hopkinson bar (SHB) at the Blast Impact and Survivability Research Unit (BISRU) at UCT. The specimens were machined from the disks obtained from laser cutting the bolt and pin holes in the PCCS and PCA plate specimens, *i.e.* the specimens

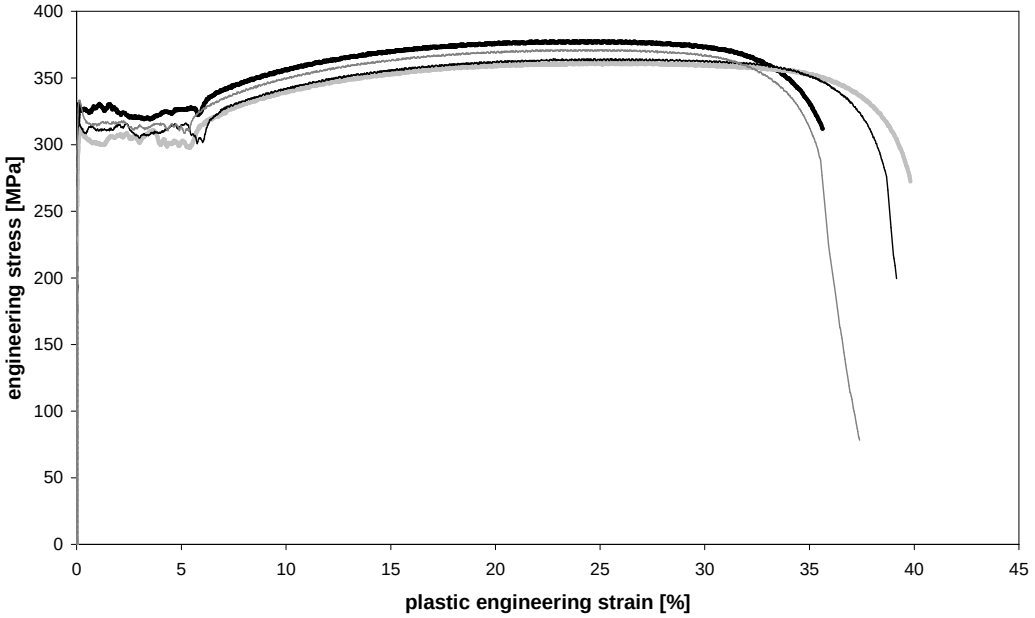

Figure B.1: Quasi-static tensile test results for the mild steel plate used in the short stand-off tests at a strain rate of $5 \times 10^{-4}\,\mathrm{s}^{-1}$.

were loaded in the through-thickness direction. Hence, the height of each specimens were dictated by the source sheet thickness, while all the specimens were machined to a nominal diameter of 3 mm.

The dynamic material tests were conducted on the small SHB in BISRU which is equipped with 12 mm diameter bars made form 17-4PH stainless steel. The input bar is 1200 mm long and strain gauged in the centre, while the output bar is 800 mm long with strain gauges at a distance of 180 mm from the specimen interface. The strain gauges have a grid length of 2 mm and are longitudinally mounted in diametrically pairs in a half bridge configuration, using a 1 MHz bandwidth amplifier and data logging card sampling at 10MHz with 12-bit resolution. A detailed review of the SHB technique is considered to be outside the scope of this thesis and a thorough description of the typical methodology implemented at BISRU is provided in Marais *et al.* [166]. The the dynamic strain rates ranged from $990\,\mathrm{s}^{-1}$ to $5000\,\mathrm{s}^{-1}$.

B.4 Short Stand-Off Blast Test Specimen Material Properties

The plate specimens used for the short stand-off blast tests were cut from from a single mild steel sheet with a nominal thickness of 1.6 mm. Examples of measured quasi-static results are shown in Figure B.1. An average yield stress of approximately 330 MPa was observed, while the flow stress at 10% strain was approximately 350 MPa. The dynamic material properties of were not measured.

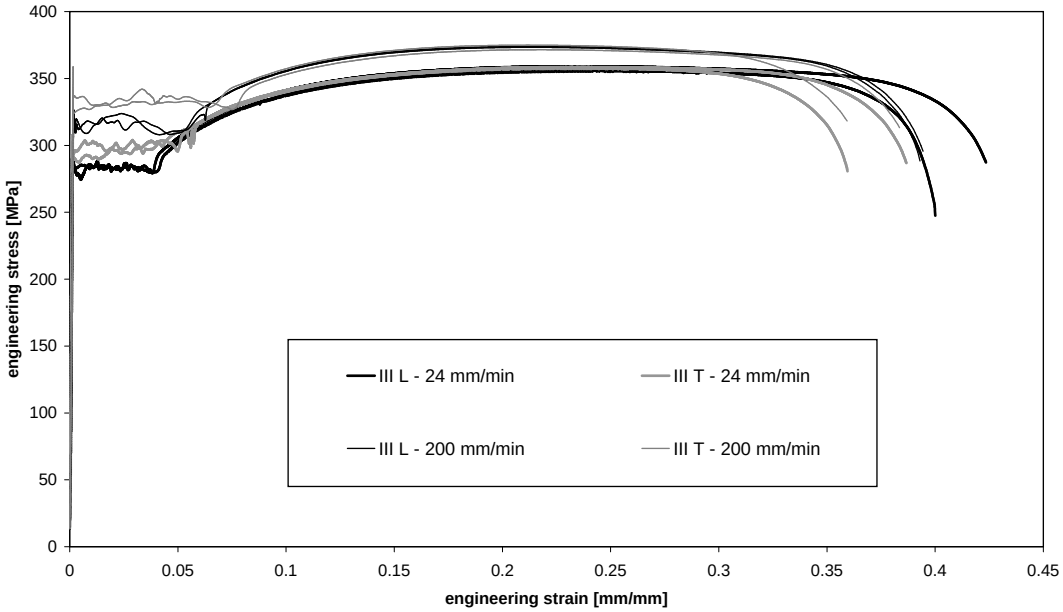

Figure B.2: Experimental data for sheet III at two quasi-static strain rates.

B.5 Blast Tube Test Specimen Material Properties

The plate specimens used for the blast tube tests were cut from five separate sheets. Sheets I, II and III were nominally of 1.6 mm thickness, while sheets IV and V had nominal thicknesses of 2 mm and 3 mm respectively.

Examples of measured quasi-static results for sheet III, which are representative of typical results for all the plates, are shown in Figure B.2. The results show that the material is rate sensitive with the results obtained at 200 mm/min being distinctly higher than that obtained at 2.4 mm/min. Furthermore, the hardening behaviour is more repeatable, in both the rolled (L)[1] and transverse (T) directions, than that of the material used for the short stand-off tests. However, the yield behaviour was inconsistent and dependent on the orientation and position of the specimen on the sheet stock. In fact, a greater degree of variation was noted in specimens cut from some of the other sheets.

Given that the yield stress is an important parameter for calculating the dimensionless deflection, it was decided to average yield stress was not reliable due to the excessive variation. Rather, an effective yield stress value was defined and scaled according to the flow stress at 10% strain, which is outside the Luder's bands and thus far more consistent and representative of the plastic deformation. The effective yield stress is obtained by dividing the flow stress at 10% strain by 350 MPa and multiplying by 330 MPa. The resulting effective yield stress for each sheet is given in Table B.1.

Figure B.3 shows typcal true stress vs. true strain curves at for different stran rate for sheet I. These curves reprentative of the curves for the other sheets which are similar and have several general features in common. Yield strength range from 280 MPa to 320 MPa. Specimens show distinct Luders type

[1] The 'L' stand for 'longitudinal'.

Table B.1: Experimental data for 1.6 mm thick PCA plates *etc*...

Plate	Average Yield [MPa]	10% flow [MPa]	Effective Yield [MPa]
Palmer	330	350	330
I	320	355	330
II	270	334	315
III	290	340	320
IV	250	330	311
V	295	360	339

quasi-static yielding behaviour, while at high strain rates the yielding behaviour is absent. The yield stress shows a significant strain rate sensitivity which is typical of mild steels, while the strain hardening rate decreases with increasing strain rate. In fact, at elevated strain rates the hardening rate is so low that a perfectly plastic model should yield reasonable accurate results, as long as rate sensitivities are included in the material models.

Figure B.4 shows the effect of strain rate on the flow stress at a plastic strain of 0.1 for all the mild steel sheets used in this work. Also shown is a selection of data from the literature to support the experimental results. Manjoine [127] tested annealed mild steel (but did not specify the chemical composition or processing), Gilat & Wu [190] tested hot rolled AISI 1020 steel, Zhao [129] tested a mild steel used in the automotive industry and Tanimura [191] tested a Japanese grade of mild steel. These references show that the result obtained in the present study compare well to previous studies on general purpose mild steels.

B.6 Material Models for High Strain Rate Plasticity

In addition to experimental data, figure B.4 also shows three theoretical curves based on the models of Cowper & Symonds [126] and Johnson & Cook [192]. The Johnson-Cook curve is based on the coefficient values of Tanimura [191], who found the value of the strain rate hardening parameter to be significantly higher than that reported by Johnson & Cook for AISI 1004 Steel. The Cowper-Symonds model with the traditional constants of $D = 40.4$ s^{-1} and $n = 5$ significantly overestimates the effect of rate rates at a 10% plastic strain. These traditional values were first reported by Cowper & Symonds to fit the yield results of Manjoine for annealed mild steel as shown in figure 2.13. The final curve in figure B.4 uses values of $D = 9254$ s^{-1} and $n = 4$ obtained as part of this work. These revised values provide remarkably a close fit considering the phenomonogical nature of the model. The results summarised in figures B.4 and 2.13 show that the Cowper & Symonds model provides a simple and accurate representation of rate sensitivity.

Previous experimental results indicate that for the plates considered in this work the strain rates can be expected to be in the order of 10^3 s^{-1}. Hence, figure B.3 suggest that the rate effect would be expected to be in the order of 2. This value for the rate effect is used frequently in chapter 7 to evaluate various approximate models. However, figure B.4 indicates that in this strain rate range, the rate effect gradient is steep and a small variation in the strain rate could have a large effect.

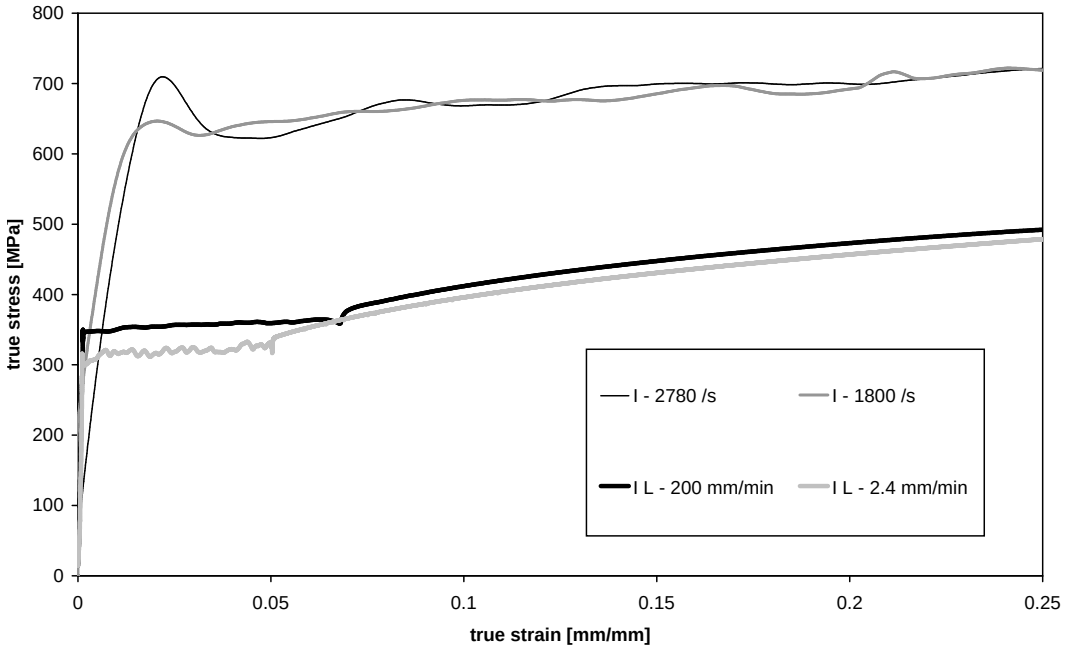

Figure B.3: Experimental data for sheet I at two quasi-static and two dynamic strain rates.

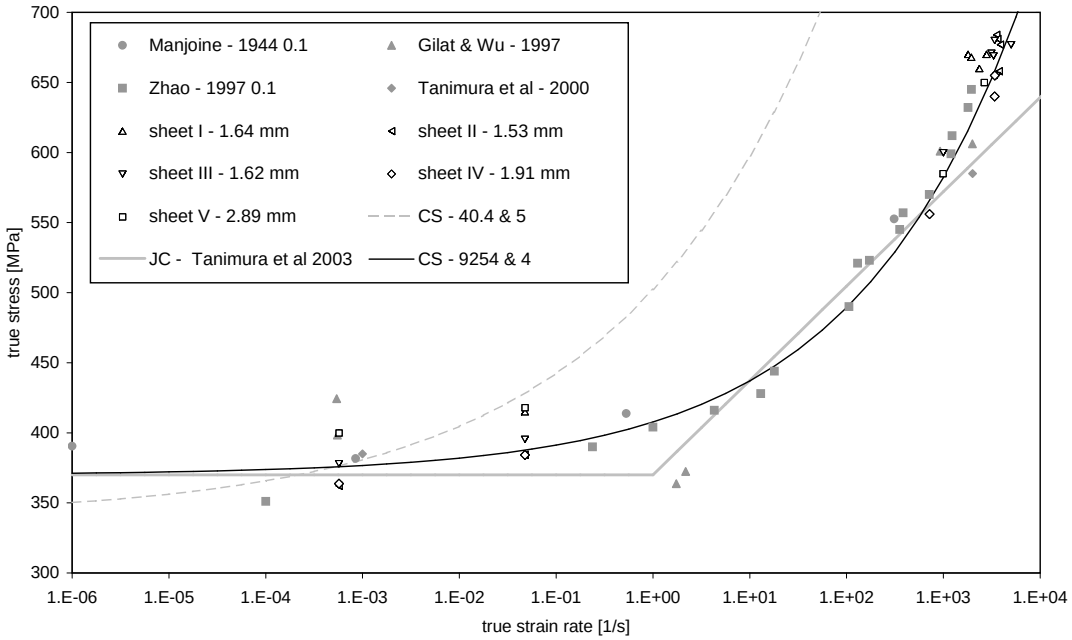

Figure B.4: Experimental data of flow strength at a strain of 0.1 for all sheets as a function of strain rate. The static flow stress σ_0 is 370 MPa.

Appendix C

Ballistic Pendulum Impulse Calculation

C.1 Introduction

This appendix contains a derivation for the detailed calculations required to interpret the motion of a ballistic pendulum.

C.2 Classical Approximate Pendulum Analysis

During its motion, the body of the ballistic pendulum maintains its horizontal orientation and can, therefore, be treated as a simple pendulum. Consider the ballistic pendulum depicted in Figure C.1. The relationship between the displacements x and y can be obtained as follows,

$$(L-y)^2 = L^2 - x^2 \quad \Rightarrow \quad 2Ly - y^2 = x^2 \tag{C.1}$$

Since the wire length L is likely to be much larger than the vertical displacement y, the following approximation can be made,

$$L >> y \quad \Rightarrow \quad 2Ly - y^2 \approx 2Ly = x^2 \quad \Rightarrow \quad y = \frac{x^2}{2L} \tag{C.2}$$

To check the region of validity of Equation (C.2) it can be compared to the exact value of y,

$$y = L - \sqrt{L^2 - x^2} \tag{C.3}$$

Equations (C.2) and (C.3) can be rewritten in dimensionless form,

$$\frac{y}{L} = \frac{1}{2}\left(\frac{x}{L}\right)^2 \quad \text{and} \quad \frac{y}{L} = 1 - \sqrt{1 - \left(\frac{x}{L}\right)^2} \tag{C.4}$$

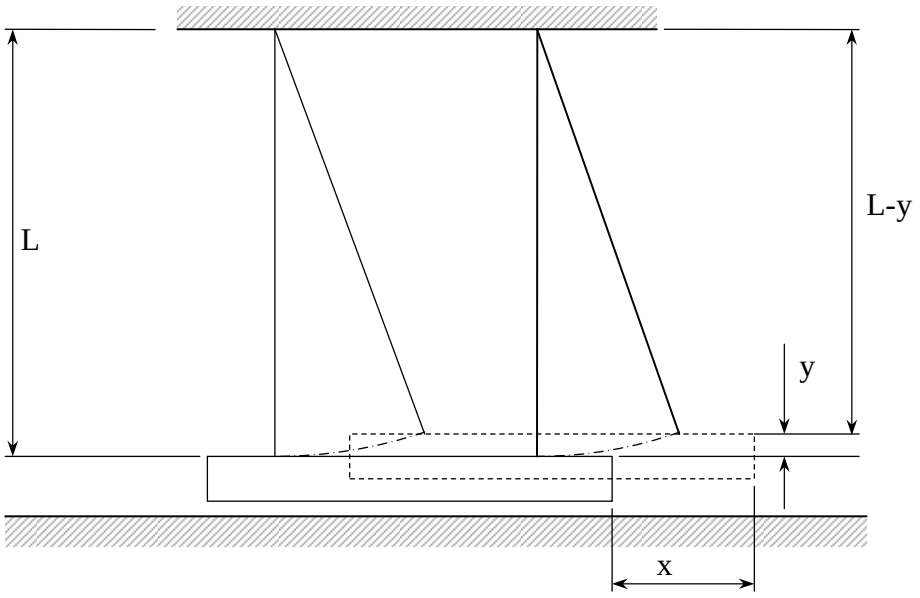

Figure C.1: Schematic diagram of a classical ballistic pendulum.

The values obtained from Equations (C.4) are compared in Table C.1. It can be seen that if the ratio of $x : L$ is $1 : 10$ or less, the error will be approximately 0.2 % or less. However, for angles greater that 10° the error becomes greater than 1 %.

A first order estimate of the natural undamped frequency can be obtained using Lord Rayleigh's method, *i.e.* an energy method. Firstly, it is assumed that the lateral displacement x will be sinusoidal and hence the velocity is,

$$x = x_{max}\, sin(\omega_n t) \quad \Rightarrow \quad v = \dot{x} = x_{max}\, \omega_n\, cos(\omega_n t) \tag{C.5}$$

The maximum kinetic and potential energy is thus,

$$E_{K,max} = \tfrac{1}{2} m v_{max}^2 = \tfrac{1}{2} m x_{max}^2 \omega_n^2 \quad \text{and} \quad E_{P,max} = mgy_{max} = mg\frac{x_{max}^2}{2L} \tag{C.6}$$

Since there is no dissipation the maximum kinetic and potential energy must be the same,

$$\tfrac{1}{2} m x_{max}^2 \omega_n^2 = mg\frac{x_{max}^2}{2L} \quad \Rightarrow \quad \omega_n = \sqrt{\frac{g}{L}} \tag{C.7}$$

Table C.1: Region of validity of Equation (C.2).

$\frac{x}{L}$	$\frac{y}{L} = \frac{1}{2}\left(\frac{x}{L}\right)^2$	$\frac{y}{L} = 1 - \sqrt{1 - \left(\frac{x}{L}\right)^2}$	% difference	angle of deflection
0.01	0.00005	0.000050001	0.002 %	0.5°
0.1	0.005	0.00501	0.2 %	5.74°
0.2	0.02	0.020204	1.01 %	11.53°

Furthermore, if the maximum displacement is measured, the initial velocity and hence maximum impulse can be obtained in several ways,

$$I = mv_{max} = mv_{max}\omega_n = mv_{max}\sqrt{\tfrac{g}{L}} = mv_{max}(2\pi f_n) \quad \Rightarrow \quad I = \frac{2\pi m x_{max}}{T_n} \tag{C.8}$$

The final expression in Equation (C.8) is the most useful since the natural period T_n is easy to measure accurately.

C.3 Effect of Damping

The motion of a ballistic pendulum is damped by air resistance and Coulomb friction arising from the recording pen. Neither of these effects are of the viscous type, i.e. neither are linearly proportional to velocity. In fact, air damping is proportional to the square of the velocity while the magnitude of the Coulomb damping force would be constant. However, the combined effect of the air and Coulomb is such that it can be approximated by viscous damping over the range of interest.

Since damping is significant, the complete differential equation for a linear damped pendulum must be considered [12],

$$\ddot{x} + 2\zeta\omega_n\dot{x} + \omega_n^2 x = 0 \quad \text{where} \quad \omega_n^2 = \sqrt{\frac{k}{m}} = \frac{2\pi}{T_n} \quad \text{and} \quad \zeta = \frac{c}{2m\omega_n} \tag{C.9}$$

Where c is the damping coefficient and ζ is the damping factor. The appropriate solution to Equation (C.9) for the case of a ballistic pendulum is,

$$x = \frac{v_0}{\omega_n} sin(\omega_d t) e^{-\zeta\omega_n t} \quad \text{where} \quad v_0 = \dot{x}_0 \quad \text{and} \quad \omega_d = \sqrt{1-\zeta^2}\,\omega_n = \frac{2\pi}{T_d} \tag{C.10}$$

Where v_0 is the initial velocity of the pendulum. The maximum forward and backward displacement of the pendulum are,

$$x_1 \quad \text{at} \quad t = \frac{T_d}{4} \quad \text{where} \quad -x_2 \quad \text{at} \quad t = \frac{3T_d}{4} \tag{C.11}$$

Hence the damping coefficient can thus be obtained by measuring these displacements,

$$\frac{x_1}{x_2} = e^{\frac{1}{2}\zeta\omega_n T_d} \quad \Rightarrow \quad \zeta\omega_n = \frac{2}{T_d} ln\left(\frac{x_1}{x_2}\right) \tag{C.12}$$

The initial impulse can thus be calculated as,

$$x_1 = \frac{v_0 T_d}{2\pi} sin\left(\frac{2\pi}{T_d}\frac{T_d}{4}\right) e^{-\frac{2}{T_d} ln\left(\frac{x_1}{x_2}\right)\frac{T_d}{4}} = \frac{v_0 T_d}{2\pi} e^{-\frac{1}{2} ln\left(\frac{x_1}{x_2}\right)} \quad \Rightarrow \quad I = \frac{2\pi m x_{max}}{T_n}\sqrt{\frac{x_1}{x_2}} \tag{C.13}$$

Note that the final expression is the same as Equation (C.8) except for the square root term. From Ttable C.2 it can be seen that the error due to damping becomes significant once the amplitude decay from x_1 to x_2 is greater than 2%. In other words, the effect of damping needs to be accounted for.

Table C.2: Effect of damping on impulse calculations.

$\frac{x_2}{x_1}$	0.999	0.99	0.98	0.95	0.9	0.75
$\left[\sqrt{\frac{x_1}{x_1}} - 1\right] \times 100\%$	0.05 %	0.5 %	1.02 %	2.60 %	5.41 %	15.47 %

C.4 Effect of Tracing Pen Non-Linearity

The motion of the pendulum is recorded on a flat surface using trancing paper and a narrow point felt tipped ink pen connected to the pendulum via a hinged bar. Since the pendulum moves in an arc, this implies that the angle of the hinged bar will change with respect to the flat surface. The change in geometry must be accounted for during the analysis of the pendulum motion. The relevant geometry for a forward and backward swing is shown in Figure C.2.

For both diagrams, the rest position of the pen is δ_0,

$$\delta_0 = \sqrt{l^2 - h^2} \tag{C.14}$$

where L is the length of the pendulum chord and l is the distance form the hinged bar attachment point to the point where the pen touched the horizontal surface. The distance L_1 from the hinge point of the pendulum to the point of the pen is thus,

$$L_1 = \sqrt{(L+h)^2 + (\delta_0 + \delta_1)^2} \tag{C.15}$$

while the angle α_1 between L_1 and the vertical is,

$$\alpha_1 = atan\left[\frac{\delta_0 + \delta_1}{L+h}\right] \tag{C.16}$$

The angle β_1 between the forward most swing of the pendulum chord and L_1 is obtained using the cosine rule,

$$\beta_1 = acos\left[\frac{L^2 + L_1^2 - l^2}{2LL_1}\right] \tag{C.17}$$

Consequently the forward most angle of the pendulum chord θ_1 is,

$$\theta_1 = \alpha_1 - \beta_1 \tag{C.18}$$

Finally, the maximum horizontal distance x_1 covered by the pendulum during the forward swing is,

$$x_1 = Lsin(\theta_1) \tag{C.19}$$

A similar process can be followed for the back swing. The distance L_2 from the hinge point of the pendulum to the point of the pen is,

$$L_2 = \sqrt{(L+h)^2 + (\delta_0 - \delta_2)^2} \tag{C.20}$$

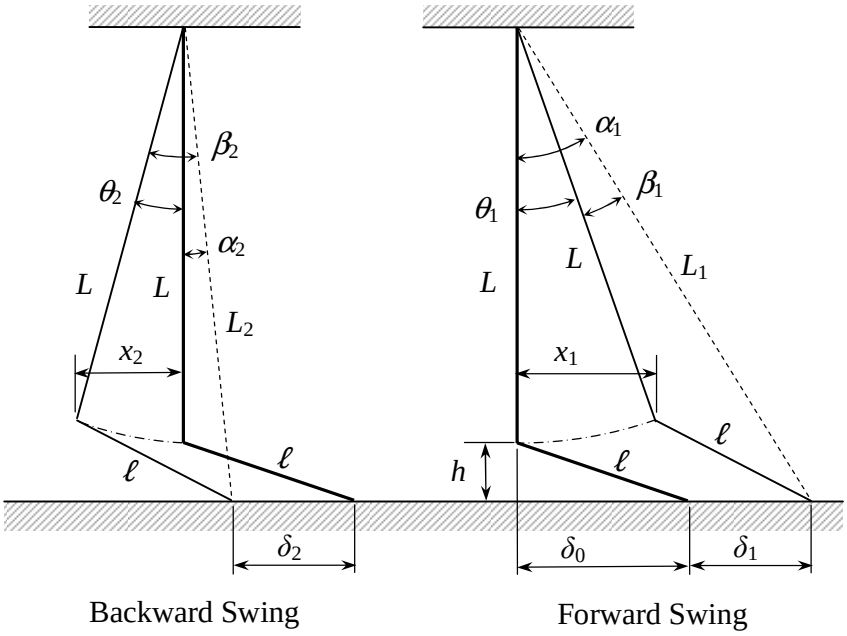

Figure C.2: Geometric diagram of the relationship between the ballistic pendulum swing and the recording pen position.

while the angle α_2 between L_2 and the vertical is,

$$\alpha_2 = atan\left[\frac{\delta_0 - \delta_2}{L + h}\right] \tag{C.21}$$

The angle β_2 between the backward most swing of the pendulum chord and L_2 is again obtained using the cosine rule,

$$\beta_2 = acos\left[\frac{L^2 + L_2^2 - l^2}{2LL_2}\right] \tag{C.22}$$

Consequently the backward most angle of the pendulum chord θ_2 is,

$$\theta_2 = \beta_1 - \alpha_2 \tag{C.23}$$

Finally, the maximum horizontal distance x_1 covered by the pendulum during the backward swing is,

$$x_2 = Lsin(\theta_2) \tag{C.24}$$

The calculation procedure is thus follows: Following a blast test, the maximum forward and backward swings of the pendulum are obtained from measuring δ_1 and δ_2 as recorded on the tracing paper by the pen. There values are then converted to maximum forward and backward swings of the pendulum x_1

and x_2 using Equations (C.14) to (C.24) given above. Finally the impulse I received by the pendulum is obtained by substituting x_1 and x_2 into Equation (C.13).

Appendix D

Detailed Calculations for PCCS Plates

D.1 Introduction

This appendix contains a record of the detailed calulation required to evaluate the integral of the Bessel function shape of a PCCS plate.

D.2 Plastic Work

The expression for plastic work results in the following expresssion for λ,

$$\lambda = 2A^2 \frac{R_o - R_i}{R_o + R_i} \int_{\frac{R_i}{R_o}\Lambda}^{\Lambda} x \left[-J_1(x) - BY_1(x)\right]^2 dx \tag{D.1}$$

The expansion of the integral takes the form,

$$\int_{\frac{R_i}{R_o}\Lambda}^{\Lambda} x \left[-J_1(x) - BY_1(x)\right]^2 dx = \int_{\frac{R_i}{R_o}\Lambda}^{\Lambda} xJ_1^2(x)dx + 2B \int_{\frac{R_i}{R_o}\Lambda}^{\Lambda} xJ_1(x)Y_1(x)dx + B^2 \int_{\frac{R_i}{R_o}\Lambda}^{\Lambda} xY_1^2(x)dx \tag{D.2}$$

These are Lommel integrals for which the solutions are well known [161] and give the result,

$$\begin{aligned}\int_{\frac{R_i}{R_o}\Lambda}^{\Lambda} x \left[-J_1(x) - BY_1(x)\right]^2 dx = &\left[\frac{x^2}{2}\left\{J_1^2(x) - J_0(x)J_2(x)\right\}\right]_{\frac{R_i}{R_o}\Lambda}^{\Lambda} \\ &+ 2B\left[\frac{x^2}{4}\left\{2J_1(x)Y_1(x) - J_0(x)Y_2(x) - J_2(x)Y_0(x)\right\}\right]_{\frac{R_i}{R_o}\Lambda}^{\Lambda} \\ &+ B^2\left[\frac{x^2}{2}\left\{Y_1^2(x) - Y_0(x)Y_2(x)\right\}\right]_{\frac{R_i}{R_o}\Lambda}^{\Lambda}\end{aligned} \tag{D.3}$$

The evaluation of this formula for several plate configurations is given below.

R_i/R_0 =	0.05	0.1	0.125	0.15385	0.2	0.3	0.4	0.5	0.6	0.7	0.8	0.9
upper case Lambda =	3.06441	3.31394	3.43515	3.57735	3.81596	4.41239	5.18307	6.24606	7.82844	10.4552	15.6981	31.4115
solve	-2E-07	3.3E-08	4.2E-07	-3E-07	-6E-07	-3E-07	-7E-07	9.9E-07	-2E-07	-5E-07	-3E-07	8E-07
B =	0.79097	1.31729	1.71889	2.47912	6.95509	-2.0299	-0.3519	0.89224	-1.0864	-4.2109	0.96498	0.98336
R_n/R_0 =	0.3889	0.44821	0.47253	0.49818	0.53563	0.60759	0.67225	0.73248	0.78966	0.84458	0.89774	0.94947
solve	1.4E-07	3E-07	-6E-07	6E-09	8.8E-08	9.1E-07	1.5E-07	-9E-07	1.4E-07	2E-08	-7E-09	1E-09
A =	1.1743	0.98451	0.84862	0.65624	0.26474	-0.9281	-2.2386	-2.0175	2.12051	-0.8626	3.38887	-4.8813
J_0(R_i)	0.99414	0.97273	0.95443	0.9257	0.8596	0.60764	0.18186	-0.2989	-0.2701	0.28663	0.15628	-0.1052
J_0(R_o)	-0.2811	-0.3473	-0.3703	-0.3895	-0.4027	-0.3397	-0.1161	0.21222	0.20961	-0.2399	-0.1398	0.09981
J_1(R_i)	0.07639	0.16343	0.20979	0.26489	0.35448	0.5271	0.57094	0.29192	-0.2785	0.08772	-0.1559	0.10515
J_1(R_o)	0.31468	0.21493	0.16454	0.10495	0.00636	-0.2064	-0.3424	-0.2217	0.20666	-0.0685	0.1405	-0.0999
J_2(R_i)	0.00293	0.0136	0.0227	0.03692	0.06934	0.18875	0.36891	0.48584	0.15158	-0.2627	-0.1811	0.11265
J_2(R_o)	0.48648	0.47704	0.46614	0.44817	0.40604	0.24615	-0.016	-0.2832	-0.1568	0.22684	0.1577	-0.1062
Y_0(R_i)	-1.2569	-0.7384	-0.5553	-0.3734	-0.1236	0.29935	0.51671	0.33499	-0.2487	0.06807	-0.162	0.10699
Y_0(R_o)	0.3554	0.26367	0.21545	0.15711	0.0579	-0.1674	-0.3299	-0.2378	0.19294	-0.057	0.14488	-0.1015
Y_1(R_i)	-4.276	-2.099	-1.6754	-1.3564	-1.0214	-0.5318	-0.0663	0.35483	0.24539	-0.2826	-0.1628	0.10712
Y_1(R_o)	0.34119	0.38993	0.40469	0.41456	0.41336	0.32301	0.08505	-0.2318	-0.1977	0.2375	0.14448	-0.1014
Y_2(R_i)	-54.558	-11.929	-7.2484	-4.5558	-2.553	-1.1028	-0.5807	-0.1078	0.35315	-0.1453	0.13602	-0.0994
Y_2(R_o)	-0.1327	-0.0283	0.02017	0.07466	0.15875	0.31377	0.36268	0.16363	-0.2435	0.10241	-0.1265	0.09504
1st R_i term	3.4E-05	0.00074	0.00206	0.00545	0.01924	0.14293	0.55637	1.12373	1.3071	2.2223	4.14775	9.15379
1st R_o term	1.10704	1.16348	1.17828	1.18745	1.19082	1.22885	1.54997	2.13114	2.31581	3.23138	5.14884	10.1541
2nd R_i term	0.31452	0.30002	0.28707	0.26598	0.21537	0.02322	-0.1727	0.02977	-0.0197	0.13312	0.00694	0.00295
2nd R_o term	0.01062	0.08781	0.11865	0.14615	0.16627	0.07026	-0.144	0.00677	-0.0069	0.13567	0.00443	0.00239
3rd R_i term	-0.5903	-0.2418	-0.1123	0.02102	0.21192	0.53701	0.65427	0.79003	1.63297	2.40447	3.82825	8.83524
3rd R_o term	0.76804	0.87592	0.94067	1.02462	1.1771	1.52684	1.70411	1.8073	2.63759	3.40186	4.82969	9.83554
integral	1.47607	2.54314	3.70818	6.75604	47.1777	4.97352	1.10341	1.77621	2.16657	18.673	1.92877	1.96645
lower case lambda	3.68327	4.03359	4.15404	4.26722	4.4088	4.61401	4.73959	4.81965	4.87106	4.90336	4.92241	4.93203
1/sqrt(lambda)	0.52105	0.49791	0.49064	0.48409	0.47626	0.46554	0.45934	0.4555	0.45309	0.4516	0.45072	0.45028

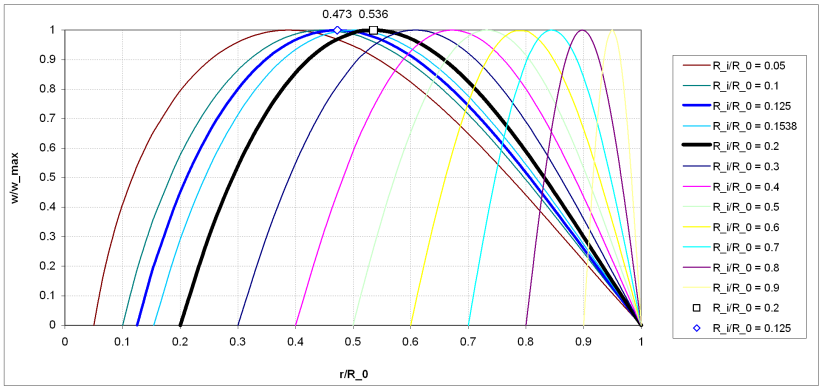

Figure D.1: PCCS-BesselShapes

Appendix E

Blast Testing Data

E.1 Introduction

This appendix contains the summarised data for the blast tests on PCA, PCCS and rigid plates conducted as part of the thesis, some of which has previous been pulished [52, 53, 182]. In the tables to follow, the entry 'no rec.' indicates that a usable data was not recorded.

E.2 Short Stand-Off Blast Loading Data

E.2.1 100 mm Plates

Table E.1: Experimental data for 100 mm diameter 1.6 mm thick PCA plates loaded with 30 mm stand-off PE4 ring charges of varying mass [52, 182]

test number	response mode	explosive mass [g]	total impulse [Ns]	bar impulse [Ns]	bar/total impulse [%]	max-max deflection [mm]	min-max deflection [mm]	ave-max deflection [mm]	final hole diameter [mm]
TC040304c	I	5	2.72	0.33	12.02	1.4	1.14	1.27	24
TC040304b	I	6	6.92	0.60	8.71	8.84	7.9	8.37	25.5
TC040304a	I	7	10.88	0.78	7.16	14.2	13.26	13.73	28.5
RP030905c	I	8	12.92	0.94	7.26	15.94	13.44	14.69	30.5
RP031009b	I	8	13.63	0.98	7.19	16.34	15.8	16.07	32
TC040313b	I	10	17.09	no rec.	no rec.	20.82	20.42	20.62	33.5

Table E.2: Experimental data for 100 mm diameter 1.6 mm thick PCCS plates loaded with 30 mm stand-off PE4 ring charges of varying mass [52, 182]

test number	response mode	explosive mass [g]	total impulse [Ns]	bar impulse [Ns]	bar/total impulse [%]	max-max deflection [mm]	min-max deflection [mm]	ave-max deflection [mm]	final hole diameter [mm]
RP030905a	I	7	5.99	2.27	37.89	1.82	1.58	1.7	-
RP031008b	I	5	6.16	2.38	38.67	2.6	1.12	1.86	-
TC040306b	I	5.5	6.51	2.51	38.53	3.5	1.28	2.39	-
TC040306a	I	6	6.59	2.62	39.76	2.13	1.52	1.825	-
RP031007b	II*	6	10.28	3.09	30.07	4.6	3.7	4.15	-
RP030904a	II*	6	10.44	2.83	27.10	4.58	3.9	4.24	-
RP030904b	II*	6.5	11.16	2.91	26.08	4.18	2.9	3.54	-
RP030919b	II	7	10.99	2.46	22.38	8.08	6.8	7.44	22.4
RP031009c	II	7	12.42	2.32	18.68	8.12	7.86	7.99	22.36
RP030905b	II	8	13.41	2.43	18.12	10.98	8.64	9.81	23
RP031009a	II	8	14.07	2.51	17.84	13.24	9.42	11.33	23.5
RP030923e	III	9	14.29	2.25	15.75	14.68	14.52	14.6	25.5
TC040318a	III	9.5	16.93	no rec.	no rec.	18.82	18.8	18.81	29
TC040313a	III	10	18.08	2.55	14.11	20.2	19.8	20	29.5

E.2.2 130 mm Plates

Table E.3: Experimental data for 130 mm diameter 1.6 mm thick PCA plates loaded with 30 mm stand-off PE4 ring charges of varying mass [182]

test number	response mode	explosive mass [g]	total impulse [Ns]	bar impulse [Ns]	bar/total impulse [%]	max-max deflection [mm]	min-max deflection [mm]	ave-max deflection [mm]	final hole diameter [mm]
RP031007c	I	4	4.84	0.38	6.13	2.82	2.6	2.71	no rec.
RP030923a	I	4	7.03	0.59	7.02	9.68	6.26	7.97	no rec.
RP031008a	I	6.5	8.41	0.45	4.70	7.66	6.9	7.28	no rec.
RP030919d	I	8.5	14.51	0.73	4.64	16.22	15.92	16.07	no rec.

Table E.4: Experimental data for 130 mm diameter 1.6 mm thick PCCS plates loaded with 30 mm stand-off PE4 ring charges of varying mass [182]

test number	response mode	explosive mass [g]	total impulse [Ns]	bar impulse [Ns]	bar/total impulse [%]	max-max deflection [mm]	min-max deflection [mm]	ave-max deflection [mm]	final hole diameter [mm]
RP030923b	I	6.5	5.61	2.74	36.44	1.6	1.38	1.49	-
RP030919c	II*	7.5	12.64	3.08	21.69	8.02	6.1	7.06	-
RP030912b	II-III	8.5	14.18	2.59	18.74	12	11.6	11.8	no rec.

[1]

[1] Note - Double check if Palmer has the final hole diameter data and/or you still have the plates.

E.2.3 160 mm Plates

Table E.5: Experimental data for 160 mm diameter 1.6 mm thick PCCS plates loaded with 30 mm stand-off PE4 ring charges of varying mass [182]

test number	response mode	explosive mass [g]	total impulse [Ns]	bar impulse [Ns]	bar/total impulse [%]	max-max deflection [mm]	min-max deflection [mm]	ave-max deflection [mm]	final hole diameter [mm]
RP030923d	I	7	6.38	2.49	29.86	1.28	1	1.14	-
RP031002a	II*	8	12.09	3.27	22.84	5.68	2.62	4.15	-
RP031007a	II*	9	14.23	3.33	20.33	7	4.02	5.51	-
RP031008c	II-III	11	19.29	2.46	11.08	15	14.72	14.86	no rec.

E.3 Blast Tube Loading Data

E.3.1 Rigid Plates

Table E.6: Experimental data for 100 mm rigid plates loaded with 10 g PE4 disk charges in blast tubes of varying length.

test number	central bar radius [mm]	shock tube length [mm]	plate thickness [mm]	total impulse [Ns]	bar impulse [Ns]	bar/total impulse [%]
TC061016j	R0	250	10	19.78	1.24	6.28
TC061016h	R0	300	10	20.52	1.11	5.40
TC061016i	R0	350	10	20.77	0.82	3.93
TC061012c	R2	250	10	19.78	no rec.	-
TC061012a	R2	300	10	20.57	no rec.	-
TC061012d	R2	300	10	20.20	no rec.	-
TC061012b	R2	350	10	21.02	no rec.	-

E.3.2 1.6 mm Thick Plates - Sheet I

Table E.7: Experimental data for 100 mm diameter PCA plates cut from Sheet I and loaded with PE4 disk charges of varying mass in a blast tube of 300 mm length with a R2 central bar.

test number	response mode	plate thickness [mm]	charge mass [g]	total impulse [Ns]	bar impulse [Ns]	bar/total impulse [%]	max-max deflection [mm]	min-max deflection [mm]	ave-max deflection [mm]	final hole diameter [mm]
TC061010c	I	1.64	10	20.69	0.79	3.81	16.89	16.54	16.72	28
TC061010g	I	1.65	10	20.86	0.84	4.01	16.84	16.4	16.62	28

Table E.8: Experimental data for 100 mm diameter PCA plates cut from Sheet I and loaded with 10 g PE4 disk charges in blast tubes of varying length with a R0 central bar.

test number	response mode	tube length [mm]	plate thickness [mm]	total impulse [Ns]	bar impulse [Ns]	bar/total impulse [%]	max-max deflection [mm]	min-max deflection [mm]	ave-max deflection [mm]	final hole diameter [mm]
TC060830f	I	050	1.65	18.21	no rec.	-	18.75	18.57	18.66	29.95
TC060628d	I	100	1.65	19.67	1.16	5.90	20.9	20.5	20.7	32.25
TC060830e	I	150	1.65	19.47	0.69	3.54	19.86	19.55	19.71	31.1
TC060829d	I	150	1.65	19.52	no rec.	-	19.1	18.7	18.9	30.8
TC060628a	I	200	1.65	20.21	1.29	6.38	19.3	18.5	18.9	30.45
TC060830d	I	250	1.65	20.49	0.95	4.64	17.8	17.6	17.7	29.4
TC060829c	I	250	1.65	20.72	no rec.	-	17.8	17	17.4	28.85
TC060829e	I	250	1.65	23.06	no rec.	-	21.4	20.4	20.9	33.4
TC060830c	I	350	1.65	21.35	0.62	2.90	16.8	16.1	16.45	27.9
TC060830a	I	400	1.65	21.61	0.66	3.05	16.4	15.5	15.95	27.3
TC060829a	I	400	1.65	21.97	no rec.	-	16.8	16.4	16.6	27.65
TC060830b	I	490	1.65	21.72	0.55	2.53	16	15.2	15.6	27
TC060829b	I	490	1.65	23.81	no rec.	-	15.4	14.9	15.15	26.6

Table E.9: Experimental data for 100 mm diameter PCA plates cut from Sheet I and loaded with PE4 disk charges of varying mass in a blast tube of 300 mm length with a R0 central bar.

test number	response mode	plate thickness [mm]	charge mass [g]	total impulse [Ns]	bar impulse [Ns]	bar/total impulse [%]	max-max deflection [mm]	min-max deflection [mm]	ave-max deflection [mm]	final hole diameter [mm]
TC061028b	I	1.65	3	5.74	0.16	2.73	2.92	2.59	2.76	20.9
TC061020f	I	1.64	4	10.05	0.33	3.33	7.76	7.37	7.57	22
TC061020e	I	1.65	5	12.31	0.45	3.68	9.76	9.32	9.54	23
TC061017h	I	1.65	6	14.05	0.59	4.18	11.42	11.15	11.29	23.6
TC061020d	I	1.65	7	15.96	0.74	4.63	13.26	12.77	13.02	25
TC061017i	I	1.64	8	17.59	0.70	3.95	14.46	14.03	14.25	25.5
TC061017l	I	1.63	9	18.73	0.72	3.84	15.35	15.05	15.2	27
TC061016g	I	1.64	10	19.84	0.94	4.74	16.15	15.86	16.01	27.5
TC061017j	I	1.64	10	20.92	0.93	4.45	16.65	16.43	16.54	27.65
TC060901c	I	1.65	10	21.46	0.82	3.82	17.26	16.9	17.08	28.1
TC060628c	I	1.65	10	21.93	0.89	4.06	18	17.3	17.65	29.95
TC060628b	I	1.65	10	22.24	no rec.	-	18.8	18.6	18.7	29.7
TC061020b	I	1.65	11	22.56	1.01	4.49	18	17.45	17.73	29
TC061020c	I	1.64	12	23.97	1.03	4.30	19.59	18.95	19.27	31
TC061017k	I	1.65	13	25.39	1.17	4.60	20.63	19.64	20.14	32

Table E.10: Experimental data for 100 mm diameter PCCS plates cut from Sheet I and loaded with PE4 disk charges of varying mass in a blast tube of 300 mm length with a R2 central bar.

test number	response mode	plate thickness [mm]	charge mass [g]	total impulse [Ns]	bar impulse [Ns]	bar/total impulse [%]	max-max deflection [mm]	min-max deflection [mm]	ave-max deflection [mm]	final hole diameter [mm]
TC061010e	I	1.65	7	16.14	3.26	20.22	4.46	3.73	4.10	-
TC061012f	I	1.64	8	17.53	no rec.	-	4.94	4.55	4.75	-
TC061010d	II	1.65	10	21.53	3.52	16.35	8.78	7.11	7.95	0
TC061010f	II	1.65	13	25.40	no rec.	-	12.48	11.41	11.95	20.5

Table E.11: Experimental data for 100 mm diameter PCCS plates cut from Sheet I and loaded with PE4 disk charges of varying mass in a blast tube of 300 mm length with a R0 central bar.

test number	response mode	plate thickness [mm]	charge mass [g]	total impulse [Ns]	bar impulse [Ns]	bar/total impulse [%]	max-max deflection [mm]	min-max deflection [mm]	ave-max deflection [mm]	final hole diameter [mm]
TC061020g	I	1.62	5	12.20	2.66	21.81	3.21	2.62	2.92	-
TC061016f	I	1.65	6	13.93	no rec.	-	3.37	3.07	3.22	-
TC061017g	II*	1.63	6.2	14.64	2.93	20.02	4.21	3.73	3.97	-
TC061017f	II*	1.64	6.5	15.18	2.91	19.15	4.93	3.73	4.33	-
TC061016e	II*	1.65	7	16.38	2.85	17.37	6.92	4.35	5.64	-
TC061016d	II	1.64	8	17.54	2.65	15.10	7.85	7.5	7.68	20.5
TC061017e	III	1.63	9	19.52	2.34	12.00	12.38	12.18	12.28	23
TC061016c	III	1.64	10	20.57	no rec.	-	14.16	13.82	13.99	24.5
TC061017c	III	1.65	10	20.68	2.46	11.87	13.56	13.36	13.46	24
TC061017d	III	1.64	13	25.76	2.42	9.40	19.57	19.21	19.39	30

E.3.3 1.6 mm Thick Plates - Sheet II

Table E.12: Experimental data for 100 mm diameter PCA plates cut from Sheet II and loaded with PE4 disk charges of varying mass in a blast tube of 300 mm length with a R0 central bar.

test number	response mode	plate thickness [mm]	charge mass [g]	total impulse [Ns]	bar impulse [Ns]	bar/total impulse [%]	max-max deflection [mm]	min-max deflection [mm]	ave-max deflection [mm]	final hole diameter [mm]
TC061102b	I	1.52	5.8	13.18	0.57	4.35	12.67	12.22	12.45	24.7
TC061102c	I	1.53	8	17.50	no rec.	-	15.01	14.38	14.70	26.6
TC061221a	I	1.54	11	22.08	no rec.	-	21.43	19.7	20.57	31.75
TC061221b	I	1.51	12	22.91	no rec.	-	22.72	21.96	22.34	34
TC061221c	I	1.53	14	26.38	no rec.	-	26.12	24.66	25.39	38.2

Table E.13: Experimental data for 100 mm diameter PCCS plates cut from Sheet II and loaded with PE4 disk charges of varying mass in a blast tube of 300 mm length with a R2 central bar.

test number	response mode	plate thickness [mm]	charge mass [g]	total impulse [Ns]	bar impulse [Ns]	bar/total impulse [%]	max-max deflection [mm]	min-max deflection [mm]	ave-max deflection [mm]	final hole diameter [mm]
TC061222g	I	1.53	5	11.86	2.52	21.29	3.53	3.39	3.46	-
TC061222i	II	1.54	9	19.24	2.51	13.02	12.37	11.44	11.91	20.35

Table E.14: Experimental data for 100 mm diameter PCCS plates cut from Sheet II and loaded with PE4 disk charges of varying mass in a blast tube of 300 mm length with a R0 central bar.

test number	response mode	plate thickness [mm]	charge mass [g]	total impulse [Ns]	bar impulse [Ns]	bar/total impulse [%]	max-max deflection [mm]	min-max deflection [mm]	ave-max deflection [mm]	final hole diameter [mm]
TC061028c	I	1.54	4	9.79	2.34	23.96	2.32	2.06	2.19	-
TC061219d	I	1.53	4.4	10.94	2.46	22.44	2.82	2.5	2.66	-
TC061219e	I	1.5	4.7	11.48	2.58	22.46	3.48	3.22	3.35	-
TC061028d	I	1.52	5	11.87	2.57	21.67	3.34	2.74	3.04	-
TC061028g	I-II*	1.55	5.5	13.41	2.83	21.08	3.51	3.18	3.35	-
TC061102k	II*	1.54	5.6	13.48	2.70	20.03	4.5	4.14	4.32	-
TC061102j	II	1.53	5.7	13.48	2.47	18.31	5	4.31	4.66	20.28
TC061102h	II	1.53	5.8	13.42	2.36	17.59	5.25	4.34	4.80	20.1
TC061102f	II	1.54	5.9	13.60	2.43	17.90	4.93	4.25	4.59	20
TC061219h	II	1.51	5.9	14.52	2.43	16.74	6.38	6.32	6.35	21.1
TC061103c	II	1.53	6	14.23	2.31	16.26	6.74	5.73	6.24	20.15
TC061028e	II	1.51	6.1	14.29	2.35	16.46	6.95	5.86	6.41	20.2
TC061103d	II	1.52	6.5	15.25	2.44	16.00	8.29	6.72	7.51	20.25
TC061219g	II	1.54	6.7	15.43	2.31	14.94	8.93	7.98	8.46	20.3
TC061219i	II	1.53	6.85	16.29	2.42	14.84	9.27	8.98	9.13	20.5
TC061102g	II-III	1.53	7	15.88	2.24	14.12	10.85	10.21	10.53	20.7
TC061028f	II-III	1.54	7.5	16.69	2.38	14.29	10.6	5.86	8.23	20.7
TC061026d	II-III	1.54	7.5	16.75	2.51	15.00	10.88	10.32	10.6	21.5
TC061103e	III	1.53	7.7	17.29	2.30	13.32	12.29	11.92	12.11	21.7
TC061102e	III	1.52	8	17.66	2.13	12.05	13.04	12.6	12.82	22.25
TC061026c	III	1.53	8.5	18.59	2.30	12.37	13.95	13.23	13.59	24
TC061028h	III	1.54	8.8	18.98	2.25	11.86	14.02	13.25	13.64	22.73
TC061103f	III-IIIb	1.54	8.9	19.37	2.59	13.39	14.12	13.95	14.04	23.25
TC061219j	III	1.54	8.95	19.34	2.17	11.24	15.14	14.83	14.99	23.95
TC061102i	III	1.53	9	19.80	2.24	11.32	15.69	15.42	15.56	24.5
TC061219k	III	1.54	9.2	19.83	2.35	11.84	15.36	15.04	15.2	24.35
TC061026b	III	1.49	9.5	19.57	2.01	10.29	16.6	16.15	16.38	25.25
TC061103g	IIIb	1.53	10	20.75	2.15	10.37	17.24	16.97	17.11	26.05
TC061103h	IIIb	1.54	11	22.22	2.66	11.97	17.56	17.16	17.36	26.6
TC061219l	IIIb	1.53	12	24.44	no rec.	-	21.6	20.55	21.08	30.6
TC061219m	IIIb	1.51	14	27.16	2.11	7.78	25.08	24.05	24.57	35.95

E.3.4 1.6 mm Thick Plates - Sheet III

Table E.15: Experimental data for 100 mm diameter PCA plates cut from Sheet III and loaded with PE4 disk charges of varying mass in a blast tube of 300 mm length with a R0 central bar.

test number	response mode	plate thickness [mm]	charge mass [g]	total impulse [Ns]	bar impulse [Ns]	bar/total impulse [%]	max-max deflection [mm]	min-max deflection [mm]	ave-max deflection [mm]	final hole diameter [mm]
TC070209a	I	1.6	7	15.08	no rec.	-	14.54	14.32	14.43	25.75
TC070228a	I	1.61	7	15.77	0.57	3.59	13.99	13.81	13.9	25.35
TC070208d	I	1.64	11	21.56	1.07	4.98	19.57	19.31	19.44	30.25
TC070208e	I	1.63	12	23.00	no rec.	-	20.06	19.53	19.80	30.95
TC070208f	I	1.61	13	24.25	no rec.	-	21.75	21.27	21.51	33.3
TC070209b	I	1.64	14	25.63	no rec.	-	22.55	21.57	22.06	33.55
TC070209c	I	1.64	15	26.58	no rec.	-	23.23	23.1	23.17	35.55
TC070301b	I	1.64	16	28.72	1.57	5.47	24.63	24.11	24.37	37.45
TC070301c	I	1.61	17	29.48	1.37	4.65	25.75	24.95	25.35	39.2

Table E.16: Experimental data for 100 mm diameter PCCS plates cut from Sheet III and loaded with PE4 disk charges of varying mass in a blast tube of 300 mm length with a R2 central bar.

test number	response mode	plate thickness [mm]	charge mass [g]	total impulse [Ns]	bar impulse [Ns]	bar/total impulse [%]	max-max deflection [mm]	min-max deflection [mm]	ave-max deflection [mm]	final hole diameter [mm]
TC061222f	I	1.61	4	9.51	2.14	22.49	2.71	2.3	2.51	-
TC070210c	I	1.64	5	11.59	2.59	22.34	3.11	2.82	2.97	-
TC061222h	I	1.63	6	13.66	2.93	21.48	4.08	3.76	3.92	-
TC061222j	I-II*	1.63	7.5	15.90	3.41	21.42	5.28	4.76	5.02	-
TC061222k	II*	1.62	8	17.12	3.77	22.02	5.77	5.1	5.44	-
TC061222l	II*	1.60	8.5	18.34	3.71	20.22	6.55	5.42	5.99	-
TC061222n	II	1.63	8.75	18.68	3.41	18.26	7.36	6.35	6.86	20.15
TC061222m	II	1.61	9	19.12	3.20	16.75	8.65	6.97	7.81	20.2
TC070210d	II	1.63	9.5	19.44	3.25	16.73	8.2	7.08	7.64	19.9
TC070210e	II	1.63	10	19.55	3.14	16.05	9.34	8.3	8.82	19.9
TC070220a	II	1.6	10.1	20.44	2.95	14.41	10.83	10.42	10.63	20.35
TC070220b	II	1.6	10.4	21.29	3.07	14.43	12.52	11.54	12.03	20.45
TC070219a	II	1.64	10.5	21.74	2.80	12.87	11.71	11.4	11.56	20.45
TC061222o	II-III	1.63	11	22.52	2.76	12.26	14.84	14.5	14.67	21
TC070219b	II	1.64	11	22.65	no rec.	-	12.46	11.62	12.04	20.45
TC061222p	III	1.62	12	23.58	2.84	12.06	16.9	16.63	16.77	22.75
TC070210f	III	1.61	13	24.40	2.70	11.06	18.61	18.36	18.49	24.6
TC070210h	III	1.64	14	25.80	3.10	12.01	17.91	17.72	17.82	24.1
TC061222q	III	1.6	14	26.94	2.80	10.39	22.12	21.41	21.77	30.35
TC070210g	III	1.64	15	26.76	2.98	11.15	20.24	19.78	20.01	26.6
TC070210i	III	1.63	16	28.45	3.09	10.86	22.99	20.9	21.95	27.9
TC070220d	III	1.63	16.5	28.79	no rec.	-	23.77	22.46	23.12	31.15
TC070219c	III	1.61	17	30.15	3.33	11.05	25.48	24.36	24.92	34.15

Table E.17: Experimental data for 100 mm diameter PCCS plates cut from Sheet III and loaded with PE4 disk charges of varying mass in a blast tube of 300 mm length with a R0 central bar.

test number	response mode	plate thickness [mm]	charge mass [g]	total impulse [Ns]	bar impulse [Ns]	bar/total impulse [%]	max-max deflection [mm]	min-max deflection [mm]	ave-max deflection [mm]	final hole diameter [mm]
TC070301a	I	1.63	5	11.34	2.75	24.25	2.89	2.62	2.76	-
TC070228i	II	1.64	8	16.80	2.43	14.47	9.91	9.02	9.47	20.6
TC070228j	II-III	1.64	8.5	17.85	2.47	13.86	11.23	10.47	10.85	21
TC070209e	III	1.61	11	21.64	no rec.	-	17.01	16.33	16.67	25.45
TC070228k	III	1.64	13	24.20	2.54	10.48	20.07	19.55	19.81	29.05
TC070228l	III	1.63	14	25.72	2.25	8.73	21.85	20.79	21.32	30.8
TC070301d	III	1.64	15	27.15	2.96	10.90	21.57	20.77	21.17	31.05
TC070301e	III	1.63	16	27.97	2.56	9.14	23.97	22.5	23.24	33.95

E.3.5 2 mm Thick Plates - Sheet IV

Table E.18: Experimental data for 100 mm diameter PCCS plates cut from Sheet IV and loaded with PE4 disk charges of varying mass in a blast tube of 300 mm length with a R0 central bar.

test number	response mode	plate thickness [mm]	charge mass [g]	total impulse [Ns]	bar impulse [Ns]	bar/total impulse [%]	max-max deflection [mm]	min-max deflection [mm]	ave-max deflection [mm]	final hole diameter [mm]
TC061229a	I	1.92	4	8.94	2.36	26.44	1.78	1.52	1.65	-
TC070228e	I	1.92	5	11.65	2.89	24.80	2.83	2.03	2.43	-
TC061229b	I	1.92	6	13.53	3.43	25.35	3.03	2.8	2.92	-
TC061221e	I	1.92	7	15.43	no rec.	-	3.84	3.43	3.64	-
TC061229c	I-II*	1.89	8	16.69	3.92	23.48	4.1	3.69	3.90	-
TC061229e	II*	1.91	8.5	18.28	4.05	22.14	4.63	3.67	4.15	-
TC061229d	II*	1.90	8.75	18.28	3.52	19.24	6.74	4.4	5.57	20.1
TC061229g	II	1.92	8.9	19.29	3.36	17.39	6.66	6.13	6.40	20.2
TC061221d	II	1.90	9	19.23	no rec.	-	7.82	6.96	7.39	20.15
TC070228f	II	1.93	9.5	18.96	3.27	17.26	6.97	6.67	6.82	20.15
TC061229i	II	1.90	10	20.93	2.99	14.30	10.39	9.95	10.17	20.6
TC070228g	II	1.93	10.5	21.28	3.23	15.16	9.26	8.23	8.75	20.35
TC061229h	III	1.89	11	22.86	3.31	14.48	13.53	13.09	13.31	22.15
TC070228h	II-III	1.93	12	23.36	3.15	13.50	12.74	12.46	12.6	21.7
TC061229j	III	1.92	13	25.56	3.42	13.40	15.99	15.5	15.75	24.05
TC070301f	III	1.93	15	27.76	3.14	11.31	17.57	16.93	17.25	25.35
TC070301g	III	1.93	17	30.34	3.55	11.71	19.19	18.96	19.08	27.8
TC070301h	III	1.93	20	32.99	3.67	11.13	21.65	21.21	21.43	30.95

Table E.19: Experimental data for 100 mm diameter PCA plates cut from Sheet IV and loaded with PE4 disk charges of varying mass in a blast tube of 300 mm length with a R0 central bar.

test number	response mode	plate thickness [mm]	charge mass [g]	total impulse [Ns]	bar impulse [Ns]	bar/total impulse [%]	max-max deflection [mm]	min-max deflection [mm]	ave-max deflection [mm]	final hole diameter [mm]
TC070130a	I	1.82	4	9.59	no rec.	-	6.48	6.26	6.37	21.5
TC070130b	I	1.93	8	17.49	no rec.	-	12.61	12.45	12.53	24.25
TC070130c	I	1.91	6	13.46	0.54	4.03	10.37	10.02	10.20	23
TC070130d	I	1.93	10	20.36	0.99	4.85	15.13	14.81	14.97	26.15
TC070131a	I	1.9	12	22.95	1.18	5.14	16.87	16.74	16.81	27.65
TC070131b	I	1.92	14	26.31	no rec.	-	18.39	17.95	18.17	28.85
TC070131c	I	1.93	16	29.27	1.41	4.82	20.57	20.28	20.43	31.5
TC070202a	I	1.91	18	30.43	no rec.	-	22.52	21.93	22.23	33.8
TC070202b	I	1.9	20	32.61	1.86	5.70	24.7	23.88	24.29	36.75

E.3.6 3 mm Thick Plates - Sheet V

Table E.20: Experimental data for 100 mm diameter PCA plates cut from Sheet V and loaded with PE4 disk charges of varying mass in a blast tube of 300 mm length with a R0 central bar.

test number	response mode	plate thickness [mm]	charge mass [g]	total impulse [Ns]	bar impulse [Ns]	bar/total impulse [%]	max-max deflection [mm]	min-max deflection [mm]	ave-max deflection [mm]	final hole diameter [mm]
TC070208a	I	2.86	4	9.79	0.40	4.06	2.75	2.66	2.71	20.75
TC070208b	I	2.90	7	15.08	0.78	5.16	6.4	6.18	6.29	21.5
TC070202e	I	2.91	10	20.35	0.98	4.81	9.04	8.64	8.84	22.5
TC070208c	I	2.9	13	23.89	1.05	4.41	10.86	10.6	10.73	23.4
TC070202d	I	2.87	16	28.95	1.75	6.03	13.73	13.46	13.60	25.15
TC070202c	I	2.9	20	33.38	1.87	5.62	15.15	14.79	14.97	26.05
TC061220h	I	2.90	21	35.13	no rec.	-	15.67	15.46	15.57	26.7

Table E.21: Experimental data for 100 mm diameter PCCS plates cut from Sheet V and loaded with PE4 disk charges of varying mass in a blast tube of 300 mm length with a R0 central bar.

test number	response mode	plate thickness [mm]	charge mass [g]	total impulse [Ns]	bar impulse [Ns]	bar/total impulse [%]	max-max deflection [mm]	min-max deflection [mm]	ave-max deflection [mm]	final hole diameter [mm]
TC070228b	I	2.91	4	9.22	2.26	24.52	0.13	0.04	0.09	-
TC070228c	I	2.90	7	15.06	3.95	26.25	1.1	0.87	0.99	-
TC061219n	I	2.9	10	20.96	5.92	28.24	2.27	1.6	1.94	-
TC070228d	I	2.86	12	23.85	6.21	26.03	2.75	2.65	2.7	-
TC061219o	I	2.9	14	26.13	6.93	26.51	3.77	2.95	3.36	-
TC061220b	I	2.89	16	29.41	7.79	26.50	4.11	3.28	3.70	-
TC061219p	II*	2.86	18	32.65	7.51	23.02	6.1	4.61	5.36	-
TC061220c	I-II*	2.9	19	33.74	no rec.	-	4.67	3.71	4.19	-
TC061220e	II	2.88	20	34.29	no rec.	-	6.39	4.97	5.68	20.1
TC061220d	II	2.89	21	35.22	no rec.	-	5.97	5.74	5.86	20.1
TC061220f	II	2.87	25	39.34	no rec.	-	8.24	6.15	7.20	20.25
TC061220g	II-III	2.89	30	44.82	no rec.	-	14.26	11.96	13.11	22.2

Appendix F

Drawings

F.1 Introduction

This appendix contains selected detailed drawings of plate specimens and instrumented ballistic pendulum parts.

F.2 Material Test Specimens

The specimen design used for the quasi-static tests are shown in Figure F.1.

F.3 Plate Specimens

The peripherally clamped annular (PCA) plate specimen dimensions are shown in Figure F.2. The peripherally clamped centrally supported (PCCS) plate specimen dimensions are identical except for the lack of a central hole. The specimens were laser cut by a local supplier, Vulcan Steel PTY LTD. The nesting pattern is shown in Figure F.3.

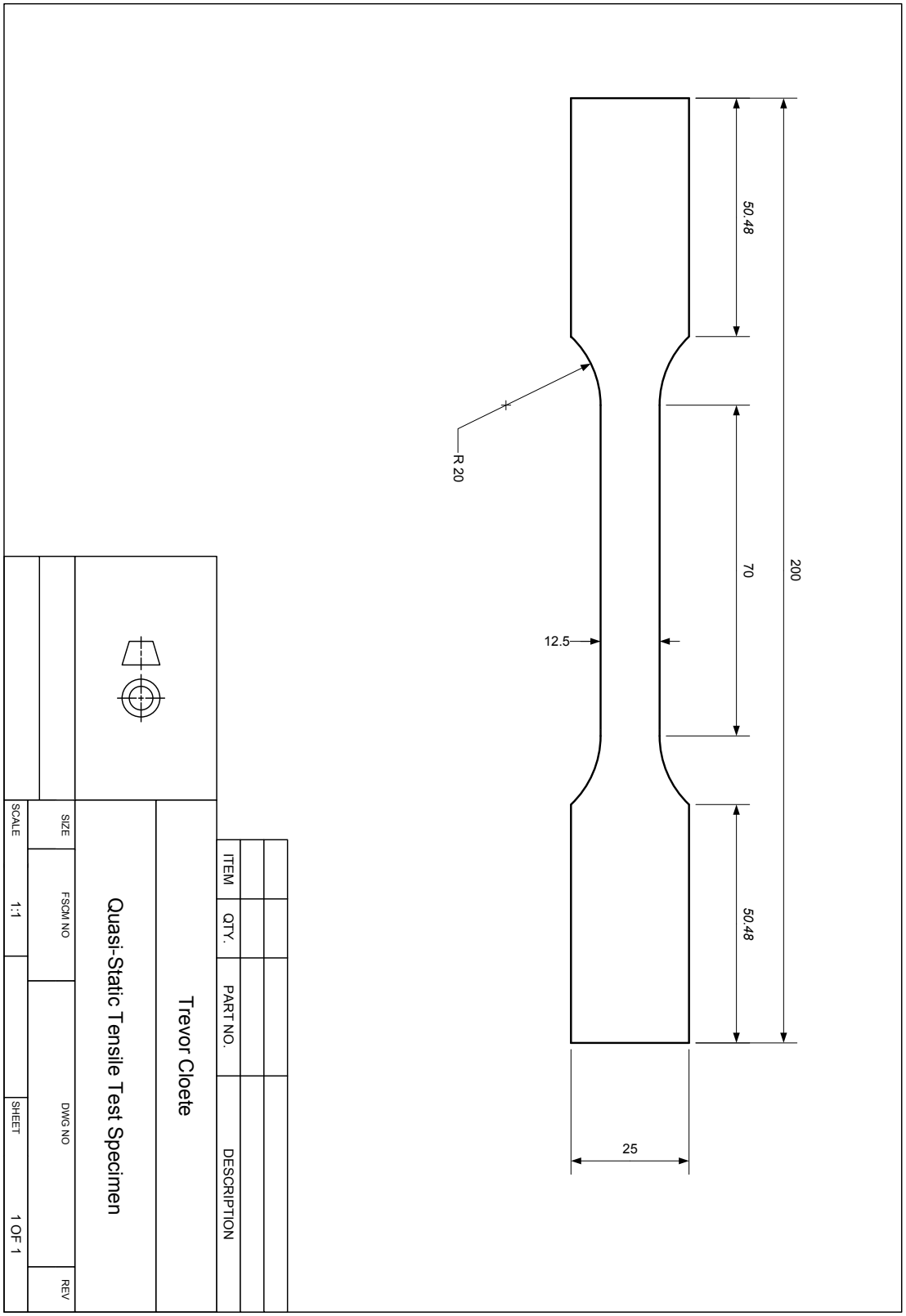

Figure F.1: Quasi-static specimen dimensions.

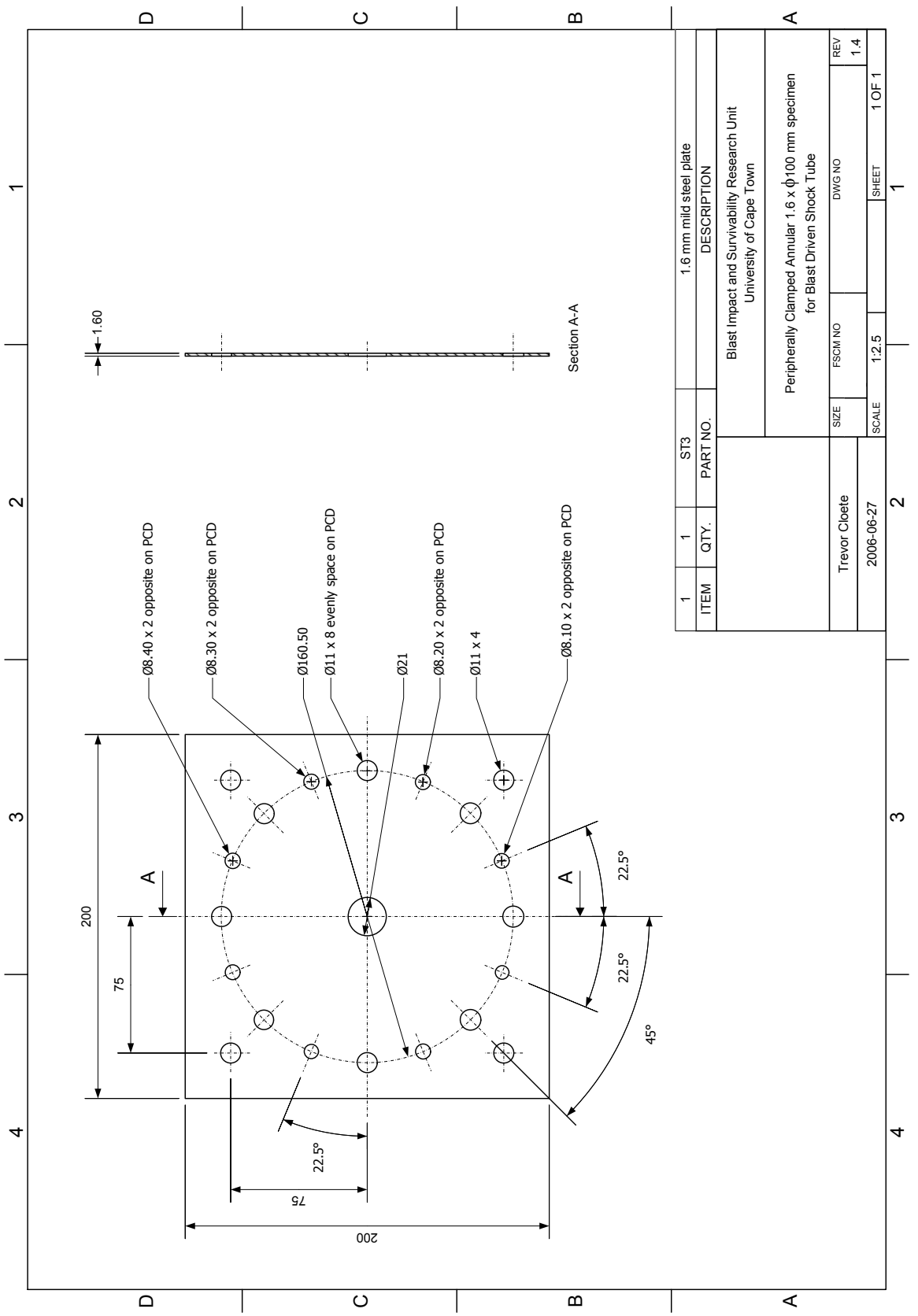

Figure F.2: Peripherally clamped annular (PCA) plate specimen dimensions.

Vulcan Laser	Task Name : T15888 Number of Sheets with Same Layout 1	Layout 1 of 1

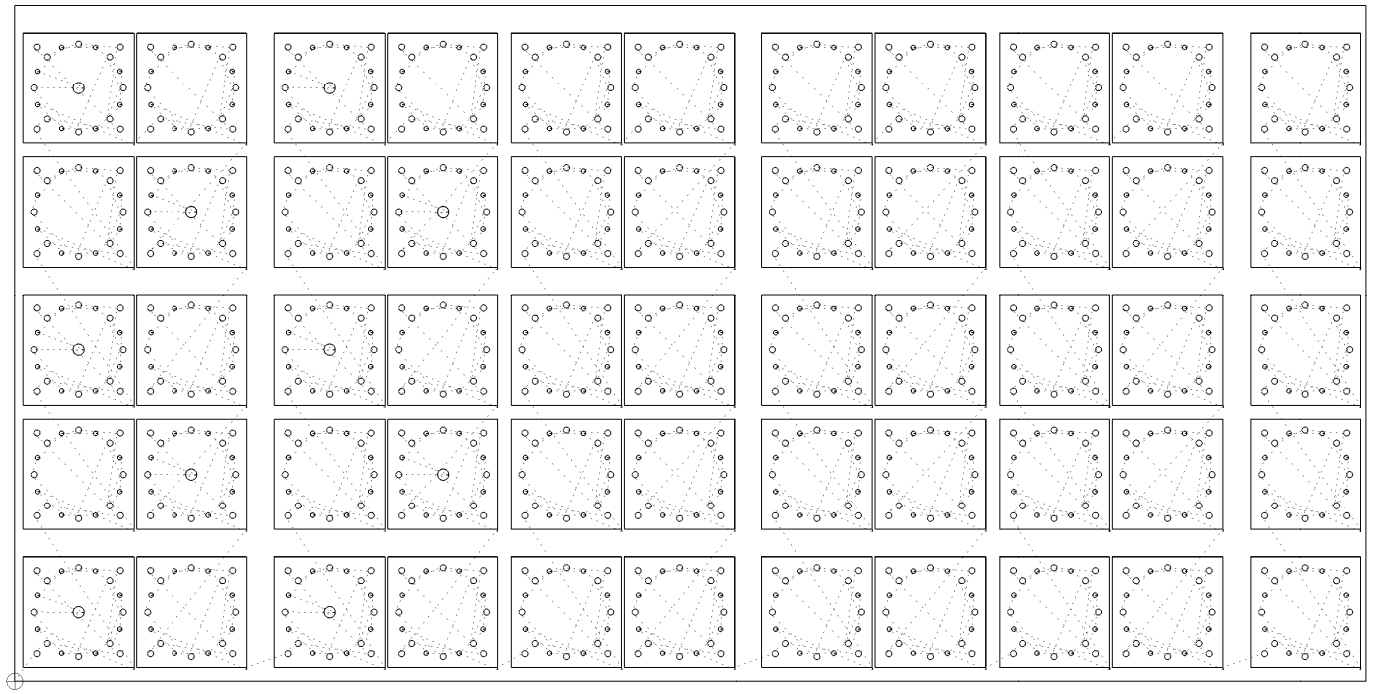

1

Figure F.3: Laser cutting pattern for sheet stock.